



IntechOpen

# Heat Transfer

Design, Experimentation and Applications

*Edited by Miguel Araiz Vega*





---

# Heat Transfer - Design, Experimentation and Applications

*Edited by Miguel Araiz Vega*

Published in London, United Kingdom

---



## IntechOpen







*Supporting open minds since 2005*



Heat Transfer – Design, Experimentation and Applications

<http://dx.doi.org/10.5772/intechopen.91485>

Edited by Miguel Araiz Vega

#### Contributors

Bayram Kiliç, Syaiful, M. Kurnia Lutfi, Raseelo Joel Joel Moitsheki, Partner Luyanda Ndlovu, Basetsana Pauline Ntsime, Vikas Poply, Jiajun Xu, Mehdi Kabirnajaf, Miguel Araiz, Raffhael Milanezi de Andrade, André Palmiro Storch, Lucas De Amorim Paulo, Antônio Bento Filho, Claysson Santos Vimieiro, Marcos Pinotti, Carlos Acosta, Miguel Rosa Oliveira Panão, Jesus Esarte, Jesús M<sup>o</sup> M. Blanco, Roger R. R Riehl, Maite Aresti, Juncal Estella, Simone Mancin, Anwar Barrak, Rangasamy Parthiban, Sudha Ganesh, Chitra Boobalan, Syed Ahsan Ahsan Sharif, Mark Kai Ming Ho, Victoria Timchenko, Guan Heng Yeoh, Marco Rottoli, Daniele Agazzi, Marcello Garavaglia, Fabio Grisoni, Marcin Trojan, Dawid Taler, Jan Taler, Luis Fonseca, Marc Salleras, Inci Donmez-Noyan, Marc Dolcet, Joaquín Santander, Denise Estrada-Wiese, Jose-Manuel Sojo-Gordillo, Alex Morata, Albert Tarancon, Gerard Gadea, Nasim Hasan, Mohd Arif, Mohaideen Abdul Khader, Naga Ramesh Korasikha, Thopudurthi Karthikeya Sharma, Gadale Amba Prasad Rao, Kotha Madhu Murthy, Takele Gameda, Raid Mohammed, Jaime Rios, I Made Arsana, Ruri Agung Wahyuono

© The Editor(s) and the Author(s) 2021

The rights of the editor(s) and the author(s) have been asserted in accordance with the Copyright, Designs and Patents Act 1988. All rights to the book as a whole are reserved by INTECHOPEN LIMITED. The book as a whole (compilation) cannot be reproduced, distributed or used for commercial or non-commercial purposes without INTECHOPEN LIMITED's written permission. Enquiries concerning the use of the book should be directed to INTECHOPEN LIMITED rights and permissions department ([permissions@intechopen.com](mailto:permissions@intechopen.com)).

Violations are liable to prosecution under the governing Copyright Law.



Individual chapters of this publication are distributed under the terms of the Creative Commons Attribution 3.0 Unported License which permits commercial use, distribution and reproduction of the individual chapters, provided the original author(s) and source publication are appropriately acknowledged. If so indicated, certain images may not be included under the Creative Commons license. In such cases users will need to obtain permission from the license holder to reproduce the material. More details and guidelines concerning content reuse and adaptation can be found at <http://www.intechopen.com/copyright-policy.html>.

#### Notice

Statements and opinions expressed in the chapters are these of the individual contributors and not necessarily those of the editors or publisher. No responsibility is accepted for the accuracy of information contained in the published chapters. The publisher assumes no responsibility for any damage or injury to persons or property arising out of the use of any materials, instructions, methods or ideas contained in the book.

First published in London, United Kingdom, 2021 by IntechOpen

IntechOpen is the global imprint of INTECHOPEN LIMITED, registered in England and Wales, registration number: 11086078, 5 Princes Gate Court, London, SW7 2QJ, United Kingdom

Printed in Croatia

British Library Cataloguing-in-Publication Data

A catalogue record for this book is available from the British Library

Additional hard and PDF copies can be obtained from [orders@intechopen.com](mailto:orders@intechopen.com)

Heat Transfer – Design, Experimentation and Applications

Edited by Miguel Araiz Vega

p. cm.

Print ISBN 978-1-83968-437-1

Online ISBN 978-1-83968-438-8

eBook (PDF) ISBN 978-1-83968-439-5

# We are IntechOpen, the world's leading publisher of Open Access books Built by scientists, for scientists

**5,400+**

Open access books available

**134,000+**

International authors and editors

**165M+**

Downloads

**156**

Countries delivered to

Our authors are among the  
**Top 1%**

most cited scientists

**12.2%**

Contributors from top 500 universities



**WEB OF SCIENCE™**

Selection of our books indexed in the Book Citation Index  
in Web of Science™ Core Collection (BKCI)

Interested in publishing with us?  
Contact [book.department@intechopen.com](mailto:book.department@intechopen.com)

Numbers displayed above are based on latest data collected.  
For more information visit [www.intechopen.com](http://www.intechopen.com)





# Meet the editor



Miguel Araiz Vega studied industrial engineering at the Public University of Navarre (UPNA), Spain, and completed his Ph.D. at the same university in 2018. The topic of his thesis was the modelization and development of a thermoelectric generator to harvest waste heat in domestic and industrial processes. He is a member of the Thermal and Fluids Research Group and the Smart Cities Institute of the UPNA. He completed a short research stay at the Royal Melbourne Institute of Technology (RMIT) in Melbourne, Australia in 2018, and he has collaborated in many research projects related to thermoelectric generation and refrigeration, and simulation, design, and optimization of heat exchangers and thermal systems. He has published fourteen manuscripts in peer-reviewed international journals and one book chapter, and he has participated in more than twenty-five international and national conferences.





# Contents

<b>Preface</b>	<b>XV</b>
<b>Section 1</b> Introduction	<b>1</b>
<b>Chapter 1</b> Introductory Chapter: Heat Transfer <i>by Miguel Araiz</i>	<b>3</b>
<b>Section 2</b> Simulations	<b>7</b>
<b>Chapter 2</b> Numerical Analysis of a Water-Cooled Condenser at Startup Conditions for Refrigeration Applications Supported with Experiments <i>by Carlos Acosta</i>	<b>9</b>
<b>Chapter 3</b> The CFD Based Method for Determining Heat Transfer Correlations on Individual Rows of Plate-Fin and Tube Heat Exchangers <i>by Dawid Taler, Jan Taler and Marcin Trojan</i>	<b>29</b>
<b>Chapter 4</b> Numerical Investigation of Heat Transfer and Fluid Flow Characteristics in a Rectangular Channel with Presence of Perforated Concave Rectangular Winglet Vortex Generators <i>by Syaiful and M. Kurnia Lutfi</i>	<b>53</b>
<b>Chapter 5</b> Survey of Some Exact and Approximate Analytical Solutions for Heat Transfer in Extended Surfaces <i>by Raseelo Joel Moitsheki, Partner Luyanda Ndlovu and Basetsana Pauline Ntsime</i>	<b>85</b>
<b>Chapter 6</b> Analysis of Liquid Cooling in Microchannels Using Computational Fluid Dynamics (CFD) <i>by Chitra Boobalan, Sudha Ganesh and Parthiban Rangaswamy</i>	<b>107</b>

<b>Chapter 7</b>	<b>121</b>
Numerical Investigation of Rising Vapour Bubble in Convective Boiling Using an Advanced 3D Hybrid Numerical Method <i>by Syed Ahsan Sharif, Mark Kai Ming Ho, Victoria Timchenko and Guan Heng Yeoh</i>	
<b>Section 3</b>	<b>145</b>
Nanofluids	
<b>Chapter 8</b>	<b>147</b>
Nanofluid as Advanced Cooling Technology. Success Stories <i>by Jesús Esarte, Roger R. Riehl, Simone Mancin, Jesús M<sup>a</sup> Blanco, Maite Aresti and Juncal Estella</i>	
<b>Chapter 9</b>	<b>165</b>
Convective Heat Transfer of Ethanol/Polyalphaolefin Nanoemulsion in Mini- and Microchannel Heat Exchangers for High Heat Flux Electronics Cooling <i>by Jaime Rios, Mehdi Kabirnajafi, Takele Gameda, Raid Mohammed and Jiajun Xu</i>	
<b>Chapter 10</b>	<b>197</b>
Nanofluid-Enhancing Shell and Tube Heat Exchanger Effectiveness with Modified Baffle Architecture <i>by I Made Arsana and Ruri Agung Wahyuono</i>	
<b>Chapter 11</b>	<b>213</b>
Heat Transfer in a MHD Nanofluid Over a Stretching Sheet <i>by Vikas Poply</i>	
<b>Section 4</b>	<b>227</b>
Design	
<b>Chapter 12</b>	<b>229</b>
Plate Heat Exchangers: Artificial Neural Networks for Their Design <i>by Bayram Kılıç</i>	
<b>Chapter 13</b>	<b>247</b>
Evolutionary Design of Heat Exchangers in Thermal Energy Storage <i>by Miguel Rosa Oliveira Panão</i>	
<b>Chapter 14</b>	<b>265</b>
Earth Air Tunnel Heat Exchanger for Building Cooling and Heating <i>by Nasim Hasan, Mohd Arif and Mohaideen Abdul Khader</i>	
<b>Chapter 15</b>	<b>283</b>
Recent Advancements in Thermal Performance Enhancement in Microchannel Heatsinks for Electronic Cooling Application <i>by Naga Ramesh Korasikha, Thopudurthi Karthikeya Sharma, Gadale Amba Prasad Rao and Kotha Madhu Murthy</i>	

<b>Chapter 16</b>	<b>311</b>
Heat Pipes Heat Exchanger for HVAC Applications <i>by Anwar Barrak</i>	
<b>Chapter 17</b>	<b>325</b>
EMbaffle® Heat Transfer Technology Step-Up in CO <sub>2</sub> Reduction <i>by Marco Rottoli, Daniele Agazzi, Marcello Garavaglia and Fabio Grisoni</i>	
<b>Section 5</b>	<b>347</b>
Thermal Management	
<b>Chapter 18</b>	<b>349</b>
Managing Heat Transfer Issues in Thermoelectric Microgenerators <i>by Marc Salleras, Inci Donmez-Noyan, Marc Dolcet, Joaquin Santander, Denise Estrada-Wiese, Jose-Manuel Sojo, Gerard Gadea, Alex Morata, Albert Tarancon and Luis Fonseca</i>	
<b>Chapter 19</b>	<b>373</b>
Transient Thermal Analysis of a Magnetorheological Knee for Prostheses and Exoskeletons during Over-Ground Walking <i>by Raphael Milanezi de Andrade, André Palmiro Storch, Lucas de Amorim Paulo, Antônio Bento Filho, Claysson Bruno Santos Vimieiro and Marcos Pinotti</i>	
<b>Chapter 20</b>	<b>389</b>
Experimental Approaches to Measurement of Vapor Quality of Two-Phase Flow Boiling <i>by Mehdi Kabirnajafi and Jiajun Xu</i>	



# Preface

Thermal energy is present in all aspects of our lives. We experience heat transfer daily when, for example, cooking or taking food out of the fridge, using a vehicle, or turning on the heating or air-conditioning system in our office. Sometimes this thermal management is not evident, but it is essential for our comfort and lifestyle. In addition, heat transfer is of vital importance in all electric power plants. Whether some fuel is burned to obtain steam or whether we want to maintain a solar panel temperature to a certain level, proper management of thermal energy is crucial to the operation of the system.

Nowadays it is even more important to control thermal transfer perfectly when designing renewable energy systems where every unit of energy requires use or when installing an efficiency measure in a process to prevent thermal losses.

Thermal energy analysis is a complex task that usually requires the use of large theoretical equations and mathematical models that can predict the behaviour of a certain system. Many approaches can be followed to study all these phenomena. Some of them involve experimental developments that include the building of test benches, rigs, and real systems to replicate the process to be studied. Others are computational models that predict the performance of the system and can be used as optimization tools when designing devices.

This book includes a large compilation of those different approaches and serves as an example of how heat transfer problems can be analysed. It is divided into the following five sections:

- “Introduction”
- “Simulations”
- “Nanofluids”
- “Design”
- “Thermal Management”

I hope this book will help engineers, researchers, and scientists to understand thermal processes better and teach them how to address heat transfer problems. I also hope it serves as an inspiration for the development of further work.

I would like to express my gratitude to all the authors who have contributed to this book. I am sure their knowledge and expertise have improved the quality of

this text. Lastly, I give thanks to IntechOpen Author Service Manager Dolores Kuzelj, whose assistance and patience have been crucial to the success of this project.

**Dr. Miguel Araiz Vega**  
Department of Engineering,  
Smart Cities Institute,  
Public University of Navarre,  
Pamplona, Spain



---

Section 1

# Introduction

---



# Introductory Chapter: Heat Transfer

*Miguel Araiz*

## 1. Introduction

Heat transfer is the field in Thermodynamics in charge of the study of the generation, conversion, exchange and use of energy in form of heat (thermal energy) between different systems. Heat can be transferred using several mechanisms such as conduction, convection, and radiation. The proper understanding of these modes of heat transfer leads to a successful design of any device in which thermal energy is involved. That is why it is so important to study and to analyze heat transfer in any application.

Thermal energy is present in any aspect of our lives. We can daily experiment heat transfer phenomena at home, when cooking or taking food out of the fridge [1], when using a vehicle to go to work [2] or turning the heating or air-conditioning system on in our office [3]. Sometimes this thermal management is not evident but it is essential for our comfort and lifestyle [4]. Besides, heat transfer is of vital importance in all the electric power plants. Whether some fuel is being burnt to get steam or if we want to maintain a PV panel temperature to a certain level, again a proper management of thermal energy is crucial to the operation of the system [5, 6].

And nowadays it is even more important to perfectly control thermal transfer when designing renewable energy systems where every unit of energy requires to be used; or when installing an efficiency measure in a process to prevent thermal losses [7, 8].

## 2. Heat transfer analysis

Thermal energy analysis is a complex task that usually requires the use of large theoretical equations and mathematical models that can predict the behavior of a certain system. It is not easy to simplify natural or forced convection, phase change phenomena, or radiation heat transfer, considering their interactions with other parts of the system under study. Therefore, most of the engineers and researchers in the thermal field turn to computational models and test benches that help them understand all these processes [9].

### 2.1 Computational simulations

A very common approach to heat transfer study is to develop a computational model making several assumptions prior to the simulations. These models use thermodynamic equations and energy balances to represent what we can expect to happen in real conditions. These computational tools are really useful since they allow us to perform tons of simulations and analyze many cases in a cost-effective manner. You can use them to optimize a certain design and be sure that it will work

properly once it has been built. Besides, by using these models a sensitive analysis can be performed to check which parameter is affecting more to the results of the system. There are many ways to develop these models, using different solving techniques. It is essential to understand the heat transfer phenomena you want to study and then check for the best method to model it.

## **2.2 Experimental analysis**

Another approach to study heat transfer problems is to design and build an experimental test bench. Sometimes it is so difficult to theoretically model a thermal energy system that it is more convenient to analyze the problem experimentally. Therefore, an experimental rig is employed to obtain useful results of the cases under study. Often, all these rigs allow the researcher to modify the boundary conditions affecting the system, so the problem can be tested under different circumstances. These test benches are also useful to validate the computational models and check if they can properly predict the behavior of the system.

## **3. Applications**

As it has been mentioned in the introduction of this chapter heat transfer appears in many daily activities. Therefore, there is a wide range of fields in which thermal energy is studied.

It is mandatory to perform a thermal analysis when developing heat exchangers designed to transport heat from one point to another. For that, it is vital to identify which kind of heat sink best fits the application (can natural convection be used, or it should include some forced convection? For example). This analysis is also useful because the conditions under which heat is being transferred will determine the material of the systems that is being used, requirements about auxiliary consumption, limit of maximum temperatures of operation, and so on.

Heat transfer analysis is also crucial in electronic applications that are continuously growing with higher consumptions, and therefore, higher thermal management requirements. As Murshed explains, power electronics are facing a huge challenge in removing high heat fluxes maintaining a low temperature in the device [10].

Conventional heat transfer approaches are still being used, but there are some other new technologies that are being included in these applications such as: nanofluids, phase change devices, and so on.

## **4. Conclusions**

The chapters included in this book are a good example of how scientists, researchers and engineers from the industry are solving heat transfer issues that appear in many fields. You will find computational models, the use of nanofluids in heat transfer devices, an optimization of a bunch of heat exchangers, and several samples of thermal management in different applications.

## **Author details**

Miguel Araiz  
Public University of Navarre, Pamplona, Spain

\*Address all correspondence to: [miguel.araiz@unavarra.es](mailto:miguel.araiz@unavarra.es)

## **IntechOpen**

---

© 2021 The Author(s). Licensee IntechOpen. This chapter is distributed under the terms of the Creative Commons Attribution License (<http://creativecommons.org/licenses/by/3.0>), which permits unrestricted use, distribution, and reproduction in any medium, provided the original work is properly cited. 

## References

- [1] Maldonado JM, de Gracia A, Zsembinszki G, Moreno P, Albets X, González MÁ, et al. Frost detection method on evaporator in vapour compression systems. *Int J Refrig*. 2020;110:75-82.
- [2] Wu J, Wei Z, Li W, Wang Y, Li Y, Sauer DU. Battery Thermal-and Health-Constrained Energy Management for Hybrid Electric Bus Based on Soft Actor-Critic DRL Algorithm. *IEEE Trans Ind Informatics*. 2021;17(6): 3751-61.
- [3] Azuatalam D, Lee WL, de Nijs F, Liebman A. Reinforcement learning for whole-building HVAC control and demand response. *Energy AI [Internet]*. 2020;2:100020. Available from: <https://doi.org/10.1016/j.egyai.2020.100020>
- [4] Mandal J, Yang Y, Yu N, Raman AP. Paints as a Scalable and Effective Radiative Cooling Technology for Buildings. *Joule*. 2020 Jul 15;4(7): 1350-6.
- [5] Wang J, Han Z, Guan Z. Hybrid solar-assisted combined cooling, heating, and power systems: A review. *Renew Sustain Energy Rev [Internet]*. 2020;133(August):110256. Available from: <https://doi.org/10.1016/j.rser.2020.110256>
- [6] Liu S, Yuan J, Deng W, Luo M, Xie Y, Liang Q, et al. High-efficiency organic solar cells with low non-radiative recombination loss and low energetic disorder. *Nat Photonics [Internet]*. 2020;14(5):300-5. Available from: <http://dx.doi.org/10.1038/s41566-019-0573-5>
- [7] Elsaid K, Kamil M, Sayed ET, Abdelkareem MA, Wilberforce T, Olabi A. Environmental impact of desalination technologies: A review. *Sci Total Environ [Internet]*. 2020;748:141528. Available from: <https://doi.org/10.1016/j.scitotenv.2020.141528>
- [8] Koochi-Fayegh S, Rosen MA. A review of energy storage types, applications and recent developments. *J Energy Storage [Internet]*. 2020;27(October 2019):101047. Available from: <https://doi.org/10.1016/j.est.2019.101047>
- [9] Giri A, Hopkins PE. A Review of Experimental and Computational Advances in Thermal Boundary Conductance and Nanoscale Thermal Transport across Solid Interfaces. *Adv Funct Mater*. 2020;30(8).
- [10] Murshed SMS. Introductory Chapter: Electronics Cooling — An Overview. In: *Electronics Cooling [Internet]*. InTech; 2016 [cited 2021 Jul 8]. Available from: <http://dx.doi.org/10.5772/63321>





Section 2

# Simulations





# Numerical Analysis of a Water-Cooled Condenser at Startup Conditions for Refrigeration Applications Supported with Experiments

*Carlos Acosta*

## Abstract

Refrigeration for commercial purposes is one of the industrial sectors with the largest energy consumption in the global market. Therefore, research and development of more efficient components such as compressors, condensers, and refrigerants continue to render promising results in terms of GWP and operational costs. However, Due to the urgency typically found in industry to develop prototypes, finding scalable solutions can be challenging. Arguably, this is the case for condenser and evaporators that are designed and assembled under the assumption that refrigeration systems operate at steady condition, where in real circumstances such systems operate under transients based on ambient temperatures or unfavorable startup conditions. The aim of this study is to characterize the thermal and fluid dynamics behavior of refrigerant R404a in a water-cooled condenser at startup conditions. The boundary conditions to solve the CFD simulations are taken from experimental values and set as user defined functions in a commercial software. The results displayed the time dependent oscillatory phase-transition details of the refrigerant throughout the domain.

**Keywords:** Heat transfer, fluid mechanics, multi-phase flow, turbulence, phase-transition

## 1. Introduction

Water-cooled condensers are commonly used in vapor compression refrigeration for industrial applications due to their high rate of heat transfer [1], simple configuration and the relatively low cost of manufacturability compared to other types of condensers [2]. On the other hand, population growth, and the exponential increase in energy consumption throughout the world keep stressing freshwater resources [3]. Typical components used in refrigeration systems such as compressors, evaporators, condensers, and refrigerants are constantly iterating to provide more energy efficient solutions [4] in order to minimize the environmental impact due to toxic molecules in refrigerants and reduce the production of residual heat [5]. Unfortunately, the steps imposed by regulatory agencies in United States and

Europe sometimes lead to production ready solutions that have not been thoroughly tested for industrial applications. Perhaps, one common example is the race in banning HFC refrigerants for compressed vapor refrigeration cycles [6]. Ideally, the components in the refrigeration system can remain intact by changing refrigerants, but this fails to be the case for most systems since the oil in the compressor and even the compressor specifications need to be tailored to the new refrigerant [7].

Virtual experimentation using numerical simulations offer great insights at the micro and macroscopic level to support design and research activities of heat exchangers, condensers and evaporators [8] given that experimental studies can reach elevated costs and access to sensorial points to capture significant physical details are difficult to incorporate in pressurized systems [9, 10]. In fact, the analysis of startup condition for physical components in thermodynamic cycles is particularly challenging given the small-time scales and the large variations detected in the variables of interest [11]. This alone calls for special attention in the sampling rate and physical location of feedback sensors given that dynamic and unstable conditions can be reached in a thermodynamic cycle by unpredicted changes in loads or variations in energetic states, and false positive readings can be measured depending on the flow characteristics through the system.

Concomitantly, the design and fabrication of condensers and heat exchangers require the knowledge and understanding of the physical and chemical phenomenon and other factors such as the properties of the working fluids or multi-phase flows [12], their regimes and states, and the geometrical characteristics of the system [13]. But rigorous experimentation in thermodynamic systems can be particularly costly because environmental chambers are often needed to obtain reproducible results [14]. Evidently, the lack of accessibility to an environmental chamber means that the ambient temperature is a random variable and the uncertainty of the experimental results can increase significantly [15] since the thermodynamic states of the thermodynamic cycle tend to fluctuate as a function of the heat rejected and the heat absorbed to and from the environment [16].

A less rigorous alternative to this approach is to perform a design of experiments at ambient conditions and execute the test multiple times to assess the error and response variations [17]. Unfortunately, this route can also lead to an expensive and time-consuming solution on top of developing variable startup conditions that can affect the performance of the system. Consequently, Numerical simulations and theoretical analysis of thermodynamic cycles should help alleviate the cost of materials, manufacturing, and redundant testing.

Heat and time-dependent multi-phase computational solutions targeting problems with complicated geometries that cannot be simplified by axisymmetric conditions or reduction of dimensions tend to be challenging to develop, and the results are always suspicious if no experimental validation is provided. Therefore, a balance between experiments and simulations seems to be the ideal recipe to obtain cost-effective solutions with solid scientific ground.

In the last few decades, significant efforts have been focused on developing more rigorous models that account for turbulent fluctuations on multi-phase flows [18–20] evidencing the complicated nature of such problems even for simple geometries [21] such as tubes and channels [22]. However, no three-dimensional studies have been reported on the CFD multi-phase modeling of R404a condensation in a medium temperature water-cooled condenser at startup conditions. This research aims to provide a study of the unsteady condensing and evaporating characteristics of R404a in a water-cooled condenser by modeling the raising temperature and pressure in the system induced by the compressed vapor entering the condenser based on experimental data.

## 1.1 Numerical analysis of turbulent phase-transition in the condensation process of refrigerant flow

Multi-phase flow refers to the flow of a mixture of phases or species such as gases in liquids or liquids in gases of different densities [23] where the liquids, and gases are considered distinct phases. There are different mathematical characterizations targeted to study multi-phase flows. For instance, for dispersed flows, one phase consists of discrete, noncontinuous elements (such as bubbles) and the second phase is considered as a continuum. This approach is widely accepted for the analysis and characterization of oil and refrigerant relationships in vapor compressed cycles, given that at certain conditions, oil can escape the compressor and affect the system performance due to the variations in the thermal properties of the mixture induced by the oil [24].

In bubbly flows or other types of applications where dispersed multiphase flows are applicable, the properties of the inhomogeneous mixture are defined relative to the continuous phase [25]. The mathematical manipulation for such flows can happen under a Lagrangian representation for the dispersed phase [26], and an Eulerian reference for the continuous phase. For the continuous phase, the material properties are defined at every point within a control volume [27], whereas in a separated flow under the Euler–Euler approach the phases are continuous but divided by a single contact surface [28].

This research focuses on the incompressible volume of fluid model where the mass transfer between phases is given by:

$$\dot{m}_v = -\dot{m}_l = \zeta\alpha_l\rho_l \left[ \frac{T - T_{sat}}{T_{sat}} \right], T > T_{sat} \quad (1)$$

for evaporation and

$$\dot{m}_l = -\dot{m}_v = \zeta\alpha_v\rho_v \left[ \frac{T_{sat} - T}{T_{sat}} \right], T < T_{sat} \quad (2)$$

for a condensation process. In the study of phase-transition of refrigerants, the saturation temperature is found based on the operating conditions of the system [29]. In this study, the inlet and outlet temperatures and pressures were measured experimentally to compute  $T_{sat}$ .

From a modeling perspective, the saturating temperature is a dominant factor in the prediction of the evaporating and condensing process. Therefore, the measured temperatures, pressures and the saturation temperature were loaded in the simulation as dynamics boundary conditions to drive the phase-transition process given the dynamic value of  $T_{sat}$ .

In order to find the quality of the mixture the volume fraction is defined as:

$$\alpha_l(\tilde{X}) + \alpha_v(\tilde{X}) = 1 \quad (3)$$

where the sum of volume occupied by the phases is 100%. Furthermore, the microscopic dynamics of the phase-transition process of refrigerants in heat exchangers and condensers can be studied by considering both the vapor and liquid as continuous and interpenetrating fluids under the Eulerian frame of reference [30]. Even though this approach is computationally expensive given that the governing equations for each phase are solved together with the momentum equation, the mass diffusion can be monitored by a straightforward calculation. For this case, the microscopic behavior of the phases can be monitored by:

$$\frac{\partial \alpha_l}{\partial t} + \nabla \cdot (\vec{u} \alpha_l) = \frac{\dot{m}_l}{\rho_l} = S_{mass} \quad (4)$$

and

$$\frac{\partial \alpha_v}{\partial t} + \nabla \cdot (\vec{u} \alpha_v) = -\frac{\dot{m}_v}{\rho_v} = -S_{mass} \quad (5)$$

for which  $\rho_l$  and  $\rho_v$  are the densities of the liquid and vapor phases. Then, the mixture density and mixture viscosity are:

$$\rho_m = \rho_l + \rho_v \quad (6)$$

and

$$\mu_m = \mu_l + \mu_v. \quad (7)$$

For each phase, the momentum conservation is given by:

$$\frac{\partial}{\partial t} (\alpha_v \rho_v \vec{u}_v) + \nabla \cdot (\alpha_v \rho_v \vec{u}_v \cdot \vec{u}_v) = -\alpha_v \nabla p + \nabla \cdot \bar{\bar{\tau}}_v + \psi_v \quad (8)$$

and

$$\frac{\partial}{\partial t} (\alpha_l \rho_l \vec{u}_l) + \nabla \cdot (\alpha_l \rho_l \vec{u}_l \cdot \vec{u}_l) = -\alpha_l \nabla p + \nabla \cdot \bar{\bar{\tau}}_l + \psi_l \quad (9)$$

where  $\psi_v$  and  $\psi_l$  are the momentum sources and the stress tensor is given by:

$$\bar{\bar{\tau}}_i = \alpha_i \mu_i \left( \nabla \vec{u}_i + \nabla \vec{u}_i^T \right) + \alpha_i \left( \lambda_i - \frac{3}{2} \mu_i \right) \nabla \cdot \vec{u}_i \bar{\bar{I}} \quad (10)$$

given that  $\lambda_i$  and  $\mu_i$  are the shear and bulk viscosities of the phase  $i$ . Then, the two equation  $\kappa - \varepsilon$  turbulent model for multi-phase flow is:

$$\frac{\partial}{\partial t} (\alpha_v \rho_v \kappa) + \nabla \cdot (\alpha_v \rho_v \kappa \vec{u}_v) = \frac{\partial}{\partial x_j} \left[ \alpha_v \left( \mu + \frac{\mu_t}{\sigma_\varepsilon} \right) \frac{\partial \kappa}{\partial x_j} \right] - \alpha_v \rho_v \varepsilon + \alpha_v G_k + S_k \quad (11)$$

for the turbulent kinetic energy  $\kappa$  and

$$\frac{\partial}{\partial t} (\alpha_v \rho_v \varepsilon) + \nabla \cdot (\alpha_v \rho_v \varepsilon \vec{u}_v) = \frac{\partial}{\partial x_j} \left[ \alpha_v \left( \mu + \frac{\mu_t}{\sigma_k} \right) \frac{\partial \varepsilon}{\partial x_j} \right] - \alpha_v C_{1\varepsilon} \frac{\varepsilon}{\kappa} G_k - \alpha_v C_{2\varepsilon} \rho_v \frac{\varepsilon^2}{\kappa} G_k + S_\varepsilon \quad (12)$$

for turbulent dissipation  $\varepsilon$  where  $\mu_t = C_\mu \rho_v \frac{\kappa^2}{\varepsilon}$  and  $C_\mu = 0.99$ .

The thermal energy in the process is conserved and computed for each phase by:

$$\frac{\partial}{\partial t} \sum_i (\alpha_i \vec{u}_i (\rho_i E_i + P)) = \nabla \cdot (K_f \nabla T) \quad (13)$$

Where the energy is  $E = h_i - \frac{p}{\rho_i} + \frac{\vec{u}_i^2}{2}$  and the enthalpy and effective thermal conductivity are:



$$h = \frac{\alpha_l \rho_l h_l + \alpha_v \rho_v h_v}{\alpha_l \rho_l + \alpha_v \rho_v} \quad (14)$$

$$h_l = C_{p,l}(T - T_o), h_v = C_{p,v}(T - T_o), \quad (15)$$

$$K_{eff} = \alpha_l K_l + \alpha_v K_v. \quad (16)$$

## 2. Experimental procedure

Since the energetic state of a refrigerant far from its critical point can only exist for stable conditions at a single pressure and temperature pair [31], it is crucial to properly identify the coupled operating pressures and temperatures to obtain the saturated temperature of the refrigerant. For this reason, an experimental setup was designed and constructed so that the inlet and outlet conditions of the water and the refrigerant under transient conditions can be detected and used as dynamic boundary conditions for the numerical simulation.

The water-cooled condenser was fabricated using copper tubing. The dimensions for the line of water, refrigerant line and copper wall separation are shown in **Table 1**. To enhance the heat transfer, thermal insulation (Polyethylene foam) was placed around the water copper jacket and the rest of the tubing connecting the components in the refrigeration system.

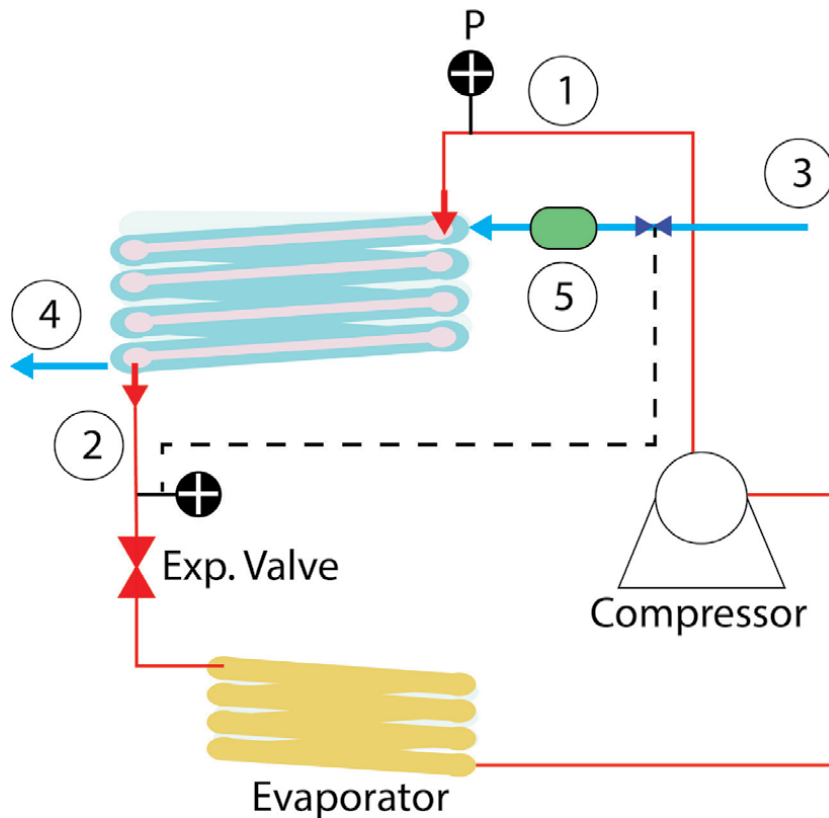
**Figure 1** shows the configuration adopted to characterize the condensing details of R404a. The figure shows the standard cycle corresponding to a vapor compression cycle including the compressor (Copeland ZB15-KCE), the water-cooled condenser, the evaporator, and the thermostatic expansion valve (Danfoss T2). The temperature and pressure of the vapor and liquid refrigerant were measured at points (1) and (2) by attaching thermocouples to the refrigeration line and connecting pressure transducers to measure the pressure drop of the refrigerant across the helix. The water inlet and outlet temperatures are monitored (3) and (4) in a non-invasive fashion.

The test methodology consisted of 6 consecutive runs for 4.75 minutes each in order to stabilize the system and reach thermal equilibrium given that an environmental chamber was not used for this study. A flow meter (5) and pressure regulator are located at the water inlet to measure the flow rate and sustain the water pressure.

**Table 2** shows the magnitude of the variables monitored to control the steady performance of the system.

Parameter	Dimension
$D_{\Omega_1}$	0.0254 [m]
$D_{\Omega_2-in}$	0.0127 [m]
$D_{\Omega_2-out}$	0.0147 [m]
$D_{\Omega_3}$	0.0127[m]
Pitch	0.031[m]
$D_{HXL}$	0.213 [m]
$L_{arc}$	3.05[m]
$A_{s-\Omega_1}$	0.3847 [m <sup>2</sup> ]
$A_{s-\Omega_2-out}$	0.2127 [m <sup>2</sup> ]
$A_{s-\Omega_3}$	0.1834[m <sup>2</sup> ]

**Table 1.**  
Parameters and dimension of the water-cooled condenser.



**Figure 1.** Schematic representation of the refrigeration system depicting the testing points measuring the inlet and outlet temperature and pressure of the refrigerant at (1) and (2), as well as the water temperature at the inlet and outlet at (3) and (4).

**Table 3** shows the sensors and instruments used for the experimental study as well as the accuracy reported by the manufacturers. The sampling rate was fixed to 100 ms using LabView 18 software and the corresponding hardware with the data acquisition system to gather the temperatures and pressures values of both water and refrigerant.

The water and refrigerant temperature at the inlet and outlet of the condenser are reported in **Figure 2** with the corresponding variation to document the test repeatability. The figure also shows the measured refrigerant pressure and the computed liquid saturation temperature using Coolprops 6.4.1 [32].

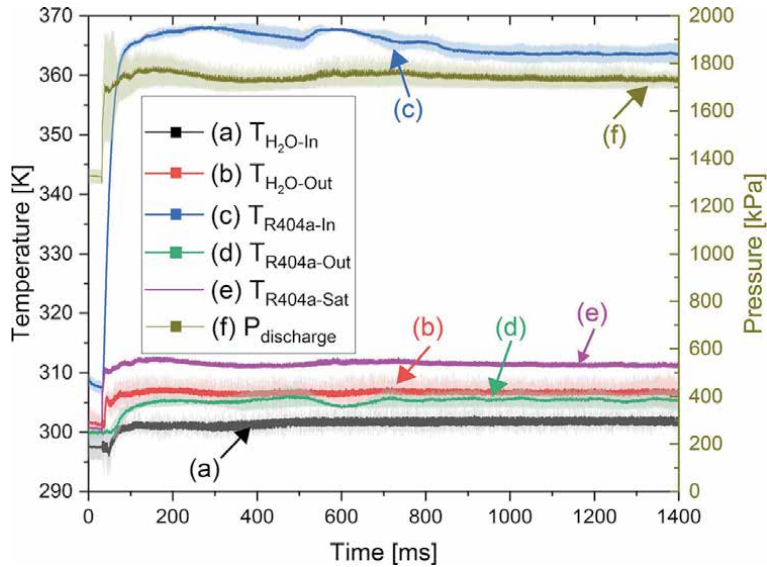
The experimental data demonstrated that the system reached maximum operating pressure close to 300 ms after starting the compressor, and a steady-state condition

Variable	Magnitude
Super-heat	$25 \pm 2.5$ [°C]
Sub-cool	$18 \pm 2.5$ [°C]
$T_{\infty}$	$22 \pm 0.9$ [°C]
$\dot{m}_{R404a}$	$0.398$ [ $\frac{kg}{s}$ ]

**Table 2.** Operational parameters of the refrigeration system.

Variable	Instrument	Accuracy
$P$	Transducer (PX-309)	0.25% Full Scale
$T$	J-Type Thermocouple	$\pm 2.2^\circ\text{C}$
$\dot{m}_{\text{H}_2\text{O}}$	2321FG	2.0% Full Scale

**Table 3.**  
Instrumentation.



**Figure 2.**  
Experimental data obtained experimentally and computed saturation temperature of R404a.

for the vapor refrigerant pressure was reached around 1200 ms after initialization. In order to characterize the startup conditions, the first 2000 ms of the average between the different experiments corresponding to each variable displayed in the **Figure 2** were programmed in ANSYS Fluent as dynamic boundary conditions.

### 3. Computational domain and boundary conditions

A time-dependent numerical model in three-dimension was developed to simulate the phase-transition and heat transfer of R404a in a water-cooled condenser. The geometry accounts for two fluid regions as well as one solid domain (copper) that separates both flows and provides the thermal mechanism for heat transfer. The computational domain ( $\Omega_1 \cup \Omega_2 \cup \Omega_3$ ) contains three distant regions belonging to the space  $\tilde{X} \rightarrow R^3$  assigned as follows:

- a. Fluid region for water ( $\Omega_1$ ).
- b. Solid copper region for physical division of water and refrigerant ( $\Omega_2$ ).
- c. Fluid region for refrigerant R404a ( $\Omega_3$ ).

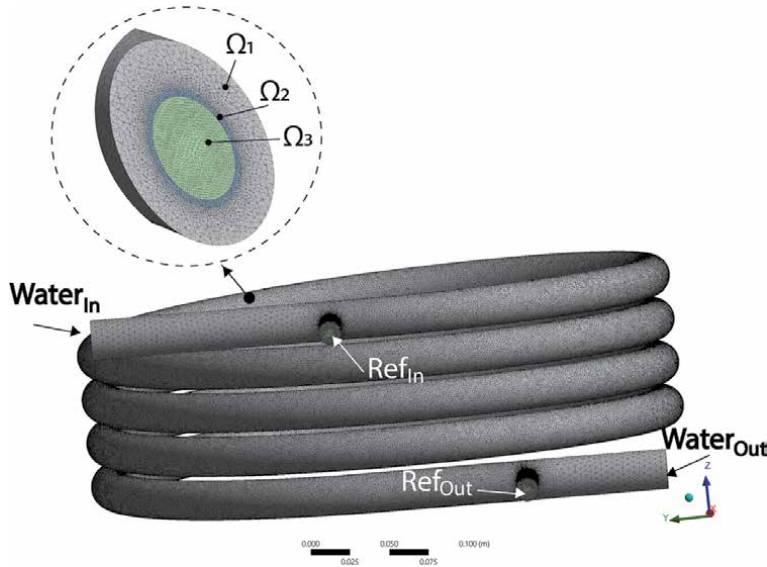
The properties of the materials and working fluids are show in **Table 4**. The temperature dependent material properties were programmed in Fluent using

Property	unit	Substance/Material			
		Water	R404a vapor	R404a liquid	Copper
$K$	$\left[\frac{W}{mK}\right]$	0.6 [33]	0.015 [34]	0.063 [34]	387.6 [35]
$\rho$	$\left[\frac{kg}{m^3}\right]$	$799.71 + 1.6040T - 3.161 \times 10^{-3}T^2$ [33]	65.24 [34]	$\rho_{l-R404a}(T)$ [34]	8978 [35]
$c_p$	$\left[\frac{J}{kg K}\right]$	4182 [36]	1221.4 [37]	1542.3 [34]	381 [35]
$\mu$	$\left[\frac{kg}{m s}\right]$	$\frac{997.2}{2.4432 \times 10^{-2}T - 6.1536}$ [38]	$\mu_{v-R404a}(T)$ [36]	$\mu_{l-R404a}(T)$ [36]	
$\xi_i$	$\left[\frac{mN}{m}\right]$			7.52 [37]	
$M$	$\left[\frac{g}{mol}\right]$	18.6 [33]	97.6 [37]		
$T_{cr-R404a}$	[K]		345.25 [39]		
$T_o-R404a$	[K]		227.15 [39]		

**Table 4.**  
Physical properties of the water, copper, and refrigerant regions.

transient data tables and user defined routines. A schematic representation of the domains describing the computational domain is shown in **Figure 3**. The figure shows the inlet and outlet faces assigned for the water and refrigerant flows. The 3D geometry was modeled in SpaceClaim from the real dimensions and the numerical solution was obtained using Ansys Fluent 19.2. The contacting surfaces were discretized with conformal elements and the computational grid was created using tetrahedral objects with a maximum Skewness of 0.74. The mesh contains 36040897 nodes and 119573669 elements with a mean size of  $3.12e-2$ [m].

The residual target (RMS) for the momentum and energy equations were set to  $1e - 3$  and  $1e - 5$  respectively. The time step was fixed to  $1e - 6$  for a total simulation time of 2 seconds.



**Figure 3.**  
Three-dimensional computational domain specifying the fluid and solid regions considered for the numerical simulation.

Model validation and verification against experimental data is an important aspect of any numerical solution. For turbulent multi-phase flows, the model validation for the phase-transition process is particularly important because the solution of the volume fraction equation depends on the saturation temperature [40]. However, the model validation and identification of the saturation temperature can be challenging if the geometry is complex enough to obstruct the path of light for particle image velocimetry and particle image thermometry or block the access of probes for electric tomography techniques [41]. Unfortunately, the phase-transition process in the water-cooled condenser complies with the restrictions mentioned above because the refrigerant phase-transition takes place in a region where standard field experimental techniques offer limited information due to the water and copper jacket around the refrigerant line. Therefore, in order to develop a model that resembles reality, the saturation temperature has been programmed as a boundary condition based on the inlet and outlet temperatures and pressures measured experimentally.

### 3.1 Boundary conditions

The inlet boundary conditions for water and refrigerant are set to the mean mass flows. The flow rate of water measured experimentally going into the system ranges from 0.21 to 0.3  $\frac{kg}{s}$  and the inlet refrigerant mass flow corresponds to the compressor mass flow provided by the manufacturer at the operating conditions.

The inlet and outlet time dependent temperature, pressures, and saturation temperature are loaded as user functions in Fluent from the experimental values shown in **Figure 2**. A no slip velocity condition was assigned to the boundary walls ( $\vec{u}_{\partial\Omega_i} = 0$ ) and a thermal insulation condition was assigned on the wall between the water and the environment. The outlet quality was set to 100% liquid given that the actual system was designed and fabricated with the charge and specifications to hold a constant sub-cool temperature after the condenser.

$\dot{m}_{in-R404a}$	0.398 $\left[\frac{kg}{s}\right]$
$P_{G-in-R404a}$	From experiments (see <b>Figure 2</b> )
$P_{G-out-R404a}$	From experiments (see <b>Figure 2</b> )
$T_{in-R404a}$	From experiments (see <b>Figure 2</b> )
$T_{out-R404a}$	From experiments (see <b>Figure 2</b> )
$x_{in-R404a}$	0
$x_{out-R404a}$	1
$\dot{m}_{in-H_2O}$	0.26 $\left[\frac{kg}{s}\right]$
$P_{out-H_2O}$	0[Pa]
$T_{in-H_2O}$	From experiments (see <b>Figure 2</b> )
$T_{out-H_2O}$	From experiments (see <b>Figure 2</b> )
$\vec{u}_{\partial\Omega_1} = \vec{u}_{\partial\Omega_2-in} = \vec{u}_{\partial\Omega_2-out} = \vec{u}_{\partial\Omega_3}$	0
$\frac{\partial T_{a\Omega_3-\infty}}{\partial n}$	0
$-Q_{\partial\Omega_2-in} = Q_{\partial\Omega_3}$	12.7[kW]
$Q_{\partial\Omega_2-in} = -Q_{\partial\Omega_1}$	12.7[kW]
$T_{Sat}$	From experiments (see <b>Figure 2</b> )

#### 4. Results and discussion

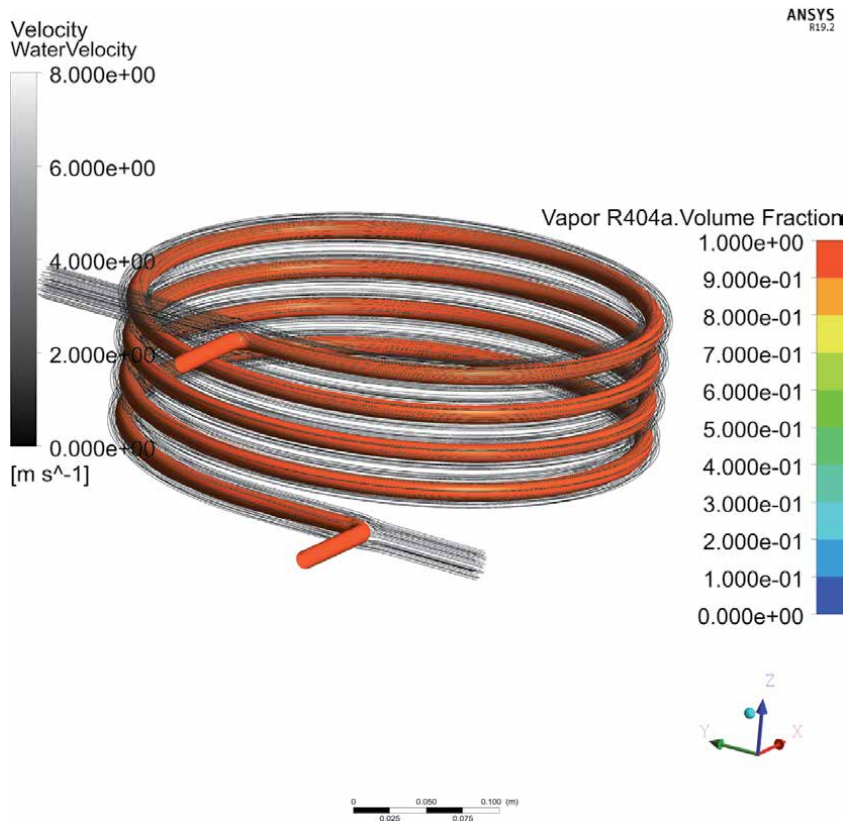
The condensing behavior and evaporating dynamics of refrigerant R404a have been simulated using the VOF approach. Due to the temperature difference, and heat flux, the refrigerant condenses throughout the spiral tubing array, whereas sporadic evaporation occurs given the inertial and body forces present in the flow. The simulation was initialized by filling the total volume of the condenser section with both, the primary fluid (liquid water) and the secondary fluid domain (refrigerant) in a vapor state.

**Figure 4** shows the domain initialization at  $t = 0.0$  s. After this instant, the water starts to flow while the refrigerant is still in a full vapor state. The magnitude and direction of the water velocity is presented by the streak line in the internal flow section, and the quality of the secondary flow is indicated by the contour interface.

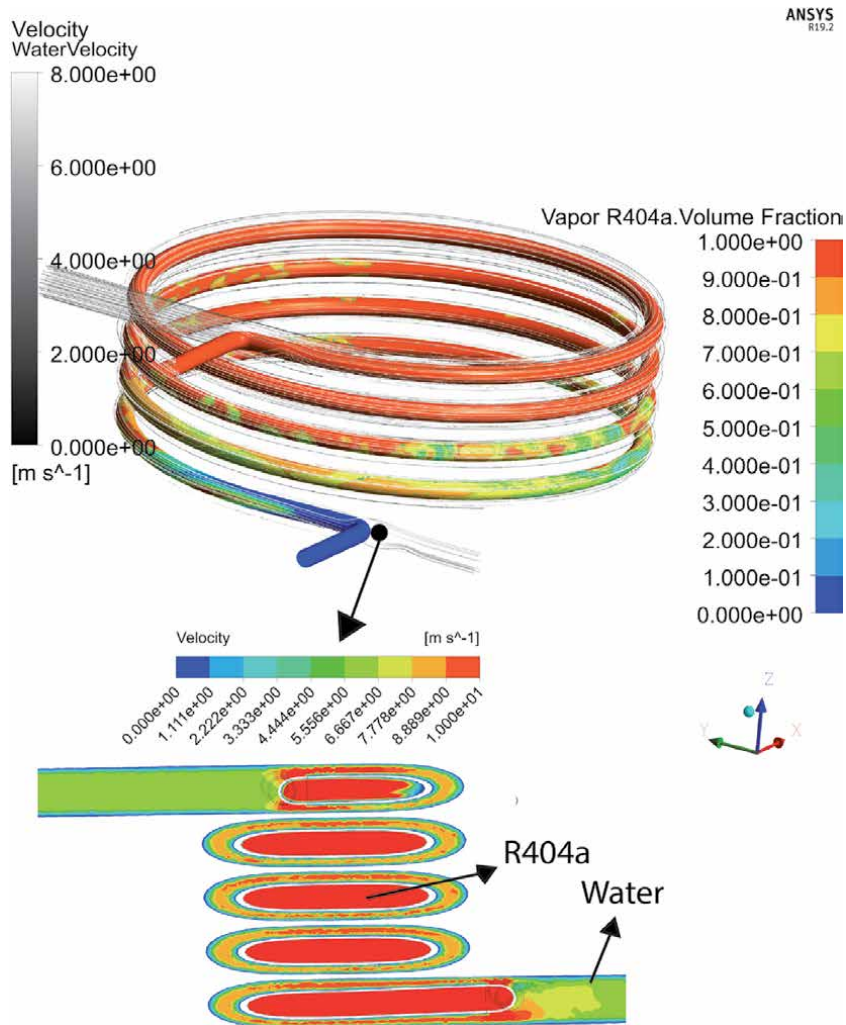
At  $t = 0.15$  s, the refrigerant leaving the condenser has fully condensed near the outlet section based on the sub-cooled temperature boundary condition. Upstream the copper tube, the refrigerant begins a phase-transitioning throughout the lower section of the spiral geometry (shown in **Figure 5**) induced by the fluid temperature distribution.

The two-phase flow in the copper tube shows complicated details, with various phase-transition patterns and irregular oscillation manifesting at the periphery of the geometry due to the centrifugal [42] and inertial forces. The mean vapor quality found in the refrigerant region is 60%.

The water around the copper elbow carrying vapor refrigerant near the inlet develops a high velocity zone due to the reduction of area enhancing the heat flux in



**Figure 4.** Numerical solution of the phase transition of R404a in the water-condenser at  $t = 0.0$  s.



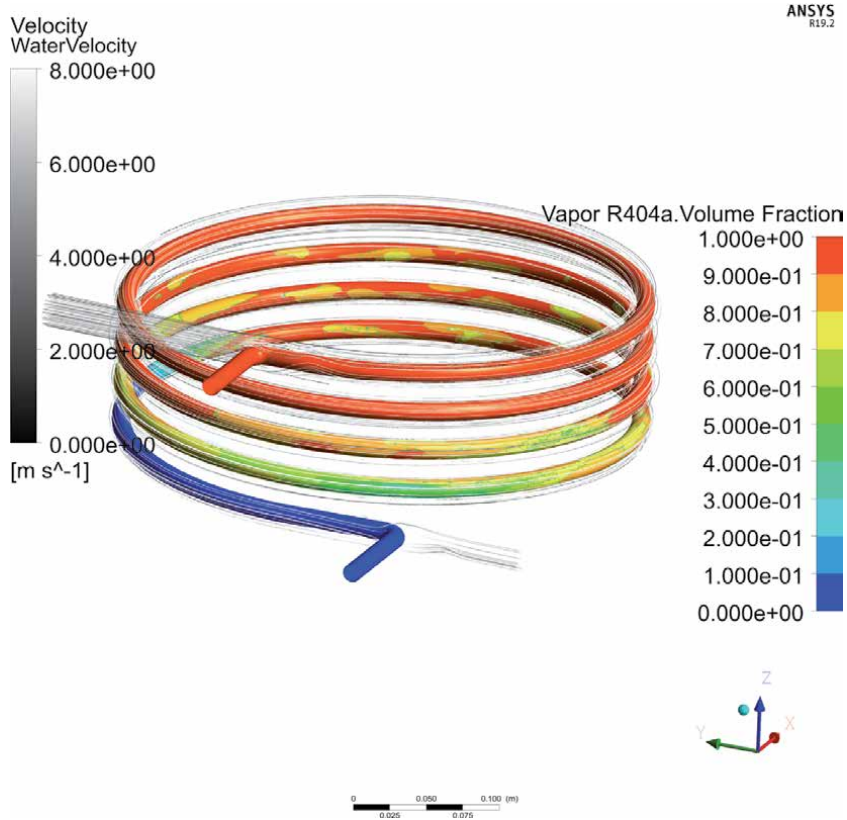
**Figure 5.**  
 Phase-transition and velocity field development at the outlet of the condenser at  $t = 0.15\ s$ .

the system [43]. On the other hand, the vapor refrigerant develops a vortex pair at the beginning of the first spiral. This is probably induced by the tube curvature close to the inlet elbow. Interestingly, no other vortices develop in subsequent curved regions which suggests that the vortex develops due to the thermal and inertial characteristics of the vapor refrigerant entering the tubular array and the proximity to the  $90^\circ$  elbow located at the inlet.

**Figure 6** shows the refrigerant phase transition details at  $0.5\ s$ . At this instant, the refrigerant has completely transitioned to liquid at the last quarter of the spiral leading to the outlet of the condenser. In the middle section of the condenser, the saturated vapor condenses and evaporates along the outer wall in repeated patterns of saturated vapor and multi-phase flow swirling due to gravity and rotational speed.

Since the wall temperature across the copper wall was assumed constant, the phase-transition region extends across a large region of the tubular array. This boundary condition prevented a flash point transition between phases [44]. Furthermore, the outlet temperature was specified to remain in a sub-cool state allowing the saturated liquid to develop further into the inner regions of the condenser.





**Figure 6.** Numerical solution of the phase transition of R404a in the water-condenser at  $t = 0.5$  s.

**Figure 7** shows the condensing and evaporating characteristics of R404a at  $t = 1.25$  s. At the tube periphery and after the first revolution, the saturated vapor begins to condense, transitioning into a two-phase flow with a 90% quality and further decreasing into a quality of 82% while displaying a parabolic profile along the outer surface wall. Then, the mixture evaporates back to a saturated vapor state before it reaches its full condensation state after the third revolution.

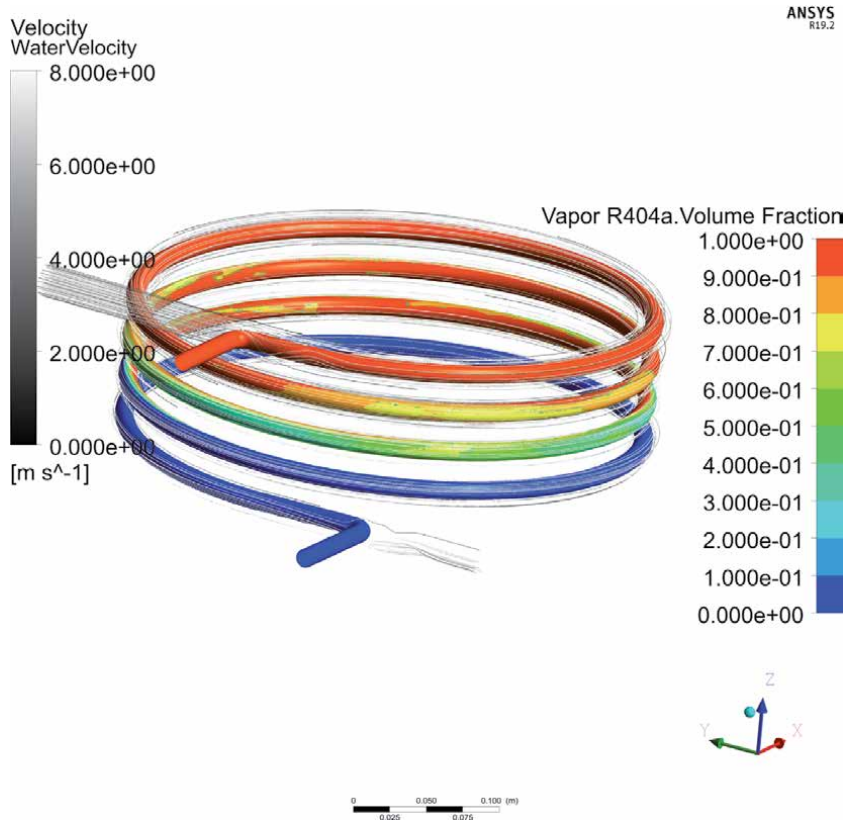
Since the heat transfer can be enhanced or penalized by geometrical factors [45], the widely used Dittus-Boelter (Eq. (17)) was employed to find the Nusselt number in the internal tubing section for the vapor refrigerant flow. Based on the fundamental restrictions of the geometry, parametric modifications to the equation determining the Nusselt number (Eq. (18)) need to be considered based on constant wall temperature assumptions [46], curvature ration [47], and fluid regime [48] such that:

$$Nu_v = \frac{\left(\frac{f}{8}\right) Re_v Pr_v}{1.07 + 12.7\left(\frac{f}{8}\right)^{0.5} (Pr_v^{0.66} - 1)} \quad 4e3 < Re < 5e6, 0.5 < Pr < 2e3 \quad (17)$$

and

$$Nu_{v-HLX} = Nu_v \left(1 + 0.35 \left(\frac{D_{\Omega_3-\infty}}{D_{HLX}}\right)\right). \quad (18)$$





**Figure 7.** Numerical solution of the phase transition of R404a in the water-condenser at  $t = 1.25$  s.

where the friction factor is given by:

$$f = (1.82 \ln Re - 1.62)^{-2} \quad (19)$$

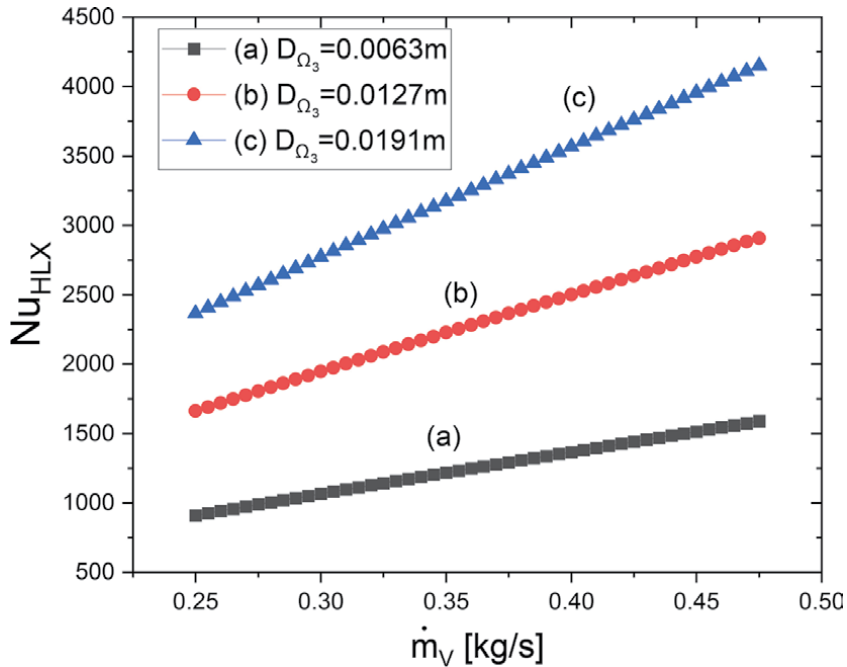
given that the Prandtl and Reynolds numbers are:

$$Pr_v = \frac{\mu_v c_{p-v}}{K_v} \quad (20)$$

and

$$Re = \frac{\rho_v \vec{u}_v D_{\Omega_3}}{\mu_v}. \quad (21)$$

**Figure 8** shows the Nusselt number with respect to vapor refrigerant mass flow as a function different tube diameter. For  $D_{\Omega_3} = 0.0063m$ , the Nusselt number calculated ranges between 900 and 1500 at different vapor mass flows. On the other hand, the Nusselt number at  $D_{\Omega_3} = 0.0191m$ , ranges between 2250 and 4200, suggesting that the heat transfer enhancement occurs by increasing the diameter of the refrigerant line and reducing the number of spirals.



**Figure 8.**  
Predicted Nusselt number as a function vapor refrigerant mass flow as a function of inlet diameter.

## 5. Conclusions

A time and temperature dependent three-dimensional multi-phase simulation with dynamics boundary conditions determined experimentally has been developed to characterize the thermal, inertial, and phase-transition details of refrigerant R404a in a water-cooled condenser at startup conditions. Given the complicated geometrical configuration of the system, where the secondary fluid (refrigerant) is concentric and flows inside the copper jacket in contact with the primary fluid (water), it becomes a challenging task to capture experimental information about the phase-transition details of the refrigerant using common optical or fluid field experimental methods such as optical tagging, particle image velocimetry, or tomography techniques. Therefore, indirect methods have been applied to obtain temperature and pressure values at the inlet and outlet sections of the condenser.

The numerical solution showed the condensing and evaporating oscillatory nature of the phase-transition throughout the spiral tubing as well as the progression of saturated liquid at the outlet of the refrigerant line. Condensation occurs due to the temperature differences between the water and the refrigerant. Evaporation takes place given the body and inertial forces present in the system that prevent further bubble nucleation to sustain the condensation process.

The velocity profiles for both water and refrigerant show vortices developing at the inlet and outlet zones due to the curvatures and elbows present in the geometry. Nusselt numbers show that heat transfer can be optimized by slightly increasing the diameter of the refrigeration line without inducing a disruption in the flow regime or affecting the manufacturability of the part.

## Acknowledgements

The author is grateful to FBD L.P. for the financial support to perform the experimental analysis.

## Conflict of interest

The author declares no conflict of interest.

## Nomenclature

$A_s$	Surface area [ $m^2$ ]
$D$	Diameter [ $m$ ]
$h$	Enthalpy [ $\frac{kJ}{kg}$ ]
$S$	Source
$T$	temperature [ $K$ ]
$t$	Time [ $s$ ]
$V$	Volume
$\vec{u}$	Velocity [ $\frac{m}{s}$ ]
$x$	Quality

## Subscripts

cr	Critical
cu	Copper
eff	Effective
l	Liquid
o	Reference
Ref	Refrigerant
sat	Saturation
v	Vapor

## Greek letters

$\alpha$	Vapor volume fraction
$\rho$	Density
$\xi$	Surface tension [ $\frac{N}{m}$ ]
$\zeta$	Mass transfer intensity [ $\frac{1}{s}$ ]
$\vec{\tau}$	Stress tensor [ $Pa$ ]
$\mu$	Viscosity
$\Omega$	3D domain

## **Author details**

Carlos Acosta  
The University of Texas at San Antonio, San Antonio, Texas

\*Address all correspondence to: carlos.acosta2@utsa.edu

## **IntechOpen**

---

© 2021 The Author(s). Licensee IntechOpen. This chapter is distributed under the terms of the Creative Commons Attribution License (<http://creativecommons.org/licenses/by/3.0>), which permits unrestricted use, distribution, and reproduction in any medium, provided the original work is properly cited. 

## References

- [1] J. Bustamante, A. Rattner and S. Garimella, "Achieving near-water-cooled power plant performance with air-cooled condensers," *Applied Thermal Energy*, vol. 105, pp. 362–371, 2016.
- [2] G. Heidinger, S. Nascimento, P. Gaspar and P. Silva, "Experimental evaluation of the thermal performance at different environmental conditions of a low temperature display case with built-in compressor and water-cooled condenser," *Applied Thermal Engineering*, vol. 144, pp. 825–835, 2018.
- [3] T. Veldkamp, Y. Wada, J. Aerts, P. Doll, S. Gosling, L. Ja, Y. Masaki, T. Oki, S. Ostberg, Y. Pokhrel, Y. Satoh, H. Kim and P. Ward, "Water scarcity hotspots travel downstream due to human interventions in the 20th and 21st century," *Nat Commun*, vol. 8, pp. 1–12, 2017.
- [4] C. Aprea, R. Mastrullo and C. Renno, "Experimental analysis of the scroll compressor performances varying its speed," *Applied Thermal Engineering*, vol. 26, no. 10, pp. 983–992, 2006.
- [5] P. Donnellan, K. Cronin and E. Byrne, "Recycling waste heat energy using vapour absorption heat transformers: A review," *Renew. Sustain. Energy Rev*, vol. 42, pp. 1290–1304, 2015.
- [6] A. Babiloni, J. Esbrí, C. Cervera, F. Molés and B. Peris, "Analysis based on EU Regulation No 517/2014 of new HFC/HFO mixtures as alternatives of high GWP refrigerants in refrigeration and HVAC systems," *International Journal of Refrigeration*, vol. 52, pp. 21–31, 2015.
- [7] "System Drop-in Testing of R-410A Replacements in Split System Heat Pump," *Air-Conditioning, Heating, and Refrigeration Institute (AHRI) Low-GWP Alternative Refrigerants Evaluation Program (Low-GWP AREP)*, vol. Test report #22., 2013.
- [8] C. Acosta, D. Yanes, A. Bhalla, R. Guo, E. Finol and J. Frank, "Numerical and experimental study of the glass-transition temperature of a non-Newtonian fluid in a dynamic scraped surface heat exchanger," *International Journal of Heat and Mass Transfer*, vol. 152, pp. 1–8, 2020.
- [9] C. Acosta, A. Bhalla and R. Guo, "Empirical and numerical determination of the freezing point depression of an unsteady flow in a scraped surface crystallizer," *Applied Thermal Engineering*, vol. 179, pp. 1–8, 2020.
- [10] Y. Shang, . Y. Zhang, . Y. Hou, B. Bai and X. Zhong, "Effects of surface subcooling on the spreading dynamics of an impact water droplet," *Physics of Fluids*, vol. 32, pp. 1–10, 2020.
- [11] S. Richter, S. Fleischer, M. Aritomi and R. Hamp, "Transient two-phase flow in arbitrary inclined tubes caused by depressurization of liquid with dissolved gasses," *International Journal of Heat and Mass Transfer*, vol. 44, no. 1, pp. 1–15, 2001.
- [12] R. Akasaka, "Thermodynamic property models for the difluoromethane (R-32) + trans-1,3,3,3-tetrafluoropropene (R-1234ze(E)) and difluoromethane + 2,3,3,3-tetrafluoropropene (R-1234yf) mixtures," *Fluid Phase Equilibria*, vol. 358, pp. 98–104, 2013.
- [13] D. Frenkel and B. Smit, *Understanding molecular simulation: from algorithms to applications*, San Diego: Academic Press, 2001.
- [14] T. He, C. Mei and J. Longtin, "Thermosyphon-assisted cooling system for refrigeration applications," *International Journal of Refrigeration*, vol. 74, pp. 165–176, 2017.
- [15] J. Kim, C. Han and S. Jeong, "Disturbance observer-based robust control against model uncertainty and

disturbance for a variable speed refrigeration system,” *International Journal of Refrigeration*, vol. 116, pp. 49–58, 2020.

[16] C. Truesdell, *The Tragicomedy of Classical Thermodynamics*, Vienna: 1971, Springer.

[17] Z. Wu and R. Du, “Design and experimental study of a miniature vapor compression refrigeration system for electronics cooling,” *Applied Thermal Engineering*, vol. 31, no. 2, pp. 385–390, 2011.

[18] S. Mimouni, A. Foissac and J. Lavieville, “CFD modelling of wall steam condensation by a two-phase flow approach,” *Nuclear Engineering and Design*, vol. 241, no. 11, pp. 4445–4455, 2011.

[19] D. Sun, J. Xu and Q. Chen, “Modeling of the evaporation and condensation phasechange problems with FLUENT,” *Heat Transf., Part B: Fundamentals*, vol. 66, no. 4, pp. 326–342, 2014.

[20] S. Mimouni, “CFD modeling of wall steam condensation: two-phase flow approach versus homogeneous flow approach,” *Sci. Technol. Nucl. Install*, 2011.

[21] H. Mohammed, D. Giddings and G. Walker, “CFD multiphase modelling of the acetone condensation and evaporation process in a horizontal circular tube,” *International Journal of Heat and Mass Transfer*, vol. 134, pp. 1159–1170, 2019.

[22] N. Padoin and C. Soares, “CFD modeling of steam condensation in industrial pipes,” *Blucher Chem. Eng. Proc*, vol. 1, no. 2, p. 12904–12911, 2015.

[23] M. Konopacki, M. Kordas, K. Fijalkowski and R. Rakocz, “Computational fluid dynamics and experimental studies of a new mixing element in a static mixer as a heat exchanger,” *Chem. Process Eng*, vol. 36, no. 1, pp. 59–72, 2015.

[24] G. Anjos, G. Oliveira and M. Norberto, “Arbitrary Lagrangian–Eulerian Method for Two-Phase Flows: Applications,” in *Encyclopedia of Two-Phase Heat Transfer and Flow III*, World Scientific, 2018, pp. 141–183.

[25] J. Parekh and R. Rzehak, “Euler–Euler multiphase CFD-simulation with full Reynolds stress model and anisotropic bubble-induced turbulence,” *International Journal of Multiphase Flow*, vol. 99, pp. 231–245, 2018.

[26] M. Göz, S. Lain and M. Sommerfeld, “Study of the numerical instabilities in Lagrangian tracking of bubbles and particles in two-phase flow,” *Comput. Chem. Eng*, vol. 28, p. 2727–2733, 2004.

[27] E. E. Michaelides, “Review—The Transient Equation of Motion for Particles, Bubbles, and Droplets,” *J. Fluids Eng.*, vol. 119, no. 2, pp. 1–16, 1997.

[28] H. Hu, “Direct simulation of flows of solid-liquid mixtures,” *International Journal of Multiphase Flow*, vol. 22, no. 2, pp. 335–352, 1996.

[29] A. Arora and S. Kaushik, “Theoretical analysis of a vapour compression refrigeration system with R502, R404A and R507A,” *International Journal of Refrigeration*, vol. 31, no. 6, pp. 998–1005, 2008.

[30] M. Zareh, H. Shokouhmand, M. Salimpour and M. Taeibi, “Numerical simulation and experimental analysis of refrigerants flow through adiabatic helical capillary tube,” *International Journal of Refrigeration*, vol. 38, pp. 299–309, 2014.

[31] S. Lee, M. Kim and S. Ro, “Thermal Conductivity of 1,1,1-Trifluoroethane (R143a) and R404A in the Liquid Phase,” *Journal of Chemical and Engineering Data*, vol. 46, no. 5, pp. 1013–1015, 2011.

[32] “Pure and Pseudo-pure Fluid Thermophysical Property Evaluation

and the Open-Source Thermophysical Property Library CoolProp,” *Industrial and Engineering Chemistry Research*, vol. 53, no. 6, pp. 2498–2508, 2014.

[33] D. Green and R. Perry, Perry’s Chemical Engineers’ Handbook, London: McGraw-Hill, 2007.

[34] B. Fadhl, L. Wrobel and H. Jouhara, “CFD modelling of a two-phase closed thermosyphon charged with R134a and R404a,” *Applied Thermal Engineering*, vol. 78, no. 5, pp. 482–490, 2015.

[35] W. Callister and D. Rethwisch, *Materials science and engineering an introduction*, Wiley, 2010.

[36] V. Geller, D. Bivens and A. Yokozeki, “Viscosity of Mixed Refrigerants, R404A, R407C, R410A, and R507C,” in *Int. Ref. and Air cond.*, West Lafayette, 2000.

[37] E. Lemmon, M. Huber and M. McLinden, NIST standard reference database 23: reference fluid thermodynamic and transport properties-REFPROP, version 8.0, Gaithersburg: Standard Reference Data, 2007.

[38] A. Gadelha, S. Neto, R. Swarnakar and A. Lima, “Thermo-Hydrodynamics of Core-Annular Flow of Water, Heavy Oil and Air Using CFX,” *Advances in Chemical Engineering and Science*, vol. 3, no. 4A, pp. 37–45, 2013.

[39] R. Heide, “The surface tension of HFC refrigerants and mixtures,” *nt J. Refrig*, vol. 20, pp. 496–503, 1997.

[40] W. Lee, *A pressure iteration scheme for two-phase flow modeling*. Multiphase Transport Fundamentals, Reactor Safety, Applications, Washington, DC: Hemisphere Publishing, 1980.

[41] C. Acosta, A. Bhalla and R. Guo, “Phase-transition temperature

determination using optical spectroscopy in a rotating flow inside a scrape surface crystallizer,” in *Photonic Fiber and Crystal Devices: Advances in Materials and Innovations in Device Applications XIV*, San Diego, 2020.

[42] H. Wu, X. Peng, P. Ye and Y. Gong, “Simulation of refrigerant flow boiling in serpentine tubes,” *Transfer*, International Journal of Heat and Mass, vol. 50, no. 5, pp. 1186–1195, 2007.

[43] H. Ito, “Flow in Curved Pipes,” *JSME international journal*, vol. 30, pp. 543–551, 1987.

[44] A. Seixlack and M. Barbazelli, “Numerical analysis of refrigerant flow along non-adiabatic capillary tubes using a two-fluid model,” *Applied Thermal Engineering*, vol. 29, no. 2, pp. 523–531, 2009.

[45] J. Abraham, E. Sparrow and W. Minkowycz, “Internal-flow Nusselt numbers for the low-Reynolds-number end of the laminar-to-turbulent transition regime,” *International Journal of Heat and Mass Transfer*, vol. 54, no. 1, pp. 584–588, 2011.

[46] R. Seban and E. McLaughlin, “Heat transfer in tube coils with laminar and turbulent flow,” *International Journal of Heat and Mass Transfer*, vol. 6, no. 5, pp. 387–395, 1963.

[47] H. Zhao, X. Li, Y. Wu and X. Wu, “Friction factor and Nusselt number correlations for forced convection in helical tubes,” *International Journal of Heat and Mass Transfer*, vol. 155, p. 119759, 2020.

[48] L. Janssen and C. Hoogendoorn, “Laminar convective heat transfer in helical coiled tubes,” *International Journal of Heat and Mass Transfer*, vol. 21, no. 9, pp. 1197–1206, 1978.





# The CFD Based Method for Determining Heat Transfer Correlations on Individual Rows of Plate-Fin and Tube Heat Exchangers

*Dawid Taler, Jan Taler and Marcin Trojan*

## Abstract

The chapter provides an analytical mathematical model of a car radiator, which includes different heat transfer coefficients (HTCs) on the first and second row of pipes. The air-side HTCs in the first and second row of pipes in the first and second pass were calculated using the correlations for the Nusselt number, which were determined by CFD simulation using the ANSYS software. Mathematical models of two radiators were built, one of which was manufactured of round tubes and the other of oval tubes. The model permits the determination of thermal output of the first and second row of tubes in the first and second pass. The small relative differences between the thermal capacities of the heat exchanger occur for different and uniform HTCs. However, the heat flow rate in the first row is much greater than the heat flow in the second row if the air-side HTCs are different on the first and second tube row compared to a case where the HTC is uniform in the whole heat exchanger. The heat transfer rates in both radiators calculated using the developed mathematical model were compared with those determined experimentally. The method for modeling of plate-fin and tube heat exchanger (PFTHE) proposed in the paper does not require empirical correlations to calculate HTCs both on the air side and on the inner surfaces of pipes. The presented method of calculating PFTHEs, considering different air-side HTCs evaluated using CFD modeling, may considerably reduce the cost of experimental research concerning new design heat exchangers implemented in manufacturing.

**Keywords:** Air-cooled heat exchangers, Air-side Nusselt number, Different heat transfer correlation on individual pipe row, CFD modeling, Empirical heat transfer correlation

## 1. Introduction

Cross-flow finned heat exchangers are used in many industrial fields. In the case of heat exchangers operating at high parameters, individual round fins are welded to the outer surfaces of the tubes. On the other hand, heat exchangers in which the temperature of the working medium is just above the ambient temperature consist

of aluminum tubes fitted with aluminum fins. These are compact heat exchangers known as plate-fin and tube heat exchangers (PFTHEs).

In finned heat exchangers with both inline and staggered tube arrangements with continuous fins, the heat transfer coefficient reaches its highest values on the first tube row (laminar flow). In subsequent rows, the HTC decreases. This is due to the large HTC values in the inlet part of channels between the fins compared to the mean coefficient on the entire fin surface.

Different methods are used to calculate heat exchangers. In the  $\epsilon$ -NTU (Effectiveness - Number of Transfer Units) method, one effectiveness value is determined for the entire heat exchanger [1]. In the P-NTU (Effectiveness - Number of Transfer Units) method, P efficiency is determined for each medium [2]. Both the above methods and the LMTD (Log Mean Temperature Difference) method assume a constant HTC value on the gas side.

Kuppan collected in his book [3] relations and diagrams to determine the efficiencies of typical heat exchangers. The temperature of the working media in large heat exchangers built from several rows of tubes can be determined by numerical models [4] based on the finite difference method or the finite volume method.

The determination of the average air-side HTC of PFTHEs built with one, two, three, and four rows of tubes have received much attention in the literature. For finned tube heat exchangers with more than four tube rows, the air-side average HTC for the entire heat exchanger is determined as for a heat exchanger built with four tube rows. Kim et al. in [5] proposed formulas to calculate wavy PFTHEs. The formulas are valid for both in-line and staggered tube arrangements and allow the determination of the air-side Nusselt number and the friction coefficient. On the other hand, the paper [6] describes correlations based on experimental measurements and applicable only to PFTHEs with a linear tube system. The paper [7] describes a study showing that increasing the number of tube rows in a continuous plain fin and tube heat exchanger under dehumidifying leads to a decrease in heat transfer. Similar studies were presented by Halici et al. in the paper [8].

The authors studied PFTHEs with a staggered tube arrangement, made of copper tubes and aluminum fins. The results of the study allowed the determination of friction and Colburn coefficients and HTC for air. The determined friction factor and heat transfer coefficient for wet surfaces were greater than for dry surfaces and decreased with the increasing number of pipe rows. Correlations for the Colburn factor presented in [5–8] were determined for whole finned heat exchangers. No correlations for Colburn factor were determined for individual tube rows in PFTHEs. Also in the works [9–10], the correlations determined were for the entire car radiator and not for individual rows.

Rich [11] performed a study of PFTHEs with a staggered tube arrangement with a higher number of tube rows (5 and 6 tube rows). The results also showed that the HTC on the air side decreases with the increasing number of rows. The tests were conducted for air velocity of less than 3.5 m/s and Reynolds number of 12000.

Marković et al. [12] based on experimental data proposed a formula to determine the air pressure drop in a finned heat exchanger with a staggered tube arrangement. In the paper [12], the Darcy-Weisbach friction factor on the air-side depends on the Reynolds number and the ratio of the total external surface area of the finned tube to the surface area of the unfinned tube.

The works [1, 3, 13, 14] contain information describing the effect of pipe dimensions, shape and wall thickness, fin size, the longitudinal and transverse pitch of tube spacing on heat transfer in PFTHE.

In addition, in [14], it is discussed how the heat output of the heat exchanger changes depending on different methods of heat transfer intensification on the inner surfaces of the tubes.

CFD simulations were used in [15–17] to determine the uniform heat transfer coefficient for the entire PFTHE.

Sun et al. presented the results of CFD simulations and experimental studies of the optimized PFTHE in their paper [15]. The optimization of the finned heat exchanger consisted of directing the airflow to the back of the tubes using appropriately prepared channels. This procedure was intended to stop the formation of dead zones, thus improving heat transfer and reducing the pressure drop on the air-side.

Numerical and experimental studies of different types of fins are presented in the paper [16]. Wavy and plain fins with radially spaced winglets around the tubes in the plate fin tube heat exchanger were discussed. Numerical calculations were carried out in the form of CFD simulations in which laminar flow was assumed for air velocities ranging from 1.5 m/s to 3.5 m/s. For air velocities above 3.5 m/s, the turbulent flow was assumed. On the other hand, experimental studies allowed the determination of correlations for the air-side Nusselt number.

Nagaosa in paper [17] used direct numerical simulation (DNS) to determine the air-side heat transfer correlation, which was then verified experimentally. Good agreement of the obtained results was achieved. Unfortunately, computer-based DNS calculations require a long time to perform.

When turbulent flow occurs on the air-side (high Reynolds numbers), the Nusselt number in the first pipe row of the PFTHE takes on lower values than the Nusselt numbers in the subsequent pipe rows. This phenomenon occurs both in heat exchangers made of smooth tubes [1–3] or single finned tubes [18] and in heat exchangers with continuous fins [11]. Kearney and Jacobi [18] determined by experimental study the Nusselt number for each row of tubes in cross-flow finned tube heat exchangers with two-rows of tubes. The results showed that for a heat exchanger with an in-line arrangement of tubes, the Nusselt number in the first row was 34% lower than the Nusselt number in the second row for a Reynolds number of about 5000 and 45% lower for a Reynolds number of about 28000. In a heat exchanger with a staggered arrangement of tubes, a 45% lower Nusselt number over the entire range of Reynolds numbers was obtained for the first row of tubes compared to the second row.

In the available literature, few works are describing mathematical models of heat exchangers considering different heat transfer coefficients on different rows of heat exchanger tubes. The works [19–20] used mathematical models of PFTHEs with different heat transfer coefficients on the first and second row of tubes to simulate steady-state operation. In work [21], calculations of PFTHEs operating under transient conditions were performed.

The paper [22] describes an analytical method for determining the required air mass flow rate of a heat exchanger used in the propane pre-cooling cycle of an LNG plant. The method can be used to control the air mass flow rate through the fin tubes of an air-cooled heat exchanger to control the outlet temperature of the working media.

The paper [23] deals with the numerical modeling of a heat exchanger with finned tubes with large fin pitch. Computer simulations were carried out to propose the optimal perforation size and design for maximum heat transfer coefficient. Fin-and-tube compact heat exchangers (FTCHEs) were investigated in [24]. The results of a three-dimensional CFD simulation for an FTCHE heat exchanger constructed from oval tubes with smooth and corrugated fins are shown. Thermal-hydraulic studies were carried out for Reynolds number in the range of 200–900. The computational results show that the average Nusselt number for FTCHE with corrugated fins can be increased up to 20% compared to the case with plain fins. The average performance value for the single- and three-wave finned oval tube compact heat exchangers increased by 5% and 15%, respectively, relative to the plain tube

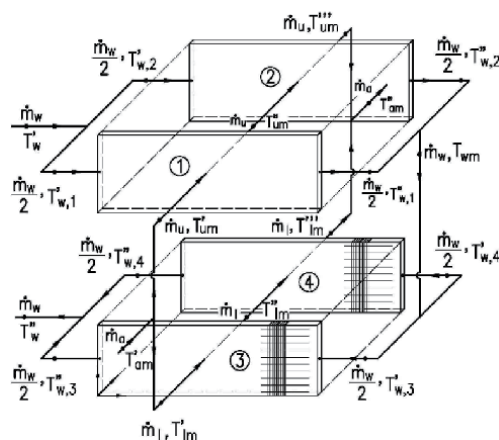
case. CFD modeling has also been used by the authors of a paper [25] to evaluate the thermo-hydraulic conditions of heat exchangers with finned tubes of circular, oval and flat cross-sections, with in-line or staggered tube arrangements. The study was carried out for small Reynolds numbers (400–900). For the selected performance criteria, it has been shown that the oval tube with the highest axial ratio is the optimum configuration that provides a heat transfer coefficient increase of 14% at Reynolds number  $Re = 400$  and 5% at Reynolds number  $Re = 900$ . In turn, the effect of different combinations of circular and elliptical tubes on the air-side flow and heat transfer characteristics of the heat exchanger was investigated in [26]. Inlet air velocities were in the range of 0.5–2.5 m/s. The CFD modeling results obtained show that at low inlet velocities, the system with the elliptical tube in front of the circular tube is better than the system with the circular tube alone. At higher air inlet velocities, the system composed of elliptical and circular tubes performs better than the heat exchanger with elliptical tubes alone. Also, the heat exchanger performance was found to be better when elliptical tubes were grouped in the upper region and round tubes in the lower region compared to the alternative arrangement of elliptical and round tubes.

An analytical mathematical model of a two-pass car radiator taking into account the different air-side HTC's on the first and second row of pipes was presented in this chapter. The results of modeling car radiators made of round and oval pipes were compared with the results of experimental research.

## 2. Mathematical model of the two-pass PFTHE with different heat transfer coefficients on each tube row

An analytical mathematical model of a two-pass radiator with two rows of pipes was developed. The first and second-row HTC's were calculated using heat transfer correlations, which were determined based on CFD (Computational Fluid Dynamics) simulations. The radiator flow diagram is shown in **Figure 1**.

The mass flow rate  $\dot{m}_w$  to the car radiator is divided into two equal parts  $\dot{m}_w/2$  flowing through the first and second row of pipes in the first pass. The starting point for building a mathematical model of a car radiator is a single-pass double-row heat exchanger (first pass of two-pass heat exchanger with two rows of tubes) (**Figure 2**).



**Figure 1.**

*Flow arrangement of the analyzed two-pass car radiator with two rows of tubes; 1 – First tube row in the first pass, 2 - second tube row in the first pass, 3 - first tube row in the second pass, 4 - second tube row in the second pass.*

## 2.1 Analytical model for the first row of pipes

The governing energy conservation equation equations for the water and air in the first tube row are

$$\frac{dT_{w,1}(x^+)}{dx^+} = -N_w^I [T_{w,1}(x^+) - T_{ma}^I(x^+)] \quad 0 \leq x^+ \leq 1 \quad (1)$$

$$\frac{\partial T_a^I(x^+, y_1^+)}{\partial y_1^+} = N_a^I [T_{w,1}(x^+) - T_a^I(x^+, y_1^+)] \quad 0 \leq x^+ \leq 1 \quad 0 \leq y_1^+ \leq 1 \quad (2)$$

where:  $x^+ = x/L_c$ ,  $y_1^+ = y_1/p_2$  dimensionless coordinates;  $x, y_1$  Cartesian coordinates (**Figure 2**)  $T_{w,1}$  the temperature of the water in the first row of pipes,  $T_a^I$  the temperature of the air in the first row of pipes.

Two local dimensionless coordinate systems were introduced ( $x^+, y_1^+$ ) and ( $x^+, y_2^+$ ) (**Figure 2**). The average air temperature  $T_{ma}^I(x^+)$  over the first-row width  $p_2$  is determined by the expression

$$T_{ma}^I(x^+) = \int_{y_1^+=0}^1 T_a^I(x^+, y_1^+) dy_1^+ \quad (3)$$

The number of heat transfer units on the water-side  $N_w^I$  and air-side  $N_a^I$  are defined as follows

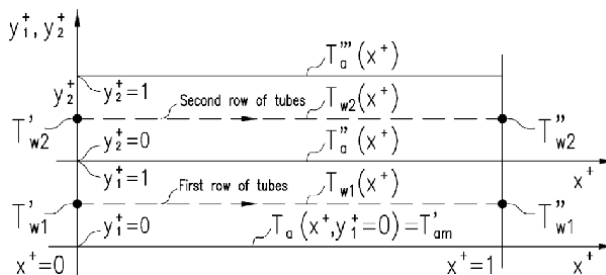
$$N_w^I = 2U^I A_{bout}^I / (\dot{m}_w \bar{c}_{pw}) \quad N_a^I = U^I A_{bout}^I / (\dot{m}_a \bar{c}_{pa}) \quad (4)$$

where:  $A_{bout}^I = n_u^I P_{out} L_c$ ,  $n_u^I$  total number of pipes in the first row of the first pass,  $A_{bout}^I$  outer surface area of the bare pipes in the first row of the first pass,  $P_{out}$  outer circumference of the plain tube,  $L_c$  length of a tube in the PFTHE, The symbol  $\bar{c}_{pw}$  means the average specific heat of water in the temperature range from  $T_w''$  to  $T_w'$ , and the average specific heat of air  $\bar{c}_{pa}$  in the temperature range from  $T_{am}'$  to  $T_{am}''$  (**Figure 2**).

The overall HTC  $U^I$  is calculated using the expression

$$\frac{1}{U^I} = \frac{A_{bout}^I}{A_{bin}^I} \frac{1}{h_{in}^I} + \frac{A_{bout}^I}{A_{wm}^I} \frac{\delta_w}{k_w} + \frac{1}{h_{oe}^I} \quad (5)$$

where:  $A_{bin}^I = n_u^I P_{in} L_c$  inner surface area of the pipes in the first row of the first pass,  $P_{in}$  inner circumference of the tube,  $h_{in}^I$  HTC on the tube inner surface in the



**Figure 2.** Diagram of a single-pass two-row heat exchanger.

first row of the first pass,  $A_{wm} = (A_{bout}^I + A_{bin}^I)/2$  mean heat transfer area of the plain tubes in the first row of the first pass,  $\delta_w$  tube wall thickness,  $k_w$  thermal conductivity of the tube material. The equivalent HTC  $h_{oe}^I$ , taking into account the heat transfer through the fins fixed to the outer surface of a plain pipe for the first row of pipes, is given by

$$h_{oe}^I = h_a^I \left[ \frac{A_{bf}^I}{A_{bout}^I} + \frac{A_f^I}{A_{bout}^I} \eta_f (h_a^I) \right] \quad (6)$$

where:  $h_a^I$  air-side HTC in the first row of tubes in the first pass,  $A_{bf}^I$  tube surface area between fins,  $\eta_f$  fin efficiency.

The boundary conditions for Eqs. (1) and (2) are as follows

$$T_{w,1}|_{x^+=0} = T'_{w,1} \quad (7)$$

$$T_a^I|_{y_1^+=0} = T'_{am} \quad (8)$$

The solution to Eqs. (1) and (2) with boundary conditions (7) and (8) is

$$T_{w,1}(x^+) = T'_{am} + (T'_{w,1} - T'_{am}) \exp \left\{ -\frac{N_w^I}{N_a^I} [1 - \exp(-N_a^I)] x^+ \right\} \quad 0 \leq x^+ \leq 1 \quad (9)$$

$$T_a^I(x^+, y_1^+) = T_{w,1}(x^+) - [T_{w,1}(x^+) - T'_{am}] \exp(-N_a^I y_1^+) \quad 0 \leq x^+ \leq 1 \quad 0 \leq y_1^+ \leq 1 \quad (10)$$

By substituting  $y_1^+ = 1$  into Eq. (10) and performing appropriate transformations the air temperature  $T_a''(x^+)$  behind the first row of pipes can be obtained

$$T_a''(x^+) = T_a^I(x^+, y_1^+ = 1) = T_{w,1}(x^+) - [T_{w,1}(x^+) - T'_{am}] \exp(-N_a^I) \quad (11)$$

Expression (9) describes the temperature  $T_{w,1}(x^+)$ . The temperature  $T'_{am}$  denotes the average air temperature after the first row of tubes. The temperature  $T_a''$  can be calculated as follows

$$T_a'' = \int_0^1 T_a''(x^+) dx = T'_{am} + \frac{N_w^I}{N_a^I} (T'_{w,1} - T'_{am}) [1 - \exp(-B)] \quad (12)$$

where  $B$  stands for

$$B = \frac{N_w^I}{N_a^I} [1 - \exp(-N_a^I)] \quad (13)$$

The temperature distribution of water and air in the first row of pipes of the first pass can be determined using Eqs. (9)–(13).

## 2.2 Analytical model for the second row of pipes

The relevant differential equations for the second row of pipes are

$$\frac{dT_{w,2}(x^+)}{dx^+} = -N_w^{II} [T_{w,2}(x^+) - T_{ma}^{II}(x^+)] \quad 0 \leq x^+ \leq 1 \quad (14)$$

$$\frac{\partial T_a^{II}(x^+, y_2^+)}{\partial y_2^+} = N_a^{II} [T_{w,2}(x^+) - T_a^{II}(x^+, y_2^+)] \quad 0 \leq x^+ \leq 1 \quad 0 \leq y_2^+ \leq 1 \quad (15)$$

where

$$N_w^{II} = 2U^{II} A_{bout}^{II} / (\dot{m}_w \bar{c}_{pw}) \quad N_a^{II} = U^{II} A_{bout}^{II} / (\dot{m}_a \bar{c}_{pa}) \quad (16)$$

Eq. (5) allows to determine the total HTC  $U^{II}$ . Heat transfer coefficient  $h_{oe}^I$  should then be replaced by  $h_{oe}^{II}$ . The effective air-side HTC  $h_{oe}^{II}$  can be calculated using Eq. (6). HTC  $h_a^I$  should then be substituted by HTC  $h_a^{II}$  for the second row of tubes. The average air temperature over the width of the second row of pipes  $T_{ma}^{II}(x^+)$  is determined as follows

$$T_{ma}^{II}(x^+) = \int_{y_2^+=0}^1 T_a^{II}(x^+, y_2^+) dy_2^+ \quad (17)$$

After taking into account that the water temperature at the inlet to the second row of pipes is  $T'_{w,2}$ , and the temperature of the air at the inlet to the second row of pipes is equal to the outlet temperature of the air from the first row of pipes the appropriate boundary conditions are

$$T_{w,2}|_{x^+=0} = T'_{w,2} \quad (18)$$

$$T_a^{II}|_{y_2^+=0} = T_a^{II}(x^+) \quad (19)$$

The solution to Eqs. (14) and (15) under boundary conditions (18) and (19) is

$$T_{w,2}(x^+) = T'_{am} + \frac{E}{D - B} [\exp(-Bx^+) - \exp(-Dx^+)] + (T'_{w,2} - T'_{am}) \exp(-Dx^+) \quad (20)$$

$$0 \leq x^+ \leq 1$$

$$T_a^{II}(x^+, y_2^+) = T_{w,2}(x^+) - [T_{w,2}(x^+) - T_a^{II}(x^+)] \exp(-N_a^{II} y_2^+) \quad (21)$$

$$0 \leq x^+ \leq 1 \quad 0 \leq y_2^+ \leq 1$$

where

$$D = \frac{N_w^{II}}{N_a^{II}} [1 - \exp(-N_a^{II})] \quad E = D (T'_{w,1} - T'_{am}) [1 - \exp(-N_a^{II})] \quad (22)$$

Eq. (13) allows to calculate the coefficient B. To determine the air temperature behind the second row of pipes  $T_a^{III}(x^+)$  (**Figure 2**), it is necessary to take into account in Eq. (21) that  $y_2^+ = 1$ . Then Eq. (20) should be substituted into Eq. (21). The resulting equation allows, after simple transformations, to write an expression for the air temperature  $T_a^{III}(x^+)$  behind the second row of pipes

$$\begin{aligned}
 T_a'''(x^+) &= T_a^{II}(x^+, y_2^+ = 1) = \\
 T_{am}' + [1 - \exp(-N_a^{II})] &\left\{ \frac{E}{D-B} [\exp(-Bx^+) - \exp(-Dx^+)] + \right. \\
 + (T'_{w,2} - T'_{am}) \exp(-Dx^+) &\left. \right\} + (T'_{w,1} - T'_{am}) [1 - \exp(-N_a^I)] \exp(-Bx^+ - N_a^{II}) \\
 0 \leq x^+ \leq 1 & \quad (23)
 \end{aligned}$$

The average air temperature after the second row of pipes  $T_{am}'''$  is determined by the formula

$$\begin{aligned}
 T_{am}''' &= \int_0^1 T_a'''(x^+) dx^+ = T_{am}' + [1 - \exp(-N_a^{II})] \left\{ \frac{E}{(D-B)B} [1 - \exp(-B)] - \right. \\
 - \frac{E}{(D-B)D} [1 - \exp(-D)] &+ \frac{(T'_{w,2} - T'_{am})}{D} [1 - \exp(-D)] \left. \right\} - \\
 - \frac{(T'_{w,1} - T'_{am})}{B} [1 - \exp(-N_a^I)] &[\exp(-B - N_a^{II}) - \exp(-N_a^{II})] \\
 & \quad (24)
 \end{aligned}$$

When the air-side HTC  $h_a^I$  on the first pipe row is equal to the HTC  $h_a^{II}$  on the second pipe row, then  $D = B$  and the denominator  $(D - B)$  is going to be zero. When  $D = B$  the formula (20) requires transformation. Writing Eq. (20) as

$$\begin{aligned}
 T_{w,2}(x^+) &= T_{am}' + \frac{E \exp(-Dx^+)}{D-B} \{ \exp[(D-B)x^+] - 1 \} \\
 + (T'_{w,2} - T'_{am}) \exp(-Dx^+) & \quad (25)
 \end{aligned}$$

and applying the L'Hôpital rule to an expression where, at  $D = B$ , the numerator and the denominator are equal to zero, one obtains

$$\begin{aligned}
 \lim_{D \rightarrow B} \frac{\exp[(D-B)x^+] - 1}{D-B} &= \lim_{z \rightarrow 0} \frac{\exp(zx^+) - 1}{z} = \lim_{z \rightarrow 0} \frac{\frac{d}{dz} [\exp(zx^+) - 1]}{\frac{dz}{dz}} = \\
 \lim_{z \rightarrow 0} \frac{x^+ \exp(zx^+)}{1} &= x^+ \\
 & \quad (26)
 \end{aligned}$$

where  $z = D - B$ .

Taking into account the relation (26) for  $D = B$  in the formula (25), i.e. for  $h_a^I = h_a^{II} = h_a$ , it takes the following form

$$\begin{aligned}
 T_{w,2}(x^+) &= T_{am}' + \{ B (T'_{w,1} - T'_{am}) [1 - \exp(-N_a^I)] x^+ + (T'_{w,2} - T'_{am}) \} \exp(-Bx^+) \\
 0 \leq x^+ \leq 1 & \quad (27)
 \end{aligned}$$

where  $N_a^I = N_a^{II} = N_a$ .

If  $h_a^I = h_a^{II} = h_a$ , then the air temperature  $T_a'''(x^+)$  after the second row of pipes is obtained with Eq. (23) after taking into account the relation (26)



$$T_a''(x^+) = T_a''(x^+, y_2^+ = 1) = T_{am}' + [1 - \exp(-N_a^I)] \times \\ \times \{ [Cx^+ + (T_{w,1}' - T_{am}') ] \exp(-Bx^+) + (T_{w,1}' - T_{am}') \exp[-(Bx^+ + N_a^I)] \} \\ 0 \leq x^+ \leq 1 \quad (28)$$

where the symbol  $C$  means

$$C = B(T_{w,1}' - T_{am}') [1 - \exp(-N_a^I)] \quad (29)$$

### 3. An analytical model of a car engine radiator

The relationships derived for the single-pass double-row PFTHE, taking into account the different HTC's on the first and second row of pipes, were used to develop an analytical mathematical model of the entire radiator, the flow diagram of which is shown in **Figure 1**. This is an engine radiator with a displacement capacity of 1600 cubic centimeters.

The constructions of coolers made of round and oval tubes are described in detail in articles [9, 10], respectively. First, the temperatures  $T_{w,1}''$  and  $T_{w,2}''$  of the liquid at the outlet from the first pass of the cooler are calculated. Then the temperature  $T_{um}$  of the liquid is calculated after mixing the liquid streams from the first and second pipe row (**Figure 1**). Water at the  $T_{um}$  temperature feeds the second pass of the automobile radiator with the water mass flow rate  $\dot{m}_w$  divided into two equal parts  $\dot{m}_w/2$  flowing through the first and second row of pipes. The air stream flows through the entire cross-section of the radiator. The mass flow rate through the first (upper) pass is  $\dot{m}_a n_u / (n_u + n_l)$ , and the second (lower) pass is  $\dot{m}_a n_l / (n_u + n_l)$ , respectively. The symbol  $\dot{m}_a$  denotes the mass flow rate of air flowing through the radiator. The symbols  $n_u$  and  $n_l$  stand respectively for the number of pipes in the first and second pass in the first row of tubes. The numbers  $n_u$  and  $n_l$  are equal ten and nine, respectively. Thermal calculations of the first and second row of pipes in the second (lower) pass have been carried out analogously to those of the first and second row in the first (upper) pass.

The thermal conductivity of aluminum tubes and fins was assumed to be  $k_w = k_f = 207 \text{ W/(m}\cdot\text{K)}$ .

### 4. Heat transfer correlations on the air-side

Based on CFD modeling performed in ANSY-CFX, the air-side heat transfer coefficient values were determined. The paper [19] provides a description of the method for determining the correlations for the average Nusselt number in the first and second row of pipes and for the entire cooler.

Nusselt number correlations for PFTHE from oval and round pipes are given below:

- oval pipe radiator

$$\text{Nu}_a^I = 30.7105 \text{Re}_a^{-0.24} \text{Pr}_a^{1/3} \quad 150 \leq \text{Re}_a \leq 330 \quad (30)$$

$$\text{Nu}_a^{II} = 0.0744 \text{Re}_a^{0.7069} \text{Pr}_a^{1/3} \quad 150 \leq \text{Re}_a \leq 330 \quad (31)$$

$$\text{Nu}_a = 1.0605 \text{Re}_a^{0.2974} \text{Pr}_a^{1/3} \quad 150 \leq \text{Re}_a \leq 330 \quad (32)$$

The Reynolds number on the air-side can be determined by knowing the hydraulic diameter and the air velocity in the smallest flow area. The hydraulic diameter for the oval tube cooler analyzed was  $d_{ha} = 1.42$  mm. The average Nusselt number on the first row of tubes varies very little (the exponent at the Reynolds number takes small values). Hydraulically and thermally developed laminar flow is characterized by a constant Nusselt number. Because the exponent at the Reynolds number for the second row of pipes takes larger values, the phenomenon of vortices forming near the front and rear stagnation points is more visible there. The heat transfer relation (32) for the average Nusselt number in a two-row bundle is similar to the expression for the average Nusselt number on a plane surface for thermally and hydraulically developing laminar flow, for which the exponent at the Reynolds number is  $1/3$ . Formulas for determining the air-side Nusselt number for an engine radiator made of circular tubes are presented below.

- round pipe radiator

$$\text{Nu}_a^I = 1.6502 \text{Re}_a^{0.2414} \text{Pr}_a^{1/3} \quad 100 \leq \text{Re}_a \leq 525 \quad (33)$$

$$\text{Nu}_a^{II} = 0.1569 \text{Re}_a^{0.5499} \text{Pr}_a^{1/3} \quad 100 \leq \text{Re}_a \leq 525 \quad (34)$$

$$\text{Nu}_a = 0.6070 \text{Re}_a^{0.3678} \text{Pr}_a^{1/3} \quad 100 \leq \text{Re}_a \leq 525 \quad (35)$$

Analyzing formulas (33) and (34), it can be observed that the exponent at Reynolds number for the first row of circular pipes is low and equals 0.2414. This indicates the dominance of laminar flow in the first row of pipes on the air-side. In the second row of tubes, the exponent at Reynolds number is higher and equals 0.5499. There are vortices at the front and rear of the tube.

However, the average Nusselt number in the first row is higher than in the second row. This is because the inlet section is located in the gap formed by two adjacent fins, which have very high values of heat transfer coefficients at the fin surfaces. This results in a greater heat flow rate absorbed by the air in the first row than in the second row. The vortices formed near the front and rear stagnation points on the surface of the second-row tube reduce the heat transfer to a large extent. The rotating air has a temperature close to that of the fin and pipe surfaces. From the heat transfer point of view, these are dead zones.

The comparison of the heat correlations determined by CFD modeling with the correlations determined based on experimental tests was carried out for two different car radiators. The flow arrangement of both radiators is the same (**Figure 1**). The first radiator is made of round pipes and the second one of the oval pipes.

## 5. Heat transfer correlations on the liquid-side

The present chapter demonstrates that by using theoretical relationships to calculate the heat transfer coefficient on the inner surfaces of the heat exchanger tubes and the use of the air-side correlations determined by CFD modeling, very similar results to experimental HTC's can be obtained.

The proposed methodology for determining the heat-transfer coefficient will reduce the cost of experimental tests for designed heat exchangers or even eliminate them. In determining the HTC for laminar flow, Gnielinski's formulas were used [27]. For the transition and turbulent flow, the formulas proposed in [28] were used.

In the range of laminar flow regime, the average HTC along the entire length of pipe  $L_t$ , assuming that the velocity profile at the pipe inlet is flat and the liquid flow is hydraulically and thermally developing, is determined by the following relationship [27].

$$\text{Nu}_{m,q} = \left[ \text{Nu}_{m,q,1}^3 + 0.6^3 + (\text{Nu}_{m,q,2} - 0.6)^3 + \text{Nu}_{m,q,3}^3 \right]^{1/3} \quad \text{Re}_w \leq 2300 \quad (36)$$

The symbol  $\text{Nu}_{m,q,1}$  designates the average Nusselt number for the developed laminar flow

$$\text{Nu}_{m,q,1} = \frac{48}{11} = 4.364 \quad \text{Re}_w \leq 2300 \quad (37)$$

The second Nusselt number  $\text{Nu}_{m,q,2}$  represents the L ev eque solution [4] for developing flow over planar surface and  $\text{Nu}_{m,q,3}$  was derived numerically for constant liquid velocity at the tube inlet

$$\text{Nu}_{m,q,2} = 3^{1/3} \Gamma(2/3) \left( \text{Re}_w \text{Pr}_w \frac{d_{hw}}{L_t} \right)^{1/3} = 1.9530 \left( \text{Re}_w \text{Pr}_w \frac{d_{hw}}{L_t} \right)^{1/3} \quad \text{Re}_w \leq 2300 \quad (38)$$

$$\text{Nu}_{m,q,3} = 0.924 \left( \text{Re}_w \frac{d_{hw}}{L_t} \right)^{1/2} \text{Pr}_w^{1/3} \quad \text{Re}_w \leq 2300 \quad (39)$$

The Nusselt number in the transition and turbulent flow range was evaluated by Taler's relationship [28].

$$\text{Nu}_w = \text{Nu}_{m,q} \Big|_{\text{Re}_w=2300} + \frac{\frac{\xi_w}{8} (\text{Re}_w - 2300) \text{Pr}_w^{1.008}}{1.084 + 12.4 \sqrt{\frac{\xi_w}{8} (\text{Pr}_w^{2/3} - 1)}} \left[ 1 + \left( \frac{d_{hw}}{L_t} \right)^{2/3} \right] \quad (40)$$

$$2300 \leq \text{Re}_w \leq 10^6 \quad 0.1 \leq \text{Pr}_w \leq 1000, \quad \frac{d_{hw}}{L_t} \leq 1$$

The Darcy-Weisbach friction factor for turbulent flow, was calculated by the Taler formula [29]

$$\xi_w = (1.2776 \log \text{Re}_w - 0.406)^{-2.246} \quad 3000 \leq \text{Re}_w \quad (41)$$

The relationship for the friction factor in the transition region was obtained using the linear interpolation [29] between the value  $\xi_w = 64/2300 = 0.02783$  for  $\text{Re}_w = 2300$  and  $\xi_w(\text{Re}_w = 3000) = 0.04355$

$$\xi_w = 0.02783 + 2.2457 \cdot 10^{-5} (\text{Re}_w - 2300) \quad 2300 \leq \text{Re}_w \leq 3000 \quad (42)$$

The Reynolds number on the water side  $\text{Re}_w = w_w d_{hw} / \nu_w$  is based on the hydraulic diameter  $d_{hw}$ . The hydraulic diameter was  $d_{hw} = 7.06$  mm for oval tubes and  $d_{hw} = d_{in} = 6.2$  mm for circular tubes. The physical properties of the water were evaluated at the mean temperature  $\bar{T}_w = (T'_w + T''_w) / 2$ .

## 6. Experimental results

Based on the experimental testing of a car radiator made of oval and round tubes (Table 1), heat transfer correlations on the air side were determined.

Geometric data	Heat exchanger of oval pipes	Heat exchanger of round pipes
Outer tube diameter $d_o$ , mm	Maximum tube diameter $d_{o,max} = 11.82$ mm Minimum tube diameter $d_{o,min} = 6.35$ mm	$d_o = 7.2$ mm
Thickness of tube wall $\delta_w$ , mm	$\delta_w = 0.4$ mm	$\delta_w = 0.5$ mm
Height $p_1$ and width $p_2$ of the apparent fin associated with one tube, mm	$p_1 = 18.5$ mm, $p_2 = 17$ mm	$p_1 = 18.5$ mm, $p_2 = 12$ mm
Fin thickness $\delta_f$ , mm	$\delta_f = 0.08$ mm	$\delta_f = 0.08$ mm
Air-side hydraulic diameter $d_{ha}$ , mm	$d_{ha} = 1.41$ mm	$d_{ha} = 1.95$ mm
Water-side hydraulic diameter $d_{hw}$ , mm	$d_{hw} = 7.06$ mm	$d_{hw} = d_o - 2\delta_w$ $d_{hw} = 6.2$ mm

**Table 1.**  
*Geometrical data of finned tubes in the heat exchanger made of oval and round tubes.*

### 6.1 Engine cooler made of oval tubes

A detailed description of the test stand for experimental research of the engine radiator constructed from oval tubes can be found in [10]. The necessary parameters, including the exponent at Reynolds number, were determined from measured data. The air parameters during the radiator studies were as follows:

- Velocity: 0.98 m/s - 2.01 m/s
- Temperature: 11°C - 15°C

The water parameters at the cooler inlet were as follows:

- Volume flow rate: 627 l/h - 2421 l/h
- Temperature: 59.6°C - 72.2°C.

The Reynolds number on the air side ranged from 150 to 330, and the water-side Reynolds number in the first (upper) pass ranged from 2500 to 11,850. When determining the air-side heat transfer correlations, the water-side HTC was calculated using (36)–(42). The following Equation for the air-side Nusselt number  $Nu_a$  was found using the experimental data

$$Nu_a = x_1 Re_a^{x_2} Pr_a^{1/3} \quad 150 \leq Re_a \leq 330 \quad (43)$$

where the parameters  $x_1$  and  $x_2$  are

$$x_1 = 0.5162 \pm 0.0116 \quad x_2 = 0.4100 \pm 0.0041 \quad (44)$$

Numbers with a sign  $\pm$  in Eq. (44) represent half of the 95% confidence interval.

### 6.2 Engine cooler made of round tubes

A test stand description of a car radiator made of round tubes can be found in [10]. Flow and heat measurements allowed to determine the air-side heat transfer correlations. The air parameters during the radiator tests were as follows:

- Velocity: 0.74 m/s - 2.27 m/s
- Temperature: 3.6°C - 15.5°C

The water parameters at the cooler inlet were as follows:

- Volume flow rate: 300 l/h - 2410 l/h
- Temperature: 50.0°C - 72.0 °C.

The water flow regime changed from laminar to transitional and then to turbulent during testing. The air-side Reynolds  $Re_a$  number ranged from 150 to 560. The Reynolds number  $Re_{w,u}$  on the water side in the first pass of the heat exchanger varied from 1450 to 16,100 during the test. The water-side HTC in round tubes was evaluated using the relationships (36)–(42). The following Equation for the air-side Nusselt number  $Nu_a$  was obtained using the least-squares method

$$Nu_a = x_1 Re_a^{x_2} Pr_a^{1/3} \quad 225 \leq Re_a \leq 560 \quad (45)$$

Based on the 70 data series, the following values of parameters  $x_1$  and  $x_2$  were found

$$x_1 = 0.5248 \pm 0.1572 \quad x_2 = 0.4189 \pm 0.0501 \quad (46)$$

Numbers with a sign  $\pm$  in Eq. (46) represent half of the 95% confidence interval.

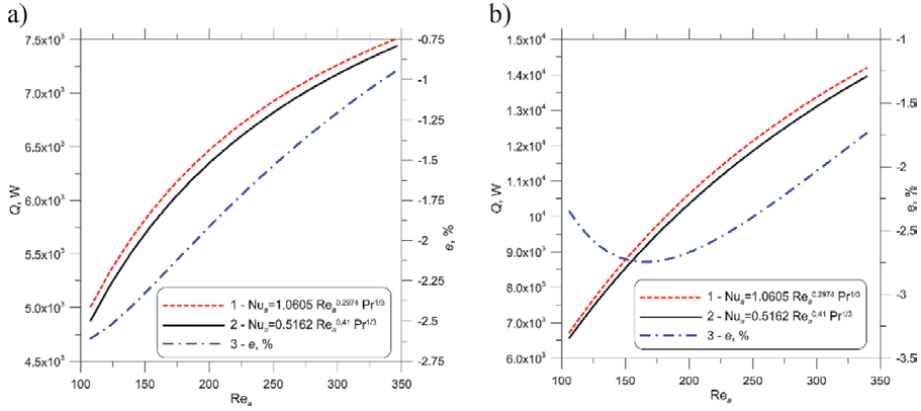
## 7. Analysis and discussion of heat flow rates from water to air transferred in the entire heat exchanger and individual rows of pipes

In the case of a radiator made of oval pipes, the results of mathematical modeling and measurements are presented as a function of the Reynolds  $Re_a$  number on the air side for two selected volume flows of water  $\bar{V}_w = 326.1$  liters/h and  $\bar{V}_w = 1273.4$  liters/h. For a car radiator built of round tubes, the results of tests and calculations are presented as a function of the Reynolds number  $Re_{w,u}$  on the water side for the first pass of the heat exchanger for the preset air velocity  $w_0$  in front of the radiator equal to 2.27 m/s.

### 7.1 Engine cooler made of oval tubes

The thermal capacity of the radiator was calculated by using an analytical mathematical model of the radiator proposed in this paper, assuming the uniform air-side HTC on both rows of pipes. **Figure 3a** shows heat flow rates calculated using the mathematical model of the PFTHE for average volumetric flow rate  $\bar{V}_w = 326.06$  liters/h, average air inlet temperature  $\bar{T}'_{am} = 13.62^\circ\text{C}$ , and average water inlet temperature  $\bar{T}'_w = 59.61^\circ\text{C}$ . The average values of  $\bar{V}_w$ ,  $\bar{T}'_{am}$ , and  $\bar{T}'_w$  were calculated based on seven measured data sets. **Figure 3b** presents heat flow rates obtained for the following data:  $\bar{V}_w = 1273.37$  liters/h,  $\bar{T}'_{am} = 14.28^\circ\text{C}$  and  $\bar{T}'_w = 60.51^\circ\text{C}$ .

The water flow in the pipes was laminar. The Reynolds number on the water-side in the first pass was between 1222 and 1287, and in the second pass between


**Figure 3.**

The heat flow rate  $Q_{w,HTC}$  from water to air in an engine cooler built with oval pipes with uniform heat transfer coefficient  $h_a$  on the air side of the whole cooler; a)  $\dot{V}_w = 326.06$  liters/h,  $\bar{T}'_{am} = 13.62^\circ\text{C}$  and  $\bar{T}'_w = 59.61^\circ\text{C}$ ; b)  $\dot{V}_w = 1273.37$  liters/h,  $\bar{T}'_{am} = 14.28^\circ\text{C}$  and  $\bar{T}'_w = 60.51^\circ\text{C}$ ; 1 - air-side equation for  $Nu_a$  based on the CFD modeling, 2 - air-side equation for  $Nu_a$  based on the experimental data, 3 - relative difference.

1358 and 1430. The velocity of the flowing air was  $w_0$ , and its values varied from 0.71 m/s to 2.2 m/s. The heat flow rates shown in **Figure 3b** were determined for the following data:  $\dot{V}_w = 1273.37$  liters/h,  $\bar{T}'_{am} = 14.28^\circ\text{C}$  and  $\bar{T}'_w = 60.51^\circ\text{C}$ . The water flow in the pipes was turbulent. The Reynolds number in the first pass of the heat exchanger on the water-side ranged from 5238 to 5440 and in the second pass from 5820 to 5883. The air velocity before the cooler varied from 0.71 m/s to 2.2 m/s. The heat transfer coefficient on the water-side was calculated using the radiator mathematical model based on Eqs. (36)–(42). The air-side HTC was calculated using Eq. (32) based on CFD simulation (Eq. 1 in **Figure 3**) or empirical Eq. (43) (Eq. 2 in **Figure 3**).

The relative difference was calculated using the expression  $e = 100(Q_2 - Q_1)/Q_2$ , where  $Q_1$  is the radiator thermal output calculated using the CFD based air-side Eq. (1) and  $Q_2$  is the radiator thermal output calculated using the empirical Eq. (2) (**Figure 3**). The analysis of the results presented in **Figure 3a** and **b** shows that the absolute value of the difference  $e$  does not exceed 2.75%. The heat flow rates based on the measurement data  $Q_{w,exp}$  and CFD simulations  $Q_{w,calc}$  were calculated as follows

$$Q_{w,exp} = \dot{V}_w \rho_w (T'_{w,exp}) \bar{c}_w (T'_{w,exp} - T''_{w,exp}) \quad (47)$$

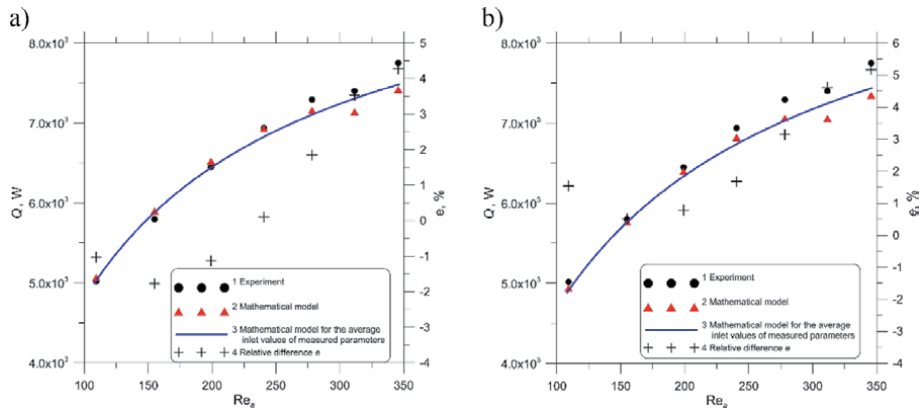
$$Q_{w,calc} = \dot{V}_w \rho_w (T'_{w,exp}) \bar{c}_w (T'_{w,exp} - T''_{w,calc}) \quad (48)$$

where:  $\bar{c}_w$  - the mean specific heat of the water in the range between the outlet  $T''_{w,exp}$  (Eq. (47)) or  $T''_{w,calc}$  (Eq. (48)) and inlet water temperature  $T'_{w,exp}$ ,  $\dot{V}_w$  - water volume flow rate measured at the car radiator inlet.

The relative difference  $e$  was calculated from the following expression

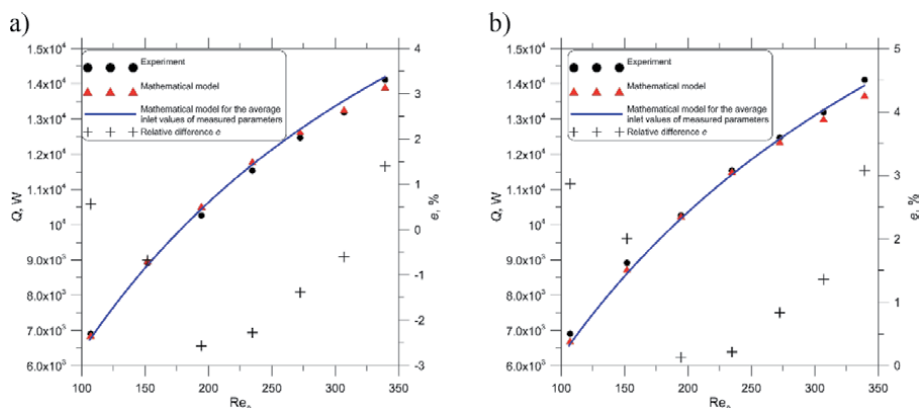
$$e = \frac{Q_{w,exp} - Q_{w,calc}}{Q_{w,exp}} 100, \% \quad (49)$$

The results of measurements and calculations of the heat transfer rate  $Q$  are shown in **Figure 4**. The results are presented for seven measurement series.



**Figure 4.** Heat transfer rate  $Q$  from hot water to air in a car radiator; 1 -  $Q_{w,exp}$  values determined using the measurement results, 2 - heat flow rate  $Q_{w,calc}$  calculated with the air-side Nusselt number  $Nu_a$  based on CFD modeling (a) or empirical correlation (b), 3 - Heat flow rate  $Q_{w,calc}$  calculated with the CFD based correlation (a) or empirical correlation (b) and the average input data from 7 measurement series:  $\bar{V}_w = 326.06$  liters/h,  $\bar{T}_{am}^I = 13.62^\circ\text{C}$  and  $\bar{T}_w = 59.61^\circ\text{C}$ , 4 - the relative difference between  $Q_{w,exp}$  and  $Q_{w,calc}$  (between 1 and 2).

Calculations were performed for averaged measurement data:  $\bar{V}_w = 326.06$  liters/h,  $\bar{T}_{am}^I = 13.62^\circ\text{C}$  and  $\bar{T}_w = 59.61^\circ\text{C}$ . The mathematical model of the car radiator was used to determine the heat flow rate  $Q$  (Entries 1 and 2). The water-side heat transfer coefficient in the radiator mathematical model used was determined with Eqs. (36–42). The water flow in the cooler tubes was laminar because the water flow rate was low. The air-side HTC was determined by Eq. (32) based on CFD modeling (**Figure 4a**) or by empirical correlation (43) (**Figure 4b**). **Figure 4** also shows the relative difference values  $e$  calculated using Eq. (49). The results presented in **Figure 4a** and **b** show an excellent agreement between the calculated and measured heat flow rates when the air-side HTC is determined using Eq. (32) based on CFD modeling.



**Figure 5.** The heat transfer rate  $Q$  from hot water to air in a car radiator; 1 -  $Q_{w,exp}$  values determined using the measurement results, 2 - heat flow rate  $Q_{w,calc}$  calculated with the air-side Nusselt number  $Nu_a$  based on CFD modeling (a) or empirical correlation (b), 3 - Heat flow rate  $Q_{w,calc}$  calculated with the CFD based correlation (a) or empirical correlation (b) and the average input data from 7 measurement series:  $\bar{V}_w = 1273.37$  liters/h,  $\bar{T}_{am}^I = 14.28^\circ\text{C}$  and  $\bar{T}_w = 60.51^\circ\text{C}$ , 4 - the relative difference between  $Q_{w,exp}$  and  $Q_{w,calc}$  (between 1 and 2).

Both when using heat transfer correlation (32) based on CFD modeling and empirical correlation (43), the relative differences  $e$  range from about (–1.5%) to about 5.2%.

**Figure 5** shows a similar comparison as in **Figure 4**, but for other averaged measurement data:  $\bar{V}_w = 1273.37$  liters/h,  $\bar{T}'_{am} = 14.28^\circ\text{C}$  and  $\bar{T}''_w = 60.51^\circ\text{C}$ . Due to the higher flow rate of water flow through a car radiator equal to  $\bar{V}_w = 1273.37$  liters/h, the flow regime of water in pipes was turbulent. The Reynolds number  $Re_{w,u}$  on the water side of the first pass pipes was between 5238 and 5440. In the lower pass, the Reynolds number  $Re_{w,l}$  was higher due to the smaller number of pipes and varied between 5820 and 5883.

It was found that the correlation for the air-side Nusselt number  $Nu_a$  determined for the entire double-row radiator based on CFD modeling provides a very good match between the calculated and measured heat flow rates transferred from hot water to air (**Figures 4** and **5**). Then, the heat flow rates transferred in the first and second row of pipes in both radiator passes were calculated taking into account different first and second row HTC. The following relationships were applied to calculate heat flow rates in each row of pipes in the first and second pass

$$Q_{1,jHTC} = \frac{\dot{m}_w}{2} \bar{c}_w (T'_w - T''_{w,1}) \quad j = 1, 2 \quad (50)$$

$$Q_{2,jHTC} = \frac{\dot{m}_w}{2} \bar{c}_w (T'_w - T''_{w,2}) \quad j = 1, 2 \quad (51)$$

$$Q_{3,jHTC} = \frac{\dot{m}_w}{2} \bar{c}_w (T'_{wm} - T''_{w,3}) \quad j = 1, 2 \quad (52)$$

$$Q_{4,jHTC} = \frac{\dot{m}_w}{2} \bar{c}_w (T'_{wm} - T''_{w,4}) \quad j = 1, 2 \quad (53)$$

The total heat transfer rate from the air to the water was calculated using the following Equation

$$Q_{t,jHTC} = \dot{m}_w \bar{c}_w (T'_w - T''_w) \quad j = 1, 2 \quad (54)$$

The symbols  $Q_{i,1HTC}$   $i = 1, \dots, 4$  designate the heat flow rate transferred in the specific pipe row (**Figure 1**) with the uniform HTC throughout the heat exchanger given by Eq. (32). The symbol  $Q_{i,2HTC}$   $i = 1, \dots, 4$  stands for the heat flow rate transferred in the particular row, with the different HTCs in the first and second pipe rows. The HTC in the first row was evaluated using Eq. (30) and in the second row by applying Eq. (31). If the air-side HTC is uniform in the whole heat exchanger, then in Eqs. (50)–(54)  $j = 1$  is assumed, and if the HTCs in the first and second tube row are not identical, then  $j = 2$  should be taken. The relative differences  $e_i$  between the heat flow rate with different HTCs in the first and second row of tubes and the heat flow rate with uniform HTC in the entire car radiator were also calculated

$$e_i = \frac{Q_{i,2HTC} - Q_{i,1HTC}}{Q_{i,2HTC}} \cdot 100 \quad i = 1, \dots, 4 \quad (55)$$

The relative  $e_t$  difference for the whole heat exchanger was calculated with a similar formula

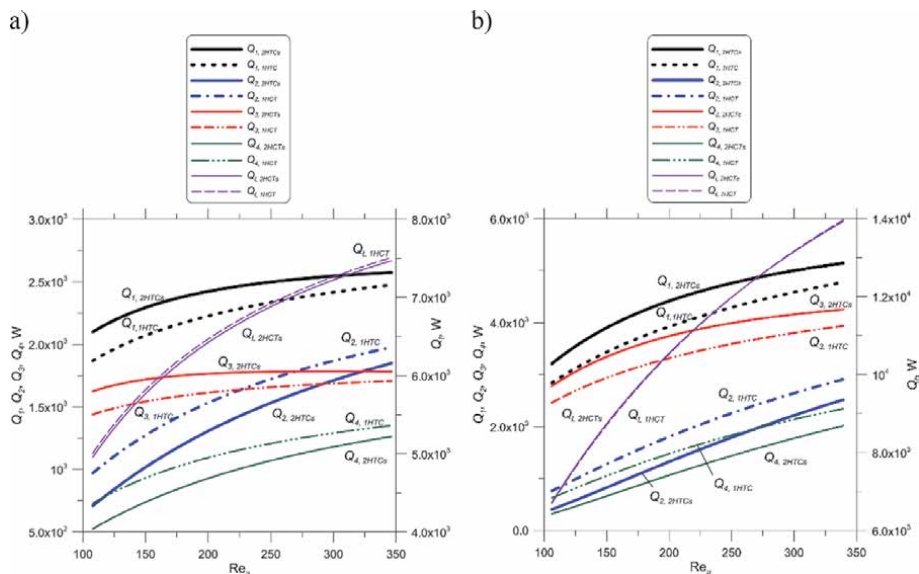
$$e_t = \frac{Q_{t,2HTC} - Q_{t,1HTC}}{Q_{t,2HTC}} \cdot 100 \quad (56)$$



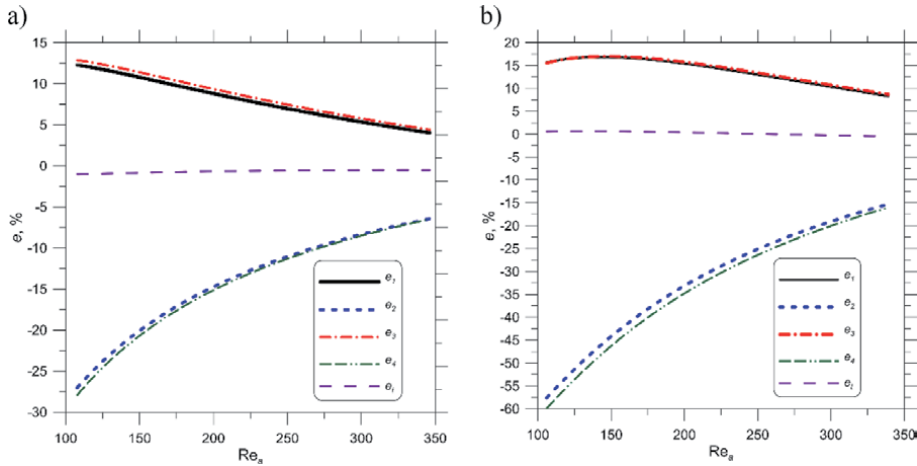
A comparison of the first and second pipe row heat flow rates in the first and second pass of the radiator and the radiator heat output for the uniform HTC throughout the radiator and different HTCs in the first and second pipe row are shown in **Figure 6a** for  $\bar{V}_w = 326.06$  liters/h and in **Figure 6b** for  $\bar{V}_w = 1273.37$  liters/h.

The results presented in **Figure 6a** and **b** show that the radiator thermal output is almost identical for the uniform HTC throughout the radiator and for different HTCs in the first and second row of tubes. As shown in **Figures 5** and **6**, the radiator capacity determined by applying a mathematical model of the car cooler using the CFD based air-side correlation for the Nusselt number is very well in line with the measurements. It can also be seen that the heat flow rates exchanged in the first row of the heat exchanger, both in first and second pass, are significantly higher for different correlations for the air-side Nusselt compared to the heat flow rates obtained assuming the same HTC in both pipe rows.

The heat capacity of the heat exchanger is almost identical with the same and different HTCs on the first and second pipe row (**Figures 5** and **6**). CFD modeling and analytical formula [19] were used to determine the air temperature increase in the entire heat exchanger. A uniform HTC for the two pipe rows was then determined from the equality condition of the calculated air temperature increases. The thermal output of the entire heat exchanger will be nearly identical with uniform and different HTCs on the first and second rows of tubes. This is because the air temperature increase on both tube rows is equal to the sum of temperature increases on the first and second tube rows.



**Figure 6.** Comparison of heat flow rates transferred from hot water to air in specific pipe row and entire PFTHE assuming that the air-side HTC is the same in both pipe rows with the corresponding heat transfer rates calculated using different HTCs in the first and second pipe rows; a)  $\bar{V}_w = 326.06$  liters/h,  $\bar{T}_{am} = 13.62^\circ\text{C}$  and  $\bar{T}_w = 59.61^\circ\text{C}$ , b)  $\bar{V}_w = 1273.37$  liters/h,  $\bar{T}_{am} = 14.28^\circ\text{C}$  and  $\bar{T}_w = 60.51^\circ\text{C}$ ;  $Q_{i,1HTC}$ ,  $i = 1, \dots, 4$  - heat flow rates transferred in specific pipe rows (**Figure 1**) assuming the same correlation (32) for the air-side Nusselt number,  $Q_{i,2HTC}$ ,  $i = 1, \dots, 4$  - heat flow rate transferred in individual pipe rows (**Figure 1**) considering different correlations for the air-side Nusselt number, Eq. (30) for the first tube row and Eq. (31) for the second tube row,  $Q_{r,1HTC}$  - car radiator output for the same heat transfer correlation (32) for all rows of pipes,  $Q_{r,2HTC}$  - car radiator output for different heat transfer correlations for the first and second tube rows, Eq. (30) for the first row and Eq. (31) for the second tube row.



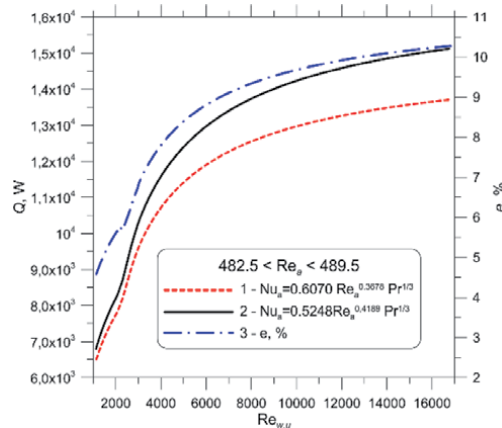
**Figure 7.** The relative differences between heat flow rates for different and uniform HTC; a)  $\bar{V}_w = 326.06$  liters/h,  $\bar{T}_{am} = 13.62^\circ\text{C}$  and  $\bar{T}_w = 59.61^\circ\text{C}$ , b)  $\bar{V}_w = 1273.37$  liters/h,  $\bar{T}_{am} = 14.28^\circ\text{C}$  and  $\bar{T}_w = 60.51^\circ\text{C}$ .

**Figure 7a** and **b** illustrate the higher heat absorption by the air in the first pipe row and the significant reduction of heat transfer in the second pipe row if different correlations for the Nusselt numbers in the first and second pipe row are taken into account compared to the respective outputs of the individual rows with a uniform HTC.

**Figure 7a** and **b** show that the more considerable differences in the exchanged heat flow through the first and second row of pipes for uniform and different HTCs are higher for the larger volume flow rate passing the cooler. The differences in the heat flow rates exchanged by the individual pipe rows with equal and different HTCs on the first and second pipe row become smaller as the air-side Reynolds number increases.

## 7.2 Engine cooler made of circular tubes

**Figure 8** depicts a comparison of the heat flow rates for the CFD based air-side correlation (35) and empirical correlation (45) for averaged measurement



**Figure 8.** The heat transfer rate  $Q_{t,HTC}$  from water to air in a car radiator made of round tubes with an equal HTC on the air side of the entire radiator as a function of the water-side Reynolds number  $Re_{w,31}$ ; 1 - air-side correlation for  $Nu_a$  based on the CFD modeling, 2 - air-side relationship for  $Nu_a$  based on the experimental data, 3 - relative difference  $e$ .

data:  $\bar{w}_0 = 2.27$  m/s,  $\bar{T}'_{am} = 8.24^\circ\text{C}$  and  $\bar{T}'_w = 70.56^\circ\text{C}$ . The volume flow rate of water  $\dot{V}_w$  at the radiator inlet varied from 309 to 2406 liters/h. The air-side Reynolds number  $Re_a$  changed from 482.5 to 489.5 and the water-side Reynolds number  $Re_{w,u}$  in the first pass of the cooler varied from 1834 to 16084.

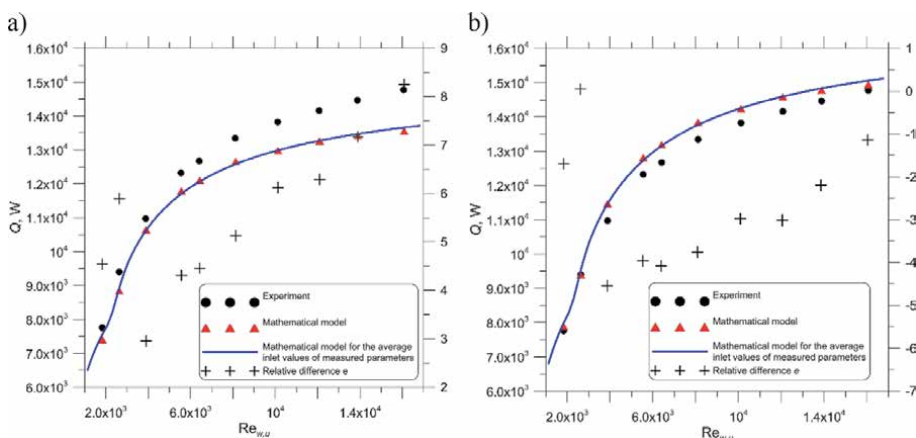
The results presented in **Figure 8** show that the capacity of the cooler constructed with round tubes calculated for the empirical correlation to the air-side Nusselt number exceeds the capacity of the cooler calculated using the correlation to the air-side Nusselt number determined by CFD modeling. The relative difference  $e$  calculated from Eq. (49) is about 5% for a water-side Reynolds number  $Re_{w,u}$  of 1800 and about 10% for a Reynolds number of 16,000 (**Figure 8**).

The relative difference  $e$  between the cooler output determined experimentally and that calculated using the mathematical model of the cooler with the air-side Nusselt number correlation obtained from CFD modeling ranges from 3% to about 8.3% (**Figure 9**). When the air-side correlation is determined experimentally, the relative difference  $e$  is smaller and ranges from  $-4$ –0% (**Figure 9b**).

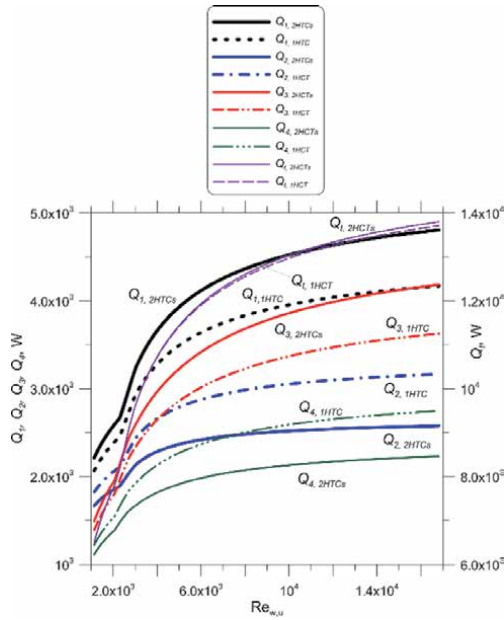
**Figure 10** shows a comparison of the heat flow rates transferred in each pipe rows assuming the same air-side heat transfer coefficient in the mathematical model of the radiator and different HTCs in the first and second tube rows.

The air in the first pipe row takes up a significantly higher heat flow rate assuming different HTCs in the first and second pipe row compared to the heat flow rate determined assuming an even HTC throughout the heat exchanger (**Figures 10 and 11**).

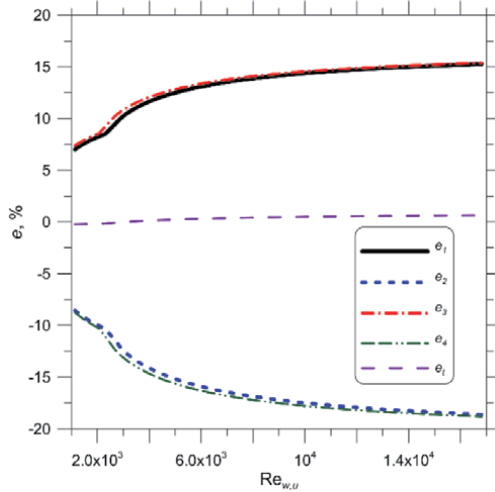
The relative differences  $e_1$  and  $e_3$  are approximately 7.5% for  $Re_{w,u}$  equal to 1000 and increase with  $Re_{w,u}$  to about 15% for the Reynolds number  $Re_{w,u}$  equal to 18,000. The relative differences of  $e_2$  and  $e_4$  are approximately  $-8\%$  for  $Re_{w,u}$  equal to 1000 and decrease with  $Re_{w,u}$  to approximately  $-18\%$  for the Reynolds number  $Re_{w,u}$  equal to 18,000. The results depicted in **Figures 10 and 11** show that the radiator thermal output is almost identical with an even HTC and different HTCs on both rows of pipes, despite the various capacities of the first and second rows of tubes.



**Figure 9.** The comparison of heat transfer rate  $Q$  from hot water to air in a car radiator as a function of the water-side Reynolds number  $Re_{w,u}$  determined experimentally and using the mathematical model of the car radiator with the uniform air-side Nusselt number  $Nu_a$  based on CFD modeling (a) and empirical correlation (b);  $e$ - relative difference.



**Figure 10.** Heat flow rates transferred from hot water to air in specific pipe row and entire car radiator assuming that the air-side HTC is the same in both pipe rows with the corresponding heat transfer rates calculated using different HTCs in the first and second pipe rows;  $\bar{w}_o = 2.27$  m/s,  $\bar{T}_{am} = 8.24^\circ\text{C}$  and  $\bar{T}_w = 70.56^\circ\text{C}$ ;  $Q_{i,1HTC}$ ,  $i = 1, \dots, 4$  - heat flow rates transferred in specific pipe rows (Figure 1) assuming the same Eq. (32) for the air-side Nusselt number throughout the radiator,  $Q_{i,2HTCs}$ ,  $i = 1, \dots, 4$  - heat flow rate transferred in individual pipe rows (Figure 1) assuming different equations for the air-side Nusselt number in the first and second tube row, Eq. (30) was used for the first tube row and Eq. (31) for the second tube row,  $Q_{r,1HTC}$  - car radiator output for the same heat transfer Eq. (32) for all rows of pipes,  $Q_{r,2HTCs}$  - car radiator output for different heat transfer equations for the first and second tube rows.



**Figure 11.** The relative differences  $e_i$  and  $e_r$  between heat flow rates for different and uniform HTCs calculated using Eq. (55) and (56);  $\bar{w}_o = 2.27$  m/s,  $\bar{T}_{am} = 8.24^\circ\text{C}$  and  $\bar{T}_w = 70.56^\circ\text{C}$ .

## 8. Conclusions

An analytical model of a two-pass car radiator with two rows of pipes was built. The use of the correlations determined by CFD modeling to calculate the air-side

heat transfer coefficient was proposed. Radiators constructed from round and oval pipes were investigated. Mathematical models of car radiators were developed, in which only one average heat transfer coefficient for the entire exchanger was used, as well as different heat transfer correlations for evaluating the air-side heat transfer coefficient on the first and second row of pipes. The use of the proposed heat exchanger calculation method will allow designing a heat exchanger with the optimum number of tube rows. Taking into account different heat transfer coefficients on each row of tubes in the calculations also allows for a more accurate calculation of the thermal output of individual rows of tubes.

The water flow regime in the tubes may be laminar, transitional, or turbulent. The results of the calculations of both tested car radiators were compared with experimental data. The compatibility of calculation and measurement results is very good. The presented method of calculating plate-fin-and-tube-heat exchangers is attractive because of eliminating costly experimental research necessary for the experimental determination of the heat transfer correlations on the air and water side.

### **Conflict of interest**

The authors declare no conflict of interest.

### **Author details**

Dawid Taler, Jan Taler\* and Marcin Trojan  
Department of Energy, Faculty of Environmental Engineering, Cracow University of Technology, Cracow, Poland

\*Address all correspondence to: [jan.taler@pk.edu.pl](mailto:jan.taler@pk.edu.pl)

### **IntechOpen**

---

© 2021 The Author(s). Licensee IntechOpen. This chapter is distributed under the terms of the Creative Commons Attribution License (<http://creativecommons.org/licenses/by/3.0>), which permits unrestricted use, distribution, and reproduction in any medium, provided the original work is properly cited. 

## References

- [1] Shah RK, Sekulic DP Fundamentals of heat exchanger design. Hoboken, New Jersey, USA: Wiley 2003.
- [2] Kakaç S, Liu H, Pramuanjaroenkij A, Heat Exchangers. Selection, Rating, and Thermal Design. 3rd ed., Boca Raton, USA: CRC Press-Taylor and Francis Group 2012.
- [3] Kuppan T, Heat exchanger design handbook. 2nd ed., Boca Raton, USA: CRC Press Taylor and Francis Group 2013.
- [4] Taler D, Numerical modelling and experimental testing of heat exchangers. Berlin-Heidelberg: Springer 2019.
- [5] Kim NH, Yun JH, Webb RL, Heat transfer and friction correlations for wavy plate fin-and-tube heat exchangers. *J Heat Trans-T ASME* 1997; 119, 560–7. DOI: 10.1115/1.2824141.
- [6] Kim NH, Youn JH, Webb RL, Air-side heat transfer and friction correlations for plain fin-and-tube heat exchangers with staggered tube arrangements. *J Heat Trans-T ASME* 1999; 121, 662–7. DOI: 10.1115/1.2826030.
- [7] Wang CC, Hsieh YC, Lin YT, Performance of plate finned tube heat exchangers under dehumidifying conditions. *J Heat Trans-T ASME* 1997; 119, 109–19. DOI: 10.1115/1.2824075.
- [8] Halici F, Taymaz I, Gündüz M, The effect of the number of tube rows on heat, mass and momentum transfer in flat-plate finned tube heat exchangers. *Energy* 2001; 26, 963–972. DOI: 10.1016/S0360-5442(01)00048-2.
- [9] Taler D, Mathematical modelling and experimental study of heat transfer in a low-duty air-cooled heat exchanger. *Energy Conversion and Management* 2018; 159, 232–243. DOI: 10.1016/j.enconman.2018.01.018.
- [10] Taler D, Taler J, Prediction of heat transfer correlations in a low-loaded plate- fin-and-tube heat exchanger based on flow-thermal tests. *Applied Thermal Engineering* 2019; 148, 641–649. DOI: 10.1016/j.applthermaleng.2018.11.060.
- [11] Rich. DG, The effect of the number of tube rows on heat transfer performance of smooth plate fin-and-tube heat exchangers. *ASHRAE Tran Pt1* 1975; 81 (Paper no. 2345), 307–17. DOI: 10.1016/S0360-5442(01)00048-2.
- [12] Marković S, Jaćimović B, Genić S, Mihailović M, Milovančević U, Otović M, Air side pressure drop in plate finned tube heat exchangers. *International Journal of Refrigeration* 2019; 99, 24–29. DOI: 10.1016/j.ijrefrig.2018.11.038.
- [13] McQuiston FC, Parker J,D, Spitler JD, Heating, ventilating, and air conditioning analysis and design. 6th ed. Hoboken, New Jersey, USA: Wiley 2005.
- [14] Webb RL, Kim NH, Principles of enhanced heat transfer. 2nd. ed., Boca Raton, USA: CRC Press 2005.
- [15] Sun Ch, Lewpiriyawong N, Loong KL, Zeng S, Lee PS, Thermal enhancement of fin and tube heat exchanger with guiding channels and topology optimisation. *International Journal of Heat and Mass Transfer* 2018; 127 (Part C), 1001–1013. DOI: 10.1016/j.ijheatmasstransfer.2018.08.093.
- [16] Li MJ, Zhang H, Zhang J, Mu YT, Tian E, Dan D, Zhang XD, Tao WQ, Experimental and numerical study and comparison of performance for wavy fin and a plain fin with radiantly arranged winglets around each tube in fin-and-tube heat exchangers. *Applied Thermal*

- Engineering 2018; 133, 298–307. DOI: 10.1016/j.applthermaleng.2018.01.012.
- [17] Nagaosa RS, Turbulence model-free approach for predictions of air flow dynamics and heat transfer in a fin-and-tube exchanger. *Energy Convers Manage* 2017; 142, 414–425. DOI: 10.1016/j.enconman.2017.03.063.
- [18] Kearney SP, Jacobi AM, Local convective behaviour and fin efficiency in shallow banks of in-line and staggered, annularly finned tubes. *J Heat Trans –T ASME* 1996; 118, 317–326. DOI: 10.1115/1.2825847.
- [19] Taler D, Taler J, Trojan M, Thermal calculations of plate-fin-and-tube heat exchangers with different heat transfer coefficients on each tube row. *Energy* 2020; 203, Paper 117806, DOI: 10.1016/j.energy.2020.117806.
- [20] Taler D, Taler J, Trojan M, Experimental Verification of an Analytical Mathematical Model of a Round or Oval Tube Two-Row Car Radiator. *Energies* 2020; 13(13), 3399, DOI: <https://doi.org/10.3390/en13133399>
- [21] Taler D, Taler J, Wrona K, Transient response of a plate-fin-and-tube heat exchanger considering different heat transfer coefficients in individual tube rows. *Energy* 2020; 95 (117023), DOI: <https://doi.org/10.1016/j.energy.2020.117023>.
- [22] Fahmy MFM, Nabih HI, Impact of ambient air temperature and heat load variation on the performance of air-cooled heat exchangers in propane cycles in LNG plants - Analytical approach. *Energy Conversion and Management* 2016; 121, 22–35.
- [23] Liu X, Yu J, Yan G, A numerical study on the air-side heat transfer of perforated finned-tube heat exchangers with large fin pitches. *International Journal of Heat and Mass Transfer* 2016; 100, 199–207, DOI: 10.1016/j.ijheatmasstransfer.2016.04.081
- [24] Gholami A, Wahid MA, Mohammed HA, Thermal-hydraulic performance of fin-and-oval tube compact heat exchangers with innovative design of corrugated fin patterns. *International Journal of Heat and Mass Transfer* 2017; 106, 573–592.
- [25] Zeeshan M, Nath S, Bhanja D, Numerical study to predict optimal configuration of fin and tube compact heat exchanger with various tube shapes and spatial arrangements. *Energy Conversion and Management* 2017; 148, 737–752. DOI: 10.1016/j.enconman.2017.06.011.
- [26] Deepakkumar R, Jayavel S, Air side performance of finned-tube heat exchanger with combination of circular and elliptical tubes. *Applied Thermal Engineering* 2017; 119, 360–372.
- [27] Gnielinski V, Heat transfer in pipe flow, chapter G1. In *VDI Heat atlas*. 2nd. ed., Heidelberg: Springer 2010, 693–699. DOI: 10.1007/978-3-540-77877-6\_34.
- [28] Taler D, A new heat transfer correlation for transition and turbulent fluid flow in tubes. *Int J Therm Sci* 2016; 108, 108–22. DOI: 10.1016/j.ijthermalsci.2016.04.022.
- [29] Taler D, Determining velocity and friction factor for turbulent flow in smooth tubes. *Int J Therm Sci* 2016; 105, 109–22. DOI: 10.1016/j.ijthermalsci.2016.02.011.





# Numerical Investigation of Heat Transfer and Fluid Flow Characteristics in a Rectangular Channel with Presence of Perforated Concave Rectangular Winglet Vortex Generators

*Syaiful and M. Kurnia Lutfi*

## Abstract

The high thermal resistance of the airside of the compact heat exchanger results in a low heat transfer rate. Vortex generator (VG) is one of the effective passive methods to increase convection heat transfer by generating longitudinal vortex (LV), which results in an increase in fluid mixing. Therefore, this study aims to analyze the convection heat transfer characteristics and the pressure drop of airflow in a rectangular channel in the presence of a concave rectangular winglet VG on a heated plate. Numerical calculations were performed on rectangular winglet pairs vortex generators (RWP VGs) and concave rectangular winglet pairs vortex generators (CRWP VGs) with a 45° angle of attack and one, two, and three pairs of VGs with and without holes. The simulation results show that the decrease in the value of convection heat transfer coefficient and pressure drop on CRWP with three perforated VG configuration is 4.63% and 3.28%, respectively, of the three pairs of CRWP VG without holes at an airflow velocity of 2 m/s.

**Keywords:** heat transfer, pressure drop, vortex generators, vortex intensity, synergy angle

## 1. Introduction

A compact heat exchanger is a heat exchanger with a large area to volume ratio so that it has a high surface area of heat transfer to volume [1]. Compact heat exchangers are widely used in the air conditioning, refrigeration, chemical, petroleum, and automotive industries. Fin and tube heat exchanger is one type of compact heat exchanger that is often encountered. One example is the condenser in air conditioning, where air is used as a refrigerant cooling medium. However, the high thermal resistance on the airside results in a low heat transfer rate [2]. Therefore, to increase the heat transfer rate, the thermal resistance needs to be lowered by increasing the convection heat transfer coefficient [3].

The method of increasing the convection heat transfer coefficient has become an interesting thing to investigate [1]. In general, the method of increasing the convection heat transfer coefficient is divided into two, namely the active method and the passive method [4]. The active method is a method that uses external energy to increase the rate of convection heat transfer, for example, by electrostatic fields, fluid vibration, and flow pulsation [1, 5]. In contrast, the passive method is a method that does not use external energy to increase the convection heat transfer rate. Passive methods are more often used than active methods because they are simpler and more effective [6]. The increase in the convection heat transfer rate in the passive method is performed by adding an insert structure and surface modification, which results in the formation of swirl flow [4, 6].

Vortex generator (VG) is an insert that produces vortices due to the formation of swirl flow, which increases the heat transfer rate [7–9]. The vortex can be divided into two, namely the transverse vortex and the longitudinal vortex [9]. The transverse vortex has a vortex axis that is perpendicular to the main flow. Meanwhile, the longitudinal vortex has a vortex axis parallel to the main flow. Longitudinal vortices are more efficient in increasing convection heat transfer because they can improve thermal performance better than transverse vortices with the same pressure drop. Longitudinal vortex causes increased fluid mixing, boundary layer modification, and flow instability resulting in increased convection heat transfer coefficient [10].

Various studies regarding the use of VGs to improve convection heat transfer have been carried out. A. Datta et al. (2016) conducted a numerical investigation of heat transfer on a rectangular microchannel installed with VGs with angle position variations in two VGs with a Reynolds number range of 200–1100 [11]. The simulation results proved that the increase in heat transfer is directly proportional to the increase in the Reynolds number and the angle of attack of VG. Installation of angle of attack of  $30^\circ$  with Reynolds number 600 is the best combination. In addition, H. Y Li (2017) conducted an experimental and numerical study on the case of fluid flow in a pin-fin heat sink mounted with a delta winglet vortex generator (DW VGs) [12]. The study was conducted to determine the effect of Reynolds number, angle of attack of VGs, and height of VGs on convection heat transfer. The results show that the increase in the Reynolds number causes a decrease in thermal resistance resulting in an increase in the convection heat transfer coefficient. The results of these studies also indicate that the angle of attack of  $30^\circ$  is the best. Meanwhile, the optimum VGs height is  $3/2 H$ .

In 2017, H.E. Ahmed et al. conducted a heat transfer study on a triangular duct with a DWP VGs in three-dimensional modeling with nanofluid flow [13]. The simulation results showed an increase in heat transfer and pressure drop of 45.7% and  $< 10\%$  respectively due to the installation of VGs and 3%  $Al_2O_3$  nanoparticles. Overall, the use of VGs and nanofluids can improve heat transfer with lower pressure drops. In addition, Syaiful et al. (2017) conducted a numerical study of the installation of CDW VGs on rectangular channels [14]. The results showed that the increase in the heat transfer coefficient due to the installation of CDWP VGs is much better than DWP VGs. However, the use of CDWP VGs results in a higher increase in pressure drop. In general, the results showed that the increase in convection heat transfer coefficient and pressure drop due to the installation of three rows of CDW VGs are 42.2–110.7% and 180–266.9%, respectively.

Then, M. Oneissi et al. (2018) conducted a numerical study on the increase in heat transfer due to the installation of DWP VGs and inclined projected winglet pair VGs with the  $k-\omega$  turbulent model [15]. In this three-dimensional simulation, the increase in heat transfer was viewed from the distribution of the Nusselt number, the coefficient of friction, and the vortices. The simulation results showed that the inclined projected winglet pair produces 7.1% better performance in increased heat

transfer than that of the DWP VGs. Zhimin Han et al. (2018) conducted a three-dimensional simulation study of the heat transfer characteristics through the perforated rectangular type of VGs [16]. In this study, the flow velocity was varied in the Reynolds number range of 214–10,703. The simulation results showed that giving holes to VGs can reduce pressure drop. The optimal thermo-hydraulic performance was observed for VGs with a hole diameter of 5 mm.

In addition, M. Samadifar et al. (2018) studied the effect of a new type of VG with variations in the angle of attack on the increase in heat transfer in the plate-fin heat exchanger in the triangular channel [17]. Six types of VGs were used in this numerical simulation, namely rectangular VG, rectangular trapezium VG, angular rectangular VG, wishbone VG, intended VG, and wavy VGs. M. Samadifar et al. performed a numerical simulation approach with turbulent  $k-\omega$  SST modeling. The simulation results showed that rectangular VGs provide a better heat transfer increase than other VGs, with an increase of 7%. The simulation results also showed that the best VGs installation is VGs with an angle of attack of 45°. Jiyang Li et al. (2019) investigated the increase in heat transfer in finless flat-tube heat exchangers due to the installation of double triangle, triangular, and rectangular VG [18]. In modeling, VGs were installed in front of the finless heat exchanger with a distance of 1 mm so that the condensation water does not hit VGs. The results showed that VGs could disturb the thermal boundary layer so that the mixing of cold and hot air increases, which results in an increase in heat transfer performance. In addition, the results also showed that the double triangle VG increases the heat transfer coefficient by 92.3% at an air velocity of 2 m/s. The double triangle VGs increase the heat transfer coefficient by 20% greater than that of the triangular and rectangular VGs but also an increase in pressure drop.

G. Lu and X. Zhai (2019) conducted a numerical investigation of the flow characteristics through the curved VG on the fin and tube heat exchanger [19]. G. Lu and X. Zhai varied the curvature and angle of attack of VG in their research. Flow characteristics were reviewed based on several non-dimensional parameters, namely  $Nu/Nu_0$ ,  $f/f_0$  and  $R = (Nu/Nu_0)/(f/f_0)^{1/3}$  with a Reynolds number range of 405–4050. Their results showed that the best thermal-hydraulic performance was obtained for VG at a curvature of 0.25 with a value of  $R = 1.06$  at a 15° angle of attack. R.K.B. Gallegos and R.N. Sharma (2019) also conducted heat transfer experiments due to the installation of VG flapping flags on the rectangular channel [20]. Their experimental results showed that VG increases the flow instability and the turbulence rate so that the Nusselt number increases by 1.34 to 1.62 times. However, VG also causes an increase in pressure drop because of the resistance to VG. This can be identified by an increase in the friction factor, which increased by 1.39–3.56 times.

The use of VG causes an increase in thermal performance, but its use has an impact on an increase in pressure drop, which results in low hydraulic flow performance. This study discusses the effect of installing RWP VGs and CRWP VGs on thermal and hydraulic performance. Thermal performance is investigated through analysis of the field synergy angle, spanwise average Nusselt number, and convection heat transfer coefficient values. Meanwhile, the hydraulic performance is analyzed through an increased pressure drop. This study aims to determine the effect of the type of VG and the effect of giving a hole on VG on thermal-hydraulic performance.

## 2. Physical model

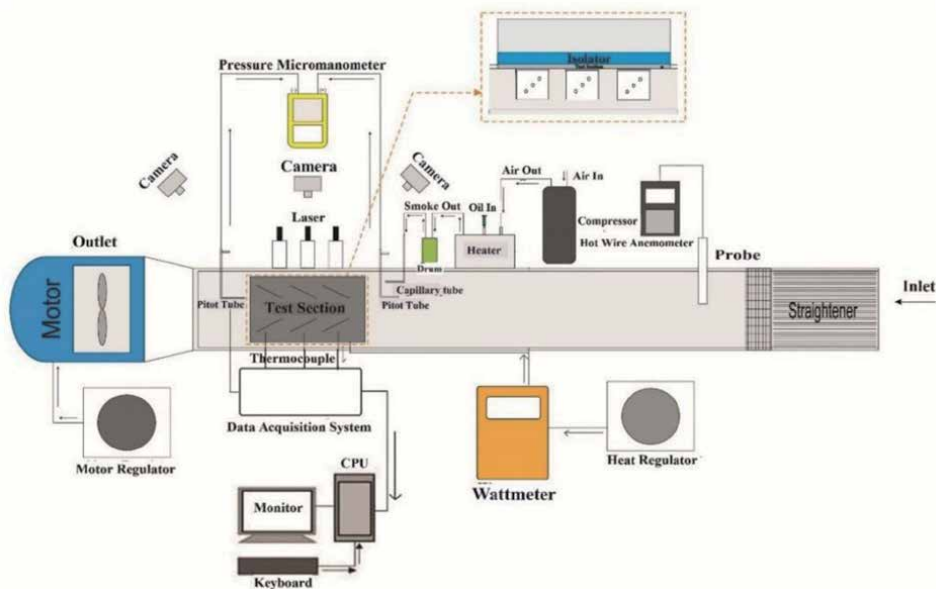
### 2.1 Experimental set-up

Experiments on the effect of VG on heat transfer and pressure drop flow were carried out in a rectangular channel made of glass with a thickness of 1 cm and a

length of 370 cm, a width of 8 cm, and a height of 18 cm, as shown in **Figure 1**. The blower sucks air into the channel from the inlet side through a straightener composed of pipes with a diameter of 5 mm and wire mesh to equalize the flow velocity. The flow velocity in the channel was varied in the range of 0.4 m/s to 2.0 m/s with an interval of 0.2 m/s using a motor regulator controlled by an inverter (Mitsubishi Electric-type FR-D700 with an accuracy of  $\pm 0.01$  Hz) and measured with a hotwire anemometer (Lutron type AM-4204 with an accuracy of  $\pm 0.05$ ). In this study, the airflow flowed through VGs with variations in the number of rows (one, two, and three rows) as well as variations with/without holes to investigate the effect on heat transfer rate and pressure drop. The VGs were mounted on a flat plate that was heated at a constant rate of 35 W using a heater that was regulated by a heater regulator and monitored by a wattmeter (Lutron DW-6060 with an accuracy of  $\pm 0.01$ ). Thermocouples K type was used to measure surface temperature, inlet and outlet temperatures, which were connected to data acquisition (Advantech type USB-4718 with accuracy  $\pm 0.01$ ) and were monitored and stored in the CPU. In the pressure drop test, two pitot tubes were installed at the inlet and outlet of the test section and connected to a micro manometer (Fluke 922 with accuracy  $\pm 0.01$ ) to monitor the pressure drop due to the installation of VGs. Flow visualization tests were also carried out to observe the longitudinal vortex formed as a result of VGs insertion. The longitudinal vortex was formed when the smoke resulting from the evaporation of oil in the heater was flowed through VGs and captured by the transverse plane formed by the luminescence of the laser beam. The camera was used to record the longitudinal vortex structure that was formed.

## 2.2 Computational model

In this study, the effects of the installation of RWP and CRWP VGs in the rectangular channel on thermal–hydraulic performance were compared. The geometry of the VG used in this study can be seen in **Figure 2**. In this simulation, VGs were made from an aluminum plate with a thickness of 1 mm with/without holes



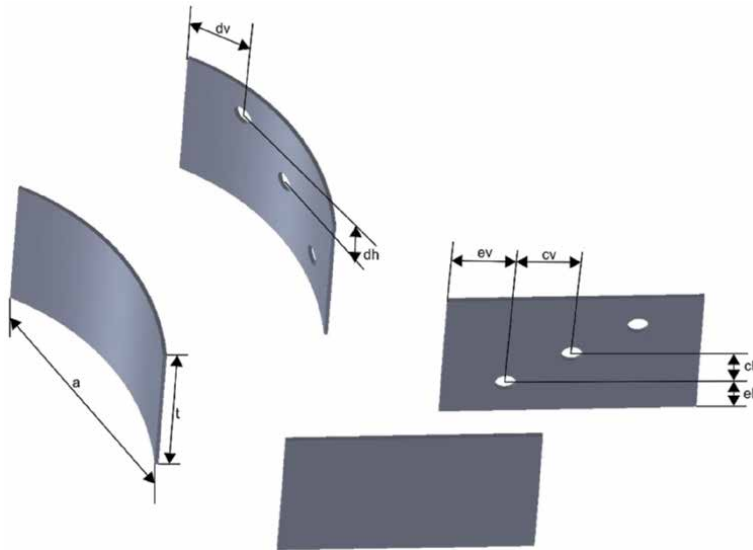
**Figure 1.**  
Schematic of experimental set-up.

with a diameter of 5 mm. **Table 1** shows the geometric parameters of the CRWP and RWP VGs. **Figure 3** is a top view of the RWP and CRWP VGs. VG with the angle of attack ( $\alpha$ )  $45^\circ$  arranged in-line in common flow-down orientation with a longitudinal pitch of 125 mm. The distance between the first row and the inlet channel is 125 mm. Meanwhile, the leading-edge transverse distance between winglet pairs VG is 20 mm. The rectangular channel modeled in this simulation has dimensions of length (P), width (L), height (H) of channels of 500 mm, 75.5 mm, 65 mm, respectively.

**Figure 4** shows the computational domain used in this modeling. This domain consists of an inlet extended region and an outlet extended region. An inlet extended region was provided to ensure that the airflow entering the channel is a fully developed flow. Meanwhile, an extended region outlet was added so that the air does not experience reverse flow in the channel.

### 2.3 Governing equations

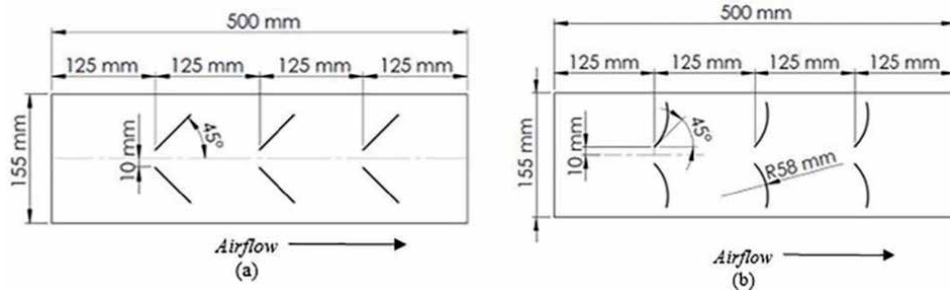
In this 3-D flow modeling, air was assumed to be steady state, incompressible and has constant physical properties. Flow can be laminar or turbulent based on its



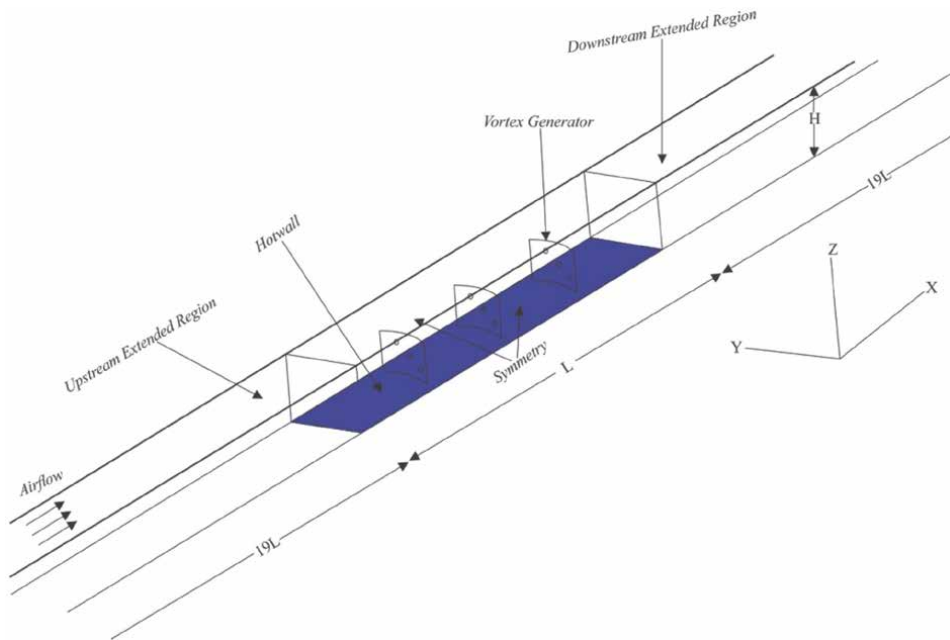
**Figure 2.**  
 Geometry of RWP and CRWP VG with and without holes.

VGs	$\alpha$ ( $^\circ$ )	a (mm)	cv (mm)	dv (mm)	ev (mm)	ch (mm)	dh (mm)	eh (mm)	t (mm)	R (mm)
CRWP without holes	45	59	—	—	—	—	—	—	40	58
CRWP with holes	45	59	15	14.56	—	—	20	9.85	40	58
RWP without holes	45	60	—	—	—	—	—	—	40	—
RWP with holes	45	60	15	—	15	20	—	10	40	—

**Table 1.**  
 Geometry parameters of vortex generator (VG).



**Figure 3.**  
Top view of (a) RWP VG, (b) CRWP VG.



**Figure 4.**  
Computational domain.

Reynolds number value. Flow velocities were set in the range of 0.4–2 m/s with 0.2 m/s intervals. The Reynolds number is determined from  $Re = \rho u_m D_h / \mu$  in the range of  $1800 < Re < 9100$ . Therefore, the flow was assumed to be laminar at a velocity of 0.4 m/s with  $Re = 1800$  and the others were turbulent. Based on these assumptions, the governing equations used to solve this case are:

Continuity equation

$$\frac{\partial u_j}{\partial x_j} = 0 \quad (1)$$

Momentum equation

$$\frac{\partial}{\partial x_j} (\rho u_i u_j) = -\frac{\partial p}{\partial x_i} + \frac{\partial}{\partial x_j} \left( \mu \frac{\partial u_k}{\partial x_i} \right) \quad (2)$$

### Energy equation

$$\frac{\partial}{\partial x_i}(\rho u_i T) = \frac{\partial}{\partial x_i} \left( \Gamma \frac{\partial T}{\partial x_i} \right) \quad (3)$$

where  $\rho$ ,  $p$ ,  $u_i$ , and  $\mu$  are the density, pressure, mean velocity on the x-axis, and dynamic viscosity, respectively. Meanwhile,  $\Gamma$  is the diffusion coefficient

$$\Gamma = \lambda / c_p$$

where  $\lambda$  is the thermal conductivity, and  $c_p$  is the specific heat of air.

The turbulent flow modeling used in this simulation is the standard  $k$ - $\omega$  model. The transport equation for the standard  $k$ - $\omega$  model consists of the turbulent kinetic energy ( $k$ ) and specific dissipation rate ( $\omega$ ) equations, respectively, which are stated as follows:

$$\frac{\partial}{\partial x_i}(\rho k u_i) = \frac{\partial}{\partial x_j} \left( \Gamma_k \frac{\partial k}{\partial x_j} \right) + G_k - Y_k + S_k \quad (4)$$

$$\frac{\partial}{\partial x_i}(\rho \omega u_i) = \frac{\partial}{\partial x_j} \left( \Gamma_\omega \frac{\partial \omega}{\partial x_j} \right) + G_\omega - Y_\omega + S_\omega \quad (5)$$

where  $\Gamma_\omega$  is the specific dissipation rate and  $\Gamma_k$  is the diffusion effectiveness of turbulence kinetic energy. The  $\Gamma_\omega$  and  $\Gamma_k$  equations are stated as follows:

$$\Gamma_\omega = \mu + \frac{\mu_t}{\sigma_\omega} \quad (6)$$

$$\Gamma_k = \mu + \frac{\mu_t}{\sigma_k} \quad (7)$$

$\sigma$  and  $\mu_t$  are the turbulent Prandtl number and turbulent viscosity, respectively. In this governing equation, the turbulent intensity can be formulated as follows:

$$I = 0.16 \Re_{D_h}^{-1/8} \quad (8)$$

### 2.4 Boundary conditions

The boundary conditions used in this computational domain are described as follows:

Inlet upstream extended region

$$u = u, v = w = 0, T = T = Const. \quad (9)$$

Outlet downstream extended region

$$\frac{\partial u}{\partial x} = \frac{\partial v}{\partial x} = \frac{\partial w}{\partial x} = \frac{\partial T}{\partial x} = 0 \quad (10)$$

Wall

$$u = v = w = 0, T = T_w \quad (11)$$

Symmetry

$$v = 0, \frac{\partial u}{\partial y} = \frac{\partial w}{\partial y} = \frac{\partial T}{\partial y} = 0 \quad (12)$$

## 2.5 Numerical method

The finite volume method (FVM) was used to analyze the thermo-hydraulic characteristics of the rectangular channel installed with VGs. Laminar flow was simulated using a laminar model, while the turbulent flow was simulated using the  $k-\omega$  model. The turbulent  $k-\omega$  model was used in this simulation because this model is suitable for modeling fluid flow in the viscous region [21]. The SIMPLE algorithm was chosen to obtain a numerical solution of the continuity and momentum equations. The governing equations for momentum, turbulent kinetic energy, specific dissipation rate and energy were discretized with a second-order upwind scheme. The convergence criterion assigned to the continuity, momentum, and energy equations was  $10^{-5}$ ,  $10^{-6}$ ,  $10^{-8}$ , respectively.

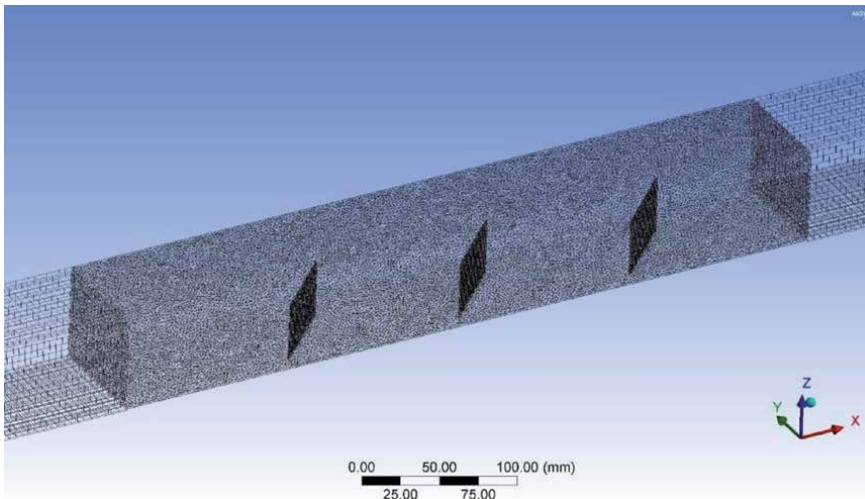
In this numerical simulation, the mesh type was differentiated between the upstream extended and downstream extended regions with the computational domain, as shown in **Figure 5**. The hexagonal mesh was used in both parts of the extended region because it has a simple geometric shape. Meanwhile, the part of the computational domain, namely the fluid and plate, uses a tetrahedral mesh because it has a more complex geometry due to the presence of VGs. The tetrahedral mesh was also used to obtain more accurate results in this area so that it can show flow separation and secondary flow in the test section.

## 2.6 Parameter definitions

The parameters used in this study are as follows:

Reynolds number

$$\Re = \frac{\rho u_m D_h}{\mu} \quad (13)$$



**Figure 5.**  
*Mesh generated.*



Nusselt number

$$Nu = \frac{hD_h}{\lambda} \quad (14)$$

where  $\rho$ ,  $u_m$ ,  $\mu$ ,  $D_h$ , and  $\lambda$  are the density, average fluid velocity, dynamic viscosity, hydraulic diameter, and thermal conductivity of the fluid, respectively.  $h$  is the convection heat transfer coefficient obtained from the following equation:

$$h = \frac{q}{A_T(T_w - T_f)} \quad (15)$$

$q$ ,  $A_T$ , and  $T_w$  are the convection heat transfer rate, heat transfer surface area, and hot wall temperature, respectively, while  $T_f$  is the bulk fluid temperature which is defined as follows:

$$T_f = \frac{T + T_{out}}{2} \quad (16)$$

$T_{in}$  is the inlet temperature and  $T_{out}$  is the temperature at the outlet side which is determined by the following equation:

$$T = \frac{\iint_A u(x, y, z)T(x, y, z)dA}{\iint_A u(x, y, z)dA} \quad (17)$$

$$T_{out} = \frac{\iint_{A_{out}} u(x, y, z)T(x, y, z)dA}{\iint_{A_{out}} u(x, y, z)dA} \quad (18)$$

$\Delta P$  is the pressure drop of fluid flow which can be formulated as  $\Delta P = P_{in} - P_{out}$  in which  $P_{in}$  and  $P_{out}$  can be described as follows:

$$P = \frac{\iint_A p dA}{\iint_A dA} \quad (19)$$

$$P_{out} = \frac{\iint_{A_{out}} p dA}{\iint_{A_{out}} dA} \quad (20)$$

## 2.7 Validation

An independent grid test was performed to ensure that the number of grids does not affect the numerical simulation results. Four different grid numbers were used for grid-independent testing. The test was carried out on the computational domain with three CRWP pairs at a velocity of 0.4 m/s. **Table 2** shows the simulation results of the variation in the number of different grids on the convection heat transfer coefficient. Because the convection heat transfer coefficient of the simulation results shows a slight difference, the optimum number of grids is determined by comparing the heat transfer coefficient from the modeling results and the results from the experiment. The smallest error from the simulation results and experimental results is used as an independent grid. Based on the comparison of the simulation results for the various numbers of grids with the experimental results, it is found that the grid with the number of elements close to 1,600,000 was chosen for use in this numerical simulation because it has the lowest error, namely 0.337%. Validation was also carried out by comparing the

Number of element	h(simulation)	h(experiment)	Error (%)
1,262,840	18.27726	18.18571	0.503
1,478,060	18.34781	18.18571	0.891
1,661,610	18.24699	18.18571	0.337
1,868,587	18.29429	18.18571	0.597

**Table 2.**  
*Grid independent test.*

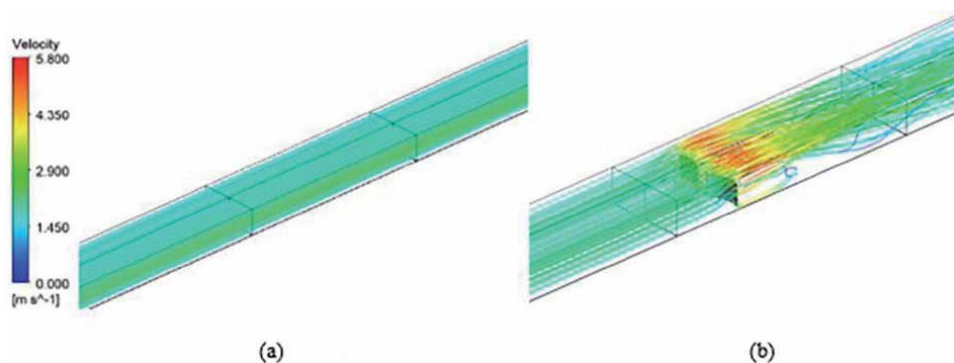
experimental results of Wu et al. (2008) and current experimental results with slightly different conditions, see Ref. [22].

### 3. Results and discussion

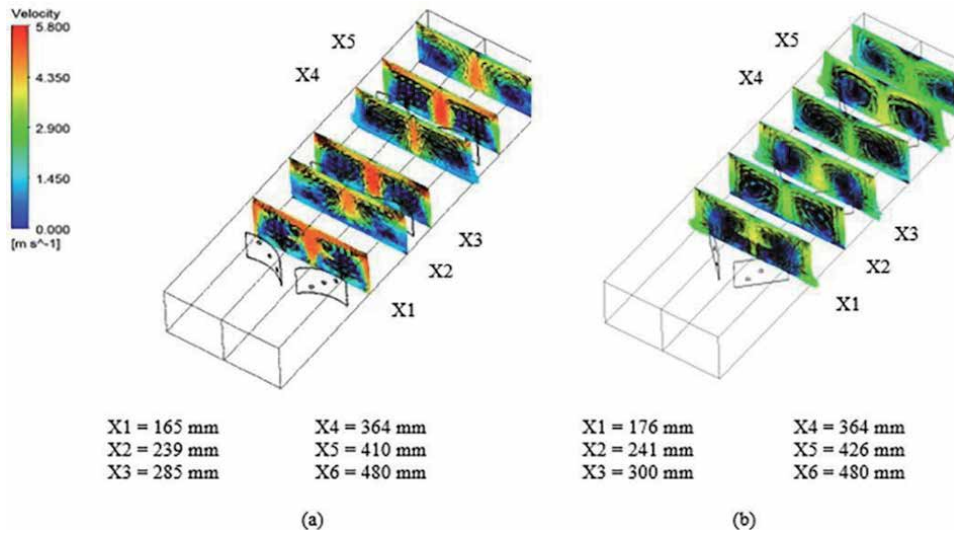
This study aims to investigate the effect of holes on VGs and the number of pairs of VGs on airflow and heat transfer characteristics. The installation of VG generates vortices and forms swirl flow so that the convection heat transfer rate on the airside increases [7–9].

#### 3.1 Flow field

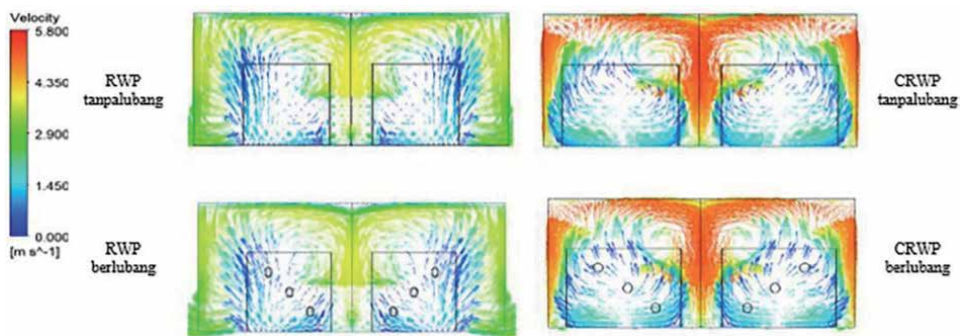
To determine the difference in flow structure in the test section, simulations were carried out on a channel with VGs and without VGs (baseline). **Figure 6(a)** is a flow in the baseline case where vortices and swirl flows are not observed. Whereas in **Figure 6(b)**, the simulation results show that the installation of VGs on the channel results in the formation of swirl flow [7], which results in longitudinal vortices due to flow separation along the VGs caused by pressure differences on the upstream and downstream VGs [10]. **Figure 7** illustrates the counter-rotating pairs of longitudinal vortices due to the installation of RVPs and CRVPs VGs with a 45° angle of attack. A strong counter-rotating longitudinal vortex forms behind the VG with the left rotating clockwise and the right rotating counterclockwise [23]. These two longitudinal vortices result in the formation of downwash flow in the center of the channel towards the lower wall of the channel and upwash flow on both sides of the channel to the upper wall of the channel. This longitudinal vortex configuration is also called common-flow-down.



**Figure 6.**  
*Velocity streamline in a channel; (a) without VG (baseline), (b) with VG.*



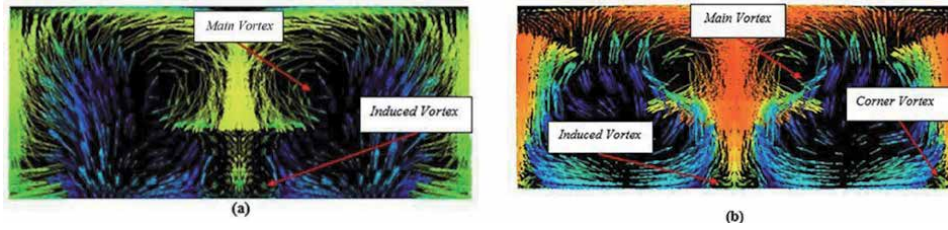
**Figure 7.**  
 Tangential velocity vector on a channel with three pairs of VG: (a) perforated CRWP and (b) perforated RWP.



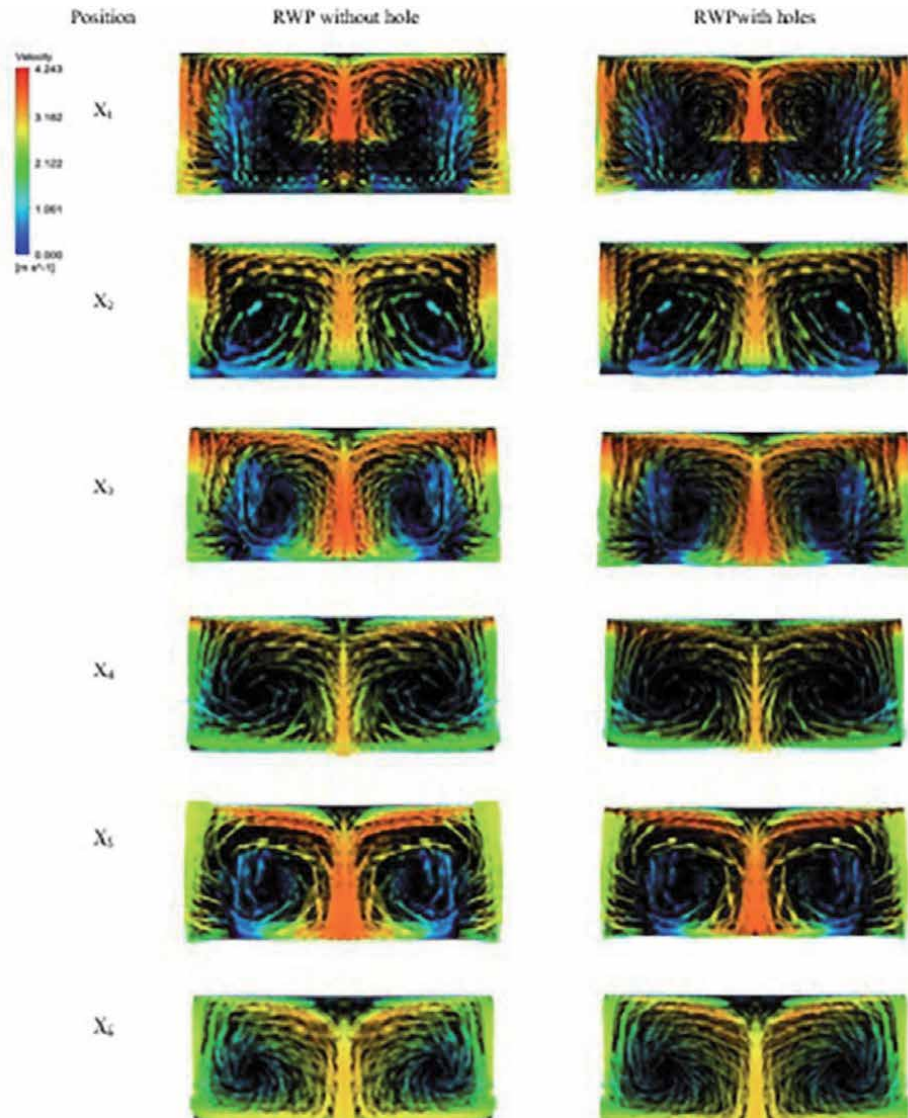
**Figure 8.**  
 Tangential velocity vector in the cross-section X1.

**Figure 8** is a comparison of tangential velocity vectors in the cross-plane X1 with three pairs of RWP and CRWP VGs for with and without holes at 2.0 m/s. The tangential velocity vector in the use of RWP and CRWP VGs is high in the down-wash region, which results in improved heat transfer [7]. In the case of CRWP VGs, the longitudinal vortex radius formed is larger than that of the RWP VGs. This is because the frontal area of the CRWP is larger, which results in a better heat transfer rate increase than that of the RWP VGs [24, 25]. The hole in VG causes a jet flow, which removes stagnant fluid in the back region of VG and increases the kinetic energy in this area so that the pressure difference before and after passing VG can be reduced [26]. Because of this decrease in the pressure difference, the longitudinal vortex strength decreases. The main vortex, induced vortex, and corner vortex are observed on CRWP VGs installation, as shown in **Figure 9**. The structure of the longitudinal vortex is formed due to several factors. The main vortex is formed due to flow separation when the flow passes through the VG wall due to the pressure difference [27]. Induced vortex is formed due to the interaction between the main vortex. Meanwhile, the corner vortex is formed as a result of the interaction between the VG wall and the main vortex.

**Figures 10** and **11** show the counter-rotating longitudinal vortex as the flow passes through the VGs. Counter-rotating longitudinal vortices are observed in the



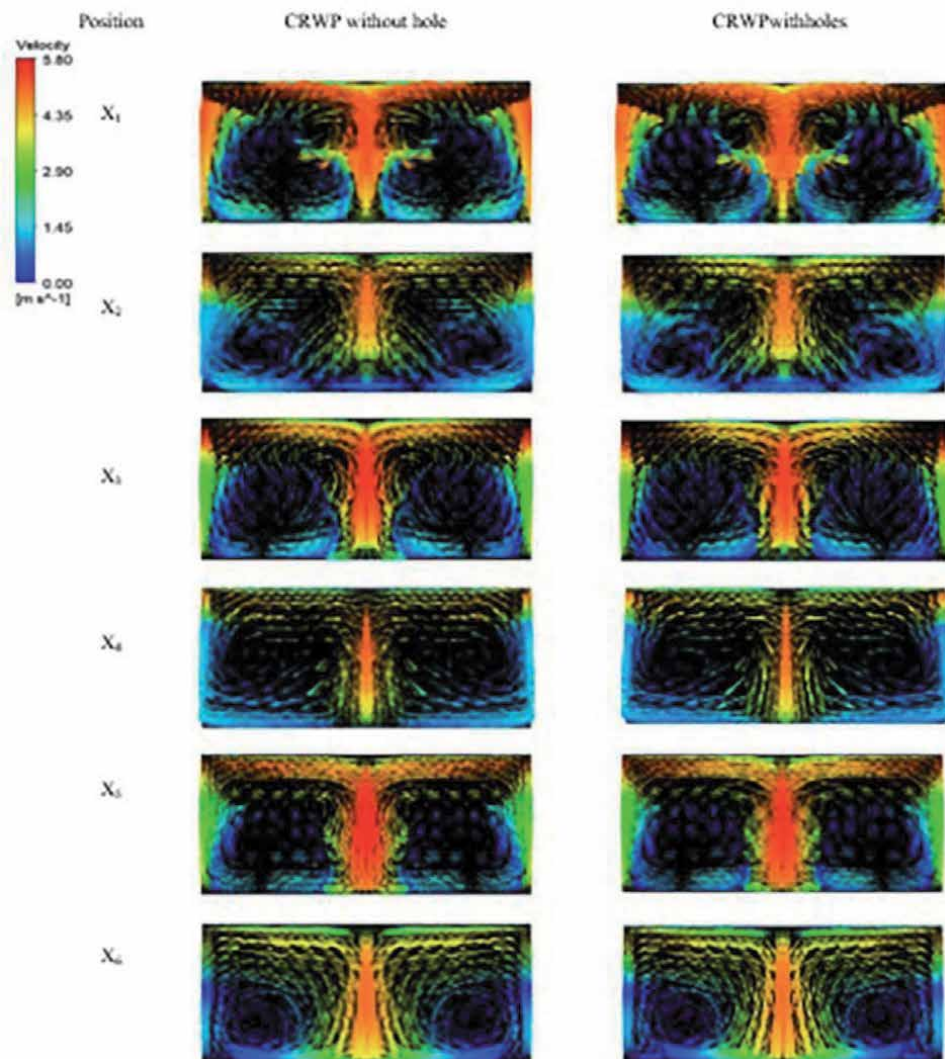
**Figure 9.** Tangential velocity vector in the cross-section  $X_1$  in the channel installed VG: (a) perforated RWP, (b) perforated CRWP.



**Figure 10.** Comparison of the tangential velocity distribution in the channel installed RWP at several cross-section positions at a velocity of 2.0 m/sec.



cross-sectional plane at positions X1 to X6 and move spirally downstream to a certain distance and sweep towards the lower wall of the channel [26]. The strength of the longitudinal vortex is observed to be greater in CRWP than in RWP. CRWP has greater longitudinal vortex strength because CRWP has a larger frontal area than that of RWP, which results in a larger longitudinal vortex radius causing in better heat transfer performance [19]. From **Figures 10** and **11**, it is observed that the longitudinal vortex in the X1 plane is stronger than that in the X2 plane for all types of VG with/without holes. This is due to viscous dissipation, which causes the longitudinal vortex to gradually weaken as the flow away from VG [28]. In the X3 plane, the longitudinal vortex strength increases compared to the X2 plane due to the addition of VGs, which results in an increase in fluid velocity in the downwash region [29]. The hole in the VG results in the weakening of the longitudinal vortex strength due to jet flow formation [26].



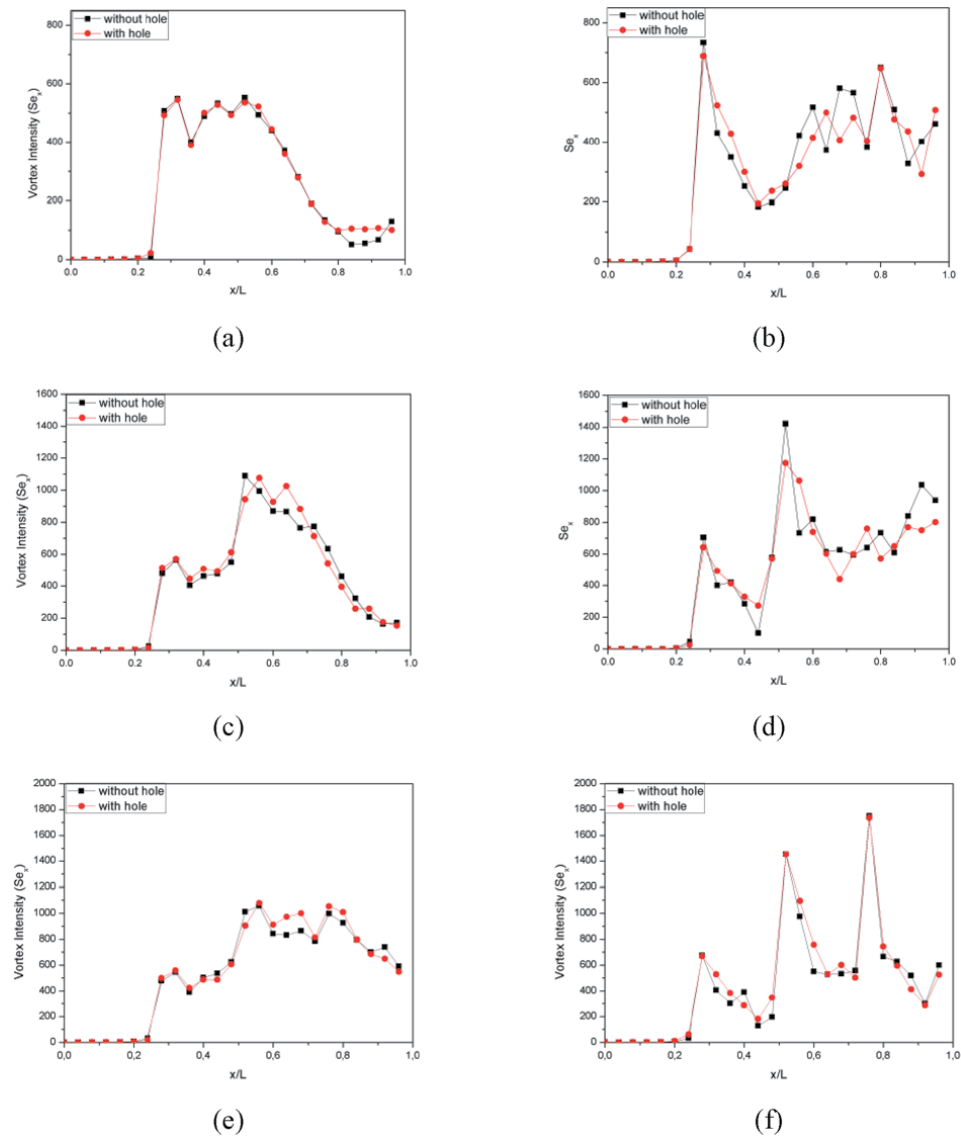
**Figure 11.** Comparison of the tangential velocity distribution in the channel installed CRWP at several cross-section positions at a velocity of 2.0 m/sec.

### 3.2 Longitudinal vortex intensity

The longitudinal vortex intensity is a dimensionless number studied by K Song et al. [30] and represents the magnitude of the inertia force induced by secondary flow to the viscous force. In this study, the longitudinal vortex intensity is defined in Eq. (22)

$$Se = \frac{\rho D_h U}{\mu} \quad (21)$$

where  $Se$  is the longitudinal vortex intensity, and  $U$  is the secondary flow velocity characteristic, which can be formulated in the following equation:



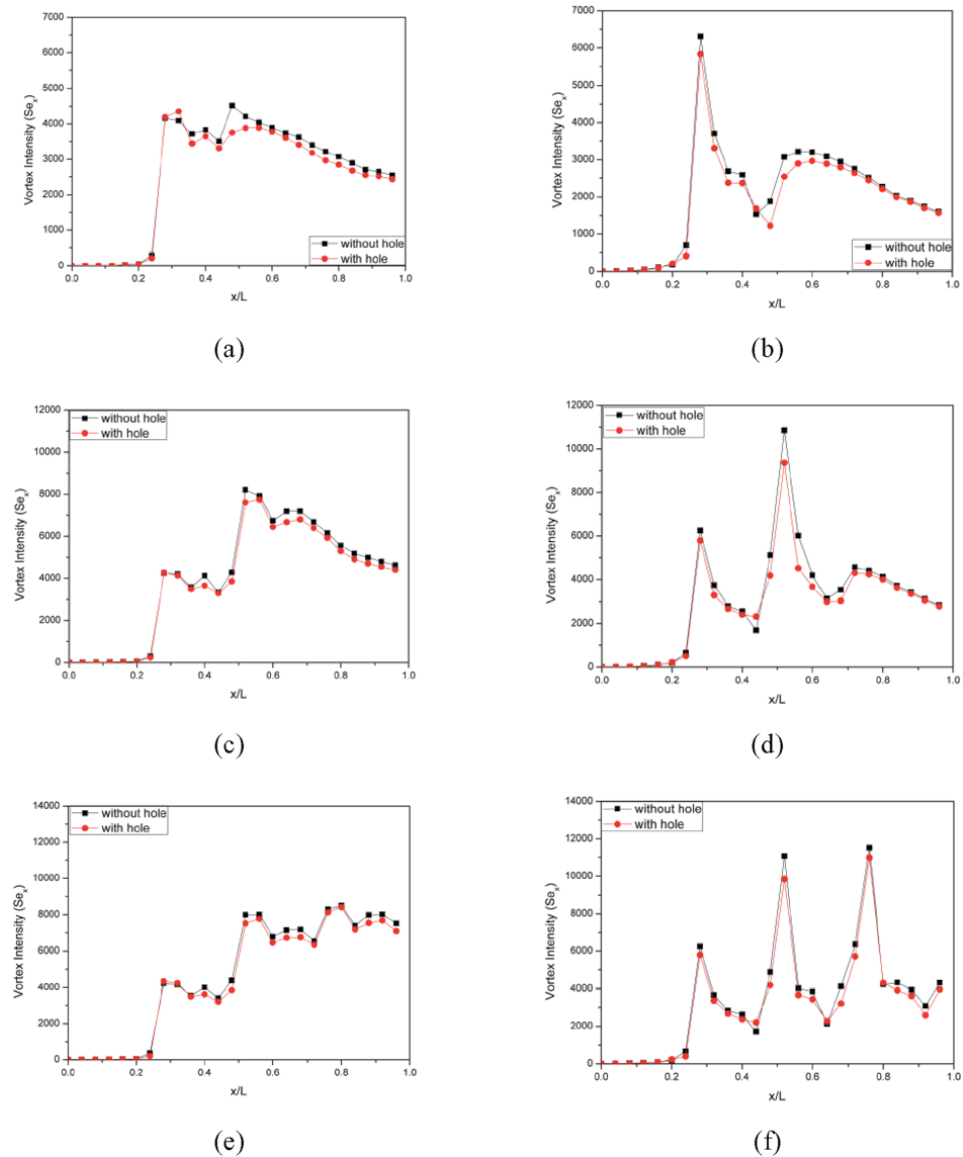
**Figure 12.** The mean spanwise longitudinal vortex intensity at a velocity of 0.4 m/s for the case of (a) one-pair RWP; (b) one-pair of CRWP; (c) two pairs RWP; (d) two-pairs CRWP; (e) three pairs RWP; (f) three-pairs CRWP.

$$U = D_h |\omega^n| = D_h \left| \frac{\partial w}{\partial y} - \frac{\partial v}{\partial z} \right| \quad (22)$$

where  $\omega^n$  is the vortices about the normal axis of the spanwise plane. The mean longitudinal vortex intensity in the spanwise plane at position  $x$  ( $Se_x$ ) is defined by Eq. (24)

$$Se_x = \frac{\rho D_h^2}{A(x)\mu} \iint_{A(x)} |\omega^n| dA \quad (23)$$

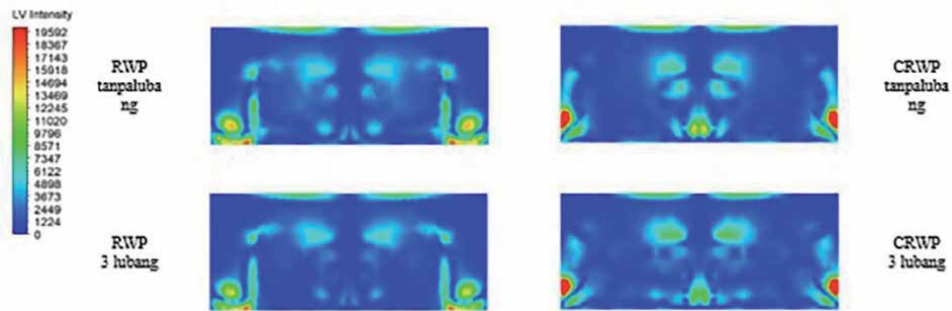
Figures 12 and 13 show the ratio of  $Se_x$  in RWP and CRWP cases at a velocity of 0.4 m/s and 2.0 m/s. In general, CRWP insertion produces a greater longitudinal



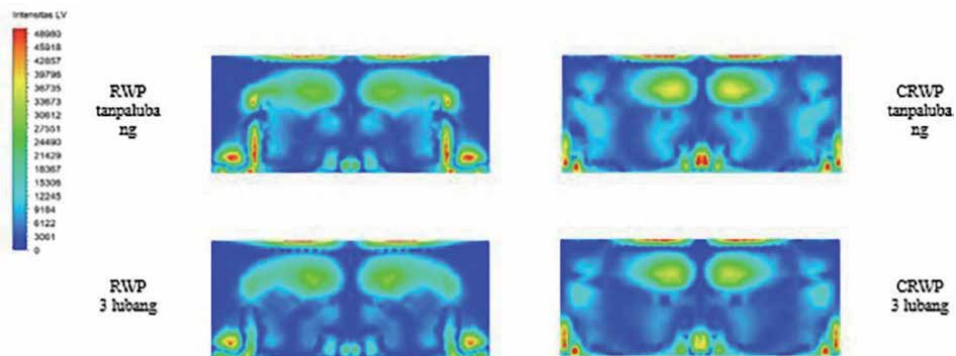
**Figure 13.** The mean spanwise longitudinal vortex intensity at a velocity of 2.0 m/s for the case of (a) one-pair RWP; (b) one-pair of CRWP; (c) two pairs RWP; (d) two-pairs CRWP; (e) three pairs RWP; (f) three-pairs CRWP.

vortex intensity than that of RWP because the frontal area of the CRWP is larger than that of the RWP and due to the instability of centrifugal force when the flow passes over the CRWP surface [19, 31]. The longitudinal distribution of the vortex intensity is shown in **Figure 14** for a velocity of 0.4 m/s and **Figure 15** for a velocity of 2.0 m/s. In the case of CRWP and RWP, the longitudinal vortex intensity tends to dissipate after passing VGs due to viscous effects [2, 26, 28]. Therefore, the installation of the second and third rows of VG reinforces the intensity of the longitudinal vortex as illustrated in **Figures 12(c)–(f)** and **Figures 13(c)–(f)** for velocities of 0.4 m/s and 2 m/s, respectively.

The hole in the VG results in a decrease in the intensity of the longitudinal vortex, as shown in **Figures 12–15**. The hole in VG causes jet flow formation, which can interfere with the generation of the longitudinal vortex [26]. For RWP VGs with a velocity of 2.0 m/s, the intensity of the longitudinal vortex experiences the highest decrease, namely 17% at  $x/L = 0.48$  for the case of one pair with holes, 11% at  $x/L = 0.4$  for the case of two pairs with holes and 13% at  $x/L = 0.48$  for the case of three pairs with holes of ones without holes. Meanwhile, in the case of CRWP VGs with a velocity of 2.0 m/s, the intensity of the longitudinal vortex experiences the highest decrease, namely 35% at  $x/L = 0.48$  for the case of one pair with holes, 14% at  $x/L = 0.68$  for the case of two pairs with holes and 22% at  $x/L = 0.68$  for the case of three pairs with holes compared to ones without holes.



**Figure 14.** The longitudinal vortex intensity for the case of three pairs of RWP and CRWP at locations  $x / L = 0.34$  and  $x/L = 0.32$  at a velocity of 0.4 m/s, respectively.



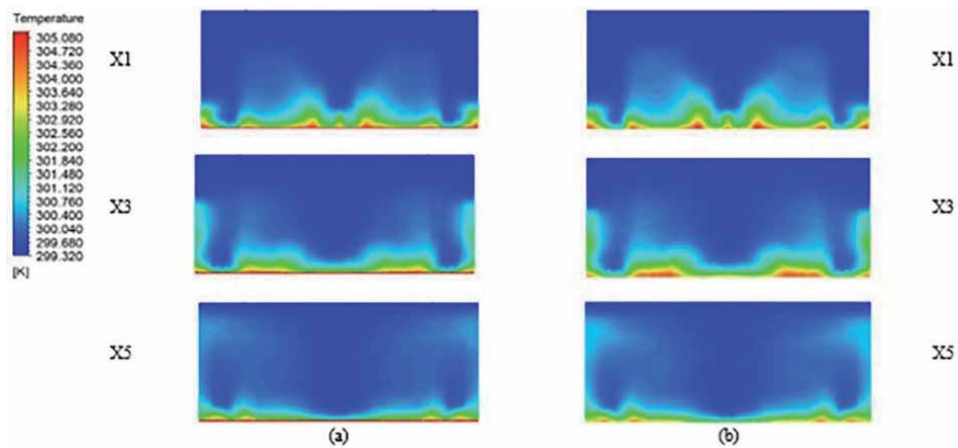
**Figure 15.** The longitudinal vortex intensity for the case of three pairs of RWP and CRWP at locations  $x / L = 0.34$  and  $x/L = 0.32$  at a velocity of 2.0 m/s, respectively.



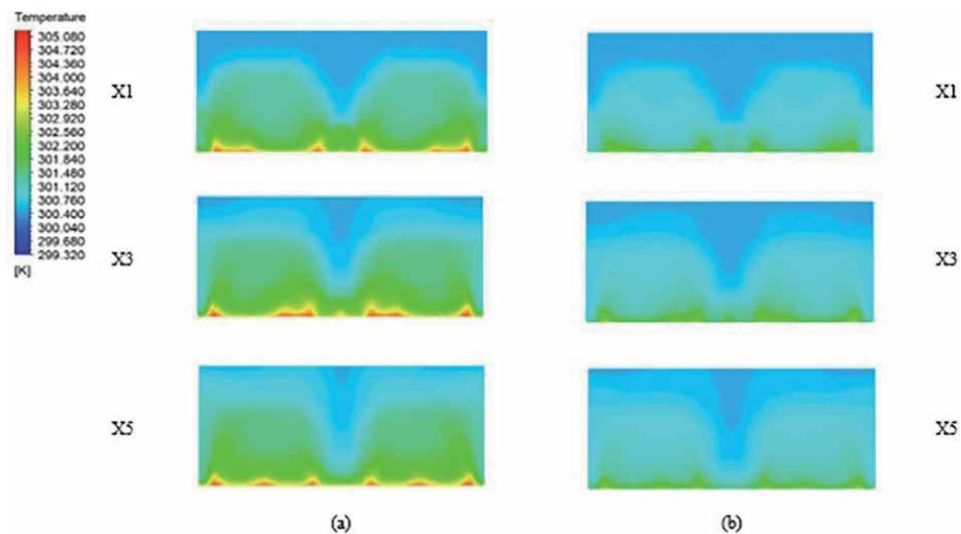
### 3.3 Temperature distribution

The temperature distribution for the RWP and CRWP cases with/without holes and the baseline in the spanwise plane at a certain position with a velocity of 2.0 m/s is shown in **Figures 16** and **17**. Visually, the temperature distribution in the channel in the presence of VG is better than the baseline. The placement of VG in the channel increases the temperature distribution due to the counter-rotating pairs of longitudinal vortices, which result in increased fluid mixing [32]. Counter-rotating pairs of longitudinal vortices produce a downwash that pushes the fluid towards the surface of the heated plate resulting in increased local heat transfer coefficients and thinning of the thickness of the thermal and dynamic boundary layers [32, 33].

Meanwhile, counter-rotating pairs of longitudinal vortices also generate upwash on the outer side of the vortex and push the hot fluid on the plate wall towards the flow-stream resulting in a decrease in the local heat transfer coefficient and a



**Figure 16.** Temperature distribution in channel with: (a) RWP without holes; (b) RWP with holes.



**Figure 17.** Temperature distribution in channel with: (a) CRWP without holes; (b) CRWP with holes.

thickening of the boundary layer as observed in **Figures 16** and **17** comparing to the baseline case, as shown in **Figure 18**. Visually, the temperature distribution in the CRWP case is more even than the temperature distribution in the RWP case. This is because CRWP produces a higher longitudinal vortex intensity than that of RWP [31]. In addition, the holes in each VG result in the formation of jet flow, which can reduce the intensity of the longitudinal vortex resulting in an increase in temperature gradient [26], as shown in **Figure 16(b)** and **17(b)**.

### 3.4 Pressure distribution

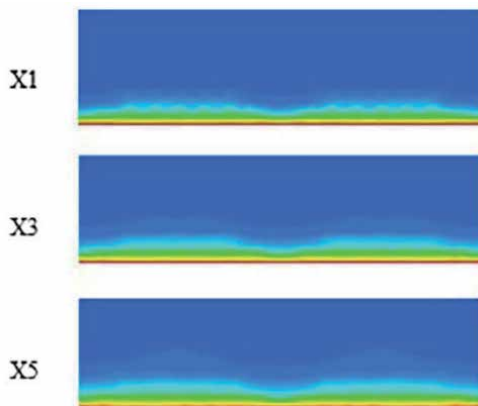
**Figure 19** shows the pressure distribution for the three-pairs RWP and CRWP cases with/without holes at a Velocity of 2.0 m/s. Installation of VG in the channel results in an increase in pressure drop due to drag generated on the flow [34, 35]. As observed in Figure 3.14, the pressure drop generated by CRWP is higher than that from RWP. This is because the frontal area of the CRWP is larger than that of the RWP, which results in a higher longitudinal vortex intensity and results in increased pressure drop [19]. A low-pressure zone is formed behind VG in the RWP and CRWP cases [26]. The hole in VG causes in the formation of jet flow, which results in a decrease in the low-pressure zone. This is because the jet flow reduces the stagnant fluid in the area behind VG and increases the kinetic energy in this area, causing the pressure difference before and after passing VG to decrease [26].

### 3.5 Mean spanwise Nusselt number

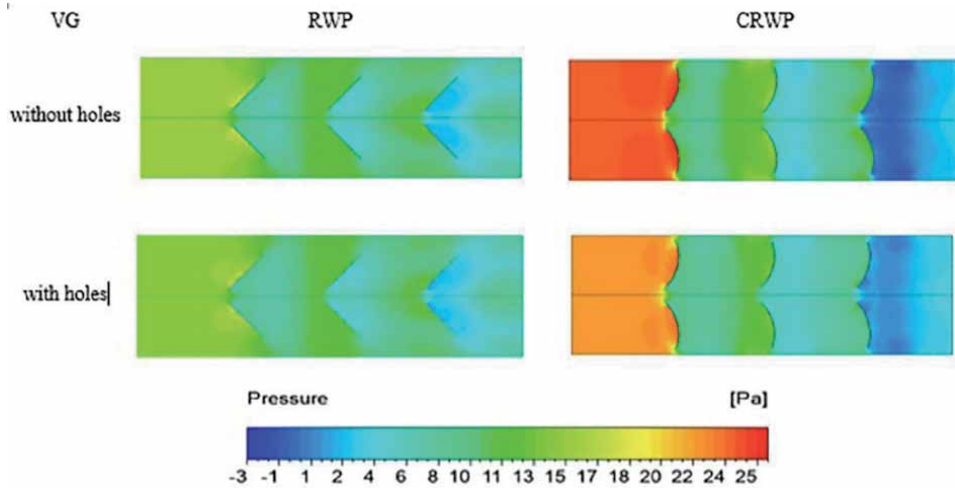
The local heat transfer improvement can be identified with the mean spanwise Nusselt number, as informed by Hiravennavar [36]. The equation used by Hiravennavar is as follows:

$$\dot{N}u_s = \frac{Bq(H/k)}{\int_0^B (T_w - T_b) dz} \quad (24)$$

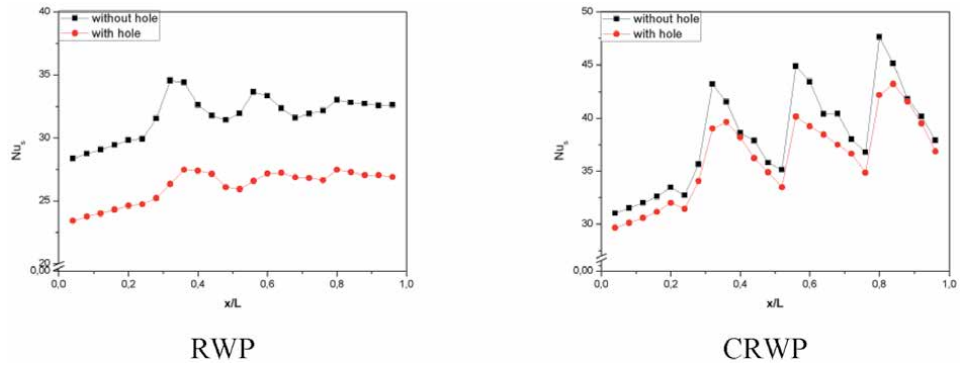
where  $B$ ,  $q$ ,  $H$ , and  $k$  are channel width, heat flux, channel height, and fluid thermal conductivity, respectively. Meanwhile,  $T_w$  and  $T_b$  are the wall temperature and bulk fluid temperature, respectively.



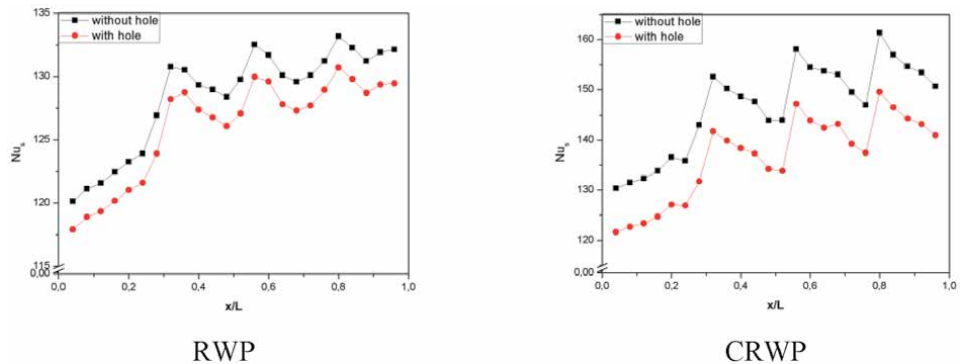
**Figure 18.**  
Temperature distribution in the channel without VG (baseline).



**Figure 19.**  
 Comparison of the pressure distribution at  $z = 0.41H$ .



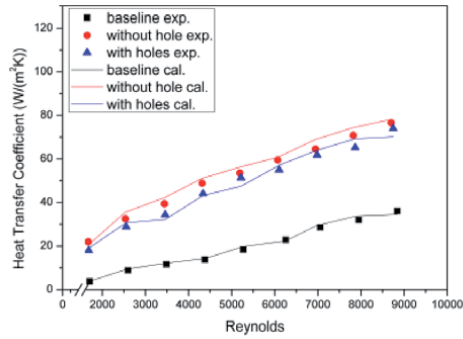
**Figure 20.**  
 Average spanwise Nusselt numbers the RWP and CRWP at a velocity of 0.4 m/s.



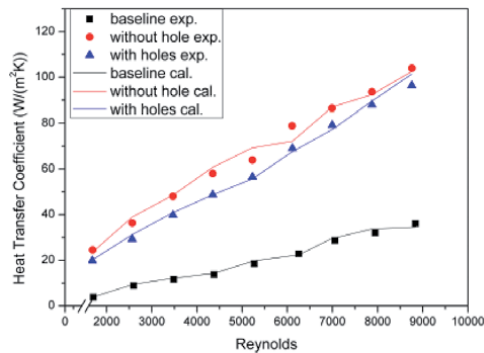
**Figure 21.**  
 Average spanwise Nusselt numbers the RWP and CRWP at a velocity of 2.0 m/s.

**Figures 20 and 21** compare the mean spanwise Nusselt numbers in the RWP and CRWP cases at velocities of 0.4 m/s and 2.0 m/s. The use of VG in the channel increases the Nusselt number [30]. **Figures 20 and 21** show that the mean spanwise Nusselt number in the CRWP case is higher than that in the RWP case. This is

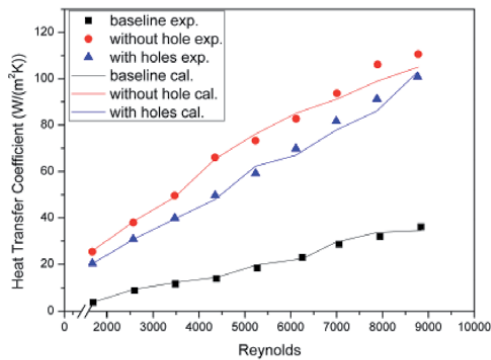
because the longitudinal vortex intensity generated by the CRWP is stronger than that of the RWP. The holes in VG result in a decrease in the mean spanwise Nusselt number because the holes in VG reduce the intensity of the longitudinal vortex [16]. The highest decrease of the average spanwise Nusselt number in perforated RWP and CRWP at a velocity of 0.4 m/s was 24% at  $x/L = 0.32$  and 11% at  $x/L = 0.56$  of VG without holes, respectively. Whereas for the same case at a velocity of 2.0 m/s, the highest reduction is 2% at  $x/L = 0.8$  and 7% at  $x/L = 0.32$ , respectively.



(a)



(b)

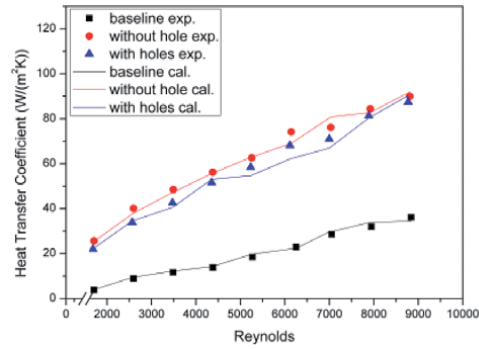


(c)

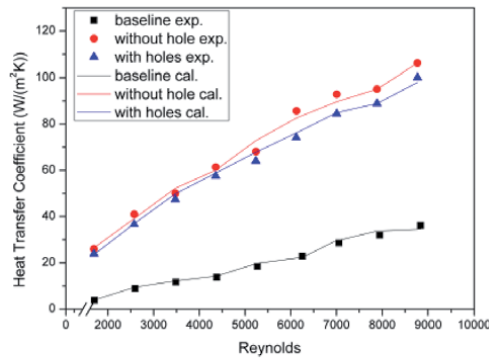
**Figure 22.** Comparison of the convection heat transfer coefficient on RWP with and without holes for installation: (a) one, (b) two, and (c) three pairs.

### 3.6 Convection heat transfer coefficient

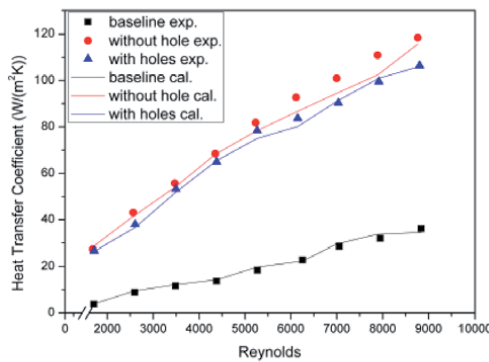
Figures 22 and 23 show the comparison of the heat transfer coefficient values due to the installation of RWP and CRWP. In general, the convection heat transfer coefficient increases with increasing Reynolds number. From Figures 22 and 23, it is found that the convection heat transfer coefficient with the CRWP installation is higher than that of the RWP. This is because CRWP produces a stronger



(a)



(b)

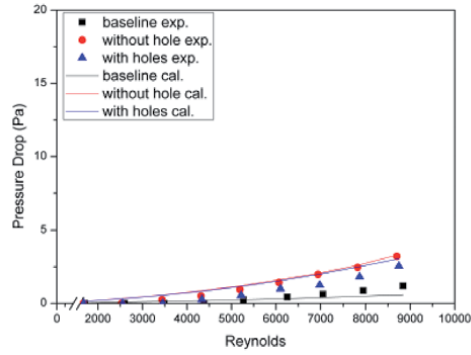


(c)

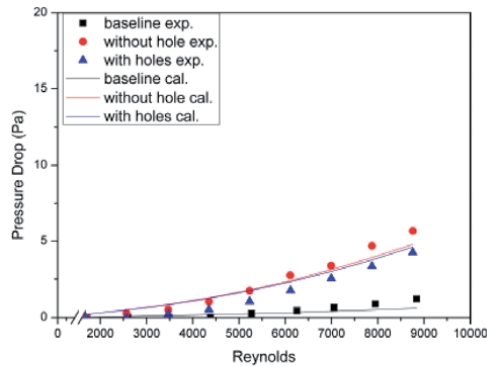
Figure 23. Comparison of the convection heat transfer coefficient on CRWP with and without holes for installation: (a) one; (b) two, and (c) three pairs.

longitudinal vortex intensity than that of RWP due to the instability of the flow as it crosses the CRWP surface [25]. The convection heat transfer coefficient in the RWP and CRWP cases with a three-pair installation configuration with holes is increased by 198% and 207%, respectively, from the baseline at the highest Reynolds number.

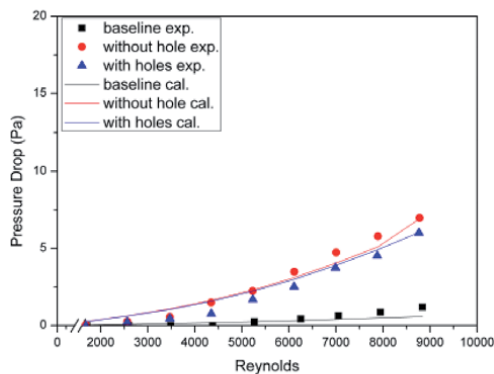
The addition of pairs of VG results in an increase in the convection heat transfer coefficient because the addition of VG pairs strengthens the longitudinal vortex



(a)



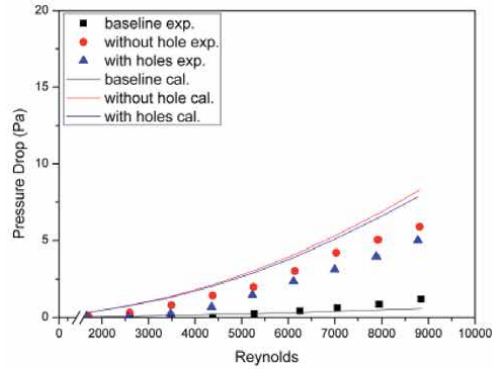
(b)



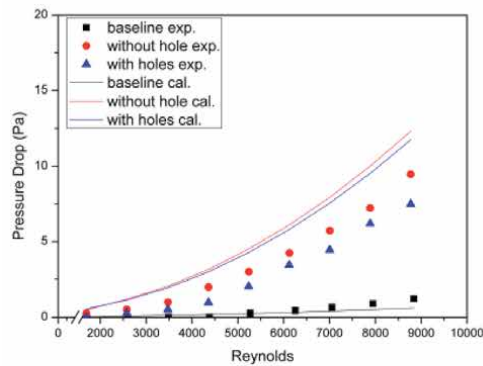
(c)

**Figure 24.** Comparison of pressure drop on RWP with and without holes for installation: (a) one; (b) two and (c) three pairs.

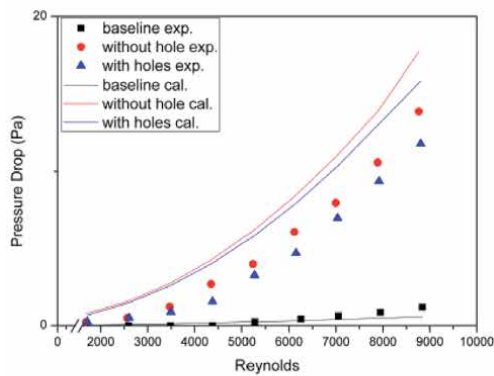
strength and interferes with the formation of boundary layers and increases fluid mixing [29]. Meanwhile, the hole in VG results in a slight decrease in the value of the convection heat transfer coefficient, as seen in **Figures 22** and **23**, because the holes in VG generate jet flow, which can weaken the intensity of the longitudinal vortex [26]. The decrease in the convection heat transfer coefficient at the highest



(a)



(b)



(c)

**Figure 25.** Comparison of pressure drop on CRWP with and without holes for installation: (a) one; (b) two and (c) three pairs.

Reynolds number for the perforated RWP and CRWP cases of three pairs is 2% and 8% of the without holes, respectively.

### 3.7 Pressure drop

A comparison of pressure drop between experiment and simulation for the RWP and CRWP cases is observed in **Figures 24** and **25**, respectively. From the two figures, it is found that the pressure drop for all cases increases with increasing Reynolds number. The main reason is the increase in the drag generated with increasing flow velocity [14]. Installation of RWP and CRWP in the channel results in an increase in pressure drop due to the drag formed on the flow. The pressure drop due to CRWP insertion is higher than RWP because CRWP produces a stronger longitudinal vortex than RWP [37]. For the perforated RWP case, the increase in pressure drop with variations of one, two, and three pairs at the highest Reynolds number is 4.26 times, 8.98 times, and 9.96 times, respectively, from the baseline. Meanwhile, for the perforated CRWP case with the highest Reynolds number in the same case, it is 12.52 times, 19.27 times, and 26.31 times from the baseline. The hole in VG causes a decrease in the pressure drop value because the hole in VG reduces fluid resistance due to the longitudinal vortex [31]. The highest reduction in pressure drop due to the hole in the RWP with variations of one, two, and three pairs is 7%, 4%, and 13%, respectively. On the other hand, the decrease in pressure drop on CRWP with the highest Reynolds number for the same case is 5%, 5%, and 11%, respectively.

### 3.8 Field synergy principle (FSP)

FSP is a method for analyzing improvement in heat transfer rate, which was informed by Guo et al. [38]. In their study, Guo et al. define the increase in the rate of heat transfer by decreasing the angle of the intersection of the velocity vector and the temperature gradient. The energy conservation equation used by Guo et al. in their research are as follows:

$$\rho C_p \int_0^{\delta_t} (U \cdot \nabla T) dy = -\lambda \frac{\partial T}{\partial y} \quad (25)$$

where  $\rho$ ,  $C_p$ , and  $\lambda$  are assumed to be constant so that the dimensionless form of Eq. (25) is

$$\mathfrak{R}_x Pr \int_0^1 (\dot{U} \cdot \nabla T) dy = Nu_x \quad (26)$$

where  $\dot{U} = U/U_\infty$ ,  $\nabla T^* = \frac{\nabla T}{(T_\infty - T_w)/\delta_t}$ ,  $y = y/\delta_t$ .  $U_\infty$  and  $T_\infty$  are the velocity and temperature of the fluid in the free stream region, respectively. Meanwhile,  $\delta_t$  is the thickness of the thermal boundary layer. Vector dot product,  $\dot{U} \cdot \nabla T$ , in Eq. (26) can be described as follows:

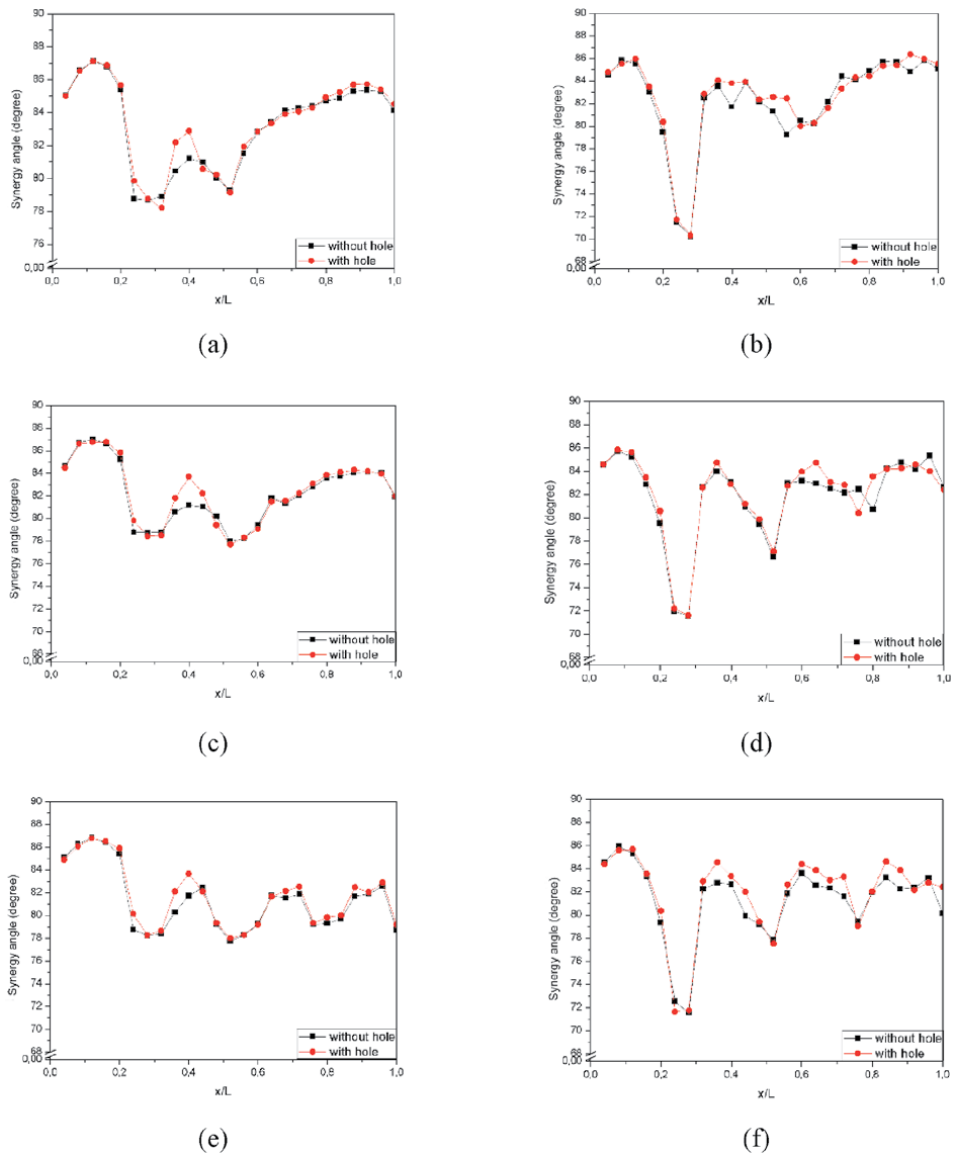
$$\dot{U} \cdot \nabla T = |\dot{U}| |\nabla T| \cos\beta \quad (27)$$

where  $\beta$  is the angle between the velocity vector and the temperature gradient. Thus, Eq. (27) can be written as follows:



$$\beta = \cos^{-1} \left( \frac{\dot{U} \cdot \nabla T}{|\dot{U}| |\nabla T|} \right) \quad (28)$$

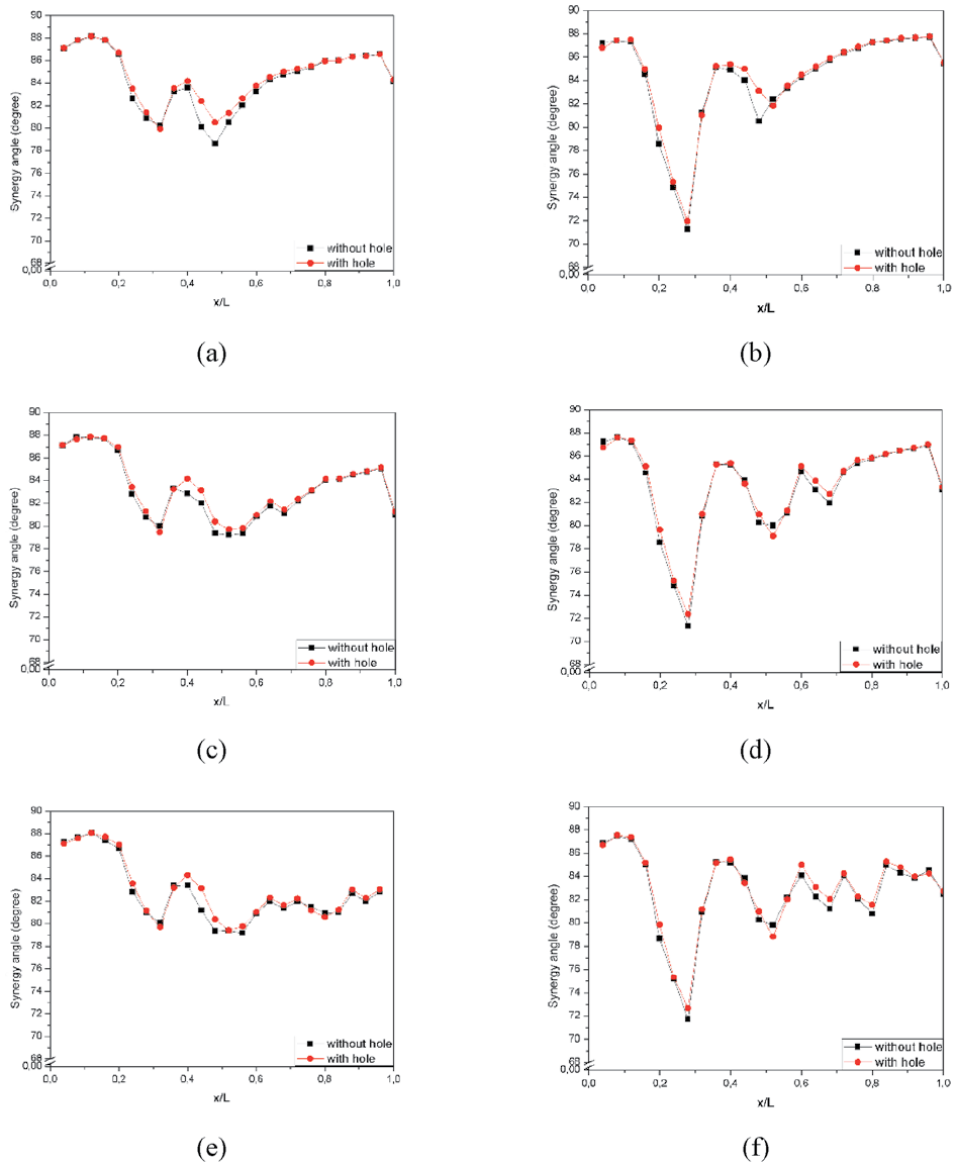
**Figures 26** and **27** illustrate the local synergy angle in the RWP and CRWP cases, respectively, with speeds of 0.4 m/s and 2.0 m/s. In general, inserting VG in the channel reduces the synergy angle because VG generates a longitudinal vortex [39]. The longitudinal vortex alters the flow and temperature fields resulting in improved heat transfer. From **Figures 26** and **27**, it can be observed that the decreased synergy angle is higher in the case of CRWP than that of RWP because the strength of the longitudinal vortex produced by CRWP is stronger than that of



**Figure 26.** Synergy angle at a speed of 0.4 m/s for the case of (a) one-pair of RWP; (b) one pair of CRWPs; (c) two pairs of RWP; (d) two-pairs of CRWP; (e) three pairs of RWP; (f) three-pairs of CRWP.

RWP [25, 40]. The lowest synergy angle in the case of three pairs of perforated RWP at a velocity of 0.4 m/s are 78.25°, 77.98°, and 79.33° at  $x/L = 0.28, 0.52,$  and  $0.76,$  respectively. Meanwhile, at velocity of 2.0 m/s, they are 81.15°, 79.42°, and 81.19° at  $x/L = 0.28, 0.52,$  and  $0.76,$  respectively.

In the case of CRWP with the same configuration, the largest synergy angles are 71.64°, 77.52°, and 79.04° at  $x/L = 0.24, 0.52,$  and  $0.76$  at 0.4 m/s, respectively. Meanwhile, at velocity of 2.0 m/s, they were 72.68°, 78.81°, and 81.57° at  $x/L = 0.28, 0.52,$  and  $0.8,$  respectively. The hole in VG increases the synergy angle due to a decrease in the heat transfer coefficient [41]. The increase in the mean synergy angle due to the addition of holes in the RWP and CRWP three pairs is 0.25° and 0.29° at a velocity of 2.0 m/s, respectively.



**Figure 27.** Synergy angle at a speed of 2.0 m/s for the case of (a) one-pair of RWP; (b) one pair of CRWPs; (c) two pairs of RWP; (d) two-pairs of CRWP; (e) three pairs of RWP; (f) three-pairs of CRWP.

## 4. Conclusion

In this study, a numerical fluid flow simulation was performed to determine the effect of installing RWP and CRWP with/without holes at 45° angle of attack on heat transfer and pressure drop in the rectangular channel. The hole in VG results in a slight decrease in the convection heat transfer coefficient. The reduction of the convection heat transfer coefficient in the channel with the installation of three pairs of perforated RWP and CRWP for the highest Reynolds number was 2% and 8% of the without holes, respectively. The hole in the VG was able to reduce the pressure drop in the channel. The highest reduction in pressure drop due to holes in RWP with variations of one, two, and three pairs was 7%, 4%, and 13%, respectively. On the other hand, the decrease in pressure drop on CRWP with the highest Reynold number for the same case was 5%, 5%, and 11%, respectively. The hole in VG caused a decrease in the mean spanwise Nusselt number in all cases. The decrease in the average spanwise Nusselt number in the perforated RWP and CRWP cases at a velocity of 0.4 m/s was the greatest of 24% at  $x/L = 0.32$  and 11% at  $x/L = 0.56$ , respectively, from those without holes. Whereas for the same case at a velocity of 2.0 m/s, the largest decrease was 2% at  $x/L = 0.8$  and 7% at  $x/L = 0.32$ , respectively. The synergy angle increased due to the holes in the RWP and CRWP. The average synergy angle increase in the use of RWP and CRWP three pairs was 0.25 and 0.29 at a velocity of 2.0 m/s, respectively.

## Acknowledgements

This work was supported by the Fundamental Research of Ministry of Education and Culture, Indonesia, with contract number: 225-110/UN7.6.1/PP/2020. The authors are grateful to all research members, especially Lab. Thermofluid of Mechanical Engineering of Diponegoro University, Indonesia.

## Author details

Syaiful\* and M. Kurnia Lutfi  
Mechanical Engineering Department of Diponegoro University, Semarang,  
Indonesia

\*Address all correspondence to: [syaiful.undip2011@gmail.com](mailto:syaiful.undip2011@gmail.com)

## IntechOpen

© 2021 The Author(s). Licensee IntechOpen. This chapter is distributed under the terms of the Creative Commons Attribution License (<http://creativecommons.org/licenses/by/3.0>), which permits unrestricted use, distribution, and reproduction in any medium, provided the original work is properly cited. 

## References

- [1] Muhammad Awais, Arafat A. Mint: Heat and mass transfer for compact heat exchanger (CHXs) design: A state-of-the-art review, *International Journal of Heat and Mass Transfer*. 2018; 127; 359–380. DOI: 10.1016/j.ijheatmasstransfer.2018.08.026
- [2] Nares Chimres, Chi-Chuan Wang, Somchai Wongwises. Mint: Effect of elliptical winglet on the air-side performance of fin-and-tube heat exchanger. *International Journal of Heat and Mass Transfer*. 2018; 123; 583–599. DOI: 10.1016/j.ijheatmasstransfer.2018.02.079
- [3] Hui Han, Shaowei Wang, Li Sun, Yuxing Li, Shuo Wang. Mint: Numerical study of thermal and flow characteristics for a fin-and-tube heat exchanger with arc winglet type vortex generators. *International Journal of Refrigeration*. 2018. DOI:10.1016/j.ijrefrig.2018.10.021
- [4] Pourya Forooghi, Mario Flory, Dirk Bertsche, Thomas Wetzel, Bettina Frohnäpfel. Mint: Heat transfer enhancement on the liquid side of an industrially designed flat-tube heat exchanger with passive inserts – Numerical investigation. *Applied Thermal Engineering*. 2017; 123; 573–583. DOI:10.1016/j.applthermaleng.2017.05.144
- [5] Benjamín Herrmann-Priesnitz, Williams R. Calderón-Muñoz, Gerardo Diaz, Rodrigo Soto. Mint: Heat transfer enhancement strategies in a swirl flow minichannel heat sink based on hydrodynamic receptivity. *International Journal of Heat and Mass Transfer*. 2018; 127; 245–256. DOI: 10.1016/j.ijheatmasstransfer.2018.07.077
- [6] R. Andrzejczyk, T. Muszynski, M. Gosz. Mint: Experimental investigations on heat transfer enhancement in shell coil heat exchanger with variable baffles geometry. *Chemical Engineering & Processing: Process Intensification*. 2018; 132; 114–126. DOI: 10.1016/j.cep.2018.08.017
- [7] Muhammad Awais, Arafat A. Bhuiyan. Mint: Heat transfer enhancement using different types of vortex generators (VGs): A review on experimental and numerical activities. *Thermal Science and Engineering Progress*. 2018; 5; 524–545. DOI: 10.1016/j.tsep.2018.02.007
- [8] H.E. Ahmed, H.A. Mohammed, M.Z. Yusoff. Mint: An overview on heat transfer augmentation using vortex generators and nanofluids: Approaches and applications. *Renewable and Sustainable Energy Reviews*. 2012; 16; 5951–5993. DOI: 10.1016/j.rser.2012.06.003
- [9] Y. Xu, M.D. Islam, N. Kharoua. Mint: Numerical study of winglets vortex generator effects on thermal performance in a circular pipe. *International Journal of Thermal Sciences*. 2017; 112; 304–317. DOI: 10.1016/j.ijthermalsci.2016.10.015
- [10] KeWei Song, Song Liu, LiangBi Wang. Mint: Interaction of counter rotating longitudinal vortices and the effect on fluid flow and heat transfer. *International Journal of Heat and Mass Transfer*. 2016; 93; 349–360. DOI: 10.1016/j.ijheatmasstransfer.2015.10.001
- [11] A. Datta, D. Sanyal, A.K. Das. Mint: Numerical investigation of heat transfer in microchannel using inclined longitudinal vortex generator. *Applied Thermal Engineering*. 2016; 108; 1008–1019. DOI:10.1016/j.applthermaleng.2016.07.165
- [12] Hung-Yi Li, Wan-Rong Liao, Tian-Yang Li, Yan-Zuo Chang. Mint: Application of vortex generators to heat transfer enhancement of a pin-fin heat

sink. *International Journal of Heat and Mass Transfer*. 2017; 112; 940–949. DOI: 10.1016/j.ijheatmasstransfer.2017.05.032

[13] Hamdi E. Ahmed, M.Z. Yusoff, M. N.A. Hawlader, M.I. Ahmed, B.H. Salman, A.Sh. Kerbeet. Mint: Turbulent heat transfer and nanofluid flow in a triangular duct with vortex generators. *International Journal of Heat and Mass Transfer*. 2017; 105; 495–504. DOI: 10.1016/j.ijheatmasstransfer.2016.10.009

[14] Syaiful, Astrid Ayutasari, Maria F. Soetanto, Ahmad Indra Siswantara, Myung-whan Bae. Mint: Thermo-Hydrodynamics Performance Analysis of Fluid Flow Through Concave Delta Winglet Vortex Generators by Numerical Simulation. *International Journal of Technology*. 2017; 7; 1276–1285. DOI: 10.14716/ijtech.v8i7.706

[15] Mohammad Oneissia, Charbel Habchid, Serge Russeila, Thierry Lemenand, Daniel Bougeard. Mint: Heat transfer enhancement of inclined projected winglet pair vortex generators with protrusions. *International Journal of Thermal Sciences*. 2018; 134; 541–551. DOI:10.1016/j.ijthermalsci.2018.08.032

[16] Zhimin Han, Zhiming Xu, Jingtao Wang. Mint: Numerical simulation on heat transfer characteristics of rectangular vortex generators with a hole. *International Journal of Heat and Mass Transfer*. 2018; 126; 993–1001. DOI: 10.1016/j.ijheatmasstransfer.2018.06.081

[17] M. Samadifar, D. Toghraie. Mint: Numerical simulation of heat transfer enhancement in a plate fin heat exchanger using a new type of vortex generators. *Applied Thermal Engineering*. 2018; 133; 671–681. DOI: 10.1016/j.applthermaleng.2018.01.062

[18] Jiyang Li, Chaobin Dang, Eiji Hihara. Mint: Heat transfer enhancement in a parallel, finless heat exchanger using a longitudinal vortex

generator, Part A: Numerical investigation. *International Journal of Heat and Mass Transfer*. 2019; 128; 87–97. DOI: 10.1016/j.ijheatmasstransfer.2018.06.049

[19] Gaofeng Lu, Xiaoqiang Zhai. Mint: Effects of curved vortex generators on the air-side performance of fin-and tube heat exchangers. *International Journal of Thermal Sciences*. 2019; 136; 509–518. DOI: 10.1016/j.ijthermalsci.2018.11.009

[20] Ralph Kristoffer B. Gallegos, Rajnish N. Sharma. Mint: Heat transfer performance of flag vortex generators in rectangular channels. *International Journal of Thermal Sciences*. 2019; 137; 26–44. DOI: 10.1016/j.ijthermalsci.2018.11.001

[21] L.H. Tang, W.X. Chu, N. Ahmed, M. Zeng. Mint: A New Configuration of Winglet Longitudinal Vortex Generator to Enhance Heat Transfer in a Rectangular Channel. *Applied Thermal Engineering*. 2016; 104; 74–84. DOI: 10.1016/j.applthermaleng.2016.05.056

[22] Syaiful, Arsanti Rakha Siwi, Tony Suryo Utomo, Yurianto, and Retno Wulandari. Mint: Numerical Analysis of Heat and Fluid Flow Characteristics of Airflow Inside Rectangular Channel with Presence of Perforated Concave Delta Winglet Vortex Generators. *International Journal of Heat and Mass Transfer Technology*. 2019; 37; 1059–1070. DOI: 10.18280/ijht.370415

[23] ZhaoqingKe, Chung-Lung Chen, Kuojiang Li, Sheng Wang, Chien-Hua Chen. Mint: Vortex dynamics and heat transfer of longitudinal vortex generators in a rectangular channel. *International Journal of Heat and Mass Transfer*. 2019; 132; 871–885. DOI: 10.1016/j.ijheatmasstransfer.2018.12.064

[24] M. Fiebig. Mint: Vortices, Generators and Heat Transfer. *Trans IChemE*. 1998; 76

- [25] Syaiful, Imam Syarifudin, Maria F. Soetanto and Myung-whan Bae. Numerical simulation of heat transfer augmentation in fin-and-tube heat exchanger with various number of rows of concave rectangular winglet vortex generator. In: MATEC Web of Conferences 159; 2018, doi: 10.1051/mateconf/201815902012
- [26] Gaofeng Lu, Guobing Zhou. Mint: Numerical simulation on performances of plane and curved winglet type vortex generator pairs with punched holes. *International Journal of Heat and Mass Transfer*. 2016; 102; 679–690. DOI: 10.1016/j.ijheatmasstransfer.2016.06.063
- [27] Zhiming Xu, Zhimin Han, Jingtao Wang, Zuodong Liu. Mint: The characteristics of heat transfer and flow resistance in a rectangular channel with vortex generators. *International Journal of Heat and Mass Transfer*. 2018; 116; 61–72. DOI: 10.1016/j.ijheatmasstransfer.2017.08.083
- [28] Leandro O. Salviano, Daniel J. Dezan, Jurandir I. Yanagihara. Mint: Thermal-hydraulic performance optimization of inline and staggered fin-tube compact heat exchangers applying longitudinal vortex generators. *Applied Thermal Engineering*. 2015; DOI: 10.1016/j.applthermaleng.2015.11.069.
- [29] Shailesh Kumar Sarangi, Dipti Prasad Mishra. Mint: Effect of winglet location on heat transfer of a fin-and-tube heat exchanger. *Applied Thermal Engineering*. 2017; 116; 528–540. DOI: 10.1016/j.applthermaleng.2017.01.106
- [30] KeWei Song, Toshio Tagawa, ZhongHao Chena, Qiang Zhang. Mint: Heat transfer characteristics of concave and convex curved vortex generators in the channel of plate heat exchanger under laminar flow. *International Journal of Thermal Sciences*. 2019; 137; 215–228. DOI: 10.1016/j.ijthermalsci.2018.11.002
- [31] Syaiful, M. S. K. Tony S. U., Agus Saryanto, and Myung-Whan Bae. Improvement of hydrodynamic performance of heated plate mounted by perforated concave delta winglet vortex generator in airflow channel: An experimental study. In: *AIP Conference Proceedings* 1983, 2018. doi: 10.1063/1.5046200
- [32] Luciano Garelli, Gustavo Ríos Rodríguez, Jonathan J. Dorella, Mario A. Storti. Mint: Heat transfer enhancement in panel type radiators using delta-wing vortex generators. *International Journal of Thermal Sciences*. 2019; 137; 64–74. DOI: 10.1016/j.ijthermalsci.2018.10.037
- [33] A. Bjerg, K. Christoffersen, H. Sørensen, J. Hærvig. Mint: Flow structures and heat transfer in repeating arrangements of staggered rectangular winglet pairs by Large Eddy Simulations: Effect of winglet height and longitudinal pitch distance. *International Journal of Heat and Mass Transfer*. 2019; 131; 654–663. DOI: 10.1016/j.ijheatmasstransfer.2018.11.015
- [34] Bittagopal Mondal, Carlos F. Lopez, Ankit Verma, Partha P. Mukherjee. Mint: Vortex generators for active thermal management in lithium-ion battery systems. *International Journal of Heat and Mass Transfer*. 2018; 124; 800–815. DOI: 10.1016/j.ijheatmasstransfer.2018.04.015
- [35] Muhammad Awais, Arafat A. Bhuiyan. Mint: Enhancement of thermal and hydraulic performance of compact finned-tube heat exchanger using vortex generators (VGs): A parametric study. *International Journal of Thermal Sciences*. 2019; 140; 154–166. DOI: 10.1016/j.ijthermalsci.2019.02.041
- [36] S.R. Hiravennavar, E.G. Tulapurkara, G. Biswas. Mint: A note on the flow and heat transfer enhancement in a channel with built-in winglet pair. *International Journal of Heat and Fluid*

Flow. 2007; 28; 299–305. DOI: 10.1016/j.ijheatfluidflow.2006.03.030

[37] Hemant Naik, S. Harikrishnan, Shaligram Tiwari. Mint: Numerical investigations on heat transfer characteristics of curved rectangular winglet placed in a channel. International Journal of Thermal Sciences. 2018; 129; 489–503. DOI: 10.1016/j.ijthermalsci.2018.03.028

[38] Z.Y. Guo, D.Y. Li, B.X. Wang. Mint: A novel concept for convective heat transfer enhancement. International Journal of Heat and Mass Transfer. 1998; 41; 2221–2225

[39] J.M. Wu, W.Q. Tao. Mint: Numerical study on laminar convection heat transfer in a rectangular channel with longitudinal vortex generator. Part A: Verification of field synergy principle. International Journal of Heat and Mass Transfer. 2008; 51; 1179–1191. DOI: 10.1016/j.ijheatmasstransfer.2007.03.032

[40] Gaofeng Lu, Guobing Zhou. Mint: Numerical simulation on performances of plane and curved winglet-Pair vortex generators in a rectangular channel and field synergy analysis. International Journal of Thermal Sciences. 2016; 109; 323–333. DOI: 10.1016/j.ijthermalsci.2016.06.024

[41] Z.Y. Guo, W.Q. Tao, R.K. Shah. Mint: The field synergy (coordination) principle and its applications in enhancing single phase convective heat transfer. International Journal of Heat and Mass Transfer. 2005; 48; 1797–1807. DOI:10.1016/j.ijheatmasstransfer.2004.11.007





# Survey of Some Exact and Approximate Analytical Solutions for Heat Transfer in Extended Surfaces

*Raseelo Joel Moitsheki, Partner Luyanda Ndlovu  
and Basetsana Pauline Ntsime*

## Abstract

In this chapter we provide the review and a narrative of some obtained results for steady and transient heat transfer through extended surfaces (fins). A particular attention is given to exact and approximate analytical solutions of models describing heat transfer under various conditions, for example, when thermal conductivity and heat transfer are temperature dependent. We also consider fins of different profiles and shapes. The dependence of thermal properties render the considered models nonlinear, and this adds a complication and difficulty to solve these model exactly. However, the nonlinear problems are more realistic and physically sound. The approximate analytical solutions give insight into heat transfer in fins and as such assist in the designs for better efficiencies and effectiveness.

**Keywords:** exact solutions, approximate solutions, Lie symmetry methods, approximate methods, heat transfer, fins

## 1. Introduction

In the study of heat transfer, a fin may be a solid or porous and stationary or moving that extends from an attached body to rapidly cool off heat of that surface. Cooling fins find application in a large real world phenomena particularly in engineering devices. Fins increase the surface area of heat transfer particularly for cooling of hot bodies. These come in different shapes, geometries and profiles. These differences provide variety of effectiveness and efficiencies. The literature with regard to the study of heat transfer in fins is well documented (see e.g. [1]). The solutions either exact, numerical or approximate analytical continue to be of immense interest and this is due to continued use of fins in engineering devices.

Much attention has been given to linear one dimensional models [2–4] whereby Homotopy Analysis Method (HAM) was used to determine series solutions for heat transfer in straight fins of trapezoidal and rectangular profiles given temperature dependent thermal properties; nonlinear one dimensional models [5] wherein preliminary group classification methods were utilised to contract invariant (symmetry) solutions; heat transfer in linear two dimensional trapezoidal fins [6]; heat transfer in two dimensional straight nonlinear fins were considered [7] wherein Lie

point symmetries and other standard methods were invoked and recently nonlinear three dimensional models [8] were considered wherein three dimensional Differential Transform Methods (DTM) were employed to construct approximate analytical solutions. The dependence of thermal properties on the temperature renders the equations highly nonlinear. The non-linearity brings an added complication or difficulty in the construction of solutions and particularly exact solutions.

Few exact solutions are recorded in the literature, for example for one dimensional problems [2–5, 9–15], two dimensions [6, 7, 16, 17]. An attempt to construct exact solutions for the three dimensional problems is found in [8], however these were general solutions. For this reason, either approximate analytical or numerical solutions are sought. However, the accuracy of numerical schemes is obtained by comparison with the exact solutions.

This chapter summarizes the work of Moitsheki and collaborators in the area of heat transfer through fin. In their work, they employed Lie symmetry methods to construct exact solutions. These methods include, the preliminary group classification, the Lie point symmetries, conservation laws and associate Lie point symmetries, non-classical symmetry methods and recently non classical potential symmetries. It appeared that most of the constructed exact solutions do not satisfy the prescribed boundary conditions. The idea then becomes, start with the simple model that satisfy the boundary conditions and compare it with the approximate solutions to establish confidence in the approximate methods, then extend analysis to problems that are difficult to solve exactly.

We acknowledge that some scholars employed many other approximate methods to solve boundary value problems (BVPs); for example the Homotopy Analysis Method [18], Collocation Methods (CM) [19], Homotopy Perturbation Methods (HPM) [20], Haar Wavelet Collocation Methods (HWCW) [21], Collocation Spectral Methods (CSM) [22], modified Homotopy Analysis Method (mHAM) [23], Spectral Homotopy Analysis Methods (SHAM) and the Optimal Homotopy Analysis Methods [24]. In this chapter we restrict discussions to Lie symmetry methods for exact solutions, and DTM and VIM for approximate analytical methods.

## 2. Mathematical descriptions

Mathematical descriptions represent some physical phenomena in terms of deterministic models given in terms of partial differential equations (PDEs). These differential equations become non-linear when heat transfer coefficient and thermal conductivity depend on the temperature (see e.g. [5]). This non-linearity was introduced as a significant modifications of the usually assumed models see e.g. [2].

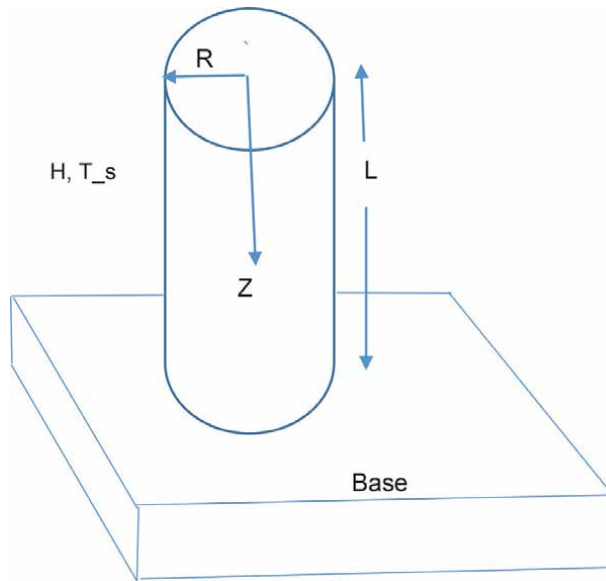
In this chapter we present a few models for various heat transfer phenomena.

### 2.1.2 + 1 dimensional transient state models

Mathematical modelling for heat transfer in fins may be three dimensional models.

#### 2.1.1 Cylindrical pin fins

We consider a two-dimensional pin fin with length  $L$  and radius  $R$ . The fin is attached to a base surface of temperature  $T_b$  and extended into the fluid of temperature  $T_f$ . The tip of the fin is insulated (i.e., heat transfer at the tip is negligibly small). The fin is measured from the tip to the base. A schematic representation of a pin fin is given in **Figure 1**. We assume that the heat transfer coefficient along the



**Figure 1.**  
 Schematic representation of a pin fin.

fin is nonuniform and temperature dependent and that the internal heat source or sink is neglected. Furthermore, the temperature-dependent thermal conductivity is assumed to be the same in both radial and axial directions. The model describing the heat transfer in pin fins is given by the BVP (see e.g. [17])

$$\rho c_p \frac{\partial T}{\partial t} = \frac{\partial}{\partial Z} \left[ K(T) \frac{\partial T}{\partial Z} \right] + \frac{1}{R} \frac{\partial}{\partial R} \left[ K(T) R \frac{\partial T}{\partial R} \right]. \quad (1)$$

The initial condition is given by

$$T(0, R, Z) = T_s, \quad 0 \leq R \leq R_a, \quad 0 \leq Z \leq L,$$

here,  $T_s$  is the temperature of the surrounding fluid.

Boundary conditions are given by

$$\begin{aligned} T(t, R, L) &= T_b, \quad 0 \leq R \leq R_a, \quad t > 0, \\ \frac{\partial T}{\partial Z} &= 0, \quad Z = 0, \quad 0 \leq R \leq R_a, \quad t > 0. \\ K(T) \frac{\partial T}{\partial R} &= -H(T)[T - T_s], \quad R = 0, \quad 0 \leq Z \leq L, \quad t > 0, \\ \frac{\partial T}{\partial R} &= 0, \quad R = R_a, \quad 0 \leq Z \leq L, \quad t > 0, \end{aligned}$$

In non-dimensionalized variables and parameters we have,

$$\frac{\partial \theta}{\partial \tau} = \frac{\partial}{\partial z} \left[ k(\theta) \frac{\partial \theta}{\partial z} \right] + E^2 \frac{1}{r} \frac{\partial}{\partial r} \left[ k(\theta) r \frac{\partial \theta}{\partial r} \right], \quad (2)$$

subject to the initial condition

$$\theta(0, r, z) = 0, \quad 0 \leq z \leq 1, \quad 0 \leq r \leq 1,$$

and boundary conditions

$$\begin{aligned}\theta(\tau, 1, r) &= 1, \quad 0 \leq r \leq 1, \quad \tau > 0, \\ \frac{\partial \theta}{\partial z} &= 0, \quad z = 0, \quad 0 \leq r \leq 1, \quad \tau > 0, \\ k(\theta) \frac{\partial \theta}{\partial z} &= -Bi h(\theta) \theta, \quad z = 0, \quad 0 \leq z \leq 1, \quad \tau > 0, \\ \frac{\partial \theta}{\partial r} &= 0, \quad r = 1, \quad 0 \leq z \leq 1, \quad \tau > 0,\end{aligned}$$

where the non-dimensional quantities  $E = \frac{L}{\delta}$ , and  $Bi = \frac{H_b \delta}{K_a}$ , are the fin extension factor and the Biot number respectively. Also,

$$\begin{aligned}t &= \frac{L^2 \rho c_p}{K_a} \tau, \quad Z = Lz, \quad R = R_a r, \\ K &= K_a k, \quad H = H_b h, \quad T = (T_b - T_s) \theta + T_s.\end{aligned}$$

where  $\tau, z, r, k, h$  and  $\theta$  are all dimensionless variables.  $K_a$  and  $H_b$  are the ambient thermal conductivity and the fin base heat transfer coefficient respectively.

Notice that other terms may be added, for example internal heat generation (source term) and fin profile.

### 2.1.2 Rectangular straight fins

Following the similar pattern, in dimensionless variables we have (see e.g. [8])

$$\frac{\partial \theta}{\partial \tau} = \frac{\partial}{\partial x} \left[ k(\theta) \frac{\partial \theta}{\partial x} \right] + E^2 \frac{\partial}{\partial y} \left[ k(\theta) \frac{\partial \theta}{\partial y} \right], \quad (3)$$

subject to the initial condition

$$\theta(0, x, y) = 0, \quad 0 \leq x \leq 1, \quad 0 \leq y \leq 1,$$

and boundary conditions

$$\begin{aligned}\theta(\tau, 1, y) &= 1, \quad 0 \leq y \leq 1, \quad \tau > 0, \\ \frac{\partial \theta}{\partial x} &= 0, \quad x = 0, \quad 0 \leq y \leq 1, \quad \tau > 0, \\ k(\theta) \frac{\partial \theta}{\partial y} &= -Bi h(\theta) \theta, \quad y = 0, \quad 0 \leq x \leq 1, \quad \tau > 0, \\ \frac{\partial \theta}{\partial y} &= 0, \quad y = 1, \quad 0 \leq x \leq 1, \quad \tau > 0,\end{aligned}$$

## 2.2 Two-dimensional steady state models

In this section we consider the two dimensional steady state models. The symmetry analysis of these models have proven to be challenging. In some cases standard method such as separations of variables have been employed to determine exact solutions.

### 2.2.1 Cylindrical pin fins

For steady state problem, the heat transfer is independent of the time variable. For example, the time derivative in Eq. (2) vanish (see e.g. [16]).

### 2.2.2 Rectangular straight fins

For steady state problem, the heat transfer is independent of the time variable. For example, the time derivative in Eq. (3) is zero (see e.g. [7]).

## 2.3 1 + 1 dimensional transient model for straight fins

### 2.3.1 Solid stationary fins

For solid stationary straight fins the model is given by (see e.g. [25, 26])

$$\frac{\partial \theta}{\partial \tau} = \frac{\partial}{\partial x} \left[ f(x)k(\theta) \frac{\partial \theta}{\partial x} \right] - M^2 \theta h(\theta), \quad 0 \leq x \leq 1. \quad (4)$$

subject to initial and boundary conditions

$$\theta(0, x) = 0, \quad 0 \leq x \leq 1, \quad \theta(\tau, 1) = 1; \quad \left. \frac{\partial \theta}{\partial x} \right|_{x=0} = 0, \quad \tau \geq 0.$$

### 2.3.2 Solid moving fins

It appear, as far as we know, this is still an open problem and in preparation.

$$\frac{\partial \theta}{\partial \tau} = \frac{\partial}{\partial x} \left[ f(x)k(\theta) \frac{\partial \theta}{\partial x} \right] - M^2 \theta h(\theta) - Pef(x) \frac{\partial \theta}{\partial x}, \quad 0 \leq x \leq 1. \quad (5)$$

subject to initial and boundary conditions

$$\theta(0, x) = 0, \quad 0 \leq x \leq 1, \quad \theta(\tau, 1) = 1; \quad \left. \frac{\partial \theta}{\partial x} \right|_{x=0} = 0, \quad \tau \geq 0.$$

### 2.3.3 Porous stationary fins

The model was considered in [27].

$$\frac{\partial \theta}{\partial \tau} = \frac{\partial}{\partial x} \left[ f(x)k(\theta) \frac{\partial \theta}{\partial x} \right] - N_c(\theta - \theta_a)^{n+1} - N_r(\theta^4 - \theta_a^4), \quad 0 \leq x \leq 1. \quad (6)$$

subject to initial and boundary conditions

$$\theta(0, x) = 0, \quad 0 \leq x \leq 1, \quad \theta(\tau, 1) = 1; \quad \left. \frac{\partial \theta}{\partial x} \right|_{x=0} = 0, \quad \tau \geq 0.$$

### 2.3.4 Porous moving fins

The model describing heat transfer in porous moving fin is considered in [28] and is given by

$$\frac{\partial \theta}{\partial \tau} = \frac{\partial}{\partial x} \left[ f(x)k(\theta) \frac{\partial \theta}{\partial r} \right] - N_c(\theta - \theta_a)^{n+1} - N_p(\theta - \theta_a)^2 - N_r(\theta^4 - \theta_a^4) - Pef(x) \frac{\partial \theta}{\partial x}, \quad 0 \leq x \leq 1. \quad (7)$$

subject to initial and boundary conditions

$$\theta(0, x) = 0, \quad 0 \leq x \leq 1, \quad \theta(\tau, 1) = 1; \quad \left. \frac{\partial \theta}{\partial x} \right|_{x=0} = 0, \quad \tau \geq 0.$$

## 2.4 1 + 1 dimensional transient model for radial fins

### 2.4.1 Solid stationary fins

For solid stationary radial fins thge model is given by

$$\frac{\partial \theta}{\partial \tau} = \frac{1}{r} \frac{\partial}{\partial r} \left[ rf(r)k(\theta) \frac{\partial \theta}{\partial r} \right] - M^2 \theta h(\theta), \quad 0 \leq r \leq 1. \quad (8)$$

subject to initial and boundary conditions

$$\theta(0, r) = 0, \quad 0 \leq r \leq 1, \quad \theta(\tau, 1) = 1; \quad \left. \frac{\partial \theta}{\partial r} \right|_{r=0} = 0, \quad \tau \geq 0.$$

### 2.4.2 Solid moving fins

For solid moving radial fins the model is given by (see e.g. [29]),

$$\frac{\partial \theta}{\partial \tau} = \frac{1}{r} \frac{\partial}{\partial r} \left[ rf(r)k(\theta) \frac{\partial \theta}{\partial r} \right] - M^2 \theta h(\theta) - f(r)Pe \frac{\partial \theta}{\partial r}, \quad 0 \leq r \leq 1. \quad (9)$$

subject to initial and boundary conditions

$$\theta(0, r) = 0, \quad 0 \leq r \leq 1, \quad \theta(\tau, 1) = 1; \quad \left. \frac{\partial \theta}{\partial r} \right|_{r=0} = 0, \quad \tau \geq 0.$$

### 2.4.3 Porous stationary fins

For solid stationary radial fins the model is given by

$$\frac{\partial \theta}{\partial \tau} = \frac{1}{r} \frac{\partial}{\partial r} \left[ rf(r)k(\theta) \frac{\partial \theta}{\partial r} \right] - N_p(\theta - \theta_a)^2 - N_r(\theta^4 - \theta_a^4), \quad 0 \leq r \leq 1. \quad (10)$$

subject to initial and boundary conditions

$$\theta(0, r) = 0, \quad 0 \leq r \leq 1, \quad \theta(\tau, 1) = 1; \quad \left. \frac{\partial \theta}{\partial r} \right|_{r=0} = 0, \quad \tau \geq 0.$$

### 2.4.4 Porous moving fins

For porous moving radial fins the model is given by

$$\frac{\partial \theta}{\partial \tau} = \frac{1}{r} \frac{\partial}{\partial r} \left[ rf(r)k(\theta) \frac{\partial \theta}{\partial r} \right] - N_p(\theta - \theta_a)^2 - N_r(\theta^4 - \theta_a^4) - f(r)Pe \frac{\partial \theta}{\partial r}, \quad 0 \leq r \leq 1. \quad (11)$$

subject to initial and boundary conditions

$$\theta(0, r) = 0, \quad 0 \leq r \leq 1, \quad \theta(\tau, 1) = 1; \quad \left. \frac{\partial \theta}{\partial r} \right|_{r=0} = 0, \quad \tau \geq 0.$$

## 2.5 One-dimensional steady state model for straight fins

Considering heat transfer in a one dimensional longitudinal fin of cross area  $A_c$  with various profiles. The perimeter of the fin is denoted by  $P$  and length by  $L$ . The fin is attached to a fixed prime surface of temperature  $T_b$  and extends to the fluid of temperature  $T_\infty$ . in non-dimensional variables, one obtains

$$\frac{d}{dx} \left[ f(x)k(\theta) \frac{d\theta}{dx} \right] - M^2 \theta h(\theta) = 0, \quad 0 \leq x \leq 1. \quad (12)$$

subject to

$$\theta(1) = 1, \quad \frac{d\theta(0)}{dx} = 0.$$

In case of a moving radial fin the term

$$f(x)Pe \frac{d\theta}{dx}$$

is added to Eq. (12).

## 2.6 One-dimensional steady state model for radial fins

Considering heat transfer in a one dimensional stationary radial fin of cross area  $A_c$  with various profiles. The perimeter of the fin is denoted by  $P$  and length by  $Lr_b - r_t$ . The fin is attached to a fixed prime surface of temperature  $T_b$  and extends to the fluid of temperature  $T_\infty$ . One may assume that at the tip of the fin  $r_t = 0$ . In non-dimensional variables, one obtains

$$\frac{1}{r} \frac{d}{dr} \left[ rf(r)k(\theta) \frac{d\theta}{dr} \right] - M^2 \theta h(\theta) = 0, \quad 0 \leq x \leq 1. \quad (13)$$

subject to

$$\theta(1) = 1, \quad \frac{d\theta(0)}{dr} = 0.$$

In case of a moving radial fin the term

$$f(r)Pe \frac{d\theta}{dr}$$

is added to Eq. (13) (see e.g. [30]).

### 3. Methods of solutions

#### 3.1 Brief account on lie symmetry methods

In this subsection we provide a brief theory of Lie point symmetries. This discussion and further account can be found in the book of Bluman and Anco [31].

##### 3.1.1 $m$ dependent and $n$ independent variables

$m$  dependent variables  $u = (u^1, u^2, \dots, u^m)$  and  $n$  independent variables  $x = (x^1, x^2, \dots, x^n)$ ,  $u = u(x)$  with  $m \geq 2$ , arise in studying systems of differential equations. We consider extended transformations from  $(x, u)$ -space to  $(x, u, u_{(1)}, u_{(2)}, \dots, u_{(k)})$ -space. Here  $u_{(k)}$  denotes the components of all  $k$ th-order partial derivatives of  $u$  wrt  $x$ .

**definition** *Total derivative.* The total differentiation operator wrt  $x^i$  is defined by

$$D_i = \frac{\partial}{\partial x^i} + u_i^\alpha \frac{\partial}{\partial u^\alpha} + u_{ij}^\alpha \frac{\partial}{\partial u_i^\alpha} + \dots + u_{i_1 i_2 \dots i_k}^\alpha \frac{\partial}{\partial u_{i_1 i_2 \dots i_k}^\alpha} + \dots, \quad i = 1, 2, \dots, n.$$

where

$$u_i^\alpha = \frac{\partial u^\alpha}{\partial x^i}, \quad u_{ij}^\alpha = \frac{\partial^2 u^\alpha}{\partial x^i \partial x^j}, \quad \text{etc.}$$

We seek the one-parameter Lie group of transformations

$$\begin{aligned} \bar{x}^i &= x^i + \varepsilon \xi^i(x, u) + O(\varepsilon^2), \\ \bar{u}^\alpha &= u^\alpha + \varepsilon \eta^\alpha(x, u) + O(\varepsilon^2), \end{aligned} \tag{14}$$

which leave the system of equation in question invariant. These transformations are generated by the base vector

$$X = \xi^i(x, u) \frac{\partial}{\partial x^i} + \eta^\alpha(x, u) \frac{\partial}{\partial u^\alpha}.$$

The  $k$ th-extended transformation of (14) are given by

$$\left. \begin{aligned} \bar{u}_i^\alpha &= u_i^\alpha + \varepsilon \zeta_i^\alpha(x, u, u_{(1)}) + O(\varepsilon^2), \\ \bar{u}_{ij}^\alpha &= u_{ij}^\alpha + \varepsilon \zeta_{ij}^\alpha(x, u, u_{(1)}, u_{(2)}) + O(\varepsilon^2), \\ \cdot &\quad \cdot \\ \cdot &\quad \cdot \\ \cdot &\quad \cdot \\ \bar{u}_{i_1 i_2, \dots, i_k}^\alpha &= u_{i_1 i_2, \dots, i_k}^\alpha + \varepsilon \zeta_{i_1 i_2, \dots, i_k}^\alpha(x, u, u_{(1)}, u_{(2)}, \dots, u_{(k)}) + O(\varepsilon^2), \end{aligned} \right\} \tag{15}$$

**Theorem 1.1** The extended infinitesimals satisfy the recursion relations



$$\left. \begin{aligned} \zeta_i^\alpha &= D_i(\eta^\alpha) - u_j^\alpha D_i(\xi^j), \\ \zeta_{ij}^\alpha &= D_j(\zeta_i^\alpha) - u_{il}^\alpha D_j(\xi^l), \\ &\vdots \\ &\vdots \\ \zeta_{i_1, i_2, \dots, i_k}^\alpha &= D_{i_k}(\zeta_{i_1 \dots i_{k-1}}^\alpha) - u_{i_1, i_2, \dots, i_{k-1} l}^\alpha D_{i_k}(\xi^l), \end{aligned} \right\} \quad (16)$$

Introducing the *Lie Characteristic function* defined by

$$W^\alpha = \eta^\alpha - \xi^j u_j^\alpha,$$

then

$$\left. \begin{aligned} \zeta_i^\alpha &= D_i(W^\alpha) + \xi^j u_{ji}^\alpha, \\ \zeta_{ij}^\alpha &= D_i D_j(W^\alpha) + \xi^k u_{kij}^\alpha, \\ &\vdots \\ &\vdots \\ \zeta_{i_1, i_2, \dots, i_k}^\alpha &= D_{i_1} \dots D_{i_k}(W^\alpha) + \xi^j u_{j i_1 i_2 \dots i_k}^\alpha. \end{aligned} \right\} \quad (17)$$

The corresponding (*k*th extended) infinitesimal generator is given by

$$X^{[k]} = \xi^i(x, u) \frac{\partial}{\partial x^i} + \eta_i^\alpha(x, u) \frac{\partial}{\partial u^\alpha} + \zeta_i^\alpha \frac{\partial}{\partial u_i} + \dots + \zeta_{i_1, i_2, \dots, i_k}^\alpha \frac{\partial}{\partial u_{i_1, i_2, \dots, i_k}}, \quad k \geq 1.$$

**Theorem 1.2** A differential function  $F(x, u, u_1, \dots, u_{(p)})$   $p \geq 0$ , is a *p*th-order differential invariant of a group *G* if

$$F(x, u, u_1, \dots, u_{(p)}) = F(\bar{x}, \bar{u}, \bar{u}_1, \dots, \bar{u}_{(p)}).$$

**Theorem 1.3** A differential function  $F(x, u, u_1, \dots, u_{(p)})$   $p \geq 0$ , is a *p*th-order differential invariant of a group *G* if

$$X^{[p]}F = 0,$$

where  $X^{[p]}$  is the *p*th prolongation of *X*.

## 3.2 Approximate methods

### 3.2.1 *p*-dimensional differential transform methods

For an analytic multivariable function  $f(x_1, x_2, \dots, x_p)$ , we have the *p*-dimensional transform given by

$$F(k_1, k_2, \dots, k_p) = \frac{1}{k_1! k_2! \dots k_p!} \left[ \frac{\partial^{k_1 + k_2 + \dots + k_p} f(x_1, x_2, \dots, x_p)}{\partial x_1^{k_1} \partial x_2^{k_2} \dots \partial x_p^{k_p}} \right] \Bigg|_{(x_1, x_2, \dots, x_p) = (0, 0, \dots, 0)} \quad (18)$$

The upper and lower case letters are for the transformed and the original functions respectively. The transformed function is also referred to as the T-function, the differential inverse transform is given by

$$f(x_1, x_2, \dots, x_p) = \sum_{k_1=0}^{\infty} \sum_{k_2=0}^{\infty} \dots \sum_{k_p=0}^{\infty} F(k_1, k_2, \dots, k_p) \prod_{l=1}^p x_l^{k_l}. \quad (19)$$

It can easily be deduced that the substitution of (18) into (19) gives the Taylor series expansion of the function  $f(x_1, x_2, \dots, x_p)$  about the point  $(x_1, x_2, \dots, x_p) = (0, 0, \dots, 0)$ . This is given by

$$f(x_1, x_2, \dots, x_p) = \sum_{k_1=0}^{\infty} \sum_{k_2=0}^{\infty} \dots \sum_{k_p=0}^{\infty} \frac{\prod_{l=1}^p x_l^{k_l}}{k_1! k_2! \dots k_p!} \left[ \frac{\partial^{k_1+k_2+\dots+k_p} f(x_1, x_2, \dots, x_p)}{\partial x_1^{k_1} \partial x_2^{k_2} \dots \partial x_p^{k_p}} \right] \Bigg|_{x_1=0, \dots, x_p=0}. \quad (20)$$

For real world applications the function  $f(x_1, x_2, \dots, x_p)$  is given in terms of a finite series for some  $q, r, s \in \mathbb{Z}$ . Then (19) becomes

$$f(x_1, x_2, \dots, x_p) = \sum_{k_1=0}^q \sum_{k_2=0}^r \dots \sum_{k_p=0}^s F(k_1, k_2, \dots, k_p) \prod_{l=1}^p x_l^{k_l}. \quad (21)$$

We now give some important operations and theorems performed in the  $p$ -dimensional DTM in **Table 1**. Those have been derived using the definition in (18) together with previously obtained results [32].

In the table

$$\delta(k_1 - e_1, k_2 - e_2, \dots, k_p - e_p) = \begin{cases} 1 & \text{if } k_i = e_i \text{ for } i = 1, 2, \dots, p. \\ 0 & \text{otherwise.} \end{cases}$$

We now provide one result of the  $p$ -dimensional DTM without proof.

**Theorem.** Proof in [32].

If

$$f(x_1, x_2, \dots, x_p) = g(x_1, x_2, \dots, x_p)h(x_1, x_2, \dots, x_p),$$

then

$$F(k_1, k_2, \dots, k_p) = \sum_{i_1=0}^{k_1} \sum_{i_2=0}^{k_2} \dots \sum_{i_p=0}^{k_p} G(k_1, k_2, \dots, k_p + i_p)H(k_1 + i_1, \dots, k_{n-1} + i_{p-1}, k_p).$$

Original function $f(x_1, x_2, \dots, x_p)$	T-function $F(k_1, k_2, \dots, k_p)$
$f(x_1, x_2, \dots, x_p) = \lambda g(x_1, x_2, \dots, x_p)$	$F(k_1, k_2, \dots, k_p) = \lambda G(k_1, k_2, \dots, k_p)$
$f(x_1, x_2, \dots, x_p) = g(x_1, x_2, \dots, x_p) \pm p(x_1, x_2, \dots, x_p)$	$F(k_1, k_2, \dots, k_p) = G(k_1, k_2, \dots, k_p) \pm P(k_1, k_2, \dots, k_p)$
$f(x_1, x_2, \dots, x_p) = \frac{\partial^{i_1+i_2+\dots+i_p} g(x_1, x_2, \dots, x_p)}{\partial x_1^{i_1} \partial x_2^{i_2} \dots \partial x_p^{i_p}}$	$F(k_1, k_2, \dots, k_p) = \frac{(k_1+i_1)! \dots (k_p+i_p)!}{k_1! \dots k_p!} (k_1 + i_1, \dots, k_p + i_p)$
$f(x_1, x_2, \dots, x_p) = \prod_{l=1}^p x_l^{e_l}$	$F(k_1, k_2, \dots, k_p) = \delta(k_1 - e_1, k_2 - e_2, \dots, k_p - e_p)$

**Table 1.** Theorems and operations performed in  $p$ -dimensional DTM.

### 3.2.2 Variational iteration methods

$$L\theta + N\theta = g(x), \quad (22)$$

where  $L$  and  $N$  are linear and nonlinear operators, respectively, and  $g(x)$  is the source inhomogeneous term. He [33], proposed the VIM where a correctional functional for Eq. (22) can be written as

$$\theta_{j+1}(x) = \theta_j(x) + \int_0^x \lambda(t)(L\theta_j(t) + N\tilde{\theta}_j(t) - g(t))dt, \quad (23)$$

where  $\lambda$  is the general Lagrange multiplier, which can be identified optimally via the variation theory, and  $\tilde{\theta}_j$  is a restricted variation, which means  $\delta\tilde{\theta}_j = 0$  [34]. The Lagrange multiplier can be a constant or a function depending on the order of the differential equation under consideration. The VIM should be employed by following two essential steps. First we determine the Lagrange multiplier by considering the following second order differential equation,

$$\theta''(x) + a\theta'(x) + b\theta(x) = g(x), \theta(0) = \alpha, \theta'(0) = \beta, \quad (24)$$

where  $a$  and  $b$  are constants. The VIM admits the use of a correctional function for this equation as follows,

$$\theta_{j+1}(x) = \theta_j(x) + \int_0^x \lambda(t)(\theta_j''(t) + a\tilde{\theta}_j'(t) + b\tilde{\theta}_j(t) - g(t))dt. \quad (25)$$

Taking the variation on both sides of Eq. (25) with respect to the independent variable  $\theta_j$  gives,

$$\frac{\delta\theta_{j+1}}{\delta\theta_j} = 1 + \frac{\delta}{\delta\theta_j} \left( \int_0^x \lambda(t)(\theta_j''(t) + a\tilde{\theta}_j'(t) + b\tilde{\theta}_j(t) - g(t))dt \right), \quad (26)$$

or equivalently

$$\delta\theta_{j+1}(x) = \delta\theta_j(x) + \delta \left( \int_0^x \lambda(t)(\theta_j''(t) + a\tilde{\theta}_j'(t) + b\tilde{\theta}_j(t) - g(t))dt \right), \quad (27)$$

which gives

$$\delta\theta_{j+1}(x) = \delta\theta_j(x) + \delta \left( \int_0^x \lambda(t)(\theta_j''(t))dt \right), \quad (28)$$

obtained upon using  $\delta\tilde{\theta}_j = 0$  and  $\delta\tilde{\theta}_j' = 0$ . Evaluating the integral of Eq. (28) by parts gives,

$$\delta\theta_{j+1} = \delta\theta_j + \delta\lambda\theta_j' - \delta\lambda'\theta_j + \delta \int_0^x \lambda''\theta_j dt, \quad (29)$$

or equivalently

$$\delta\theta_{j+1} = \delta(1 - \lambda'|_{t=x})\theta_j + \delta\lambda\theta_j' + \delta \int_0^x \lambda''\theta_j dt. \quad (30)$$

The extreme condition of  $\theta_{j+1}$  requires that  $\delta\theta_{j+1} = 0$ . Equating both sides of Eq. (30) to 0, yields the following stationary conditions

$$1 - \lambda'|_{t=x} = 0, \quad (31)$$

$$\lambda|_{t=x} = 0, \quad (32)$$

$$\lambda''|_{t=x} = 0. \quad (33)$$

This in turn gives

$$\lambda = t - x. \quad (34)$$

In general, for the  $n^{\text{th}}$  order ordinary differential equation, the Lagrange multiplier is given by,

$$\lambda = \frac{(-1)^j}{(j-1)!} (t-x)^{j-1}. \quad (35)$$

Having determined  $\lambda$  and substituting its value into (23) gives the iteration formula

$$\theta_{j+1}(x) = \theta_j(x) + \int_0^x (t-x) \left( \theta_j''(t) + a\theta_j'(t) + b\theta_j(t) - g(t) \right) dt, \quad (36)$$

The iteration formula Eq. (36), without restricted variation, should be used for the determination of the successive approximations  $\theta_{j+1}(x), j \geq 0$ , of the solution  $\theta(x)$ . Consequently, the solution is given by

$$\theta(x) = \lim_{j \rightarrow \infty} \theta_j(x). \quad (37)$$

## 4. Survey of some solutions

In this section we demonstrate the challenge in the construction of exact solution for heat transfer in pin fin. Also, we consider the work in [5].

### 4.1 Some exact solutions

#### 4.1.1 Example 1

Given the power law thermal conductivity in heat transfer through pin fins, that is in Eq. (3)  $k(\theta) = \theta^n$ . The model admits four finite symmetry generators. Amongst the others, the two dimensional Lie subalgebra is given by

$$X_1 = \frac{\partial}{\partial z}, \quad X_2 = z \frac{\partial}{\partial z} + r \frac{\partial}{\partial r} + \frac{2\theta}{n} \frac{\partial}{\partial \theta}$$

Notice that

$$[X_1, X_2] = X_1,$$

and hence we start the double reduction first with  $X_1$  which implies  $(\tau, r, \theta)$  are invariants and leads to a steady state problem. Hence writing  $\theta = F(\tau, r)$  and substitute in the original equation, one obtains

$$F_\tau = E^2 \frac{1}{r} \frac{\partial}{\partial r} (r F^n F_r).$$

$X_2$  becomes

$$X_2^* = r \frac{\partial}{\partial r} + \frac{2F}{n} \frac{\partial}{\partial F}.$$

This symmetry generator leads to the first order ODE

$$g'(\gamma) = 4E^2 \left( \frac{n+1}{n^2} \right) g(\gamma)^{n+1}.$$

In terms of original variables one obtains the general exact solution

$$\theta(\tau, r) = r^{n/2} \left[ -4E^2 \left( \frac{n+1}{n^2} \right) \tau + c_1 \right]^{-1/n}.$$

The difficulty for group-invariant solutions is the satisfaction of the imposed or prescribed boundary conditions. This has been seen in two dimensional steady state problems [7, 16], and 1 + 1 D transient problems [25]. Perhaps the most successful attempt in in [26]. For nonlinear steady state problems, some transformation such as Kirchoff [7, 16], may linearise the two dimensional problems which then becomes easier to solve using standard methods. Linearisation of nonlinear steady state one dimensional problems is possible when thermal conductivity is a differential consequence of heat transfer coefficient [5].

#### 4.1.2 Example 2

In [5], preliminary group classification is invoked to determine the thermal conductivity which lead to exact solutions. It turned out that given a power law heat transfer coefficient, thermal conductivity also takes the power law form. Given Eq. (12) with both  $k(\theta)$  and  $h(\theta)$  given by  $\theta^n$  then one obtains the solution

$$\theta(x) = \left[ \frac{\cosh(\sqrt{n+1} Mx)}{\cosh(\sqrt{n+1} M)} \right]^{1/(n+1)}. \quad (38)$$

The expressions for fin efficiency and effectiveness can be explicit in this case. Furthermore, this solution led to the benchmarking of the approximate analytical solutions [35]. With established confidence in approximate methods, then one may solve other problems that are challenging to solve exactly.

## 4.2 Some approximate solutions

### 4.2.1 Three dimensional DTM

In this subsection we consider heat transfer in a cylindrical pin fin. We consider thermal conductivity given as a linear function of temperature  $1 + \beta\theta$  and a power

law heat transfer coefficient. The three dimensional DTM solution of Eq. (2) is given by

$$\begin{aligned} \theta(\tau, r, z) = & c\tau + c\tau r + c\tau r^2 + c\tau r^3 + c\tau r^4 + c\tau r^5 + c\tau r^6 + c\tau r^7 + \dots \dots \\ & + c\tau z^2 - \frac{Bic^{m+1}}{(1 + \beta c)} \tau r z^2 - \frac{5c}{2E^2} \tau r^2 z^2 + \frac{10Bic^{m+1}}{9E^2(1 + \beta c)} \tau r^3 z^2 + \dots \dots \\ & + c\tau z^3 - \frac{Bic^{m+1}}{(1 + \beta c)} \tau r z^3 - \frac{9c}{2E^2} \tau r^2 z^3 + \frac{2Bic^{m+1}}{E^2(1 + \beta c)} \tau r^3 z^3 + \dots \dots \\ & \vdots \end{aligned} \tag{39}$$

One may determine the value of  $c$  by invoking the boundary at the base of the fin, as such

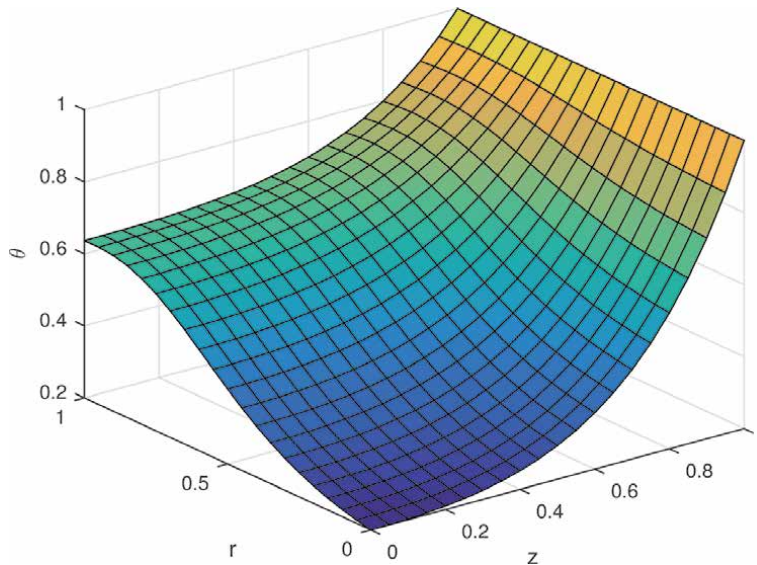
$$c\tau + c\tau r + c\tau r^2 + \dots + c\tau - \frac{Bic^{m+1}}{(1 + \beta c)} \tau r - \frac{5c}{2E^2} \tau r^2 \dots + c\tau - \frac{Bic^{m+1}}{(1 + \beta c)} \tau r - \frac{9c}{2E^2} \tau r^2 + \dots = 1.$$

To plot a three dimensional figure for this solution one may fix temperature, say at  $\tau = 0.4$  The results are shown in **Figure 2**.

#### 4.2.2 Two dimensional DTM

The two dimensional DTM solution for a steady heat transfer through the cylindrical fin is given by

$$\theta(r, z) = c - \frac{Bic^{m+1}}{1 + \beta c} r + \dots + cz^2 - \frac{Bic^{m+1}}{1 + \beta c} z^2 r + \dots + cz^3 - \frac{Bic^{m+1}}{1 + \beta c} z^3 r + \dots \tag{40}$$



**Figure 2.** Approximate analytical solutions for a two-dimensional cylindrical spine fin with a constant thermal conductivity ( $\beta = 0$ ) for  $\tau = 0.4$ . The parameters are set such that  $E = 2$ ,  $Bi = 0.2$ , and  $m = 3$ . (see also, [8]).

and  $c$  is obtained from

$$c - \frac{Bic^{m+1}}{1 + \beta c} r + \dots + c - \frac{Bic^{m+1}}{1 + \beta c} r - \frac{12c + 18\beta c^2 + 4E^2\beta c^2 + \frac{4E^2\beta Bi^2 c^{2m+2}}{(1+\beta c)^2}}{4E^2(1 + \beta c)} r^2 + \dots = 1.$$

This solution is plotted in **Figure 3**

#### 4.2.3 Comparison of one dimensional exact, DTM and VIM solutions

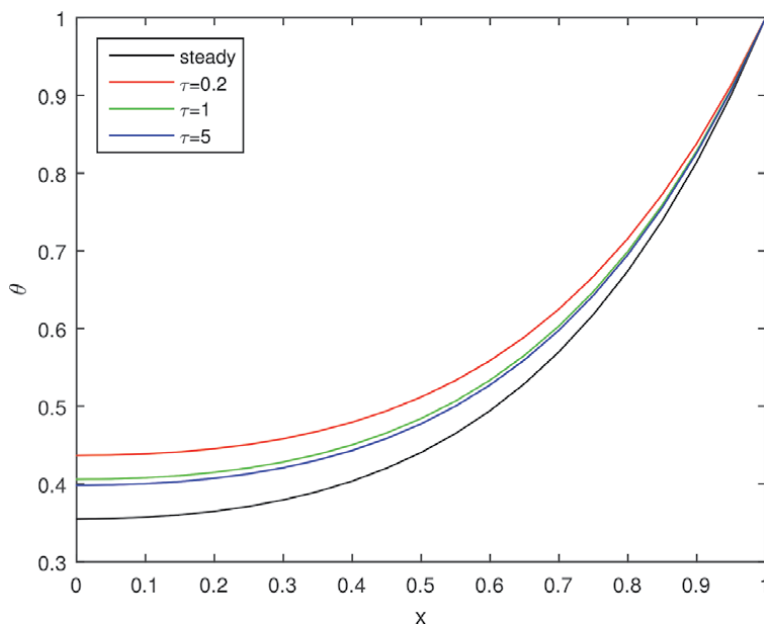
Here the solutions for the one dimensional heat transfer problems are compared, namely the exact solution given in Eq. (38). The VIM solutions is given by

$$\theta(x) = c + \frac{3c^2M^2x^2}{2} - \frac{3c^5M^2x^2}{2} + \frac{c^7M^2x^2}{2} + \frac{c^5M^4x^4}{8} - \frac{3c^7M^4x^4}{2} + \frac{5c^9M^4x^4}{4} - \frac{c^{11}M^4x^4}{4} + \dots \quad (41)$$

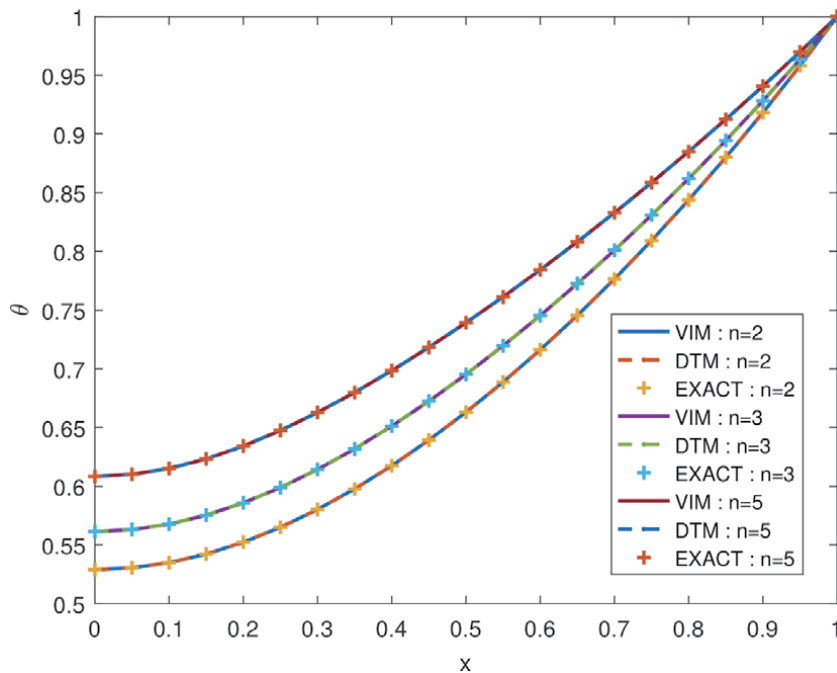
The constant  $c$  may be obtained using the boundary condition at the fin base. The DTM solution is given by (see [35])

$$\theta(x) = c + \frac{3c^2M^2x^2}{2} - \frac{c^2M^2x^2}{6} + \frac{c^2M^2(3 - 4M^2c)x^4}{48} + \frac{c^2M^2(1 - 16M^2c)x^5}{240} - \dots \quad (42)$$

Likewise, the constant  $c$  is obtained using the boundary conditions. These solutions are depicted in **Figure 4**.



**Figure 3.** Approximate analytical solutions for a two-dimensional cylindrical spine fin with a constant thermal conductivity ( $\beta = 0$ ) for  $\tau = 0.4$ . The parameters are set such that  $E = 2$ ,  $Bi = 0.2$ , and  $m = 3$ . (see also, [8]).



**Figure 4.**

A temperature distribution in a rectangular fin for varying values of  $n$ ,  $M = 1.7$ . (see also [36]).

## 5. Outlook and some concluding remarks

The interest in heat transfer through fins will continue unabated. This is brought about by applications of fins in engineering appliances. The solutions to the problems give insight into effectiveness and efficiency of different fins. In this chapter we provided a summary of some of the work in recent times. In particular, we reviewed the exact and approximate analytical solutions. We demonstrated that although the models describing heat transfer seem to be simple, they are in fact challenging to solve exactly. When constructed, the exact solutions are used as benchmarks for the approximate solutions. It appears that some models including contracting or expanding have attracted some attention. The analysis of these problems provide insight into heat transfer phenomena and assist in the design of fins. The challenge is the construction of exact solutions, however one may construct approximate analytical solutions. The problems discussed here are not exhaustive.

### Conflict of interest

The authors declare no conflict of interest.

### Nomenclature

$A_c$	Cross-sectional area
$Bi$	Biot number
$E$	Aspect ratio



$h$	dimensionless heat transfer coefficient
$H$	Heat transfer coefficient
$H_b$	Heat transfer coefficient at the base of the fin
$h$	Dimensionless thermal conductivity
$K_a$	Thermal conductivity of the fluid
$K$	Thermal conductivity of the fin
$L$	Length of the fin
$R$	Radius
$R_a$	Radius
$t$	time
$T_b$	Base temperature
$T_s$	Fluid temperature
$x$	Dimensionless fin length
$X$	Fin length
$y$	Dimensionless fin length
$Y$	Fin length
$Z$	Length of a cylindrical pin fin. Greek letters
$\tau$	Dimensionless time
$\theta$	dimensionless temperature

## Author details

Raseelo Joel Moitsheki<sup>1\*</sup>, Partner Luyanda Ndlovu<sup>1</sup> and Basetsana Pauline Ntsime<sup>2</sup>

<sup>1</sup> School of Computer Science and Applied Mathematics, University of the Witwatersrand, Johannesburg, South Africa

<sup>2</sup> Department of Mathematical Science, College of Science, Engineering and Technology, University of South Africa, Florida, South Africa

\*Address all correspondence to: [raseelo.moitsheki@wits.ac.za](mailto:raseelo.moitsheki@wits.ac.za)

## IntechOpen

© 2021 The Author(s). Licensee IntechOpen. This chapter is distributed under the terms of the Creative Commons Attribution License (<http://creativecommons.org/licenses/by/3.0>), which permits unrestricted use, distribution, and reproduction in any medium, provided the original work is properly cited. 

## References

- [1] A.D. Kraus, A. Aziz and J. Welte, *Extended Surface Heat Transfer*, Wiley, New York, 2001. <https://onlinelibrary.wiley.com/doi/pdf/10.1002/9780470172582.fmatter> [Accessed: 15 September 2020]
- [2] F. Khani and A. Aziz, Thermal Analysis of a Longitudinal trapezoidal fin with temperature-dependent thermal conductivity and heat transfer coefficient, *Communications in Nonlinear Science and Numerical Simulation*. 2010;15(3): 590–601. <https://www.sciencedirect.com/science/article/abs/pii/S1007570409002202> [Accessed: 15 September 2020]
- [3] F. Khani, M. A. Raji, and H. H. Nejad, Analytical solutions and efficiency of the nonlinear fin problem with temperature-dependent thermal conductivity and heat transfer coefficient, *Communications in Nonlinear Science and Numerical Simulation*. 2009;14(8): 3327–3338. <https://www.sciencedirect.com/science/article/abs/pii/S1007570409000355> [Accessed: 16 September 2020]
- [4] F. Khani and M.A. Raji, S.H. Nezhad, A series solution of the fin problem with a temperature-dependent thermal conductivity, *Communications in Nonlinear Science and Numerical Simulation*. 2009;14(7): 3007–3017. <https://www.sciencedirect.com/science/article/abs/pii/S1007570408004115> [Accessed: 16 September 2020]
- [5] Moitsheki RJ, Hayat T, Malik Y, Some exact solutions of the fin problem with a power law temperature-dependent thermal conductivity, *Nonlinear Analysis: Real World Applications* 2010;(11)5: 3287–3294 <https://www.sciencedirect.com/science/article/pii/S1468121809003459> [Accessed: 16 September 2020]
- [6] H.S. Kang and D.C. Look, Two dimensional trapezoidal fins analysis, *Computational Mechanics*. 1997; 19: 247–250 <https://link.springer.com/article/10.1007/s004660050173> [Accessed: 16 September 2020]
- [7] R.J. Moitsheki and A. Rowjee, Steady Heat Transfer through a two-dimensional rectangular straight fin <http://downloads.hindawi.com/journals/mpe/2011/826819.pdf> [Accessed: 16 September 2020]
- [8] N. Fallo and R.J. Moitsheki, Approximate Analytical Solutions for Transient Heat Transfer in Two-Dimensional Straight Fins, *Nonlinear Dynamics and Systems Theory*. 2019;19: 133–140, [http://www.e-ndst.kiev.ua/v19n1-SI/3\(67\).pdf](http://www.e-ndst.kiev.ua/v19n1-SI/3(67).pdf) [Accessed: 14 September 2016]
- [9] R.J. Moitsheki and M.D. Mhlongo, Classical Lie point symmetry analysis of a steady nonlinear omne-dimensionalsl fin problem. *Journal of Applied Mathematics*. 2012; Article ID 671548, 13 pages. <https://www.hindawi.com/journals/jam/2012/671548/> [Accessed: 14 September 2020].
- [10] R.J. Moitsheki, Steady heat transfer through a radial fin with rectangular and hyperbolic profiles, *Nonlinear Analysis: Real World Applications* 2011;12(2):867–874 <https://www.sciencedirect.com/science/article/pii/S1468121810001975> [Accessed: 15 September 2020].
- [11] R.J. Moitsheki, Steady one dimensional heat flow in a longitudinal triangular and parabolic fin, *Communications in Nonlinear Science and Numerical Simulation*. 2011;16(10): 3971–3980 <https://www.sciencedirect.com/science/article/abs/pii/S1007570411000426> [Accessed: 15 September 2020].
- [12] A. Moradi, Analytical solutions for fin with temperature dependant heat transfer coefficient, *International*

Journal of Engineering and Applied Sciences, 2011;3(2): 1–12. <https://dergipark.org.tr/en/download/article-file/217660> [Accessed: 20 September 2020].

[13] M. Turkyilmazoglu, An optimum profile of a special pin fin: full solutions, International Journal of Numerical Methods for Heat and Fluid Flow. 2020. Ahead of print. <https://www.emerald.com/insight/content/doi/10.1108/HFF-11-2019-0801/full/html> [Accessed: 30 September 2020]

[14] M. Turkyilmazoglu, Heat transfer through longitudinal fins, Journal of Thermophysics and Heat Transfer. Journal of Thermophysics and Heat Transfer. 2014;28(4): 806–811. <https://arc.aiaa.org/doi/abs/10.2514/1.T4348?journalCode=jtht> [Accessed: 15 September 2020]

[15] M. Turkyilmazoglu, Exact heat-transfer solutions to radial fins of general profile. Journal of Thermophysics and Heat Transfer. 2016;30(1): 89–93. <https://arc.aiaa.org/doi/abs/10.2514/1.T4555> [Accessed: 15 September 2020]

[16] R.J. Moitsheki and C. Harley, Steady thermal analysis of two-dimensional cylindrical pin fin with a nonconstant base temperature. Mathematical Problems in Engineering. 2011; Article ID 132457. 17 pages. <https://www.hindawi.com/journals/mpe/2011/132457/> [Accessed: 15 September 2020]

[17] N. Fallo, R.J. Moitsheki and O.D. Makinde, Analysis of heat transfer in a cylindrical spine fin with variable thermal properties, Defect and Diffusion Forum, 2018;387: 10–22 <https://www.scientific.net/DDF.387.10> [Accessed: 15 September 2020]

[18] A. Moradi, A.P.M. Fallah, T. Hayat, O.M. Aldossary. On solution of natural convection and radiation heat transfer problem in a moving porous fin. Arabian J Sci Eng. 2014;39:1303–12.

<https://link.springer.com/article/10.1007/s13369-013-0708-9> [Accessed: 15 September 2020]

[19] M.G. Sobamowo, Analysis of heat transfer in porous fin with temperature-dependent thermal conductivity and internal heat generation using Chebychev Spectral Collocation Method, Journal of Computational Applied Mechanics. 2017;48(2): 271–284. [https://jcamech.ut.ac.ir/article\\_63384.html](https://jcamech.ut.ac.ir/article_63384.html) [Accessed: 15 September 2020]

[20] H.A. Hoshyar, I. Rahimpetroudi, D.D. Ganji, A.R. Majidian, Thermal performance of porous fins with temperature-dependent heat generation via the homotopy perturbation method and collocation method. Journal of Applied Mathematics and Computational Mechanics. 2015;14(4): 53–65 <http://amcm.pcz.pl/?id=view&volume=14&issue=4&article=6> [Accessed: 15 September 2020]

[21] G. Oguntala and R. Abd-Alhameed, Haar Wavelet Collocation Method for thermal analysis of porous fin with temperature-dependent thermal conductivity and internal heat generation, Journal of Applied and Computational Mechanics. 2017;3(3): 185–191. <https://bradscholars.brad.ac.uk/handle/10454/12045> [Accessed: 15 September 2020]

[22] Y. Sun, J. Ma, B. Li and Z. Guo, Prediction of nonlinear heat transfer in a convective-radiative fin with temperature dependent properties by the collocation spectral method. Numerical Heat Transfer Part B Fundamentals. 2015;69(1):68–83 <https://www.tandfonline.com/doi/abs/10.1080/10407782.2015.1081043?journalCode=unhb20> [Accessed: 15 September 2020]

[23] S.S. Motsa, P. Sibanda and S. Shateyi, A new spectral-homotopy analysis method for solving a nonlinear

- second order BVP, *Communications in Nonlinear Science and Numerical Simulation*. 2010; 15(9): 2293–2302 <https://www.sciencedirect.com/science/article/abs/pii/S1007570409004754> [Accessed: 07 October 2020]
- [24] M. Esmailpour and D.D. Ganji, Solution of the Jeffery–Hamel flow problem by optimal homotopy asymptotic method. *Computers and Mathematics with Applications*. 2010;59(11), 3405–3411. <https://www.sciencedirect.com/science/article/pii/S0898122110002002> [Accessed:07 October 2020]
- [25] R.J. Moitsheki and C. Harley, Transient heat transfer in longitudinal fins of various profiles with temperature-dependent thermal conductivity and heat transfer coefficient, *Pramana Journal of Physics*. 2011;77: 519–532. <https://link.springer.com/article/10.1007/s12043-011-0172-6> [Accessed: 31 September 2020]
- [26] M.D. Mhlongo, R.J. Moitsheki and O.D. Makinde, Transient response of longitudinal rectangular fins to step change in base temperature and in base heat flow conditions, *International Journal of Heat and Mass Transfer*. 2013;57(1), 117–125. <https://www.sciencedirect.com/science/article/abs/pii/S0017931012007788> [Accessed: 01 October 2020]
- [27] P.L. Ndlovu, The significance of fin profile and convective-radiative fin tip on temperature distribution in a longitudinal fin, *Nano Hybrids and Composites*. 2019;26: 93–105. <https://www.scientific.net/NHC.26.93> [Accessed: 7 September 2020]
- [28] P.L. Ndlovu, Analytical study of transient heat transfer in a triangular moving porous fin with temperature dependant thermal properties, *Defect and Diffusion Forum*. 2019;393:31–46. <https://www.scientific.net/DDF.393.31> [Accessed:12 September 2020]
- [29] P.L. Ndlovu and R.J. Moitsheki, Analysis of transient heat transfer in radial moving fins with temperature-dependent thermal properties, *Journal of Thermal Analysis and Calorimetry*. 2019;138: 2913–2921. <https://link.springer.com/article/10.1007/s10973-019-08306-5> [Accessed:29 September 2020]
- [30] P.L. Ndlovu and R.J. Moitsheki, Analysis of temperature distribution in radial moving fins with temperature dependent thermal conductivity and heat transfer coefficient. *International Journal of Thermal Sciences*. 2019;145: 106015 <https://www.sciencedirect.com/science/article/abs/pii/S1290072919301784> [Accessed: 10 September 2020]
- [31] G.W. Bluman and S. Anco, *Symmetry and Integration Methods for Differential Equations*. Applied Mathematical Sciences, Springer, New York. 2002. <https://www.springer.com/gp/book/9780387986548> [Accessed: 7 September 2020]
- [32] A. Kurnaz, G. Oturanç and M.E. Kiris, n-Dimensional differential transformation method for solving PDEs. *International Journal of Computer Mathematics*. 2005;82(3) 369–380. <https://www.tandfonline.com/doi/abs/10.1080/0020716042000301725> [Accessed: 5 September 2020]
- [33] J.H. He, Variational iteration method — a kind of non-linear analytical technique: some examples, *International Journal of Non-Linear Mechanics*. 1999;(34) 699—708. <https://tarjomefa.com/wp-content/uploads/2018/06/9165-English-TarjomeFa.pdf> [Accessed: 20 September 2020]
- [34] A.M. Wazwaz, The variational iteration method for solving linear and nonlinear ODEs and scientific models with variable coefficients. *Central European Journal of Engineering*, 2014; 4: 64–71. <https://link.springer.com/artic>

le/10.2478/s13531-013-0141-6  
[Accessed: 15 September 2020]

[35] P.L. Ndlovu and R.J. Moitsheki, Analytical solutions for steady heat transfer in longitudinal fins with temperature-dependent properties. *Mathematical Problems in Engineering*. 2013, Article ID 273052. <https://www.hindawi.com/journals/mpe/2013/273052/> [Accessed: 22 September 2020]

[36] P.L. Ndlovu and R.J. Moitsheki, Predicting the Temperature Distribution in Longitudinal Fins of Various Profiles with Power Law Thermal Properties Using the Variational Iteration Method. *Defect and Diffusion Forum*, 387: 403–416 <https://www.scientific.net/DDF.387.403> [Accessed: 10 December 2020]



# Analysis of Liquid Cooling in Microchannels Using Computational Fluid Dynamics (CFD)

*Chitra Boobalan, Sudha Ganesh and Parthiban Rangaswamy*

## Abstract

Liquid cooling is an extremely successful process to remove excess heat generated, with the usual procedure of heat transfer using coolant in desktop PCs. In this regard, heat transfer with minimal size equipment can be achieved by the addition of nanosized solid particles to the base fluid. The hybrid nanofluid is synthesized by dispersing the synthesized mono nanofluid in a volume fraction of 0.2 iron oxide with 0.8 fractions of graphene nanofluid to form a graphene/iron oxide combination. These nanoparticles increase the heat transfer coefficient as they have high thermal conductivity when compared to conventional heat transfer fluids like water or ethylene glycol. Stability is increased and sedimentation is reduced because of the large surface area of a nanoparticle. FLUENT, the most widely used computational fluid dynamics (CFD) software package, based on the finite volume method, and is used to run the thermal simulations for estimating the base temperature of the heat sink. The scope of this chapter is to find the base temperature of the heat sink using simulations. The experimentally measured base temperature is 310.01 K and in the simulation, it is 310.81 K for the flow rate of 0.75LPM. All the simulated surface temperatures are compared with experimentally determined temperatures for simulation validation.

**Keywords:** microchannel, nanocoolant, base temperature, CFD

## 1. Introduction

Liquid cooling in microchannels is a highly successful method of removing excess heat from the circuits, with water being the most common heat transfer fluid on the desktop. The important advantage of using water cooling over air cooling is due to enhanced thermal properties of water (higher thermal conductivity and heat capacity property).

The noteworthy development of power densities in the Central Processing Unit (CPU) chips and also the reduction of their surface area contribute to the production of high heat flux. Computers and the processor's thermal management and its operation without overheating are a difficult task nowadays. The increase of transistors used in the circuit has reached up to 580 million. Microelectronics devices are safe on their operating temperature for the range of 70–80 °C and the reliability is decreased 5% for every degree rise in temperature. One sensible manner is to

use liquid fluid to gain the generated heat by convective means and deliver it to the external surroundings. Also, convective systems have the potential to be designed for various configurations. As proved in [1], bulk heat transfer is more significant than the thermal properties for most applications because bulk transport is the main reason for heating or cooling. This micron-sized particle, when used in low volume fractions prevents particles clogging and also reduces the pressure drop.

PC coolers are helpful for this reason using appropriate working liquids coolant. They will greatly enhance the system's cooling performance. Heat sinks are equipped for simultaneous cooling of several chips and also processor supply circuits, graphic cards, and CPU. In employing a heat sink very low flow rates of coolants are required and thereby the noise generations are also minimal as mentioned in [2].

This liquid cooling is categorized into active and passive cooling. The principle of an active liquid cooling system for computers is the same as that used in combustion engines, with the coolant being water which is circulated by a pump. This Heat sink made of microchannels is mounted on the CPU and sometimes on the components like GPU and Northbridge and cooled typically a radiator. The radiator itself is cooled externally by employing a fan [3].

Both active liquid cooling systems and passive liquid cooling systems are used depending upon the requirements. The passive system often discards a fan or a water pump, hence the reliability of the system can be theoretically increased and or making it quieter than active systems. However, they are much less efficient in discarding the heat and thus also need to have much more coolant and thus a much bigger coolant reservoir (giving more time to the coolant to cool down).

Although liquid cooling under forced convection enables higher heat dissipation rates, air cooling is the most common technique for heat removal. The primary advantage of air cooling is its easy operability with less noise. Forced air-cooling processes may be further classified into serial and parallel flow systems. In a serial system, the air stream is passed over successive rows of modules or boards, so that each row is treated by the same air that has been preheated by the previous row. The power and airflow requirements are the key factors in serial airflow resulting in an extensive air temperature rise across the machine. Parallel airflow systems can be used to reduce the temperature rise in the cooling air. In this system, the printed circuits or modules are all equipped with a parallel air supply. In this method, each board or module is supplied with a fresh supply of cooling air [4].

## **2. Nano coolants in microchannels for CPU cooling**

In this connection, heat transfer equipment with minimal size can be achieved by adding solid small-sized particles [5]. These particles have high thermal conductivity when compared to conventional coolants like water or ethylene glycol [6]. If the suspended particle size is in the order of microns and millimeter lot of problems like particle settlement, corrosion and more pressure drop needs to be overcome. Because of these drawbacks, milli-size or micron-size particles are not used widely. Choi and Eastman [7] tried suspending nanometer particles in a solution. The nano-sized particle and their low volume fractions prevent particles from clogging and also reduce the pressure drop. Stability is increased and sedimentation of the particle is decreased due to its increased surface area of particles [8]. The efficiency in heat removal is improved since heat transfer takes place at the particle surface. Nanosheets comprising MAXene obtained from  $Ti_3SiC_2$  MAX phase ternary carbides can be a probable nanocoolant with very efficient thermal management. It is synthesized via shear-induced micromechanical delamination technique. It is also



known as 'rheo-controlled' nanofluid. The thermal conductivity increments are about 45% at 323 K [9]. The corrosion effect of nano coolant accompanying material loss needs to be analyzed. Coolants such as graphene nanoparticles, corrosive water, and ethylene glycol were studied and their effects on parameters like the temperature of the coolant, inlet pressure, and rpm of the pump were recorded [10]. He also confirmed that the corrosion effect was the same for both the base coolant and nanocoolant [11]. The suspended graphene nanoparticles with water as a base solvent and for various volume fractions and measured its convection coefficients for the temperature range of 30 °C to 80 °C. The heat transfer characteristics of hybrid nanofluid (HyNF) flow through the tubular heat exchanger were also studied by [12]. They examined the various parameters like thermal conductivity and heat transfer coefficient under forced convection. The experiments were performed for various nanoparticles ranging from 0.1% to 1.0% volume concentrations added in the base fluid. The results showed that the bulk heat transfer coefficient was maximum by 48.4% up to 0.7% volume concentration of HyNC.

## 2.1 CPU cooling with hybrid nanofluid

Labib et al. [13] employed two different base fluids of water and ethylene glycol and analyzed the effect of convective heat transfer mixing of Al<sub>2</sub>O<sub>3</sub> nanoparticles. The CFD results are validated with the experimental data for Al<sub>2</sub>O<sub>3</sub>/water nanofluid. The results revealed that Ethylene Glycol base fluid gives better heat transfer enhancement than that of water. The mixture of Al<sub>2</sub>O<sub>3</sub> nanoparticles into CNTs/water nanofluid is a new concept of combined/hybrid nanofluid that can profitably increase convective heat transfer. Eshgarf and Afrand [14] studied the rheological behavior of COOH functionalized MWCNTs–SiO<sub>2</sub>/EG–water hybrid nanocoolant for application in cooling systems. They prepared the stable suspension of MWCNTs and SiO<sub>2</sub> nanoparticles (50:50 volume%) in a specified amount of a binary mixture of EG–water (50:50 vol.%) for the temperature range of 27.5–50 °C. From the results, it is inferred that the apparent viscosity generally increases with an increase in the solid volume fraction and decreases with increasing temperature.

Naquiuddin et al. [15] showed geometrically graded microchannel heat sink for improvements in thermal performances. They showed for a heat load of 2000 W, the average temperature of the microchannel can be reduced to 69.6°Celsius with a temperature variation of 3° Celsius. Microchannel heat sink with micro-scale ribs and grooves for chip cooling is also investigated with CFD studies [16]. The performances of various heat sink parameters like trapezoidal, rectangular, and triangular-shaped microchannel with different channel width and aspect ratio was analyzed. The rectangular microchannel showed the best performance with the aspect ratio among 8.904–11.442. The rectangular microchannel has the lowest thermal resistance, followed by the trapezoid and triangle microchannel. Wang et al. [17] designed a heat sink with micro-scale ribs and grooves for chip cooling. The cooling efficiency is more for rib-grooved microchannel than the conventional smooth rectangular microchannel through experimental and numerical approaches. The Nusselt number of rib-grooved microchannel can be 1.11–1.55 times that of a smooth microchannel. He also studied the apparent friction factor for various relative rib heights of 0.6, 0.73, and 0.85 μm.

## 2.2 Synthesis of nanofluid

For nanofluid synthesis, there are many key factors to be considered [18]. Stable nanofluid [19] can be formed by one and two-step methods [20]. Both one-step and two-step methods can produce nanoparticles in suspension and also agglomeration

of particles. Thus, it is required to synthesis a suspension of non-agglomerated and also well-monodispersed nanoparticles in the liquid are the key steps for the enhancement of the thermal properties of nanofluid.

To withstand the operating temperature it should high thermal stability

- i. For the homogeneity of the medium, its dispersion should be uniform
- ii. Chemical compatibility and ease of chemical manipulation.

### 2.2.1 Synthesis of graphene nanoparticle

Graphene oxide nanopowders are used for graphene synthesis. Quartz crucible filled with GO is kept inside the muffle furnace at 500 °C followed by the process of thermal exfoliation–reduction under air atmosphere for 4 min. The prepared graphene powder temperature is reduced to the air ambient temperature.

### 2.2.2 Synthesis of iron oxide nanoparticle

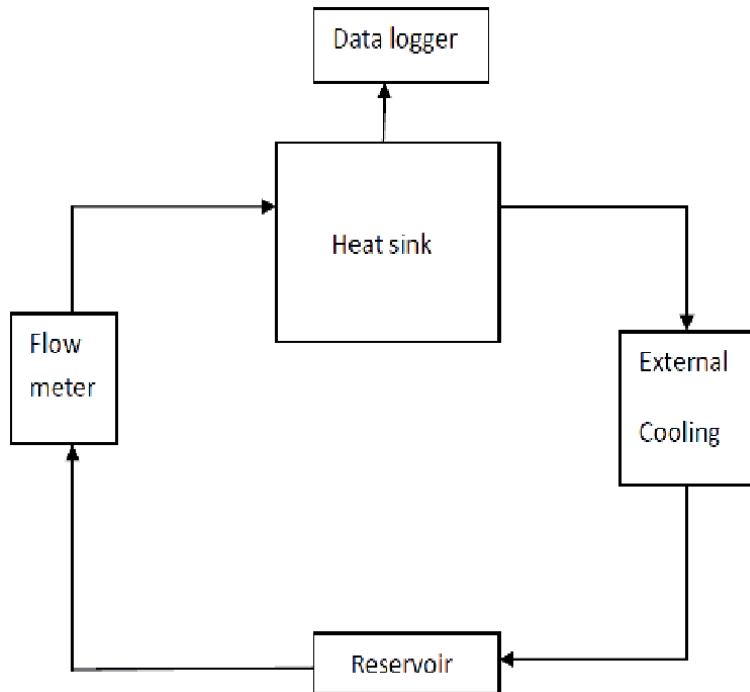
In 5 mL of distilled water, Iron (II) chloride tetrahydrate powder and 50 mL of isobutanol were added after which  $Fe^{2+}$  ions were formed. The aqueous organic mixture was heated to 75 °C, added dropwise for 2 hours with 0.8 M NaOH and stirred for 30 min at 500 rpm. The synthesized iron oxide nanoparticles were washed with distilled water at 75 °C and dried in an oven at 50 °C. The dried particles of iron oxide nanoparticles were calcined for 2 h at 300 °C, 100 minutes at 400 and 600 °C. The hybrid nanofluid was prepared by dispersing the synthesized mono nanofluid in a volume fraction of 0.2 iron oxide with 0.8 fractions of graphene nanofluid to form graphene/iron oxide combination. The prepared hybrid fluid thermal properties as given in **Table 1** are used for further simulations.

### 2.2.3 Experimental set up

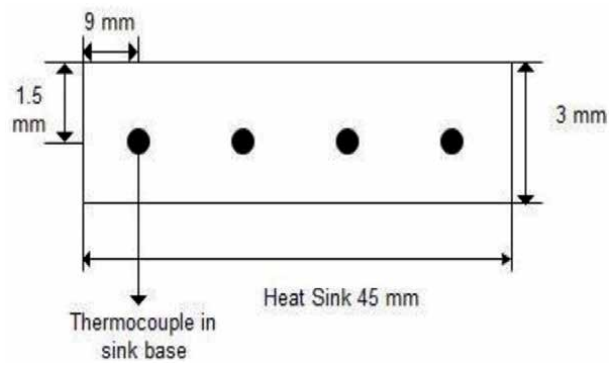
**Figure 1** illustrates the heat sink used in the experimental setup [21]. **Figure 2** depicts the channel in the fabricated heat sink fitted with Four number of K-type thermocouples Thermocouples. The fabricated dimension of the heat sink comprising microchannels is tabulated in **Table 2**. Around 1 L of hybrid coolant is prepared and it is filled in the reservoir tank. It then flows to the test loop includes a needle valve in order to facilitate the different volumetric flow rates of synthesized hybrid nanocoolant. Omega rotameter (+1% full-scale accuracy) was used to measure the flow rate ranging from 0.35 to 0.75 LPM. The coolant enters the inlet port of the fabricated sink and absorbs the heat generated at the bottom of the sink due to its enhanced thermal properties and exits through the outlet port. This coolant is further cooled to its inlet temperature in a radiator as depicted in the cycle. **Figure 3** represents the fabricated heat sink made of copper with inlet

Coolant - type	Density (kg/m <sup>3</sup> )	Specific heat (J/kg/K)	Thermal conductivity (W/mK)	Viscosity (cp)
G-Feo	1049.13	3795	1.209	1.4
De-ionisedwater	995.6	4178	0.615	1.0

**Table 1.**  
Thermo-physical properties of nano coolants at 303 K for volume fraction 0.1%.



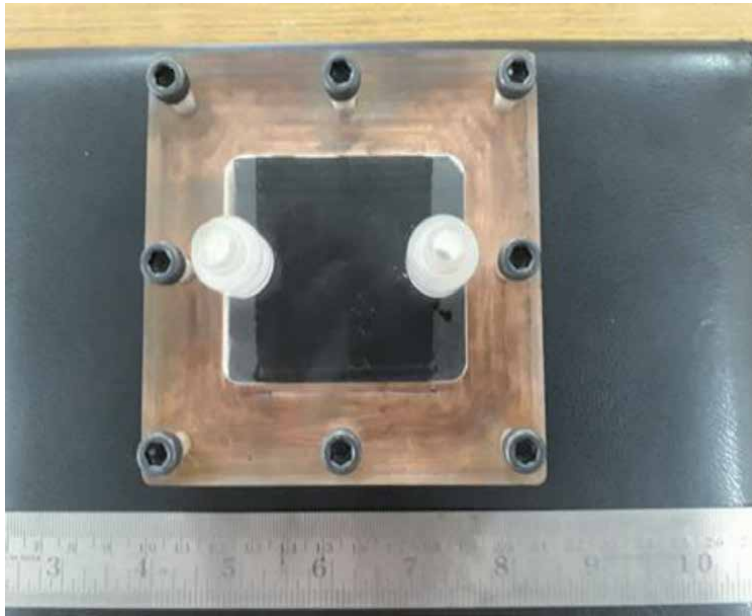
**Figure 1.**  
 Experimental flow diagram.



**Figure 2.**  
 Microchannel side view with thermocouples.

Various Fin parts	Dimensions (mm)
Width	55
Length	45
Height of fin	3
Width of microchannel	0.5
Heat sink base thickness	3

**Table 2.**  
 Heat sink dimension mm.



**Figure 3.**  
*Microchannel with inlet and exit ports.*

and outlet ports. The average temperature of the four thermocouples indicates the experimentally measured base temperature of the heat sink.

### 3. Computational fluid dynamics (CFD) in microchannels

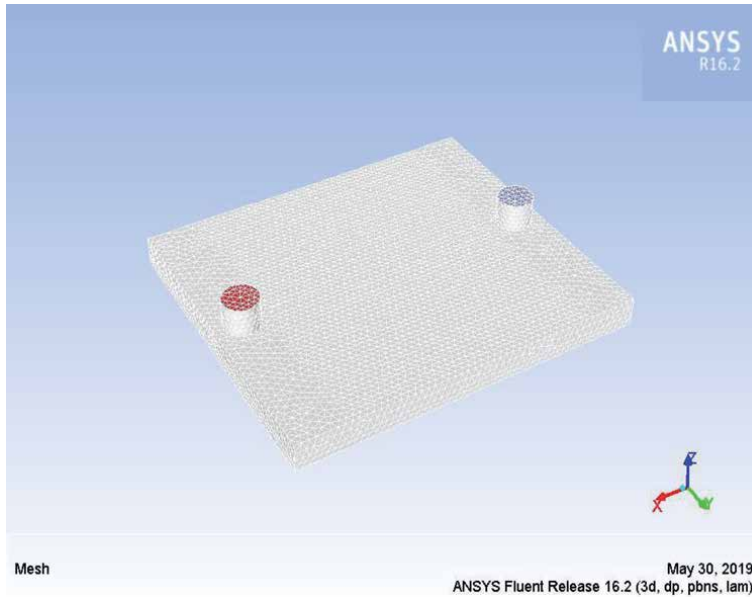
FLUENT, the most widely used Computational Fluid Dynamics (CFD) software package, based on the finite volume method, and was used to run the thermal simulations. Meshes were created, with 117353 elements, together in the fluid and solid domain. In order to simulate a fully developed flow, tubes at the inlet and outlet are selected with a length equals to 10 tube diameters.

<b>Properties of cell mesh</b>	
Total number of elements	117353
Elements in fluid domain	77408
Elements in the solid domain	39948
<b>Orthogonal quality</b>	
Interior fluid	0.099
Interior solid	0.1176
Minimum fluid	0.207
Minimum solid	0.164
Maximum fluid	0.990
Maximum solid	0.989

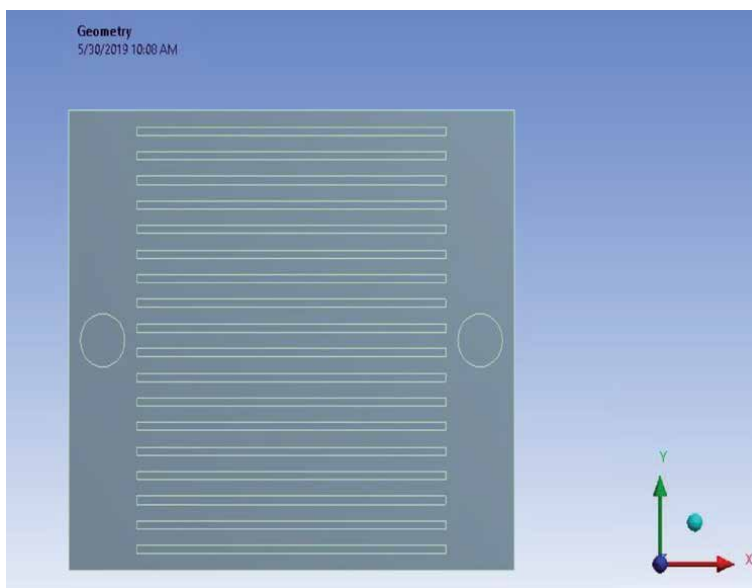
**Table 3.**  
*Generated grid values.*

The fluid flow BCs used in the CFD are as follows:

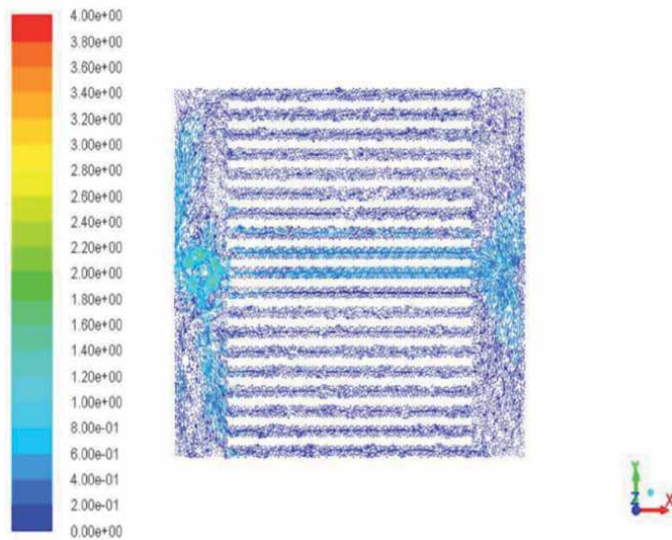
- i. A constant inlet mass flow rate condition, ranging from 0.005 to 0.013 kg/s.
- ii. A constant heat flux  $134.839 \text{ kW/m}^2$  [22] as the reference is set at the base wall of the heat sink.



**Figure 4.**  
*Heat sink with mesh.*



**Figure 5.**  
*Top view of heat sink geometry.*



**Figure 6.**  
*Top view of microchannel showing velocity vector.*

As a basic assumption, a fully developed flow (pressure outlet) is imposed. At all walls, a zero velocity (No-slip condition) boundary condition is applied and simulations are performed until the steady-state value of  $T$  base is attained. The generated grid values are tabulated in **Table 3**.

Mesh with three different sizes was generated for the grid independency test. With maximum mesh size of 2 mm (mesh-1), 1 mm (mesh-2) and 0.75 mm (mesh-3) respectively. The change in Average temperature values between (mesh-2) and (mesh-3) is only about 0.4%. So, mesh-2 with a size of 1 mm is used in further simulations. The typical microchannel with final meshing is shown in **Figure 4**. The top view of the heat sink without meshing is shown in **Figure 5**.

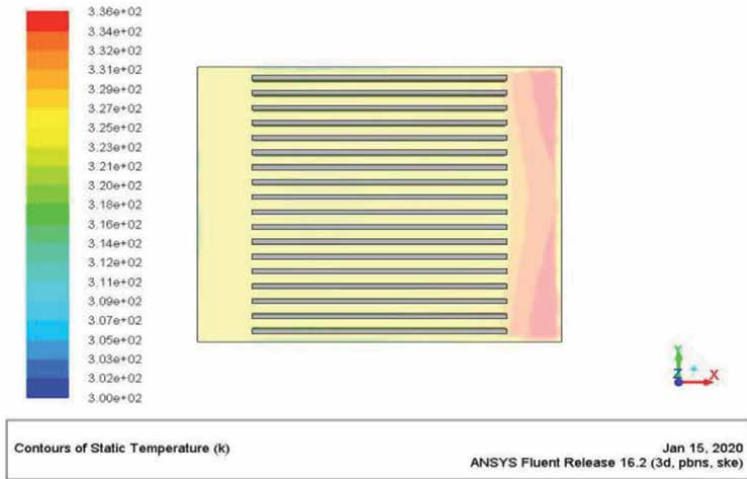
Simulations are performed for laminar flow in the channel path of the fabricated heat sink and examined for various conditions. **Figure 6** indicates the top view of the microchannel with the velocity vector showing the fluid flow directions. The direction of the velocity vector indicates the flow of the hybrid coolant from the inlet to the outlet port through the microchannels.

#### 4. Various contours of graphene - iron oxide

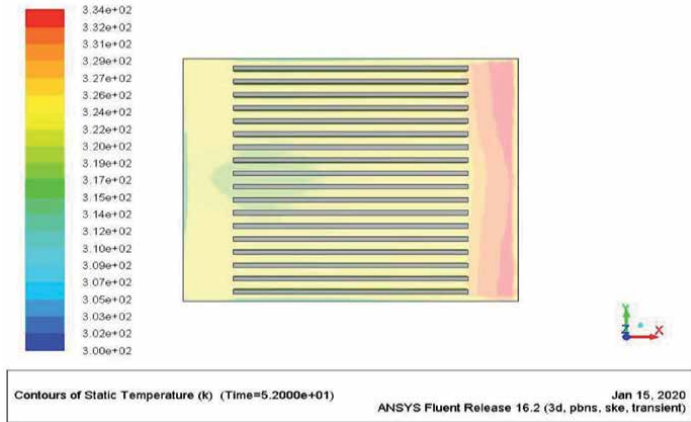
The temperature contours of graphene - iron oxide coolant are shown in **Figures 7–9** for 0.05 volume %, 0.075 volume %, and 0.1 volume % respectively. These contours represent the temperature distribution all along the length of the channel from inlet to exit port in the X direction. From these contours, it is implicit that the coolant temperature increases as it flows along the length of the channel. From **Figure 9**, it is inferred that more heat is absorbed for 0.1 vol % graphene - iron oxide coolant and the base plate temperature of the heat sink was 310.81 K for 0.1 volume fraction of coolant for the flow rate of 0.75 LPM.

##### 4.1 Wall base temperature

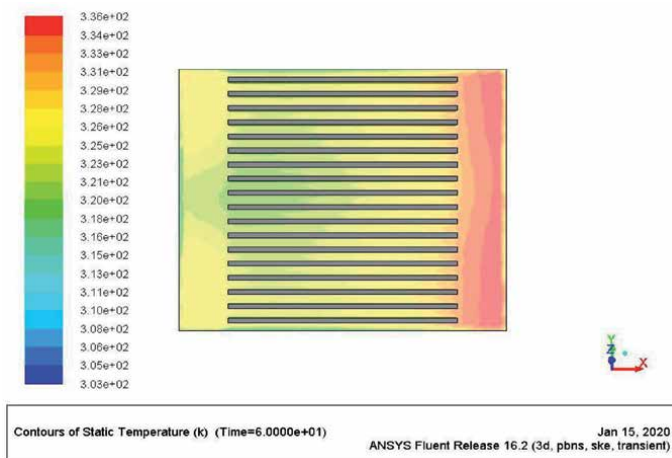
The processor operating temperature (heat sink base temperature) under various flow rates for different coolant concentration is represented in **Figure 10**. It is inferred



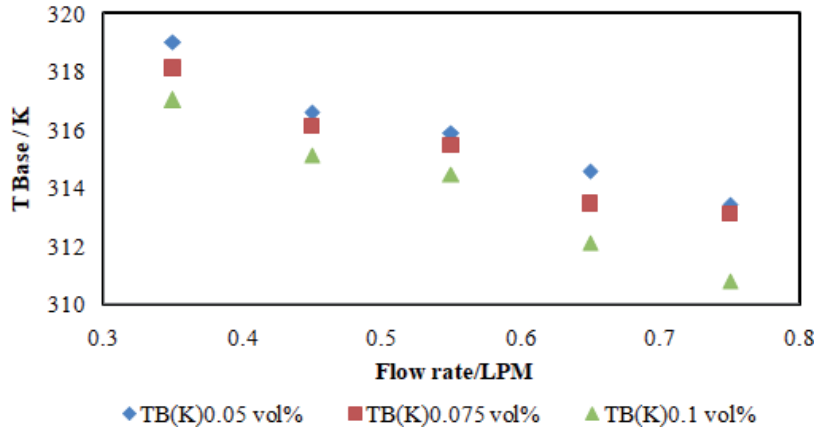
**Figure 7.**  
*Temperature contours for 0.05 volume % graphene-iron oxide.*



**Figure 8.**  
*Temperature contours for 0.075 volume % graphene-iron oxide.*



**Figure 9.**  
*Temperature contours for 0.1 volume % - graphene-iron oxide.*

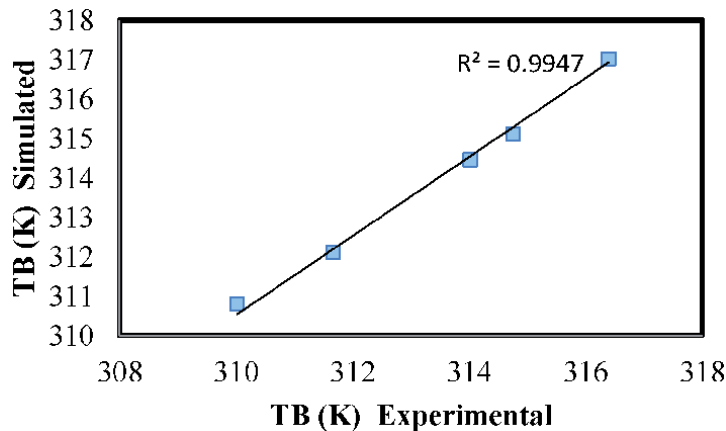


**Figure 10.**  
Simulated base temperature versus flow rate - graphene-iron oxide.

from the graph representing the lowest temperature of 310.01 K for the concentration of 0.1 vol. % graphene-iron oxide system for 0.5 mm fin spacing while for water it is 317.05 K. These hybrid coolants because of their high thermal conductivity are capable of removing more heat when used in microchannels. The percentage reduction in base temperature when using graphene-iron oxide is 1.96%.

## 5. Comparison of simulated and experimental base temperatures

**Figure 11** shows the comparison of simulated and experimental base temperatures for 0.1 volume % graphene – iron oxide and the correlation coefficient was found to be 0.994 which validates the model.



**Figure 11.**  
Validation of experimental and simulated values of T base – 0.1 volume % graphene-iron oxide.

## 6. Conclusion

The present work indicates the usage of graphene as one of the components in the synthesis of hybrid nanofluids for CPU cooling by microchannel cooling



techniques. In this, graphene-iron oxide nanocoolants are used at three different volume fractions and base temperatures are measured. The experimental temperature is 310.01 K and in the simulation, it is 310.81 K for the flow rate of 0.75LPM. A comparison is made between the experimentally measured base temperatures and the simulated temperatures correlation coefficient was obtained to validate the model.

## Author details


Chitra Boobalan<sup>1</sup>, Sudha Ganesh<sup>2</sup> and Parthiban Rangaswamy<sup>1\*</sup>

1 Department of Chemical Engineering, Sri Sivasubramaniya Nadar College of Engineering, Kalavakkam, Tamilnadu, India

2 Department of Chemical Engineering, Sri Venkateswara College of Engineering, Pennalur, Tamilnadu, India

\*Address all correspondence to: [parthibanr@ssn.edu.in](mailto:parthibanr@ssn.edu.in)

## IntechOpen

© 2021 The Author(s). Licensee IntechOpen. This chapter is distributed under the terms of the Creative Commons Attribution License (<http://creativecommons.org/licenses/by/3.0>), which permits unrestricted use, distribution, and reproduction in any medium, provided the original work is properly cited. 

## References

- [1] Roberts NA, Walker DG. Convective performance of nanofluids in commercial electronics cooling systems. *Applied Thermal Engineering*. 2010;30(16):2499-2504.
- [2] Rafati M, Hamidi AA, Niaser MS. Application of nanofluids in computer cooling systems (heat transfer performance of nanofluids). *Applied Thermal Engineering*. 2012 Dec 1;45:9-14.
- [3] Alagesan S, Duraisamy S, Raman M. Experimental investigation on thermal performance of plate fin heat sinks with nano PCM. *Thermal Science*. 2019(00):357.
- [4] Ojha S. CFD analysis on forced convection cooling of electronic chips[thesis]; 2009.
- [5] Zengyuan G. FRONTIER OF HEAT TRANSFER—MICROSCALE HEAT TRANSFER [J]. *Advances in Mechanics*. 2000;1
- [6] Choi SU, Eastman JA. Enhanced heat transfer using nanofluids. University of Chicago, U.S. Patent 6,221,275; 2001.
- [7] Choi SU, Eastman JA. Enhancing thermal conductivity of fluids with nanoparticles. Argonne National Lab., IL (United States); 1995.
- [8] Heris SZ, Esfahany MN, Etemad G. Numerical investigation of nanofluid laminar convective heat transfer through a circular tube. *Numerical Heat Transfer, Part A: Applications*. 2007 Sep 21;52(11):1043-1058.
- [9] Mahesh KV, Linsha V, Mohamed AP, Ananthakumar S. Processing of 2D-MAXene nanostructures and design of high thermal conducting, rheo-controlled MAXene nanofluids as a potential nanocoolant. *Chemical Engineering Journal*. 2016 Aug 1;297:158-169.
- [10] Xian HW, Sidik NA. Erosion-corrosion effect of nanocoolant on actual car water pump. In *IOP Conference Series: Materials Science and Engineering* 2019 (Vol. 469, No. 1, p. 012039). IOP Publishing.
- [11] Kumar KD, Gowd BU. Convective heat transfer characteristics of graphene dispersed nanofluids. *Int. J. Mech. Eng. Robot. Res.* 2012;2:250-260.
- [12] Madhesh D, Kalaiselvam S. Experimental analysis of hybrid nanofluid as a coolant. *Procedia Engineering*. 2014;97:1667-1675.
- [13] Labib MN, Nine MJ, Afrianto H, Chung H, Jeong H. Numerical investigation on effect of base fluids and hybrid nanofluid in forced convective heat transfer. *International Journal of Thermal Sciences*. 2013 Sep 1;71:163-171.
- [14] Eshgarf H, Afrand M. An experimental study on rheological behavior of non-Newtonian hybrid nano-coolant for application in cooling and heating systems. *Experimental Thermal and Fluid Science*. 2016 Sep 1;76:221-227.
- [15] Naqiuddin NH, Saw LH, Yew MC, Yew MK, Yusof F. Numerical study of the geometrically graded micro-channel heat sink for high heat flux application. *Energy Procedia*. 2017 Dec 1;142:4016-4021.
- [16] Wang G, Niu D, Xie F, Wang Y, Zhao X, Ding G. Experimental and numerical investigation of a microchannel heat sink (MCHS) with micro-scale ribs and grooves for chip cooling. *Applied Thermal Engineering*. 2015 Jun 25;85:61-70.

[17] Wang H, Chen Z, Gao J. Influence of geometric parameters on flow and heat transfer performance of micro-channel heat sinks. *Applied Thermal Engineering*. 2016 Aug 25;107:870-879.

[18] Parametthanuwat T, Rittidech S, Pattiya A, Ding Y, Witharana S. Application of silver nanofluid containing oleic acid surfactant in a thermosyphon economizer. *Nanoscale research letters*. 2011 Dec;6(1):1-0.

[19] Garg P, Alvarado JL, Marsh C, Carlson TA, Kessler DA, Annamalai K. An experimental study on the effect of ultrasonication on viscosity and heat transfer performance of multi-wall carbon nanotube-based aqueous nanofluids. *International Journal of Heat and Mass Transfer*. 2009 Oct 1;52(21-22):5090-5101.

[20] Zarringhalam M, Karimipour A, Toghraie D. Experimental study of the effect of solid volume fraction and Reynolds number on heat transfer coefficient and pressure drop of CuO–water nanofluid. *Experimental Thermal and Fluid Science*. 2016 Sep 1;76:342-351.

[21] Didarul IM, Kenyu O, Minoru Y, Izuru S. Study on heat transfer and fluid flow characteristics with short rectangular plate fin of different pattern. *Experimental Thermal and Fluid Science*. 2007 Feb 1;31(4):367-379.

[22] Intel Pentium 4 Processors 570/571, 560/561, 550/551, 540/541, 530/531 and 520/521. 2005. Supporting Hyper-Threading Technology Datasheet. Available from: <<http://www.intel.com/design/pentium4/datashts/302351.htm>>. may 2005.



# Numerical Investigation of Rising Vapour Bubble in Convective Boiling Using an Advanced 3D Hybrid Numerical Method

*Syed Ahsan Sharif, Mark Kai Ming Ho,  
Victoria Timchenko and Guan Heng Yeoh*

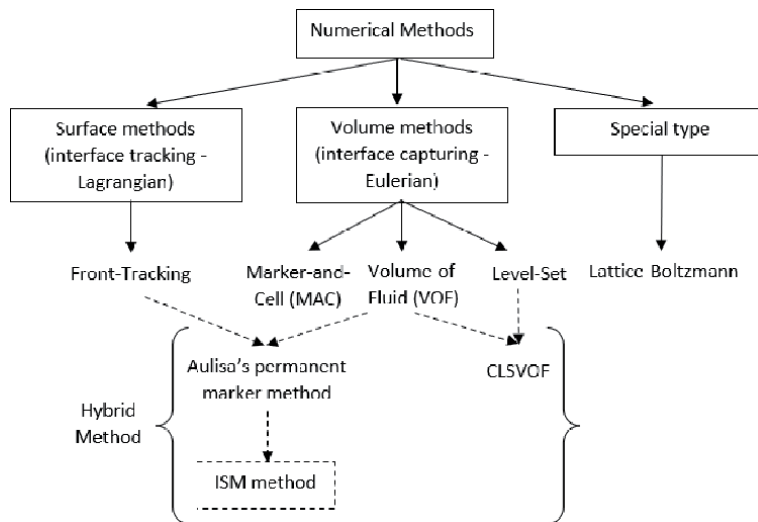
## Abstract

This chapter introduces an advanced and new type of Three-Dimensional (3D) numerical method called the InterSection Marker (ISM) method. The ISM method - a hybrid Lagrangian–Eulerian 3D front-tracking algorithm specifically crafted for multi-phase flow simulation. The method was used to simulate rising vapour bubble behaviour in Convective boiling conditions. Two applications: bubble growth and bubble condensation due to the convective action, were investigated. Numerically obtained bubble properties, such as size, shape and velocity, are compared well against the past works, and the ISM method proved to be an efficient numerical tool for the interface tracking of multi-phase flow CFD simulations involving heat and mass transfer.

**Keywords:** InterSection Marker (ISM) method, interfacial heat and mass transfer, convective boiling, vapour bubble, bubble condensation

## 1. Introduction

Multi-phase flow simulation, such as vapour bubbles is complicated. Various numerical methods, such as Front-tracking, Marker and Cell, Volume of Fluid, Level Set, Lattice-Boltzmann, were invented to mimic such phenomena – see **Figure 1**. These methods, however, have their own characteristics strengths and weaknesses (e.g. see summary in [1, 2]). Hybrid methods, as a result, have emerged to harness the merits of their parent methods to improve accuracy and to tackle complex multi-phase flow applications. Combining the strength of the VOF method and the Front-Tracking method, Aulisa et al. [3] Three-Dimensional (3D) method tracks the interface as a Lagrangian but finds the intersection of the surface mesh with control volume faces and locally remeshes the surface contour while preserving the tracked volume. Aulisa’s method, however, requires permanent markers which cannot be seeded or removed after the simulation is executed, and leads to resolution issues for spherical bubble expansion problem. To improve the method prescribed in Aulisa et al. [3], InterSection Marker (ISM) method [4] was devised. The ISM method eliminated the need for permanent markers and addressed the



**Figure 1.**  
Taxonomy of selective numerical methods for multi-phase flows, and the introduction to the ISM method.

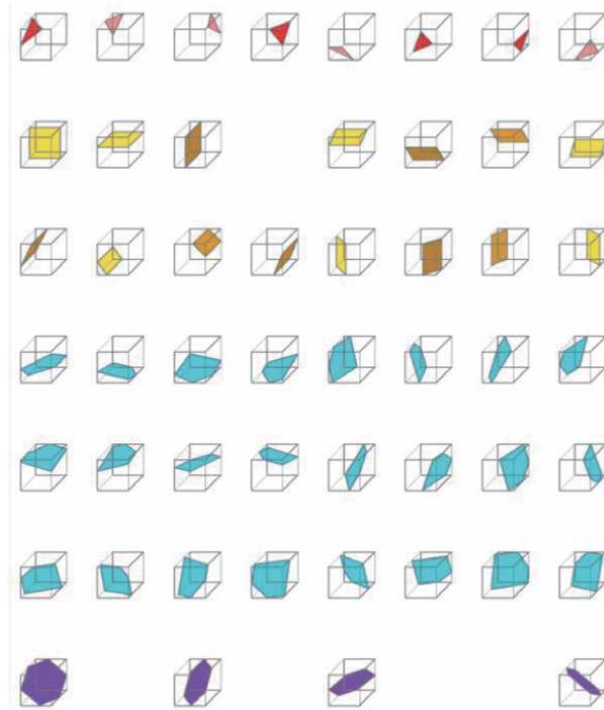
local surface resolution issue in volume inflationary type problems. The ISM method was previously successfully applied to air bubble rise simulations which were adiabatic in nature [5]. However, ISM method's ability to calculate interfacial area more accurately (uncertainty in the order of 1–2%) than conventional VOF methods proved it an ideal candidate for multi-phase simulations involving heat and mass transfers across the interface, such as rising vapour bubbles in superheated or sub-cooled water. During the simulation, the predicted vapour bubble properties such as size, shape and velocity were compared against the past works and found to be in good agreement.

## 2. A brief introduction to the InterSection marker (ISM) method

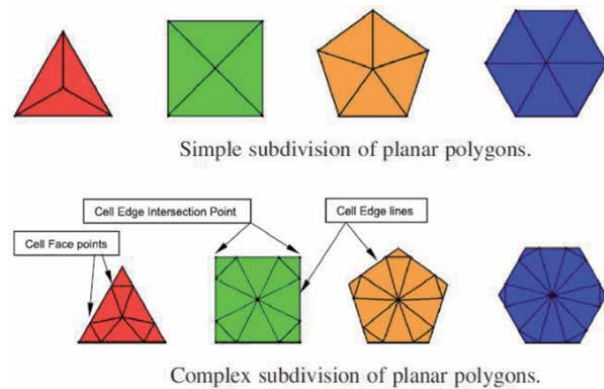
In the search for higher surface tracking fidelity, the InterSection Marker (ISM) method [4, 5] was developed where the proper determination of the interfacial area is critical, such as for the heat and mass transfers process across the interface separating two-phase fluids. An in-depth description of the ISM method is out of the scope of this chapter, and the reader should consult [4, 5] for details. Below, however, highlight the key features of the ISM method to provide the reader with a basic understanding.

The ISM method uses a Lagrangian surface mesh co-located within a uniform Eulerian mesh where upon flow-field quantities such as pressure, velocity and temperature are calculated. The total surface is modelled as a connected series of discrete interfaces (planar polygons), each located within their own *cubic control volume* (CCV). Each planar polygon intersects the edges of the control volume, and the combination of cell-edge intersections uniquely identifies the type of polygon a control volume holds.

The ISM method identifies the type of interface residing in a cell by the combination of cell-edge intersections that interface makes. Total of 51 combinations of basic set of planar-type interfaces had been identified: 8 intersection marker combinations for 3 sided interfaces, 15 for 4 sided, 24 for 5 sided, and 4 for 6 sided – see **Figure 2**. Given the combination of cell edge intersections is unique, a *look-up* table can be used to identify the type of interface located within each cell [4, 5] in a manner similar to that used in the marching cube method [6]. Further subdivisions



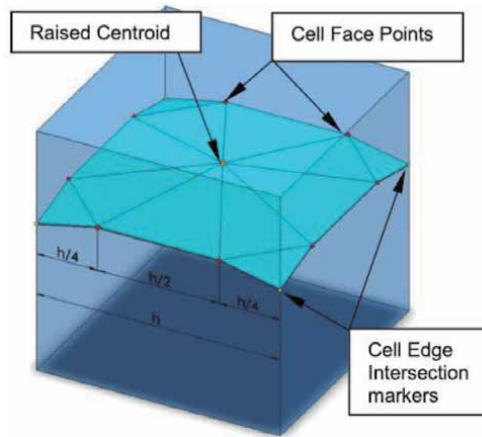
**Figure 2.**  
 Planar surfaces co-located within cubic cells can be of 3 to 6 sides.



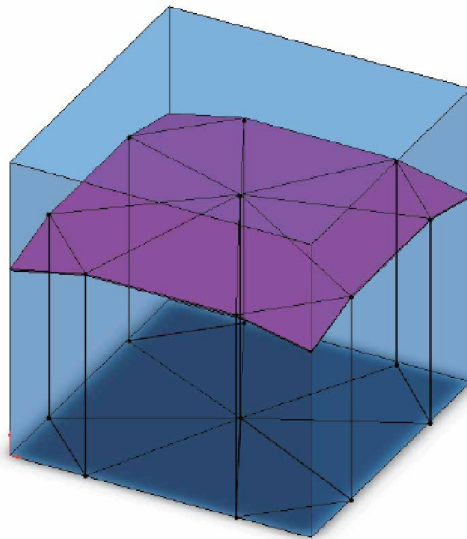
**Figure 3.**  
 Subdivision of planar polygons.

of these polygons are carried out to maintain planar surface during translation/ deformation – see **Figure 3**. A triangular tessellation pattern is the preferred option because three points randomly translated will always form a plane. Additional intersection-marker combinations of non-planar-type interfaces were also identified (details in [4, 5]), which are necessary to prevent the modelled interface from collapsing and folding onto itself.

After identification of the planar polygons and their sub-divisions, the next step in the ISM method is to identify the component points of the interface – as shown in **Figure 4**: (i) the intersection markers where the interface crosses the control volume cell edges, (ii) the cell face conservation points which allow composite curves to be modelled, and (iii) the raised centroid whose position is calculated to satisfy volumetric conservation. The Volume-of-fluid (VOF) is then calculated by



**Figure 4.**  
*ISM Interface points.*



**Figure 5.**  
*VOF calculation.*

summing the volumes of individual triangular columns – refer to **Figure 5**. For the surface translation and the remeshing process, see Ho et al. [4].

### **3. Simulation of rising vapour bubble in convective boiling conditions using the ISM method**

Here, two examples of rising vapour bubble simulations due to the convective boiling conditions are illustrated. Firstly, vapour bubble growth in superheated water; secondly, bubble condensation in sub-cooled boiling conditions.

#### **3.1 Vapour bubble growth during rising due to the natural-convective action**

In nucleate pool boiling, Vapour bubble typically attains its maximum size at the moment of departure. After lift-off, vapour bubble, however, could continue to grow during its ascent in the presence of favourable condition – a layer of



superheated liquid which exists close to the heated surface and is metastable in nature [7]. Although the bubble growth rate in this region is not that significant with compared to the initial pre-departure growth, the bubble will grow for the convective action (convective boiling) with the presence of superheated liquid. Vapour bubble size, shape, and rise velocity for this superheated liquid region can significantly affect the heat and mass transfer mechanism involve. It is thus critical to understand and predict the behaviour and properties of rising and simultaneously growing vapour bubbles. In this section, the growth of a rising vapour bubble is numerically investigated in quiescent superheated water under the influence of buoyancy and surface tension forces with special emphasis given to heat and mass transfers due to the convective action.

### 3.1.1 Numerical features

Both the water and the vapour phases can be assumed to experience the same 'mixture velocity' at any local point within the computational domain, and the two-fluid system can be approximated as a one-fluid mixture. The mixture density and viscosity of each control volume can be calculated based on the volume fraction ( $\alpha$ ), which has the following values:

$$\alpha = \begin{cases} 1 & \text{liquid phase} \\ 0 < \alpha < 1 & \text{interface} \\ 0 & \text{gas phase} \end{cases} \quad (1)$$

The variable density and viscosity are then estimated using the  $\alpha$  value:

$$\rho = (1 - \alpha)\rho_g + \alpha\rho_l \quad (2)$$

$$\mu = (1 - \alpha)\mu_g + \alpha\mu_l \quad (3)$$

Where: Subscripts  $l$  and  $g$  indicate liquid (water) and gas (vapour) phases.

When the mass transfer is considered, a source term needs to be added to the  $\alpha$ -transport equation:

$$\frac{\partial \alpha}{\partial t} + \nabla \cdot (\alpha V) = \left(\frac{1}{\rho}\right) S_{mass} \quad (4)$$

Where:  $S_{mass}$  is the interfacial mass transfer source term.

Similarly, the continuity equation becomes:

$$\nabla \cdot V = \left(\frac{1}{\rho_g} - \frac{1}{\rho_l}\right) S_{mass} \quad (5)$$

The Momentum equation is:

$$\frac{\partial \rho V}{\partial t} + \nabla(\rho V \cdot V) = -\nabla p + \rho g + \nabla \cdot \mu(\nabla V + \nabla V^T) + F_\sigma \quad (6)$$

Where:  $p$ ,  $g$  and  $F_\sigma$  are the pressure, gravity and surface tension force respectively.

The Energy equation is:

$$\frac{\partial}{\partial t}(\rho E) + \nabla(V(\rho E + p)) = \nabla(k \nabla T) + S_{heat} \quad (7)$$

Where:  $S_{heat}$ ,  $E$ ,  $T$  and  $k$  are the interfacial heat transfer source term, energy, temperature and thermal conductivity respectively.

$S_{heat}$  can simply be obtained by multiplying  $S_{mass}$  by the change of enthalpy ( $h_{fg}$ ) for phase-change as [8]:

$$S_{heat} = S_{mass} \times h_{fg} \quad (8)$$

Vapour bubble growth was simulated using the convective heat transfer mechanism and change in enthalpy (phase-change), and the source term can be presented as [9]:

$$S_{mass} = a_{if} \cdot \frac{h_{if} \Delta T_{super}}{h_{fg}} \quad (9)$$

Where:  $a_{if}$  is the interfacial bubble surface area per unit volume;  $h_{if}$  is the convective heat transfer coefficient;  $\Delta T_{super}$  is the liquid superheat. Using the ISM method's capability of calculating interfacial surface area more precisely (than the conventional VOF models), local bubble interfacial surface areas (cell-wise) were used to evaluate the total mass transfer onto the growing bubble.

Thus, Eq. (9) can be written as:

$$S_{mass} = \sum_n S_{mass\_cell(n)} = \sum_n \frac{h_{if} \times a_{b\_cell(n)} \times \Delta T_{super}}{h_{fg}} \quad (10)$$

Where:  $S_{mass\_cell(n)}$  is the 3D spatial interfacial cell-by-cell mass transfer rate onto the growing bubble.  $a_{b\_cell(n)}$  is the local bubble surface (interfacial) area at the interface cell and can be obtained from the ISM simulation (see **Figures 4** and **5**).  $\Delta T_{super}$  is the liquid superheat.  $h_{if}$  can be calculated by the following evaporation correlation:

$$Nu_{evap} = \frac{h_{if} D_b}{k_l} \rightarrow h_{if} = \frac{k_l}{D_b} \times Nu_{evap} \quad (11)$$

Evaporative Nusselt number ( $Nu_{evap}$ ) can be calculated from the correlations.  $Nu_{evap}$  depends on the mechanism of fluid flow, the properties of the fluid, and the geometry. Numerous heat transfer correlations have been proposed for convective heat and mass transfer from the sphere for specific applications and conditions. To identify an appropriate  $Nu_{evap}$ , selective and widely acceptable correlations were considered (see **Table 1**), and were plotted against the Bubble Reynolds number ( $Re_b$ ) [10]. It was found, for small  $Re_b$ , there is not much difference among the correlations. However, for higher  $Re_b$ , a significant discrepancy exists among the correlations. Hughmark [13] is not only chosen for its broad-application and popularity, but also for providing median range values (not too high or low) for higher Reynolds number. Bubble Reynolds number ( $Re_b$ ) in the correlation can be expressed as:

$$Re_b = \frac{\rho_l U_b D_b}{\mu_l} \quad (12)$$

Where Bubble rise velocity ( $U_b$ ) can be calculated as:

$$U_b = \frac{C_z^{n+1} - C_z^n}{\Delta t} \quad (13)$$

Reference	Correlation Proposed ( $Nu_{evap} = Nu$ )	Valid For
Ranz and Marshall [11]	$Nu = 2 + 0.6Re^{1/2}Pr^{1/3}$	$0 \leq Re < 200$
Whitakar [12]	$Nu = 2 + (0.4Re^{1/2} + 0.06Re^{2/3})Pr^{0.4} \left(\frac{\mu}{\mu_s}\right)^{1/4}$	$3.5 \leq Re \leq 7.6 \times 10^4$ $0.71 \leq Pr \leq 380$ $1.0 \leq (\mu/\mu_s) \leq 3.2$
Hughmark [13]	$Nu = 2 + 0.6Re^{0.5}Pr^{0.33}$	$0 \leq Re < 776.06$ $0 \leq Pr < 250$
	$Nu = 2 + 0.27Re^{0.62}Pr^{0.33}$	$776.06 \leq Re$ $0 \leq Pr < 200$
Akiyama [14]	$Nu = 0.37Re^{0.6}Pr^{1/3}$	Laminar Flow
McAdams [15]	$Nu = 0.37Re^{0.6}$	$17 < Re < 70,000$

**Table 1.**  
 Evaporative Nusselt number correlations [10].

Where  $C_z$  is the location of bubble centre in upward, z-direction. Sphere-equivalent Bubble Diameter ( $D_b$ ) is calculated as:

$$D_b = \sqrt[3]{\frac{6V_b}{\pi}} \quad (14)$$

In-a-nut-shell  $h_{if}$  depends on the variables below:

$$h_{if} = f(\rho_l, \mu_l, k_l, Pr, U_b, D_b) \quad (15)$$

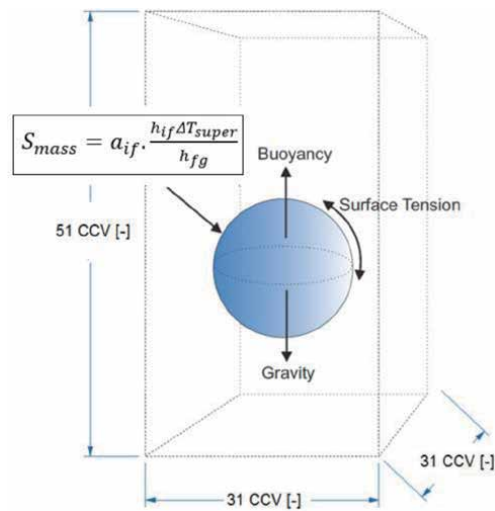
First four variables are for water properties at saturation temperature and are constant (for isothermal condition). However, the last two variables are for the vapour bubble and will change continuously for added mass onto the bubble and corresponding varying rise velocity. As such  $h_{if}$  needs to be calculated at each time-step for varying bubble diameter and velocity. As a result, values for the interfacial mass transfer source term ( $S_{mass}$ ) will also change in each time step. This demonstrates, even for the isothermal condition, the complex physics behind a growing vapour bubble.

Coupled with an in-house variable-density and variable-viscosity single-fluid flow solver, the ISM interface tracking method was employed to simulate single vapour bubble growth (test sizes 2.5 mm, 3 mm, 4 mm) in quiescent water under the influence of gravity and surface tension forces. Detail descriptions of all the numerical features are not the scope of this chapter. **Table 2**, however, shows the salient features used during the numerical simulation. Interested readers could get further information from the relevant references.

Simulations were carried out in a computational domain of  $31 \times 51 \times 31$  Cubic Control Volumes (CCV) with an initial spherical bubble of radius  $5h$  (where  $h$  is the width of the non-dimensional cubic control volume) – see **Figure 6**. Other mesh sizes, such as  $21 \times 31 \times 21$  and  $41 \times 61 \times 41$ , were also investigated, but the mesh size of  $31 \times 51 \times 31$  is maintained the same as the previous successful ISM application of Ho et al. [5] to minimise numerical error and optimise computational time. See Ho et al. [4, 5] for ISM fidelity and sensitivity testing. The centre of the bubble was located in line with the centre of the cavity, at a distance of  $15.5h$  from each side wall and at a distance of  $15.5h$  from the bottom boundary. All thermos-physical properties were taken at the saturation temperature of  $100^\circ\text{C}$ . To check the effect of liquid superheat on the bubble growth, a wide variety of liquid superheat temperatures,  $\Delta T_{super}$  ( $1^\circ\text{C}$ ,  $15^\circ\text{C}$ , and  $35^\circ\text{C}$ ) were considered during the testing. Variable time steps (in the range

Description	Method/Mechanism/Platform	Reference
Surface construction, Interface advection and remeshing	ISM method (Hybrid Eulerian–Lagrangian)	[4]
Coupling between ISM interface tracking method and in-house variable-density and variable-viscosity single-fluid flow solver	Immersed Boundary Method (IBM)	[16]
Surface (interfacial) tension	Continuum Surface Force (CSF)	[17]
3D surface curvature	Paraboloid Least Square fitting method	—
Pressure–velocity coupling	Semi-Implicit Method for Pressure-Linked Equations (SIMPLE) algorithm	[18]
Discretisation schemes	Finite volume formulation - hybrid and central schemes	—
Compiler for ISM interface tracking algorithm and the flow solver program	Intel Visual ForTran Composer XE 2011	—
CFD result Visualisation	Techplot	—

**Table 2.**  
Numerical features.



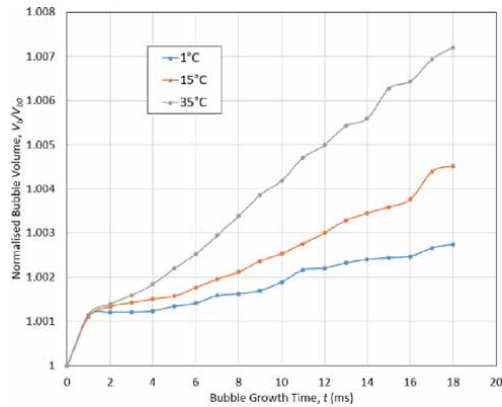
**Figure 6.**  
Schematic diagram of test setup (not-to-scale).

of  $1 \times 10^{-4}$  to  $1 \times 10^{-5}$ ) were also used and found to have insignificant effects on the numerical results. In terms of the computational efforts by using the ISM method, it took 1–3 days to simulate the transient bubble growth process on a personal computer with 2.2 GHz quad-core processor and 16 GB RAM.

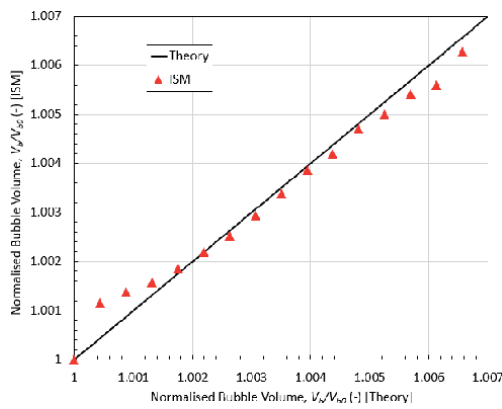
### 3.1.2 Numerical results

#### 3.1.2.1 Size

Normalised bubble volumes of growing bubble over time are plotted in **Figure 7**. As the interfacial mass transfer source term ( $S_{mass}$ ) is directly proportional to the



**Figure 7.** Normalised bubble volume over time ( $D_{bo} = 3 \text{ mm}$ ) [10].



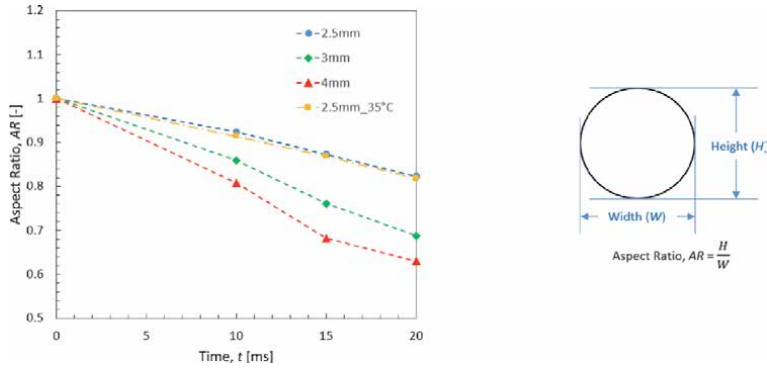
**Figure 8.** Comparison with theory ( $D_{bo} = 3 \text{ mm}$ ,  $\Delta T_{super} = 35 \text{ }^\circ\text{C}$ ) (adapted from [10]).

liquid superheat (See Eq. (9)), the bubble was growing at higher rates for larger liquid superheats. For all cases, bubble growth started to vary from 1–2 ms, as in addition to liquid superheat bubble velocity also began to play a critical role in the bubble growth. Bubble volume growth ratios obtained during the numerical simulation are compared with the theory in **Figure 8** and found to be in good agreement. The deviation is less than 1% and is obvious, as fixed  $h_{if}$  values are used in the entire theoretical calculations; on the other hand,  $h_{if}$  values in the numerical simulations are always changing for varying bubble velocities. It is to be noted, normalised bubble volume of a growing bubble due to the convective action can be evaluated analytically as [10]:


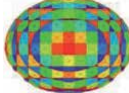

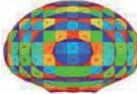
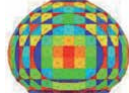
$$\frac{V_b}{V_{b0}} = \left( 1 + \frac{2h_{if}\Delta T_{super}t}{\rho_l D_{b0} h_{fg}} \right)^3 \quad (16)$$

### 3.1.2.2 Shape

Aspect Ratio ( $AR$ ) is used to quantify the bubble shape, and is defined by the bubble height by width.  $AR$  value of 1.0 indicates the bubble is in a perfect spherical shape. Values less than 1.0 designate the bubble is an oblate spheroid.  $AR$  for



**Figure 9.**  
Comparison of aspect ratio, AR ( $\Delta T_{super} = 1 \text{ }^\circ\text{C}$ ).

Point	Bubble Characteristics	Shape obtained in Numerical Simulation	Clift et al. [19] Shape Regime
A	2.5 mm bubble, $\Delta T_{super} = 1 \text{ }^\circ\text{C}$ , Simulation time = 0.1 ms, $Re = 10$ , $Eo = 0.997$		Spherical
B	2.5 mm bubble, $\Delta T_{super} = 1 \text{ }^\circ\text{C}$ , Simulation time = 31.1 ms, $Re = 1700$ , $Eo = 0.997$		Ellipsoidal
C	3 mm bubble, $\Delta T_{super} = 35 \text{ }^\circ\text{C}$ , Simulation time = 10 ms, $Re = 1800$ , $Eo = 1.43$		Ellipsoidal
D	3 mm bubble, $\Delta T_{super} = 35 \text{ }^\circ\text{C}$ , Simulation time = 20 ms, $Re = 2300$ , $Eo = 1.43$		Ellipsoidal-Wobbling
E	4 mm bubble, $\Delta T_{super} = 35 \text{ }^\circ\text{C}$ , Simulation time = 10 ms, $Re = 4200$ , $Eo = 2.55$		Ellipsoidal-Wobbling

**Table 3.**  
Bubble shape validation (cases with selective simulation time are chosen for demonstration). All bubbles are on the same scale for comparison.

various bubbles are plotted in **Figure 9**. With the increase of initial bubble size, bubble deformed at a higher rate and became flattened/oblate spheroid. The liquid superheat also has direct effects on the bubble shape. For the same size bubble, with the increase of liquid superheat, the bubble deformed at a higher rate (i.e. became oblate) due to the increased rate of mass transfer.

Numerically obtained bubble shapes are also compared with the shape regimes of Clift et al. [19] and found to be in good agreement (see **Table 3**). Here, Eötvös number ( $Eo$ ) is defined as

$$Eo = \frac{(\rho_l - \rho_g)gD_b^2}{\sigma} \quad (17)$$

As  $Eo$  is fixed for the same-sized individual bubble, during its ascend the bubble will go through different shape regimes based on its velocity or  $Re$  (see [19] for details). For, 2.5 mm, 3 mm and 4 mm bubbles, this transformation is from spherical-to-ellipsoidal-to-wobbling. It is to be noted that the boundary of these shape regimes is not strictly defined, and for the small bubble, such as 2.5 mm bubble could transform from spherical shape to the wobbling direct based on  $Re$ . At the later stage, numerical bubble shapes also reveal unstable features and disturbance on the interface. Larger bubble, 4 mm, in this case, became reverse-heart like shape with disturbance on the bottom.

### 3.1.2.3 Velocity

When an adiabatic bubble is released from a stationary position, its velocity continues to rise until it reaches to its terminal velocity regime where the bubble continues to rise at a constant velocity, i.e. no acceleration [19–21]. Growing vapour bubble also showed similar velocity profile during its ascend during the numerical simulation [10]. Initially, the velocity rose exponentially after the release of the bubble from its stationary position. The bubble then entered into a relatively stable velocity regime. Generally, with the increase of the bubble size, the bubble reaches to its stable velocity regime more quickly for the larger buoyancy force resulted from larger bubble volume.

The rise velocities ( $U_{stb}$ ) of growing bubbles in the stable regime are benchmarked against similar terminal velocity ( $U_{ter}$ ) regime of adiabatic bubbles in **Table 4**. Overall, with the increase of the bubble size,  $U_{stb}$  decreases, and the simulation results compared well with the high-low ranges reported by Clift et al. [19]. ISM's results follow the lower limit, as for the growing bubbles,  $U_{stb}$  is lower than a comparable adiabatic bubble's  $U_{ter}$ . This is because the drag force increases at a larger rate due to the deformed frontal area (i.e. bubble shape) of a growing bubble for continually added mass which reduces the bubble rise velocity [22, 23]. Sideman and Taitel's [24] experiments also exhibited similar trends for evaporated growing bubbles.

Initial Bubble Diameter, $D_0$ [mm]	Liquid Superheat, $\Delta T_{Super}$ [°C]	Numerically obtained average rise velocity of a growing bubble in stable regime, $U_{Stb}$ [cm/s]	Terminal Velocity, $U_{ter}$ [cm/s] of Adiabatic Bubble
			Experimental (High - Low) [10]
2.5	1	20.28	28–17
	15	19.98	
	35	19.60	
3	1	20.98	26–17.5
	15	20.12	
	35	19.70	
4	1	17.12	25–18
	15	16.98	
	35	16.94	

**Table 4.** Bubble velocity comparison (adapted from [10]).

Although small in magnitude, it is observed, with the increase of the liquid superheat,  $U_{stb}$  decreases for a same-sized bubble. This is due to the same reason: with the increase of added mass at a higher rate for higher liquid superheat (see Eq. (9)), the bubble deformed at a faster rate causing more drag force and reduced velocity. Sideman and Taitel's [24] also overserved similar phenomena of reduced bubble velocity with the increase of temperature.

### 3.1.3 Conclusion

Below summarised the major findings based on the numerical results obtained using the ISM method:

- As the interfacial mass transfer source term ( $S_{mass}$ ) is directly proportional to the liquid superheat, the bubble was growing at higher rates for larger liquid superheats.
- The bubble deforms more with the increase of the size. The liquid superheat also has a direct effect on the bubble shape. For a same-sized bubble, with the increase of liquid superheat, the bubble deforms at a higher rate due to the increased rate of mass transfer.
- When an adiabatic bubble is released from a stationary position, its velocity continues to rise until it reaches to its terminal velocity regime where the bubble continues to rise at a constant velocity (i.e. no acceleration). A growing bubble also shows similar trends. In the stable velocity regime, however, the growing bubble velocity ( $U_{stb}$ ) is generally lower than the terminal velocity ( $U_{ter}$ ) of an adiabatic bubble. For the continuously added mass, the growing bubble shape deforms more rapidly than an adiabatic bubble causing higher drag force and reduced velocity.
- With the increase of the liquid superheat,  $U_{stb}$  decreases for a same-sized bubble. This is due to the same reason: with the increase of added mass at a higher rate for higher liquid superheat, the bubble deformed at a faster rate causing more drag force and reduced velocity.

## 3.2 Vapour bubble condensation in sub-cooled boiling condition

Vapour bubble condensation in subcooled liquid where the water temperature is below saturation is an important physical phenomenon [25]. Subcooled boiling flow is one of such examples and can be found in boilers, steam generators, nuclear reactors, and other engineering systems. To optimise the design and to make these systems safe, it is critical to understand and predict the behaviour of bubbles behaviour in subcooled boiling flows. As the presence of vapour bubbles has a significant effect on the heat transfer characteristics of a system as well as pressure drops and flow instability [8, 26]. Vapour bubble life and collapse during condensation can be either inertia (for high liquid subcooling and high Jacob number) or heat transfer controlled (for low liquid subcooling and low Jacob number). Using the ISM method, this section discusses the heat transfer controlled vapour bubble condensation in quiescent water where the bubble reduction rate is longer, and the process is controlled by the heat transfer at the interface. In order to simulate the condensing bubble, the source terms were modelled in the CFD governing equations to account for heat and mass transfers from the bubble. During the simulation, the predicted condensing vapour bubble properties such as size reduction rate,



shape and velocity were compared against the past works and found to be in good agreement.

### 3.2.1 Numerical features

Likewise, bubble growth due to the convective action in the previous section, vapour bubble size reduction (i.e. condensation) was simulated using the same convective heat transfer mechanism due to the temperature gradient between vapour and water phase. Eq. (1)–(8) are also applicable here.  $S_{mass}$ , however, needs to be treated in the opposite way for mass loss from the vapour bubble.

Thus,

$$S_{mass} = \sum_n S_{mass_{cell(n)}} = \sum_n \frac{h_{if} \times a_{b_{cell(n)}} \times \Delta T_{sub}}{h_{fg}} \quad (18)$$

Where:  $S_{mass_{cell(n)}}$  is the 3D spatial interfacial cell-by-cell mass transfer rate from the condensing bubble;  $a_{b_{cell(n)}}$  is the local bubble surface area at the interface cell and can be obtained from the ISM simulation (see **Figure 4**).  $\Delta T_{sub}$  is the liquid subcooling. Interfacial (convective) heat transfer coefficient ( $h_{if}$ ) can be calculated by the following condensation correlation:

$$Nu_{cond} = \frac{h_{if} D_b}{k_l} \rightarrow h_{if} = \frac{k_l}{D_b} \times Nu_{cond} \quad (19)$$

Eq. (12)–(14) can also be used here to determine Reynolds number, Bubble Velocity and Bubble Diameter. Next using this  $Re_b$ , Condensate Nusselt number ( $Nu_{cond}$ ) can be calculated from the correlations. **Table 5** shows some of the notable relations found in the literature. A preference was given to the relations having Jacob number ( $Ja$ ) – a dimensionless number which is usually used for boiling, evaporation and condensation applications. To check the model's sensitiveness, Condensing bubble volume reduction with time for various correlations was investigated [31]. The correlations exhibit a wide discrepancy in volume reduction rates,

Reference	Correlation Proposed	Valid For
Zeitoun et al. [25]	$Nu_{cond} = 2.04 Re_b^{0.61} \alpha^{0.328} Ja_1^{-0.308}$	For Steam-Water flow at near atmospheric pressure and for void fraction up to 30 percent.
Kim & Park [27]	$Nu_{cond} = 0.2575 Re_b^{0.7} Pr_1^{-0.4564} Ja_1^{-0.2043}$	$Re_b = 1000-6000$ $18 < Ja < 36$ $1.87 < Pr < 2.03$ $0.8 \text{ mm} < D < 6 \text{ mm}$
Lucic & Mayinger [28]	$Nu_{cond} = 1.46 Re_b^{0.61} Pr_1^{0.33} Ja_1^{-0.31}$	$Re_b \approx 1000 - 3400$ $Ja \approx 10 - 30$
Yuan et al. [29]	$Nu_{cond} = 0.6 Re_b^{1/2} Pr_1^{1/3} (1 - Ja_1^{0.1} Fo_{b0})$	For Narrow channel $Re_b = 335-1770$ $Pr \approx 1.7$ $Ja = 20-60$
Warrier et al. [30]	$Nu_{cond} = 0.6 Re_b^{1/2} Pr_1^{1/3} (1 - 1.2 Ja_1^{9/10} Fo_{b0}^{2/3})$	$20 < Re_b < 700$ $1.8 < Pr < 2.9$ $12 < Ja < 100$

**Table 5.**  
 Condensate Nusselt number correlations.

especially with the progress of simulation time. The reasons being these co-relations were developed for specific media and test setups and are valid for a range of parameters only. Warriar et al. [30], for instance, reported an uncertainty of  $\pm 25\%$  when they benchmarked their correlation with others.

Considering the scope of current work and relevance, and for validation purposes, Kim and Park [27] is applied during the numerical simulations. Jacob number ( $Ja$ ) is defined as:

$$Ja_l = \frac{\rho_l C_{pl} \Delta T_{sub}}{\rho_g h_{fg}} \quad (20)$$

Where:  $C_{pl}$  is the liquid (water) specific heat.

For condensation, vapour bubble size and corresponding bubble rise velocity will change continuously. As such,  $h_{if}$  needs to be calculated at each time-step for varying bubble size and velocity. As a result, values for the interfacial mass transfer source term ( $S_{mass}$ ) will also change in each time step.

Numerical test setups are the same as the previous application. For numerical test cases, 2 mm, 3 mm and 4 mm initial sized bubbles with various liquid subcooling were considered to check the effect of liquid subcooling on the bubble condensation rates. To validate ISM simulation results further, other odd bubble sizes (e.g. 1.008 mm and 4.9 mm) were also considered.

### 3.2.2 Numerical results

#### 3.2.2.1 Size

The ISM simulation results were validated against past-correlations. In literature, Bubble history ( $\beta$ ) has been expressed as the transient form consisting of the Fourier number ( $Fo$ ), and is formulated as, for instance [25, 27]:

$$\beta = (1 - 5.67 Re_b^{0.61} \alpha^{0.328} Ja_l^{0.692} Fo_0)^{0.72} \quad (21)$$

$$\beta = (1 - 0.6695 Re_b^{0.7} Ja_l^{0.7957} Pr^{0.4564} Fo_0)^{0.7692} \quad (22)$$

Where: Bubble history ( $\beta$ ) which is defined as:

$$\beta = \frac{D_b}{D_{b0}} \quad (23)$$

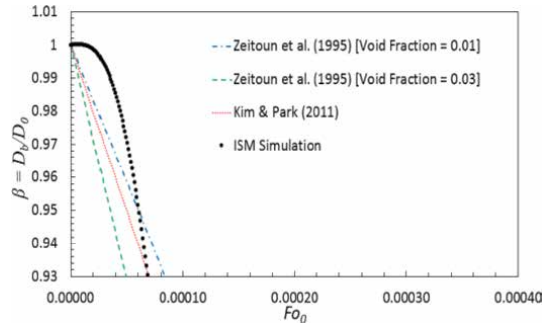
Where: the subscript 0 indicates the initial state. Therefore,  $D_{b0}$  is the initial bubble diameter, and  $D_b$  is the instantaneous bubble diameter.

The Fourier number ( $Fo_0$ ) is based on the initial bubble size and is written as:

$$Fo_0 = \frac{at}{D_0^2} \quad (24)$$

Where:  $a$  is the thermal diffusivity.

Bubble history ( $\beta$ ) obtained during the numerical simulation is plotted against past correlations in **Figure 10**. Depending on the bubble size, liquid subcooling and Reynolds number ( $Re$ ), the bubble size reduced at varying rates. The bubble was condensing at a higher rate for larger liquid subcooling and higher Reynolds number. The ISM simulation, however, shows discrepancy at the beginning of the condensation stage. The reason being: fixed Reynolds numbers were used to



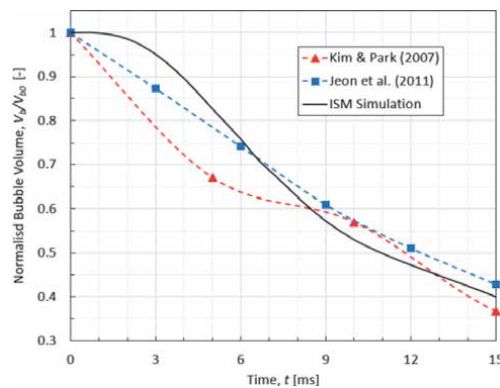
**Figure 10.** Bubble history comparison between correlations and ISM simulation [31]. [ $D_{b0} = 4 \text{ mm}$ ,  $\Delta T_{\text{sub}} = 10 \text{ }^\circ\text{C}$ ,  $Re = 500$ ,  $Ja = 30$ ].

calculate the correlated  $\beta$  values. The interfacial (convective) heat transfer coefficient ( $h_{if}$ ) is proportional to the bubble velocity, so higher the bubble velocity higher the bubble condensation rate. As the bubble was released from a stationary position (with zero velocity and Reynolds number), it took some time for the bubble to reach a reasonable rise velocity (similar to the terminal velocity regime of an adiabatic bubble) and corresponding Reynolds number. Numerical results show close agreement with past correlations at the later stage of condensation after the bubble achieved relatively higher velocity values.

The ISM simulation results were also compared against past experimental results – see **Figure 11**. The ISM simulation results show good agreement, and the overall bubble condensation trends closely follow other benchmarked case of Kim and Park [27] (deviation in the range of 5–15%). The differences between the experimental and ISM numerical simulation are noticeable for different initial test conditions, bubble shapes, and so on.

### 3.2.2.2 Shape

Generally, small bubble keeps its spherical shape during its rise for high surface tension forces. Bubble shape deformation accelerates with the increase of its size and becomes ellipsoidal or spherical cap or wobbling. Since 2 mm and 3 mm condensing bubbles quickly loss their mass and become small, their shape is generally limited to spherical or ellipsoidal. A larger bubble, e.g. 4 mm condensing bubble, on



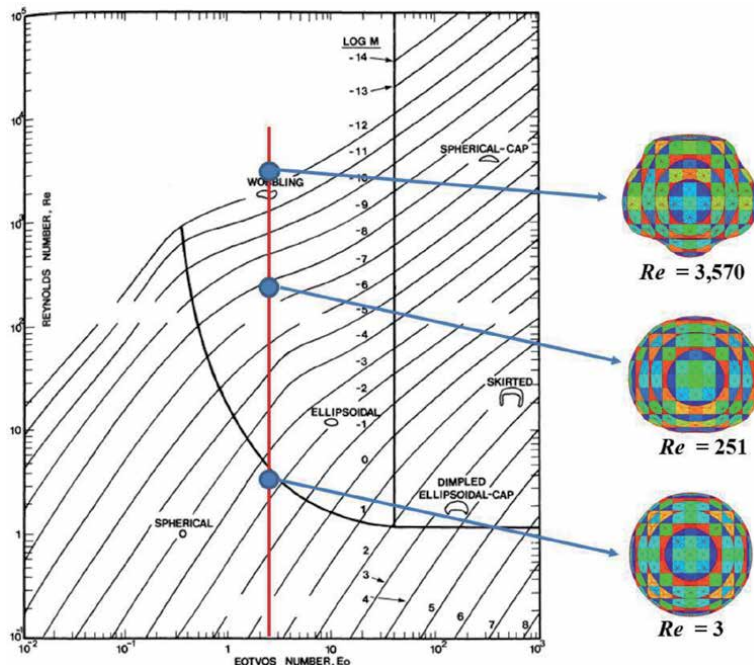
**Figure 11.** Comparison of normalised bubble volume [31]. [ $D_{b0} = 4.9 \text{ mm}$ ,  $\Delta T_{\text{sub}} = 12 \text{ }^\circ\text{C}$ ].

the other hand, is going through a series of interesting shape evolution, as such, it is considered to compare against Clift et al. [19] shape regimes. A series of instantaneous bubble status points were considered, and their corresponding  $Re$  were calculated using bubble velocity obtained from the ISM simulation for comparison. With the increase of bubble velocity and its corresponding higher  $Re$ , the bubble was deforming from spherical to ellipsoidal to wobbling shape regimes. **Figure 12** demonstrates the bubble shapes obtained from the ISM simulation have excellent agreement with Clift et al. [19] shape regimes.

Bubble shapes obtained in the ISM simulation were also compared with Kamei and Hirata's [32] experimentation and found to be a good agreement – see **Table 6**. The condensing bubble was keeping its spherical shape because of small size and high surface tension forces during its rise. **Table 6** also shows the comparison of shapes with past numerical works (Zeng et al. [33] and Samkhaniani and Ansari [34]).

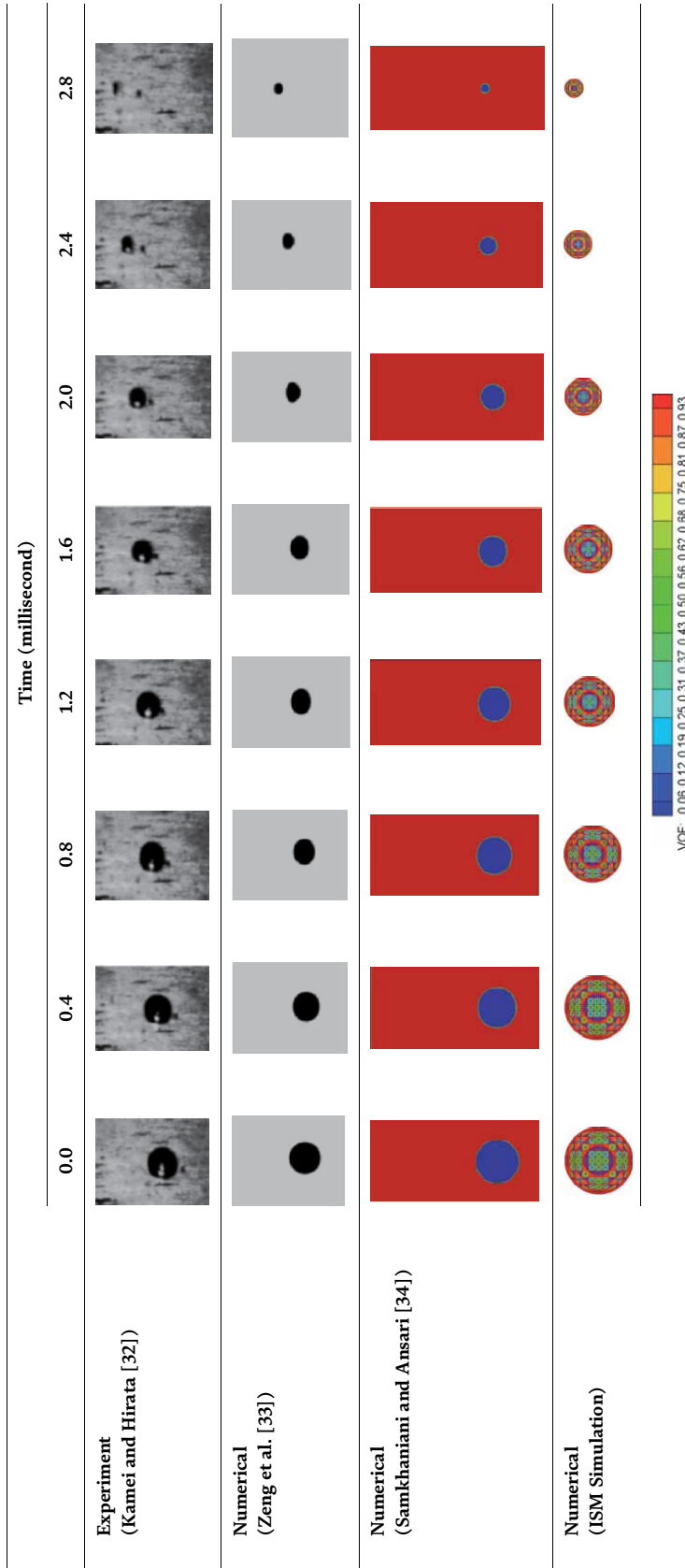
### 3.2.2.3 Velocity

Likewise growing bubble, the rise velocity of condensing bubbles is different from adiabatic bubbles [8]. For continuous reduction in bubble size (i.e. volume) in subcooled boiling flow condition, bubble rise velocity and shape are also always changing. From **Figure 13**, it is evident that with the increase of liquid Subcooling bubble rise velocity continues to increase. The findings are consistent with [8] numerical results. The deviation is the result of different test setups; however, **Figure 13** overall indicates the trends of higher the liquid Subcooling higher the bubble rise velocity. Bubble buoyancy force decreases for continuous reduction of bubble volume. The drag force is also reduced for smaller bubble frontal area; however, the resulted net effect is positive buoyancy force acting upwards, and the bubble rise velocity increases continuously.

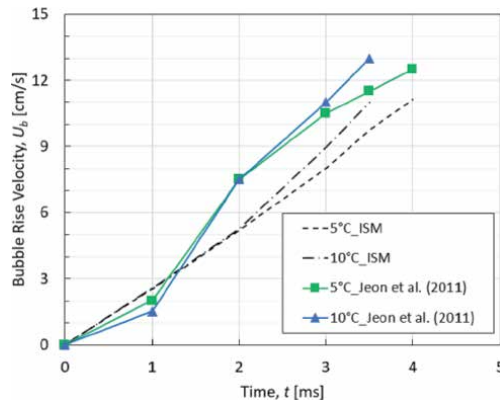


**Figure 12.**

Bubble shape validation with Clift et al. [19]. Test case:  $D_{bo} = 4 \text{ mm}$ ,  $\Delta T_{sub} = 25 \text{ }^\circ\text{C}$ , Eötvös number,  $Eo = 2.55$  (adapted from [31]). All bubbles are on the same scale for comparison.



**Table 6.** Bubble shape comparison between past experimental/numerical results and ISM simulation ( $D_{bo} = 1.008 \text{ mm}$ ,  $\Delta T_{sub} = 2.5^\circ\text{C}$ ) (adapted from [31]).

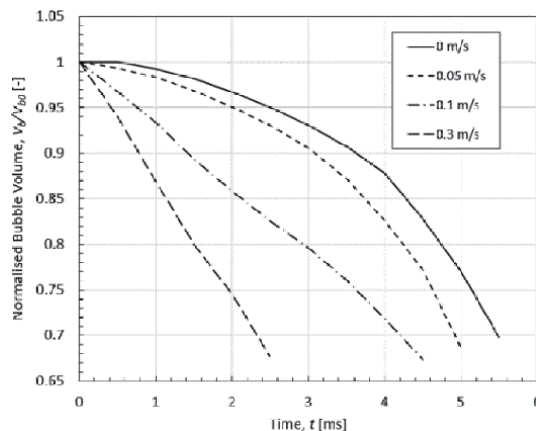


**Figure 13.** 3 mm bubble rise velocity comparison with Jeon et al. [8]. (as demonstrated in [31]).

### 3.2.2.4 Effects of fluid flow and varying temperature fluid field

Effects of fluid flow and varying temperature fluid field on bubble condensation were also investigated. With the increase of fluid flow velocity, the bubble was condensing at a higher rate (see **Figure 14**). This is because the relative bubble velocity increases for same-directional (positive) fluid flow velocity resulting in the higher mass transfer or mass loss from the bubble (see Eq. (18)–(19)). **Table 7** depicts the effects of fluid flow velocity on the bubble shape. With a rapid mass loss for a higher fluid flow field, the bubble was deforming at a higher rate and becoming unstable with relatively shorter life span.

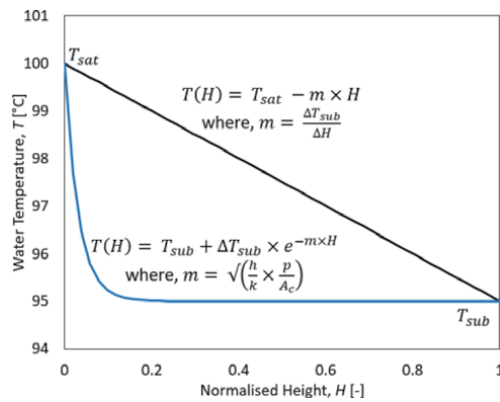
For varying temperature fluid field, two models were considered: (i) linear and (ii) exponential – see **Figure 15**. The Linear model can be applied to thermal stratification of hot water tanks and the natural systems, such as lakes and ponds. The exponential model is more suitable for the convective boiling application and hence was applied to current numerical study. Because of the computational domain and the relative higher heat transfer coefficient ( $h$ ) value for convective boiling condition ( $h = 8,000 \text{ W/m}^2 \text{ }^\circ\text{C}$  was used in **Figure 15**), the temperature of fluid field is rapidly achieving the liquid bulk-temperature. As a result, the effects of varying temperature field, in this instance, were minimal on both condensing bubble size and shape. See **Figure 16** and **Table 8**.



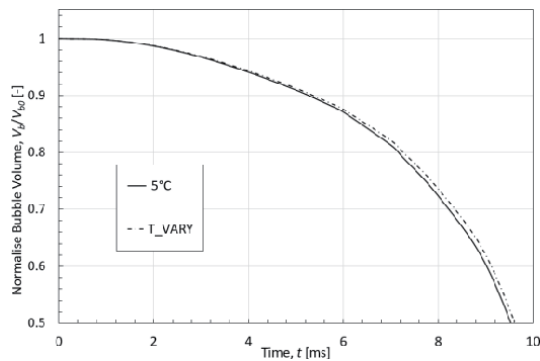
**Figure 14.** Bubble condensation rates for various fluid flow velocity [ $D_{bo} = 2 \text{ mm}$ ,  $\Delta T_{sub} = 5 \text{ }^\circ\text{C}$ ].

Flow Velocity [m/s]	Simulation Time, $t$ [ms]				
	0	1.5	3	4.5	6
0					
0.05					[N/A]
0.1				[N/A]	[N/A]
0.3			[N/A]	[N/A]	[N/A]

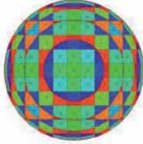

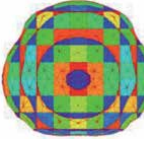
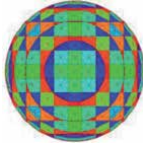

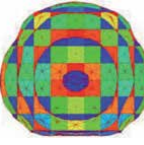
**Table 7.**  
 Condensing bubble shape comparison for various fluid flow velocity [ $D_{bo} = 2 \text{ mm}$ ,  $\Delta T_{sub} = 5 \text{ }^\circ\text{C}$ ]. All bubbles are on the same scale for comparison.



**Figure 15.**  
 Temperature models.



**Figure 16.**  
 2 mm bubble condensation rates [ $D_{bo} = 2 \text{ mm}$ ,  $\Delta T_{sub} = 5 \text{ }^\circ\text{C}$ ].

$\Delta T_{sub}$ [°C]	Simulation Time, $t$ [ms]			Maximum Rise Velocity (cm/s)
	0	5	8.75	
5				6.9
T_VARY				6.5

**Table 8.**

Condensing bubble shape comparison for varying temperature field [ $D_{bo} = 2$  mm,  $\Delta T_{sub} = 5$  °C]. All bubbles are on the same scale for comparison.

### 3.2.3 Conclusion

Following critical observations were observed during Condensing bubble simulation:

- Bubble reduction rate depends on the liquid subcooling and bubble velocity. Higher the liquid subcooling higher the bubble reduction rate.
- Same is true for the bubble velocity. The interfacial (convective) heat transfer coefficient ( $h_{if}$ ) is proportional to the bubble velocity. As such, higher the bubble velocity higher the bubble condensation rate.
- Precaution should be taken during the selection of an appropriate Condensate Nusselt number ( $Nu_{cond}$ ) correlation. As the numerical results can vary significantly and should be chosen based on the applications.
- Bubble deforms at a higher rate for larger bubble sizes during ascend. For higher surface tension force, smaller bubbles tend to keep their original spherical shape.
- Liquid subcooling also contributes to the bubble shape determination as heat and mass transfers across the interface cause distortion. With higher liquid subcooling, bubbles get smaller quickly and maintain spherical shape.
- When an adiabatic bubble is released from a stationary position, the rise velocity of the bubble continues to rise until it reaches a stable velocity regime. Whereas for condensing bubble, the rise velocity is always changing for continual heat and mass transfers.
- With the increase of liquid subcooling, rise velocity of the condensing bubble increases.
- With the increase of fluid flow velocity, both bubble condensation rates and shape deformation increase.
- Varying temperature field in this particular instance had minimal effects on condensing bubble size and shape.



## 4. Summary

The InterSection Marker (ISM) – a new type of 3D interface tracking method was used to simulate the evaporative growth and condensation of a rising vapour bubble due to convective boiling conditions. The ISM method's ability to calculate interfacial area more accurately than conventional VOF methods proved it an ideal candidate for multi-phase flow simulations involving heat and mass transfers across the interface. During the simulation, the predicted vapour bubble properties such as size, shape and velocity were compared against the past works and found to be in good agreement.

## Conflict of interest

The authors declare no conflict of interest.

## Nomenclature

### Roman

$a$	Thermal diffusivity, $\text{m}^2/\text{s}$
$a_{if}$	Interfacial area between phases per unit volume, $\text{m}^2/\text{m}^3$
$c_p$	Specific heat, $\text{kJ}/\text{kg}^\circ\text{C}$
$C_z$	Location of bubble centre in the z-direction
$D_b$	Sphere-equivalent Bubble Diameter, $\text{m}$
$Eo$	Eötvös number, –
$Fo$	Fourier number, –
$g$	Gravity, $\text{m}/\text{s}^2$
$h_{if}$	Interfacial (convective) heat transfer coefficient, $\text{W}/\text{m}^2^\circ\text{C}$
$h_{fg}$	Enthalpy for vaporisation, $\text{kJ}/\text{kg}$
$Ja$	Jacob number, –
$k_l$	Thermal conductivity, $\text{W}/\text{m}^\circ\text{C}$
$Nu$	Nusselt number, –
$p$	Pressure, $\text{Pa}$
$Re$	Reynolds number, –
$S_{heat}$	Interfacial heat transfer source term, $\text{W}/\text{m}^3$
$S_{mass}$	Interfacial mass transfer source term, $\text{kg}/\text{m}^3\text{s}$
$t$	Time, $\text{s}$
$\Delta T_{sub}$	Liquid subcooling, $^\circ\text{C}$
$\Delta T_{super}$	Liquid superheat, $^\circ\text{C}$
$U_b$	Bubble rise velocity, $\text{m}/\text{s}$
$U_{ter}$	Bubble terminal velocity, $\text{m}/\text{s}$
$U_{stb}$	Evaporating bubble velocity in the stable regime, $\text{m}/\text{s}$
$V_b$	Bubble volume, $\text{m}^3$

### Greek symbols

$\alpha$	Volume fraction
$\beta$	Bubble History
$\mu$	Dynamic viscosity, $\text{kg}/\text{ms}$
$\rho$	Density, $\text{kg}/\text{m}^3$
$\sigma$	Surface tension force, $\text{N}/\text{m}$

*Subscripts*

<i>O</i>	Initial/Original
<i>b</i>	Bubble
<i>cell</i>	Cell
<i>cond</i>	Condensation
<i>evap</i>	Evaporation
<i>if</i>	Interfacial
<i>g</i>	Gas (vapour) phase
<i>heat</i>	Heat
<i>l</i>	Liquid (water) phase
<i>mass</i>	mass
<i>stb</i>	Stable
<i>ter</i>	Terminal

*Acronym*

3D	Three-Dimensional
AR	Aspect Ratio
CCV	Cubic Control Volumes
CFD	Computational Fluid Dynamics
IBM	Immersed Boundary Method
ISM	InterSection Marker
SIMPLE	Semi-Implicit Method for Pressure-Linked Equations
VOF	Volume-of-fluid

**Author details**

Syed Ahsan Sharif<sup>1\*</sup>, Mark Kai Ming Ho<sup>2</sup>, Victoria Timchenko<sup>1</sup>  
and Guan Heng Yeoh<sup>1</sup>


1 School of Mechanical and Manufacturing Engineering, University of New South  
Wales, Kensington, NSW, Australia

2 Australian Nuclear Science and Technology Organisation (ANSTO),  
Lucas Heights, NSW, Australia

\*Address all correspondence to: sharif.syed@gmail.com

**IntechOpen**

---

© 2021 The Author(s). Licensee IntechOpen. This chapter is distributed under the terms of the Creative Commons Attribution License (<http://creativecommons.org/licenses/by/3.0>), which permits unrestricted use, distribution, and reproduction in any medium, provided the original work is properly cited. 

## References

- [1] van Sint Annaland M, Deen NG, Kuipers JA. Numerical simulation of gas bubbles behaviour using a three-dimensional volume of fluid method. *Chemical engineering science*. 2005;60(11):2999–3011.
- [2] van Sint Annaland M, Dijkhuizen W, Deen NG, Kuipers JA. Numerical simulation of behavior of gas bubbles using a 3-D front-tracking method. *AIChE Journal*. 2006;52(1):99–110.
- [3] Aulisa E, Manservigi S, Scardovelli R. A surface marker algorithm coupled to an area-preserving marker redistribution method for three-dimensional interface tracking. *Journal of Computational Physics*. 2004;197(2):555–584.
- [4] Ho M, Yeoh G, Reizes J, Timchenko V. The intersection marker method for 3D interface tracking of deformable surfaces in finite volumes. *International Journal for Numerical Methods in Fluids*. 2016;81(4):220–244.
- [5] Ho M, Yeoh GH, Reizes JA, Timchenko V. Bubble flow simulations using the intersection marker (ISM) interface tracking method. *International Journal of Numerical Methods for Heat & Fluid Flow*. 2018;28(1):118–137.
- [6] Lorensen WE, Cline HE. Marching cubes: A high resolution 3D surface construction algorithm. *ACM siggraph computer graphics*. 1987;21(4):163–169.
- [7] Holman, JP. *Heat Transfer*. 7<sup>th</sup> ed. McGraw-Hill International (UK) Limited; 1992.
- [8] Jeon SS, Kim SJ, Park GC. Numerical study of condensing bubble in subcooled boiling flow using volume of fluid model. *Chemical engineering science*. 2011;66(23):5899–5909.
- [9] Yeoh, GH, Tu, J. *Computational Techniques for Multi-Phase Flows*. 1<sup>st</sup> ed. Oxford: Butterworth-Heinemann; 2010.
- [10] Sharif SA, Ho MK, Timchenko V, Yeoh, GH. Three-Dimensional simulation of natural-convective vapour bubble growth in superheated water by a new interface tracking method. Submitted for Publication in *International Journal of Heat and Fluid Flow*, 2021a.
- [11] Ranz WE, Marshall WR. Evaporation from drops. *Chem. Eng. Prog.* 1952;48(3):141–146.
- [12] Whitaker S. Forced convection heat transfer correlations for flow in pipes, past flat plates, single cylinders, single spheres, and for flow in packed beds and tube bundles. *AIChE Journal*. 1972; 18(2):361–370.
- [13] Hughmark GA. Mass and heat transfer from rigid spheres. *AIChE Journal*. 1967;13(6):1219–1221.
- [14] Akiyama M. Bubble collapse in subcooled boiling. *Bulletin of JSME*. 1973;16(93):570–575.
- [15] McAdams, WH. *Heat Transmission*. 3<sup>rd</sup> ed. New York: McGraw-Hill Book Company; 1954.
- [16] Peskin CS. Numerical analysis of blood flow in the heart. *Journal of computational physics*. 1977;25(3): 220–252.
- [17] Brackbill JU, Kothe DB, Zemach C. A continuum method for modeling surface tension. *Journal of computational physics*. 1992;100(2):335–354.
- [18] Patankar SV, Spalding, DB. *A Calculation Procedure for Heat, Mass and Momentum Transfer in Three-Dimensional Parabolic Flows*. *International Journal of Heat and Mass Transfer*. 1972;15:1787–1806.

- [19] Clift, R, Grace, JR, Weber, ME. Bubbles, Drops, and Particles. New York: Academic Press; 1978.
- [20] Zhang Y, McLaughlin JB, Finch JA. Bubble velocity profile and model of surfactant mass transfer to bubble surface. *Chemical engineering science*. 2001;56(23):6605–6616.
- [21] Hua J, Lou J. Numerical simulation of bubble rising in viscous liquid. *Journal of Computational Physics*. 2007; 222(2):769–795.
- [22] Wanchoo RK. Terminal velocity equation for a two-phase bubble in an immiscible liquid medium. *Chemical Engineering Communications*. 1993;120(1):111–117.
- [23] Sharif SA, Ho MK, Timchenko V, Yeoh, GH. Gravity-driven Bubble Rise Simulation. In: Professor Yeoh, GH, editor. *Handbook of Multiphase Flow Science and Technology*. Springer; 2019.
- [24] Sideman S, Taitel Y. Direct-contact heat transfer with change of phase: evaporation of drops in an immiscible liquid medium. *International Journal of Heat and Mass Transfer*. 1964;7(11): 1273–1289.
- [25] Zeitoun, O, Shoukri, M, Chatoorgoon, V. Interfacial Heat Transfer between Steam Bubbles and Subcooled Water in Vertical upward flow. *Journal of Heat Transfer*. 1995;117: 402–407.
- [26] Al Issa S, Weisensee P, Macián-Juan R. Experimental investigation of steam bubble condensation in vertical large diameter geometry under atmospheric pressure and different flow conditions. *International Journal of Heat and Mass Transfer*. 2014;70:918–929.
- [27] Kim SJ, Park GC. Interfacial heat transfer of condensing bubble in subcooled boiling flow at low pressure. *International Journal of Heat and Mass Transfer*. 2011;54(13–14):2962–2974.
- [28] Lucic A, Mayinger F. Transport phenomena in subcooled flow boiling. *Heat and mass transfer*. 2010;46(10): 1159–1166.
- [29] Yuan D, Pan L, Chen D, Wang X. Condensation heat transfer coefficient at vapour-liquid interface of subcooled flow boiling in vertical narrow rectangular channel. *Nuclear Power Engineering*. 2009;30(5):30–34.
- [30] Warriar GR, Basu N, Dhir VK. Interfacial heat transfer during subcooled flow boiling. *International journal of heat and mass transfer*. 2002; 45(19):3947–3959.
- [31] Sharif SA, Ho MK, Timchenko V, Yeoh, GH. Simulation of rising condensing vapour bubble in rectangular channel using an interface tracking method. Submitted for Publication in *AIChE Journal*, 2021b.
- [32] Kamei S, Hirata M. Condensing phenomena of a single vapor bubble into subcooled water. *Experimental Heat Transfer*. 1990;3(2):173–182.
- [33] Zeng Q, Cai J, Yin H, Yang X, Watanabe T. Numerical simulation of single bubble condensation in subcooled flow using OpenFOAM. *Progress in Nuclear Energy*. 2015;83:336–346.
- [34] Samkhaniani N, Ansari MR. Numerical simulation of bubble condensation using CF-VOF. *Progress in Nuclear Energy*. 2016;89:120–131.

---

Section 3

# Nanofluids

---



# Nanofluid as Advanced Cooling Technology. Success Stories

*Jesús Esarte, Roger R. Riehl, Simone Mancin, Jesús M<sup>a</sup> Blanco, Maite Aresti and Juncal Estella*

## Abstract

Nanofluids are defined as heat transfer fluids with enhanced heat transfer properties by the addition of nanoparticles. Nanofluid's stability, nanoparticles' type and their chemical compatibility with the base fluid are essential not only to increase the nanofluid's thermophysical properties but also to ensure a long-lasting and thermal efficient use of the equipment in which it is used. Some of these aspects are discussed in this chapter. Likewise, the improvement in terms of the heat transfer capacity (thermal resistance) that the use of nanofluids has on the heat pipes-thermosyphons is shown. On the other hand, the improvement in energy efficiency that nanofluid causes in a vapor compression system is also presented.

**Keywords:** nanofluid, heat pipe, vapor compression, battery refrigeration

## 1. Introduction

In an increasingly digitized society with a growing trend in the interconnection of things (IoT and AI), the volume of information circulating through the network and to be processed is constantly growing. This information must be processed in high-speed processing and storage servers, which means that the density of heat to be dissipated has increased considerably in recent decades. This heat flux increase, together with technological advances that allow the miniaturization of electronics, forces thermal engineers to seek advanced solutions in heat dissipation. Advances in the field of electronics, and in particular power electronics, have resulted in a significant increase in heat flux density at the component level. Meeting component temperature requirements and ensuring maximum system performance requires more efficient, lower-volume cooling technologies. As a result, thermal management is becoming increasingly important and critical to the electronics industry. The need for thermal management has increased over the past decade and the prediction is that a steeper increase is yet to come in the coming years.

In parallel, other applications have demanded an increasing thermal management capability that were not even considered less than a decade ago. The advent of electric vehicles with the use of Li-Ion batteries has become a new edge for the development of reliable and high-performance thermal management systems. Due to the fact that this type of battery can be charged within minutes and present a high density of energy that can be delivered to the vehicle's systems, overheating became an issue that can potentially cause accidents, which unfortunately have

already been reported in some applications. This type of issue is generally caused by heat concentration in specific areas of the battery resulting in temperature overshooting with consequent potential fire and loss of the device. Such an issue has been reported with more frequency as new vehicles that utilize electric propulsion are gaining interest from different markets, which require proper addressing using reliable thermal management systems. As a potential solution for this issue, temperature homogenization can be applied in order to minimize heat concentration, which also contributes to increasing the battery's lifetime.

On the other hand, conventional vapor compression refrigeration has, in recent years, suffered from the consequences of international environmental legislation relating to fluorinated refrigerants "HFCs". In this regard, Europe has adopted the "F-GAS" regulation, which establishes deadlines for the use of these refrigerants due to their negative impact on the climate. The climate impact of a substance is commonly expressed as the global warming potential (GWP). The lower the GWP, the more climate-friendly the substance. Most of the HFCs have a very high GWP and are hence potent greenhouse gases. Most of the HFCs are used as refrigerants in refrigeration and air conditioning. To mitigate emissions of substances with a high GWP and comply with the F-Gas Regulation, each sector needs to find solutions to quickly switch to low GWP refrigerants. The F-gas regulation is committed to so-called clean refrigerants (hydrocarbons, CO<sub>2</sub>, HFOs) due to their zero or very low GWP. However, the use of these refrigerants often implies a reduction in the efficiency of the refrigerators as well as an extra effort to redesign them.

Under this scenario, thermal and refrigeration engineers are forced to find solutions, not only in terms of the type of refrigerant (more respectful with the environment) but also in terms of new refrigeration technologies (acoustic, thermocaloric, thermoelectric, nanofluids ...) that meet new challenges in heat dissipation and cooling. Nanofluids are envisioned as one of these solutions. Although there is little bibliography at this regard, recent works show the interest of nanofluids as key enabling technology to meet the environmental challenges vapor compression systems must face. For example, Gokulnath G [1] presents an analysis of the effect of different nano-refrigerants on a domestic refrigerator performance. Haque [2] analyzes the behavior of a domestic refrigerator when using a polyol-ester-based nano-lubricant.

Nanofluids are defined as heat transfer fluids with enhanced heat transfer properties by the addition of nanoparticles. When formulating a nanofluid, a fundamental aspect to consider is its stability, since its thermophysical properties pretty much depend on it. Adding dispersants in the two-phase systems is an easy and economic method to enhance the stability of nanofluids. Although surfactant addition is an effective way to enhance the dispersibility of nanoparticles, surfactants might cause several problems [3]. In this chapter an analysis of the effect of nanoparticles not only on the stability of the nanofluid but also on its thermal conductivity is carried out.

The use of nanofluids is already being seen in different applications - technologies, in this chapter some application cases are shown.

## **2. Nanofluids**

Nanofluids [4] are a type of fluid made up of a base fluid to which nanoparticles (<100 nm) are added in order to increase its thermophysical properties.. Nanoparticles manipulation and in turn nanofluid formulation requires high security measures and therefore must be handled in controlled environments, **Figure 1**.





**Figure 1.**  
*Nanoparticles handling laboratory.*

Metallic nanoparticles are among the most interesting ones due to their high thermal conductivity. This nanoparticles addition makes the nanofluid thermal conductivity increase [5, 6] as well as its viscosity which is a negative effect as far as pressure drop is concerned.

Despite the amount of research carried out so far, which shows that the use of nanofluids increase the heat transfer coefficients, there is still much to understand in the area of nanofluids, for example, depending on which cooling technology (LHP, HP) the nanofluid is used in, other forces (capillarity) apart from the viscous and gravitational forces come into play requiring a better fluid–structure interaction understanding [7]. This interaction is given, among others, by the surface tension and the contact angle between the fluid and the porous medium. Since the contact angle is affected by the addition of nanoparticles [8–10] the capillary forces are altered and with them the LHP capillary pumping. From a theoretical point of view, the phenomena that take place at the nanoparticle level (Brownian movement, plasma, ...) that make the heat transfer coefficients improve are not clear. In the bibliography there are several theoretical models [11–19] that try to shed light on the matter but their predictions differ from the experimental values [20–22]. This theoretical field requires a greater research effort to be able to give answers to the real behavior of nanofluids.

Nanoparticles not only increase the thermal conductivity of the base fluid but also act as sources of bubble generation in boiling processes, thus increasing the boiling coefficients, important in LHPs and HPs [23, 24].

Nanoparticles stability [25, 26] in the fluid is key to have a nanofluid that ensures an enhancement of the device thermal performance over time. Different techniques are used for such purpose: surfactant addition, sonication and surface charge change.

The addition of nanoparticles to a base fluid, as mentioned above in the section, basically alters its viscosity and its thermal conductivity. These alterations depend pretty much on the nanoparticle size and concentration as shown in the following sections. This influence is reflected in the following analysis carried out for the base fluid polyol-ester when it is doped with different types of nanoparticles (CuO, Al<sub>2</sub>O<sub>3</sub> and TiO<sub>2</sub>).

## 2.1 Nanoparticles size - viscosity

As mentioned above, nanofluid viscosity [27] is an important property as far as thermal performance and fluid flow are concerned. As shown by the rheological analyzes carried out by different researchers [28, 29]. Among the several works regarding oil based nanofluids, Resiga et al. [30] investigated the rheological properties of highly concentrated transformer oil-based magnetic nanofluids; the results confirmed that the nanofluids were Newtonians in all concentrations except at the highest concentration of 20.8 vol%. Murshed et al. [31] experimentally studied the viscosity of silicone oil (SO) based  $\text{TiO}_2$  and  $\text{SiO}_2$  nanofluids confirming the nanofluids' Newtonian nature. Chen and Xie. [32] reached the same conclusion for carbon nanotubes (TCNT)-nanofluids. At low shear rates, Newtonian behavior of silicone oil (Syltherm 800) based diamond-graphene nanofluid was observed by Yang et al. [33]. The same authors [34] investigated the effects of multi-walled carbon nanotubes (MWCNT) loading, surfactant concentration and dispersion energy (ultrasonication) on the thermal conductivity and steady shear viscosity of oil (PAO6)- based-nanofluids. Polyisobutene succinimide (PIBSI) was used as surfactant. The results showed that at low shear conditions the nanofluid viscosity was governed by the PIBSI, observing a 0.1 to 0.07 Pa shear stress decrease. They also analyzed the concentration of CNT versus viscosity, it was observed that the viscosity increased for any concentration other than 3% by weight.

Heris et al. [35] studied the rheological properties of ZnO nanoparticles dispersed in mineral oil (MO) based lubricant as a function of the volume fraction in the range 0.01–0.6% and temperature from 0 to 60 °C. The results showed that the investigated nanolubricants were found to behave as yield stress fluids as mineral oil and the viscosity ratio was increased by the nanoparticle loadings. The effects of the temperature were noticeable at high temperature and concentration.

Kole and Dey [36] dispersed 40 nm diameter CuO nanoparticles at a volume fraction higher than 0.005 in gear oil and concluded that for a 10–50 °C temperature range the nanofluid shear rate was below  $30 \text{ s}^{-1}$ . For ultra-low concentration, it was observed a viscosity increase with increasing volume fraction.

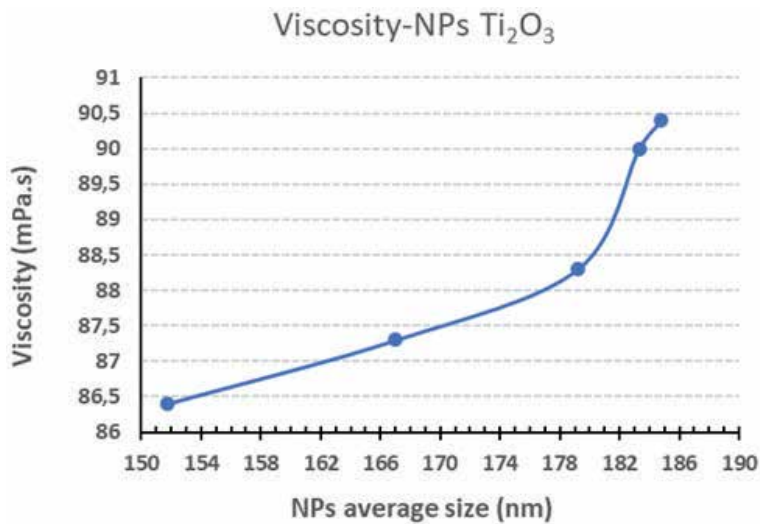
Moreover, Saedinia et al. [37] investigated the viscosity of CuO/oil-based nanofluids with 50 nm nanoparticle for weight fraction ranging from 0.2% to 2%. Newtonian nature was noticed in the shear rate range of  $0\text{--}15 \text{ s}^{-1}$  for all the investigated temperatures and concentrations.

When analyzing the  $\text{Ti}_2\text{O}_3$  nanoparticles size on the 1 wt%. polyol-ester nanofluid, **Figure 2**, it is observed that viscosity increases with the increase of NP size. This increase becomes steeper for a specific size (180 nm). This result agrees with other researchers' work [38, 39]. Although, it could be expected that viscosity would decrease with increasing NP size [40], this performance depends to a great extent on the NP concentration, which can cause a decrease or an increase in viscosity as the size of the NPs increases [41].

In any refrigeration application, the nanofluid must be pumped to flow through the pipe and this pumping work is greater the higher the viscosity. In terms of efficiency, this work must be as low as possible and consequently the nanofluid viscosity.

## 2.2 Thermal conductivity

The enhancement of the thermal conductivity of the base fluid is the primarily objective of the addition of nanoparticles. The literature showed that the thermal conductivity of nanofluids is higher compared to the base fluids; this is confirmed also in the case of oil-based nanofluids. Nonetheless, just a few works were devoted to investigate the thermal conductivity of this kind of nanofluids.



**Figure 2.**  
*Influence of NPs size on viscosity. 1 wt% nanofluid of Ti<sub>2</sub>O<sub>3</sub> NPs in polyol-ester.*

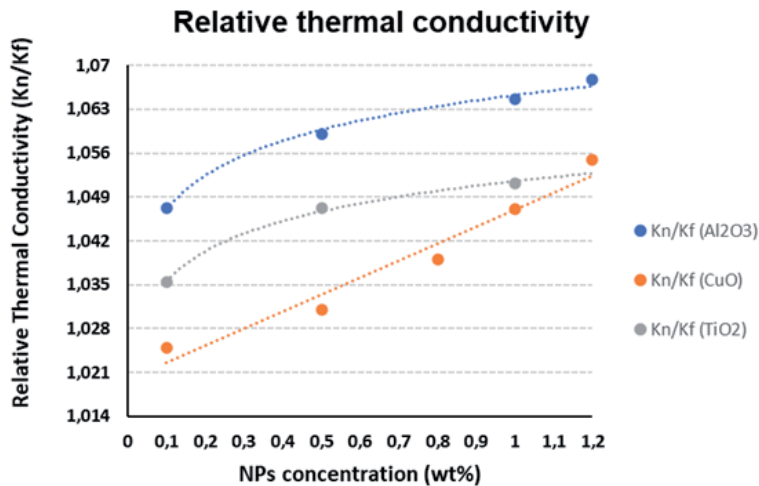
Saeedinia et al. [37] investigated the thermal conductivity of CuO/oil nanofluid. The authors, measured the thermal conductivity at different temperatures ranging between 24 and 70 °C and at two concentrations of 1 wt% and 2 wt. %. The results showed a remarkable enhancement in the thermal conductivity of the studied nanofluid with temperature. With increasing the temperature, the agglomeration of nanoparticles is hindered, and thus the thermal conductivity is enhanced because of the more uniform of nanoparticles dispersion.

Wang et al. [42] studied the effects of temperature and solid concentration on the thermal conductivity of oil-based nanofluids containing graphite nanoparticles. The results highlighted that when adding 1.36%vol. of graphite a 36% enhancement in the thermal conductivity was achievable. The authors also found that the thermal conductivity enhancement was not linear with nanoparticle concentration. The temperature showed a weak effect on the thermal conductivity enhancement but when increasing temperature, the thermal conductivity also increased.

Aberoumand et al. [43] experimentally investigated the thermal conductivity of silver/heat transfer oil nanofluid at different values of concentration and temperatures. The authors found that while the thermal conductivity of the base fluid showed a decreasing trend as the temperature increased that of the nanofluid increased with the temperature. This trend has been found for all the investigated concentrations. The authors stated that this phenomenon can be explained considering the Brownian motion which are enhanced when increasing temperature. Aberoumand et al. [44] experimentally demonstrated that for a nanofluid composed of 1% wt CuO nanoparticles on engine oil, the thermal conductivity increased by 49%.

Colangelo et al. [45] The effect of adding a different amount of Oleic Acid surfactant to Al<sub>2</sub>O<sub>3</sub>/diathermic oil NF on the thermal conductivity, in different temperatures (30 to 50 °C) and three concentrations of 0.3, 0.7, and 1 vol.%, has been investigated by. Their results showed that adding surfactant does not affect the thermal conductivity of the NF. Moreover, increasing the solid concentration of the surfactant has also no effect on the thermal conductivity enhancement. They reported the maximum enhancement of 4% at the solid concentration of 1 vol. %.

**Figure 3** shows the thermal conductivity variation with variation in nanoparticle concentration from 0.1 wt% to 1.1 wt% at ambient temperature. It is apparent from



**Figure 3.** Influence of NPs concentration on thermal conductivity for different NPs (CuO, Ti<sub>2</sub>O<sub>3</sub> and Al<sub>2</sub>O<sub>3</sub>) and concentrations. Polyol-ester as base fluid.

**Figure 3** that thermal conductivity increases with increasing the NPs concentration [46]. However, in the cases of Al<sub>2</sub>O<sub>3</sub> and TiO<sub>2</sub>, the thermal conductivity increase is less the higher the concentration. The “CuO” nanofluid exhibits a linearly increasing behavior with concentration.

The effect of the type of nanoparticle is clearly observed in **Figure 3**. Al<sub>2</sub>O<sub>3</sub> nanoparticles provide the largest thermal conductivity increase compared to the other two.

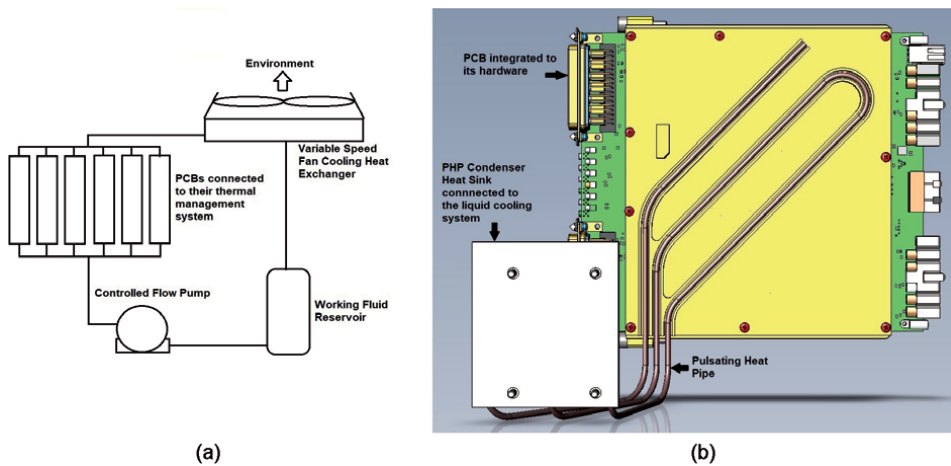
### 3. Application cases

#### 3.1 Passive cooling devices

Nanofluids can be potentially applied as working fluids in active (mechanically driven) and passive (capillary action, slug/plug dynamics) systems. Thermal management devices employing either concepts can benefit from the advantages of using nanofluids in order to enhance their heat transport capabilities.

Liquid cooling systems use a pump to drive the liquid to the heat source (or sources) in contact with a dedicated heat exchanger (or multiple heat exchangers). Heat is then absorbed by the working fluid and transported by the lines to a condenser (one or multiple), where the heat is rejected to a medium (environmental air, liquid reservoir, etc) with low temperature. Since the liquid cooling system is a closed circuit, the working fluid operates in a cycle absorbing and rejecting heat. As a necessity from its design, liquid cooling systems require a reservoir used to self-control the working fluid being used by the system, which will be determined by the flow rate at which it is operating. **Figure 4a** presents an schematics of a liquid cooling system.

As a promising technology for complex thermal management systems, Pulsating Heat Pipe (PHPs), also known as Oscillating Heat Pipes (OHPs) can potentially use nanofluids as their working fluids, due to the fact that they do not present a wick structure that could compromise their overall thermal performance. Their simple construction based on a meandering tube bent in several parallel curves operate by means of liquid slugs and vapor plugs motion [46], transporting the heat absorbed



**Figure 4.**  
*(a) schematic, and (b) CAD representation of the thermal control system arrangement.*

from a source and rejecting it in a sink. This kind of device can be considered a special type of heat pipe and was introduced by Akachi [47]. There are several applications in thermal control systems that PHPs can be utilized, from structures to electronics cooling, as well as thermal management of sensitive equipment such as those related to aerospace and surveillance. Given the potential use of PHPs as an effective thermal control device, investigations have been carried out towards the improvement of their overall efficiency, which leads to the search of alternative and more effective working fluids. In this case, the addition of solid nanoparticles in the working fluid has shown important improvements in its thermal conductivity that can potentially benefit PHPs [48].

Another thermal control device that can benefit from the improvements given by nanofluids is called Loop Heat Pipe (LHP). Given its architecture, LHPs are high efficient thermal control devices that can transport heat over long distances. It is built with a capillary evaporator responsible for generating capillary pressure that drives the working fluid throughout the loop. It is directly connected to a heat source where it absorbs the heat transferring it to the working fluid causing its evaporation. Due to the presence of a fine pore structure (wick), it generated capillary pressure that pushed the vapor towards the condenser, where it condenses back to liquid phase. By the capillary pressure action, liquid is sent back to the evaporator to complete the cycle. A compensation chamber (or reservoir) present at the capillary evaporator's inlet, which is hydraulically connected to the evaporator's core, will supply or drain the working fluid depending on the heat loads that are applied [49]. Depending of the level of accuracy needed to control the heat source, the LHP can present a pressure control regulator that sets the device's operation temperature with great precision [50, 51]. The potential in applying nanofluids in LHPs has been presented, showing a considerable enhancement in their performance. However, since the pressure drop increases with the use of nanofluids, the overall performance can be compromised due to limitations in the capillary pressure generation by the evaporator [52, 53].

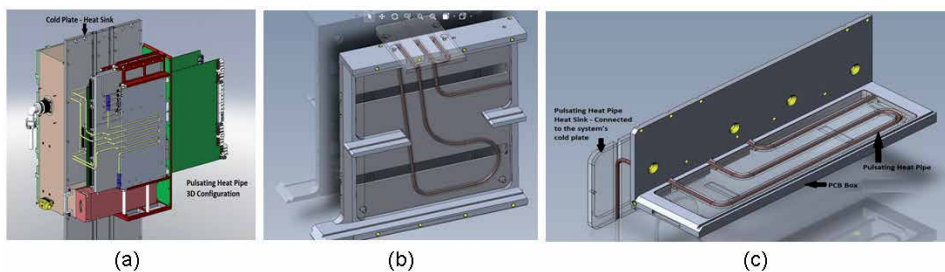
Due to the potential in using nanofluids in thermal control devices, PHPs have been designed and integrated in a hybrid thermal management system installed in a surveillance system. This hybrid thermal management system was composed of a liquid cooling loop that connected several heat sources by heat exchangers, where PCBs were directly attached, in order to keep their electronic components within the required levels of temperature. A magnetic pump with variable flow rate was

responsible for driving the working fluid throughout the loop, in order to guarantee that the heat generated would be properly absorbed and rejected. However, some PCBs were located far from the heat exchangers, which required the use of PHPs to connect the PCBs to them in order to transport the heat generated by the electronics to be properly rejected in a heat sink, while keeping their temperature according to the project's requirements. Due to the complexity of the system, along with the presence of hundreds of PCBs, several PHPs were designed, built and integrated to their dedicated heat sink, which were connected to the liquid cooling system. All the heat generated by the PCBs was transported to a condenser, responsible for dissipating it to the environmental air. According to the project's requirements, the hybrid system had to operate between +5 and + 50 °C of ambient temperature for a maximum humidity level of 95%. The schematics of such arrangement is presented by **Figure 4a** and **b** presents the hybrid setup where the pulsating heat pipe and the heat sink are connected [54].

The nanofluid selected for this application was composed of de-ionized water as the base fluid and CuO nanoparticles, since this combination presents a stable chemical compatibility. The solid nanoparticles presented an average diameter of 29 nm with 98% of purity. The nanoparticles concentration varied from 3.5 wt% to 20 wt%, which were used to compare their effects on the system's thermal performance while operating in real conditions.

As mentioned before, several PHPs were designed, built and integrated in this surveillance system, which showed to be a very complex thermal management problem to be solved. The PHPs had different configurations regarding their total effective length, number of turns, etc. all due to the fact that they were operating under different heat loads. The different designs for the PHPs are shown in **Figure 5** with the representation of their integration with their respective PCB [54]. The PHPs were charged with a nanofluid formed with de-ionized water (base fluid) and CuO (nanoparticles), with the same characteristics as the ones applied to the liquid cooling system. The nanoparticles concentration ranged from 2.0 wt% to 3.5 wt%. Due to the PHPs requirements towards the temperature homogenization of all their related PCBs, the heat dissipation capabilities of the entire thermal management system could be optimized.

Due to the thermal management characteristics at which a given device must operate, such as those found in heavy duty processing demands of computer clusters, as well as some electronics found in avionics, etc., a specific design is required. For high heat densities, PHPs are not indicated as thermal control devices due to their limitation in transporting the heat, which can generate concentrated heat loads and an eventual device's failure. In this case, LHPs are the most indicated to be applied as they can efficiently remove the heat from concentrated areas, being known to operate in applications where the heat flux in the heat source can be as



**Figure 5.** PHPs with nanofluids applied to the thermal control of PCBs. (a) low, (b) medium, (c) high thermal load configuration.



much as  $100 \text{ W/cm}^2$ , or even above that. There are different architecture configurations for LHPs destined to the thermal control of high heat density electronics, being able to operate with a regular working fluid or with a nanofluid, such as shown by **Figure 6** [52–54].

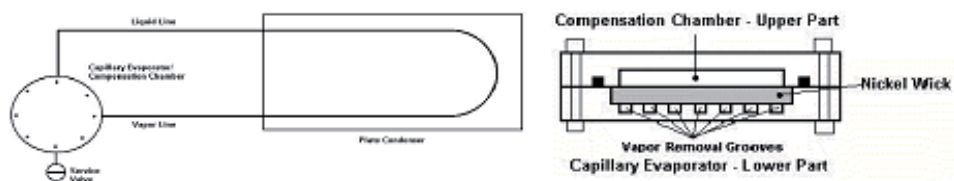
Nanofluids have been reported to increase by up to 20% the heat transport capability in LHPs, even though they were facing higher pressure drops as nanofluids present a higher viscosity when compared to the base fluid's only. In this case, a better assessment regarding the LHP's thermal characteristics must be well balanced in order to not compromise its performance and cause a system's failure.

A subject that is commonly neglected by some researchers and manufacturers is related to the degree of chemical compatibility between the base fluid, the solid nanoparticles and the material used to build a PHP and a LHP, since they operate with their working fluid at saturation conditions. This is a key factor to ensure instant operation of those devices as soon as heat is administrated to their evaporator, being promptly absorbed by latent heat. If chemical incompatibility is found between the working fluid, solid nanoparticles and other materials used to build the device, the working fluid will begin its degradation resulting in the generation of non-condensable gases (NCGs). The velocity at which the degradation will occur will depend on the materials and working fluid involved, as well as with the operational temperature. Incompatible materials and fluids, such as water and aluminum, ammonia and copper, etc., will present a degradation much faster than known compatible materials and fluids, such as water and copper, ammonia and aluminum.

The NCGs generated during the base fluid's degradation will be accumulated at the coldest part of the PHP/LHP (condenser), being accumulated there during the device's operation. Since more NCG will be accumulated, the device will lose its condensation capability, compromising the heat rejection by the system that will end up causing an increase in the evaporator's temperature and, finally, the device's failure due to a dryout caused by the lack of liquid returning to the evaporator.

A process that has been often neglected by many professionals working with PHPs/LHPs and heat pipes, as well as with nanofluids, is called *aging*. This process forces the system to generate as much NCG as possible under controlled conditions that will eventually guarantee that the device will operate for a long time without the effect of NCGs [55].

As part of the manufacturing processes of any device like PHPs, LHPs and heat pipes, the aging process will be executed after the vacuum/charging procedure applied to those devices. The vacuum/charging procedure is of great importance and must be carefully controlled in order to ensure that the device will properly operate under the designed requirements. In this case, the device must reach a vacuum level that is adequate for its operation, which is also applied as a final cleaning process and moisture removal to any device. Prior to transferring the working fluid to the device, it needs to go through a process called *outgassing* that

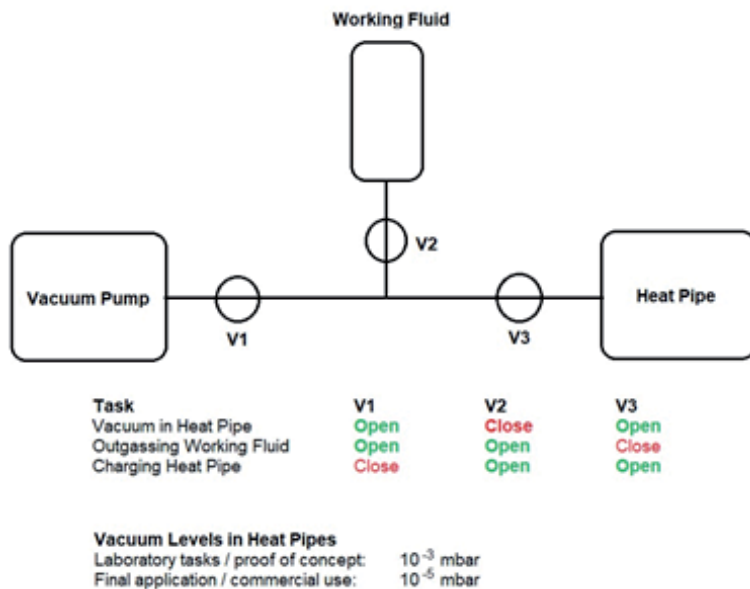


**Figure 6.**  
*Loop heat pipes applied to computer clusters thermal control.*

will bring the working fluid to its saturation condition at the local temperature. Along with this, the *outgassing* will eliminate any dissolved gases present in the working fluid that will certainly contribute to the NCG generation and compromise the device's performance. This is not a complex process to be executed and can be done as presented by **Figure 7**. The technician needs to pay attention to the valves sequence to ensure that the device will be properly evacuated at the required vacuum level, as well as the adequate outgassing of working fluid prior to transfer it to the device. In order to perform the vacuum in the device, valves V1 and V3 must be open, keeping V2 closed. Upon reaching the required vacuum level and no leaks have been detected, the working fluid is outgassed by opening V1 and V2 keeping V3 closed. Once the outgassing has been completed, the technician can transfer the working fluid to the device by closing V1 while opening V2 and V3, ensuring that the required inventory of working fluid is properly transferred to the device [55].

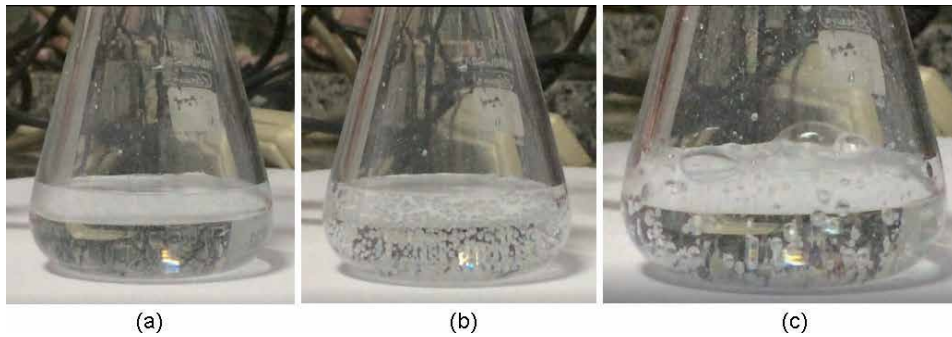
When using low pressure working fluids, such as water, methanol, and acetone, it is possible to watch the entire outgassing process when using a clear glass bottle. During this process, all dissolved gases that will be removed from the working fluid will present a “boiling” pattern, indicating that the vacuum pump is bringing the internal volume to the working fluid's saturation condition. **Figure 8** presents the outgassing process being executed for deionized water. In the case of a nanofluid, due to the addition of solid nanoparticles, the resulting working fluid can result in a dark substance that can present some difficulties to see the outgassing occurring. A trained technician can overcome this issue and perform the outgassing as needed, as shown by **Figure 9** for the case of CuO-deionized water nanofluid (concentration of 2 wt%).

The outgassing process will be over once the bubbles stop appearing in the working fluid. This is the time when the working fluid can be transferred to the device. Nanofluids present a faster outgassing process due to the presence of solid nanoparticles. The working fluid volume that needs to be transferred to the device will determine the time required for the outgassing process, as well as the vacuum pump's speed.

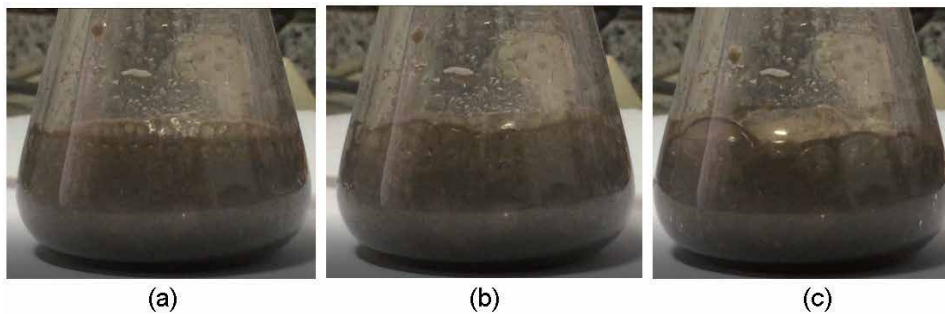


**Figure 7.** Charging process of a heat pipe operating at saturation conditions.





**Figure 8.**  
*Outgassing process for the de-ionized water: (a) beginning of the process; (b) dissolved gases being released; (c) intense release of dissolved gases.*



**Figure 9.**  
*Outgassing process for the CuO- water nanofluid: (a) beginning of the process; (b) dissolved gases being released; (c) intense release of dissolved gases.*

### 3.2 Active cooling -vapor compression

Another potential application for nanofluids is vapor compression refrigeration “VCS”. In these systems, the working fluid is circulated actively through a compressor. The compressor generates the pressure difference necessary for the refrigerant to circulate. During its journey, the refrigerant undergoes a cyclical phase change, condensation-evaporation, which gives it a greater heat transport capacity compared to liquid cooling.

The coefficient of performance “COP” of the VCS systems can be improved in two ways: firstly, by increasing heat abstraction rate in evaporator, and secondly, by reducing the work done in a compressor. The use of nanoparticles to increase the COP of vapor compression systems is something that has already been confirmed, as evidenced by the research works on the matter [54, 55]. Some works are more focused on the increase of heat transfer rates [56–58] while others are on the compressor lubrication improvement [59, 60].

The present work aims to provide more scientific information about nano-lubricants and how they influence the COP of a vapor compression system. The refrigeration system used for determining the COP values was built in-house, **Figure 10** and whose characteristics are listed in **Table 1**.

The Polyol ester lubricant is doped at 1.5% by weight with two types of nanoparticles (Cu and CuO). Both the clean lubricant and the two formulated nano-lubricants are tested on the bench in order to record the corresponding COP. The results are shown in **Table 2**.

The level of lubricant in the refrigerant circuit also has its effect on the COP of the refrigerator, as shown in **Figure 11**.



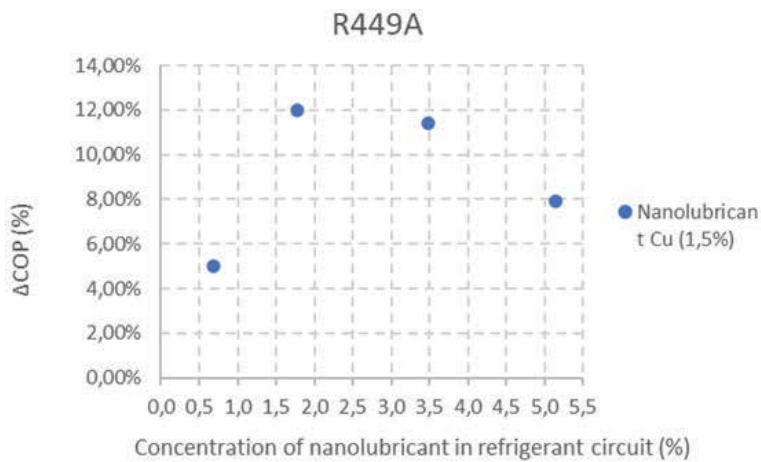
**Figure 10.**  
VC system to test nano-lubricant effects on COP.

Cooling capacity	400W
Compressor	Secop SC12MLX
Refrigerant	R449A
Charges mass	400gr

**Table 1.**  
Components' technical characteristics.

Lubricant	COP	COP increase
Polyol ester	1.25	---
Polyol ester +1.5% Cu	1.41	12%
Polyol ester+3%Cu	1.31	5%

**Table 2.**  
COP improvement.



**Figure 11.**  
Effect of the 1.5%Cu nano-lubricant on the VCS's COP.

## 4. Conclusion

- In view of what is stated in this chapter, it can be concluded that: nanofluids is a promising science to improve the heat transfer capacity of different technologies
- It is applicable to different sectors with minimal investment cost
- Nanofluid stability continues to be a challenge and therefore an open door to research
- A greater understanding of the causes that make the thermophysical properties of nanofluid improve is still necessary, more theoretical research is required
- The large amount of experimental research work carried out to date positions nanofluids as a key enabling technology for the advancement of thermal and cooling management in the immediate future.

## Author details

Jesús Esarte<sup>1\*</sup>, Roger R. Riehl<sup>2</sup>, Simone Mancin<sup>3</sup>, Jesús M<sup>a</sup> Blanco<sup>4</sup>, Maite Aresti<sup>1</sup> and Juncal Estella<sup>1</sup>

1 NAITEC-Research Center for Automotive and Mechatronics, Pamplona, Spain

2 National Institute for Space Research – INPE/DMC, São José dos Campos, Brazil


3 Department of Management and Engineering University of Padova, Padova, Italy

4 UPV-University of Basque Country, Bilbao, Spain

\*Address all correspondence to: [jesarte@naitec.es](mailto:jesarte@naitec.es)

## IntechOpen

---

© 2021 The Author(s). Licensee IntechOpen. This chapter is distributed under the terms of the Creative Commons Attribution License (<http://creativecommons.org/licenses/by/3.0>), which permits unrestricted use, distribution, and reproduction in any medium, provided the original work is properly cited. 

## References

- [1] Gokulnath G and Prabhu A.R.G, Performance Analysis of a Nano Refrigerant Mixtures in a Domestic Refrigeration System, 2017 Applied Science 508-516
- [2] Haque M.E, Bakar Kadirgama K, Noor M M, and Shakaib, Performance of a domestic refrigerator using nanoparticles-based polyolester oil lubricant, 2016 J. Mech. Eng. Sci., 1778-1791.
- [3] Y. Hwang, J. K. Lee, C. H. Lee et al., Stability and thermal conductivity characteristics of nanofluids. *Thermochimica Acta*, vol. 455, no. 1-2, pp. 70-74, 2007
- [4] Wei Yu and Huaqing Xie. "A Review on Nanofluids: Preparation, Stability Mechanisms, and Applications. *Journal of Nanomaterials*, 2012.
- [5] Koo, J., Kleinstreuer, C., A new thermal conductivity model for nanofluids, *Journal of Nanoparticle Research*, 6 (2006) 577-588.
- [6] Chein, R. and Huang, G., Analysis of microchannel heat sink performance using nanofluids, *Applied Thermal Engineering*, 25 (2005) 3104-3114.
- [7] Riehl, R. R., Performance evaluation when using nanofluids in loop heat pipe and pulsating heat pipe, in: *Proceedings of the 37<sup>th</sup> International Conference on Environmental Systems (ICES)*, July 10-15 (2007), Chicago, IL USA, paper 2007-01-3193.
- [8] M. Hernaiz, V. Alonso, P. Estellé, Z. Wu, B. Sundén, L. Doretto, S. Mancin, N. Çobanoğlu, Z.H. Karadeniz, N. Garmendia, M. Lasheras-Zubiarte et al. The contact angle of nanofluids as thermophysical property. *Journal of Colloid and Interface Science*, Volume 547, 1 July 2019, Pages 393-406
- [9] M.H.Buchmann, N. Garmendia, et al. "The contact angle of nanofluids as thermophysical property". *Journal of Colloid and Interface Science*. Volume 547, 1 July 2019, Pages 393-406
- [10] Gimeno-Furio A., Mancin S. (2020) Effects of Carbon Nanohorn Based Nanofluids Pool Boiling on Optical Properties and Wettability of Different Metal Surfaces, *Heat Transfer Engineering*, DOI: 10.1080/01457632.2020.1818407
- [11] Ghadimi, A., Saidur, R., Metselaar H. S. C., "A Review of Nanofluid Stability Properties and Characterization in Stationary Conditions", *International Journal of Heat and Mass Transfer*, 4051-4068, Elsevier, Jul. 2011.
- [12] Riehl, R. R., Development of Copper-Methanol Heat Pipes: Thermal Performance Evaluation for Electronics Cooling, *Heat Powered Cycles Conference*, Nottingham, UK, June 26-29, 2016.
- [13] Liu, Z. H., and Zhu, Q. Z., "Application of Aqueous Nanofluids in a Horizontal Mesh Heat Pipe", *Energy Conversion and management*, 292-300, Elsevier, Jul. 2010.
- [14] Wang, P. Y., and Chen, X. J., and Liu, Z. H., and Liu, Y. P., "Application of Nanofluid in an Inclined Mesh Wicked Heat Pipes", *Thermochimica Acta*, 100-108, Elsevier, Apr. 2012.
- [15] Kumaresan, G., and Venkatachalapathy, S., Arsvatham, L. G., Wongwises, S., "Comparative Study on Heat Transfer Characteristics of Sintered and Mesh wick heat pipes using CuO Nanofluids", *International Communications in Heat and Mass Transfer*, 208-215, Elsevier, Aug. 2014.
- [16] Liu, Z. H., and Li, Y. Y., and Bao, R., "Thermal Performance of Inclined

Grooved Heat Pipes Using Nanofluids”, *International Journal of Thermal Sciences*, 1680-1687, Elsevier, Apr. 2010.

[17] Wang, G. S., and Song, B., and Liu, Z. H., “Operation Characteristics of Cylindrical Miniature Grooved Heat Pipe Using Aqueous CuO Nanofluids”, *Experimental Thermal and Fluid Science*, 1415-1421, Elsevier, Jul. 2010.

[18] Kumaresan, G., and Venkatachalapathy, S., “A Review on Heat Transfer Enhancement Studies of Heat Pipes Using Nanofluids”, *Frontiers in heat pipes*, (FHP) 3-043001, 2012.

[19] Chien, H.-T., Tsai, C.-I., Chen, P.-H., and Chen, P.-Y. “Improvement on Thermal Performance of a Disk-Shaped Miniature Heat Pipe with Nanofluid”, *ICEPT 2003. Fifth International Conference on Electronic Packaging Technology. Proceedings. (IEEE Cat. No.03EX750)*, 389. IEEE, Shanghai, China (2003).

[20] Yang, X. F., and Liu, Z. H., and Zhao, J., “Heat Transfer Performance of a Horizontal Micro-Grooved Heat Pipe Using CuO Nanofluid”, *Journal of Micromechanics and Microengineering*, 035038, IOP Pub., Feb. 2008.

[21] Marcelino, E., Oliveira, D., Riehl, R. R., “A Review on Thermal Performance of CuO-water Nanofluids Applied to Heat Pipes and Their Characteristics”, *ITherm - The Intersociety Conference on Thermal and Thermomechanical Phenomena in Electronic Systems*, May 31–June 3, Las Vegas, NV USA, 2016.

[22] Venkatachalapathy, S., Kumaresan, G., Suresh, S., “Performance analysis of cylindrical heat pipe using nanofluids – An experimental study”, *International Journal of Multiphase Flow* 72 (2015) 188-197.

[23] Tong, B. Y., Wong, T. N., Ooi, K. T., Closed-loop pulsating heat pipe, *Applied Thermal Engineering*, 21 (2001) 1845-1862.

[24] Yu, W., Choi, S. U. S., The role of interfacial layers in the enhanced thermal conductivity of nanofluids: a renovated Maxwell model, *Journal of Nanoparticle Research*, 5 (2003) 167-171.

[25] Riehl, R. R., “Analysis of Loop Heat Pipe Behaviour Using Nanofluid”, *Heat Powered Cycle Int. Conf.*, Newcastle, UK, 2006.

[26] Zhang, Y., *Nanofluids Research, Development and Applications*, 1<sup>st</sup> ed., Nova Science Inc., New York, 2013, Chaps. 2,3.

[27] S.M. Sohel Murshed, Patrice Estellé, A state of the art review on viscosity of nanofluids, *Renewable and Sustainable Energy Reviews* 76 (2017) 1134-1152.

[28] Sharma AK, Tiwari AK, Dixit AR. Rheological behavior of nanofluids: a review. *Renew Sustain Energy Rev* 2016;53:779-91

[29] Murshed SMS, Leong KC, Yang C. Thermophysical properties of nanofluids. In: Sattler KD, editor. *Handbook of nanophysics: nanoparticles and quantum dots*. Boca Raton: Taylor & Francis; 2010

[30] Resiga DS, Socoliuc V, Boros T, Borbath T, Marinica O, Han A, Vekas L. The influence of particle clustering on the rheological properties of highly concentrated magnetic nanofluids. *J Colloid Interface Sci* 2012;373:110-5.

[31] Murshed SMS, Santos FJV, Nieto de Castro CA. Investigations of viscosity of silicone oil-based semiconductor nanofluids. *J Nanofluid* 2013;2:261-6

[32] Chen L, Xie H. Silicon oil based multiwalled carbon nanotubes nanofluid with optimized thermal conductivity enhancement. *Colloid Surf A: Physicochem Eng Asp* 2009;352:136-40.

- [33] Yang Y, Oztekin A, Neti S, Mohapatra S. Particle agglomeration and properties of nanofluids. *J Nanopart Res* 2012;14:852.
- [34] Yang Y, Grulke EA, Zhang ZG, Wu G. Thermal and rheological properties of carbon nanotube-in-oil dispersions. *J Appl Phys* 2006;99:114307.
- [35] Heris SZ, Razbani MA, Estellé P, Mahian O. Rheological behavior of zinc-oxide nanolubricants. *J Dispers Sci Technol* 2015;36:1073-9
- [36] Kole M, Dey TK. Effect of aggregation on the viscosity of copper oxide-gear oil nanofluids. *Int J Therm Sci* 2011;50:1741-7
- [37] Saeedinia M, Akhavan-Behabadi MA, Razi P. Thermal and rheological characteristics of CuO-base oil nanofluid flow inside a circular tube. *Int Commun Heat Mass Transf* 2012;39:152-9
- [38] R. Prasher, et al., "Measurements of nanofluid viscosity and its implications for thermal applications". [J], *Appl. Phys. Lett.* 89 (13) (2006) 255.
- [39] M.H. Esfe, et al. "An experimental investigation, sensitivity analysis and RSM analysis of MWCNT (10)-ZnO(90)/10W40 nanofluid viscosity". [J], *J.Mol. Liq.* 288 (2019) 111020.
- [40] Xichen Hu, et, al. "Experimental investigation and mechanism analysis: Effect of nanoparticle size on viscosity of nanofluids". *Journal of Molecular Liquids* 314 (2020) 113604
- [41] S.P. Jang, et. al. "Particle concentration and tube size dependence of viscosity of Al<sub>2</sub>O<sub>3</sub> – water nanofluids flowing through micro-and minitubes". *J. Appl. Phys. Lett.* 91 (24) (2007) 243112
- [42] B. Wang, X. Wang, W. Lou, J. Hao, Thermal conductivity and rheological properties of graphite/oil nanofluids, *Colloids Surf. A Physicochem. Eng. Asp.* 414 (Nov. 2012) 125-131
- [43] S. Aberoumand, A. Jafarimoghaddam, M. Moravej, H. Aberoumand, K. Javaherdeh, Experimental study on the rheological behavior of silver-heat transfer oil nanofluid and suggesting two empirical based correlations for thermal conductivity and vis-cosity of oil based nanofluids, *Appl. Therm. Eng.* 101 (May 2016) 362-372.
- [44] S. Aberoumand, A. Jafarimoghaddam, Experimental study on synthesis, stability, thermal conductivity and viscosity of Cu-engine oil nanofluid, *J. Taiwan Inst. Chem. Eng.* 71 (Feb. 2017) 315-322.
- [45] G. Colangelo, E. Favale, P. Miglietta, M. Milanese, A. de Risi, Thermal conductivity, viscosity and stability of Al<sub>2</sub>O<sub>3</sub>-diathermic oil nanofluids for solar energy systems, *Energy* 95 (Jan. 2016) 124-136
- [46] Ovais Gulzar et. al. "Experimental study on thermal conductivity of mono and hybrid Al<sub>2</sub>O<sub>3</sub>-TiO<sub>2</sub> nanofluids for concentrating solar collectors". *International Journal of Energy Research.* (2020), 1-15.
- [47] Akachi, H., Polasek, F., Stulc, P., Pulsating Heat Pipes, *Proceedings of the 5<sup>th</sup> International Heat Pipe Symposium*, Melbourne, Australia, pp. 208-217, 1996.
- [48] Yu, W., Choi, S. U. S., "The role of interfacial layers in the enhanced thermal conductivity of nanofluids: a renovated Maxwell model", *Journal of Nanoparticle Research*, 5, 2003, pp. 167-171.
- [49] J. Esarte, A. Bernardine, et al. "Performance assessment of a Three-Dimensional printed porous media produced by Selective Laser Melting technology for the optimization of Loop

Heat Pipe wicks". Applied Science 2019, 9 2905; doi:10.3390/app9142905.

[50] Riehl, R. R., Thermal Performance and Development of a Dual Evaporator Loop Heat Pipe, *Heat Pipe Science and Technology, An International Journal*, 4(1-2), 105-117, 2013

[51] Riehl, R. R., "Current Developments on Pulsating Heat Pipes and Dual-Evaporators Loop Heat Pipes", 18<sup>th</sup> Workshop on Thermophysics Applications in Microgravity, March 24, the Aerospace Corporation, El Segundo, CA, USA 2014.

[52] Riehl, R. R. "Utilization of Passive Thermal Control Technologies in Cooling Electronics: A Brief Review, *Heat Pipe Science and Technology, An International Journal*, 7 (3-4), 161-183, 2016.

[53] Riehl, R. R., Murshed, S. M. S., Life Time Expectancy Prediction and Ageing Process of Heat Pipes Using Nanofluids, *Heat Transfer Engineering*, DOI: 10.1080/01457632.2020.1818423

[54] Haque M.E, Bakar Kadirgama K, Noor M M, and Shakaib, Performance of a domestic refrigerator using nanoparticles-based polyolester oil lubricant, 2016 J. Mech. Eng. Sci., 1778-1791

[55] Kamaraj N, Experimental analysis of Vapour Compression Refrigeration System using the refrigerant with Nano particles, 2016 Int journal of mech. engg. 16-25

[56] Kedarnath B, Enhancement of COP using Nanoadditives in Domestic Refrigerator 2015 Int journal of Applied sci.engg.tech.282-286

[57] Kamaraj N, Experimental analysis of Vapour Compression Refrigeration System using the refrigerant with Nano particles, 2016 Int journal of mech. engg. 16-25

[58] Soliman AMS Taher SH Abdel-Rahman AK and Ookawara S, Performance enhancement of vapor compression cycle using nano materials, 2015 Int. Conf. Renew. Energy 821-826

[59] Kannan P and Manivanana A, Theoretical analysis of a vapour compression refrigeration system with R134a , R290 , R600a & various ratio of R290 / R600a, 2016 IJRASET 143-146

[60] Veera Raghavalu K, Govindha Rasu N. "Review on Applications of NanoFluids used in Vapour Compression Refrigeration System for Cop Enhancement". *Materials Science and Engineering* 330 (2018)





# Convective Heat Transfer of Ethanol/Polyalphaolefin Nanoemulsion in Mini- and Microchannel Heat Exchangers for High Heat Flux Electronics Cooling

*Jaime Rios, Mehdi Kabirnajafi, Takele Gameda, Raid Mohammed and Jiajun Xu*

## Abstract

The present study experimentally and numerically investigates the flow and heat transfer characteristics of a novel nanostructured heat transfer fluid, namely, ethanol/polyalphaolefin nanoemulsion, inside a conventionally manufactured minichannel of circular cross section and a microchannel heat exchanger of rectangular cross section manufactured additively using the Direct Metal Laser Sintering (DMLS) process. The experiments were conducted for single-phase flow of pure polyalphaolefin (PAO) and ethanol/PAO nanoemulsion fluids with two ethanol concentrations of 4 wt% and 8 wt% as well as for two-phase flow boiling of nanoemulsion fluids to study the effect of ethanol nanodroplets on the convective flow and heat transfer characteristics. Furthermore, the effects of flow regime of the working fluids on the heat transfer performance for both the minichannel and microchannel heat exchangers were examined within the laminar and transitional flow regimes. It was found that the ethanol/PAO nanoemulsion fluids can improve convective heat transfer compared to that of the pure PAO base fluid under both single- and two-phase flow regimes. While the concentration of nanoemulsion fluids did not reflect a remarkable distinction in single-phase heat transfer performance within the laminar regime, a significant heat transfer enhancement was observed using the nanoemulsion fluids upon entering the transitional flow regime. The heat transfer enhancement at higher concentrations of nanoemulsion within the transitional regime is mainly attributed to the enhanced interaction and interfacial thermal transport between ethanol nanodroplets and PAO base fluid. For two-phase flow boiling, heat transfer coefficients of ethanol/PAO nanoemulsion fluids were further enhanced when the ethanol nanodroplets underwent phase change. A comparative study on the flow and heat transfer characteristics was also implemented between the traditionally fabricated minichannel and additively manufactured microchannel of similar dimensions using the same working fluid of pure PAO and the same operating conditions. The results revealed that although the DMLS fabricated microchannel posed a higher pressure loss, a substantial heat

transfer enhancement was achieved as compared to the minichannel heat exchanger tested under the same conditions. The non-post processed surface of the DMLS manufactured microchannel is likely to be the main contributor to the augmented heat transfer performance. Further studies are required to fully appreciate the possible mechanisms behind this phenomenon as well as the convective heat transfer properties of nanoemulsion fluids.

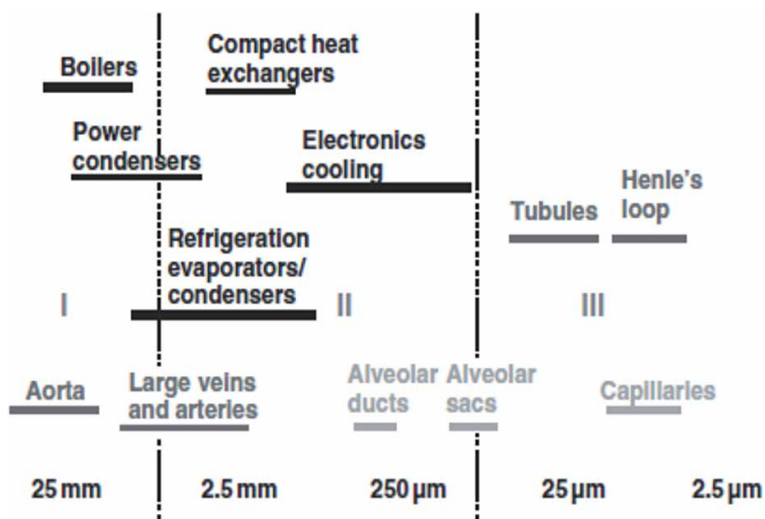
**Keywords:** ethanol/polyalphaolefin nanoemulsion, minichannel, additively manufactured microchannel, single-phase flow, two-phase flow boiling, heat transfer enhancement

## 1. Introduction

Fluid flow within the channels can be viewed as the heart for plenty of natural and industrial systems. Heat and mass transfer are carried out along the walls of channels existing in biological systems, for instance blood vessels, kidney, lungs, and brain, as well as in many of industrial systems, for example heat exchangers, air separation plants, water desalination systems, and nuclear power reactors [1].

**Figure 1** illustrates a range of channel dimensions applied for different systems. While the smallest channel dimensions are observed in the biological systems undergoing mass transport, the larger dimensions are employed for the transportation of fluids. From a technological point of view, a steady transition from the larger channel dimensions, order of magnitudes of 10 to 25 mm, to the smaller channel dimeters, order of magnitudes of tens to hundreds of  $\mu\text{m}$ , can be seen in the recent years.

Generally, the energy transport process takes place along the channel wall, while the bulk flow occurs through the channel's cross-sectional area. The transport rate varies with the surface area, being in a linear proportion to the channel diameter ( $D$ ), while the flow rate shows a direct proportion to the cross-sectional area ( $D^2$ ). Hence, the ratio of channel surface area to the volume is proportional to  $1/D$ . Obviously, a reduction in the channel diameter leads to the increase in the ratio of surface area to volume.



**Figure 1.** Channel diameter ranges applied for different applications [2].

By shifting to the smaller channel dimensions, some of the conventional principles of fluid flow, mass transport, and energy transport need to undergo reevaluation for validation or possible revisions. The following three main reasons can be mentioned to address the difference in the fluid flow modeling between conventional and mini/microchannels [3]:

- i. some changes realized in the fundamental principles; as an illustration, the continuum hypothesis may not be valid for gas flows in mini/microchannels, or a deviation arisen from an enhanced effect of some forces (e.g., electrokinetic),
- ii. uncertainties originating in those factors extracted empirically from experiments on the large-size channels, for instance pressure loss coefficients of fluid flow at the tube entrance and exit,
- iii. uncertainties originating from microscale measurements, either in geometry or operating conditions.

In the heat transfer applications, the reasons which drive such a shift towards smaller flow passages are as follows [2]:

- i. Substantial enhancement of heat transfer,
- ii. Improved dissipation of heat flux in the microelectronic circuits and devices,
- iii. Development of micro-scale devices which require the equally small cooling systems.

The use of smaller channels provides a better performance in heat transfer, albeit accompanied mostly with an increase in the pressure drop. An optimal balance between these parameters results in the various channel dimensions for different applications. Take as an illustration, in automobile industry, the dimensions of flow passages in evaporators and radiators have reached to nearly 1 mm as a result of the balance between the cleanliness standards, heat transfer, and pumping power. Similarly, the high heat fluxes generated by microelectronic devices as well as the geometric and dimensional constraints imposed by the micro-scale devices and microelectromechanical systems (MEMS) require a drastic reduction in the dimensions of flow channels designed for their cooling systems. Also, the mirrors used for high-power laser devices employ the cooling systems having extremely small footprint. The continuous advances in the fields of genetic and biomedical engineering are contingent upon the precise transport control and thermal control of fluid flow in the micro-scale passages. Hence, a solid understanding of heat transfer process and fluid flow in such micro-scale systems is crucial to the design and operation.

### **1.1 Classification of flow channels**

The hydraulic diameter can serve as an indicator for taking into account a channel's dimensions and then classifying the flow channels. The reduction in channel dimensions has different impacts on various processes. Although the derivation of particular criteria based on different process parameters seems to be fascinating, a simple dimensional-based classification is typically employed in the literature due to the abundance of process parameters arising in the transition from

conventional to micro dimensions. The channel classification suggested in [4] has categorized the range of 1–100  $\mu\text{m}$  as the microchannels, 100  $\mu\text{m}$  to 1 mm as the mesochannels, 1–6 mm as the compact passages, and the range above 6 mm as the conventional channels.

Kandlikar et al. [3] improved their channel classification reported earlier in [5], and then presented a more general classification according to the minimum channel dimension, shown in **Table 1**. In this table,  $D$  indicates the channel diameter. However, in case the channel is non-circular, the smallest channel dimension is recommended to be taken for  $D$ ; for instance, in a rectangular channel the smaller side is considered for  $D$ . This channel classification may be used for either of single-phase or two-phase flow applications.

For the case of phase-change heat transfer in particular, the channels with various scales are classified according to the Bond number proposed by Cheng et al. [6] for expressing the transition from macroscale heat transfer to microscale heat transfer. Bond number takes into consideration the impacts of pressure, temperature, and some thermophysical properties of a fluid and is given as follows:

$$Bo = \left( \frac{D_h}{l_C} \right)^2 \quad (1)$$

where  $D_h$  stands for hydraulic diameter, and  $l_C$  accounts for capillary length expressed as:

$$l_C = \sqrt{\frac{\sigma}{g(\rho_1 - \rho_V)}} \quad (2)$$

For water at 373 K, the capillary length ( $l_C$ ) of water is practically 2.72 mm. Based on Cheng's et al. classification, the channels with the range of a hydraulic diameter ( $D_h$ ) between 600  $\mu\text{m}$  and 4,720  $\mu\text{m}$  can be considered as minichannels for the applications using water as the base liquid. **Table 2** shows the channel classification based on Bond Number (Bo) for water at 373 K.

Channel Classification	Smallest Channel Dimension (D)
Conventional Channels	$D \geq 3 \text{ mm}$
Minichannels	$3 \text{ mm} \geq D \geq 200 \mu\text{m}$
Microchannels	$200 \mu\text{m} \geq D \geq 10 \mu\text{m}$
Transitional Microchannels	$10 \mu\text{m} \geq D \geq 1 \mu\text{m}$
Transitional Nanochannels	$1 \mu\text{m} \geq D \geq 0.1 \mu\text{m}$
Nanochannels	$0.1 \mu\text{m} \geq D$

**Table 1.**  
Channel classification based on dimensions.

Channel Classification	Bond Number (Bo)	Hydraulic Diameter
Microchannels	$Bo < 0.05$	$D_h < 600 \mu\text{m}$
Minichannels	$0.05 < Bo < 3$	$600 \mu\text{m} < D_h < 4720 \mu\text{m}$
Macrochannels	$Bo > 3$	$D_h > 4720 \mu\text{m}$

**Table 2.**  
Channel classification based on bond number for water at 373 K.

In the present study, we follow and meet both the selection criteria stated above for channel classification (i.e., **Tables 1** and **2**) to ensure proper differentiation in performance between minichannels and microchannels as well as proper collection of the literature associated with heat transfer of mini and/or microchannels.

## 1.2 Ethanol/polyalphaolefin nanoemulsion: a novel heat transfer fluid

A variety of industries and military sectors have faced the challenge of finding effective and efficient thermal management solutions as the electronic systems used can output heat flux as high as  $100 \text{ W/cm}^2$  [7–11]. While many advanced works have been performed to develop high performance heat exchangers with varieties of shape, size and tube surface augmentation, the bottleneck of improvement has fall into how to develop efficient heat transfer fluids with significantly improved thermal properties over those currently available. To date, several heat transfer fluid candidates have been reported, which include, but not limited to, nanofluids [12–34], dilute emulsion [35, 36], and emulsion [37–41]: Nanofluid has been intensively studied since it was proposed in 1995 by Choi [42]. It is consisted of a mixture of solid nanoparticles and base fluid, and it has been reported to be potentially useful in applications such as nuclear power system, solar collector, and compact high power density electronics system. Emulsion and dilute emulsion fluid are essentially similar systems made of a mixture of two immiscible liquids, while the “dilute emulsion” has 5 vol% or less dispersed component. Using emulsion to enhance heat transfer can be dated back to 1959 by Moore [43], and it has attracted interests of researchers [35–45]. One of the most detailed descriptions of how emulsions boil is the work of Bulanov and Gasanov [38–41, 44, 45], in which they proposed chain-reaction boiling of the droplets as an explanation for the observed superheated droplets and bubble dynamics on the heat surface. In addition, Rosele [46] et al. carried out an experimental study of boiling heat transfer from a horizontal heated wire, including visual observations in which the heat transfer could be enhanced in dilute emulsions compared to that of water as a base fluid.

Recently, the authors have proposed a new type of heat transfer fluid called “nanoemulsion” [47]. Nanoemulsion is a suspension of liquid nanodroplets formed by self-assembly inside another immiscible fluid, as part of a broad class of multiphase colloidal dispersions [48]. The nanoemulsion eliminates the presence of solid particles, which usually cause abrasion and erosion issues even with extremely fine particles such as nanoparticles [49–53], and instead, uses liquid nanostructures [54–63]. The droplets typically have a length scale less or equal to 50 nm, which makes the nanoemulsion fluid thermodynamically stable and transparent to natural light. A comparison of nanoemulsion with emulsion (dilute emulsion) is represented in **Table 3** [47, 48].

Property	Nanoemulsion	Emulsion
Appearance	Transparent	Turbid
Interfacial tension	Ultra-low ( $\ll 1 \text{ mN/m}$ )	Low
Droplet size	$< 50 \text{ nm}$	$> 500 \text{ nm}$
Phase stability	Thermodynamically stable	Thermodynamically unstable
Preparation	Self-assembly	Need of external shear
Viscosity	Newtonian	Non-Newtonian

**Table 3.**  
 Comparison of Nanoemulsion and emulsion (dilute emulsion).

Pool boiling heat transfer studies of nanoemulsion fluids have shown that: (i) the thermophysical properties of the nanoemulsion fluids are found to be better than that of the base fluid [54, 55]; and (ii) an appreciable increase in heat transfer coefficient (HTC) and critical heat flux (CHF) can be observed in nanoemulsion fluids when the phase-changeable nanodroplets formed inside undergo nucleation [57, 61, 62].

Convective heat transfer of conventional heat transfer fluids inside mini/microchannel heat exchangers has been extensively studied due to its capability to remove high heat fluxes [33, 36, 64–66]. However, relatively few studies have been carried out to investigate the application of novel heat transfer fluids inside mini/microchannels. The recent development of nanotechnology has led to the improvement of heat transfer coefficient using novel nanostructured working fluids. While there are some recent experimental studies addressing the possibility of using nanostructured heat transfer fluids inside micro/nanostructured surface to enhance heat transfer [26, 31, 34], other recent studies showed that the use of nanofluids and nanotube coating offers a lower heat transfer coefficient at the coated surface compared to the bare surface [67–70].

Despite the significant enhancement observed in pool boiling heat transfer of nanoemulsion fluids compared to the base fluids, it remains inconclusive whether the same optimistic outlook can be expected in the convective heat transfer of nanoemulsion fluids. The present study aims to numerically and experimentally investigate the flow and heat transfer characteristics of ethanol/PAO nanoemulsion inside a conventionally manufactured minichannel and compares them with those of a microchannel heat exchanger manufactured additively.

## **2. Experimental approach**

### **2.1 Preparation of nanoemulsion**

To minimize the impact of the differences in thermophysical properties of the two constitutive fluids on the convective heat transfer experiments, ethanol and PAO fluids were used to prepare the nanoemulsion for this study since their thermal conductivity values are very similar. Dioctyl sulfosuccinate sodium salt (Sigma Aldrich) was used as a surfactant to form the nanoemulsion.

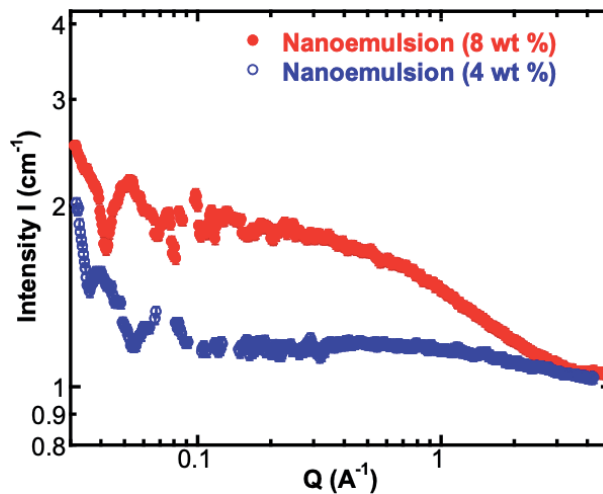
In the preparation process, the first step was to add the dioctyl sulfosuccinate sodium salt (Sigma Aldrich) into PAO fluid. The mixture was stirred until the dioctyl sulfosuccinate sodium salt was completely dissolved. The second step is to inject ethanol into the base fluid and mix them well until the mixture became transparent. In the present study, ethanol (4 or 8 percentage of ethanol by weight) is added into PAO to form 4 wt % or 8 wt % Ethanol/PAO nanoemulsion fluids respectively.

#### *2.1.1 Structural properties*

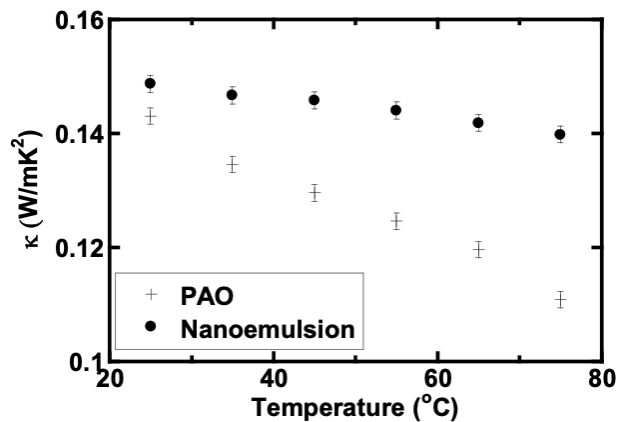
**Figure 2** shows the small angle neutron scattering (SANS) experimental results of ethanol nanodroplets measured by NG7 SANS beamline at NIST Center for Neutron Research (NCNR), and the data was reduced to extract the structural information following the protocol provided by NCNR [71, 72]. It was found that the ethanol nanodroplets formed inside the nanoemulsion fluids have a radius of less than 1 nm on average.

#### *2.1.2 Thermophysical properties*

Thermal conductivity and viscosity are macroscopically observable parameters that affect the thermal performance of the fluids. **Figure 3** shows the thermal



**Figure 2.** Small angle neutron scattering curves for 4 wt % and 8 wt % ethanol/PAO nanoemulsion heat transfer fluids.

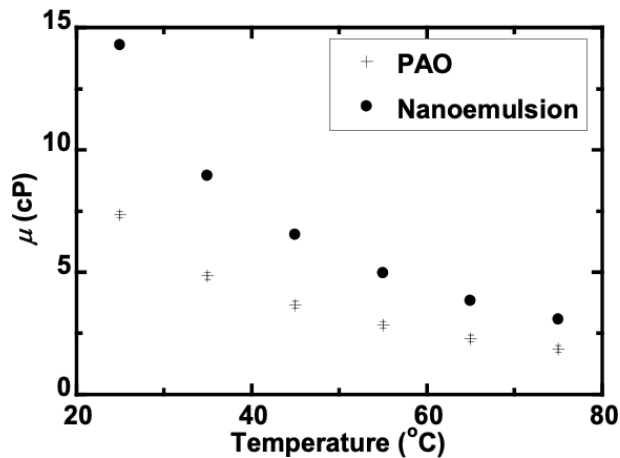


**Figure 3.** Thermal conductivity of the pure PAO and 8 wt % ethanol/PAO nanoemulsion at temperature range of 25 ~ 75°C.

conductivities of the base PAO fluid and 8 wt % Ethanol/PAO nanoemulsion fluid and their dependence upon temperature. Thermal conductivity of the pure PAO and Ethanol/PAO nanoemulsion fluids was measured in the temperature range from 25–75°C using the 3 $\omega$ -wire method [56]. As represented in **Figure 3**, the Ethanol/PAO nanoemulsion fluid experimented here exhibits a higher thermal conductivity compared to pure PAO: a 3.9% increase which agrees well with the earlier study [57]. In addition, the thermal conductivity decreases with higher temperature but at a substantially lower rate compared to pure PAO.

Similarly, the viscosity of the Ethanol/PAO nanoemulsions was measured using a commercial viscometer (Brookfield DV-I Prime) from 25–75°C. In general, the viscosity is found to decrease with increasing temperature in most heat transfer fluids, which is also observed in the proposed Ethanol/PAO nanoemulsion, that is, a decrease from 14.3 cP to 3.05 cP as illustrated in **Figure 4**, which agrees well with the authors' previous study [57].

The thermophysical properties considered in the present study for ethanol/PAO nanoemulsion and pure PAO fluids to conduct experimental heat transfer tests are summarized in **Table 4**.



**Figure 4.** Dynamic viscosity of the pure PAO and ethanol/PAO Nanoemulsion fluids at temperature range of 25 ~ 75°C.

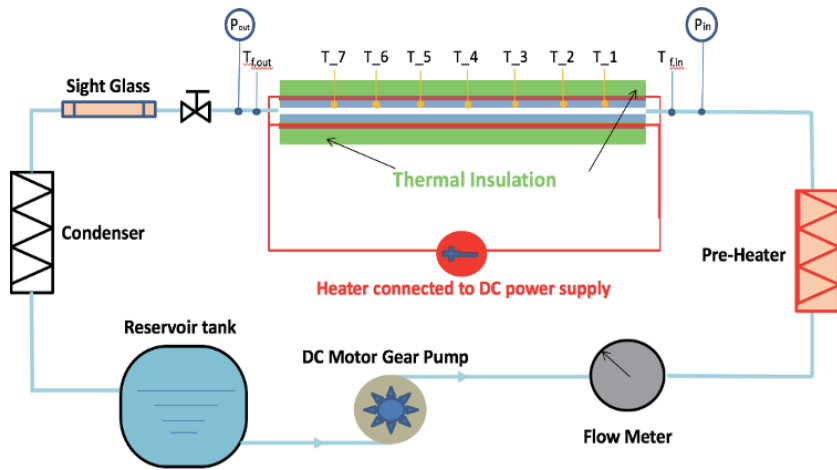
Property	4 wt % Nanoemulsion	8 wt % Nanoemulsion	PAO
Density ( $kg/m^3$ )	794	792	798
Conductivity (W/m-K)	0.148	0.149	0.143
Viscosity (kg/m-s)	$13.8 \times 10^{-3}$	$14.3 \times 10^{-3}$	$7.34 \times 10^{-3}$
Nanodroplet radius (nm)	0.5	0.8	N/A

**Table 4.** Thermophysical properties of ethanol/PAO Nanoemulsion and PAO at 25°C.

## 2.2 Experimental apparatus

The convective heat transfer tests of nanoemulsion fluids were carried out for two heat exchangers comprising a conventionally manufactured minichannel of 12 circular channels and an additively manufactured microchannel of 30 rectangular channels, both with the same exterior heat exchanger geometry. A schematic of the test loop setup built to conduct experiments is shown in **Figure 5**. The test apparatus consists mainly of a horizontal test section of either minichannel or microchannel heat exchanger, three gear pumps, a fluid reservoir, a flow sight glass, preheating section, condenser, and data acquisition system to measure and record the pressure, temperature, and mass flow rate. In the present study, the heat transfer tests were performed under a uniform wall heat flux applied on the top and bottom surfaces of the minichannel and microchannel heat exchangers. A programmable DC power supply with 0.05% power uncertainty was used to electrically heat up the test sections in order to obtain the constant wall heat flux. Furthermore, the preheating section was also electrically heated by a circulator, and the inlet fluid temperature is controlled at a desired value before entering the test sections. The inlet and outlet fluid temperatures were measured by two K-type thermocouples. The test section was carefully wrapped using an insulation material with a thermal conductivity of  $0.043 W/(m.K)$ . A layer of aluminum foil was then wrapped on the outside of thermal insulation layer. The heat losses through the insulation layer were estimated to be lower than 2% of total heat losses and it was neglected in thermal performance calculations in the present study. Pressure drops of the test section were measured by two GP-50 differential pressure transducers with a working range of 0–200 kPa and an uncertainty of 0.25%. For all the tests conducted, both minichannel and

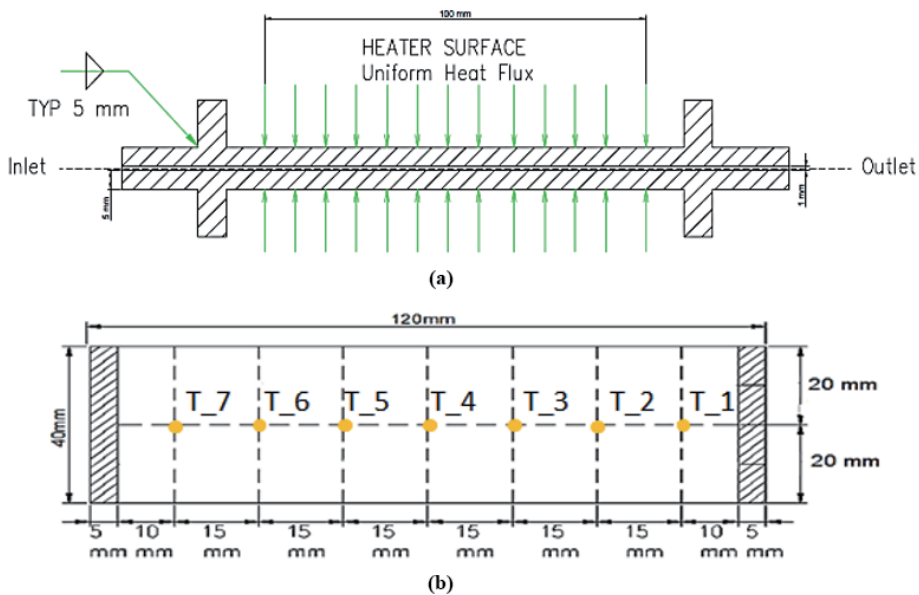




**Figure 5.**  
 Schematic of the test apparatus.

microchannel heat exchangers were placed horizontally to the ground. The liquid in the reservoir was first preheated to a preset temperature of 75°C. The liquid flow rate was adjusted to the desired value and monitored by a digital paddle wheel flow meter (Micro-Flow™). Within the experiments, the fluid temperature and surface temperature were automatically recorded by the data acquisition system. The test system reached steady-state conditions while the changing rates of all the set parameters mentioned above were less than 0.2%. The entire test rig was fully automated using the National Instrument LabVIEW software and data acquisition devices (National Instruments Corp., Austin, TX, USA).

**Figure 6(a)** and **(b)** depict the side-view and top-view of the test sections respectively, in which seven thermocouples were attached to the top surface of both minichannel and microchannel heat exchangers and were used to measure the local



**Figure 6.**  
 Schematic of the test sections (both mini- and microchannels): (a) side view, (b) top view with wall-mounted thermocouples.

Geometry					
Test Section	Material	Cross Section	Orientation	Channel Diameter	Length
Microchannel	316 L Steel	Rectangular	Horizontal	640 $\mu$ m $\times$ 760 $\mu$ m	120 mm
Minichannel	Aluminum	Circular	Horizontal	1 mm	120 mm
Operating Conditions at Inlet of Test Sections					
Loop	Working Fluid	$T_{in}$	$P_{in}$	Heat Flux	Mass Flux
Single-Phase Flow	Nanoemulsion	75°C	159 kPa	13–44 kW/m <sup>2</sup>	1063–8504 Kg/m <sup>2</sup> -s
Two-Phase Flow	Nanoemulsion	75°C	159 kPa	13–44 kW/m <sup>2</sup>	630–5037 Kg/m <sup>2</sup> -s

**Table 5.**  
Geometry of the test sections along with operating conditions used.

wall temperatures as shown in **Figure 6(b)** where each red dot represents one wall-mounted thermocouple.

**Table 5** summarizes geometry of both test sections (minichannel and microchannel) coupled with the operating conditions applied to conduct experimental tests for single-phase flow and two-phase flow as well as to conduct numerical analysis of heat transfer performance for comparison purposes.

### 2.2.1 Data processing

In the present study, the average heat transfer coefficient  $h$  is used and expressed as follows:

$$h = \frac{q_{wall}}{T_s - T_f} \quad (3)$$

where  $q_{wall}$  is the local heat flux estimated by considering the local heat loss as shown in Eqs. (4) and (5) for minichannel and microchannel respectively,  $T_s$  is the average local surface temperature measured by the wall-mounted thermocouples along the channel direction calculated by Eq. (6),  $T_f$  is the fluid's bulk mean temperature calculated by Eq. (7).

$$q_{wall} = \frac{Q}{n(\pi DL)} \quad (4)$$

$$q_{wall} = \frac{Q}{n(2HL + 2WL)} \quad (5)$$

$$T_s = \frac{1}{7} \sum_{x=1}^{x=7} T_x \quad (6)$$

$$T_f = \frac{1}{2} (T_{f,in} + T_{f,out}) \quad (7)$$

The average Nusselt number of nanoemulsion fluid can be expressed by:

$$Nu = \frac{h D_h}{k_f} \quad (8)$$

in which  $D_h$  is the hydrodynamic diameter for either of minichannel or microchannel.

The Reynolds number of the flow can also be calculated as follows:

$$Re = \frac{\rho VD}{\mu} \quad (9)$$

Total pressure loss along the test sections is calculated by:

$$\Delta P = \Delta P_{friction} + \Delta P_{minor} \quad (10)$$

and the friction factor is calculated by:

$$f = \Delta P_{friction} \frac{2D}{\rho LV^2} \quad (11)$$

To take the shape of the channel's cross-section into consideration, the Poiseuille number (Po) can be found to be only a function of microchannel's aspect ratio:

$$Po = f \times Re = \frac{4\pi^2(1 + \varepsilon^2)}{3\sqrt{\varepsilon}(1 + \varepsilon)} \quad (12)$$

in which  $\varepsilon = H/W$ .

### 2.2.2 Uncertainty propagation

The uncertainties for different parameters involved in the experimental tests are listed in **Table 6**.

An uncertainty analysis is performed from the measurement uncertainties using calculus and the principle of superposition of errors. In general, for a variable F that is a function of several variables such as  $F = F(a, b, c, \dots)$ , the squares of the

Parameter	Uncertainty
Temperature (°C)	±0.1
Flow velocity (m/s)	±6%
Position of the thermocouples (m)	±0.01
Dimensions of the minichannel (m)	±0.002
Dimensions of the microchannel (m)	±0.002
Power input (W)	±0.5%
Heat flux (W/m <sup>2</sup> )	±0.5%
Pressure (Pascal)	±0.25%

**Table 6.**  
 Uncertainties sources for the experimental tests.

Calculated Variable	Uncertainty
Heat transfer coefficient, $h$	±6%
Nusselt number, $Nu$	±8%
Reynolds number, $Re$	±6%
Friction factor, $f$	±10%

**Table 7.**  
 Uncertainties for heat transfer performance parameters.

uncertainty in  $F$  is the sum of the square of the uncertainties due to each independent variable,  $\delta F = \left[ \left( \frac{\partial F}{\partial a} \delta a \right)^2 + \left( \frac{\partial F}{\partial b} \delta b \right)^2 + \left( \frac{\partial F}{\partial c} \delta c \right)^2 + \dots \right]^{0.5}$  where  $\delta a$  stands for the uncertainty due to variable  $a$ . The uncertainties of the heat transfer performance parameters are calculated and represented in **Table 7**.

### 3. Conventionally manufactured minichannel heat exchanger

**Figure 7** illustrates the minichannel heat exchanger of 12 circular channels designed and fabricated conventionally to conduct the experimental tests. The material and geometry of the minichannel test section was shown earlier in **Table 5**, coupled with the operating conditions engaged to run the experiments.

Using the PAO base fluid, the flow and heat transfer characteristics of the minichannel test section were carefully evaluated to verify the integrity of the experimental facility and test procedures. The experiments on the PAO base fluid were first performed, and the test results were used as baseline data to compare with those of Ethanol/PAO nanoemulsion fluids of 4% and 8% wt% ethanol. A range of heat fluxes addressed earlier in **Table 3** was selected as heat inputs to simulate single-phase and two-phase flow heat transfer conditions. All the experiments performed in the present study were repeated five times, and the relative errors of test data were found to be less than 5%. The SANS measurements were performed on the samples only prior to initiating the experiments. However, previous studies on a similar water/PAO system have demonstrated that there are no remarkable structure changes of the nanodroplets before and after pool boiling tests inside an enclosed system [63].

#### 3.1 Results and discussions

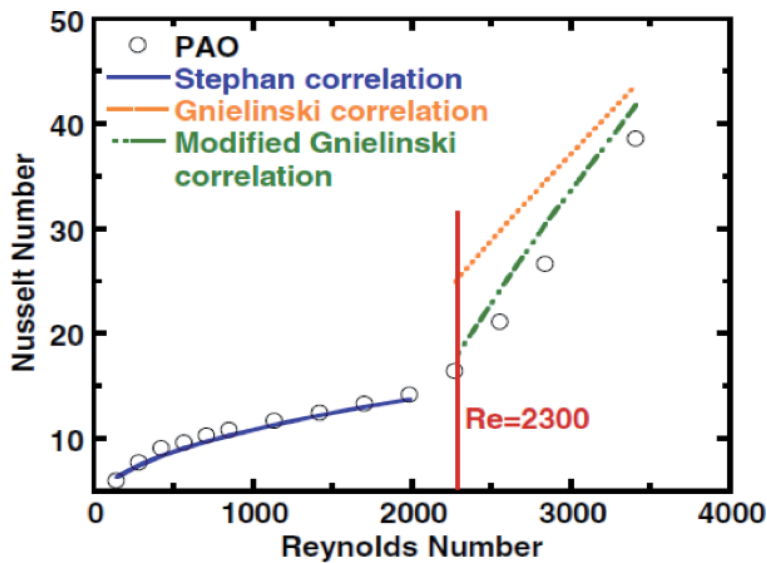
##### 3.1.1 Experimental results

###### 3.1.1.1 Single-phase results of PAO Base fluid

**Figure 8** illustrates variations of average Nusselt number with Reynolds for the pure PAO base fluid and compares the results with the empirical heat transfer correlations tabulated in **Table 8**. While Stephan correlation was used to predict



**Figure 7.** Traditionally manufactured minichannel heat exchanger developed for the present comparative study.



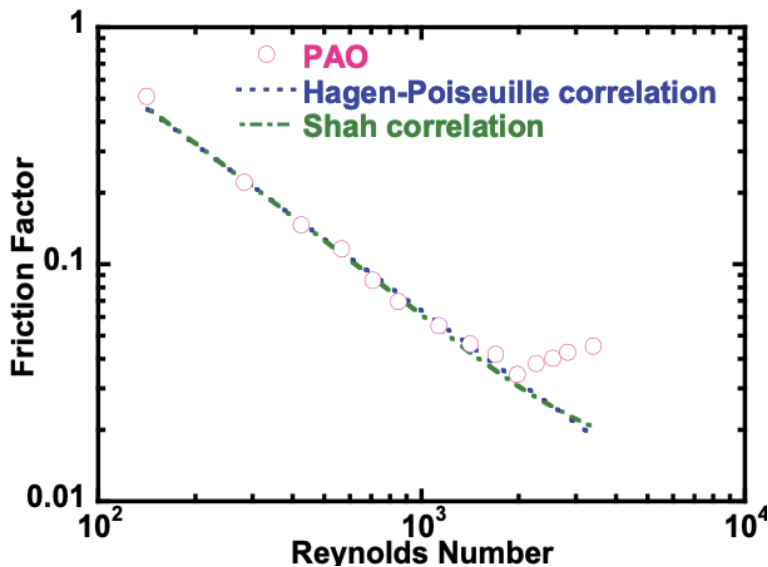
**Figure 8.**  
 Average Nusselt number versus Reynolds number for pure PAO fluid.

Correlation	Conditions	Validity Range
<b>Stephan correlation [73]</b> $Nu = 4.364 + \frac{0.086(RePr_D)^{1.33}}{1+0.1Pr(Re_D^2)^{0.83}}$	Laminar flow in a circular pipe	$Re < 2300$
<b>Gnielinski correlation [73]</b> $Nu = \frac{(f/8)(Re-1000)Pr}{1+12.7\sqrt{f/8}(Pr^{1/3}-1)}$ where $f = \frac{1}{(1.82 \log(Re) - 1.64)^2}$	Constant wall heat flux, fully developed turbulent and transitional flow	$3000 < Re < 5 \times 10^4$
<b>Modified Gnielinski correlation [74]</b> $Nu = \frac{(f/8)(Re-1000)Pr}{1+12.7\sqrt{f/8}(Pr^{1/3}-1)}$ where $f = 3.03 \times 10^{-12} \cdot Re^3 - 3.67 \times 10^{-8} \cdot Re^2 + 1.46 \times 10^{-4} \cdot Re - 0.151$	Constant wall heat flux, transitional flow in a straight circular pipe	$2300 < Re < 4500$

**Table 8.**  
 Empirical heat transfer correlations used for comparison purposes with their validity ranges.

heat transfer characteristics within the laminar regime [73], the Gnielinski correlation was exploited for fully developed turbulent flow regime [73] and modified Gnielinski correlation [74] was used for comparison purposes within the transitional flow regime. As shown by the measured data and empirical correlations in **Figure 8**, the Nusselt number consistently increases with the Reynolds number, however it starts to increase at a greater rate for Reynolds greater than 2300 (critical Reynolds), which indicates a transition from laminar to turbulent flow regime. As represented in this figure, the experimental heat transfer results show good agreements with the empirical correlations in both laminar and transitional flow regimes.

**Figure 9** shows variations of friction factor with Reynolds number for the pure PAO base fluid and compares the results with the empirical friction factor correlations listed in **Table 9**. The Hagen-Poiseuille correlation was used to predict flow characteristics within the fully developed laminar flow regime inside a circular minichannel [73] whereas the Shah correlation was used to include the entrance effect within the hydrodynamically developing region [73]. As represented in



**Figure 9.**  
Friction factor versus Reynolds number for pure PAO fluid.

Correlation	Conditions	Validity Range
Hagen-Poiseuille correlation [73] $f \cdot Re = 64$	Laminar flow in a circular channel	$Re < 2300$
Shah correlation [73] $f \cdot Re \approx 4 \left( \frac{3.44}{\sqrt{\xi}} + \frac{16 + 0.3125\xi - \frac{3.44}{\sqrt{\xi}}}{1 + 2.12 \times \frac{10^{-4}}{\xi^2}} \right)$ where $\xi = \left( \frac{L}{D} \right) / Re$	Laminar flow inside circular channel with consideration of entrance length	$Re < 2300$

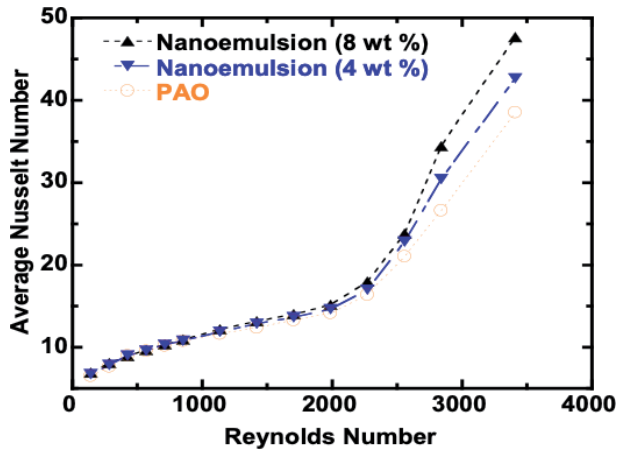
**Table 9.**  
Empirical friction factor correlations used for comparison purposes with their validity ranges.

**Figure 9**, the measured values of friction factor for the pure PAO flowing inside the minichannel agree well with the empirical correlations during laminar flow regime. The friction factor decreases when Reynolds number increases up to around 2000. Afterwards, the friction factor starts to increase sharply for Reynolds greater than 2000, which indicates transition from laminar to turbulent flow regime.

### 3.1.1.2 Single-phase results of ethanol/PAO nanoemulsions

After confirming the integrity of the test loop using the experimental results of pure PAO fluid, heat transfer and flow characteristics of Ethanol/PAO nanoemulsion fluids with 4 and 8 wt% ethanol were experimentally investigated by following a similar test procedure.

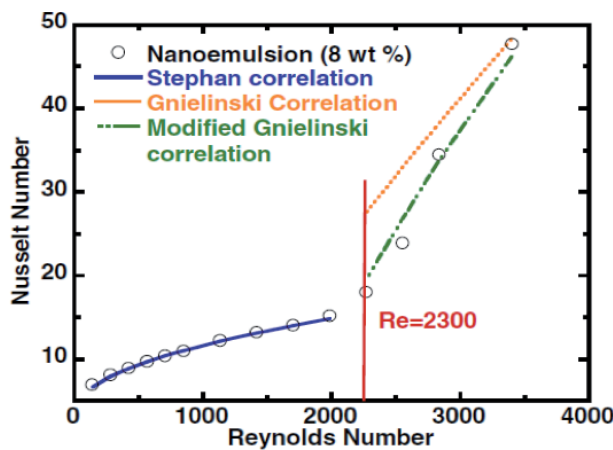
**Figure 10** represents variations of average Nusselt for the base fluid and nanoemulsion fluids against a range of Reynolds lying in the laminar and transitional flow regimes. As shown in this figure, Nusselt increases with Reynolds for all the working fluids tested in the present study within either laminar regime ( $Re < 2300$ ) or transitional regime ( $Re > 2300$ ). **Figure 10** also illustrates that increase in ethanol concentration of nanoemulsion fluids does not reflect a remarkable distinction in heat transfer performance within the laminar regime. However, when ethanol concentration of nanoemulsions increases from pure PAO (0%) to 8 wt% nanoemulsion, Nusselt number exhibits significant enhancements within the



**Figure 10.**  
 Nusselt number versus Reynolds for pure PAO and nanoemulsion fluids.

transitional and the early stage of turbulent flow regimes. The results show a 24% increase in average Nusselt number for 8 wt% nanoemulsion fluid and a 11% increase in average Nusselt for 4 wt% nanoemulsion fluid compared to that of pure PAO at the same Reynolds number of 3400. The heat transfer enhancement in the transitional regime can be attributed to the enhanced interaction and interfacial thermal transport between ethanol nanodroplets and PAO base fluid, so that the increase in density and size of nanodroplets at higher concentrations of ethanol can contribute to a stronger mixing and mass exchange effects within the transitional and turbulent flow regimes.

**Figure 11** compares experimental heat transfer data for 8 wt% ethanol/PAO nanoemulsion with conventional heat transfer correlations suggested in the literature for internal flow. As shown in this figure, the experimental results agree very well with those predicted by the empirical correlations in both laminar and transitional flow regimes. While the classical Gnielinski correlation overestimates the Nusselt number for the transitional flow, the Stephan and modified Gnielinski correlations provide a better prediction of Nusselt number for the laminar and transitional flow regimes, respectively.



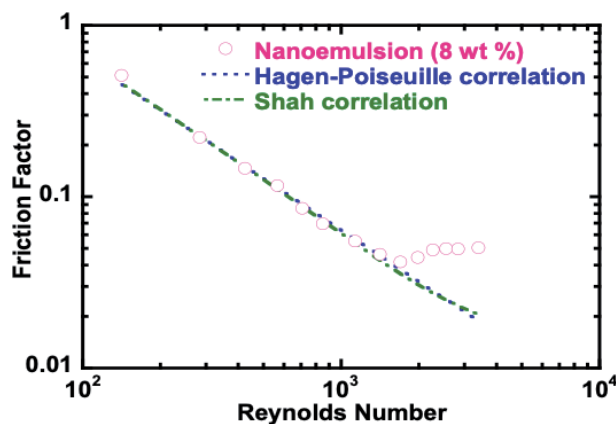
**Figure 11.**  
 Nusselt number versus Reynolds for 8 wt% ethanol/PAO nanoemulsion.

**Figure 12** represents variations of friction factor with Reynolds number for 8 wt % ethanol/PAO nanoemulsion, and compares the experimental results with those predicted by the empirical correlations, in which a very similar trend can be observed with that of the single-phase PAO base fluid as previously shown in **Figure 9**. As illustrated in **Figure 12**, the friction factor of nanoemulsion within the laminar regime decreases consistently with Reynolds number up to the Reynolds of 2000, indicating a slightly earlier entrance into the transitional flow regime compared to that of the pure PAO. Upon entering the transitional regime, friction factor is found to increase and then starts to flat out at Reynolds number of around 3000. As clearly seen in this figure, the experimental data measured for friction factor of nanoemulsion showed good agreements with those predicted by the Hagen-Poiseuille and Shah correlations.

### 3.1.1.3 Two-phase results of ethanol/PAO nanoemulsions

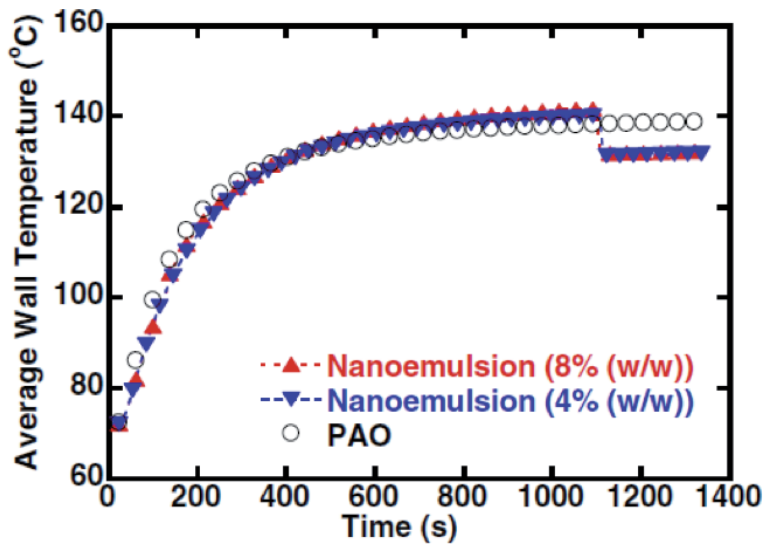
One of the reasons to replace conventional heat transfer fluids with nanoemulsion is to achieve significant heat transfer enhancements when the phase changeable nanodroplets undergo nucleation. Previous studies have demonstrated a significantly improved heat transfer coefficient and critical heat flux using nanoemulsion with phase changeable nanodroplets undergoing the nucleate boiling [57, 61, 62]. In the present study, the ethanol nanodroplets formed inside the nanoemulsion are expected to function as phase change nuclei at elevated temperatures during the two-phase flow boiling experiments. The maximum flow rate needs to be limited to less than 4.46 m/s (or  $Re = 1136$ ) to maintain a wall temperature high enough to trigger flow boiling. Accordingly, all the flow boiling data collected and shown in the present study reflect heat transfer behavior within the laminar flow regime.

**Figure 13** represents the variations of average transient wall temperature data for all the tested working fluids (4 and 8 wt% ethanol/PAO nanoemulsions and pure PAO) with time, which overlapped well with each other within single-phase flow regime. However, the wall temperatures of nanoemulsions started to deviate from the single-phase trend line, followed by a sudden drop in the wall temperature which indicates an increase in heat transfer coefficients due to the flow boiling. Using the sight flow indicator located next to the outlet of the minichannel test section, it was observed that there were bubbles coming out of the minichannel heat exchanger, which confirms that the ethanol nanodroplets underwent nucleation



**Figure 12.** Friction factor versus Reynolds number (Nanoemulsion fluid).





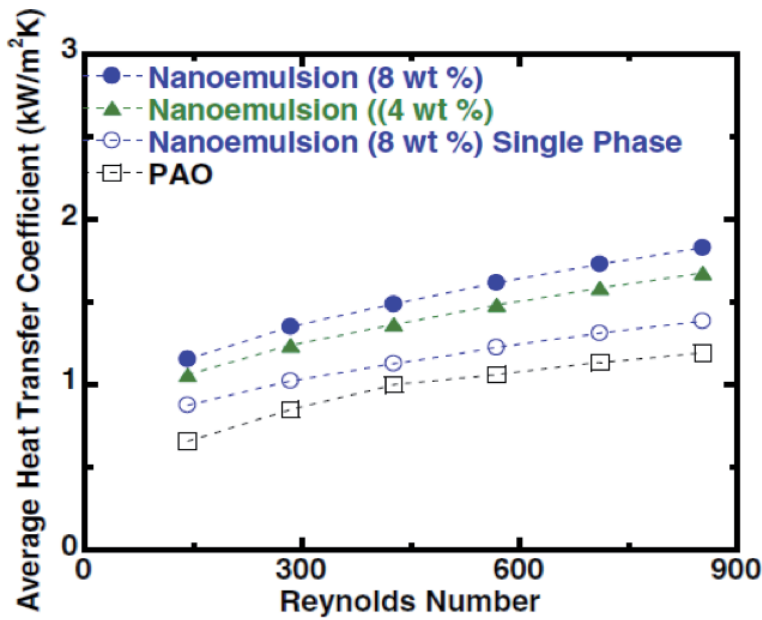
**Figure 13.**  
*Evolution of the average wall temperature with time for pure PAO and nanoemulsions.*

and the flow lies in the state of two-phase flow boiling. Another interesting observation was the delay in nucleation boiling temperature or the onset of nucleate boiling (ONB). As illustrated in **Figure 13**, the nucleation did not start until the average surface temperature of the minichannels reached a temperature around 140°C while the boiling temperature for ethanol is 78°C. Similar findings of delayed ONB were previously reported for pool boiling experiments of sub-cooled ethanol/PAO nanoemulsion fluids [57]. The delayed ONB can be attributed to the inefficient thermal transport between each surfactant molecule and its surrounding PAO fluid, in which the PAO molecules are not packed closely near the hydrophilic head-group of the surfactant molecule and could not provide efficient thermal pathway in between the micelles and base fluid [59, 60].

**Figure 14** shows the variations of average heat transfer coefficient with Reynolds number for flow boiling of nanoemulsion fluids, and compares them with those of single-phase flow of pure PAO and nanoemulsions. In addition to the fact that the Ethanol/PAO nanoemulsion fluids exhibit slightly higher heat transfer coefficients (HTCs) compared to those of pure PAO in single-phase flow due to the minor improvement in thermophysical properties, the HTCs were found to be significantly enhanced when the nanoemulsion fluids underwent two-phase flow boiling. It is also apparent that the phase change of the ethanol nanodroplets is the main contributor to the heat transfer improvement. **Figure 14** also reveals that the ethanol concentration of nanoemulsion has a positive impact on the overall heat transfer coefficients in both single-phase flow and two-phase flow boiling. As shown in this figure, an average HTC enhancement of 50 ~ 70% was achieved with Ethanol/PAO nanoemulsion compared to that of the PAO base fluid.

### 3.1.2 Simulation results

The prototype of the minichannel heat exchanger was designed using CREO software and then the model was imported to COMSOL-Multiphysics to conduct numerical heat transfer analysis for the same geometry and operating conditions summarized in **Table 5**. The following assumptions were adopted to conduct the simulations: no slip boundary condition, normal inflow velocity, uniform wall heat



**Figure 14.** Average heat transfer coefficient versus Reynolds for single-phase and two-phase flow of the working fluids.

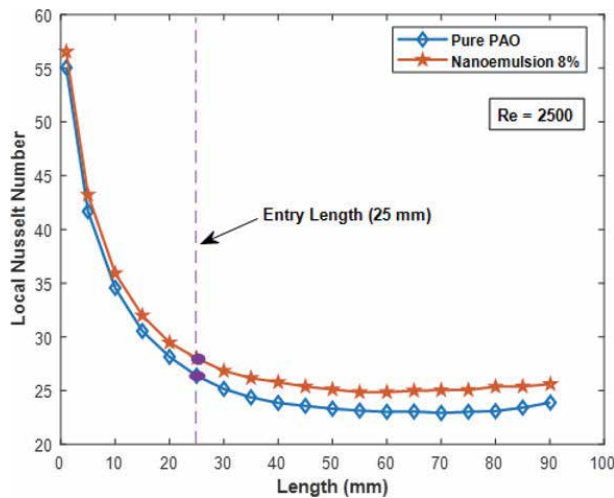
flux boundary conditions imposed on the top and bottom surfaces of the minichannel heat exchanger, and thermophysical properties of the working fluids are set to remain constant for the values addressed earlier in **Table 4**.

Three types of meshes were developed in the present study to examine accuracy of simulation results as well as to confirm mesh independency of the results, including finer, fine, and normal. The size settings for each mesh are shown in **Table 10**. The finer mesh size was eventually chosen as it allows to conduct sufficiently accurate analysis while still maintaining a reasonable computational time.

**Figure 15** represents the variations of local Nusselt number at a certain Reynolds number of 2500 (i.e., the beginning of transitional regime) along the minichannel heat exchanger with the same geometry and dimensions used previously for the experimental investigations as summarized in **Table 5**. As illustrated in this figure, the local Nusselt number decreases along the minichannel at early positions and then reaches relatively constant values of 23 and 26 for the pure PAO and 8 wt%

Description	Finer	Fine	Normal
Calibrate for	Fluid dynamics	Fluid dynamics	Fluid dynamics
Maximum element size	0.148	0.212	0.4
Minimum element size	0.016	0.04	0.12
Curvature factor	0.4	0.5	0.7
Resolution of narrow regions	0.95	0.8	0.7
Maximum element growth rate	1.08	1.13	1.4
Number of elements	684,571	200,829	86,383
Mesh shape	Triangle	Triangle	Triangle
Computational time	14 min 25 sec	3 min 19 sec	1 min 22 sec

**Table 10.** Mesh types developed to conduct numerical analysis.



**Figure 15.** Variations of local Nusselt number along the minichannel at  $Re = 2500$  for pure PAO and 8% ethanol/PAO nanoemulsion fluids with the entrance effects

Ethanol/PAO nanoemulsion, respectively, within the fully developed transitional region. This reveals a heat transfer enhancement of around 13% at a certain Reynolds number of 2500 using the 8 wt% nanoemulsion fluid compared to that of the pure PAO inside the minichannel heat exchanger.

This is important to point out that while the simulation results in **Figure 15** show the Nusselt values of 23 and 26 for the fully developed flows of pure PAO and 8% nanoemulsion, respectively, the experimental results of pure PAO and 8% nanoemulsion introduced earlier in **Figures 8** and **11** show the Nusselt values of around 21 and 24 at the same Reynolds of 2500, respectively. This indicates a relative deviation of approximately 9% between the model and experimental results.

As also observed from the simulation results in **Figure 15**, there is a declining trend of Nusselt number along the early locations of the minichannel. The significantly higher Nusselt number at the early locations and its subsequent sharp drop is due to the thermal entrance region at the inlet of the minichannel test section where the internal liquid single-phase flows are still neither thermally nor hydrodynamically fully developed. As a result of having a thermally developing flow in the entrance region, the thermal boundary layer is extremely thin which causes larger values of Nusselt and HTC compared to those of locations outside the entrance region where both of the working fluids are fully developed.

The hydrodynamic ( $x_{fd,hyd}$ ) and thermal ( $x_{fd,th}$ ) entry lengths for an internal flow in a circular channel can be calculated as follows, respectively [73]:

$$\frac{x_{fd,hyd}}{D} \approx 0.05 Re_D \quad (13)$$

$$\frac{x_{fd,th}}{D} \approx 0.05 Re_D Pr \quad (14)$$

The hydrodynamic entry length for the transitional flows of PAO and 8% nanoemulsion in the minichannel was found to be 25 mm. As demonstrated in **Figure 15**, the local Nusselt numbers for each of the working fluids take relatively constant values after the entry length of 25 mm where the boundary layer develops fully across the cross section of the microchannel and appears to be independent of

the channel length. Since the working fluids are PAO and nanoemulsion with Prandtl numbers greater than 1 ( $Pr > 1$ ), the hydrodynamic boundary layer develops more quickly than the thermal boundary layer ( $x_{fd,th} > x_{fd,hyd}$ ).

## **4. Additively manufactured microchannel heat exchanger**

### **4.1 Additive manufacturing of microchannel prototype**

While micro- and minichannels show promising potential and have been incorporated in a wide variety of unique, compact, and efficient cooling applications, manufacturing of micro- and minichannels made of high temperature alloys is still a challenging task. Recently, additive manufacturing (AM) technology has shown its promising application in manufacturing [75–79]. The use of additive manufacturing, or widely known as 3D printing technique, has revolutionized the traditional manufacturing process, which now eliminates the traditional constrictions in geometry design and manufacturability. AM based manufacturing technique has opened the design potential of traditionally impossible geometries and structures.

The metal based additive manufacturing techniques, including: Selective Laser Melting (SLM), Selective Laser Sintering (SLS), and Electron Beam Melting (EBM), are the most widely studied. Of the aforementioned techniques, Direct Metal Laser Sintering (DMLS) method, as a subset of the SLS process, is particularly appropriate for building production-grade parts due to its ability to use high temperature alloys in the process [77, 80–83].

With DMLS, thin layers of atomized fine metal powder are evenly distributed using a coating mechanism onto a substrate plate, usually metal, that is fastened to an indexing table that moves in the vertical (Z) axis. This takes place inside a chamber containing a tightly controlled atmosphere of inert gas, either argon or nitrogen at oxygen levels below 500 parts per million. Once each layer has been distributed, each 2D slice of the part geometry is fused by selectively melting the powder. This is accomplished with a high-power laser beam, usually an ytterbium fiber laser with hundreds of watts. The laser beam is directed in the X and Y directions with two high frequency scanning mirrors. The laser energy is intense enough to permit full melting (welding) of the particles to form solid metal. The process is repeated layer after layer until the part is complete.

One of the unique characteristics of DMLS manufacturing process is that the surfaces of manufactured parts are intrinsically rough due to the nature of laser sintering process [80]. While the outward-facing surfaces can be smoothed via machining, internal surfaces cannot be post-processed easily. Stimpson et al. examined the effects of surface roughness on flow structures in DMLS parts containing microchannels [84]. In another study, Snyder et al. [85] analyzed the effect of building direction on flow structures in similar DMLS parts, paying particular attention to the different roughness features generated by different printing orientations. The authors of both studies [84, 85] reported relative roughness values ranging between 20% and 38% of the channel hydraulic diameters and proved that correlations for friction factor and heat transfer are no longer valid for surfaces with such high roughness values. Thus, it is imperative to characterize the internal surface of DMLS manufactured parts.

Many investigations have also been conducted to study flow behavior in microchannels of different cross-sections such as rectangular, circular, trapezoidal, triangular, and elliptical [86–88]. Rectangular and trapezoidal cross-sections have been extensively studied for a wide range of applications, mainly due to practical considerations such as fabrication techniques, cost, and ease of manufacturing.

Most researchers have employed rectangular cross-sections for studying friction and pressure drop in microchannels. Since microchannels length is normally long (compared to other dimensions), inlet and exit effects have been neglected in most works.

In the present study, the additively manufactured microchannel heat exchanger was developed using the EOSINT M280 machine at the University of the District of Columbia (UDC). The machine takes advantage of the DMLS technique to 3D print the designed prototype. **Figure 16** represents the EOSINT M280 machine which can be used to seamlessly manufacture complex heat exchanger designs. The process parameters (material scaling, layer thickness, and beam offset) applied to the machine are listed in **Table 11**. Adjusting process parameters and investigating different building directions to understand their impacts on the prototype performance is beyond the scope of this study.

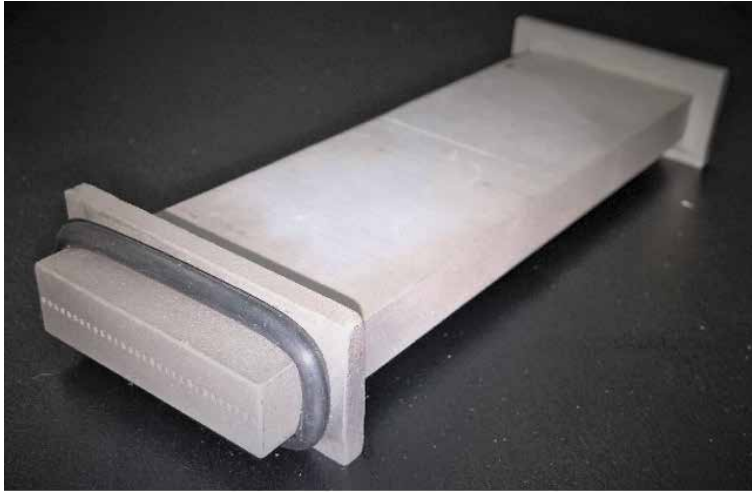
Using the aforementioned fabrication process, a rectangular cross-sectional microchannel heat exchanger was designed and additively manufactured with 316 L Stainless Steel. Each channel is designed to be  $640\mu\text{m}$  in width and  $760\mu\text{m}$  in height, with a length of  $120\text{ mm}$ . A total of 30 microchannels were fabricated along the center of the heat exchanger. Flanges were manufactured on each end of the heat exchanger to fit the existing test loop and facilitate the experimental investigations. **Figure 17** represents the additively manufactured microchannel heat exchanger developed for the present study.



**Figure 16.**  
 EOSINT M280 machine used to develop the microchannel prototype.

Parameter	Setting
Material	316 L Stainless Steel
Process Gas	Nitrogen
Laser Power	400 W
Material Scaling X	0.045%
Material Scaling Y	0.16%
Beam Offset	0.11 mm
Layer Thickness	40 micrometer
Software	EOSTATE Magics RP (materialize)

**Table 11.**  
 Settings applied to EOSINT M280 machine to develop the prototype.



**Figure 17.** Additively manufactured (AM) microchannel heat exchanger developed for the present study.

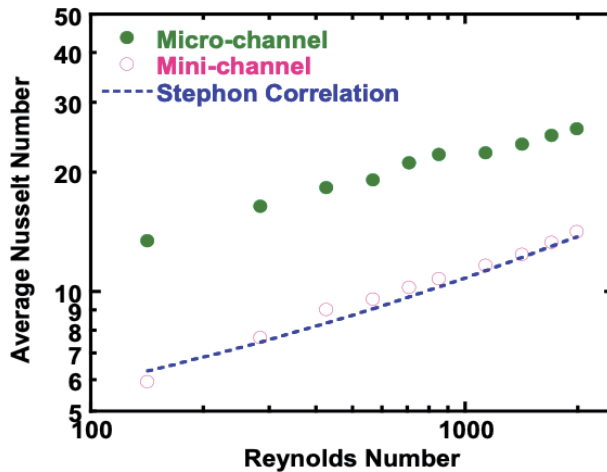
To characterize internal surfaces of the part including the roughness of each surfaces and true cross-section area, a computed X-ray tomography (CT Scan) was used. The CT scan takes a series of 2D images of an object and then incorporates them to form a 3D reconstruction of the object using the software algorithms. Through this method, the external and internal surfaces can be determined along with the channel surface roughness. An arithmetic roughness average,  $R_a$ , was calculated using the height differences between the CT scan data and the designed channel wall surface. The results have shown that the  $R_a/D_h$  value is 0.23.

## 4.2 Results and discussions

### 4.2.1 Experimental results

After verifying the integrity of the experimental configuration and test procedures, heat transfer and flow characteristics of the single-phase flow of pure PAO fluid inside the additively manufactured microchannel were experimentally investigated and then compared with those of minichannel heat exchanger introduced earlier. All the experiments conducted in the present study were repeated five times, and the relative errors of test data were found to be less than 5%. Since Poiseuille number remains constant with variations of Reynolds in the laminar regime, the experimental data for each set was averaged over the laminar flow regime.

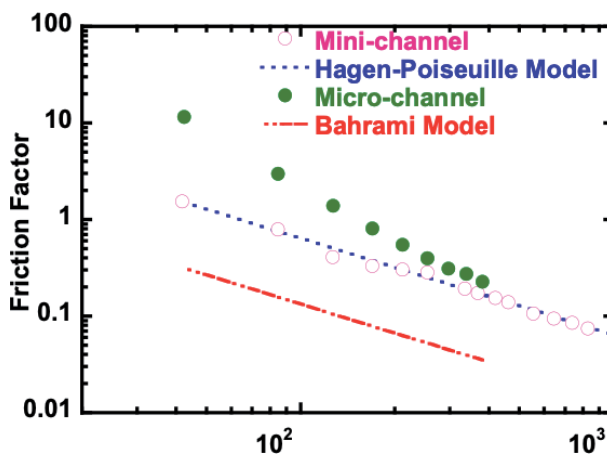
**Figure 18** represents the variations of the measured average Nusselt number with Reynolds for single-phase flow of the pure PAO within the laminar regime ( $100 < Re < 2000$ ) for both microchannel and minichannel heat exchangers. As shown in this figure, while the Nusselt number gradually increases with Reynolds for both microchannel and minichannel, a significant enhancement of heat transfer is observed using the microchannel compared to the minichannel heat exchanger under the same operating conditions. Furthermore, the experimental results were compared with the Stephan's correlation for internal flow. As illustrated in **Figure 18**, the Stephan's correlation underestimates the Nusselt number inside the microchannel whereas it agrees well with the minichannel. The main reason for the reflected deviation is attributed to the larger surface roughness of the additively manufactured microchannel using the DMLS technique compared to that of the



**Figure 18.** Average Nusselt number versus Reynolds for the pure PAO fluid in both minichannel and microchannel heat exchangers.

traditionally manufactured minichannel heat exchanger. Stimpson et al. [84] and Snyder et al. [85] have investigated the effects of surface roughness and printing orientation on flow structures in DMLS manufactured parts and proved that the existing empirical correlations for heat transfer and friction factor are no longer valid for the additively fabricated surfaces with high roughness values. This is also important to point out that the non-post processed surface of the DMLS manufactured microchannels is likely to be the main contributor to the augmented heat transfer performance. Future study is then required to better appreciate the possible mechanisms behind the phenomenon observed here.

**Figure 19** shows the variations of friction factor with a range of Reynolds numbers lying in the laminar regime for both the minichannel and microchannel heat exchangers. As clearly represented in this figure, the friction factor decreases with the increase of Reynolds number for both the test sections experimented in the present study. It can also be observed that the average friction factor of the PAO fluid inside the AM microchannel remains noticeably higher compared to that of the minichannel, and the entrance effect is more pronounced at lower Reynolds



**Figure 19.** Friction factor versus Reynolds number for the pure PAO fluid in both minichannel and microchannel heat exchangers.

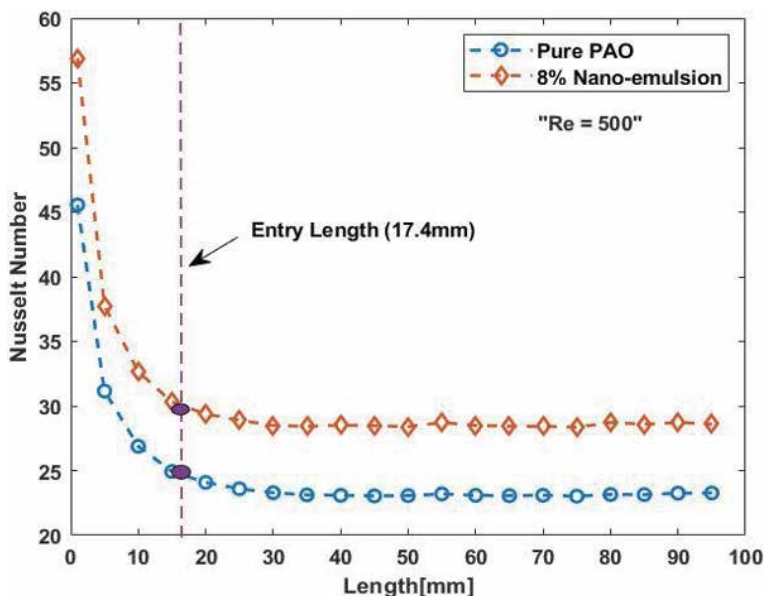


numbers. Similar to the heat transfer measurements, the friction factor measurements were compared and validated with classical empirical correlations proposed in the literature. As illustrated in **Figure 19**, the friction factor of the PAO fluid flowing inside the minichannel agrees well with the classical Hagen-Poiseuille correlation within the laminar regime. Considering the relatively large dimensions of the microchannel ( $H = 780\mu\text{m} \times W = 640\mu\text{m}$ ), Baharmi model [89] underestimates the friction factor, and it is likely due to the rough internal surface of the DMLS manufactured microchannel as discussed earlier.

#### 4.2.2 Simulation results

The prototype of the microchannel heat exchanger was designed using CREO software and then the model was imported to COMSOL-Multiphysics to conduct numerical heat transfer analysis for the same geometry and operating conditions summarized in **Table 5**. The following assumptions were adopted to conduct the simulations: no slip boundary condition, normal inflow velocity, uniform wall heat flux boundary conditions imposed on the top and bottom surfaces of the microchannel heat exchanger, and thermophysical properties of the working fluids are set to remain constant for the values listed earlier in **Table 4**. To confirm mesh independency of the simulation results and compare their accuracies, three types of meshes were developed, including finer, fine, and normal. The finer mesh size was ultimately chosen as it provides sufficiently accurate analysis while still sustaining a reasonable computational time.

**Figure 20** represents the variations of local Nusselt number at a certain Reynolds number of 500 along the microchannel heat exchanger with the same geometry and dimensions used previously for the experimental investigations as listed in **Table 5**. As shown in this figure, the local Nusselt number decreases along the microchannel at early positions and then reaches relatively constant values of 22 and 29 for the pure PAO and 8 wt% Ethanol/PAO nanoemulsion, respectively, within the fully developed laminar region. This reveals a heat transfer enhancement of around 32%



**Figure 20.** Variations of local Nusselt number along the microchannel at  $Re = 500$  for pure PAO and 8% ethanol/PAO nanoemulsion fluids with the entrance effects.



at a certain Reynolds number of 500 using the 8 wt% nanoemulsion fluid compared to that of the pure PAO inside the microchannel heat exchanger.

This is important to note that while the simulation results in **Figure 20** show a Nusselt value of 22 for the fully developed flow of pure PAO, the experimental results introduced in **Figure 18** show a Nusselt value of almost 20 at the same Reynolds of 500, which indicates a relative deviation of approximately 10% between the simulation and experimental results. This deviation is mainly due to the development of model which fails to study the effect of the DMLS manufactured surfaces on the flow and heat transfer characteristics.

As vividly seen from the simulation results in **Figure 20**, there is a declining trend of local Nusselt number along the early locations of the microchannel. The significantly higher Nusselt number at the early locations and its subsequent sharp drop is due to the thermal entrance region at the inlet of the microchannel test section where the internal liquid single-phase flows are still neither thermally nor hydrodynamically fully developed. As a result of having a thermally developing flow in the entrance region, the thermal boundary layer is extremely thin which causes larger values of Nusselt and HTC compared to those of locations outside the entrance region where both of the working fluids are fully developed.

Using the Eq. (13), the hydrodynamic entry length for the laminar flows of PAO and nanoemulsion in the microchannel was found to be 17.5 mm. As illustrated in **Figure 20**, the local Nusselt numbers for each of the working fluids take relatively constant values after the entry length of 17.5 mm where the boundary layer develops fully across the cross section of the microchannel and appears to be independent of the channel length. Since the working fluids are PAO and nanoemulsion with Prandtl numbers greater than 1 ( $Pr > 1$ ), the hydrodynamic boundary layer develops more quickly than the thermal boundary layer.

## 5. Conclusions

In this study, the flow and heat transfer characteristics of a novel nanostructured heat transfer fluid (i.e., ethanol/polyalphaolefin nanoemulsion) inside a minichannel of circular cross section and a microchannel of rectangular cross section were investigated experimentally and numerically. The experiments were performed for single-phase flow of pure PAO and ethanol/PAO nanoemulsion fluids of 4 wt% and 8 wt% concentrations within the laminar and transitional regimes as well as for two-phase flow boiling of nanoemulsion fluids within the laminar flow regime.

It was revealed that the nanoemulsion fluids thermally outperformed the pure PAO base fluid in single-phase flow of transitional regime, however, it does not reflect an appreciable improvement in single-phase heat transfer performance within the laminar flow regime. The significant heat transfer enhancement achieved at higher concentrations of nanoemulsion within the transitional regime is mainly attributed to the enhanced interaction and interfacial thermal transport between ethanol nanodroplets and PAO base fluid. For two-phase flow boiling, heat transfer coefficients of ethanol/PAO nanoemulsion fluids were further enhanced once the ethanol nanodroplets underwent phase change. A comparative study was also conducted on the flow and heat transfer characteristics of pure PAO between the traditionally manufactured minichannel and additively manufactured microchannel under the same operating conditions. Despite the higher friction factor and pressure loss, significant heat transfer enhancements were achieved using the additively manufactured microchannel compared to the traditionally fabricated minichannel heat exchanger under the same operating conditions, so that

the gained heat transfer enhancement through the microchannel is more prominent than its drawback of increased pressure loss. The non-post processed surface of the DMLS manufactured microchannel is believed to be the main contributor to the augmented heat transfer and pressure drop. Further studies are needed to fully understand the possible mechanisms behind it, and also to gain a deeper insight into the phase-change heat transfer characteristics of nanoemulsion fluids.

## **Acknowledgements**

The authors gratefully acknowledge financial support from NASA MUREP Institutional Research Opportunity Grant under Cooperative Agreement #80NSSC19M0196, and National Science Foundation (NSF) for supporting this work via grant HRD-1601156. In addition, the authors would also like to acknowledge the financial support from National Science Foundation (NSF) under award HRD-1914751.

## **Author details**

Jaime Rios, Mehdi Kabirnajafi, Takele Gameda, Raid Mohammed and Jiajun Xu\*  
Center for Advanced Manufacturing in Space Technology and Applied Research  
(CAM-STAR), University of the District of Columbia, Washington D.C., USA

\*Address all correspondence to: [jiajun.xu@udc.edu](mailto:jiajun.xu@udc.edu)

## **IntechOpen**

---

© 2021 The Author(s). Licensee IntechOpen. This chapter is distributed under the terms of the Creative Commons Attribution License (<http://creativecommons.org/licenses/by/3.0>), which permits unrestricted use, distribution, and reproduction in any medium, provided the original work is properly cited. 

## References

- [1] Kabirnajafi, M., Xu, J. Experimental Approaches to Measurement of Vapor Quality of Two-Phase Flow Boiling. Heat Transfer - Design, Experimentation and Applications, INTECH, Edited by Miguel Araiz, 2020, ISBN: 978-1-83968-438-8.
- [2] Kandlikar, S.G., Steinke, M.E. Examples of microchannel mass transfer processes in biological systems, Proceedings of 1st International Conference on Minichannels and Microchannels, Rochester, NY, April 24–25, 2003, Paper ICMM2003–1124, ASME 933–943.
- [3] Kandlikar, S.G., Garimella, S., Li, D., Colin, S., King, M. Heat transfer and fluid flow in minichannels and microchannels, Elsevier, 2006, ISBN: 0-0804-4527-6.
- [4] Mehendale, S.S., Jacobi, A.M., Shah, R.K. Fluid flow and heat transfer at micro- and meso-scales with applications to heat exchanger design. Appl. Mech. Rev., 2000, 53: 175–193.
- [5] Kandlikar, S.G., Grande, W.J. Evolution of microchannel flow passages – thermohydraulic performance and fabrication technology, Heat Transfer Eng., 2003, 24: 3–17.
- [6] Cheng, P., Wu, H.Y., Hong, F.J. Phase-change heat transfer in microsystems, J. Heat Transfer, Trans. ASME, 2007, 129: 101–107.
- [7] Dewan, A., Mahanta, P., Raju, K. S., and Kumar, P. S., 2004, “Review of passive heat transfer augmentation techniques,” Proceedings of the Institution of Mechanical Engineers Part a-Journal of Power and Energy, 218 (A7), pp. 509–527.t
- [8] Agostini, B., Fabbri, M., Park, J. E., Wojtan, L., Thome, J. R., and Michel, B., 2007, “State of the art of high heat flux cooling technologies,” Heat Transfer Engineering, 28(4), pp. 258–281.
- [9] Ebadian, M. A., and Lin, C. X., 2011, “A Review of High-Heat-Flux Heat Removal Technologies,” Journal of Heat Transfer-Transactions of the Asme, 133 (11).
- [10] Inaba, H., 2000, “New challenge in advanced thermal energy transportation using functionally thermal fluids,” International Journal of Thermal Sciences, 39(9–11), pp. 991–1003.
- [11] Zimparov, V., 2002, “Energy conservation through heat transfer enhancement techniques,” International Journal of Energy Research, 26(7), pp. 675–696.
- [12] Xuan, Y. M., and Li, Q., 2003, “Investigation on convective heat transfer and flow features of nanofluids,” Journal of Heat Transfer-Transactions of the Asme, 125(1), pp. 151–155.
- [13] Evans, W., Fish, J., and Keblinski, P., 2006, “Role of Brownian motion hydrodynamics on nanofluid thermal conductivity,” Applied Physics Letters, 88(9).
- [14] Heris, S. Z., Etemad, S. G., and Esfahany, A. N., 2006, “Experimental investigation of oxide nanofluids laminar flow convective heat transfer,” International Communications in Heat and Mass Transfer, 33(4), pp. 529–535.
- [15] Kim, S. J., Bang, I. C., Buongiorno, J., and Hu, L. W., 2006, “Effects of nanoparticle deposition on surface wettability influencing boiling heat transfer in nanofluids,” Applied Physics Letters, 89(15).
- [16] Ma, H. B., Wilson, C., Borgmeyer, B., Park, K., Yu, Q., Choi, S. U. S., and Tirumala, M., 2006, “Effect of

nanofluid on the heat transport capability in an oscillating heat pipe,” *Applied Physics Letters*, 88(14).

[17] Prasher, R., Song, D., Wang, J. L., and Phelan, P., 2006, “Measurements of nanofluid viscosity and its implications for thermal applications,” *Applied Physics Letters*, 89(13).

[18] Chein, R., and Chuang, J., 2007, “Experimental microchannel heat sink performance studies using nanofluids,” *International Journal of Thermal Sciences*, 46(1), pp. 57–66.

[19] Khodadadi, J. M., and Hosseinizadeh, S. F., 2007, “Nanoparticle-enhanced phase change materials (NEPCM) with great potential for improved thermal energy storage,” *International Communications in Heat and Mass Transfer*, 34(5), pp. 534–543.

[20] Buongiorno, J., Hu, L. W., Kim, S. J., Hannink, R., Truong, B., and Forrest, E., 2008, “Nanofluids for enhanced economics and safety of nuclear reactors: An evaluation of the potential features, issues, and research gaps,” *Nuclear Technology*, 162(1), pp. 80–91.

[21] Coursey, J. S., and Kim, J., 2008, “Nanofluid boiling: The effect of surface wettability,” *International Journal of Heat and Fluid Flow*, 29(6), pp. 1577–1585.

[22] Milanova, D., and Kumar, R., 2008, “Heat transfer behavior of silica nanoparticles experiment in pool boiling,” *Journal of Heat Transfer-Transactions of the Asme*, 130(4).

[23] Merabia, S., Koblinski, P., Joly, L., Lewis, L. J., and Barrat, J. L., 2009, “Critical heat flux around strongly heated nanoparticles,” *Physical Review E*, 79(2), p. 4.

[24] Shima, P. D., Philip, J., and Raj, B., 2009, “Magnetically controllable nanofluid with tunable thermal

conductivity and viscosity,” *Applied Physics Letters*, 95(13).

[25] Wang, L. Q., and Wei, X. H., 2009, “Nanofluids: Synthesis, Heat Conduction, and Extension,” *Journal of Heat Transfer-Transactions of the Asme*, 131(3).

[26] Boudouh, M., Gualous, H. L., and De Labachellerie, M., 2010, “Local convective boiling heat transfer and pressure drop of nanofluid in narrow rectangular channels,” *Applied Thermal Engineering*, 30(17–18), pp. 2619–2631.

[27] Wong, K. V., and De Leon, O., 2010, “Applications of Nanofluids: Current and Future,” *Advances in Mechanical Engineering*, p. 11.

[28] Yu, W., Xie, H. Q., Wang, X. P., and Wang, X. W., 2011, “Significant thermal conductivity enhancement for nanofluids containing graphene nanosheets,” *Physics Letters A*, 375(10), pp. 1323–1328.

[29] Hampton, M. A., Nguyen, T. A. H., Nguyen, A. V., Xu, Z. P., Huang, L. B., and Rudolph, V., 2012, “Influence of surface orientation on the organization of nanoparticles in drying nanofluid droplets,” *Journal of Colloid and Interface Science*, 377, pp. 456–462.

[30] Park, S. D., Lee, S. W., Kang, S., Kim, S. M., and Bang, I. C., 2012, “Pool boiling CHF enhancement by graphene-oxide nanofluid under nuclear coolant chemical environments,” *Nuclear Engineering and Design*, 252, pp. 184–191.

[31] Chehade, A. A., Gualous, H. L., Le Masson, S., Fardoun, F., and Besq, A., 2013, “Boiling local heat transfer enhancement in minichannels using nanofluids,” *Nanoscale Research Letters*, 8, pp. 1–20.

[32] Hadad, K., Rahimian, A., and Nematollahi, M. R., 2013, “Numerical

- study of single and two-phase models of water/Al<sub>2</sub>O<sub>3</sub> nanofluid turbulent forced convection flow in VVER-1000 nuclear reactor,” *Annals of Nuclear Energy*, 60, pp. 287–294.
- [33] Ray, D. R., Das, D. K., and Vajjha, R. S., 2014, “Experimental and numerical investigations of nanofluids performance in a compact minichannel plate heat exchanger,” *International Journal of Heat and Mass Transfer*, 71, pp. 732–746.
- [34] Yu, L. Y., Sur, A., and Liu, D., 2015, “Flow Boiling Heat Transfer and Two-Phase Flow Instability of Nanofluids in a Minichannel,” *Journal of Heat Transfer-Transactions of the Asme*, 137(5).
- [35] Roesle, M. L., and Kulacki, F. A., 2010, “Boiling of Dilute Emulsions-Toward a New Modeling Framework,” *Industrial & Engineering Chemistry Research*, 49(11), pp. 5188–5196.
- [36] Morshed, A., Paul, T. C., Fang, R. X., Khan, J. A., and Asme, 2013, “Flow boiling Characteristics of Dilute Emulsion in Microchannel,” *Proceedings of the Asme International Mechanical Engineering Congress and Exposition - 2012, Vol 7, Pts a-D*, pp. 2085-2091.
- [37] Kotlarchyk, M., Chen, S. H., and Huang, J. S., 1982, “TEMPERATURE-DEPENDENCE OF SIZE AND POLYDISPERSITY IN A 3-COMPONENT MICRO-EMULSION BY SMALL-ANGLE NEUTRON-SCATTERING,” *Journal of Physical Chemistry*, 86(17), pp. 3273–3276.
- [38] Bulanov, N. V., Skripov, V. P., and Khmylnin, V. A., 1984, “Heat Transfer to Emulsion with superheating of its disperse phase,” *J. Eng. Phys.*, pp. 1-3.
- [39] Bulanov, N. V., Skripov, V. P., and Khmylnin, V. A., 1993, “Heat Transfer to Emulsion with a low-boiling disperse phase,” *Heat Transfer Res*, pp. 786-789.
- [40] Bulanov, N. V., 2001, “An analysis of the heat flux density under conditions of boiling internal phase of emulsion,” *High Temperature*, 39(3), pp. 462–469.
- [41] Bulanov, N. V., Gasanov, B. M., and Turchaninova, E. A., 2006, “Results of experimental investigation of heat transfer with emulsions with low-boiling disperse phase,” *High Temperature*, 44(2), pp. 267–282.
- [42] Choi, S. U. S., and Eastman, J. A., 1995, *ASME International Mechanical Engineering Congress & Expositio*.
- [43] Moore, G. R., 1959, “Vaporization of Superheated Drops in Liquids,” *Aiche Journal*, 5(4), pp. 458–466.
- [44] Bulanov, N. V., and Gasanov, B. M., 2005, “Experimental setup for studying the chain activation of low-temperature boiling sites in superheated liquid droplets,” *Colloid Journal*, 67(5), pp. 531–536.
- [45] Bulanov, N. V., and Gasanov, B. M., 2008, “Peculiarities of boiling of emulsions with a low-boiling disperse phase,” *International Journal of Heat and Mass Transfer*, 51(7–8), pp. 1628–1632.
- [46] Rosele, M. L., 2010, “Boiling of Dilute Emulsions,” PhD dissertation, University of Minnesota.
- [47] Trinh V., Xu J., An Experimental Study on Flow and Heat Transfer Characteristics of Ethanol/Polyalphaolefin Nanoemulsion Flowing Through Circular Minichannels. *Nanoscale Research Letters*, 2017, 12: 216. DOI 10.1186/s11671-017-1984-1.
- [48] Kumar, P., and Mittal, K. L., 1999, *Handbook of microemulsion science and technology*, New York: Marcel Dekker.
- [49] Shanthi, R., Anandan, S. S., and Ramalingam, V., 2012, “HEAT

TRANSFER ENHANCEMENT USING NANOFLUIDS: An Overview,” *Thermal Science*, 16(2), pp. 423–444.

[50] Wang, X. Q., and Mujumdar, A. S., 2008, “A REVIEW ON NANOFLUIDS - PART I: THEORETICAL AND NUMERICAL INVESTIGATIONS,” *Brazilian Journal of Chemical Engineering*, 25(4), pp. 613–630.

[51] Kakac, S., and Pramuanjaroenkij, A., 2009, “Review of convective heat transfer enhancement with nanofluids,” *International Journal of Heat and Mass Transfer*, 52(13–14), pp. 3187–3196.

[52] Murshed, S.M., Nieto de Castro, C. A., Lourenco, M. J. V., Lopes, M. L. M., and Santos, F. J. V., 2011, “A review of boiling and convective heat transfer with nanofluids,” *Renewable & Sustainable Energy Reviews*, 15(5), pp. 2342–2354.

[53] Wang, X. Q., and Mujumdar, A. S., 2008, “A REVIEW ON NANOFLUIDS - PART II: EXPERIMENTS AND APPLICATIONS,” *Brazilian Journal of Chemical Engineering*, 25(4), pp. 631–648.

[54] Yang, B., and Han, Z. H., 2006, “Thermal conductivity enhancement in water-in-FC72 nanoemulsion fluids,” *Applied Physics Letters*, 88(26).

[55] Han, Z. H., and Yang, B., 2008, “Thermophysical characteristics of water-in-FC72 nanoemulsion fluids,” *Applied Physics Letters*, 92(1).

[56] Xu, J., Liu, X., Yang, B., 2009, THERMOPHYSICAL CHARACTERISTICS OF SELF-ASSEMBLED ETHANOL/POLYALPHAOLEFIN NANOEMULSION FLUIDS. ASME IMECE 2009, Nov. 13-19, 2023–2026.

[57] Xu, J., Wu, C. W., and Yang, B., 2010, “Thermal- and Phase-Change Characteristics of Self-Assembled

Ethanol/Polyalphaolefin Nanoemulsion Fluids,” *Journal of Thermophysics and Heat Transfer*, 24(1), pp. 208–211.

[58] Han, Z. H., Yang, B., Qi, Y., and Cumings, J., 2011, “Synthesis of low-melting-point metallic nanoparticles with an ultrasonic nanoemulsion method,” *Ultrasonics*, 51(4), pp. 485–488.

[59] Xu, J., Yang, B., and Hammouda, B., 2011, “Thermal conductivity and viscosity of self-assembled alcohol/polyalphaolefin nanoemulsion fluids,” *Nanoscale Research Letters*, 6.

[60] Xu, J., Hammouda, B., and Yang, B., 2012, “Thermophysical Properties and Pool Boiling Characteristics of Water in Polyalphaolefin Nanoemulsion Fluids,” ASME, Proceedings of ASME Micro/Nanoscale Heat & Mass Transfer International Conference 2012.

[61] Xu, J., and Yang, B., 2012, “Novel Heat Transfer Fluids: Self-assembled Nanoemulsion Fluids,” *Nanotechnology*, D.J.N. Govil, ed., Studium Press LLC.

[62] Xu, J., Yang, B., and Hammouda, B., 2013, “Thermophysical Properties and Pool Boiling Characteristics of Water-in-Polyalphaolefin Nanoemulsion Fluids,” *Journal of Heat Transfer-Transactions of the Asme*, 135(9).

[63] Xu, J., Hammouda, B., Cao, F., and Yang, B., 2015, “Experimental study of thermophysical properties and nanostructure of self-assembled water/polyalphaolefin nanoemulsion fluids,” *Advances in Mechanical Engineering*, 7 (4): 1–8.

[64] Xu, J., Yang, B., 2012, Thermophysical Properties and Pool Boiling Characteristics of Water in Polyalphaolefin Nanoemulsion Fluids. ASME 2012, Int. Conference on Micro/Nanoscale Heat and Mass Transfer, Atlanta, GA, USA. MNHMT2012-75232, 321-325.

- [65] Kandlikar, S.G., Grande, W.J. Evaluation of single-phase flow in microchannels for high heat flux chip cooling—thermohydraulic performance enhancement and fabrication technology. *Heat Transfer Eng.*, 2004, 25(8): 5–16.
- [66] Cooke, D., Kandlikar, S.G. Pool boiling heat transfer and bubble dynamics over plain and enhanced microchannels. *J Heat Transfer Trans ASME*, 2011, 133(5):052902–052901.
- [67] Ahn, H.S., Sathyamurthi, V., and Banerjee, D., 2009, “Pool Boiling Experiments on a Nano-Structured Surface,” *IEEE Transactions on Components and Packaging Technologies*, 32(1), pp. 156–165.
- [68] Sathyamurthi, V., Ahn, H. S., Banerjee, D., and Lau, S. C., 2009, “Subcooled Pool Boiling Experiments on Horizontal Heaters Coated with Carbon Nanotubes,” *Journal of Heat Transfer-Transactions of the ASME*, 131(7).
- [69] Morshed, A., Rezwana, A. A., and Khan, J. A., 2014, “Two-phase convective flow in microchannel with nanoporous coating,” 10th International Conference on Mechanical Engineering (ICME 2013), 90, pp. 588-598.
- [70] Kumar, C. S. S., Suresh, S., Aneesh, C. R., Kumar, M. C. S., Praveen, A. S., and Raji, K., 2015, “Flow boiling heat transfer enhancement on copper surface using Fe doped Al<sub>2</sub>O<sub>3</sub>-TiO<sub>2</sub> composite coatings,” *Applied Surface Science*, 334, pp. 102–109.
- [71] Hammouda, B., SANS from Polymers-Review of the Recent Literature. *Polymer Reviews* 2010, 50 (1), 14–39.
- [72] Hammouda, B.; Krueger, S.; Glinka, C. J., Small-angle neutron scattering at the national institute of standards and technology. *Journal of Research of the National Institute of Standards and Technology* 1993, 98 (1), 31–46.
- [73] Bergman T.A., Levine A.S., Incropera F.P., Dewitt D.P., *Fundamentals of Heat and Mass Transfer*, John Wiley & Sons Inc., 7th Edition, 2011, ISBN 13 978–0470–50197-9.
- [74] Abraham JP, Sparrow EM, Minkowycz WJ., 2011, Internal-flow Nusselt numbers for the low-Reynolds-number end of the laminar-to-turbulent transition regime. *Int J Heat Mass Transf* 54:584–588.
- [75] Frazier, W. E., 2014, “Metal Additive Manufacturing: A Review,” *Journal of Materials Engineering and Performance*, 23(6), pp. 1917–1928.
- [76] Mellor, S., Hao, L., and Zhang, D., 2014, “Additive manufacturing: A framework for implementation,” *International Journal of Production Economics*, 149, pp. 194–201.
- [77] Yap, C. Y., Chua, C. K., Dong, Z. L., Liu, Z. H., and Zhang, D. Q., 2014, STATE-OF-THE-ART REVIEW ON SELECTIVE LASER MELTING OF NON-FERROUS METALS.
- [78] Giannatsis, J., and Dedoussis, V., 2009, “Additive fabrication technologies applied to medicine and health care: a review,” *International Journal of Advanced Manufacturing Technology*, 40(1–2), pp. 116–127.
- [79] Levy, G. N., Schindel, R., and Kruth, J. P., 2003, “Rapid manufacturing and rapid tooling with layer manufacturing (LM) technologies, state of the art and future perspectives,” *Cirp Annals-Manufacturing Technology*, 52(2), pp. 589–609.
- [80] Longhitano, G. A., Larosa, M. A., Munhoz, A. L. J., Zavaglia, C. A. D., and Ierardi, M. C. F., 2015, “Surface Finishes for Ti-6Al-4V Alloy Produced by Direct

Metal Laser Sintering,” *Materials Research-Ibero-American Journal of Materials*, 18(4), pp. 838–842.

[81] Kruth, J. P., Wang, X., Laoui, T., and Froyen, L., 2003, “Lasers and materials in selective laser sintering,” *Assembly Automation*, 23(4), pp. 357–371.

[82] Gibson, I., and Shi, D. P., 1997, “Material properties and fabrication parameters in selective laser sintering process,” *Rapid Prototyping Journal*, 3(4), pp. 129–136.

[83] Krauss, H., Zeugner, T., and Zaeh, M. F., 2015, “Thermographic Process Monitoring in Powderbed Based Additive Manufacturing,” *Proc. 41st Annual Review of Progress in Quantitative Nondestructive Evaluation (QNDE)*, pp. 177-183.

[84] Stimpson, C. K., Snyder, J. C., Thole, K. A., and Mongillo, D., 2016, “Roughness Effects on Flow and Heat Transfer for Additively Manufactured Channels,” *Journal of Turbomachinery*, 138(5), pp. 051008-051008-051010.

[85] Snyder, J. C., Stimpson, C. K., Thole, K. A., and Mongillo, D., 2016, “Build Direction Effects on Additively Manufactured Channels,” *Journal of Turbomachinery*, 138(5), pp. 051006-051006-051008.

[86] Sadaghiani, A. K., Saadi, N. S., Parapari, S. S., Karabacak, T., Keskinöz, M., and Kosar, A., 2017, “Boiling heat transfer performance enhancement using micro and nano structured surfaces for high heat flux electronics cooling systems,” *Applied Thermal Engineering*, 127, pp. 484–498.

[87] Zhang, J., Diao, Y. H., Zhao, Y. H., and Zhang, Y. N., 2017, “An experimental investigation of heat transfer enhancement in minichannel: Combination of nanofluid and micro fin structure techniques,” *Experimental*

*Thermal and Fluid Science*, 81, pp. 21–32.

[88] Harirchian, T., and Garimella, S. V., 2008, “Microchannel size effects on local flow boiling heat transfer to a dielectric fluid,” *International Journal of Heat and Mass Transfer*, 51(15–16), pp. 3724–3735.

[89] Bahrami, M., Yovanovich, M. M., and Culham, J. R., 2006, “Pressure Drop of Fully-Developed, Laminar Flow in Microchannels of Arbitrary Cross-Section,” *Journal of Fluids Engineering*, 128(5):1036–1044.



# Nanofluid-Enhancing Shell and Tube Heat Exchanger Effectiveness with Modified Baffle Architecture

*I Made Arsana and Ruri Agung Wahyuono*

## Abstract

As shell and tube heat exchanger is widely employed in various field of industries, heat exchanger design remains a constant optimization challenge to improve its performance. The heat exchanger design includes not only the architectural geometry of either the shell and tube configuration or the additional baffles but also the working fluid. The baffle design including the baffle angle and the baffle distance has been understood as key parameter controlling the overall heat exchanger effectiveness. In addition, a room of improvement is open by substituting the conventional working fluid with the nanomaterials-enriched nanofluid. The nanomaterials, e.g.  $\text{Al}_2\text{O}_3$ ,  $\text{SiO}_2$ ,  $\text{TiO}_2$ , increases the thermal conductivity of the working fluids, and hence, the more efficient heat transfer process can be achieved. This chapter provide an insight on the performance improvement of shell and tube heat exchanger by modifying the baffle design and utilizing nanofluids.

**Keywords:** Design optimization, Geometry, Conductivity, Heat exchanger performance, Computational fluid dynamics

## 1. Introduction

Heat exchanger is considered a vital component in thermal process required in a wide range of industries. This heat exchanger is typically employed for condensation, sterilization, pasteurization, fractionation, distillation, and crystallization [1–3]. This implies that the heat exchanger shall possess an optimized design to yield the highest possible effectiveness while having a compact dimension. In general, heat transfer in a heat exchanger is substantially dominated by convection and conduction. The convection is significantly affected by the geometry of the heat exchanger and some dimensionless numbers, including Reynolds number ( $Re$ ), Nusselt number ( $Nu$ ) and Prandtl numbers ( $Pr$ ) [1–7]. It should be noted that  $Re$ ,  $Nu$  and  $Pr$  are dependent on the flow rate and fluid properties including the density, absolute viscosity, specific heat and thermal conductivity.

Practically, various heat exchangers have been developed and the shell and tube heat exchanger has been intensively employed in industries as it shows some favorable features, i.e. easy maintenance, robust construction, and higher construction reliability [8–12]. The shell and tube heat exchanger mainly comprise of shell, tubes,

front head, rear head, baffles, and nozzle. For high performance shell and tube heat exchanger, which shows high effectiveness ( $\epsilon$ ), several parameters affecting the heat and mass transfer process should be optimized, including the working fluid and material selection, flow rate, temperature, heat transfer rate, pressure drop, shell and tube dimension and composition, as well as baffle distance and cut, and pitch range [8–14]. Considering the architecture of heat exchanger, baffles arrangement is one of the important parameters that will increase the heat transfer and hence the effectiveness. For instance, reducing the baffle gaps could induce high pressure drop while setting the baffle gap too far could lead to less efficient heat transfer. In addition, improper baffle arrangement will lead to additional mechanical vibration which can damage the heat exchanger apparatus, and hence lower the reliability of the heat exchanger.

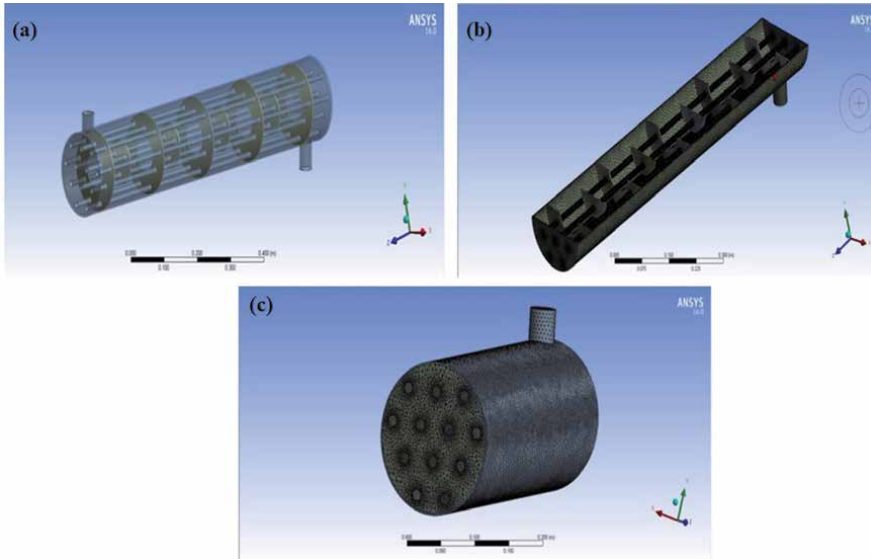
Other practical problem arising in industry is that the heat exchanger frequently faces unfavorable thermal properties of its working fluid, i.e. water, ethylene glycol, or oil, leading to the lower heat transfer effectiveness [14]. Therefore, it is necessary to improve the thermal properties of working fluids, one of which is by adding functional nanoparticles into the working fluid [15–17]. Recent studies have investigated the improvement of heat transfer effectiveness in nanofluids bearing various metal oxide semiconductor nanoparticles, e.g.  $\text{Al}_2\text{O}_3$ ,  $\text{TiO}_2$ ,  $\text{CuO}$ , and  $\text{SiO}_2$  [15–26]. Among these materials,  $\text{TiO}_2$  is one of the widely exploited nanoparticles for increasing the heat transfer effectiveness as it shows superior chemical and thermophysical stability [18–23]. Nonetheless, it should be noted that the utilization of high concentration of nanoparticles should be avoided since it may cause blockage of the fluid flow as well as induce fouling [18, 19]. Still, the use of nanoparticles in the base fluid (nanofluid) can be considered an alternative approach to improve both the thermal conductivity of the working fluid and the long-term stability by maintaining lower pressure drop in the system [20]. Some literature report that the use of nanofluids enhances the heat transfer effectiveness particularly under laminar flow condition by increasing both the concentration of nanoparticles in nanofluids and the Reynolds number [15–21]. These results suggest that the use of nanofluids increases the convection coefficient within the heat transfer process.

Considering the abovementioned facts, it is quite clear that the heat transfer process in the heat exchanger can be improved in many ways. Particularly for shell and tube heat exchanger, enhancing the heat exchanger effectiveness which is discussed in this chapter can be achieved by modifying the baffle architecture and by utilizing nanofluids with functional nanoparticles. The baffle arrangement discussed in this chapter includes the baffle distance and the baffle type which was investigated by experimental and numerical method using computational fluid dynamics (CFD). Meanwhile, the effect of nanofluid substitution to the working fluid has been investigated experimentally by varying the concentration of nanoparticles, i.e.  $\text{Al}_2\text{O}_3$  in water and  $\text{SiO}_2@\text{TiO}_2$  in water: ethylene glycol.

## 2. Experimental and numerical approach to evaluate the effect of baffle arrangement to the heat exchanger effectiveness

Baffle modification in this chapter includes baffle types, baffle angle and baffle distance. Modification of baffle type and angle was investigated experimentally using the experimental setup of laboratory scale of heat exchanger shown in **Figure 1** [11]. The baffle type was varied using helical and double segmental baffle, whilst the baffle angle was set in the range of  $5^\circ$ ,  $6^\circ$ , and  $7^\circ$ . The pressure drop and the temperature difference between inlet and outlet of heat exchanger were





**Figure 2.** (a) The 3D model of shell and tube heat exchanger meshed with tetrahedral/hexahedral meshing type at different angle, and the corresponding (b) horizontal and (c) vertical cross-sectional 3D model of heat exchanger. Figures from Ref. [27] used with permission.

No.	Specification	Boundary conditions
1	Inlet	Mass flow inlet
2	Shell	Adiabatic wall
3	Tube	Convection wall
4	Baffle	Adiabatic wall
5	Outlet	Outflow

**Table 1.** Boundary conditions of shell and tube heat exchangers.

$$\frac{\partial}{\partial t}(\rho E) + \nabla \cdot (\vec{v}(\rho E + p)) = \nabla \cdot k_{eff} \nabla T + \nabla \cdot (\bar{\tau}_{eff} \cdot \vec{v}) + S_h \quad (1)$$

where  $k_{eff}$  is the effective conductivity which is the sum of  $k$  and  $k_t$  (thermal conductivity for the presence of turbulence). The two terms on the right side represent the energy transfer by conduction and viscosity dissipation. Meanwhile, the energy transfer was calculated as follow [17, 18]:

$$\frac{\partial}{\partial t}(\rho h) + \nabla \cdot (\vec{v} \rho h) = \nabla \cdot (k \nabla T) + S_h \quad (2)$$

where  $\rho$  was the density,  $h$  was the sensible enthalpy,  $k$  was the conductivity constant,  $T$  was the surface temperature, and  $S_h$  was the volumetric heat source. The Eq. (1) and (2) were complemented by the continuity and conservation of momentum:

$$\nabla \cdot u = 0 \quad (3)$$

$$\rho \frac{du}{dt} = F - \nabla p + \mu \nabla^2 u \quad (4)$$

where  $p$  was normal pressure ( $\text{N/m}^2$ ),  $F$  was body force on solid region. For a faster convergence of numerical calculation, the Boussinesq model was considered. This model set the fluid density as a function of temperature:

$$\rho = \rho_0(1 - \beta(T - T_0)) \quad (5)$$

where  $\beta$  was thermal expansion coefficient ( $1/\text{K}$ ),  $T_0$  dan  $\rho_0$  represented the operational parameter. This model was accurate as long as the density changes were small, or it was valid if satisfying for  $\beta(T - T_0) < < 1$ .

The final step in CFD was the post processing stage including the data visualization in the form of a contour of static temperature, pressure, and velocity profile. Data analysis was carried out to determine the temperature distribution in the shell and tube heat exchanger with different baffle distances. The heat exchanger effectiveness ( $\varepsilon$ ) was calculated in every variation of baffle distance using NTU method which considers the following steps [19]:

The rate of heat capacity ( $C$ ) was calculated as

$$C_c = \dot{m}_c \times Cp_c \quad (6)$$

$$C_h = \dot{m}_h \times Cp_h \quad (7)$$

where the smallest value  $C_{min}$  considers:

$$C_{min} = > \text{If } C_h < C_c \text{ then } C_h = C_{min} \quad (8)$$

$$C_{min} = > \text{If } C_c < C_h \text{ then } C_c = C_{min} \quad (9)$$

The maximum heat transfer ( $q_{max}$ ) was calculated as follow:

$$q_{max} = C_{min} \times (T_{h,in} - T_{c,in}) \quad (10)$$

$$q_{in} = q_{out} \quad (11)$$

$$q_h = q_c \quad (12)$$

$$= \dot{m}_h \times C_h \times (T_{h,in} - T_{h,out}) \quad (13)$$

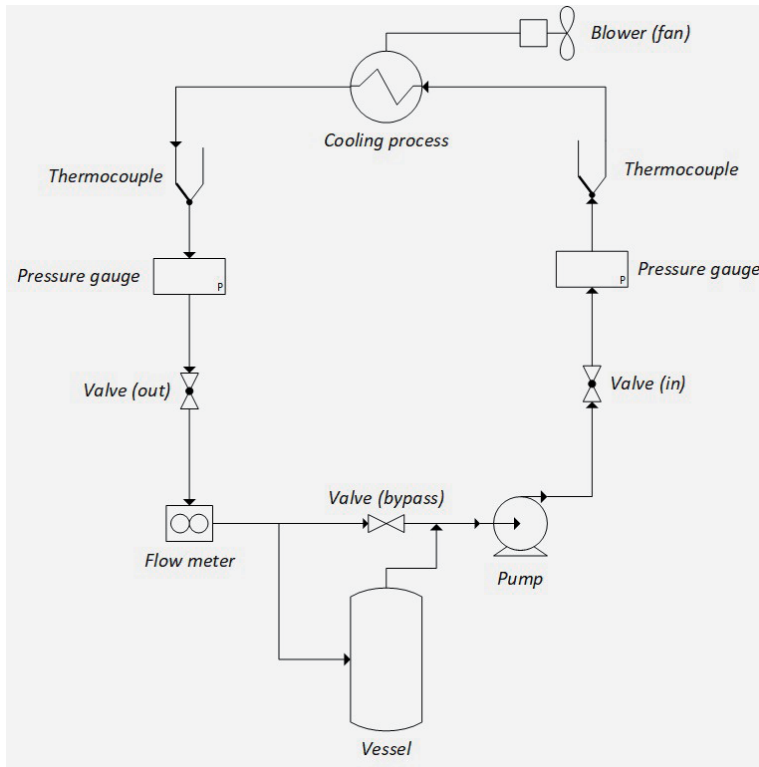
$$= \dot{m}_c \times C_c \times (T_{c,out} - T_{c,in}), \quad (14)$$

and the effectiveness ( $\varepsilon$ ) of the heat exchanger can then be calculated as follow:

$$\varepsilon = \frac{q_{actual}}{q_{max}} \quad (15)$$

### 3. Experimental approach to evaluate the effect of nanoparticles concentration in nanofluid to the heat exchanger effectiveness

The effectiveness of heat transfer using different nanofluids was assessed in the laboratory scale of experimental heat transfer system (automobile radiator training kit) which includes a closed loop of hot and cold flow (**Figure 3**). The heat exchanger was finned-tube cross flow heat exchanger (Suzuki). The nanoparticle used was  $\text{Al}_2\text{O}_3$  and  $\text{SiO}_2@\text{TiO}_2$ . The  $\text{SiO}_2@\text{TiO}_2$  in a mixture of EG:water (1:1 v/v) nanofluid was utilized as the hot fluid in the system. The concentration was varied in the range of 0–0.025% mass fraction of  $\text{SiO}_2@\text{TiO}_2$  to EG:water base fluids. The system was functionalized with the calibrated thermocouples, flow meter and



**Figure 3.** The schematic of heat exchanger system for investigating the effect nanofluid concentration to its effectiveness.

pressure gauges. The schematic diagram of the automobile radiator training kit is shown in **Figure 1**.

Performance of heat exchanger using different concentration of  $\text{SiO}_2@\text{TiO}_2$  was evaluated by the heat transfer effectiveness. Heat transfer parameters of nanofluids were determined by joint experimental and theoretical approach, *i.e.* only conductivity is directly determined from transient hot wire measurements. The other parameters are determined as follows:

- Density of nanofluids

$$\rho_{nf} = (1 - \varphi)\rho_{bf} + \varphi\rho_{pf} \quad (16)$$

- Viscosity of nanofluids (Einstein equation)

$$\mu_{nf} = (1 + 2.5\varphi)\mu_{bf} \quad (17)$$

- Reynolds number (Re)

$$\text{Re} = \frac{\rho \times V \times D_h}{\mu} \quad (18)$$

- Nusselt number ( $Nu$ ) of external flow

$$Nu = 0.683 \times \text{Re}^{0.38} \times \text{Pr}^{0.37} \times \left(\frac{\text{Pr}}{\text{Pr}_s}\right)^{0.25} \quad (19)$$

- Nusselt number ( $Nu$ ) of internal flow

$$Nu = 0.0265 \times Re^{0.8} Pr^{0.36} \quad (20)$$

- Convection coefficient ( $h_{nf}$ ) of nanofluids

$$h_{nf} = 0.295 \left( \frac{k_w}{D_h} \right) Re^{0.64} Pr^{0.32} \left( \frac{\pi}{2} \right) \quad (21)$$

- Convection coefficient ( $h$ ) of air

$$h = \frac{Nu \times k_f}{D_h} \quad (22)$$

Once all above parameters were determined, the overall heat transfer coefficient ( $U$ ) was estimated. For a single tube heat exchanger,  $U$  was determined as follows:

$$U = \frac{1}{\frac{1}{h_i} + \frac{\Delta x}{k_w} + \frac{1}{h_o}} \quad (23)$$

Finally, the heat transfer rate which involves convection and conduction was evaluated by the following:

$$Q = U \times A \times \Delta T_{LMTD} \quad (24)$$

where

$$\Delta T_{LMTD} = \frac{(T_{h,in} - T_{c,out}) - (T_{h,out} - T_{c,in})}{\ln \left[ \frac{(T_{h,in} - T_{c,out})}{(T_{h,out} - T_{c,in})} \right]} \quad (25)$$

## 4. Improvement of heat exchanger effectiveness

As previously mentioned, in this section effect of baffle architecture, including type, angle, and distance, and the nanoparticle type and concentration in nanofluids toward the heat exchange effectiveness will be discussed.

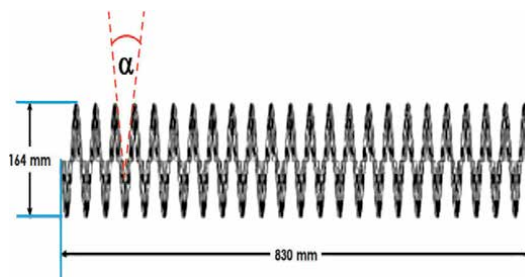
### 4.1 Effect of baffle arrangement

As stated in the introduction, the baffle arrangement plays significant role in the operation of heat exchanger. All thermal properties and performance of heat exchanger upon modification of baffle type, angle and distance are summarized in **Table 2**. In general, the efficiency of heat transfer process can be indicated by the temperature difference in either the hot or the cold fluid flow in the shell and tube heat exchanger, which is later used to determine the effectiveness.

Regarding the baffle selection, in this work helical and double segmental baffle were evaluated. While the baffle distance is different for both, *i.e.*, 1.64 and 1 cm for helical and double-segmental baffle, respectively, the baffle distance does not give significant effect to the performance. **Table 2** gives the experimental results and indicates that the  $\Delta T_c$  for heat exchanger with helical baffles is higher than that with double segmental baffles, *i.e.*, 17.7°C vs. 14.4°C. This condition in turn yields

Baffle Modification	Parameter	$\Delta T$ (°C)	$\Delta P$ (kPa)	$\epsilon$
Baffle Type	Helical (distance: 164 mm)	17.7	7.36	0.35
	Double Segmental (distance: 100 mm)	14.4	14.48	0.30
Baffle angle (°) ( <i>Helical baffle</i> )	6	25.4	123.9	0.50
	7	21.4	88.4	0.45
	8	15.7	70.7	0.32
Baffle angle (°) ( <i>Double segmental baffle</i> )	15	24	183.4	0.48
	30	13.7	179.5	0.27
	45	4.7	178.1	0.09
Baffle Distance (cm) ( <i>Disc and doughnut baffle</i> )	0.3	48.0	1.95	0.93
	0.6	8.0	2.98	0.20
	0.9	9.0	2.21	0.15

**Table 2.** Summarized parameters in heat exchanger upon baffle modification. The data was compiled from Ref. [11, 27–29].



**Figure 4.** The helical baffle angle ( $\alpha$ ) configuration in the shell and tube heat exchanger.

effectiveness of 0.35 which is 15% higher than the effectiveness of shell and tube heat exchanger using double segmental baffles.

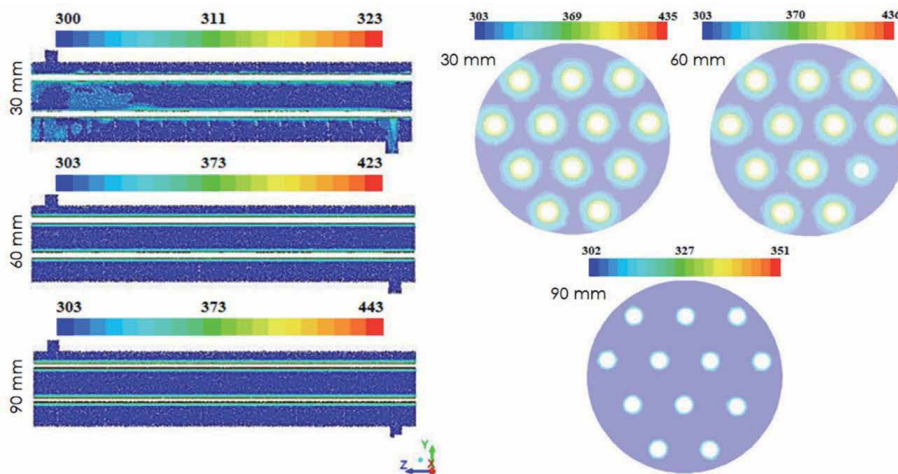
As both helical and double segmental baffle show comparable performance when used in shell and tube heat exchanger, the discussion is directed to effect of baffle angle to the heat exchanger performance. The variation of the baffle angle also influences the  $\Delta T_c$ . Smaller baffle angle tends to decrease  $\Delta T_c$ . This is plausibly since more baffles leads to a lower heat transfer passing through the tube due to the flow disturbance by the large number of baffles (see configuration **Figure 4**). The smaller angle, it will absorb the heat faster so that the heat transfer from hot to cold fluid stream becomes less efficient. As noted in **Table 2**, the heat exchange effectiveness drops from 0.50 to 0.32 by changing the baffle angle from 5° to 7°. This trend is somewhat similar to the effect of changing double segmental baffle angle from 15° to 45° which leads to decreasing  $\Delta T_c$ ,  $\Delta P$  and effectiveness quite significantly.

While smaller baffle angle is advantageous for heat exchanger, smaller baffle distance is also preferable for heat exchanger. This is confirmed by both experimental and numerical study. The effect of baffle distance in helical baffled shell and tube heat exchanger as assessed by computational fluid dynamics (CFD) approach shows that distancing the baffles from 30 to 90 cm decreases  $\Delta T_c$  from 48.0 to 9.0° C which results in a decreasing effectiveness from 0.93 to 0.15. The CFD results can be evaluated from the static temperature profile as displayed in **Figure 5**. As shown,

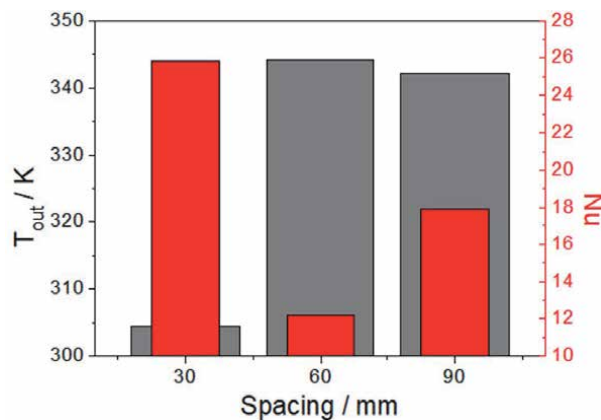


it is clear that the temperature profile of the fluid flow in the heat exchanger with a baffle distance of 30 mm is substantially different from others. The non-uniform temperature distribution is observed in the first quarter of the heat exchanger due to the turbulence flow as there are dead spaces and recirculation zones. Nonetheless, this phenomenon significantly enhances the thermo-hydraulic performance. A more uniform temperature profile in the shell side of the heat exchangers with baffle distance of 60 and 90 mm is observed. Taking a close look at the temperature distribution around the arranged tubes (Figure 5, right), significant radial distribution of temperature from the outer surface of tubes is visible for heat exchanger using 30 and 60 mm baffle distance whilst a subtle temperature changes in the surrounding the tubes is observed for heat exchanger using 90 mm-distanced baffle. At this juncture, 30 mm baffle distance is preferable for shell and tube heat exchanger design.

Other thermophysical properties of heat exchangers with a variation of the baffle distance can also be deduced from CFD, e.g. outflow temperature ( $T_{out}$ ) and Nusselt number (Nu) as shown in Figure 6. The outflow temperature ( $T_{out}$ ) of hot



**Figure 5.** Cross sectional at y-axis (left) and z-axis (right) of steady state static temperature distribution in heat exchanger using 30, 60, and 90 mm baffle distance. The color code unit is K. figures from Ref. [27] used with permission.



**Figure 6.** Thermophysical parameters deduced from numerical calculation, including outlet temperature ( $T_{out}$ ), and Nusselt number (Nu).

stream is the lowest for the utilization of 30 mm-distanced baffles while heat exchanger using baffle distance of 60 and 90 mm shows  $T_{out}$  which is on par. This result indicates that the shell and tube heat exchanger with 30 mm baffle distance has the highest heat transfer from the hot to the cold fluid flow. Further, the Nusselt number displays similar trend. The highest Nu is observed for the heat exchanger using 30 mm-distanced baffles. Increasing the baffle distance from 30 mm to 60 and 90 mm lowers the Nu down to 12 and 18, respectively. It should be noted that higher Nu reflects a more efficient convection favorable in the shell and tube heat exchanger.

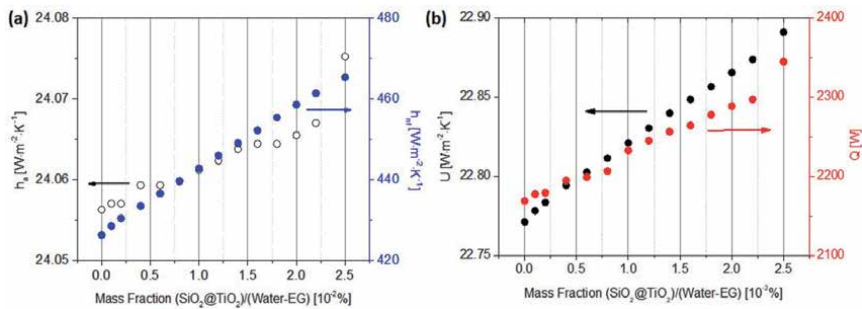
#### 4.2 Effect of Nanofluids materials and concentration

It is already mentioned that the use of nanoparticles in nanofluid is to increase the conductivity of the base fluid and hence, the overall thermal transfer coefficient. Here, we used both ultra-low concentration (0.002–0.025%) and typical doping concentration (0.5–1.5%) of nanoparticles in the corresponding base fluids for the use of  $Al_2O_3$  and core-shell  $SiO_2@TiO_2$ , respectively [10, 15]. In general, the heat transfer performance of nanofluids can be indirectly assessed by the dynamic of temperature changes in either the hot ( $T_h$ ) or cold ( $T_c$ ) fluid flow and the altered U value upon changing the nanoparticle concentration in the base fluid. These two parameters are summarized in **Table 3**.

To begin the discussion, the use of nanofluids at the lowest concentration will be first discussed. In this work, we have employed a core-shell  $SiO_2@TiO_2$  nanoparticles enriched water-ethylene glycol (EG) mixture. The result show that the  $T_c$  of outflow is higher with increasing concentration of  $SiO_2@TiO_2$  nanofluids. This observation indicates that the higher the concentration of nanofluids, the higher the heat is transferred as the thermal conductivity of  $SiO_2@TiO_2$  increases. Furthermore, the addition of  $SiO_2@TiO_2$  to the base fluid can result in an increase in the value of the convection coefficient of nanofluid as shown **Figure 7(a)**. It is also interesting to note that changing the mass fraction of  $SiO_2@TiO_2$  affects the convection coefficient of the air blown to the heat exchanger due to increasing contact surface area during the heat transfer process. The addition of  $SiO_2@TiO_2$  nanoparticles at a concentration of 0.025% increases the heat transfer coefficient by 9.2%.

Nanofluids	Nanoparticle concentration (% v/v)	U ( $Wm^{-2} K^{-1}$ )	$\Delta T_c$ ( $^{\circ}C$ )	$\epsilon$
$SiO_2@TiO_2$ in Water-EG	0	22.76	11.4	0.203
	0.002	22.78	11.6	0.208
	0.008	22.82	12.8	0.218
	0.010	22.84	13.4	0.222
	0.016	22.86	15.0	0.224
	0.020	22.88	15.4	0.238
	0.025	22.90	16.9	0.246
$Al_2O_3$ in Water	0	29.93	10.7	0.178
	0.5	30.14	15.0	0.261
	1.0	30.19	18.4	0.350
	1.5	30.31	24.7	0.422

**Table 3.** Summarized parameters of the thermal properties of nanofluids and the shell and tube heat exchanger upon the utilization of nanofluids [10, 15].



**Figure 7.** (a) The estimated convection coefficient of air ( $h_a$ ) and SiO<sub>2</sub>@TiO<sub>2</sub> nanofluids ( $h_{nf}$ ). (b) the overall heat transfer coefficient ( $U$ ) and heat rate ( $W$ ) in heat exchanger using different concentration of SiO<sub>2</sub>@TiO<sub>2</sub> nanofluids. Figures from ref. [15] used with permission.

Evaluating the total heat transfer coefficient, the results show that there is no significant increase. Only slight increase of about 0.03–0.07% is observed for each increment of mass fraction. At the same flow rate (8 liter per min) increasing the concentration of SiO<sub>2</sub>@TiO<sub>2</sub> nanoparticles up to 0.025% yields an increasing heat transfer rate up to 18.11% (from 2168  $W \cdot m^{-2}$  to 2344  $W \cdot m^{-2}$ ). This heat transfer rate is higher than that of water based nanofluid containing TiO<sub>2</sub> nanoparticles: At a concentration of 0.25%, the heat transfer rate is only enhanced by 11% [30]. This further implies that the heat transfer rate of the low concentration SiO<sub>2</sub>@TiO<sub>2</sub> nanofluids can be improved by increasing the flowrate of nanofluids in the heat exchanger. In general, the effectiveness of heat transfer using different SiO<sub>2</sub>@TiO<sub>2</sub> concentration is linearly increasing with increasing the mass fraction of nanoparticles in the base fluid. It is shown that the effectiveness of heat transfer increases by 1.6–2% for increasing mass fraction by 0.005%. Overall, there is an increase in the effectiveness of heat exchanger by 21% (from 0.203 to 0.246) when the water:EG base fluid is added with 0.025% SiO<sub>2</sub>@TiO<sub>2</sub>. The results indicate that the additional nanoparticles shows better performance of heat exchanger than another study using EG:water (3:2) based nanofluid containing only 0.02% TiO<sub>2</sub> which shows an increase of effectiveness by 13% [22].

For higher concentration of nanoparticles, *i.e.*, Al<sub>2</sub>O<sub>3</sub> in the base fluid of water shows similar trend as compared to the SiO<sub>2</sub>@TiO<sub>2</sub> in water:EG nanofluid. Addition of merely 0.5% Al<sub>2</sub>O<sub>3</sub> already increases  $\Delta T_c$  by 5°C. Further increasing nanoparticles concentration from up to 1.5% results in  $\Delta T_c$  of 24.7°C (*vs.* 10.7°C for pure water as working fluid). Interestingly, the  $U$  value does not change significantly as also observed for SiO<sub>2</sub>@TiO<sub>2</sub> in water:EG nanofluid. The  $U$  value for base fluid of water is known 29.93  $W \cdot m^{-2} \cdot K^{-1}$  while the deployment of Al<sub>2</sub>O<sub>3</sub> up to 1.5% volume fraction only improves  $U$  value up to 30.31  $W \cdot m^{-2} \cdot K^{-1}$ . Of course, the observed effects in the Al<sub>2</sub>O<sub>3</sub>-water nanofluid can be explained by the same phenomena as previously discussed in the SiO<sub>2</sub>@TiO<sub>2</sub> in water:EG nanofluid.

## 5. Conclusion

In this chapter, we have shown that improvement of shell and tube heat exchanger effectiveness can be achieved by optimizing the baffle architecture and by using nanofluids to substitute the conventional working fluid. We have investigated the effect of baffle type and baffle distance in the laboratory scale of shell and tube heat exchanger using experimental and numerical approach, respectively. In

general, the heat exchanger effectiveness is affected by the baffle arrangement and type. It is found that helical baffle is preferable than double segmental baffle which yields 15% higher effectiveness. Larger baffle separation distance consistently shows a significantly decreasing heat transfer rate as indicated by lower  $\Delta T$ . This in turn lowers the heat exchanger effectiveness quite substantially. In addition, angle also quite essential to optimize. For the utilization of helical baffle, only changing  $5^\circ$  to  $7^\circ$  already lowers the effectiveness from 0.50 down to 0.32.

The utilization of nanofluid has been demonstrated to enhance the heat transfer process yielding higher effectiveness. Even at the extremely low concentration of nanoparticles, *i.e.*, 0.002 to 0.025%, the water-ethylene glycol based nanofluids containing  $\text{SiO}_2@\text{TiO}_2$  core-shell nanoparticles enable enhancement of heat exchanger effectiveness by 20%. This finding is essential as it is not necessary to use high concentration of nanoparticles to improve heat exchanger effectiveness while avoiding fouling inside the tubing system of shell and tube heat exchanger. Another set of examples has been shown that using water based working fluid using  $\text{Al}_2\text{O}_3$ . Increasing volume fraction of  $\text{Al}_2\text{O}_3$  nanoparticles significantly boosts the effectiveness up to 0.422 which is plausibly a result of increasing thermal conductivity of the water base fluid.

## Acknowledgements

Financial support by the Center of Research and Development (*Lembaga Penelitian dan Pengabdian Kepada Masyarakat*) of Universitas Negeri Surabaya and the directorate of research and community development (*Direktorat Riset dan Pengabdian Kepada Masyarakat*) of Institut Teknologi Sepuluh Nopember is highly acknowledged. Authors also would like to thank to the Mechanical Engineering Department and Heat Transfer Laboratory of Universitas Negeri Surabaya for their technical support.

## Conflict of interest

Authors declare that there is no conflict of interest.

## Nomenclature

$C_c, C_h$	Heat capacity of hot and cold fluid, $\text{W}/^\circ\text{C}$
$\dot{m}_h, \dot{m}_c$	mass flow rate, $\text{kg}/\text{s}$
$C_{p,h}, C_{p,c}$	Specific heat of hot and cold fluid, $\text{J}/\text{kg } ^\circ\text{C}$
$h$	Enthalpy, $\text{J}/\text{kg } ^\circ\text{C}$
$q_{max}$	Maximum heat transfer (W)
$q_{actual}$	Actual heat transfer (W)
$T$	Temperature, $^\circ\text{C}$ or K
$u$	Velocity of the medium, $\text{m}/\text{sec}$ .
$V$	Volume, $\text{m}^3$
$\varepsilon$	heat exchanger effectiveness, n.d

## Subscripts

h, c	Refers to hot and cold fluid
i, o	Refers to inflows and outflows

## Greek symbols

$\beta$	Extinction or attenuation coefficient, $\text{m}^{-1}$
$\theta$	Polar or cone angle measured from normal of surface, rad.
$\rho_f$	Density of a fluid. $\text{kg}/\text{m}^3$
$\sigma_{scat}$	Scattering coefficient, $\text{m}^{-1}$
$\sigma_{abs}$	Scattering coefficient, $\text{m}^{-1}$
$\phi$	Azimuthal angle, rad.
$\Phi$	Scattering phase function
$\Omega$	Solid angle, sr

## Author details


I Made Arsana<sup>1\*</sup> and Ruri Agung Wahyuono<sup>2</sup>

1 Department of Mechanical Engineering, Faculty of Engineering, Universitas Negeri Surabaya, Surabaya, East Java, Indonesia

2 Department of Engineering Physics, Faculty of Industrial Technology and System Engineering, Institut Teknologi Sepuluh Nopember, Surabaya, Indonesia

\*Address all correspondence to: [madearsana@unesa.ac.id](mailto:madearsana@unesa.ac.id)

## IntechOpen

© 2021 The Author(s). Licensee IntechOpen. This chapter is distributed under the terms of the Creative Commons Attribution License (<http://creativecommons.org/licenses/by/3.0/>), which permits unrestricted use, distribution, and reproduction in any medium, provided the original work is properly cited. 

## References

- [1] Mazubert A, Fletcher DF, Poux M, Aubin J. Hydrodynamics and mixing in continuous oscillatory flow reactors – Part I: Effect of baffle geometry. *Chem. Eng. Process.: Process Intensification* 2016; 108; 78–92. DOI:10.1016/j.cep.2016.07.015
- [2] Akbar FR, Arsana IM. Effect of Wire Pitch on Capacity of Single Staggered Wire and Tube Heat Exchanger Using Computational Fluid Dynamic Simulation. *International Journal of Engineering*. 2020;33;1637–1642. DOI: 10.5829/ije.2020.33.08b.22
- [3] Arsana IM, Susianto, Budhikarjono K, Altway A. Optimization of The Single Staggered Wire and Tube Heat Exchanger. *MATEC Web of Conferences*. 2016;58; 01017. DOI: 10.1051/mateconf/20165801017
- [4] Javaran EJ, Nassab SAG, Jafari S. Numerical Simulation of a Three-Layered Radiant Porous Heat Exchanger Including Lattice Boltzmann Simulation of Fluid Flow. *International Journal of Engineering Transaction A: Basics*. 2011; 24; 301–319. DOI:10.5829/idosi.ije.2011.24.03a.09
- [5] He X, Zhao H, Chen X, Luo Z, Miao Y. Hydrodynamic Performance Analysis of the ducted propeller Based on the Combination of Multi-Block Hybrid Mesh and Reynolds Stress Model. *Journal of flow control, Measurement, and Visualization*. 2015; 3; 67–74. DOI:10.4236/jfcmv.2015.32007
- [6] Assari MR, Tabrizi HB, Parvar M, Farhani MA. Experimental Investigation of Sinusoidal Tube in Triplex-Tube Heat Exchanger during Charging and Discharging Processes Using Phase Change Materials. *International Journal of Engineering Transactions A: Basics*. 2019; 31(7); 999–1009. DOI:10.5829/ije.2019.32.07a.13
- [7] Maurya RS, Singh S. Numerical Investigation of Isothermal Flow Around. Impingement Plates in a Shell and Tube Heat Exchanger. *Journal of Thermal Engineering*. 2017; 3(5);1442–1452. DOI:10.18186/journal-of-thermal-engineering.338901
- [8] Singh G, Nandan A. Experimental Study of Heat Transfer Rate in a Shell and Tube Heat Exchanger with Air Bubble Injection (technical note). *International Journal of Engineering Transactions B: Application*. 2016; 29(8); 1160–1166. doi: 10.5829/idosi.ije.2016.29.08b.16
- [9] Thakur G, Singh G, Thakur M, Kajla S. An experimental study of nanofluids Operated Shell and Tube Heat Exchanger with Air Bubble Injection. *International Journal of Engineering Transaction A: Basics*. 2018; 31; 136–143. DOI: 10.5829/ije.2018.31.01a.19
- [10] Arsana IM, Agista DR, Ansori A, Sutjahjo DH, Effendy M. The Effect of Nanofluid Volume Fraction to The Rate of Heat Transfer Convection Nanofluid Water- $\text{Al}_2\text{O}_3$  on Shell and Tube Heat Exchanger. *Journal of Physics: Conference Series*. 2020;1569;032048. DOI: 10.1088/1742-6596/1569/3/032048
- [11] Arsana IM, Rasyid AHA, Drastiawati NS, Ariyanto SR. The Influence of Baffle Gap to The Effectiveness of Shell and Tube Heat Exchanger with Helical Baffle. *Journal of Physics: Conference Series*. 2020;1569; 042091. DOI: 10.1088/1742-6596/1569/4/042091.
- [12] Lei Y, Li Y, Jing S, Song C, Lyu Y, Wang F. Design and performance analysis of the novel shell-and-tube heat exchangers with lower baffles. *Appl. Thermal Eng.* 2017; 125: 870–879. DOI: 10.1016/j.applthermaleng.2017.07.081
- [13] Sreedhar V, Chandra GR, Kanth TNR, Somaiah A. Experimental

Investigation on Shell and Tube heat Exchanger Using Segmental and Disc-Doughnut Type Baffles. *Int. J. Mechanical Engineering and Technol.* 2017; 8(12): 975–984.

[14] Sarkar S, Singh KK, Shenoy KT. CFD Modeling of Pulsed Disc and Doughnut Column: Prediction of Axial Dispersion in Pulsatile Liquid-Liquid Two-Phase Flow. *Ind. Eng. Chem. Res.* 2019; 58(33): 15307–15320. <https://doi.org/10.1021/acs.iecr.9b01465>

[15] Arsana IM, Muhimmah LC, Nugroho G, Wahyuono RA. Enhanced Heat Transfer Effectiveness Using Low Concentration SiO<sub>2</sub>-TiO<sub>2</sub> Core-Shell Nanofluid in a Water/Ethylene Glycol Mixture. *Journal of Engineering Physics and Thermophysics.* 2021; 94(2): 439-446.

[16] Rusu MM, Wahyuono RA, Fort CI, Dellith A, Dellith J, Ignaszak A, Vulpoi A, Danciu V, Dietzek B, Baia L. Impact of drying procedure on the morphology and structure of TiO<sub>2</sub> xerogels and the performance of dye-sensitized solar cells. *J. Sol-Gel Sci. Technol.* 2017; 81(3): 693–703.

[17] Ebrahimnia-Bajestan E, Moghadam MC, Niazmand H, Daungthongsuk W, Wongwises S. Experimental and numerical investigation of nanofluids heat transfer characteristics for application in solar heat exchangers. *International Journal of Heat Mass Transfer.* 2016; 92: 1041–1052.

[18] Davarnejad R, Kheiri M. Numerical Comparison of Turbulent Heat Transfer and Flow Characteristics of SiO<sub>2</sub>/Water Nanofluid within Helically Corrugated Tubes and Plain Tube. *International Journal of Engineering, Transaction B: Applications.* 2015; 28: 1408–1414.

[19] Duangthongsuk W, Wongwises S. Measurement of temperature-dependent thermal conductivity and

viscosity of TiO<sub>2</sub>-water nanofluids. *Experimental Thermal Fluid Science.* 2009; 33: 706–714.

[20] Barzegarian R, Moraveji MK, Aloueyan A. Experimental investigation on heat transfer characteristics and pressure drop of BPHE (brazed plate heat exchanger) using TiO<sub>2</sub>-water nanofluid. *Experimental Thermal Fluid Science.* 2016; 74: 11–18.

[21] Azmi WH, Hamid KA, Mamat R, Sharma KV, Mohamad MS. Effects of working temperature on thermo-physical properties and forced convection heat transfer of TiO<sub>2</sub> nanofluids in water – ethylene glycol mixture. *Applied Thermal Engineering.* 2016; 106: 1190–1199.

[22] Reddy MCS, Rao VV. Experimental studies on thermal conductivity of blends of ethylene glycol-water-based TiO<sub>2</sub> nanofluid. *International Community Heat Mass Transfer.* 2013; 46: 31–36.

[23] Bhanvase BA, Sarode MR, Putterwar LA, Abdullah KA, Deosarkar MP, Sonawane SH. Intensification of convective heat transfer in water/ethylene glycol based nanofluids containing TiO<sub>2</sub> nanoparticles. *Chemical Engineering Process.* 2014; 82: 123–131.

[24] Hamid KA, Azmi WH, Mamat R, Sharma KV. Experimental investigation on heat transfer performance of TiO<sub>2</sub> nanofluids in water-ethylene glycol mixture, *International Community Heat Mass Transfer.* 2016; 73: 16–24.

[25] Davarnejad R, Ardehali RM. Modeling of TiO<sub>2</sub>-water Nanofluid Effect on Heat Transfer and Pressure Drop, *International Journal of Engineering, Transaction B: Applications.* 2014; 27: 195–202.

[26] Pirhayati M, Akhavan-Behabadi MA, Khayat M. Convective Heat

Transfer of Oil based Nanofluid Flow inside a Circular Tube, *International Journal of Engineering, Transaction B: Applications*. 2014; 27; 341–348.

[27] Arsana IM, Wiyanto T, Wijanarko DV, Soeryanto, Wahyuono RA, Numerical Investigation on The Performance of Shell and Tube Heat Exchanger with Modified Disc and Doughnut Baffle Distance. (submitted)

[28] Arsana IM, Setyawan R. Simulation Study on Effect of Baffle Angle to the Heat Exchanger Effectiveness on Shell and Tube Heat Exchanger Using Helical Baffle. (submitted)

[29] Nada QA, Arsana IM, Study on New-Orientation of Baffle in Shell and Tube Heat Exchanger using Double Segmental Baffle. (submitted)

[30] Eiamsa-ard SK, Kiatkittipong K, Jedsadaratanachai W. Heat Transfer Enhancement of  $\text{TiO}_2$ /Water Nanofluid in A Heat Exchanger Tube Equipped with Overlapped Dual Twisted-tapes. *Engineering Science and Technology, an International Journal*. 2015; 18; 336–350.



# Heat Transfer in a MHD Nanofluid Over a Stretching Sheet

*Vikas Poply*

## Abstract

The intention behind carrying out this research work is to analyze the heat transfer characteristics in a Magnetohydrodynamic (MHD) boundary layer nanofluid flow over a stretching sheet. Two phase representation of nanofluid studied the consequence of Brownian motion along with thermophoresis. The major purpose of study is to investigate the significant role of prominent fluid parameters thermophoresis, Brownian motion, Eckert number, Schmidt number and magnetic parameter on profile of velocity, temperature distribution and concentration. Runge–Kutta Fehlberg (RKF) method was adopted to numerically solve the non-linear governing equations and the linked boundary conditions by use of shooting technique. Over all the consequence of prominent fluid parameters are explained via graphs, whereas distinction of several valuable engineering quantities like skin friction coefficient, local Nusselt number and local Sherwood number are also tabulated. The finding of present study helps to control the rate of heat transportation as well as fluid velocity in any manufacturing processes and industrial applications to make desired quality of final product.

**Keywords:** heat transfer, nanofluid, stretching sheet, MHD flow

## 1. Introduction

In various fields of science and technology rapid progress has urged the researchers to extend their study towards the regime of boundary layer flow over a stretching sheet. The boundary layer flow behavior towards a linearly or non-linearly stretching sheet plays a significant role for solving engineering problems and possess vast applications in manufacturing and production processes including metal spinning, rubber sheet manufacturing, production of glass fibers, wire drawing, extrusion of polymer sheets, petroleum industries, polymer processing etc. In these cases, the final product of desired characteristics depends on the rate of cooling in the process and the process of stretching. The dynamics of the boundary layer fluid flow over a stretching surface originated from the pioneering work of Crane [1] and he examined the incompressible steady boundary layer fluid flow caused by stretching sheet which moves in its own plane with linear velocity due to the uniform stress applications. This problem is particularly interesting as Crane [1] obtained the exact solution of 2D Navier–Stokes equations. Afterthat, Gupta and Gupta [2] extend Crane [1] work over different mathematical geometries. Yoon et al. [3] studied the theoretical and experimental results using Coulomb friction model by considering punch-sheet interface. Also, Sarma and Rao [4] examined the viscoelastic fluid flow by considering stretched sheet. In view of this, Vajravelu [5]

studied flow and heat transfer in a viscous fluid over a nonlinear stretching sheet without using the impact of viscous dissipation. Cortell [6] examined heat and fluid flow transportation over a nonlinear stretching sheet for two different types of thermal boundary conditions, prescribed surface temperature (PST) and constant surface temperature (CST). The influence of heat transfer on the stagnation point flow of a third-order fluid over a shrinking surface has been studied by Nadeem et al. [7]. Recently, Prasad et al. [8] examined the mixed convection heat transfer aspects with variable fluid flow properties over a non-linear stretching surface.

Fluid heating and cooling are important in many industries such as power, manufacturing and transportation. Effective cooling techniques are greatly needed for cooling any sort of high energy device. Common heat transfer fluids such as water, ethylene glycol, and engine oil have limited heat transfer capabilities due to their low heat transfer properties. In contrast, metals have thermal conductivities up to three times higher than these fluids, so it is naturally desirable to combine the two substances to produce a heat transfer medium that behaves like a fluid, but has the thermal of a metal. Since last two decades, study of nanofluid has urged the researcher's attention due to their heat transportation rate. Nanofluid comes in existence when we add a small quantity of nano-sized  $10^{-9} - 10^{-7}$  particles to the base fluids. Low heat transportation fluids like fluorocarbons, glycol, deionized water, etc. have badly thermal conductivity and therefore deliberated necessary for heat transfer coefficient surrounded by heat transfer medium and surface. The nanoparticles are typically made up of metals (*Al, Cu*), nitrides (*AlN, SiN*), carbides (*Sic*), oxides (*Al<sub>2</sub>O<sub>3</sub>*), or nonmetals (carbon nanotubes, Graphite, etc.) and the base fluid (conductive fluid) is usually water or ethylene glycol. Also, it has been experimentally proved that rate of heat conduction of nanofluids is more than rate of heat conduction of the base fluids. The concept of nanofluid was initially proposed by Choi and Eastman [9] to indicate engineered colloids composed of nanoparticles dispersed in a base fluid. An MIT based comprehensive survey has been done by Buongiorno [10] for convective transportation in nanofluids by considering seven slip conditions that may produce a relative velocity within the base fluid and nanoparticles. Only two (Brownian motion and thermophoresis) out of these seven slip mechanisms were found to be important mechanisms. By adopting Buongiorno's model, Kuznetsov and Nield [11] explored the nanofluid boundary layer uniform convecting fluid flow.

In recent years, MHD fluid flow has gained researchers attention due to its controllable heat transfer rate. Magnetohydrodynamics (MHD) effect also play and influential role in controlling the rate of cooling as well as segregation of molten metal's from various non-metallic impurities. Magnetohydrodynamic (MHD) fluid flow has enormous utilization in manufacturing processes, even in the industrial areas as well. The terminology "Magnetohydrodynamic" is combination of three elementary terms magneto that stands for magnetic field, hydro that stands for fluid/liquid and dynamics that stands for evolution of particles. The existence of external magnetic field gives rise to Lorentz drag force which acts on the fluid, so potentially altering the characteristics of fluid flow especially velocity, temperature and concentration. Grouping of electromagnetism Maxwell's equation and fluid mechanics Navier's stokes equations therefore provides Magnetohydrodynamic (MHD) relation [12, 13]. Hayat et al. [14] studied the MHD fluid flow transportation over stretching surfaces. Later, the influence of viscous and Ohmic dissipation (i.e. joule heating) in nanofluid has been presented by Hussain et al. [15]. Vajravelu and Canon [16] studied the flow behavior of fluid towards a non-linear stretching sheet. Further, Matin et al. [17] analyzed the entropy effect in MHD nanofluid flow over stretching surface. Shawky et al. [18] studied the Williamson nanofluid flow in porous medium and he acknowledged that enhancement in non-Newtonian parameter escalates skin friction

coefficient along with the rate of heat transfer. Basir et al. [19] examined the consequences of Peclet and Schmidt number in existence of partial slip towards a stretching surface. After that, rate of heat transfer along with partial slip condition was generalized by Pandey and Kumar [20]. Recently, Vinita and Poply [21] discussed MHD slip fluid flow of nanofluid in the existence of free stream velocity or outer velocity towards a stretching surface. Vinita et al. [22] studied MHD fluid flow with variable slip conditions over non-linear stretching surface. Furthermore, non-linearity effect towards the stretching surface under different physical circumstances has been examined by researchers in [6, 23–25].

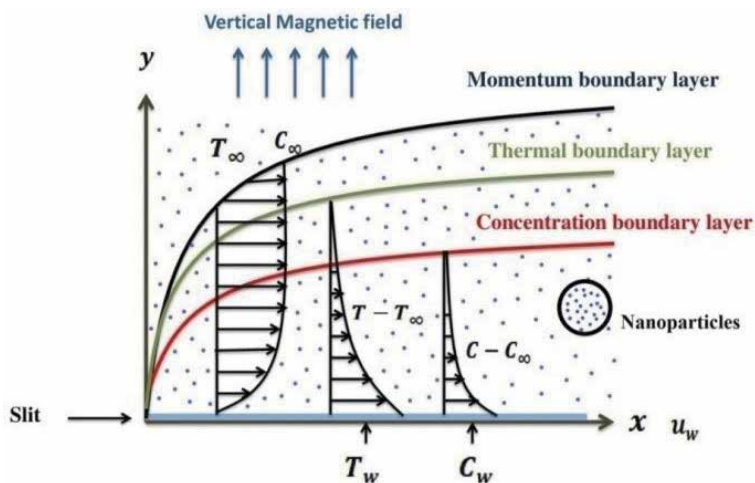
The outcomes of current study reveal that the results obtained is very significant in the formation of quality object in various manufacturing processes like polymer engineering, paper technology, wire and plastic industries. This study holds important industrial application, particularly in the field of extrusion where the fluid dispersed with particles is used to augment the strength and durability of the material.

## 2. Materials and methods

In present analysis, 2-D incompressible fluid flow in MHD nanofluid over linear stretching sheet has been considered. Linear behavior generates flow and sheet is stretched in both direction of  $x$  axis with stretching velocity  $u_w = ax$ , where  $a$  and  $x$  denotes a constant and stretching surface coordinate respectively.  $T_w = T_\infty + T_0x^m$  at  $y = 0$ , where  $T_0$  refers to the positive constant,  $T_\infty$  refers to the ambient temperature attained and  $m$  refers to the physical parameter known as surface temperature parameter. Also, by introducing  $m = 0$ , we have a special case of constant surface temperature (CST). **Figure 1** represents the physical model of the current study. The continuity, momentum, energy and concentration equations of the incompressible nanofluid boundary layer flow are as follows [10]

$$\frac{\partial u}{\partial x} + \frac{\partial v}{\partial y} = 0 \quad (1)$$

$$u \frac{\partial u}{\partial x} + v \frac{\partial u}{\partial y} = \nu \frac{\partial^2 u}{\partial y^2} - \frac{\sigma B^2}{\rho} u \quad (2)$$



**Figure 1.**  
 Physical model and coordinate system.

$$u \frac{\partial T}{\partial x} + v \frac{\partial T}{\partial y} = \tau \left[ D_B \frac{\partial C}{\partial y} \frac{\partial T}{\partial y} + (D_T/T_\infty) \left( \frac{\partial T}{\partial y} \right)^2 \right] \quad (3)$$

$$u \frac{\partial C}{\partial x} + v \frac{\partial C}{\partial y} = D_B \frac{\partial^2 C}{\partial y^2} + \frac{D_T}{T_\infty} \frac{\partial^2 T}{\partial y^2} \quad (4)$$

Boundary conditions are given as:

$$u = u_w, v = 0, T = T_w, C = C_w \text{ at } y = 0 \quad (5)$$

$$u \rightarrow 0, T \rightarrow T_\infty, C \rightarrow C_\infty \text{ as } y \rightarrow \infty \quad (6)$$

Here horizontal and vertical velocities are represented by  $u$  and  $v$ , respectively. Also  $\nu$  denotes kinematic viscosity,  $\rho$  is the density of fluid,  $\tau = \frac{(\rho c)_p}{(\rho c)_f}$  defines a proportion of heat capacities,  $D_T$  reflects thermophoretic diffusion coefficient,  $B$  is the magnetic field intensity,  $D_B$  denotes Brownian diffusion coefficient,  $\sigma$  represents electrical conductivity

The fundamental Eqs. (1)-(4) with boundary conditions (5) and (6) are transformed using similarity variables

$$u = ax f'_\delta(\xi), v = -\sqrt{a\nu} f_\delta(\xi) \quad (7)$$

$$\phi_\delta(\xi) = \frac{C - C_\infty}{C_w - C_\infty}, \theta_\delta(\xi) = \frac{T - T_\infty}{T_w - T_\infty}, \xi = y \sqrt{\frac{a}{\nu}}$$

Inserting Eq. (7) into Eqs. (2)-(4), the governing Eqs. (1)-(4) takes the form

$$f_\delta''' + f_\delta f_\delta'' - M f_\delta' - f_\delta'^2 = 0 \quad (8)$$

$$\frac{1}{Pr} \theta_\delta'' + f_\delta \theta_\delta' - f_\delta' \theta_\delta + Nb \theta_\delta' \phi_\delta' + Nt \theta_\delta'^2 + Ec f_\delta'^2 + MSc f_\delta'^2 = 0 \quad (9)$$

$$\phi_\delta'' + \frac{1}{2} Sc f_\delta \phi_\delta' + \frac{Nt}{Nb} \theta_\delta'' = 0 \quad (10)$$

The relevant boundary conditions are reduced to

$$f_\delta(\xi) = 0, f_\delta'(\xi) = 1, \theta_\delta(\xi) = 1 \text{ and } \phi_\delta(\xi) = 1 \text{ at } \xi = 0 \quad (11)$$

$$f_\delta'(\xi) \rightarrow 0, \phi_\delta(\xi) \rightarrow 0 \text{ and } \theta_\delta(\xi) \rightarrow 0 \text{ as } \xi \rightarrow \infty \quad (12)$$

where prime denotes derivative with respect to  $\xi$  and the key crucial parameters are defined by:

$$M = \frac{\sigma B^2}{a}, Nt = \frac{(\rho c)_p D_T (T_w - T_\infty)}{(\rho c)_f \nu T_\infty}, Sc = \frac{\nu}{D_B}, Pr = \frac{\nu}{\alpha}, \quad (13)$$

$$Ec = \frac{u_w^2}{C_p (T_w - T_\infty)} \text{ and } Nb = \frac{(\rho c)_p D_B (C_w - C_\infty)}{(\rho c)_f \nu}$$

Here  $M$  is the magnetic parameter,  $Nt$  is the thermophoresis parameter,  $Sc$  is the Schmidt number,  $Pr$  is Prandtl number,  $Ec$  is the Eckert number and  $Nb$  is the Brownian motion parameter. Also, the physical quantities of interest skin friction coefficient, local Nusselt number and local Sherwood number are respectively defined as:

$$Cf_x = \frac{\tau_w}{\rho u_w^2}, Nu_x = \frac{xq_w}{k(T_w - T_\infty)} \text{ and } Sh_x = \frac{xq_m}{D_B(C_w - C_\infty)} \quad (14)$$

where  $\tau_w$ ,  $q_w$  and  $q_m$  are wall shear stress, local heat flux and local mass flux at the stretching surface serially given as:

$$\tau_w = \mu \alpha x^{\frac{1}{2}} \sqrt{\frac{a}{\nu}} f''_\delta(0), q_w = -k(T_w - T_\infty) \sqrt{\frac{a}{\nu}} \theta'_\delta(0) \text{ and } q_m = -D_B(C_w - C_\infty) \sqrt{\frac{a}{\nu}} \phi'_\delta(0) \quad (15)$$

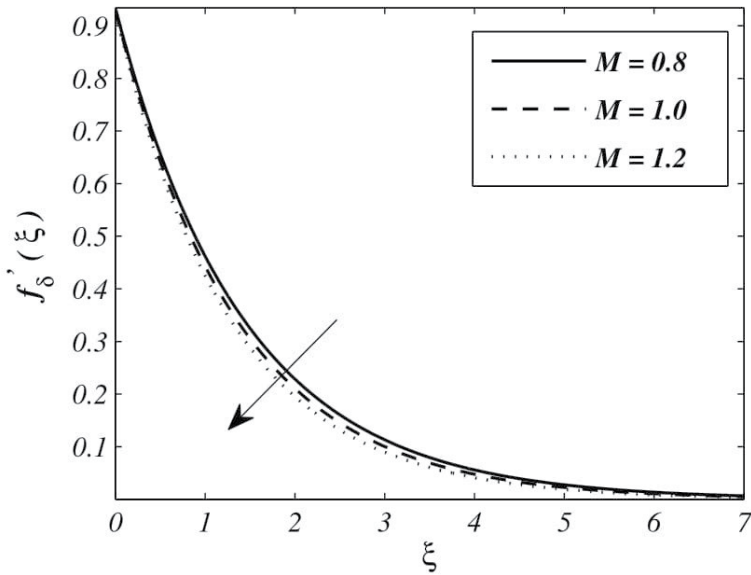
### 3. Results and discussion

Present study finds numerical solution of differential Eqs. (8)–(10) subjected to the boundary conditions (11) and (12) that are computed using RKF method by applying shooting technique. The main reason behind to solve the present problem are to determine the impact of prominent fluid parameters namely Eckert number  $Ec$ , thermophoresis  $Nt$ , Brownian motion parameter  $Nb$ , Schmidt number  $Sc$  and magnetic parameter  $M$  on  $f'_\delta(0)$ ,  $\theta'_\delta(0)$  and  $\phi'_\delta(0)$ . **Table 1** demonstrate the impact of fluid parameters  $Nb$ ,  $Nt$ ,  $Ec$ ,  $Sc$  and  $M$  on skin friction coefficient  $f''_\delta(0)$ , local Nusselt number  $-\theta'_\delta(0)$  and local Sherwood number  $-\phi'_\delta(0)$  by taking fixed entries of fluid parameters Prandtl number,  $Pr$  as 5.0 and surface temperature parameter  $m$  as 1.0.

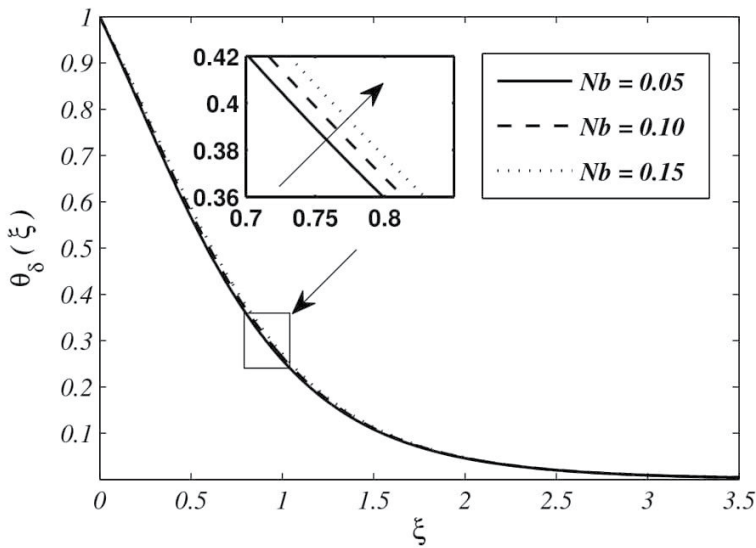
**Figure 2** manifests variation in fluid velocity against magnetic parameter  $M$  (0.8, 1.0, 1.2). This figure shows that existence of magnetic parameter  $M$  resists the fluid particle to move freely and main reason behind the resistance is that magnetic parameter  $M$  produces Lorentz force and this magnetism behavior can be adopted for controlling the fluid movement. Thus, enhancement in the value of magnetic parameter  $M$  causes the declination of velocity distribution

$Nb$	$Nt$	$Ec$	$Sc$	$M$	$f''_\delta(0)$	$-\theta'_\delta(0)$	$-\phi'_\delta(0)$
0.1	0.2	0.4	1.5	1.0	-0.62674	0.72369	-0.41288
					-0.69140	0.78127	-0.55822
					-0.74178	0.82246	-0.66610
0.05	0.2	0.4	1.5	1.0	-0.69140	0.82355	-1.77998
					-0.69140	0.78127	-0.55822
					-0.69140	0.74045	-0.15292
0.1	0.2	0.4	1.5	1.0	-0.69140	0.78127	-0.55822
					-0.69140	0.73298	-0.95811
					-0.69140	0.68790	-1.28267
0.1	0.2	0.0	1.5	1.0	-0.69140	2.18627	-3.19235
		0.1			-0.69140	1.83840	-2.54049
		0.2			-0.69140	1.48829	-1.88419
0.1	0.2	0.4	1.1	1.0	-0.69140	0.81074	-0.78101
			1.4		-0.69140	0.78800	-0.60993
			1.7		-0.69140	0.76889	-0.46155
0.1	0.2	0.4	1.5	0.8	-0.65763	0.95086	-0.85564
				1.0	-0.69140	0.78127	-0.55882
				1.2	-0.72329	0.61783	-0.27004

**Table 1.** Values of skin friction coefficient  $f''_\delta(0)$ , local Nusselt number  $-\theta'_\delta(0)$  and local Sherwood number  $-\phi'_\delta(0)$  for crucial fluid parameters  $Nb, Nt, Ec, Sc$  and  $M$  with fixed entries of  $Pr = 5.0$  and  $m = 1.0$ .



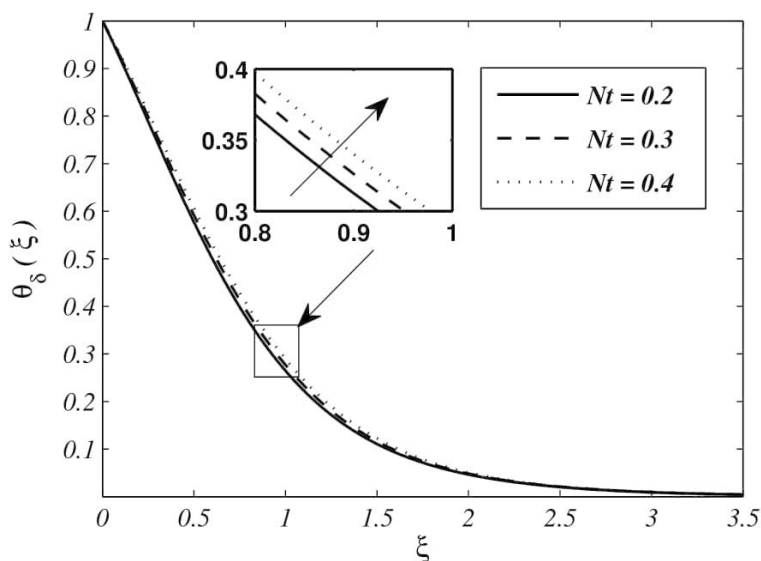
**Figure 2.**  
Impact of magnetic parameter  $M$  on velocity profile  $f'_\delta(\xi)$ .



**Figure 3.**  
Impact of Brownian motion parameter  $Nb$  on temperature profile  $\theta_\delta(\xi)$ .

**Figure 3** examines temperature distribution variation against the fluid parameter Brownian motion parameter  $Nb$  (0.05, 0.10, 0.15). The striking of atoms or molecules of the fluid particles with each other will create an arbitrary motion called Brownian motion of suspended (pendulous) particles and that will enhance width of boundary layer. Hence, fluid temperature increases for higher Brownian motion parameter  $Nb$  and in consequence local Nusselt number decreases.

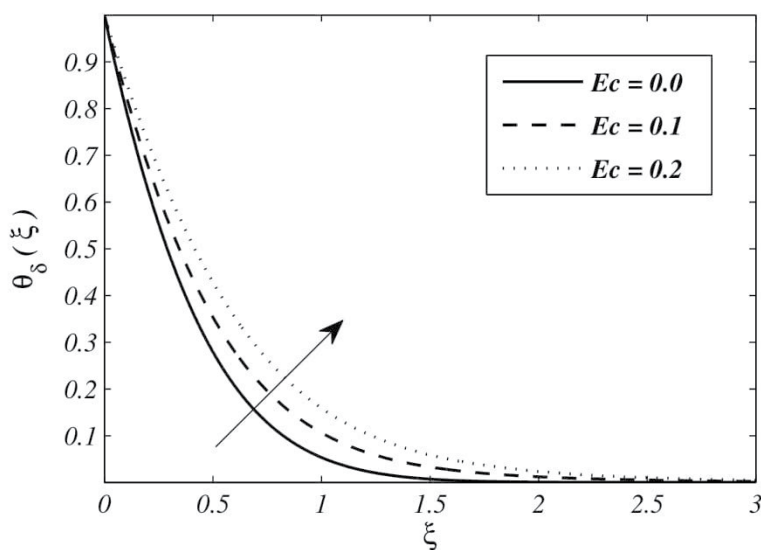
**Figure 4** deliberates the impact of fluid temperature under the consequence of thermophoresis parameter  $Nt$  (0.2, 0.3, 0.4). Temperature gradient falls down for higher values of thermophoresis parameter  $Nt$  that result in reduction of



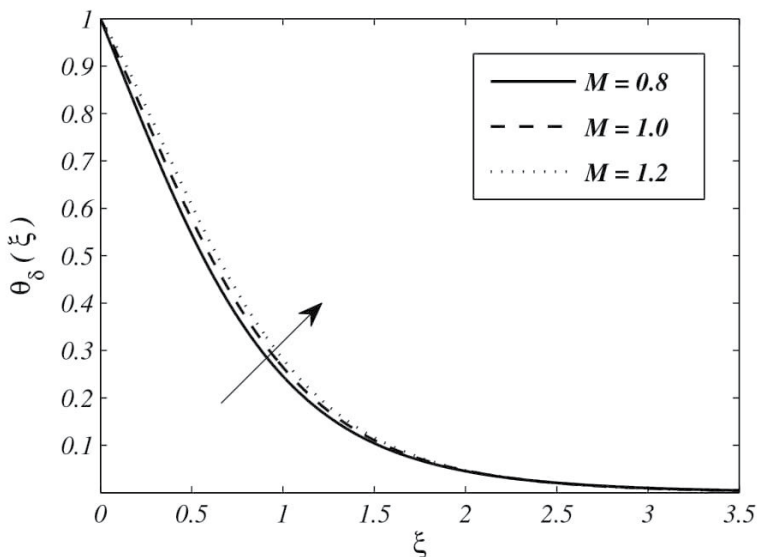
**Figure 4.**  
 Impact of thermophoresis parameter  $Nt$  on temperature profile  $\theta_\delta(\xi)$ .

conduction of nanoparticles. Thus, width of boundary layer enhances due to reallocation of ultrafine particles from hotter to colder part and hence, temperature enhances for higher thermophoresis parameter  $Nt$  that can be seen in **Figure 4**.

**Figure 5** demonstrate fluid temperature variation against Eckert number  $Ec$  (0.0, 0.1, 0.2). A dimensionless quantity  $Ec$  is the fraction of advective transportation and heat dissipation potential. As Eckert number  $Ec$  enhances, thermal buoyancy effect raises that results in increasing temperature and that is the main reason behind the conversion of kinetic energy into thermal energy. Hence, fluid temperature enhances because of this conversion effect. Consequently, declination in Nusselt number  $Nu_x$  is noticed that can be seen via **Table 1**.



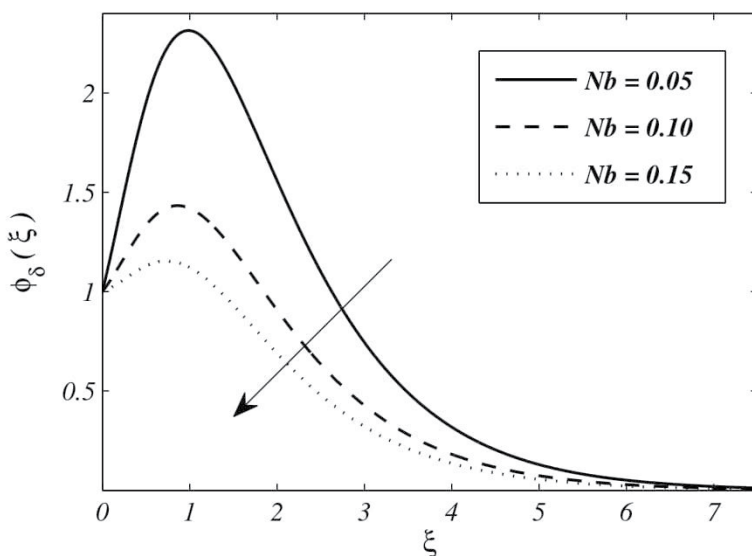
**Figure 5.**  
 Impact of Eckert number  $Ec$  on temperature profile  $\theta_\delta(\xi)$ .



**Figure 6.**  
Impact of magnetic parameter  $M$  on temperature profile  $\theta_{\delta}(\xi)$ .

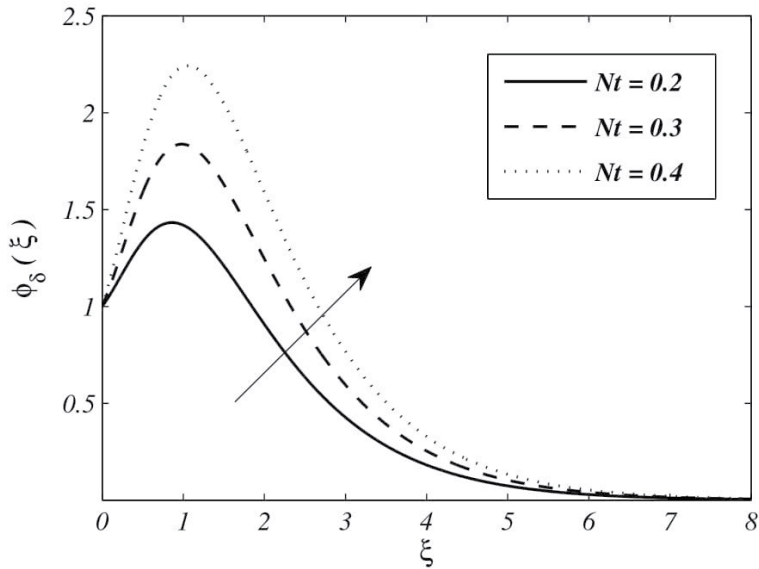
**Figure 6** reflects variation of temperature distribution against magnetic parameter  $M$ . With an increases in magnetic parameter  $M$ , velocity profile decreases because of generation of Lorentz force that consequently intensify the boundary thickness and rate of heat transportation and hence fluid temperature enhances as shown via **Figure 6**.

**Figure 7** manifests the impact of Brownian motion parameter  $Nb$  (0.05, 0.10, 0.15) on nanoparticle concentration  $\phi_{\delta}(\xi)$ . With an increase in the value of Brownian motion parameter  $Nb$ , fluid particles collides with each other with higher speed which results in increase in the nanoparticle concentration and consequently, local Sherwood number reduces as depicted in the **Table 1**.



**Figure 7.**  
Impact of Brownian motion parameter  $Nb$  on Concentration profile  $\phi_{\delta}(\xi)$ .

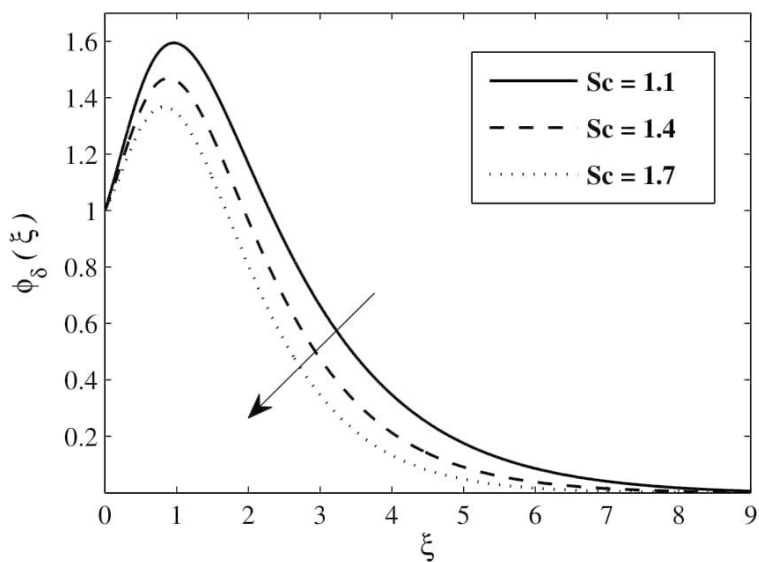




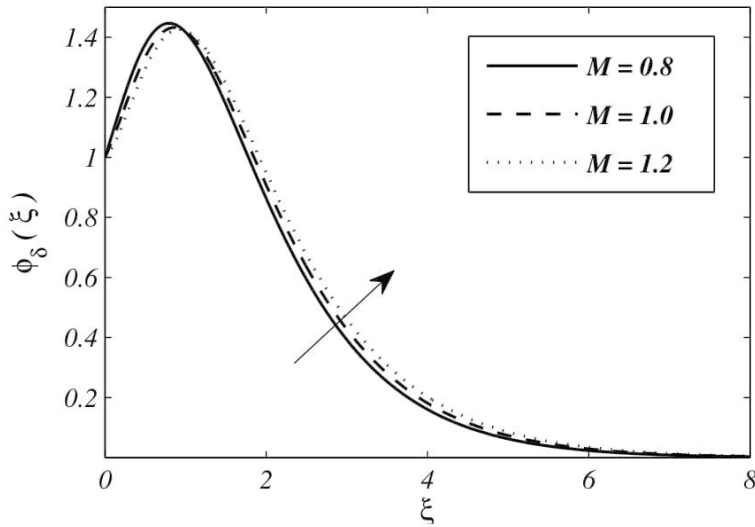
**Figure 8.**  
Impact of thermophoresis parameter  $Nt$  on Concentration profile  $\phi_\delta(\xi)$ .

**Figure 8** portrays variation for nanoparticle volume fraction  $\phi_\delta(\xi)$  against thermophoresis parameter  $Nt$  (0.2, 0.3, 0.4). This graph shows that with an increase in thermophoresis parameter, nanoparticle concentration increases. Basically, in case of thermophoresis force applied by a particle on the other particle will generate the movement of particles from hotter to colder part and hence fluid moves from hotter to colder region and hence intensification in the nanoparticle volume fraction is observed via **Figure 8**.

**Figure 9** portrays the impact of Schmidt number  $Sc$  (1.1, 1.4, 1.7) on profile of nanoparticle concentration. Intensification in the value of physical parameter  $Sc$ ,



**Figure 9.**  
Impact of Schmidt number  $Sc$  on Concentration profile  $\phi_\delta(\xi)$ .



**Figure 10.**  
Impact of magnetic parameter  $M$  on Concentration profile  $\phi_{\delta}(\xi)$ .

declination in mass diffusivity is observed. Due to this effect nanoparticle concentration decreases.

**Figure 10** reflects the variation for nanoparticle concentration  $\phi_{\delta}(\xi)$  against the magnetic parameter  $M$  (0.8, 1.0, 1.2). With increase in magnetic parameter  $M$ , rate of mass transportation decreases that consequently increase nanoparticle concentration and hence reduction in the value of local Sherwood number is notice as seen in **Table 1**.

#### 4. Conclusions

Present study reflects the heat, mass and flow transportation of Magneto-hydrodynamic (MHD) nanofluid towards a sheet which is stretched linearly. Key findings of current analysis are summarized as:

1. Skin friction coefficient elevates with increment in magnetic parameter  $M$  due to produced Lorentz force that ultimately improves local Sherwood number along with Nusselt number for higher magnetic parameter  $M$ .
2. Fluid temperature enhances for greater values of physical parameters Eckert number  $Ec$ , Brownian motion parameter  $Nb$  and thermophoresis parameter  $Nt$ .
3. An enhancement in the profile of nanoparticle concentration is noticed for greater values of thermophoresis parameter  $Nt$ . Whereas, it declines for Brownian motion parameter  $Nb$  and Schmidt number  $Sc$ .

#### Nomenclature

$x, y$	Cartesian coordinates
$B$	Magnetic field intensity
$a$	Positive constant

$m$	Surface temperature parameter
$Sc$	Schmidt number
$C$	Concentration
$C_w$	Nanoparticle volume fraction
$q_m$	Mass flux
$Pr$	Prandtl number
$Nu_x$	Nusselt number
$Nt$	Thermophoresis parameter
$T_\infty$	Ambient temperature attained
$Sh_x$	Sheerwood number
$v$	Vertical velocity
$D_B$	Brownian diffusion coefficient
$Nb$	Brownian motion parameter
$T$	Temperature
$u_w$	Stretching velocity
$D_T$	Thermophoresis diffusion coefficient
$T_w$	Temperature at the sheet
$q_w$	Hass flux
$C_\infty$	Ambient nanoparticle volume fraction
$u$	Horizontal velocity
$M$	Magnetic parameter

### Greek symbols

$\nu$	Kinematic viscosity
$\beta$	Casson fluid parameter
$\sigma$	Electrical conductivity
$\xi$	Similarity variable
$\alpha_m$	Thermal diffusivity
$\tau$	Ratio of heat capacities
$\theta_\delta$	Non-dimensional temperature
$\phi_\delta$	Non-dimensional nanoparticle concentration

### Author details

Vikas Poply  
Kishanlal Public College, Rewari, Haryana, India

\*Address all correspondence to: [vikaspoply@gmail.com](mailto:vikaspoply@gmail.com)

### IntechOpen

© 2020 The Author(s). Licensee IntechOpen. This chapter is distributed under the terms of the Creative Commons Attribution License (<http://creativecommons.org/licenses/by/3.0>), which permits unrestricted use, distribution, and reproduction in any medium, provided the original work is properly cited. 

## References

- [1] L. J. Crane, "Flow past a stretching plate," *Zeitschrift für angewandte Mathematik und Physik ZAMP*, vol. 21, pp. 645–647, July 1970.
- [2] P. S. Gupta and A. S. Gupta, "Heat and mass transfer on a stretching sheet with suction or blowing," *The Canadian Journal of Chemical Engineering*, vol. 55, pp. 744–746, Dec. 1977.
- [3] B. B. Yoon, R. S. Rao, and N. Kikuchi, "Sheet stretching: A theoretical-experimental comparison," *International Journal of Mechanical Sciences*, vol. 31, pp. 579–590, Jan. 1989.
- [4] M. S. Sarma and B. N. Rao, "Heat transfer in a viscoelastic fluid over a stretching sheet," *Journal of Mathematical Analysis and Applications*, vol. 222, pp. 268–275, 1998.
- [5] K. Vajravelu, "Viscous flow over a nonlinearly stretching sheet," *Appl. Math. Comput.*, vol. 124, pp. 281–288, Dec. 2001.
- [6] R. Cortell, "Viscous flow and heat transfer over a nonlinearly stretching sheet," *Applied Mathematics and Computation*, vol. 184, pp. 864–873, Jan. 2007.
- [7] S. Nadeem, A. Hussain, and K. Vajravelu, "Effects of heat transfer on the stagnation flow of a third order fluid over a shrinking sheet," *Zeitschrift für Naturforschung A*, vol. 65, pp. 969–994, Nov. 2010.
- [8] K. Prasad, K. Vajravelu, and P. Datti, "Mixed convection heat transfer over a non-linear stretching surface with variable fluid properties," *International Journal of Non-Linear Mechanics*, vol. 45, pp. 320–330, Apr. 2010.
- [9] S. U. S. Choi and J. A. Eastman, "Enhancing thermal conductivity of fluids with nanoparticles," *ASME International Mechanical Engineering Congress and Exposition*, pp. 1–9, Nov. 1995.
- [10] J. Buongiorno, "Convective transport in nanofluids," *Journal of Heat Transfer*, vol. 128, pp. 240–250, March 2006.
- [11] A. Kuznetsov and D. Nield, "Natural convective boundary-layer flow of a nanofluid past a vertical plate," *International Journal of Thermal Sciences*, vol. 49, pp. 243–247, Feb. 2010.
- [12] C. Mamaloukas, S. Spartalis, and H. P. Mazumdar, "MHD flow of a Newtonian fluid over a stretching sheet: an approximate solution," *International journal of Computational and Numerical Analysis and Applications*, vol. 1, pp. 299–310, 2002.
- [13] R. Tamizharasi and V. Kumaran, "Pressure in MHD/Brinkman flow past a stretching sheet," *Communications in Nonlinear Science and Numerical Simulation*, vol. 16, pp. 4671–4681, Dec. 2011.
- [14] T. Hayat, M. Qasim, and S. Mesloub, "MHD flow and heat transfer over permeable stretching sheet with slip conditions," *International Journal for Numerical Methods in Fluids*, vol. 66, pp. 963–975, July 2011.
- [15] A. Hussain, M. Malik, T. Salahuddin, S. Bilal, and M. Awais, "Combined effects of viscous dissipation and joule heating on MHD sisko nanofluid over a stretching cylinder," *Journal of Molecular Liquids*, vol. 231, pp. 341–352, Apr. 2017.
- [16] K. Vajravelu and J. Cannon, "Fluid flow over a nonlinearly stretching sheet," *Applied Mathematics and Computation*, vol. 181, pp. 609–618, Oct. 2006.

- [17] M. H. Matin, M. R. H. Nobari, and P. Jahangiri, "Entropy Analysis in Mixed Convection MHD flow of Nanofluid over a Non-linear Stretching Sheet," *Journal of Thermal Science and Technology*, vol. 7, no. 1, pp. 104–119, 2012.
- [18] H. M. Shawky, N. T. M. Eldabe, K. A. Kamel, and E. A. Abd-Aziz, "MHD flow with heat and mass transfer of Williamson nanofluid over stretching sheet through porous medium," *Microsystem Technologies*, vol. 25, pp. 1155–1169, Apr. 2019.
- [19] M. F. Md Basir, M. J. Uddin, A. I. Md. Ismail, and O. A. Bg, "Nanofluid slip flow over a stretching cylinder with schmidt and pcllet number effects," *AIP Advances*, vol. 6, pp. 1-15, May 2016.
- [20] A. K. Pandey and M. Kumar, "Boundary layer flow and heat transfer analysis on cu-water nanofluid flow over a stretching cylinder with slip," vol. 56, no. 4, pp. 671–677, Dec. 2017.
- [21] V. Vinita and V. Poply, "Impact of outer velocity MHD slip flow and heat transfer of nanofluid past a stretching cylinder," *Materials Today: Proceedings*, Vol. 26, pp. 3429-3435, 2020.
- [22] Vinita, Poply V, Goyal R, Sharma N., "Analysis of the velocity, thermal, and concentration MHD slip flow over a nonlinear stretching cylinder in the presence of outer velocity," *Heat Transfer*, 2020; 1–27. <https://doi.org/10.1002/htj.21941>.
- [23] Goyal R, Vinita, Sharma N, Bhargava R., "GFEM analysis of MHD nanofluid flow toward a power-law stretching sheet in the presence of thermodiffusive effect along with regression investigation," *Heat Transfer*, 2020;1–23. <https://doi.org/10.1002/htj.21873>.
- [24] Poply V, Singh P, Choudhary KK, "Analysis of laminar boundary layer flow along a stretching cylinder in the presence of thermal radiation," *WSEAS Trans Fluid Mech.*, vol. 8, pp. 159-164, 2013.
- [25] P. Rana and R. Bhargava, "Flow and heat transfer of a nanofluid over a nonlinearly stretching sheet: A numerical study," *Communications in Nonlinear Science and Numerical Simulation*, vol. 17, pp. 212– 226, Jan. 2012.



---

Section 4

# Design

---





# Plate Heat Exchangers: Artificial Neural Networks for Their Design

*Bayram Kılıç*

## Abstract

Heat exchangers are installation components in which two fluids with different temperatures are separated from each other with the help of plates and these plates make heat transfer between two fluids. The biggest advantage of plate heat exchangers over other type of heat exchangers is their heat transfer efficiency. The thinness of the plates separating the two fluids compared to other material alternatives increases the amount of heat transfer and thus reduces the heat losses that may occur during heat transfer. Plate heat exchangers are not only efficient but also prevent the formation of residue and dirt that can accumulate over time in the used applications. It also protects the system against excessive pressure that may occur in the installation. In this study, some information about plate heat exchangers is given such as classification, plate geometry, pressure losses, and thermal calculations. Also, the data obtained from the experimental work were used to obtain some relativity in order to use it in plate heat exchangers and artificial neural networks (ANN) method was used for this purpose. Artificial neural network method is used in many engineering applications. The most important advantages of this method are rapid formation, simple formation and high learning capacity.

**Keywords:** plate heat exchanger, heat transfer, artificial neural networks, thermodynamic

## 1. Introduction

One of the most common and used processes in engineering practice is the heat exchange between two or more fluids at different temperatures. The devices in which these changes are made are generally called heat exchangers (HEX) and in practice they are used in power plants, chemical industries, heating, air conditioning, cooling, vehicles, electronic devices, use of alternative energy sources, can be found in many places. As can be seen from the above written, HEXs that is used in various applications in practice, can be used in different structures, capacities, sizes and types according to the intended use. HEXs are the most important heat transfer equipments of the industry and they can be seen in different kinds and capacities at almost every stage of chemistry, power plants, cooling, heating and air conditioning processes under different names such as evaporator, condenser, heater and cooler. From the point of view of machine and chemical engineering education, the HEXs are a very good application for this branch of science which contains all of the basic subjects of these engineering branches: materials, strength, thermodynamics and heat transfer science. As it can be understood, HEXs are always used in daily life. Thus, the design ought to be followed up to the best detail, and the nearest investigation results ought

to be gotten by utilizing related projects, and studies ought to be directed to improve the designs. Decreasing the amount of heat transferred in the HEX causes the performance of the HEX to reduce. This implies loss of performance in the energy system utilizing HEXs. The improvement of heat transfer permits the system dimensions to be kept at the proper values, thus reducing system cost and operating costs.

In the case of plate heat exchangers (PHEX), the surfaces with the basic heat transfer are made of thin metal plates. These metal surfaces might be level or wavy. They can be examined in three groups: sealed plate, spiral plate and lamellar. Heating, cooling and ventilation applications achieve the high efficiency, affordability and compact design they require thanks to PHEXs. By replacing tubular HEXs with daytime HEXs with PHEXs, PHEXs have gained a rapidly increasing market share in the entire industry. The wide selection range of plates in various sizes and materials provides superior flexibility to PHEXs. This flexibility is a great advantage for many thermal process HEXs [1].

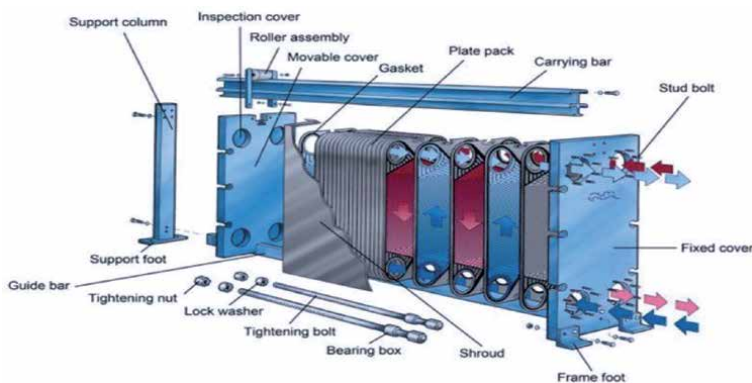
Some correlations can be obtained using the data obtained from experimental studies and then these correlations can be used in energy applications. Artificial neural networks (ANN) method is mostly used for this purpose in energy applications. Artificial neural networks estimate the output value corresponding to this data using, data that makes up the network. It is known that artificial intelligence methodologies are used in the analysis of PHEXs as in energy systems. However, an analysis using ANN methodology for heat transfer rate and effectiveness in PHEXs for different surface angles has been performed in a small number. This study focuses on the usability of ANN methodology for performance analysis of PHEXs.

## 2. Plate heat exchangers

In PHEXs, the surfaces with the basic heat transfer are made of thin metal plates. These metal surfaces might be level or wavy. They generally have a higher total heat transfer coefficient than shell-tube type HEXs. **Figure 1** shows the structure of a PHEX.

Plate heat exchangers; They can be examined in three groups as sealed plated, spiral plated and lamellar [1]:

- a. Heat exchangers with sealed plates; Heat exchangers with sealed plates are made by packing the thin metal plates into a frame and packing them. On each side of each metal plate there are holes for fluid to pass through. When the plates are assembled and packed, using appropriate seals prevents the fluids from



**Figure 1.**  
The structure of the plate heat exchanger [2].

intermixing and leaking out. The hot and cold fluids flow through the spaces between the plates without mixing. The plates are made wavy to provide rigidity, to stabilize the distance between the plates and to improve heat transfer.

- b. Spiral PHEXs; Plate type heat exchangers in which heat transfer surfaces are formed from plates and not formed by cylindrical pipes. Spiral plate heat exchangers are obtained by spirally wrapping two elongated thin metal plates 150–1800 mm wide each for a fluid, forming two spiral parallel edges. A uniform clearance can be maintained between the two plates. Both sides of the plates are covered with sealed covers. Various flow configurations are possible and different types of spiral heat exchangers can be manufactured depending on the flow configurations.
- c. Lamellar heat exchangers; It is obtained by placing a bundle made of pipes (lamella) placed in a body. The lamella is usually held together by a point or an electric sewing source. One of the fluids flows through the lamellar tubes and flows through the other fluid lamellae. There are no surprise plates in the body. The flow is single-pass and the same direction or opposite flow arrangement can be used.

## 2.1 Design of plate heat exchangers

The heat exchangers are mainly regarded as pressure vessels. For this reason, the choice of design pressure, design temperature and appropriate material is crucial in the design of PHEXs. Once these criteria are established, the necessary calculations are made for the design. In the design of a PHEX, the surface  $A$  for heat transfer, the logarithmic mean temperature difference ( $\Delta T_m$ ) and the total heat transfer coefficient ( $K$ ), pressure drop, physical size and economics are significant factors.

## 2.2 The importance of material used in plate heat exchangers

One of the factors that enable PHEXs to work without problems for long years in the desired thermal conditions is that the heat exchanger material is of a certain quality. In order for materials to be subjected to ISO 9001 quality testing, it is necessary to mark each item for retrospective analysis.

## 2.3 Plate material

It is very important to choose the plate material according to the flow rate used and the maximum desired working strength. Generally, the plate materials given in **Table 1** are used and the most commonly used material type is 1.440 / AISI 316 [2, 3].

AISI 304	NI 200/201
AISI 316	G-30
AISI 316 L	C-4
254 SMO	INCONEL 625
654 SMO	INCONEL 825
TITANYUM	MONEL 400
Ti - PD	TANTALUM
C-276	C - 22

**Table 1.**  
 Material types of heat exchangers.

PHEXs are produced from different materials in today. These alternative materials are aluminum, carbon steel, stainless steel, nickel alloys, zirconium and titanium. For many chemical processes, Zirconium is a cost-effective material of construction in shielding process equipment systems from destructive corrosive leaks. With incredibly high resistance to corrosion, Zirconium HEXs can withstand some of the harshest situations. This translates to decreased maintenance expense, with downtime kept to a minimum. Copper has many preferred specifications for thermally efficient and durable HEXs. Above all else, copper is an perfect conductor of heat. This means that copper's high thermal conductivity allows heat to pass through it speedly. Other required specifications of copper in HEXs include its corrosion resistance, biofouling resistance, maximum allowable stress and internal pressure, creep rupture strength, fatigue strength, hardness, thermal expansion, specific heat, antimicrobial specifications, yield strength, high melting point, ease of fabrication, and ease of joining.

In chemical processes, the use of titanium HEXs has been found to be a cost-effective method of resisting leaks from corrosion on a process line. Titanium HEXs has superior corrosion resistance, high heat transfer efficiency, non-breaking property and provide an extended service life compared to other materials.

#### **2.4 Gasket material**

In plate heat exchangers it is the limit factor contour. Therefore, it is very important to choose the 'right' gasket material. Various sealing types according to application are listed below. One of the most important points that should not be forgotten is that the exchanger gaskets are produced in three qualities, normal, sulfur and peroxide. These three quality seal materials are peroxidized when compared with each other, and the material always ensures the best performance in terms of operating conditions [4, 5].

#### **2.5 Plate geometries used in plate heat exchangers**

Almost all plates used today are of the fishermen type. Traditionally, fish hatch plates are now made with two arrows, one is the "high-theta" with high resistance to flow and the other is the "low-theta" with low resistance against flow.

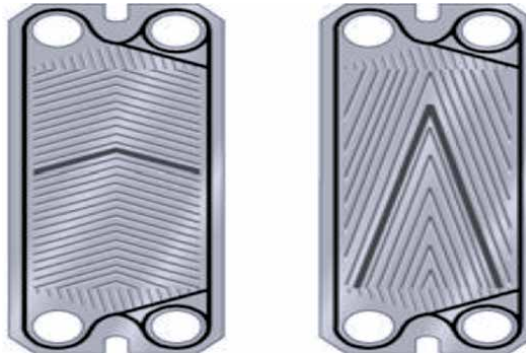
These two types of plates can be combined in three different ways, each with different characteristics in terms of heat transfer and pressure drop.

The symmetrical plates and the primary and secondary sides are geometrically identical and the plate deck can best be used on only one side. A later innovation is the asymmetrical plaque, these two teams have arrows, one high-theta and the other low-theta. Plates having different plate geometries are given in **Figures 2–6**

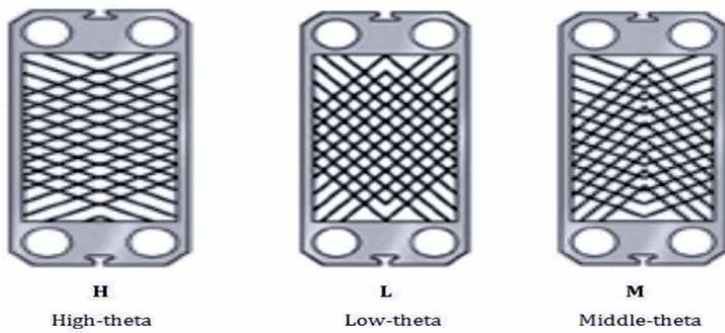
These two plates can be combined in the form of six different flow channels, each with different heat transfer characteristics. Gasket materials commonly used in plate heat exchangers are given **Table 2**.

The asymmetric plates also provide asymmetrical plate deck formation, where the geometry of the primary side is different from the geometry of the secondary side. These two aspects can be used separately in the best way, thus reducing the required heat transfer surface and providing better utilization of the existing pressure reduction.

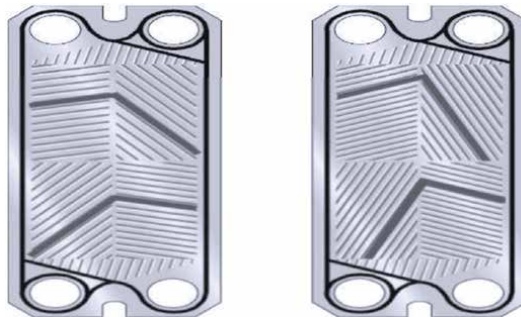
Plates are manufactured in different thicknesses up to 8 mm by 0.4 mm in accordance with the designed pressure rating and maintenance stability. Thin plates are not used in cleaning applications and other applications where the unit needs to be opened. The most commonly used materials in geothermal applications are AISI 316, 254 SMO and commercial pure (grade 1) titanium. Other high alloy materials are also used where geothermal fluids are very corrosive.



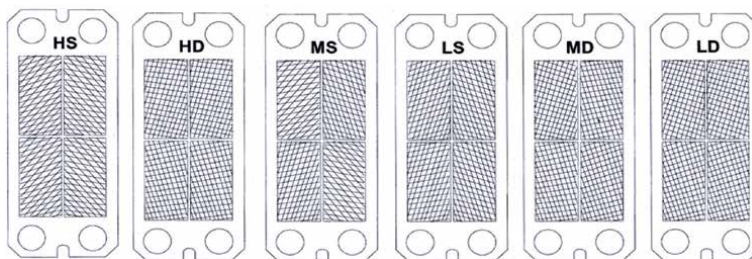
**Figure 2.**  
*Two arrowhead chevron plates.*



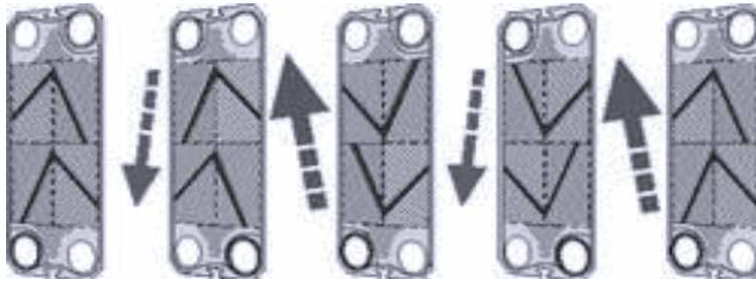
**Figure 3.**  
*Three different channels by combining two symmetrical plates.*



**Figure 4.**  
*Asymmetrical high and low-theta plates.*



**Figure 5.**  
*Six different flow channels combined from two different platters.*



**Figure 6.**  
*Asymmetric best use at PHE.*

Nitrile (Nbr)
Hnbr
Etilen Propilen (Epdm)
Florokarbon (Fpm)
Viton Gf
PTFE Encapsulated NBR

**Table 2.**  
*Gasket materials commonly used in plate heat exchangers.*

### 3. Thermodynamic analysis of plate heat exchangers

If the heat transfer in a HEX is assumed to be only between the fluids in it and the absence of a heat loss in the center, it can be written in the PHEX with the following relation [6–9]:

$$\begin{aligned} \dot{Q} &= \text{Heat in the HEX (W)}. \\ &= \text{Heat given by the hot fluid (W)}. \\ &= \text{Heat received by the cold fluid (W)}. \\ K &= \text{Total heat transfer coefficient (W/m}^2\text{°K)} \end{aligned}$$

$$\dot{Q} = K A \Delta T_m \quad (1)$$

The temperatures given and received during the cooling and heating of hot and cold fluids can be found by the mass fluxes of fluids and the enthalpy of entrances and exits and can be written as [10]:

$$\dot{Q} = \dot{m}(h_i - h_o) \quad (2)$$

If the temperatures of the fluids change when the heat is taken and given, the amount of heat that passes is [10]:

$$\dot{Q} = \dot{m}_h c_{ph} (T_{hi} - T_{ho}) = \dot{m}_c c_{pc} (T_{co} - T_{ci}) \quad (3)$$

After a certain period of operation, particles, metal salts or various chemical elements may accumulate in the fluids on the heat exchanger surfaces. Occasionally, due to corrosive effects, an oxidation layer may form on these surfaces. All these

layers are brought to an additional thermal resistance during heat transfer. This contamination resistance (or factor), as indicated by the  $R_f$  symbol, can be found as follows, in the sense that the thermal resistances of the heat transfer surfaces are dirty and clean [1]:

$$R_f = \frac{1}{K_{dirty}} - \frac{1}{K_{clean}} \quad (4)$$

Due to the roughness of the metal surfaces, there is a contact resistance between these two surfaces due to the poor contact between the two metals. The contact resistance on two surfaces causes a decrease in temperature on these surfaces. In order to take these situations into consideration, a resistance definition can be made as follows [1]:

$$R_t = \frac{(T_A - T_B)}{\frac{\dot{Q}}{A}} \quad (5)$$

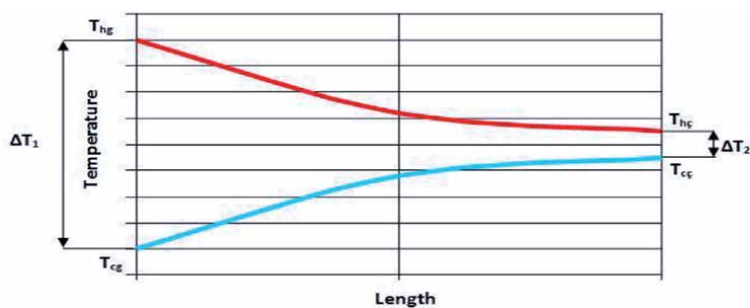
Consequently, the total heat transfer coefficient at the surface of the HEX can be found by the following Eq. [1]:

$$\frac{1}{K} = \frac{1}{\alpha_1} + R_{f1} + \frac{\delta_1}{\lambda_1} + R_{t,1-2} + \frac{\delta_2}{\lambda_2} + R_{t,2-3} + \frac{\delta_3}{\lambda_3} + R_{f2} + \frac{1}{\alpha_2} \quad (6)$$

In the construction of the heat calculations of the heat exchangers, the expression of the mean logarithmic temperature difference ( $\Delta T_m$ ) is required if Eq. (1) is used. The mean logarithmic temperature difference value is determined by the flow rate in the heat exchanger. **Figure 7** and **Figure 8** show temperature distributions along the length of the HEX when the flow is parallel and opposite.

The mean logarithmic temperature difference ( $\Delta T_m$ ) can be expressed as:

$$\Delta T_m = \frac{\Delta T_1 - \Delta T_2}{\ln \frac{\Delta T_1}{\Delta T_2}} \quad (7)$$



**Figure 7.**  
 Temperature distribution in a parallel flow HEX [1].



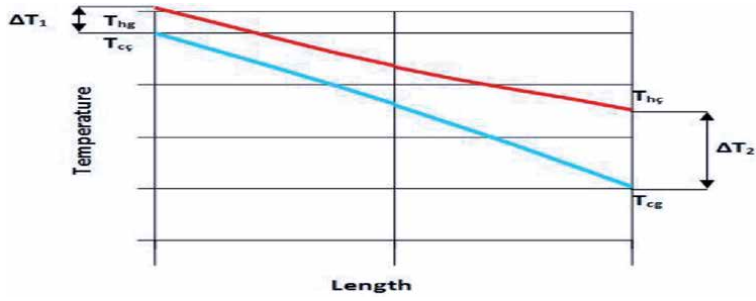


Figure 8. Temperature distribution in the reverse flow HEX [1].

If the last equation is moved to Eq. (1):

$$\dot{Q} = \frac{KA(\Delta T_1 - \Delta T_2)}{\ln \frac{\Delta T_1}{\Delta T_2}} \quad (8)$$

expression is obtained.

The efficiency of HEXs can be calculated with the help of the following Equation [11]:

$$\varepsilon = \frac{\dot{Q}}{\dot{Q}_{\max}} \quad (9)$$

$C_h = \dot{m}_h c_{ph}$  and  $C_c = \dot{m}_c c_{pc}$  are the thermal capacity values of hot and cold fluids, the actual heat transfer in the HEX can be written as [12, 13]:

$$\dot{Q} = C_h (T_{hi} - T_{ho}) = C_c (T_{co} - T_{ci}) \quad (10)$$

If the  $\dot{Q}_{\max}$  value is defined as the maximum possible heat transition, it can be written as follows, provided that it is smaller than the  $C_h$  or  $C_c$  thermal capacity outputs [14, 15]:

$$\dot{Q}_{\max} = C_{\min} (T_{hi} - T_{ci}) \quad (11)$$

### 3.1 Determination of heat transfer rate and effectiveness in plate heat exchangers using alternative an approach

Artificial Neural Network (ANN) was designed for the generalizations of biological nervous systems' mathematical models. When the simplified neurons were introduced, the first steps were taken towards the neural networks, which are also known as connectionist models or parallel distributed processing. The artificial neurons are the main component of the process, and they are also known as simply neurons and nodes. In order to represent the effects of synapses in a simplified mathematical neuron model, the connection weights modulating the effects of associated input signals are utilized, while the nonlinear characteristics of neurons are represented by using the transfer function. Then, the impulse of neuron is



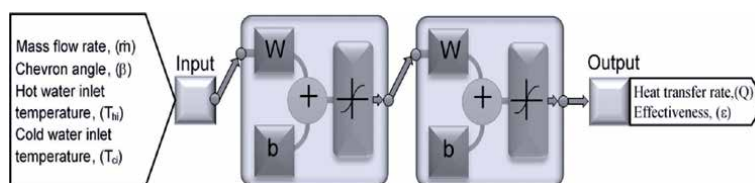
calculated as the weighted sum of the input signals and transformed by the transfer function. The artificial neurons are provided with the capability of learning by adjusting the weights in accordance with the preferred learning algorithm.

The data obtained from the experimental work [16] were used to obtain some relativity in order to use it in PHEXs and ANN method was used for this purpose. ANN method is used in many engineering applications. The most important advantages of this method are rapid formation, simple formation and high learning capacity. Two methods are used in thermal calculations in PHEXs. These methods are mean logarithmic temperature difference and effectiveness-NTU methods. In this study, the data obtained from the experiments [16] (hot water inlet–outlet temperature, cold water inlet–outlet temperature, flow rate and plate surface angle) are quite suitable for using the mean logarithmic temperature difference method. These experimental data are the input variables of the network created for the ANN method. The effectiveness and the heat transfer rate of the PHEX are output variables. All data and calculated results obtained from experimental data can be modeled with ANN method and can be used to obtain results depending on different variables.

MATLAB Toolbox was used for ANN methodology. In the training of the data, the number of neurons in the hidden layer was changed between 3 and 12. 80% of the 227 data obtained from the experiments were randomly selected for training and 20% for testing. The generated network has 4 input variables as hot water inlet temperature ( $T_{hi}$ ), cold water inlet temperature ( $T_{ci}$ ), fluid flow ( $m$ ) and plate surface angle ( $\beta$ ). Effectiveness ( $\epsilon$ ) is output variable. The generated artificial neural network is shown schematically in **Figure 9**. In the created network, LOGSIG is selected as the transfer function, Forward Back Prop for the network type, and TRAINLM and TRAINSCG as the training function. The number of epochs used was 1000 values. Each network is run 10 times in order to get the best value.

To obtain the best result from ANN method, different algorithms and hidden neurons are used in different numbers. The values of root mean square error (RMSE), the coefficient of determination ( $R^2$ ) and coefficient of variation (cov) obtained for heat transfer rate and effectiveness value are given in **Tables 3 and 4**. The performance evaluation criteria obtained from the ANN model are given in **Table 5**. The best  $R^2$  value for heat transfer rate was obtained as 0.999636 for the TRAINLM-5 training function. For the best effectiveness value,  $R^2$  value was 0.999565 for the TRAINLM-12 training function.

In determining the heat transfer rate and effectiveness of the PHEX, the equations obtained from the ANN method were used. In the above equations,  $E_i$  is the neuron summation function and  $F_i$  is the neuron activation function.  $E_i$  represents the input variables and  $b_n$  represents the bias value. The coefficients used in the formulas represent the weight values of each neuron's summation function of the hidden layer of the training network. In the above equations, hot water inlet temperature ( $T_{hi}$ ), cold water inlet temperature ( $T_c$ ), fluid flow ( $m$ ) and plate surface angle ( $\beta$ ) are used in ANN as 4 input variables. The weight coefficients and bias values used for the determination of the heat transfer rate and effectiveness are given in **Tables 6 and 7** respectively.



**Figure 9.** Schematic representation of artificial neural network [17].

Algorithm-Neuron	RMSE	cov	R <sup>2</sup>
Lm-3	53.5148	0.02003	0.999618
Lm-4	52.7873	0.01975	0.999628
<b>Lm-5</b>	<b>52.2255</b>	<b>0.01954</b>	<b>0.999636</b>
Lm-6	58.6761	0.02196	0.999540
Lm-7	54.9293	0.02056	0.999597
Lm-8	63.3763	0.02372	0.999464
Lm-9	57.5448	0.02153	0.999558
Lm-10	60.1653	0.02251	0.999517
Lm-11	58.8812	0.02203	0.999537
Lm-12	129.645	0.04852	0.997758
SCG-3	95.9341	0.03590	0.998772
SCG-4	76.4545	0.02861	0.999220
SCG-5	75.8600	0.02839	0.999232
SCG-6	61.0010	0.02283	0.999503
SCG-7	71.3101	0.02669	0.999321
SCG-8	61.6170	0.02306	0.999493
SCG-9	63.3772	0.02372	0.999464
SCG-10	54.6721	0.02046	0.999601
SCG-11	62.3508	0.02333	0.999481
SCG-12	59.8349	0.02239	0.999522

*The bold values are the best values of root mean square error (RMSE), the coefficient of determination (R<sup>2</sup>) and coefficient of variation (cov) obtained from the ANN model for to estimate of heat transfer rate and effectiveness.*

**Table 3.**

*The statistical values of the network for predicting the heat transfer rate.*

Heat transfer rate in the plate heat exchanger can be calculated by the following equations depending on the hot water inlet temperature ( $T_{hi}$ ), cold water inlet temperature ( $T_c$ ), fluid flow ( $m$ ) and plate surface angle ( $\beta$ ) [17].

$$E_6 = -112.6039F_1 + 83.284F_2 - 89.934F_3 - 70.4233F_4 + 229.4711F_5 - 107.9219 \quad (12)$$

$$\dot{Q} = \left( \frac{1}{1 + e^{-E_6}} \right) 3920 \quad (13)$$

Similarly, the effectiveness in the PHEX can be calculated from the following equations depending on the hot water inlet temperature ( $T_{hi}$ ), cold water inlet temperature ( $T_c$ ), fluid flow ( $m$ ) and plate surface angle ( $\beta$ ) [17].

$$E_{13} = 21.3112F_1 - 2.7185F_2 + 21.2966F_3 + 7.2653F_4 - 0.056092F_5 - 26.4603F_6 - 19.2568F_7 - 12.4354F_8 + 3.0543F_9 - 46.6099F_{10} + 58.215F_{11} + 0.28895F_{12} - 1.5743 \quad (14)$$

$$\varepsilon = \frac{1}{1 + e^{-E_{13}}} \quad (15)$$

Algorithm-Neuron	RMSE	cov	R <sup>2</sup>
Lm-3	0.0102575	0.022758	0.999475
Lm-4	0.0096802	0.021477	0.999532
Lm-5	0.0134191	0.029773	0.999101
Lm-6	0.0097002	0.021522	0.999530
Lm-7	0.0099292	0.022030	0.999508
Lm-8	0.0097623	0.021660	0.999524
Lm-9	0.0100210	0.022234	0.999498
Lm-10	0.0096225	0.021350	0.999538
Lm-11	0.0109986	0.024403	0.999396
<b>Lm-12</b>	<b>0.0093323</b>	<b>0.020706</b>	<b>0.999565</b>
SCG-3	0.0124508	0.027625	0.999226
SCG-4	0.0109349	0.024261	0.999403
SCG-5	0.0129422	0.028715	0.999164
SCG-6	0.0114423	0.025387	0.999346
SCG-7	0.0121871	0.027040	0.999258
SCG-8	0.0118729	0.026343	0.999296
SCG-9	0.0112524	0.024966	0.999368
SCG-10	0.0101688	0.022562	0.999484
SCG-11	0.0109066	0.024199	0.999406
SCG-12	0.0113416	0.025164	0.999358

The bold values are the best values of root mean square error (RMSE), the coefficient of determination (R<sup>2</sup>) and coefficient of variation (cov) obtained from the ANN model for to estimate of heat transfer rate and effectiveness.

**Table 4.**  
 The statistical values of the network for predicting the effectiveness.

Thermodynamic Values	Method	Comparison Parameters		
		R <sup>2</sup>	RMSE	cov
Heat transfer rate	ANN	0.999636	52.2255	0.01954
Effectiveness	ANN	0.999565	0.0093323	0.020706

**Table 5.**  
 Performance evaluation criteria obtained from the ANN model.

Neuron position (w <sub>ni</sub> )	I <sub>1</sub> (T <sub>hi</sub> )	I <sub>2</sub> (T <sub>ci</sub> )	I <sub>3</sub> ( $\dot{m}$ )	I <sub>4</sub> ( $\beta$ )	b <sub>n</sub>
1	1.8443	10,5531	2.1624	-1.2641	18.7258
2	56.9616	-52.142	27.1211	-0.0728	-20.0211
3	-0.38653	0.42041	-2.0398	-5.9629	4.8897
4	-2.6099	2.2846	3.6669	8.8609	-7.3451
5	-40.8109	37.1115	-105.8138	33.7376	27.9695

**Table 6.**  
 The weight coefficients and bias values used for the determination of the heat transfer rate.

Neuron position ( $w_{ni}$ )	$I_1 (T_{hi})$	$I_2 (T_{ci})$	$I_3 (\dot{m})$	$I_4 (\beta)$	$b_n$
1	11.1556	11.7598	39.362	9.2238	47.3869
2	-37.921	46.173	-7.0158	-4.478	-2.4622
3	16.3938	-38.169	-35.378	-4.640	39.5329
4	13.9183	-1.3878	-10.187	13.3089	3.5955
5	92.1152	8.6141	28.7158	-49.57	-16.817
6	31.4252	-30.344	3.3642	25.2838	-23.704
7	-14.906	11.1061	-9.057	-9.2724	10.1669
8	23.2713	-4.3873	-49.1203	20.2264	4.1424
9	68.8739	-72.556	34.7909	-44.281	13.6961
10	-0.13074	3.2502	1.8366	11.4214	-8.3915
11	-10.7511	12.7919	-3.6727	13.7598	-7.913
12	35.966	58.1377	91.3142	3.7576	-46.231

**Table 7.**  
Weight coefficients and bias values used to determine of the effectiveness.

Temperature $T_{hi} (^{\circ}\text{C})$	Temperature $T_{ci} (^{\circ}\text{C})$	Flow rate $\dot{m}$ (kg/s)	Plate surface angle $\beta (^{\circ})$	Heat transfer rate (W)		Error (%)
				Actual values	ANN	
32.8	25	0.167	30	2167	2191	1.09
44.6	37.1	0.167	30	2167	2144	1.08
51.1	43.6	0.167	30	2167	2166	0.07
58.1	50.1	0.167	30	2377	2354	0.97
31.8	26.6	0.239	30	2195	2204	0.40
39.3	34	0.239	30	2295	2284	0.48
44.7	39.4	0.239	30	2295	2319	1.05
37.9	34.3	0.321	30	2144	2115	1.37
45.5	41.9	0.321	30	2144	2159	0.68
34.8	28.4	0.263	60	3077	3103	0.85
53.3	46.8	0.263	60	3407	3393	0.40
19.2	15.7	0.39	60	2608	2609	0.06
26.4	21.9	0.39	60	3259	3254	0.17
37.5	33.1	0.39	60	3422	3421	0.04
45.2	40.8	0.39	60	3585	3572	0.37
32.1	29	0.517	60	3023	3055	1.06
45.7	42.5	0.517	60	3455	3419	1.04

**Table 8.**  
Comparison of the actual values of the heat transfer rate with the estimated values obtained in the ANN model.

The actual values of the heat transfer rate and the predicted values and error values obtained in the ANN model are given in **Table 8**. Eq. (16) is used in the calculation of error values [18].

$$Error = \frac{|A^e - A^p|}{A^e} \times 100 \quad (16)$$

Where,  $A^e$  is the data obtained from experiments and  $A^p$  is the estimates obtained from ANN. As seen in **Table 8**, the highest error value is 1.37. It has been determined that this value is an acceptable error value.

Similarly, the actual values of the effectiveness and the predicted values and error values obtained in the ANN model are given in **Table 9**. As seen in **Table 9**, the highest error value is 1.23. This value is also determined to be an acceptable error value.

### 3.2 Pressure drop in heat exchangers

In all HEXs there is a close physical and economic relationship between heat transfer and pressure drop. In a heat exchanger intended to be designed for a constant heat capacity, increasing fluid velocities increases the heat transfer coefficient and allows smaller heat exchangers (compact). In this way, a smaller size or more

Temperature $T_{hi}$ (°C)	Temperature $T_{ci}$ (°C)	Flow rate $m$ (kg/s)	Plate surface angle $\beta$ (°)	Effectiveness		Error (%)
				Actual values	ANN	
21.2	15.4	0.167	30	0.40	0,396	0.95
44.6	37.1	0.167	30	0.41	0,409	0.22
51.1	43.6	0.167	30	0.41	0,407	0.73
31.8	26.6	0.239	30	0.42	0,423	0,71
39.3	34	0.239	30	0.43	0,435	1.23
22.4	18.9	0.321	30	0.43	0,426	0.91
29.1	25.5	0.321	30	0.42	0,423	0.69
34.8	28.4	0.263	60	0.44	0,445	1.14
41.4	34.9	0.263	60	0.45	0,453	0.62
53.3	46.8	0.263	60	0.48	0,477	0.63
26.4	21.9	0.39	60	0.44	0,439	0.20
45.2	40.8	0.39	60	0.50	0,501	0.22
21.8	19.1	0.517	60	0.44	0,443	0.77
32.1	29	0.517	60	0.45	0,452	0.40
38.8	35.7	0.517	60	0.48	0,481	0.13
45.7	42.5	0.517	60	0.50	0,505	0.90
54.3	51	0.517	60	0.52	0,521	0,21

**Table 9.**  
 Comparison of the actual values of the effectiveness with the estimated values obtained in the ANN model.

compact heat exchanger design can be achieved at the same capacity with a lower investment cost. On the other hand, increasing the velocities of the fluids causes the pressure drop in the heat exchanger to increase. This increases the investment cost of the pump due to the operating costs of the system and the growth of the pump or fan, as it increases the power of the pump or fan. Therefore, in the design of a HEX, the heat transfer and pressure drop must be considered together and the most appropriate solution for the system should be sought.

Since the flow model is very complex even in the simplest heat exchangers, approximate solutions and experimental findings are utilized in the determination of pressure drop as well as theoretical analyzes. The total pressure drop in a HEX is considered in two ways, the pressure drop in the straight pipe and the local pressure drop. The pressure drop in the straight pipe indicates the pressure drop from the rubbing in the flowing fluid in the fixed section piping or conduits. The local pressure drop is the loss of flow and direction changes in the flow. Unlike fluids at the same temperature, the natural convection caused by the temperature distribution in the heat exchangers may cause an additional pressure loss (or sometimes gambling).

The total pressure loss in a heat exchanger is summed separately from the pressure losses in each step of the exchanger.

### 3.3 Local losses

Cross-sectioning, rotation, separation, or coupling of fluid as it flows through a channel also causes pressure losses. These are generally called local losses. Changes in the velocity and direction of the fluid create Eddy movements (eddies) that cause energy loss. Although local losses occur at very short distances, they remain effective over a long period of time throughout the flow. These losses are generally [1];

$$\Delta P_y = \zeta \frac{\rho v^2}{2} \quad (17)$$

form. Where  $\zeta$  is called the local loss coefficient and can be found from the relevant sources for various local loss factors either using formulas or diagrams.

### 3.4 Pressure loss caused by acceleration of the fluid and lifting force

The pressure loss during the acceleration of the fluid, in fixed cross-sections,

$$\Delta P_{iv} = \rho_o v_o^2 - \rho_i v_i^2 \quad (18)$$

Where  $v_o$ ,  $v_i$  are the fluid velocity at inlet and outlet of the flow channel;  $\rho_o$ ,  $\rho_i$  again indicate the density of the fluid at the inlet and outlet of the channel. The fluid is assumed to be incompressible, and in fluid fluids this value is the order of magnitude that other pressure losses can be neglected.

### 3.5 Pressure loss in sealed plate heat exchangers

The pressure loss in this type of heat exchanger is [19];

$$\Delta P_{gasketplate} = \lambda_{gasketplate} \frac{L_p \rho v^2}{d_h 2} \quad (19)$$

Turbulent flow;

$$\lambda_{gasketplate} = 1,22 \text{Re}^{-0,252} \quad (20)$$

Due to the protrusions on the plates, turbulence can pass through the Reynolds numbers, which are smaller than the values given in the flow flat exit channels. Therefore, in the case of sealed PHEXs, the flow at values such as  $\text{Re} > 100\text{--}400$  is assumed to be turbulent.

### 3.6 The power required to maintain fluid motion

First, the pressure losses in the HEX and the pressure losses in the piping up to the heat exchanger are calculated. Later, the fan or pump power required to move the fluid in this system by calculating the sum of the pressure losses in the heat exchanger up to the HEX [20],

$$N = \frac{\dot{m} \sum (\Delta P)_t}{\rho \eta} \quad (21)$$

can be found in the equation.

## 4. Conclusions

PHEXs are the most frequently used heat transfer equipments in energy applications and can be under various names such as evaporators and condensers in almost every stage of chemistry, petrochemical industry, power plants, cooling, heating and air conditioning process in various types and capacities. From the point of view of machine and chemical engineering education, plate heat exchangers are a very good application for this branch of science which contains all of the basic subjects of these engineering branches: materials, strength, thermodynamics and heat transfer science. As can be seen, PHEXs are a commonly used construction in our daily lives. For this reason, its design should be done in detail, analysis results should be obtained with analysis programs and studies should be done to improve the designs. Decreased the amount of heat transferred in the PHEX causes the performance of the HEX to decrease. This means loss of capacity in energy system with plate heat exchanger. The regulation of heat transfer permits the system dimensions to be kept at the proper values, thus decreasing system cost and operating costs.

In this study, some equations were obtained to use in the plate heat exchangers by using the data obtained from the experimental work. ANN methodology was used for this purpose. As a result of the equations obtained for heat transfer and efficiency values in ANN application, approximate results were obtained at the value of 1.37 which is the highest error value for the real value heat transfer value and 1.23 for the efficiency value. When we look at the literature it is seen that these values are acceptable error values.

### Conflict of interest

“The authors declare no conflict of interest.”

## **Author details**

Bayram Kılıç  
Technical Sciences Vocational School, Burdur Mehmet Akif Ersoy University,  
Burdur, Turkey

\*Address all correspondence to: bayramkilic@mehmetakif.edu.tr

## **IntechOpen**

---

© 2021 The Author(s). Licensee IntechOpen. This chapter is distributed under the terms of the Creative Commons Attribution License (<http://creativecommons.org/licenses/by/3.0>), which permits unrestricted use, distribution, and reproduction in any medium, provided the original work is properly cited. 



## References

- [1] Genceli O. Isı Değiştiricileri. Birsen Yayınevi, İstanbul, Türkiye, 1999. 424 p.
- [2] <https://ekinendustriyel.com/brazed-heat-exchanger/the-structure-of-plate-heat-exchanger/>
- [3] Camilleri R, Howey DA, McCulloch MD. Predicting the flow distribution in compact parallel flow heat exchangers. *Applied Thermal Engineering*. 2015;90:551-558.
- [4] Çengel YA, Boles MA. Mühendislik Yaklaşımıyla Termodinamik. McGraw-Hill, 1994. 867 p.
- [5] David K, Paul L. Evaluating of heat exchanger surface coatings. *Applied Thermal Engineering*. 2010;30:2333-2338.
- [6] Dovic D, Palm B, Svaic S. Generalized correlations for predicting heat transfer and pressure drop in plate heat exchanger channels of arbitrary geometry. *International Journal of Heat and Mass Transfer*. 2009;52:4553-4563.
- [7] Dwivedi AK, Das SK. Dynamics of plate heat exchangers subject to flow variations. *International Journal of Heat and Mass Transfer*. 2007;50:2733-2743.
- [8] Faizal M, Ahmed MR. Experimental studies on a plate heat exchanger for small temperature different applications. *Experimental Thermal and Fluid Science*. 2012;36:242-248.
- [9] Afonso IM, Cruz P, Maia JM, Melo LF. Simplified numerical simulation to obtain heat transfer correlations for stirred yoghurt in a plate heat exchanger. *Food and Bioproducts Processing*. 2008;86:296-303.
- [10] Gherasim I, Taws M, Galanis N, Nguyen CT. Heat transfer and fluid flow in a plate heat exchanger part I. Experimental investigation. *International Journal of Thermal Sciences*. 2011;50:1492-1498.
- [11] Gut JAW, Fernandes R, Pinto JM, Tadini CC. Thermal model validation of plate heat exchangers with generalized configurations. *Chemical Engineering Science*. 2004;59:4591-4600.
- [12] Gyuwan H, Sangkwon J. Pressure loss effect on recuperative heat exchanger and its thermal performance. *Cryogenics*. 2010;50:13-17.
- [13] Hajabdollahia H, Hajabdollahib Z. Investigating the effect of properties variation in optimum design of compact heat exchanger using segmented method. *Chemical Engineering Research and Design*. 2016;112:46-55.
- [14] Idario P, Nascimento E, Garcia C. Heat transfer performance enhancement in compact heat exchangers by using shallow square dimples in flat tubes. *Applied Thermal Engineering*. 2016;96:659-670.
- [15] Karthik P, Kumaresan V, Velraj R. Experimental and parametric studies of a louvered fin and flat tube compact heat exchanger using computational fluid dynamics. *Alexandria Engineering Journal*. 2015;54:905-915.
- [16] Kılıç B. Experimental investigation of effects to heat transfer of plate geometry with dynamic and thermal parameters in the plate heat exchangers. Ph.D. Thesis, Süleyman Demirel University, The Graduate School of Natural and Applied Sciences, Isparta, Turkey. 2013. (in Turkish)
- [17] Kılıç B, İpek O, Şencan Şahin A. A comparative computational intelligence approach for heat transfer analysis of corrugated plate heat exchangers. *Environmental Engineering and Management Journal*. 2018;17(8):1831-1840.

[18] Selbas R, Sencan A, Kılıç B. Alternative approach in thermal analysis of plate heat exchanger. *Heat Mass Transfer*. 2009;45:323-329.

[19] Pandey SD, Nema VK. An experimental investigation of exergy loss reduction in corrugated plate heat exchanger. *Energy*. 2011;36:997-3001.

[20] Reppich M. Use of high performance plate heat exchangers in chemical and process industries. *International Journal of Thermal Science*. 1999;38:999-1008.

# Evolutionary Design of Heat Exchangers in Thermal Energy Storage

*Miguel Rosa Oliveira Panão*

## Abstract

The efficiency and ability to control the energy exchanges in thermal energy storage systems using the sensible and latent heat thermodynamic processes depends on the best configuration in the heat exchanger's design. In 1996, Adrian Bejan introduced the Constructal Theory, which design tools have since been explored to predict the evolution of the architecture in flow systems. This chapter reviews the fundamental knowledge developed by the application of the constructal principle to the energy flows in the design of heat exchangers of thermal energy storage systems. It introduces the Sveltteness and scale analysis, as two constructal tools in the evolutionary design of engineering flow systems. It also includes the analysis on essential scales of several configurations, or energy flow architectures, toward establishing the main guidelines in the design of heat exchangers for storing thermal energy.

**Keywords:** thermal energy storage, heat exchangers, constructal theory, phase-change materials, flow architecture

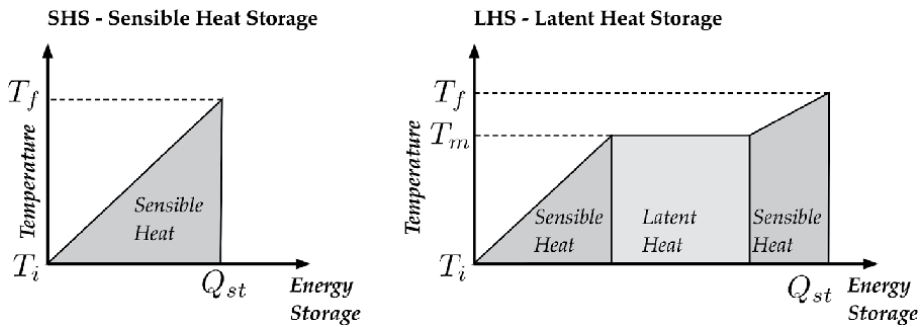
## 1. Introduction

Engineering systems capture a fraction of the total amount of thermal energy available from renewable sources, and to increase the energy system reliability, the research and development of the flow architecture in thermal energy storage systems is of paramount importance.

One of the crucial issues is the characteristic fluctuations in the availability of energy from renewable resources and wasted energy in industrial processes. The design of efficient thermal energy storage systems is an essential step toward meeting the consumption demands of electricity and heat [1]. Therefore, there is growing attention in the development of thermal energy storage systems to produce adequate energy savings and utilization, with a relevant impact on numerous and diverse applications [2, 3].

There are two basic approaches to thermal energy storage. One using the sensible heat without phase-change (SHS - Sensible Heat Storage), and another using the sensible heat *and* phase-change (LHS - Latent Heat Storage), as depicted in **Figure 1**. The thermal balance describing each approach is given by

$$Q_{st}^{SHS} = V_{SHS} \rho_l c_{p,l} (T_f - T_i) \quad (1)$$



**Figure 1.** Thermal energy storage modes based on the sensible heat (SHS - left) and latent heat (LHS - right).

$$Q_{st}^{LHS} = V_{LHS} [\rho_s c_{p,s} (T_m - T_i) + h_{sl} + \rho_l c_{p,l} (T_f - T_m)] \quad (2)$$

where  $V$  is the storage material volume,  $\rho_l, c_{p,l}$  are the fluid or melted material's density and specific heat, respectively,  $h_{sl}$  is the latent heat of fusion of the Phase-Change Material (PCM), and  $\rho_s, c_{p,s}$  are the PCM density and specific heat in its solid state,  $T_i$  and  $T_f$  are the initial and final temperatures of the energy storage process and  $T_m$  corresponds to the melting temperature of the PCM in the LHS case.

In both approaches, the upper limit for the final temperature is the saturation value associated with the vaporization of the liquid. Because of its high heat capacity, water is the most used fluid for SHS. However, theoretically, Huang et al. [4] showed the energy stored in a water-based system is one order of magnitude lower than the energy stored in a PCM. And, experimentally, Kaygusuz [5] showed evidence of a PCM system able to store up to 60% of its theoretical maximum, which represents almost the double value of the theoretical storage capacity in water-based systems. These results were the motivation for further investment in the development of LHS systems. Compared to single-phase heat storage systems, LHS systems store the same amount of energy using more compact systems, reducing production and maintenance costs.

In LHS systems, **Figure 1** on the right represents the three theoretical stages of the storage process. Initially, the Thermal Storage Material (TSM) is in its solid-state, and it stores (charges) energy through:

Step 1) the sensible heat until the melting temperature;

Step 2) the latent heat component until a complete phase-change of the TSM from solid to liquid. In this stage, the time of the melting process depends on the advancement of the solid-liquid interface (melting front), according to the configuration of the thermal fluid circuit of the heat exchanger (HE) immersed in the TSM;

Step 3) after the total liquefaction of the TSM, energy storage continues until the liquid reaches the saturation temperature of the next phase-change without compromising the volume of the Thermal Storage facility.

The storage of energy in these steps depends on the thermal properties of TSM, and the thermodynamics of the storage process. Still, the main challenge is the design of heat exchangers, as the engineering system that enables the flow of energy from the sources (renewable and non-renewable) to the TSM, disregarded in recent comprehensive reviews on thermal energy storage [6, 7]. Namely, this design has a significant impact on the charging and discharging times, if using renewable energy sources, given their limited time-window throughout the day.

The standard approach in the design of heat exchangers is to optimize the thermal and hydrodynamic energy flows. It uses an iterative process based on

previous work, and typical working conditions, such as the amount of fouling and pressure drop in the system, testing a significant number of trial-and-error designs until the values for the heat transfer performance, hydrodynamic effects and longevity are within pre-established requirements. A common trait in this standard approach is the lack of evaluation criteria grounded on the underlying physical processes. Constructal design distinguishes from the standard approach in providing the evaluation criteria in such a way. Therefore, the purpose of this chapter is to synthesize and present an evolutionary design approach (not optimization) using tools based on constructal theory. Therefore, the novelty is to include the architecture of thermal energy storage systems at the design stage [8] and investigate the best way to introduce the freedom to morph to overcome the shortcomings on charging and discharging periods due to prescribed, rigid and fixed designs when subjected to daily and seasonal changes.

## 2. Design tools in constructal theory

In 1996, Adrian Bejan [9], professor at Duke University, proposed a Constructal Theory to explain the evolution of configurations in nature stating,

*“for a finite-size flow system (not infinitesimal, one particle, or sub particle) to persist in time (to live) it must evolve with freedom such that it provides easier and greater access to what flows.”*

In practice, when using the constructal theory in engineering, one finds the best direction for the flow structures emerging from of what facilitates movement, designated as *constructal design*. And this design establishes a relation between what flows (energy, fluids, people, etc.) and the geometry of the flow architecture, in such a way that it becomes a global property of the engineering system. This property, the *Svelteness*, is a tool in constructal design.

In thermal energy storage, there are several length and time scales competing in the unfolding heat transfer processes, characterized by mass, momentum and energy balances of the system. However, not all the terms correspond to the dominant scales setting the overall result of charging and discharging of energy. A *scale analysis* is the second tool in constructal design explored in this section, allowing a proper definition of the relevant scales, and their implication to the heat exchanger design.

### 2.1 Svelteness of flow configuration

The *Svelteness* ( $S_v$ ) is this global geometric property of the flow space, which guides the engineering practice in the assessment of the flow design performance. This property corresponds to the relation between two length scales of the flow system configuration: an external ( $L_e$ ); and an internal length ( $L_i$ ), usually associated with the volume as  $V^{1/3}$ .

$$S_v = \frac{L_e}{L_i} \quad (3)$$

According to Bejan and Lorente [10], the evolutionary direction is that of *vascularization*, implying an increase of the Svelteness. Therefore, as an example applied to TES, what is the best constructal design solution for a simple tube inside a tank?

Should the design be a PCM in the inner tube and having the thermal fluid flowing through the tank (see [11]), or the opposite (see [12])?

In this example, the inner tube and tank are cylindrical with a length of  $L$ , and diameter of  $d$  and  $D$ , respectively. Therefore, the Svelteness in both cases has  $L$  as its external length scale. However, the volume associated to the thermal fluid depends on the situation. When the PCM is inside the inner tube, the volume where the thermal fluid flows is  $V = (\pi/4)(D^2 - d^2)L$ , and in the opposite case,  $V = (\pi/4)d^2L$ . If  $Sv^i$  corresponded to the case where the energy flows inward to the PCM on the inner tube, and  $Sv^o$  when it flows outward to the PCM in the tank, the relation between Sveltenesses would be

$$\frac{Sv^o}{Sv^i} = \left[ \left( \frac{D}{d} \right)^2 - 1 \right]^{1/3} \quad (4)$$

If a larger Svelteness points in the evolutionary design of the outward energy flow from the thermal fluid inside the inner tube,  $Sv^o/Sv^i > 1$ , thus  $D^2/d^2 > 2$ , and  $D^2/d^2 < 2$  otherwise. Consider the case of choosing the best design to favor the flow of energy inward to a PCM inside a tube, as in the work of Ghoneim [11]. What should be the value of the void fraction  $\phi$ , which is the ratio between the thermal fluid volume ( $V_{tf}$ ) and the storage tank volume ( $V_{st}$ )? First, the volume of thermal fluid is the difference between the storage tank volume and the volume of all tubes containing the PCM energy storage material,  $V_{tf} = V_t - n_t V_t$ , with  $n_t$  as the number of tubes and  $V_t = (\pi/4)d^2L$  as the volume of each tube. Therefore, one defines the void fraction as

$$\phi = 1 - \frac{n_t V_t}{V_{st}} \quad (5)$$

Considering  $D$  as the external diameter containing the tube diameter  $d$ , and the thermal fluid circulating in the tank, the storage tank volume should equal the total volume of all the tubes with the “necessary” thermal fluid volume,  $V_{st} = n_t(\pi/4)D^2L$ , thus, using this reasoning in the void fraction implies that

$$\frac{D^2}{d^2} = \frac{1}{1 - \phi} \quad (6)$$

Considering the previous constructal analysis using the Svelteness, storing energy with PCM material inside the tubes is only worthy when  $D^2/d^2 < 2$ . Therefore, when applied to Eq. (6), it points to the need of void fraction values of  $\phi < 0.5$ . In fact, all the LHS systems investigated using the configuration of Ghoneim [11], choose  $\phi = 0.3 < 0.5$ . Constructal theory corroborates this option, but indicates that  $\phi$  could assume higher values, eventually leading to the insertion of more tubes with PCM, allowing the storage of more energy.

On the other hand, recent works as that of Agyenim et al. [12], point toward having the PCM in the tank, instead of inside the inner tubes, and in these cases with a single tube through which circulates the thermal fluid,  $D^2/d^2 = 7.35 > 2$ .

## 2.2 Method of scale analysis

*Scale analysis* or *scaling* is a problem solving method useful to obtain essential and expedite information of several energetic processes [13]. It is not the same as a

the dimensional analysis performed in fluid mechanics, but to assess the importance of the order of magnitude of the parameters involved in heat transfer processes, and extract the relevant scales from their governing equations. For more details on the principles of scale analysis, see Bejan [13] (pp. 17–20). Here, one uses an example to illustrate the method.

Consider the example above of an LHS system with the PCM inside a tube and the thermal fluid circulating around it. If there is a sudden change in the thermal fluid temperature ( $T_f$ ), how long will it take for that perturbation to reach the PCM material at the central axis of the tube? Assuming heat transfer by diffusion in cylindrical coordinates, and that changes in the thermal diffusivity ( $\alpha$ ) are negligible within that time scale, the energy equation for the thermal energy storage process is

$$\frac{\partial T}{\partial t} = \frac{\alpha}{r} \frac{\partial^2 T}{\partial r^2} \quad (7)$$

Scaling means using the symbol  $\sim$  to establish the order of magnitude of a differential term with the main parameters of the flow configuration. Therefore,

$$\frac{\partial T}{\partial t} \sim \frac{\Delta T}{\tau} \quad (8)$$

$$\frac{\alpha}{r} \frac{\partial^2 T}{\partial r^2} \sim \alpha \frac{\Delta T}{(d/2)^2} \quad (9)$$

where  $\tau$  corresponds to the time scale under evaluation,  $\Delta T$  to the temperature difference between the tube's boundary and the center, and  $d$  is the tube's diameter. In scaling terms, Eq. (7) becomes,

$$\frac{\Delta T}{\tau} \sim \alpha \frac{\Delta T}{(d/2)^2} \quad (10)$$

which solved for the time scale results in

$$\tau \sim \frac{(d/2)^2}{\alpha} \quad (11)$$

Bejan [13] contains the synthesis for all the rules in a scale analysis. However, the example above is enough to explain the procedure applied later in section 3. The following section exemplifies the application of constructal theory as an evolutionary design method to develop heat exchangers in sensible and latent heat storage engineering systems.

### 3. Constructal theory in thermal energy storage heat exchangers

One of the essential elements in a constructal theory analysis is the freedom to morph of flowing configurations. Therefore, once we identify what is the flow under analysis, one can better understand what its freedom to morph means. On the other hand, the heat exchanger in thermal energy storage corresponds to the structure obtained after morphing through which energy flows from a source, usually the thermal fluid, to the storage material (e.g. a solid or a phase-change material, PCM). Depending on the storage material, the heat transfer mechanisms vary, and, accordingly, the energy storage scales. For example, if the material is solid, the heat

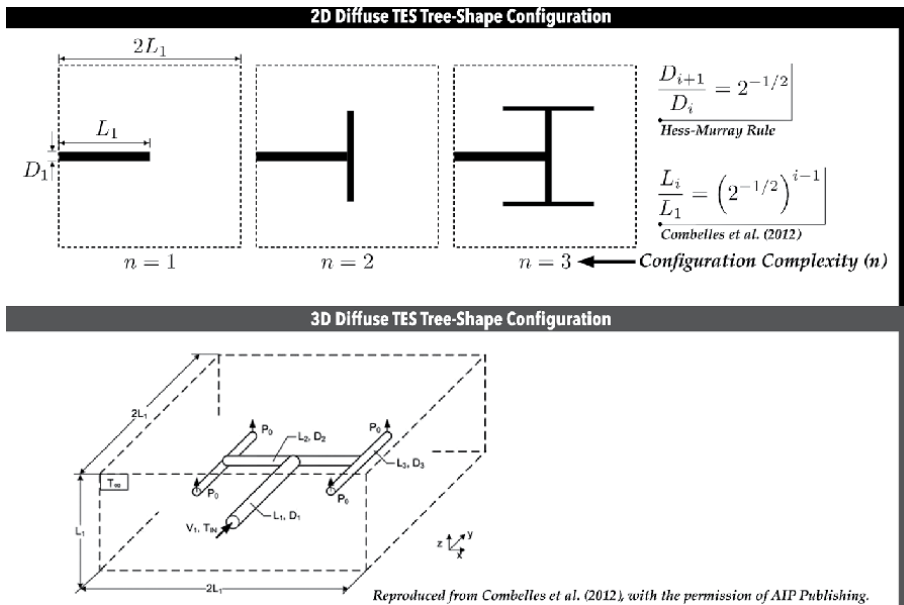
transfer mechanism is diffusion and the mode is the one on the left of **Figure 1**. But if one uses a PCM, the energy storage story follows the second mode on the right, involving natural convection, a melting process, a solid–liquid interface moving boundary, and all these elements lead to additional complexity of the heat exchanger, affecting the energy storage scales.

### 3.1 Heat exchangers in sensible heat storage

Consider an underground volume of solid with a network of channels through which a thermal fluid transports energy for storage purposes. The storage mechanism is heat diffusion from the channels outer area to the volume of solid. What should be the structure of the channels network? Combelles et al. [14] explored this TES system with tree-shaped configurations of 2D channels made of parallel plates the length  $L_1$  and  $D_1$  of width within an area of  $2L_1 \times 2L_1$ , and 3D pipes configured within a solid of  $2L_1 \times 2L_1 \times L_1$  of volume, as depicted in **Figure 2**.

The first step is to characterize the architecture of each configuration type (2D or 3D) in terms of their Sveltiness, as the global property of the system, which relates the external length scale given by the total length of the flow network,  $L_{total} = \sum_{i=1}^n L_i$ , depending on its complexity ( $n$ ), and the internal flow length scale varying with the 2D or 3D nature of the flow. If the flow network is bi-dimensional, the internal length scale corresponds to  $A_f^{1/2}$  with  $A_f = \sum_{i=1}^n 2^{i-1} L_i D_i$ , while in the three-dimensional configuration, this scale is  $V_f^{1/3}$  with  $V_f = \sum_{i=1}^n 2^{i-1} \frac{\pi}{4} D_i^2 L_i$ . When one increases the complexity of the flow network, Lorente et al. [15] show the relation between the length and diameter of one branch ( $i$ ) and the next ramification ( $i + 1$ ) follows the Hess-Murray rule. Thus,

$$\frac{L_{i+1}}{L_i} = \frac{D_{i+1}}{D_i} = 2^{-1/2} \tag{12}$$



**Figure 2.** 2D and 3D diffusive TES tree-shape configurations.



which developed to depend on the length and diameter of the first branch ( $L_1, D_1$ ), simplify to

$$L_i = L_1 \left( 2^{-1/2} \right)^{i-1} \quad (13)$$

$$D_i = D_1 \left( 2^{-1/2} \right)^{i-1} \quad (14)$$

The Sveltiness for both general configurations, considering the relations in Eqs. (13) and (14), depends on two major features of the configuration: its complexity ( $\psi(n)$ ); and the geometrical relation between the length and diameter of the first channel ( $L_1/D_1$ ).

$$Sv_k = \psi_k(n) \left( \frac{L_1}{D_1} \right)^{q_k} \text{ with } k = \{2D, 3D\} \quad (15)$$

and

$$\begin{cases} \psi_{2D}(n) = \frac{1 - 2^{-n/2}}{1 - 2^{-1/2}} n^{-1/2} & \wedge q_{2D} = 1/2 \\ \psi_{3D}(n) = 2 \left( \frac{3+2\sqrt{2}}{1-2^{-n}\sqrt{2^n}} \right)^{1/3} (1 - 2^{-n/2}) & \wedge q_{3D} = 2/3 \end{cases}$$

If the Sveltiness indicates the evolution of the flow configuration, one should connect the flow architecture complexity,  $\psi_k(n)$ , and the geometry of the initial channel, with the scales associated to the storage of energy.

The amount of energy stored depends on the material, but in this TES system, the relevant scale is the storage time and the evolution of the temperature in the conductive solid. Considering the solid is, initially, at  $T_0$ , and the inflowing thermal fluid is at  $T_{in}$ , in time, the average temperature in the solid ( $T_{avg}$ ) evolves toward  $T_{in}$ . Therefore, Combelles et al. [14] analyzes the evolution of this diffusive thermal storage configuration with a dimensionless thermal potential as

$$\theta_{avg} = \frac{T_{avg} - T_0}{T_{in} - T_0} \quad (16)$$

This analysis focuses on the timescales of energy storage and the corresponding effect of the configuration complexity (number of bifurcations,  $n$ ). Considering the fluid, there are two essential timescales:

- the timescale of fluid traveling the  $n$  channels;

$$t_f = \sum_{i=1}^n \frac{L_i}{V_i} = \psi_f(n) \left( \frac{L_1}{V_1} \right) \sim \frac{L_1}{V_1} \quad (17)$$

since  $\psi_f(n) = \frac{2^{-3n/2}-1}{2^{3/2}-1}$  varies between 1 and 1.55, which means  $\psi_f(n) \sim 1 \forall n \geq 1$ ;

- and the timescale of thermal diffusion across the channel;

$$t_c \sim \frac{D_1^2}{\alpha_f} \quad (18)$$

Combelles et al. [14] argue that in the case where thermal diffusion in the channel's boundary layer is a slower process than the fluid traveling through the

channels,  $t_f < t_c$ , and the temperature of the fluid at exit is practically unchanged. It is a relevant result to establish a stable boundary condition.

The third timescale, and the longer, corresponds to the time it takes to store energy in the solid volume,  $t_s$ , meaning the timescale to heat the entire volume by thermal diffusion, expressed as

$$t_s \sim \frac{L_1^2}{\alpha_s} \quad (19)$$

From the numerical simulations, the evolution of the dimensionless thermal potential  $\theta_{avg}(t)$  is given by

$$\theta_{avg}(t) = 1 - \exp\left(-C\frac{t}{\tau}\right) \quad (20)$$

where  $C$  is a scale parameter, and  $\tau$  is the TES response time given by

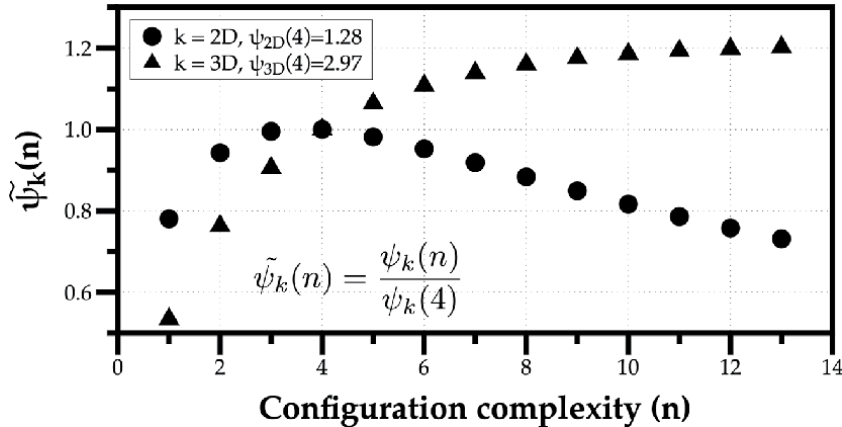
$$\tau = \frac{m_s c_{p,s}}{\dot{m}_f c_{p,f}} \quad (21)$$

with  $m_s = \rho_s 4L_1^3$  as the solid mass (and  $\rho_s$  its density),  $c_{p,s} = \frac{k_s}{\rho_s \alpha_s}$  is the solid specific heat, and  $\dot{m}_f c_{p,f} = \left(\frac{k_f}{\alpha_f}\right) \frac{\pi}{4} D_1^2 V_1$  is the thermal capacity rate of the fluid. Considering Eq. (15), and introducing it in the TES response time results in

$$\tau = \frac{16}{\pi} \left(\frac{Sv_k}{\psi_k(n)}\right)^{2/q_k} \frac{\tilde{\alpha}}{\tilde{k}} t_f \quad (22)$$

with  $\tilde{\alpha} = \alpha_f/\alpha_s$  and  $\tilde{k} = k_f/k_s$ . The results from the numerical simulations in both 2D and 3D configurations reported in Combelles et al. [14] evidence the decrease of the diffuse TES system response time with a higher complexity of the flow network, which is consistent with the relation obtained in Eq. (22) for a fixed  $Sv_k$  as considered in their simulations.

**Figure 3** shows the results for the complexity degree scale ( $\psi_k(n)$ ) normalized by the value obtained for  $n = 4$ :  $\tilde{\psi}_k(n) = \psi_k(n)/\psi_k(4)$ . In a 2D configuration, one obtains a maximum of the scale associated to the complexity degree at  $n = 4$  (which



**Figure 3.** Evolution of the scale associated to the complexity degree of the flow network in relation to its maximum,  $\tilde{\psi}_k(n)$ .

is the maximum complexity investigated in Combelles et al. [14]). In the 3D configuration,  $\tilde{\psi}_{3D}(n)$  shows a monotonic behavior, although for  $n > 10$ , the increase of one level of complexity generates a variation of less than 1% in diminishing returns. The maximum complexity explored by Combelles et al. [14] was  $n = 4$  and adding one level of complexity would produce an increment of only 6.4% compared to 10.6% between  $n = 3$  and 4.

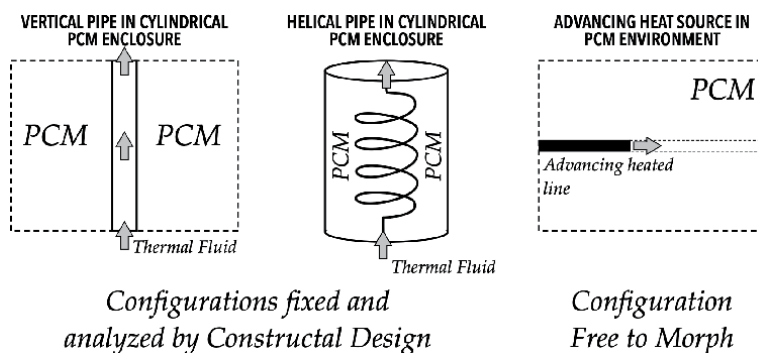
In absolute terms, the constructal design of heat exchangers in diffusive TES systems suggests the choice of a 3D configuration, rather than a 2D, for a faster energy storage, since it leads to  $\psi_{3D}$  complexity scale factors of 1.6 to 2.3 times higher than the 2D scale, allowing shorter charging times. However, in applications where a 2D configuration is more appropriate, the level of complexity should not go beyond 4 dendritic bifurcations.

### 3.2 Heat exchangers in latent heat storage

Energy storage systems using the latent heat of a certain phase-change material (PCM) rely on the heat transfer mechanisms of diffusion and natural convection. Initially, the PCM is in its solid state and it stores heat by diffusion close to the channel containing the thermal fluid, or fin, until it reaches the fusion (or melting) temperature ( $T_m$ ), creating a melting frontline. Thereafter, a solid–liquid interfacial boundary develops and the melting history consists in two distinct periods: invasion; and consolidation.

The invasion period corresponds to the time interval until the solid–liquid interface reaches a distance equivalent to the process characteristic length. The consolidation period corresponds to the remaining time until all the PCM in the LHS system is in its liquid state. These periods do not, necessarily, correspond to the timescales associated to the diffusive and convective heat transfer processes. The charging and discharging times of LHS depend on the heat exchanger design and the dominant heat transfer mechanisms through which energy flows from its source to the PCM.

There are several design configurations investigated with a constructal approach for the heat exchangers using phase-change to store energy in PCM. **Figure 4** presents three configurations reported in the literature. The configurations with a vertical pipe [15] is the less prone to morphing. The helical pipe [16] in a cylindrical PCM enclosure is fixed, but the ability to vary the number of turns and the diameter of each turn increases the system's freedom to morph. Finally, an advancing heat source line invading the PCM material aims at the theoretical design with the greatest freedom to morph [17]. One of the novelties in constructal design of engineering systems is determining the Sveltiness as expression of its architecture, and the system's freedom to morph, considering an evolutionary path toward



**Figure 4.** Heat exchanger configurations investigated with a constructal theory approach.

vascularization, i.e. an increase of its Svelteness. The constructal analysis of all designs also implies the investigation of length and timescales associated with heat transfer mechanisms, and the possible effect of the Svelteness in these scales.

Lorente et al. [15] performed a scale analysis to analyze the latent thermal energy storage where energy flows from the thermal fluid circulating inside a central vertical pipe and the surrounding PCM. The dominant heat transfer mechanism is natural convection. The Svelteness in this case would have the height of the enclosure ( $L_e = H$ ) as external length scale, and an internal length scale based on the volume occupied by the thermal fluid as  $L_i = (\frac{\pi}{4}d^2H)^{1/3}$ , with  $d$  as the diameter of the vertical pipe. The final outcome relating the Svelteness with the heat exchanger geometry leads to

$$H/d = (\pi/4)^{1/3} Sv^{3/2} \quad (23)$$

The maximum energy one can store in this first TES configuration is  $Q_{max} = \frac{\pi}{4}(D^2 - d^2)H\rho h_{sl}$ , with  $\rho$  as the PCM density and  $h_{sl}$  as its latent heat of fusion. According to Lorente et al. [15], the time-scale of the melting history ( $\tau_m$ ) considers natural convection as the dominant heat transfer mechanism where friction dominates buoyancy forces, thus, resulting in

$$\tau_m = \frac{Q_{max}}{\pi dk \Delta T C Ra_H^{1/4}} \quad (24)$$

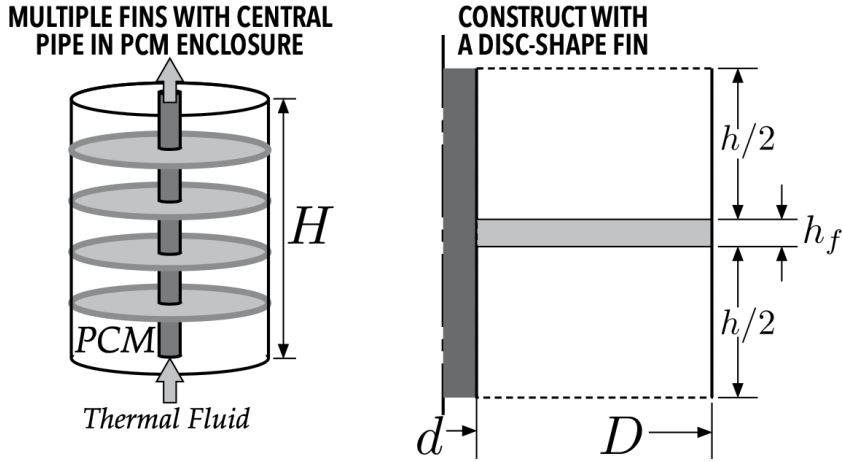
The relation between the maximum amount of energy stored and this time-scale, including Eq. (23) in (24) leads to  $Q_{max}/\tau_m \sim Sv^{-3/2}$ . Considering that evolution in constructal theory occurs toward the vascularization of flow architectures, implying the increase of their Svelteness, in this case, it leads to decreasing  $Q_{max}/\tau_m$ , instead of increasing as desired. This is an interesting result from the constructal design point of view because it indicates that natural convection generated by the vertical pipe alone is not the best heat transfer mechanism for a faster energy storage in LHS. However, one should point that their simplified scale analysis, and numerical simulations, which considers an annular moving melting front, seems unrealistic when confronted with later experimental works such as Zhang et al. [18], with time-scales of one order of magnitude lower than those predicted in Lorente et al. [15] –  $O(\tau_m) \sim 10^2$  h. Nonetheless, this result points to the need of a better solution to facilitate the flow access of energy between a surface heated by a thermal fluid and the PCM. The works of Ogoh and Groulx [19], and Kamkari and Shokouhmand [20], are examples where fins around the main energy source facilitate its flow to the PCM for storage during charging, promoting heat transfer by diffusion and mitigating natural convection.

Considering the case of Ogoh and Groulx [19], **Figure 5** depicts the adding of disc-shape fins to the original vertical pipe in cylindrical PCM enclosure configuration, where each disc-shape fin corresponds to a *construct* (represented on the right).

The total height of the cylinder ( $H$ ), in terms of constructs corresponds to  $H = n(h + h_f)$ , with  $n$  as the number of constructs,  $h$  the total height of the PCM inside a construct, and  $h_f$  as the fin thickness. Therefore, the interval between annular fins becomes

$$h = \frac{H}{n} - h_f \quad (25)$$

Considering the Svelteness ( $Sv$ ) for this construct as the ratio between the external characteristic length based on the upper and bottom areas of the disc-shape fin,  $L_e = [\frac{\pi}{2}(D^2 - d^2)]^{1/2}$ , and the internal characteristic length given by the annular



**Figure 5.**  
 Disc-shape fin constructs applied to a vertical pipe in cylindrical PCM enclosure.

disc volume,  $L_i = \left[ \frac{\pi}{4} (D^2 - d^2) h_f \right]^{1/3}$ , considering Eq. (25), one can express the ratio between the space between fins ( $h$ ) and the external diameter of the enclosure ( $D$ ) as

$$\frac{h}{D} = \frac{H}{nD} - \frac{\sqrt{2\pi}}{Sv^3} \quad (26)$$

Ogoh and Groulx [19] argue for a neglecting effect of convection between annular fins, thus, the energy stored by phase-changing the PCM from solid to its liquid state occur by conduction. In this sense, the most important scale characterizing the melting front ( $\delta$ ) departs from the annular disc fin. The balance between the conduction heat flux ( $q''$ ) supplied to the melting front and the rate of melting can be described as

$$q'' dt = \rho h_s d\delta \quad (27)$$

Assuming a linear temperature distribution across this layer where the heat transfer occurs by diffusion, one could quantify the heat flux as  $q'' = k \frac{\Delta T}{\delta}$ , which applied in Eq. (27) results in

$$\delta = \sqrt{a\tau} \quad (28)$$

with  $a = \frac{2k\Delta T}{\rho h_s}$ , where  $\Delta T = T_w - T_m$ , with  $T_w$  as the temperature of the fin wall,  $T_m$  the fusion temperature of the PCM, and  $\tau$  corresponds to the timescale of energy storage. To understand the evolution of the configuration based on this scale, one could argue that the charging finishes when  $h \sim 2\delta$ , thus, replacing this scale in Eq. (26), and solving it as a function of the Sveltiness, results in

$$Sv \sim \sqrt{2\pi} \left( \frac{nD}{H - 2n\sqrt{a\tau}} \right) \quad (29)$$

Therefore, since  $Sv > 0$ , it implies  $H - 2n\sqrt{a\tau} > 0$ , resulting in an upper theoretical limit for this timescale as

$$\tau < \left( \frac{H}{2n} \right)^2 \frac{1}{a} = \tau_{max} \quad (30)$$

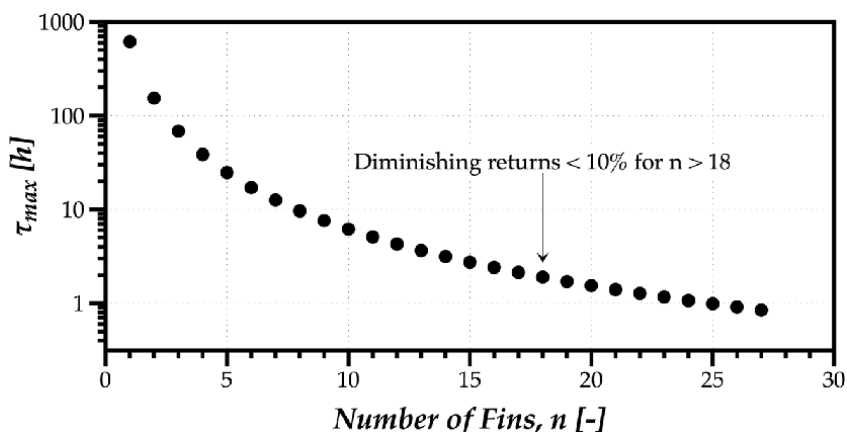
**Figure 6** shows the results for this limit considering the properties reported in [19].

The constructal design analysis of this heat exchanger indicates diminishing returns of less than 10% for a number of fins above  $n > 18$ , which is coherent with the numerical results presented by Ogoh and Groulx [19]. Applying the timescale defined by Eq. (30) to the experimental conditions in the work of Kamkari and Shokouhmand [20], which explore the effect of no fins with the cases of 1 and 3 fins, for the later case,  $\tau_{max}$  is roughly  $1.3\times$  the value measured for the total melting process. In the case of the experiments with 1 fin, the results for  $\tau_{max}$  are significantly larger, evidencing the role of natural convection in delaying the heat transfer to the PCM.

The helical coil illustrated in **Figure 4** is an alternative to the vertical pipe, and a geometry where the freedom to morph is larger because of the ability to change the helix diameter, number of turns and pitch angle. Alailami et al. [16] explored the morphing ability of the system in its design stage to optimize the storage of energy analyzing two scales. The timescale of heat penetrating the storage material from the boundaries of the helical coil to the cylinder diameter,  $\tau_c = D^2/\alpha$ ; and the temperature difference,  $T(t) - T_{tf}$ , scaled by the initial condition,  $T(0) - T_{tf}$ , with  $T_{tf}$  as the temperature of the thermal fluid. When Alailami et al. [16] simulated the evolution of the scaled average temperature -  $T_{avg}^* = \frac{T_{avg}(t^*) - T_{tf}}{T(0) - T_{tf}}$  - its value decreased with the scaled time -  $t^* = t/\tau_c$  - meaning the average temperature of the energy storage material approaches the temperature of the thermal fluid.

Afterward, focusing the analysis on  $t^* = 0.3$ , and varying the helical coil diameter -  $D_h = \zeta D$  - and pitch height -  $H_h = \varepsilon H$  - obtained as function of the cylinder diameter ( $D$ ) and height ( $H$ ), the authors reached an optimum diameter and pitch length of the helical coil, corresponding to  $\zeta = 0.6$ , and  $\varepsilon = 0.3$ , respectively.

Without using the work of Alailami et al. [16], Joseph et al. [21] performed an experiment of this configuration to store energy in a PCM. The authors used unoptimized values for the helical coil ( $\zeta \approx 0.7$ ,  $\varepsilon \approx 0.2$ ), from the Alailami et al. [16] point of view. However, the PCM configuration showed promising results storing 20% more energy than its equivalent mass in water. Also, the charging process in the PCM facility was slower and the authors attribute this result to the unoptimized heat exchanger design, justifying the need of more research on this topic.



**Figure 6.** Variation of limit timescale for the energy stored in a PCM through annular fins distributed around a vertical pipe inside a cylindrical enclosure.

The last geometry in **Figure 4** is theoretical and corresponds to the greatest freedom to morph through an advancing heated line that can bifurcate at some point. The analysis performed by Bejan et al. [17] focus on the invasion (line advances until the storage boundaries) and consolidation (all PCM melts) stages, and introduces a tree invasion pattern with a complexity level up to  $n = 2$  branching events. The results of this theoretical analysis point to the acceleration of the charging times. However, the conversion of this approach into a practical application is still a challenge, since there is no technology capable of this kind of morphing inside a PCM solid environment.

A final comment concerns the possible contribution of constructal design to optimize the total cost of heat exchanger design methods, which is not a direct correlation. As shown by Azad and Amidpour [22], since the constructal design provides an evolutionary perspective on the optimum geometric features of heat exchangers, it can lead to a substantial reduction of the total cost, compared to more standard design approaches. Namely, in the aforementioned work, the authors used constructal theory to optimize shell and tube heat exchangers, and the new approach allowed to reduce this cost by 50%. However, the application of a similar reasoning in the development of heat exchangers for thermal energy storage is in need of more research.

#### **4. Conclusions**

Thermal energy storage is one of the preeminent options to face the energy challenges of this century, providing a high energy saving potential and effective utilization. However, in these systems, the architecture of the heat exchangers through which energy flows, during charge and discharge, is of paramount importance. While most approaches optimize heat exchanger designs, the one presented in this chapter, based on constructal theory, follows an evolutionary design, meaning that the configuration explored at the design stage is dynamic and free to morph. It is not pre-defined, rigid, or still, but considers how it should evolve toward the greater access of the energy currents that flow through it.

Thermal energy storage systems follow two thermodynamic processes using the sensible heat of the energy storage material, or, besides the sensible heat, also the latent heat, as in Phase-Change Material (PCM). After introducing the general considerations on these systems, this chapter presents two design tools in constructal theory: the Svelteness, as a global property of any flow system, which tends to increase and evolve toward vascularization; and the scale analysis, as an expedite problem solving tool that allows obtaining relevant information of the several energetic processes involved.

Using the design tools presented, this chapter reviews and further explores the constructal theory approach in the development of heat exchangers for sensible and latent thermal energy storage configurations. The analysis evidences the explanatory potential of the constructal approach, increasing the sensibility of the engineer to the advantages of including the freedom to morph at the design stage of heat exchangers in thermal energy storage.

#### **Acknowledgements**

The author would like to acknowledge project UIDB/50022/2020 and UIDP/50022/2020 of ADAI for the financial support for this publication.

## Nomenclatures and Abbreviations

$c_p$	Specific heat [ $\text{J}\cdot\text{kg}^{-1}\text{K}^{-1}$ ]
$d, D$	Diameter [m]
$H, h$	Height [m]
$h_{sl}$	Latent heat of fusion [J/kg]
$k$	Thermal conductivity [ $\text{W}\cdot\text{m}^{-1}\text{K}^{-1}$ ]
$L$	Length [m]
$m$	Mass [kg]
$\dot{m}$	Mass flow rate [kg/s]
$n$	Number of tubes or Complexity degree [-]
$Q_{st}$	Energy stored [J]
$r$	radial coordinate [m]
Ra	Rayleigh number [-]
Sv	Svelteness [-]
$T$	Temperature [K]
$t$	time [s]
$T_f$	Final temperature [K]
$T_i$	Initial temperature [K]
$T_m$	Melting temperature [K]
$V$	Volume [ $\text{m}^3$ ]

### Greek Symbols

$\alpha$	Thermal diffusivity [ $\text{m}^2/\text{s}$ ]
$\delta$	Length [m]
$\Delta T$	Temperature difference [K]
$\varepsilon$	Scale factor [-]
$\zeta$	Scale factor [-]
$\theta$	Normalized temperature difference [-]
$\rho$	Density [ $\text{kg}/\text{m}^3$ ]
$\tau$	Timescale [s]
$\phi$	Void fraction

### Subscripts

<i>avg</i>	average
<i>c</i>	cylinder
<i>e</i>	external
<i>f</i>	fluid, fin
<i>h</i>	helical
<i>i</i>	internal, inner
<i>m</i>	melting
<i>max</i>	maximum
<i>o</i>	outward
<i>s</i>	solid
<i>st</i>	stored
<i>t</i>	tube
<i>tf</i>	thermal fluid
2D	Two-dimensional
3D	Three-dimensional
HE	Heat Exchanger
LHS	Latent Heat Storage



PCM	Phase-Change Material
SHS	Sensible Heat Storage
TES	Thermal Energy Storage
TSM	Thermal Storage Material


## Author details

Miguel Rosa Oliveira Panão  
ADAI, LAETA, Department of Mechanical Engineering, University of Coimbra,  
Coimbra, Portugal

\*Address all correspondence to: [miguel.panao@dem.uc.pt](mailto:miguel.panao@dem.uc.pt)

## IntechOpen

---

© 2021 The Author(s). Licensee IntechOpen. This chapter is distributed under the terms of the Creative Commons Attribution License (<http://creativecommons.org/licenses/by/3.0>), which permits unrestricted use, distribution, and reproduction in any medium, provided the original work is properly cited. 

## References

- [1] Zsiborács H, Baranyai NH, Vincze A, Zentkó L, Birkner Z, Máté K, Pintér G. Intermittent renewable energy sources: The role of energy storage in the European power system of 2040. *Electronics*. 2019 Jul;8(7):729.
- [2] Wu S, Yan T, Kuai Z, Pan W. Thermal conductivity enhancement on phase change materials for thermal energy storage: A review. *Energy Storage Materials*. 2020 Mar 1;25:251–95.
- [3] Soares N, Costa JJ, Gaspar AR, Santos P. Review of passive PCM latent heat thermal energy storage systems towards buildings energy efficiency. *Energy and Buildings*. 2013 Apr 1;59:82–103.
- [4] Huang BK, Toksoy M, Cengel YA. Transient response of latent heat storage in greenhouse solar system. *Solar Energy*. 1986 Jan 1;37(4):279–92.
- [5] Kaygusuz K. Experimental and theoretical investigation of latent heat storage for water based solar heating systems. *Energy Conversion and Management*. 1995 May 1;36(5):315–23.
- [6] Sarbu I, Sebarchievici C. A comprehensive review of thermal energy storage. *Sustainability*. 2018 Jan;10(1):191.
- [7] Alva G, Lin Y, Fang G. An overview of thermal energy storage systems. *Energy*. 2018 Feb 1;144:341–78.
- [8] Clemente MR, Panãeo MR. Introducing flow architecture in the design and optimization of mold inserts cooling systems. *International Journal of Thermal Sciences*. 2018 May 1;127:288–93.
- [9] Bejan A. *Freedom and Evolution: Hierarchy in Nature, Society and Science*. Springer Nature; 2019 Dec 6.
- [10] Bejan A, Lorente S. *Design with Constructal Theory*. Wiley; 2008.
- [11] Ghoneim AA. Comparison of theoretical models of phase-change and sensible heat storage for air and water-based solar heating systems. *Solar Energy*. 1989 Jan 1;42(3):209–20.
- [12] Agyenim F, Eames P, Smyth M. A comparison of heat transfer enhancement in a medium temperature thermal energy storage heat exchanger using fins. *Solar Energy*. 2009 Sep 1;83(9):1509–20.
- [13] Bejan A. *Convection Heat Transfer*. 4th Ed., John Wiley & Sons; 2013.
- [14] Combelles L, Lorente S, Anderson R, Bejan A. Tree-shaped fluid flow and heat storage in a conducting solid. *Journal of Applied Physics*. 2012 Jan 1;111(1):014902.
- [15] Lorente S, Bejan A, Niu JL. Phase change heat storage in an enclosure with vertical pipe in the center. *International Journal of Heat and Mass Transfer*. 2014 May 1;72:329–35.
- [16] Alalaimi M, Lorente S, Bejan A. Thermal coupling between a helical pipe and a conducting volume. *International Journal of Heat and Mass Transfer*. 2015 Apr 1;83:762–7.
- [17] Bejan A, Ziaei S, Lorente S. The S curve of energy storage by melting. *Journal of Applied Physics*. 2014 Sep 21;116(11):114902.
- [18] Zhang P, Meng ZN, Zhu H, Wang YL, Peng SP. Melting heat transfer characteristics of a composite phase change material fabricated by paraffin and metal foam. *Applied Energy*. 2017 Jan 1;185:1971–83.
- [19] Ogoh W, Groulx D. Effects of the number and distribution of fins on the storage characteristics of a cylindrical latent heat energy storage system: a

numerical study. *Heat and Mass Transfer*. 2012 Oct 1;48(10):1825–35.

[20] Kamkari B, Shokouhmand H. Experimental investigation of phase change material melting in rectangular enclosures with horizontal partial fins. *International Journal of Heat and Mass Transfer*. 2014 Nov 1;78:839–51.

[21] Joseph A, Kabbara M, Groulx D, Allred P, White MA. Characterization and realtime testing of phasechange materials for solar thermal energy storage. *International Journal of Energy Research*. 2016 Jan;40(1):61–70.

[22] Azad AV, Amidpour M. Economic optimization of shell and tube heat exchanger based on constructal theory. *Energy*. 2011 Feb 1;36(2):1087–96.



# Earth Air Tunnel Heat Exchanger for Building Cooling and Heating

*Nasim Hasan, Mohd Arif and Mohaideen Abdul Khader*

## Abstract

The computational fluid dynamic (CFD) is an influential method for measuring Heat transfer profiles for typical meteorological years. CFD codes are managed by numerical algorithms that may undertake fluid glide headaches. CFD offers the numerical results of partial differential equations with main airflow and heat transfer in a discretized association. The complex fluid glide and the warmth transfer publications worried in any heat exchanger can be determined with the help of the CFD software program (Ansys Fluent). A study states and framework which implicitly rely on the computational fluid dynamics, which is being formulated for computing the efficiency-related parameters of the thermal part and the capability of the EATHE system for cooling. A CFD simulation program is being used for modeling the system. The framework is being validated with the help of the simulation set-up. A thermal model was developed to analyze thermal energy accumulated in soil/ground for the purpose of room cooling/heating of buildings in the desert (hot and dry) climate of the Bikaner region. In this study, the optimization of EATHE design has been performed for finding the thermal performance of straight, spiral, and helical pipe earth air tunnel heat exchanger and Heat transfer rate for helical pipe was found maximum among all designs.

**Keywords:** computational fluid dynamic, straight pipe, spiral pipe, helical pipe, heat exchanger for earth to air, design

## 1. Introduction

The current world scenario facing an energy crisis because of the depletion of fossil fuels, so we are in need to find alternative sources of energy which can satisfy future energy needs. Non-conventional sources of energy are better alternatives that can be found abundantly on earth [1]. Air-conditioning is a commonly used household and industrial appliance for cooling. The common working fluids used in these devices are CFCs are hazardous to human beings and depletes the ozone layer of the atmosphere. Alternative refrigerants are developed by scientists to overcome the problems associated with energy consumption, environmental pollution, and performance [2, 3]. In this regard one of the alternatives is EATHE. EATHE are modern devices in which tubes are buried under the earth at 1.5 m to 2.5 m. the temperature will remain constant at this depth and it is equal to the annual average temperature. The constant temperature will remain lower in summer and it can be utilized for cooling, similarly, it can be utilized for heating in winter conditions. EATHE is made up of metallic, concrete, or plastic tubes which are buried under the

earth which can utilize the heat capacities of the earth for heating and cooling conditions. TEATHE is used as a source in the winter and sink in the summer. EATHE can be effectively used as a cooling system if the cooling load requirements are met or else it can assist the cooling systems by saving an enormous amount of energy. Many researchers have found out that EATHE can reduce energy consumption enormously and it can be used for building heating and cooling conditions [4–6]. The important factors which affect the performance of the EATHE system are surface condition, temperature, and moisture [7]. Earth to air heat exchanger model has been developed for calculating thermal performance in cooling mode and CFD model is compared with experimental data, 6.07% variation have found while comparing outlet temperature of earth pipe air heat exchanger in CFD model and experimental setup. This variation may be due to the coefficient of friction of the material which is used in simulation taken, irregularities such as insulation, and joints of experimental set-up [8]. CFD model of different diameters of chlorinated polyvinyl chloride pipes has been used for finding thermal performance of heat exchanger for the earth to air in a cooling mode where temperature fall has reduced while decreasing pip diameter and vice versa [9]. In this work, the CFD model of the earth air pipe heat exchanger has been used for finding thermal performance for building heating and cooling purposes. Temperature fall has occurred in cooling mode is 18.590 C and while heating mode, the temperature rises 12.8°C [10]. In this work, the CFD model was validated with an experimental setup where a maximum variance of 7% between the experimental and simulation results is founded [11]. CFD model of different diameter of chlorinated polyvinyl chloride pipes has used for finding thermal performance of heat exchanger for earth to air in cooling mode where temperature fall has reduced while decreasing pip diameter and vice versa [12].

## **2. Methodology**

### **2.1 Description of CFD model**

CFD is an authoritative method to locating the heat and mass transfer from a few years. Computational fluid dynamic codes are measured through numerical algorithms which could take a look at fluid waft headaches. Computational fluid dynamics offers numerical outcomes by the utilization of the (PDE) partial differential equations which leading airflow and heat transmission during a discretized arrangement, complicated liquid motion, and therefore the heat transmission guides involved in any warmth exchanger are often detected through a computational fluid dynamic software program, like FLUENT. Computational fluid dynamic codes in fluent cover 3 elements as shown in **Figure 1** [11].

- Pre-processor are containing input of a motion hassle to a CFD package with the aid of that means of geometry of the area of interest. The CFD place generating grid to subdivision of fluid place. The place is dividing into several sub-areas. The sub-regions are a grid-iron (or mesh) of cells (or manage volumes or factors), with or hint the place border.
- Solver tactics restricted the transfer capacity method for resolving the main equations of the liquid flow and heat transmission.
- put up-processor displays results of the recreations by way of course plots, define plots, charts, moving photographs, and many others.

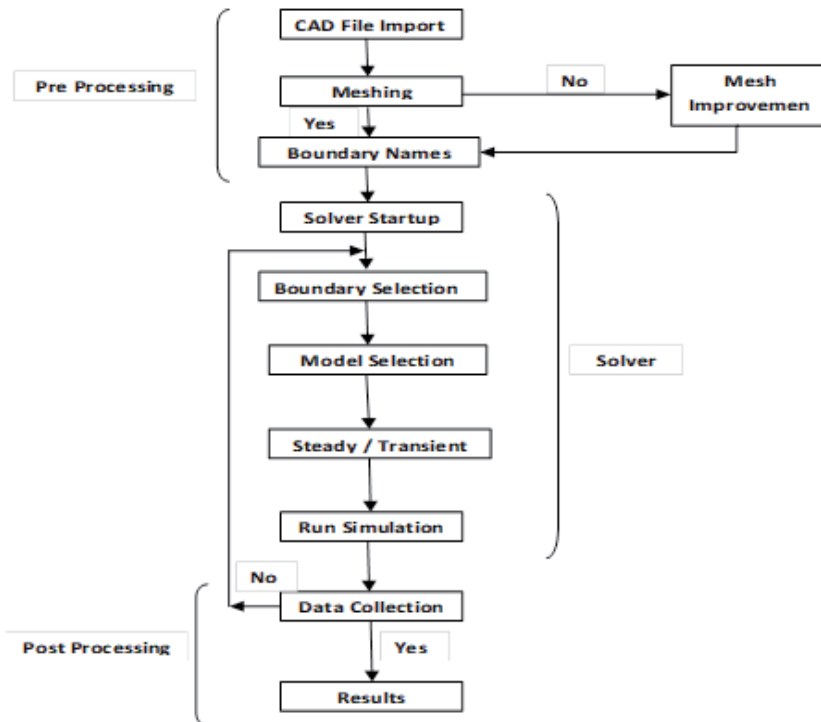


Figure 1.  
CFD flow chart [11].

## 2.2 Model specifications

The present CFD EATHE model is prepared by using CATIA P3 V5R14. The CATIA is a very important tool for preparing geometry. Since the EATHE model is cylindrical. The model has been considering three parts via outer, middle and, inner which are the material of soil, PVC pipe, and air (fluid) respectively. There are three types of model straight pipe, spiral pipe, and helical pipe heat exchanger for the earth-to-air model which is shown in Figures 2–7.

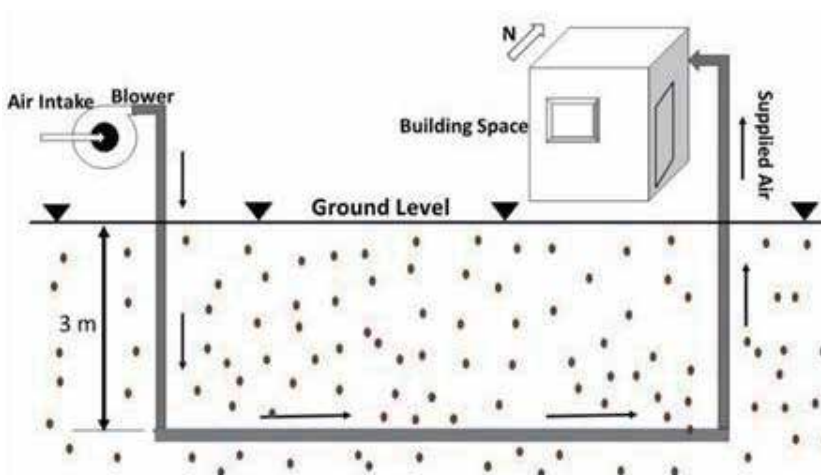
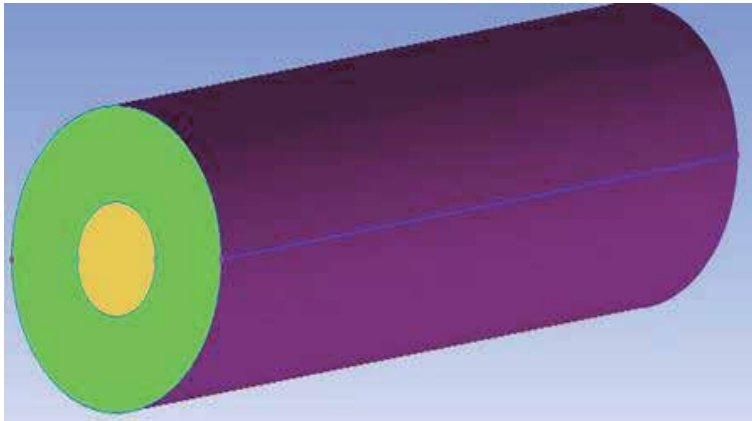
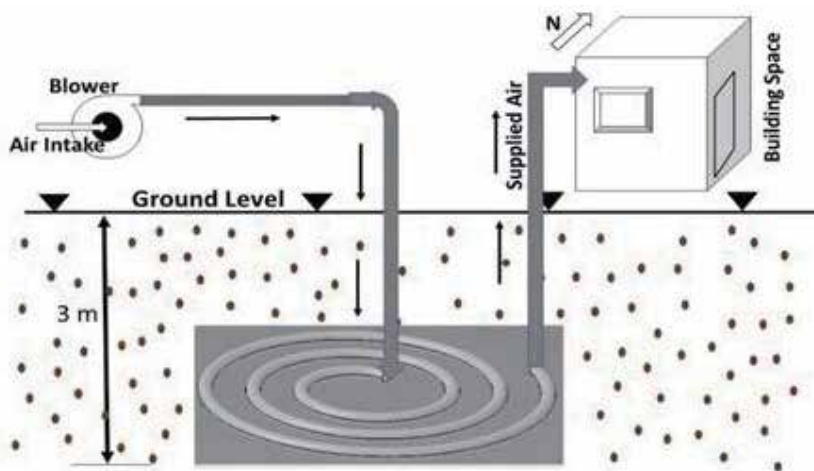


Figure 2.  
Straight pipe heat exchanger for earth to air.



**Figure 3.**  
*Model of straight pipe EATHE.*



**Figure 4.**  
*Spiral pipe heat exchanger for earth to air.*

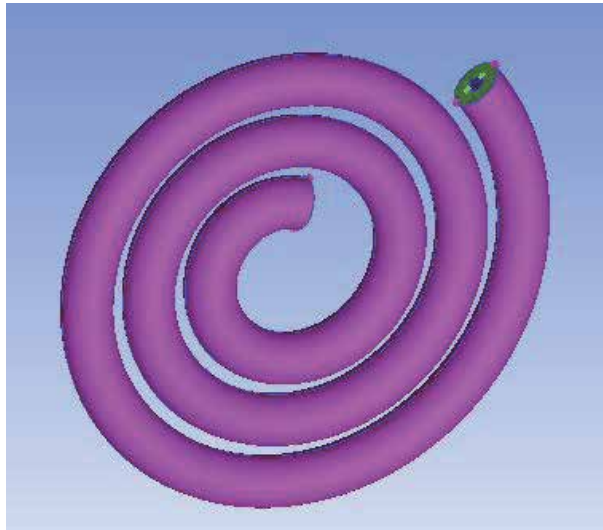
### 2.3 Meshing

The next step of the pre-processing stage is the generation of mesh to be used in the ANSYS ICEM is used for generating the mesh of the geometry. The tetrahedral meshing is used to mesh the heat exchanger for the earth-to-air model which is shown in **Figure 8**. Since air enters from the one end of the pipe this is the 'inlet' and leaves from the 'outlet' created in the model. In the present analysis, CFD simulations performed using an unstructured grid. The mesh is used proximity and curvature-based. One of the geometry meshing algorithms picks a different mesh method by default. The sizing parameters are selected based on the size of the model. The 'relevance centre' and 'smoothing' specification of each mesh is set to fine. The minimum element size and maximum element size both are set to 0.011 mm and 0.15 mm respectively.

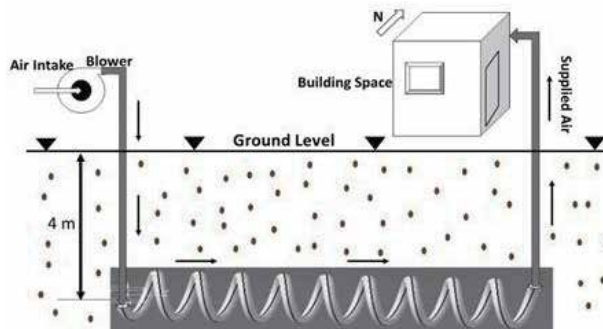
### 2.4 Boundary conditions

The present study is the optimization of EATHE performance. This study is performed for the desert climate of western Bikaner Rajasthan India. The Bikaner has

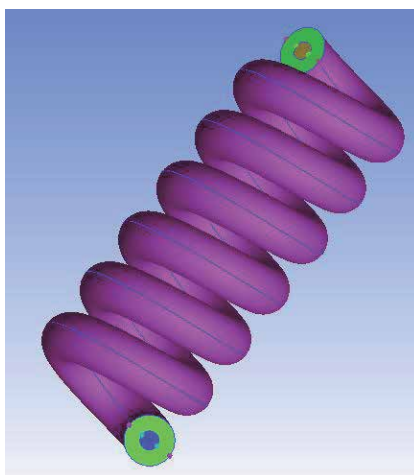




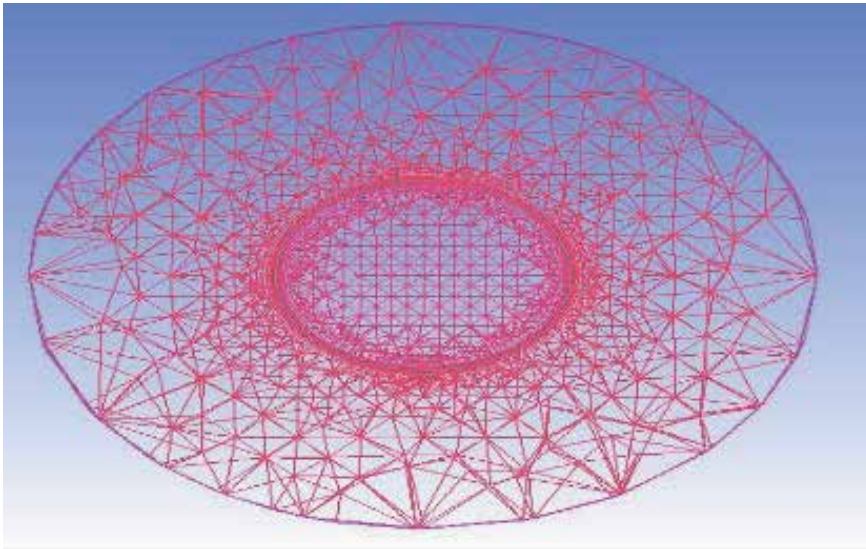
**Figure 5.**  
*Model of spiral pipe EATHE.*



**Figure 6.**  
*Helical pipe heat exchanger for earth to air.*



**Figure 7.**  
*Model of helical pipe EATHE [8].*



**Figure 8.**  
*Meshing model.*

a geological area of East Longitude 28 01' and North Latitude 73 019'. Arranged at a normal elevation of 797 Feet, Bikaner has extraordinary temperatures. As the region lies in the betray region, outrageous warmth in summer and frosty in winter is normal for forsaking. Both day and night temperature increments bit by bit and achieves their most extreme esteems in April, May, and June. The temperature fluctuates from 47°C in summer to around 0°C in winter. Climate is for the most part dry and hot except amid the storm time frame. The dampness is most noteworthy in August with mean day by day relative moistness is 71% in the morning and 52% at night. The EATHE is displayed as two coupled warmth exchange forms, to be specific, convection warm exchange among air streaming in the tube and the tube inner surface, and conduction warm exchange between the pipe external surface and the dirt condition. The external distance across the dirt barrel encompassing the EATHE pipe is taken as four times the pipe width. The external distance across the dirt barrel encompassing the EATHE pipe is taken as four times the pipe width to restrict the emphasis time. To analyze the EAHE system, the following assumptions are made.

1. The temperature of soil throughout the length and depth of pipe is constant.
2. Thermal properties and heat flux are considered to remain constant.
3. Airflow throughout the EATHE is incompressible.
4. Friction and joint losses during the air flow are neglected
5. Engineering materials used are considered homogenous and isotropic.

In this EATHE CFD designed model, air as fluid supplied to the model with Maximum temperature of summer.

Heat gain/released by air to surroundings calculated by

$$Q = \dot{m}C_p(T_{out} - T_{in}). \quad (1)$$

Where.

$Q$  = heat extract or released by the soil to surrounding soil via pipe material (W).

$\dot{m}$  = mass flow rate (kg/sec).

$C_p$  = specific heat (W/m-K).

$T_{out}$  = Temperature of air at the outlet EATHE.

$T_{in}$  = Temperature of air at the inlet EATHE.

Mass conservation Law: The equation for continuity equation or mass conservation law is written as

$$\frac{\partial u}{\partial x} + \frac{\partial v}{\partial y} + \frac{\partial w}{\partial z} = 0 \quad (2)$$

Conservation Law of energy: neither the energy can be created nor destroyed, it only changes its form which stated by the law of energy conservation. The equation can be written as:

$$u \frac{\partial T}{\partial x} + v \frac{\partial T}{\partial y} + w \frac{\partial T}{\partial z} = \alpha \left[ \frac{\partial^2 T}{\partial x^2} + \frac{\partial^2 T}{\partial y^2} + \frac{\partial^2 T}{\partial z^2} \right] \quad (3)$$

(Newton's second law also known as Navier–Stokes equation): the flowing is momentum equation:

Momentum equation in X-direction:

$$u \frac{\partial u}{\partial x} + v \frac{\partial u}{\partial y} + w \frac{\partial u}{\partial z} = \frac{1}{\rho} \frac{\partial p}{\partial x} + \nu \left[ \frac{\partial^2 u}{\partial x^2} + \frac{\partial^2 u}{\partial y^2} + \frac{\partial^2 u}{\partial z^2} \right] \quad (4)$$

Momentum equation in Y-direction:

$$u \frac{\partial v}{\partial x} + v \frac{\partial v}{\partial y} + w \frac{\partial v}{\partial z} = \frac{1}{\rho} \frac{\partial p}{\partial y} + \nu \left[ \frac{\partial^2 v}{\partial x^2} + \frac{\partial^2 v}{\partial y^2} + \frac{\partial^2 v}{\partial z^2} \right] \quad (5)$$

Momentum equation in Z-direction:

$$u \frac{\partial w}{\partial x} + v \frac{\partial w}{\partial y} + w \frac{\partial w}{\partial z} = \frac{1}{\rho} \frac{\partial p}{\partial z} + \nu \left[ \frac{\partial^2 w}{\partial x^2} + \frac{\partial^2 w}{\partial y^2} + \frac{\partial^2 w}{\partial z^2} \right] \quad (6)$$

In Eqs. (2)–(6) the velocity components in  $x$ -,  $y$ -, and  $z$ -directions are  $u$ ,  $v$ , and  $w$  and temperature and pressure are  $T$  and  $p$  of the flowing air [13].

Thermal properties of sandy and sandy soil used for CFD EATHE which is shown in **Table 1**.

Property	Sandy Loam Soil
Thermal Conductivity ( $\kappa$ ) W/m-K	1.26
Density ( $\rho_s$ ) (kg/m <sup>3</sup> )	2215
Specific heat ( $C_s$ ) J/kg-K	1260

**Table 1.**  
Soil properties.

### 3. Result and discussion

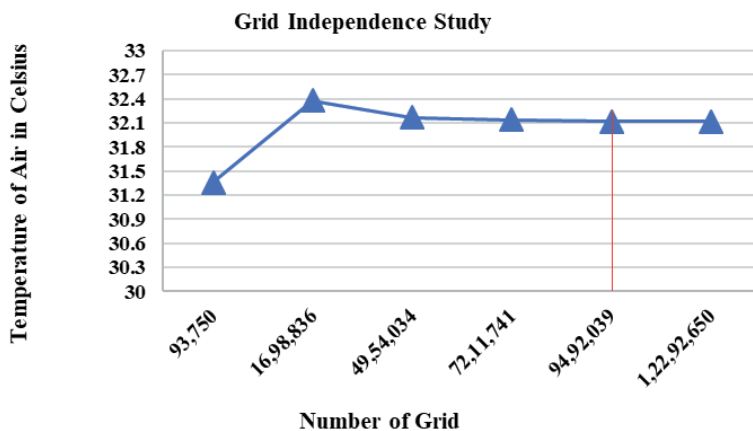
#### 3.1 Grid independence study

The result of CFD analysis is based upon the number of grid elements or size of meshing. If the number of elements is increased, the computational result quality will be good at a certain limit and if the number of elements is decreased, the computational result quality will be poor. In the present study number of an element is depending on the size of the element, if the size of an element increases the number of an element is decreases and vice versa. For good quality of computational fluid dynamic result, we need to reduce the size of an element. Due to reduce in size the resulting quality will improve at a certain size of an element. After a certain size, the CFD result will be constant. Performance of computational fluid dynamic evaluation at the specific variety of detail is called grid independence. For the heat exchanger for the earth-to-air model, the grid independence study has been executed with an exceptional quantity of mesh elements is shown in **Table 2** and **Figure 9**.

The maximum and minimum detail size 0.15 and 0.011 is a stander heat exchanger for earth to air model. This size of an element is further utilized for the earth air tunnel model optimization of the design.

Minimum size of element (mm)	Maximum size of element (mm)	Number of element	Outlet temperature of EATHE (°C)
0.11	1.5	93,750	31.36
0.0275	0.375	16,98,836	32.38
0.0157	0.214	49,54,034	32.17
0.0129	0.176	72,11,741	32.14
0.011	0.15	94,92,039	32.12
0.0095	0.13	1,22,92,650	32.12

**Table 2.**  
Grid independence study with different number of mesh element.



**Figure 9.**  
Graph of temperature v/s number of grids [11].

### 3.2 Validation of model to experimental data

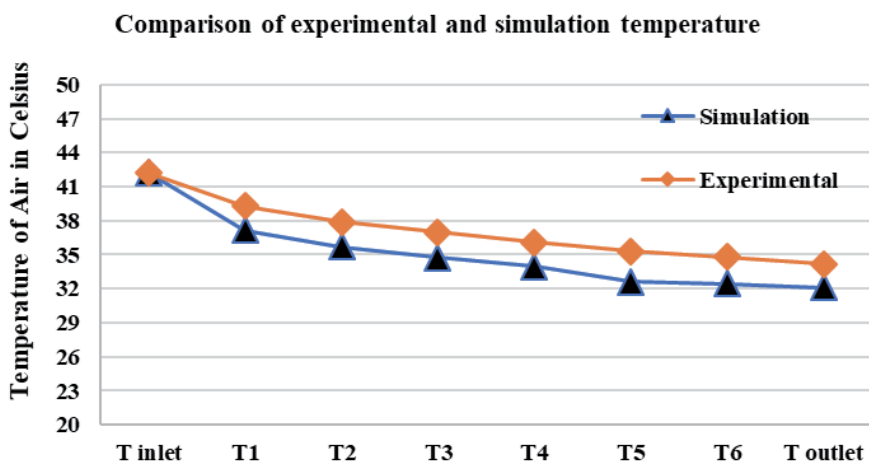
A CFD-based EATHE model was developed to forecast the thermal performance of the EATHE system. The developed CFD model was validated using the previously published results by Bansal et al. [3]. They conducted the experiments to determine the cooling performance of the EATHE system for the hot and dry climate of Ajmer (Western India) with pipes of two different materials-PVC and mild steel. Both the pipes have 0.15 m inner diameter, 23.42 m length, and were enshrouded 2.7 m below the ground surface in the horizontal position. The properties of air, soil and PVC is shown in **Table 3**. Experimental and simulation temperature results along the pipe length for PVC pipe at a velocity of 5 m/s are shown in **Figure 10**. The temperature predicted by the CFD model at all the points, except at the inlet point, along the pipe length is lower than the experimental results. It is also observed that temperature deviation varies between 0% to a maximum of 7.62%, and this deviation in temperatures may be contributed by the variation in the coefficient of friction (from actual friction coefficient of pipe) used in a simulation for the pipe material.

### 3.3 Optimizing the design of heat exchanger for earth to air

The fluid flow analysis for a different design of earth to air heat exchanger has been evaluated by using the computational fluid dynamic fluent model for the cooling mode of the hot and dry climate of the Bikaner region, the ambient temperature of the Bikaner region is considered 47.6°C for the inlet temperature of optimizing the design of heat exchanger for the earth to air. In this analysis, the

Material	Thermal conductivity (w/m K)	Density (kg/m <sup>3</sup> )	Specific heat capacity (j/kg K)
Air	0.0242	1.225	1006
Soil	0.52	2050	1840
PVC	0.16	1380	900

**Table 3.**  
 Physical and thermal parameters used in validation [3].



**Figure 10.**  
 Graph of temperature v/s length of EATHE [8].

simulation of optimizing the design heat exchanger for the earth to air has been carried out to find the temperature of air under the steady-state conditions by keeping the soil around the pipe of the heat exchanger for the earth to air at a constant temperature of 300°K. The fluid flow analysis of optimizing the design heat exchanger for the earth to air system has been considered the outer surface of the soil thickness with 200 mm which is fourth times the diameter of the heat exchanger for the earth to air pipe. The solution of the governing equation shows the temperature profile of fluid which is air with different pipe designs of heat exchanger for the earth to air. Different design of heat exchanger for the earth to air pipe like straight pipe, spiral pipe, and a helical pipe has been selected for analysis. This all types of heat exchanger for the earth to air has been carried out for finding the thermal performance of heat exchanger for the earth to air and find out the optimum design of heat exchanger for the earth to air. The analysis has been performed for hot and dry climate of Bikaner where maximum outdoor temperature was found as 47.6°C and was taken as inlet design temperature for heat exchanger. The various material properties like thermal conductivity, density, and specific heat capacity are used for different types of pipe material is used in simulation which is shown in **Table 4**.

### 3.3.1 Straight pipe heat exchanger for earth to air

Heat exchanger for the earth to an air of straight pipe length, diameter, and velocity 20 m, 0.15 m and 2 m/s respectively have been used for analysis. The ambient temperature of the Bikaner region is 47.6°C is used for the analysis of heat exchanger for the earth to air. There are eight temperature sensors ( $T_{inlet}$ , T1, T2, T3, T4, T5, T6 and  $T_{outlet}$ ) are inserted in a pipe at equal distance of 3.34 m to find out temperature at a different section. Straight pipe heat exchanger for the earth to air, air temperature falls from 47.60 C to 28.340 C.

**Figure 11** represents the contour plot of temperature distribution in the air. The fluid flow analysis of a straight pipe heat exchanger for the earth to air is evaluated by using the computational fluid dynamic fluent model for cooling mode for the hot and dry climate of the Bikaner region.

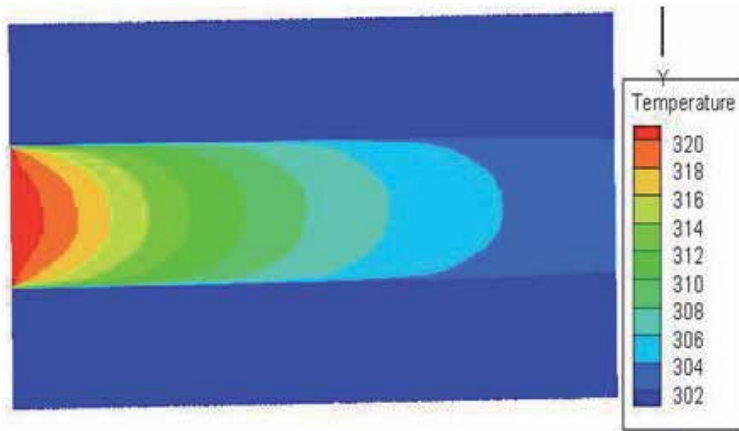
### 3.3.2 Spiral pipe heat exchanger for earth to air

**Figure 12** represents the contour plot of temperature distribution in air and the red color denotes the maximum temperature range, and the blue color shows the minimum temperature range.

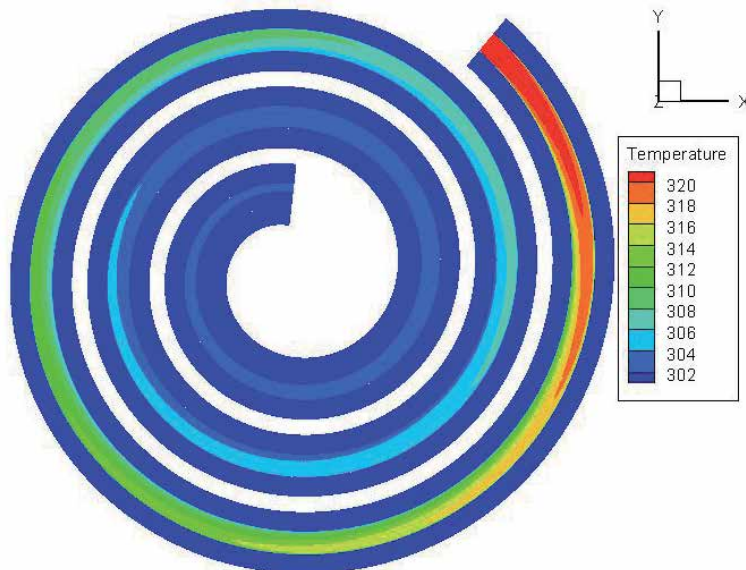
Heat exchanger for the earth to an air of spiral pipe length, diameter, and velocity 20 m, 0.15 m, and 2 m/s respectively have been used for analysis. The ambient temperature of the Bikaner region is 47.6°C is used for the analysis of heat exchanger for the earth to air. There are eight temperature sensors

Material Name	Density (kg/m <sup>3</sup> )	Specific Heat Capacity (J/kgK)	Thermal Conductivity (W/mK)
Air	1.225	1006	0.0242
Sandy Loam Soil (Bikaner)	2215	1260	1.26
HDPE	940	2000	0.4

**Table 4.**  
*Properties of material.*



**Figure 11.**  
*Contour plot of temperature distribution along straight pipe.*



**Figure 12.**  
*Contour plot of temperature distribution along spiral pipe.*

( $T_{inlet}$ ,  $T_1$ ,  $T_2$ ,  $T_3$ ,  $T_4$ ,  $T_5$ ,  $T_6$ , and  $T_{outlet}$ ) are inserted in a pipe at an equal distance of 3.34 m to find out temperature at a different section. Spiral pipe heat exchanger for the earth to air, air temperature falls from 47.60 C to 28.310 C.3.3.3.

### 3.3.3 Helical pipe heat exchanger for earth to air

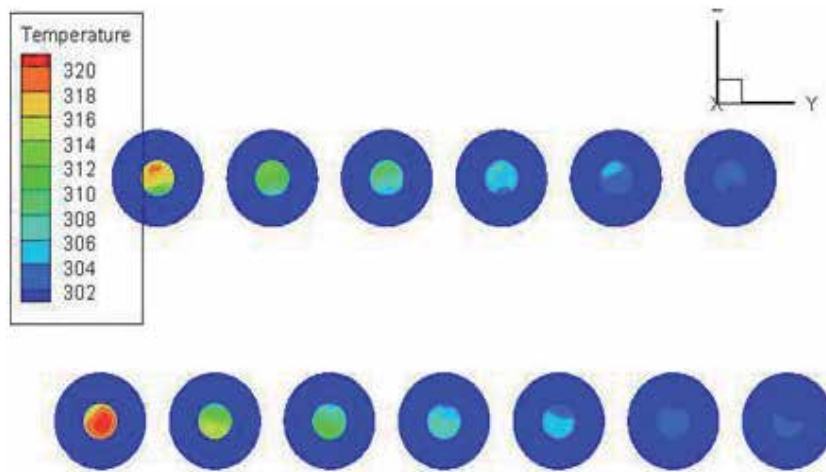
Heat exchanger for the earth to air of helical pipe length, diameter, and velocity 20 m, 0.15 m, and 7 m/s respectively have been used for analysis. The ambient temperature of the Bikaner region is 47.6°C is used for the analysis of heat exchanger for earth to air. There are eight temperature sensors ( $T_{inlet}$ ,  $T_1$ ,  $T_2$ ,  $T_3$ ,  $T_4$ ,  $T_5$ ,  $T_6$  and  $T_{outlet}$ ) are inserted in a pipe at equal distance of 3.14 m to find out temperature at a different section. In a helical pipe heat exchanger for the earth to air, the air temperature falls from 47.60 C to 28.230 C which is shown in **Figure 13**.



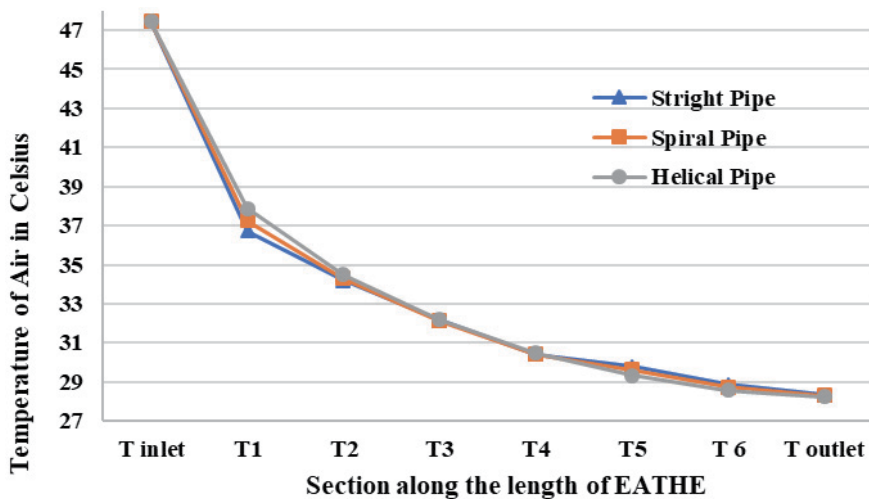
**Figure 13** represents the contour plot of temperature Distribution of air along the length of helical pipe. The fluid flow analysis of helical pipe heat exchanger for earth to air is evaluated by using the computational fluid dynamic fluent model for cooling mode for the hot and dry climate of the Bikaner region.

The fluid flow and heat transfer analysis for EATHE is performed using the CFD fluent model using a different design condition. The performance is compared in terms of temperature drop and heat transfer rate in **Figure 14**.

**Figure 15** shows the graph of heat transfer rate versus length of earth pipe. The heat transfer rate along the pipe length follows the same trend as the temperature followed. The heat transfer rate is achieved in a straight, spiral, and helical pipe is 10403.86w, 10420.19w, and 10463.79w respectively.

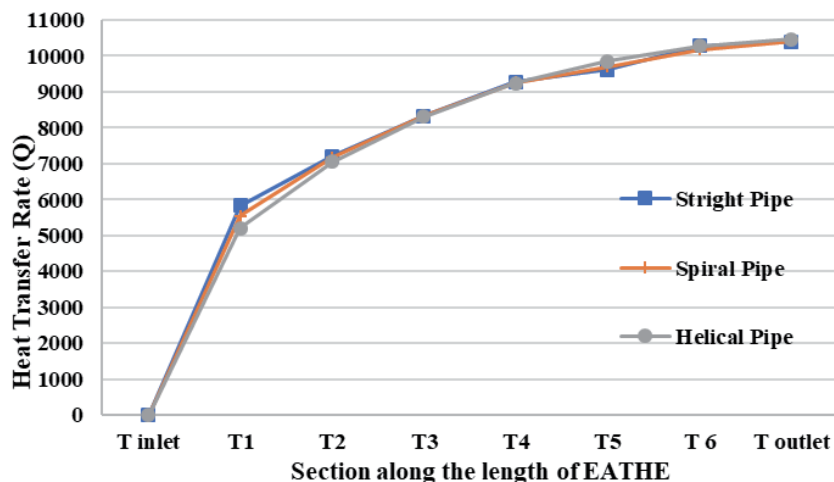


**Figure 13.**  
Contour plot of temperature distribution along helical pipe.



**Figure 14.**  
Graph of temperature v/s length for straight, spiral and helical pipe EATHE.

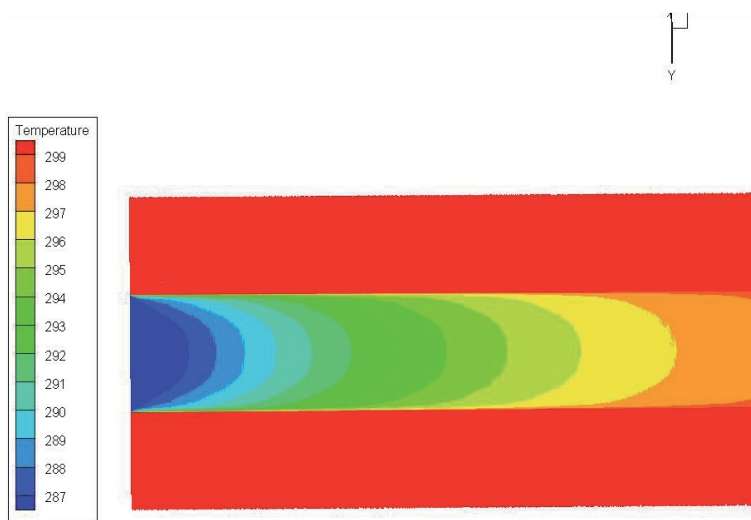




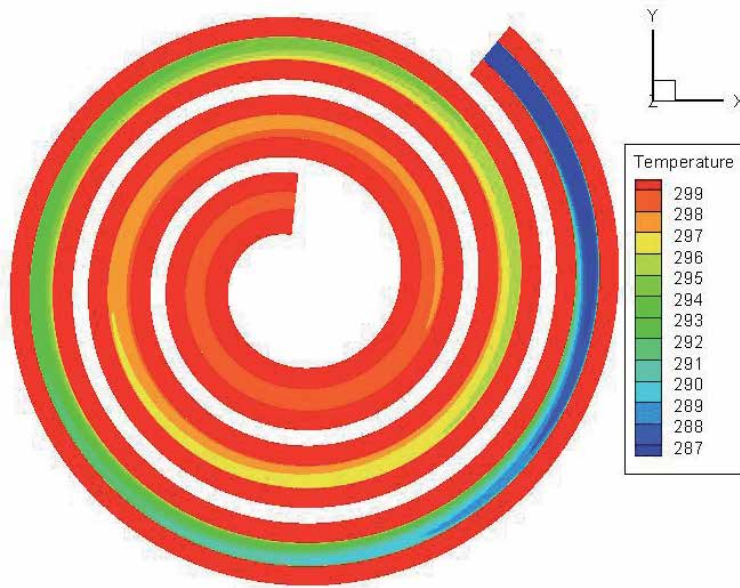
**Figure 15.**  
 Graph of heat transfer rate v/s section length.

### 3.4 CFD analysis of heat exchanger for earth to air for heating space

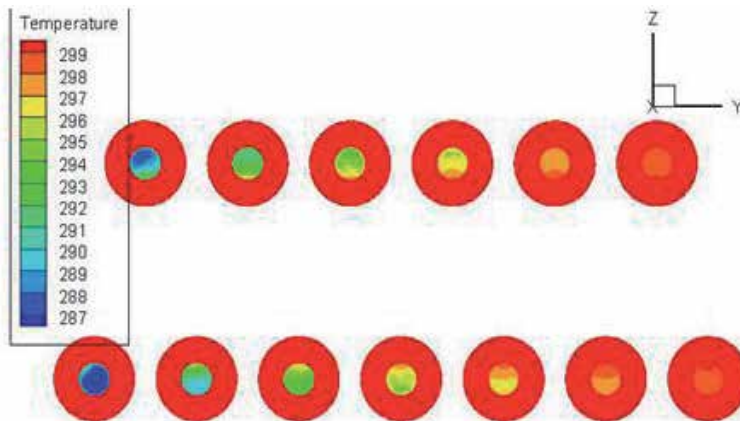
Computational model of earth to air heat exchanger has been analyzed for space heating of building. Warmness exchanger for earth to air consists of length, diameter, pipe fabric, and airspeed 20 m, 0.15, PVC and 2 m/s respectively. This all parameter of heat exchanger for earth to air has been executed for locating the thermal. The ambient average temperature of the Bikaner region in the wintertime is 12.80°C. There are 8 thermocouples are inserted in a pipe at an equal distance of 3.14 m to discover the temperature at each section. Air temperature rise in a straight, spiral, and helical pipe is 12.81°C, 13.29°C, and 13.25°C respectively which is shown in **Figure 16**. **Figures 17–19** show the temperature couture plot of heat exchanger for the earth to air for heating of building in the winter session.



**Figure 16.**  
 Temperature couture plot of straight pipe for heating mode.



**Figure 17.**  
Temperature contour plot of spiral pipe for heating mode.



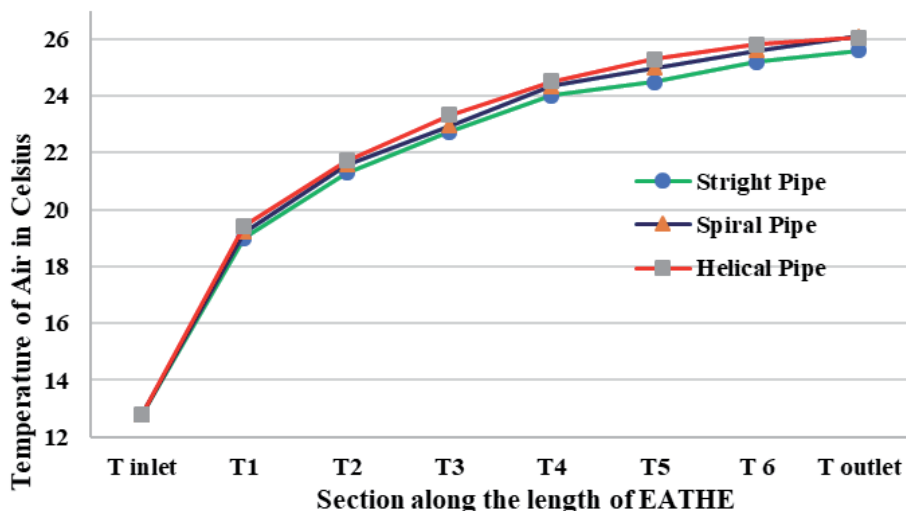
**Figure 18.**  
Temperature contour plot of helical pipe for heating mode.

**Figure 20** illustrates the variations of heat transfer rates along the pipe length of heat exchanger. The heat transfer rate along the pipe length follows the same trend as the temperature followed. The heat transfer rate in a straight, spiral, and helical pipe is 6974.014w, 7235.335w, and 7213.558w respectively.

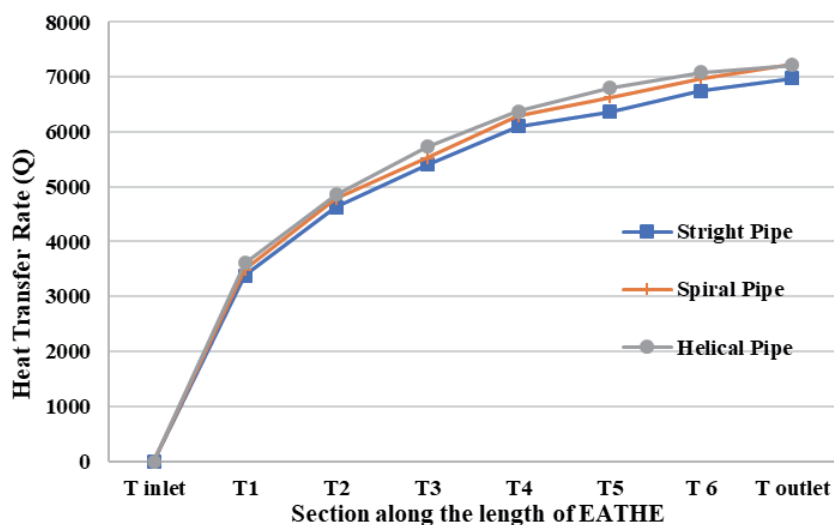
#### 4. Conclusion

From the above results and discussion, the following conclusion are drawn.

- The different design variants of earth to air heat exchanger i.e. spiral pipe, straight pipe, and the helical pipe have been analyzed for finding cooling and heating of the building.



**Figure 19.**  
 Graph of EATHE temperature v/s length.



**Figure 20.**  
 Graph of heat transfer rate v/s section length.

- Air temperature falls in straight, spiral, and helical pipe is 19.11°C, 19.14°C, and 19.22°C respectively.
- Air temperature rise in the straight, spiral, and helical pipe is 12.81°C, 13.29°C, and 13.25°C respectively.
- The heat transfer rate achieved in the straight, spiral, and helical pipe are 6974.014w, 7235.335w, and 7213.558w respectively.
- The heat transfer rate is achieved in the straight, spiral, and helical pipe is 10403.86w, 10420.19w, and 10463.79w respectively.

## **Author details**

Nasim Hasan<sup>1\*</sup>, Mohd Arif<sup>1</sup> and Mohaideen Abdul Khader<sup>2</sup>

1 Mechanical Engineering Department, Mettu University, Mettu, Ethiopia

2 Mai-nefhi College of Engineering, Mai Nefhi, Eritrea

\*Address all correspondence to: nasimhasan78@gmail.com

## **IntechOpen**

---

© 2021 The Author(s). Licensee IntechOpen. This chapter is distributed under the terms of the Creative Commons Attribution License (<http://creativecommons.org/licenses/by/3.0>), which permits unrestricted use, distribution, and reproduction in any medium, provided the original work is properly cited. 

## References

- [1] T. S. Bisoniya, A. Kumar, and P. Baredar, "Experimental and analytical studies of earth-air heat exchanger (EAHE) systems in India: A review," *Renewable and Sustainable Energy Reviews*, vol. 19, pp. 238–246, 2013.
- [2] V. Bansal, R. Misra, G. D. Agrawal, and J. Mathur, "Performance analysis of earth-pipe-air heat exchanger for winter heating," *Energy and Buildings*, vol. 41, no. 11, pp. 1151–1154, 2009.
- [3] V. Bansal, R. Misra, G. D. Agrawal, and J. Mathur, "Performance analysis of earth-pipe-air heat exchanger for summer cooling," *Energy and Buildings*, vol. 42, no. 5, pp. 645–648, 2010.
- [4] N. K. Bansal, M. S. Sodha, and S. S. Bharadwaj, "Performance of Earth-air tunnel system," *International Journal of Energy Research*, vol. 7, no. 4, pp. 333–345, 1983. S. S. Bharadwaj and N. K. Bansal, "Temperature distribution inside ground for various surface conditions," *Building and Environment*, vol. 16, no. 3, pp. 183–192, 1981.
- [5] M. Santamouris, A. Argiriou, and M. Vallindras, "Design and operation of a low energy consumption passive solar agricultural greenhouse," *Solar energy*, vol. 52, no. 5, pp. 371–378, 1994.
- [6] R. Kumar, S. C. Kaushik, and S. N. Garg, "Heating and cooling potential of an earth-to-air heat exchanger using artificial neural network," *Renewable Energy*, vol. 31, no. 8, pp. 1139–1155, 2006.
- [7] S. Milun, T. Kilić, and O. Bego, "Measurement of soil thermal properties by spherical probe," *IEEE Transactions on Instrumentation and Measurement*, vol. 54, no. 3, pp. 1219–1226, 2005.
- [8] Hasan, N., Mathur, Y. B., and Khader, M. A. (2018). Validation of earth air tunnel heat exchanger CFD model to experimental setup. *IOSR Journal of Engineering*, 8(01), V2.
- [9] Hasan, N., Sheikh, M. Y., Bulcha, A., and Adeba, J. (2019, August). Numerical investigation of chlorinated polyvinyl chloride pipe earth air tunnel heat exchanger at different pipe diameter. In *AIP conference proceedings* (Vol. 2134, No. 1, p. 030003). AIP publishing LLC.
- [10] Hasan, N., Tibba, I. G. S., Mosisa, F. T., and Daniel, A. (2018, September). Ground tunnel as renewable energy utilization of ground energy as a source and sink for building heating and cooling. In *AIP Conference Proceedings* (Vol. 2018, No. 1, p. 020005). AIP Publishing LLC.
- [11] Hasan, N., Mathur, Y. B., and Khader, M. A. (2018). Validation of earth air tunnel heat exchanger CFD model to experimental setup. *IOSR Journal of Engineering*, 8(01), V2.
- [12] Hasan, N., Sheikh, M. Y., Bulcha, A., and Adeba, J. (2019, August). Numerical investigation of chlorinated polyvinyl chloride pipe earth air tunnel heat exchanger at different pipe diameter. In *AIP conference proceedings* (Vol. 2134, No. 1, p. 030003). AIP publishing LLC.
- [13] Agrawal, K.K., Bhardwaj, M., Misra, R. et al. Optimization of operating parameters of earth air tunnel heat exchanger for space cooling: Taguchi method approach. *Geotherm Energy* 6, 10 (2018). <https://doi.org/10.1186/s40517-018-0097-0>



# Recent Advancements in Thermal Performance Enhancement in Microchannel Heatsinks for Electronic Cooling Application

*Naga Ramesh Korasikha, Thopudurthi Karthikeya Sharma,  
Gadale Amba Prasad Rao and Kotha Madhu Murthy*

## Abstract

Thermal management of electronic equipment is the primary concern in the electronic industry. Miniaturization and high power density of modern electronic components in the energy systems and electronic devices with high power density demanded compact heat exchangers with large heat dissipating capacity. Microchannel heat sinks (MCHS) are the most suitable heat exchanging devices for electronic cooling applications with high compactness. The heat transfer enhancement of the microchannel heat sinks (MCHS) is the most focused research area. Huge research has been done on the thermal and hydraulic performance enhancement of the microchannel heat sinks. This chapter's focus is on advanced heat transfer enhancement methods used in the recent studies for the MCHS. The present chapter gives information about the performance enhancement MCHS with geometry modifications, Jet impingement, Phase changing materials (PCM), Nanofluids as a working fluid, Flow boiling, slug flow, and magneto-hydrodynamics (MHD).

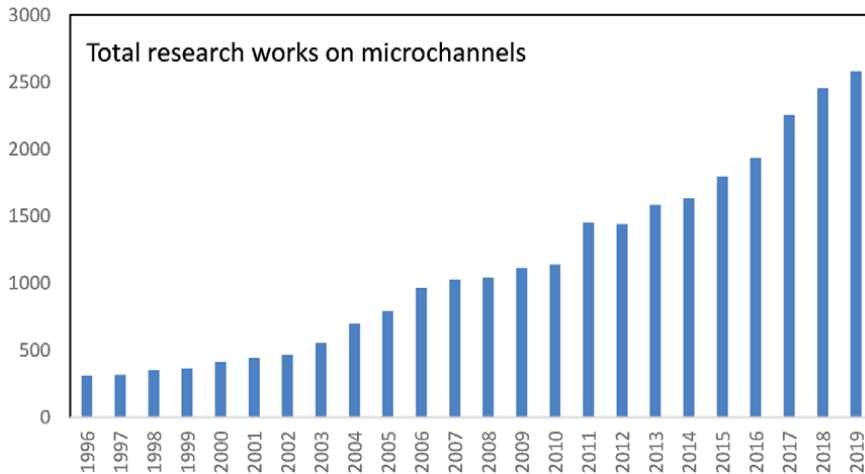
**Keywords:** Microchannel heat sink (MCHS), Heat transfer enhancement, Jet impingement, Phase changing materials (PCM), Flow boiling, Slug flow, Magneto hydrodynamics

## 1. Introduction

Thermal management of electronic components is the major concern to make the efficient high powered energy system [1–3]. The modern researchers' attention is on the development of efficient heat exchanging devices for thermal management of electronic components [4, 5]. Miniaturization has a noticeable footprint on heat exchanger technology and which makes the heat exchangers as compact and efficient. The life and overall efficiency of a thermal energy system are highly affected by its heat exchanger's efficiency. The microchannel heat sink is an inventive and highly compact heat dissipating device, so it is the most suitable for the application of thermal management of electronics. The performance and the life span of the electronic component with high power density is highly dependent on its heat dissipation capacity [6]. The performance of an electronic component is enhanced

S.G. Kandlikar and W.J. Grande [7]	S.S. Mehendale et al. [8]
Conventional channels: $D_h < 43$ mm	Conventional channels: $D_h < 46$ mm
Mini-channels: $0.2$ mm $< D_h < 3$ mm	Compact passages: $1$ mm $< D_h < 6$ mm
Micro-channels: $10$ $\mu\text{m} < D_h < 200$ $\mu\text{m}$	Meso-channels: $0.1$ mm $< D_h < 1$ mm
Transitional channels: $0.1$ $\mu\text{m} < D_h < 10$	Micro-channels: $1$ $\mu\text{m} < D_h < 100$ $\mu\text{m}$

**Table 1.**  
The classification of the mini and microchannels.



**Figure 1.**  
The increment of studies performed on the micro-channels from the year 1996 to 2019 [15].

by providing an efficient heat absorbing device like MCHS. The MCHS is also used in many other applications like LED cooling, fuel cells, refrigeration, combustors, chemical industry and food industry, etc. Huge literature availability on MCHS indicates the capacity of this technology.

The categorization of the microscale channels is different from the conventional flow channels, and it is done by considering the channel's hydraulic diameter. So many classifications are available from the literature. Many authors followed the classification given by S.G. Kandlikar and W.J. Grande [7] and S.S. Mehendale et al. [8], which is produced in **Table 1**.

The microchannel heat sink was first developed in 1981 for electronic cooling applications, which has rectangular cross-sectional channels made of silicon. In this study, the maximum thermal resistance of  $0.09$   $^{\circ}\text{C}/\text{W}$  was observed at the heat flux of  $790$   $\text{W}/\text{cm}^2$  over the  $1$   $\text{cm}^2$  area [9]. Since then, noticeable work has been done to improve the micro-channels' fluid flow and heat transfer performance by improving the channel geometry, surface roughness of the channel, channel aspect ratio, working fluid and substrate materials, etc. The thermal resistance of  $0.070$   $\text{C}/\text{W}$  was achieved for the MCHS developed for thermal management of the diode laser array manufactured by Indium phosphide (InP) [10]. The hydraulic diameter and aspect ratio of the channel was proved to be has a noticeable impact on the thermal and hydraulic behavior of the M [11].

Initially, few studies claimed that the conventional correlations and theories are not applicable for the micro and mini channels. Eventually, researchers cleared about these ambiguities and concluded that the inaccuracies in the microchannel dimensional measurements are the main reason for the deviation of the results produced from the conventional correlations. The uncertainties in experiments

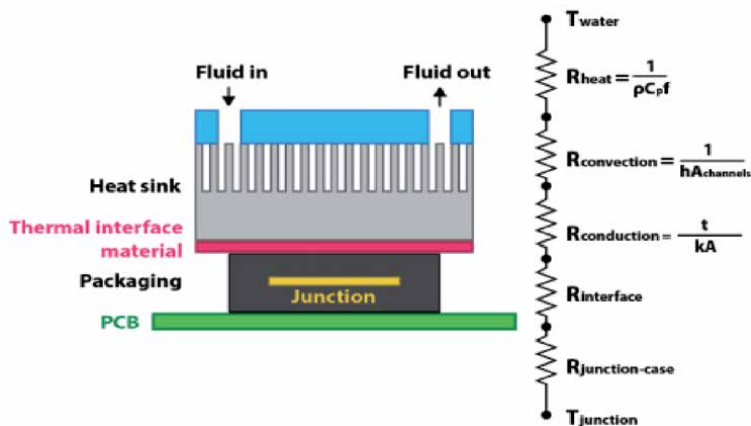


were proved to be dominated by the uncertainties in the diameter measurement, which may cause the 20% deviation in the measurement of Poiseuille's number [12]. In this analysis,  $fRe$  (Poiseuille's number) data for microscale stroke flow showed negligible deviation from the macroscale stroke flow. 3% uncertainty in the channel width and channel height leads to the 21% uncertainty in calculating the friction factor [13]. The electric double-layer effect, entrance effect, and entrance effect are also possible causes for the deviation of pressure drop, apart from the measurements' errors. To find the possible inaccuracies and partial thermal in the MCHS, enhanced thermal characterization methods were developed [14]. **Figure 1** represents the increment of studies performed on the micro-channels from the year 1996 to 2019 [15].

## 2. Microchannel heatsink (MCHS)

The heat sink is a heat-absorbing device that takes heat from its surroundings by the various modes of heat transfer by using working fluids. Miniaturization makes the heat sinks as efficient and compact. MCHSs have fluid flow channels in the size of microns. MCHS application is found in the high-powered density energy system with less space availability. These applications include the computer components cooling (Storage devices, CPUs and GPUs, etc.) [16], thermal management of high power density electronic components (IGBTs) [17], cooling of fuel cells [18], diode laser arrays [19], and combustors [20], etc. Electronic cooling is the major application of the MCHS. **Figure 2** represents the schematic diagram of the transistor with a liquid-cooled heat sink.

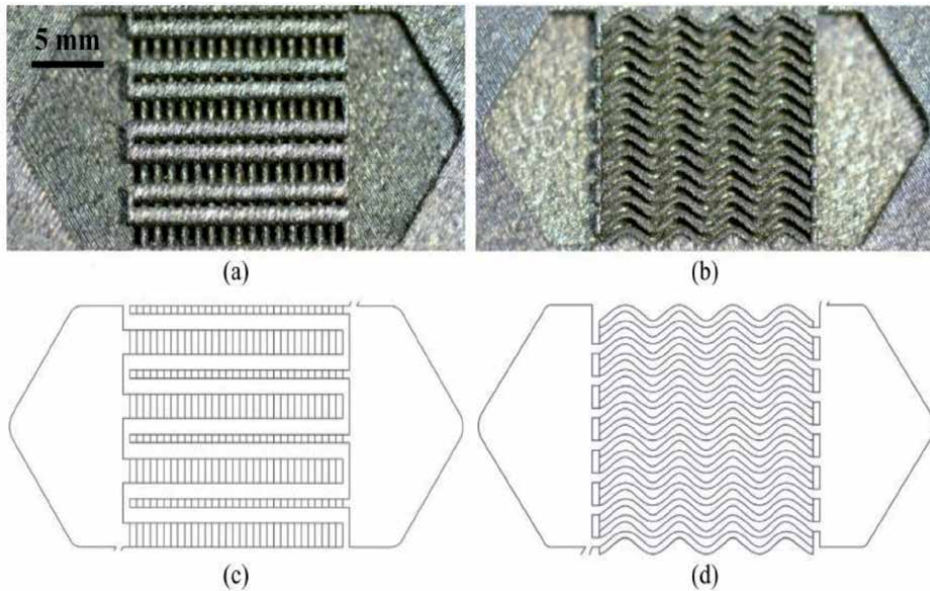
Fabrication of MCHS is the biggest hurdle to perform the experimental investigations. Laser cutting [22], dry and wet etching [23–25], micro-cutting [26], and ultrasonic micro-machining [27] are very expensive fabrication methods for MCHS. Most of the researcher's attention is on developing a new low-cost manufacturing method with good surface characteristics. Kaikan Diao, Yuyuan Zhao [28] studied the performance of the sintered Copper microchannel manufactured by a low-cost fabrication method. This study proved that the pressure drop in the sintered copper microchannel was higher than the microchannel machined conventionally and noticeably lower than the porous Copper microchannel fabricated by the Lost carbonate sintering method (LCS). Ivel L. Collins et al. [29] performed the direct-metal-laser-sintering



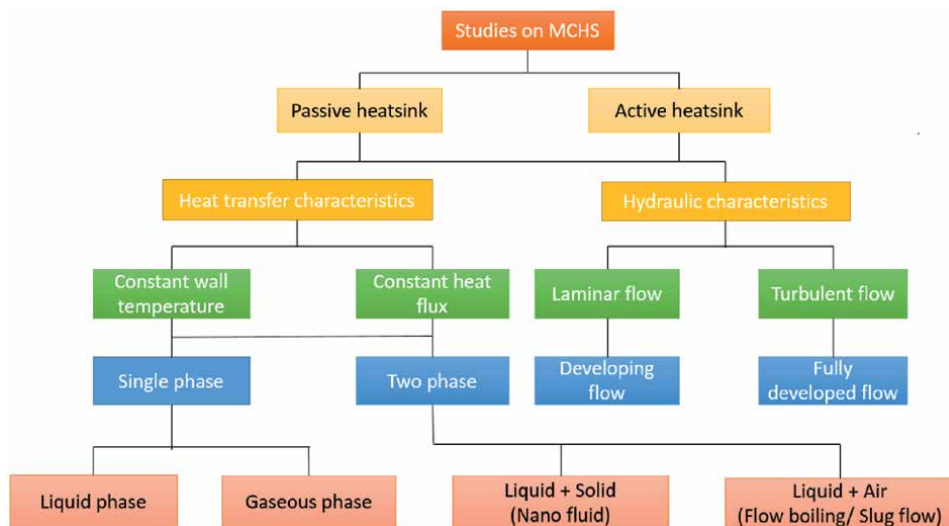
**Figure 2.** Schematic diagram of the transistor with liquid-cooled heatsink [21].

method (DMLS) for manufacturing of two MCHS models, PMM (permeable membrane MCHS) and MMC (manifold MCHS) heat-sinks shown in **Figure 3**.

The analysis method implemented for the study of MCHS is also plays a key role in the accuracy of the study. Initially, researchers and scientists depended on expensive experimental methods only for their research but the development of numerical methods has upturned the studies on microfluidics. Novel computational fluid dynamic (CFD) techniques have been developed for accurate analysis of the MCHS. 3-dimensional simulation models give an accurate result than 2-dimensional simulation models but computational time is less for a 2-dimensional model. Similar outcomes were found in the 2D and 3D simulation model studies conducted on the



**Figure 3.** Images of the (a, c) manifold MCHS and (b, d) permeable membrane MCHS [29].



**Figure 4.** Schematic of various studies on micro-channel heatsinks (MCHS) [15].

microchannel fluid micro-mixing [30]. S. A. Si Salah et al. [31] implemented the control-volume FEM (CVFEM) to study microchannel flow, which has the advantages of both finite element method and the finite volume method. The slug flow in the microchannel of serpentine shape was studied using a Coupled-level-set and volume of fluid (CLSVOF) method, which accurately predicted heat transfer and fluid flow performance liquid–liquid 2-Phase flow [32]. J. Rostami and A. Abbassi [33] implemented the Eulerian–Lagrangian method to analyze the  $\text{Al}_2\text{O}_3$ -water fluid flow in the wavy channeled heat sink. Shuzhe Li et al. [34] and Zhibin Wang et al. [35] were also used the coupled level set and volume of fluid method for their study on coalescence between the moving liquid and the droplets in the microchannel. A flexible coupled-level-set and volume of fluid (flexCLV) method [36], Lattice Boltzmann method (LBM) [37, 38]. The coupled LBM [39] was also implemented for the accurate prediction of complex problems. **Figure 4** shows the schematic of types of studies performed on the microchannel heat sinks.

### 3. Thermal performance-enhancing techniques

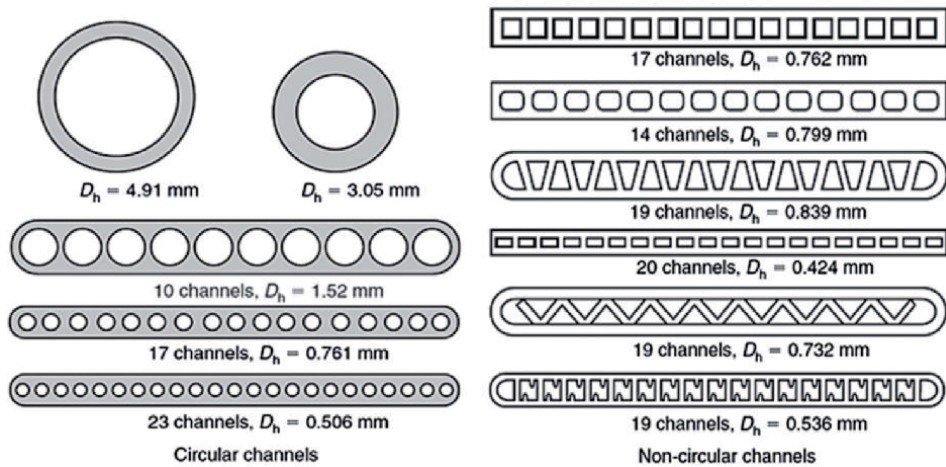
It is clear from the studies in the literature that MCHS has an eminent future in the field of thermal management of electronic equipment. The work performed on the micro-channel heat sink by Tuckerman and Pease [9] attracted the researchers towards the MCHS. Researchers and scientists have been working on MCHS to develop new ways to enhance heat transfer in micro-channels. The details of the few thermal performance-enhancing techniques developed for MCHS are produced in this section.

#### 3.1 Geometric improvements

The microchannel geometry has a major impact on its heat transfer and fluid flow performance. The improvement of the microchannel geometry is a possible technique to decrease the pressure drop with a significant increase of the heat transfer. Various cross-sectional shapes of micro-channels used for the analysis are presented in **Figure 5**. Microchannel with a Trapezoidal-shaped cross-section has a good thermal performance than the rectangular channel [41]. The effect of the different parameters like aspect ratio (AR) [42], hydraulic diameter, channel spacing [31], channel width, channel height, etc., on the heat transfer behavior of microchannel, were also studied.

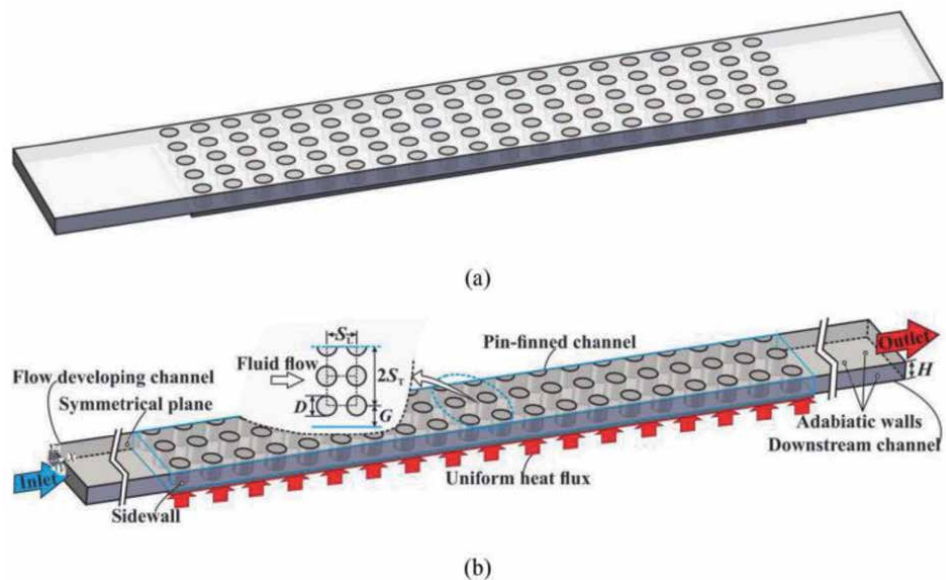
An experimental analysis performed on the rectangular microchannel with the working fluids FC770 and water proved that the critical Reynolds number (Re) increases to 2400 from 1700 with a reduction of aspect ratio (AR) to 0.25 From 1 [43]. The reduction of friction factor with increasing the AR was also noticed initially, and then it started increasing. The increase of both the Nusselt number (Nu) and the pressure loss with the channel height reduction was observed in the numerical study on MCHS with transfer channels [44]. The flow channel size shows a noticeable effect on the hydraulic performance as it was decreasing from the macro scale to the micro-scale. The effect on the hydraulic behavior of the microchannel was negligible as the space between the micro-channels decreases from 50  $\mu\text{m}$  to 0.5  $\mu\text{m}$  [31]. The Nu and Poiseuille number are found to be raised with rising the AR and side angle [45].

Some studies on MCHS have introduced the ribs, internal fins into the flow channels and changes the shape of the passage so that the area of heat transfer increased. A considerable decrease of pressure drop was noticed when the rectangular-shaped ribs and the sinusoidal cavities are provided to the MCHS [46]. In the various category of offset ribs on the channel sidewalls, the best performance was observed with the forward triangular ribs and the rectangular ribs showed the worst behavior at the Re

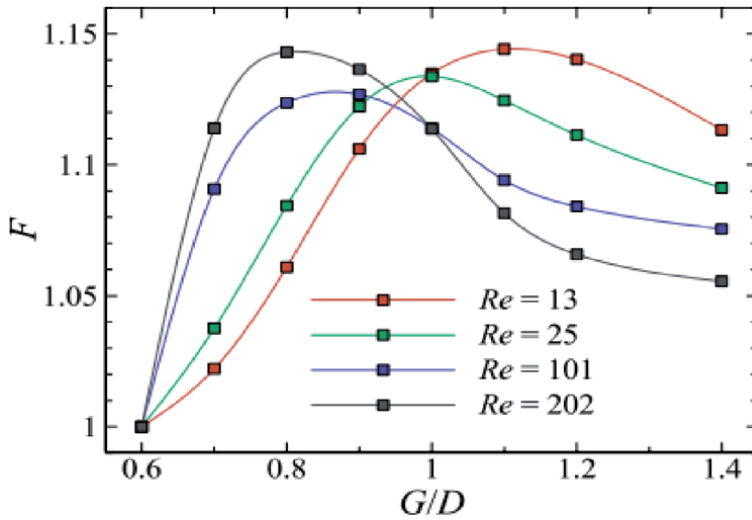


**Figure 5.** Various cross-sections of micro/mini channels used for studies [40].

less than 350 [47]. The increase of heat transfer was also observed by providing the internal fins with the increase of pressure drop, as a cumulative effect, the microchannel performance was increased. The proximity from the wall of the large row of pin fins showed the greatest effect on the velocity field, distribution of flow, temperature distribution, and streamline structure. As the gap between the pin-fins increases, the heat transfer is noticed to increase first and then decrease. The fin structured microchannel with equal gap and diameter shows better thermal performance [48]. A schematic model of finned MCHS is produced in **Figure 6**. The effect of proximity from the sidewall on the thermal performance is represented in **Figure 7**.



**Figure 6.** Schematic model of finned MCHS, (a) physical model and (b) boundary conditions [48].



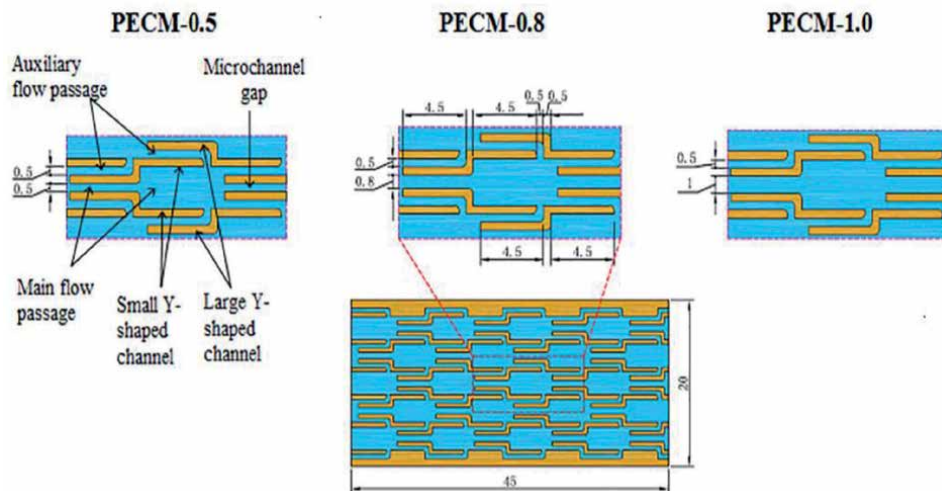
**Figure 7.**  
 The influence of proximity from the sidewall on the thermal performance of MCHS [48].

The large heat transfer (HT) enhancement was found in the periodically converging and the diverging and periodically expanded and constrained MCHS. 46.8–160.2% improvement in HT was noticed in the converging and the diverging MCHS (**Figure 8**) [49]. 50–117% improvement of heat transfer was found in the periodically expanded and constrained MCHS (**Figure 9**) in the range of  $Re$  from 150 to 820 [50].

An experimental study on periodic jetting and throttling MCHS (**Figure 10**) has concluded that the mean temperature and maximum temperature in the throttling

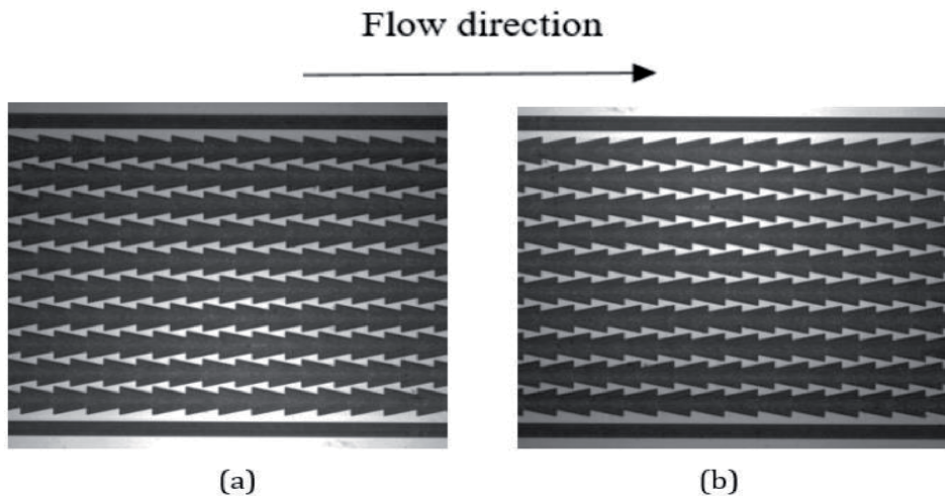


**Figure 8.**  
 Physical model of periodic converging–diverging microchannel [49].



**Figure 9.**  
 Design of the periodic expanded and constrained MCHS [50].



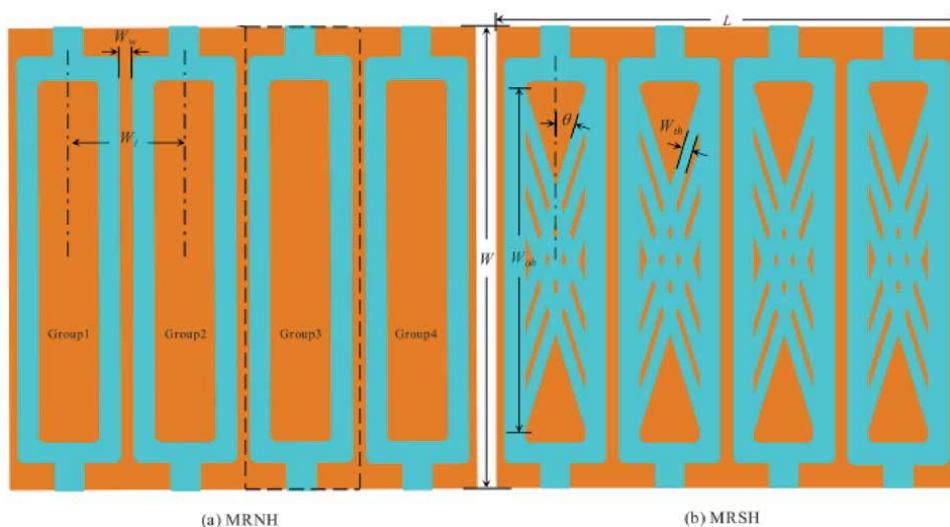


**Figure 10.**  
Physical model of (a) jetting MCHS (b) throttling MCHS [51].

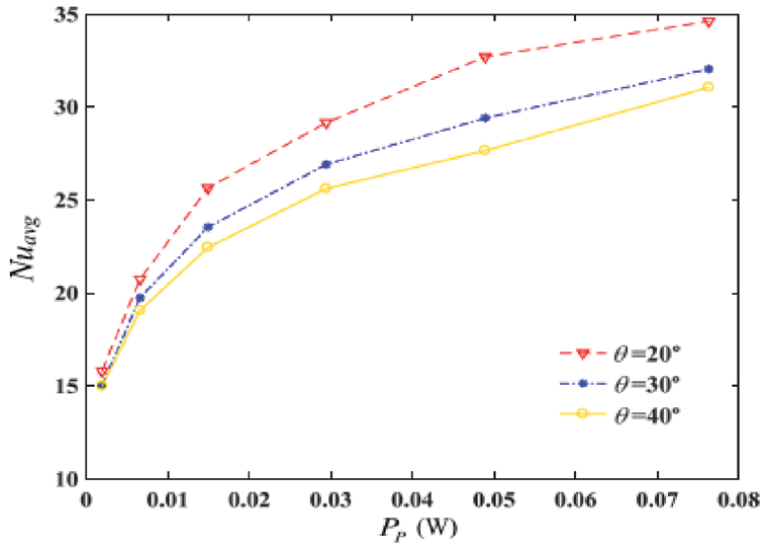
MCHS are less than the jetting MCHS with huge pressure loss [51]. The heat transfer rate in the trapezoid cross-sectional MCHS with grooved structure was noticed to be improved by 28% because of the breaking and regeneration of the thermal and hydrodynamic boundary layer [41].

Huan-ling Liu et al. [52] developed new annular MCHS designs, MRNH and MRSH presented in **Figure 11**, and concluded that the consistency of the substrate temperature of the interleaved structure was better than the sequential structure. The increase of the total thermal resistance was noticed with rising the slant angle in the MRSH design. The variation of the average Nu with the pumping power is represented in **Figure 12**.

Some of the researchers [53–55] investigated the effect of the channel surface-roughness on the thermal performance of MCHS. Their work disclosed that the HT in MCHS was augmented for rough-surfaced channels and its effect is very significant at high Re. Yan Ji et al. [56] analyzed the low Knudsen number (Kn) gas



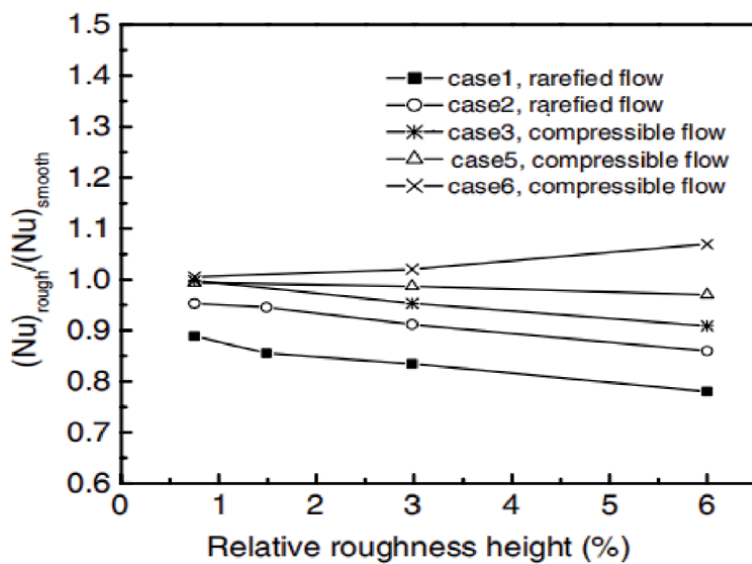
**Figure 11.**  
Schematic design of MCHS, (a) MRNH (b) MRSH configuration [52].



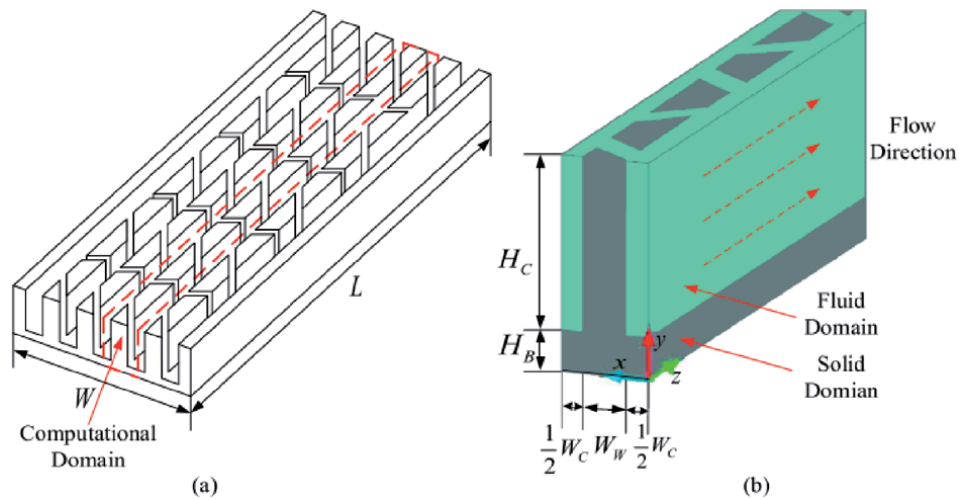
**Figure 12.**  
 The variation average nu with pumping power at three slant angles [52].

flow in rough channels and observed a decrease of local heat flux with increasing the relative roughness for rarefied and compressible flow. The variation Nu with the roughness is shown in **Figure 13**.

Secondary flow in MCHS is an effective method to reduce the pressure drop, which is a major limitation in the above-discussed models. One of the secondary flow MCHS models is shown in **Figure 14**. The maximum enhancement in heat transfer in secondary flow MCHS was obtained by optimizing the ratio of the parameters of secondary channel width to the main channel width ( $\alpha$ ), the ratio of secondary channel half-pitch to the main channel width ( $\beta$ ), and tangent value of the angle of the secondary channel ( $\gamma$ ) [57].



**Figure 13.**  
 Variation of nu with the relative roughness [56].



**Figure 14.** Design of (a) secondary flow MCHS (b) computational domain [57].

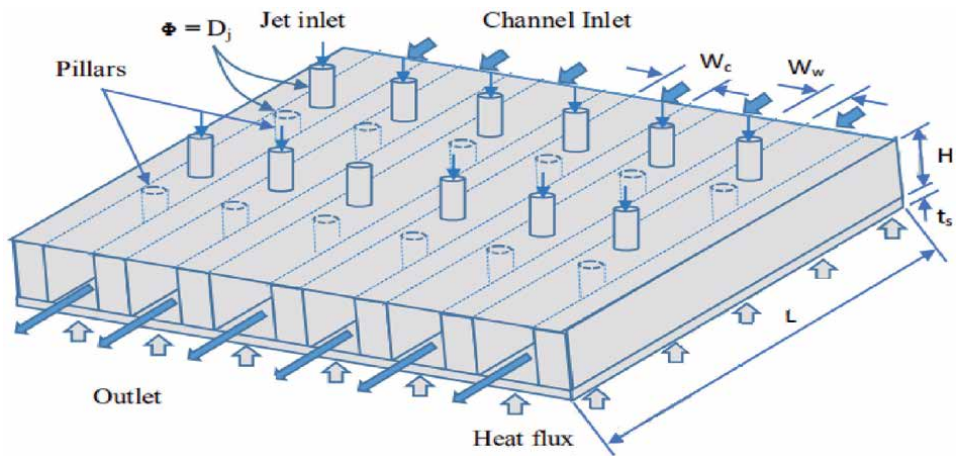
A novel MCHS model namely, permeable membrane MCHS (PMM) and manifold microchannel heatsink (MMC) manufactured by Direct metal laser sintering method using an aluminum alloy was studied experimentally and noticed the better performance of the PMM heat sink [29]. **Figure 3** shows the images of PMM and MMC heat sinks.

### 3.2 Jet impingement arrangement

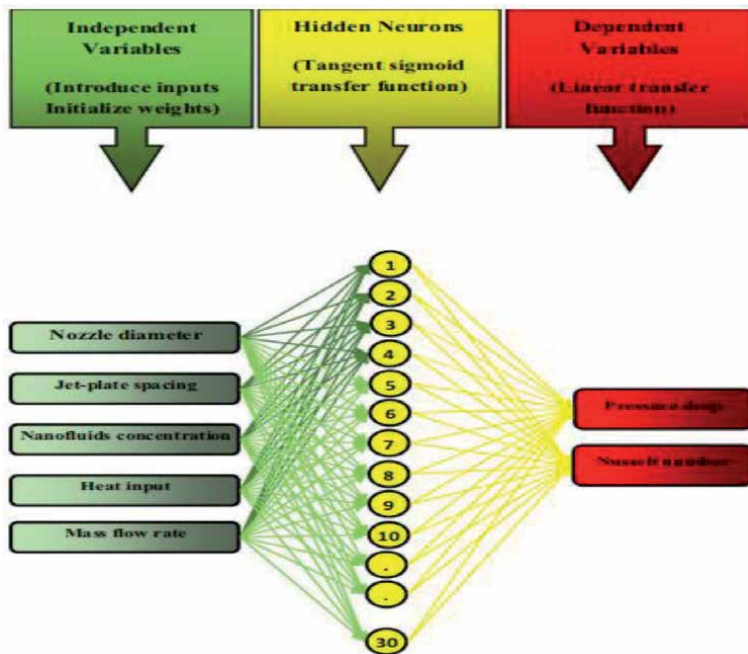
A microchannel heat sink with a jet impingement arrangement is an active heat sink with high heat transfer coefficients. Jet impingement in the flow of a fluid using liquid coolants produces very high heat transfer coefficients and it is more significant in the stagnation region [58–60]. Substantial work has been performed on the jet impingement, with various working fluids, at various nozzle configurations, standoff distances, and lengths. Jet impingement in heat sinks shows uniform temperature distribution for both micro-scale and macro-scale applications. Microscale jet impingement is most suitable for dissipating the heat from high-powered electronic systems [61]. Hybrid MCHS with micro jet impinging developed for photovoltaic solar cell cooling was enhanced the solar cell electrical efficiency by 39.7% [62]. The numerical study conducted on the hybrid MCHS with a slot-jet module and various channel cross-sections revealed that the trapezoidal channel shows the better cooling effect [63]. The decreasing order of the pressure drop in the various channels at the fixed flow rate was circular cross-section, a trapezoidal cross-section, and rectangular cross-section. The rectangular channel was not favorable for impingement jet to produce vorticities, so it has a low-pressure loss. Afzal Husain et al. [64] modeled a new hybrid MCHS with impingement and pillars (**Figure 15**). It was noticed that the MCHS model with the low jet pitch to diameter ratio produces a greater heat transfer coefficient. The hybrid MCHS design with the ratio of standoff (distance between jet impingement surface and nozzle exit) to the diameter of the jet close to 2 and 3 results in low thermal resistance and pumping power.

P. Naphon et al. [65] applied the ANN model (**Figure 16**) of the Levenberg–Marquardt Backward propagation (LMB) training algorithm and Computational





**Figure 15.** Schematic model of the hybrid MCHS with pillars and jet impingement [64].



**Figure 16.** Optimal ANN model proposed by P. Naphon et al. [65].

fluid dynamics to study the jet impingement of Nanofluids in the MCHS. The maximum deviation of the predicted results from the measured data was found to be 1.25%. With increasing the nozzle level, the heat transfer from the heat sink module to Nanofluid was tended to decrease, which causes the high fins tip temperature. Generally, there are two different jet impingement arrangements: the free-surface and submerged jet-arrays [66]. The schematic model of the free surface and submerged jet arrays are produced in **Figure 17**.

The heat transfer was also enhanced effectively by introducing various shapes of dimples on the HT surface with impinging jets [67]. Convex dimple arrangement

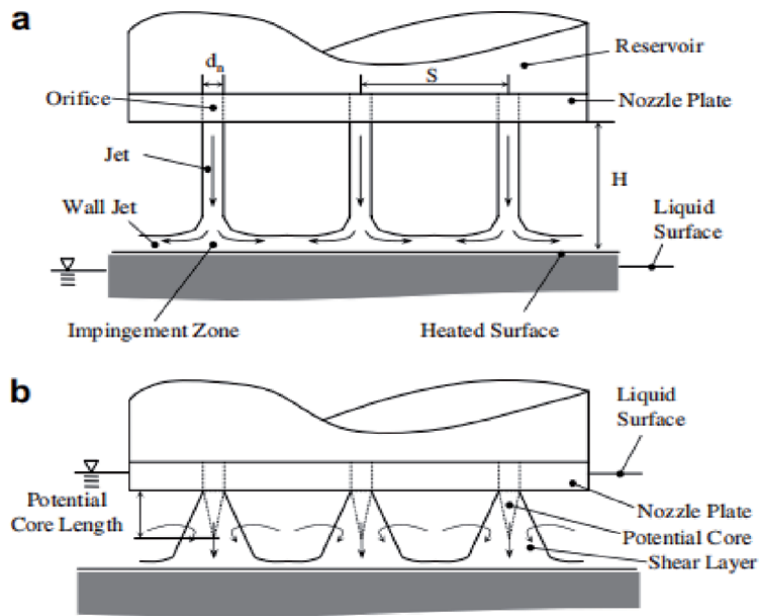


Figure 17. Schematic model of (a) free-surface jet-arrays and (b) submerged jet-arrays [66].

has superior overall performance among the three arrangements studied and it has a high heat transfer rate and lowest pressure loss. The single nozzle with a convex dimple arrangement is presented in Figure 18.

### 3.3 Nanofluid as the working fluid

Thermo-physical properties of the Nanofluids are superior among various working fluids, so which are suitable for high heat transfer applications.

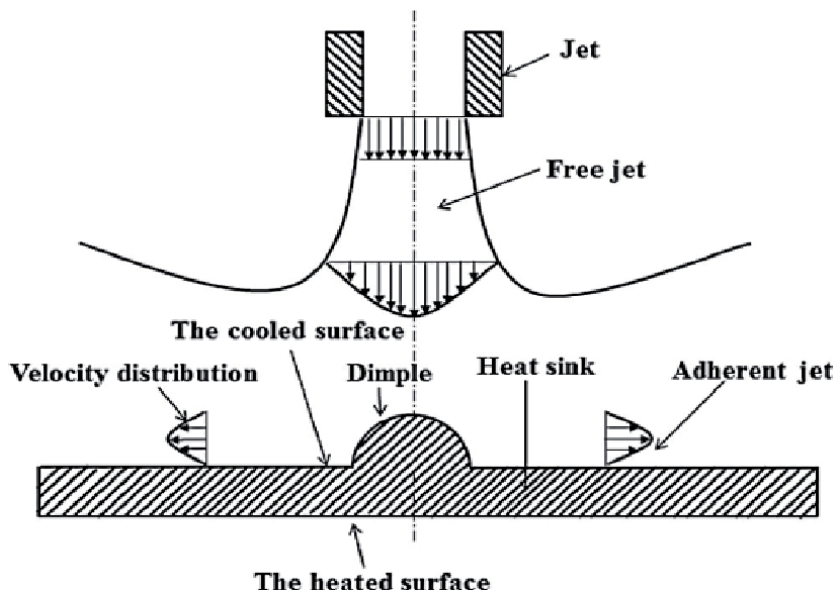
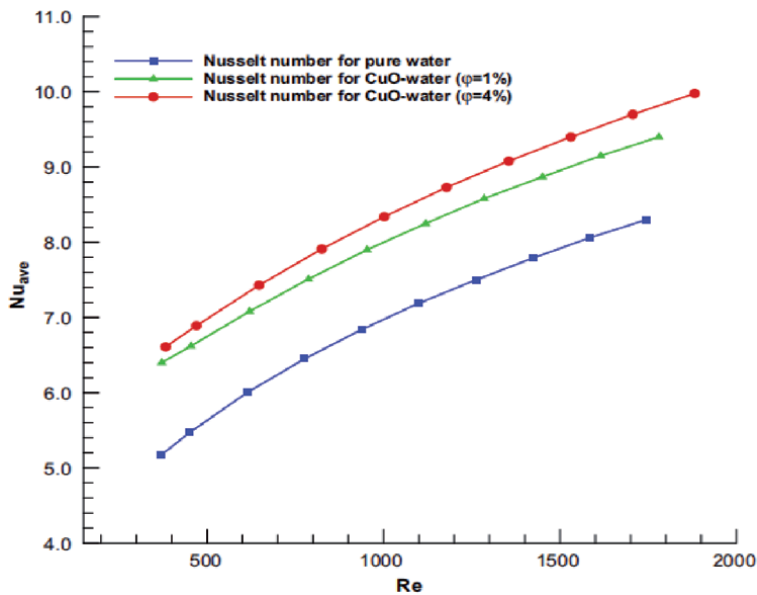


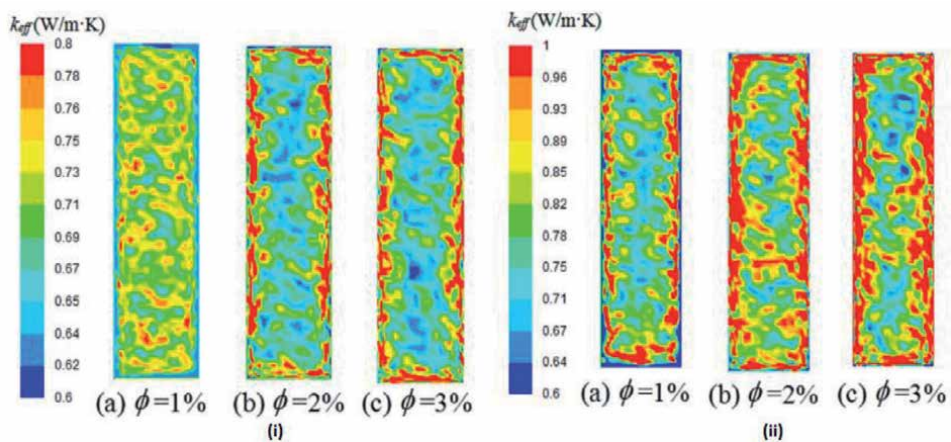
Figure 18. Schematic diagram of single nozzle with convex dimple arrangement [67].

Significant research has been done on MCHS with Nanofluids using experimental and single and multi-phase CFD models. Multi-phase methods are noticed to be more precise compared to the single-phase numerical methods [68]. The inaccuracy of the 2-phase mixture method and the 1-phase methods for 1% Nanofluid compared to the experimental results were found to be 11.39% and 32.6% respectively [69].

Ayoub Abdollahi et al. [70] proved that the water-based SiO<sub>2</sub> Nanofluid has the best performance among the four water-based SiO<sub>2</sub>, CuO, Al<sub>2</sub>O<sub>3</sub>, and ZnO Nanofluids. In a similar study conducted on the hexagonal channeled MCHS using various water-based Nanofluids, it was observed that Al<sub>2</sub>O<sub>3</sub>-water Nanofluid has the highest heat transfer coefficient [71]. The analysis on CuO-Water Nanofluid flow in trapezoidal channeled MCHS proved that the thermal performance of heat sink



**Figure 19.** The variation of average nu with Reynolds for various nanofluid volume fractions [72].



**Figure 20.** Distribution of nanofluid thermal conductivity at the outlet with various mass Flux (i) 0.0001 kg/s, (ii) 0.0003 kg/s [75].

was enhanced by increasing the Nanofluid volume fraction with a penalty of high pumping power [72]. The variation of Average Nu with the Reynolds number ( $Re$ ) is shown in **Figure 19**.

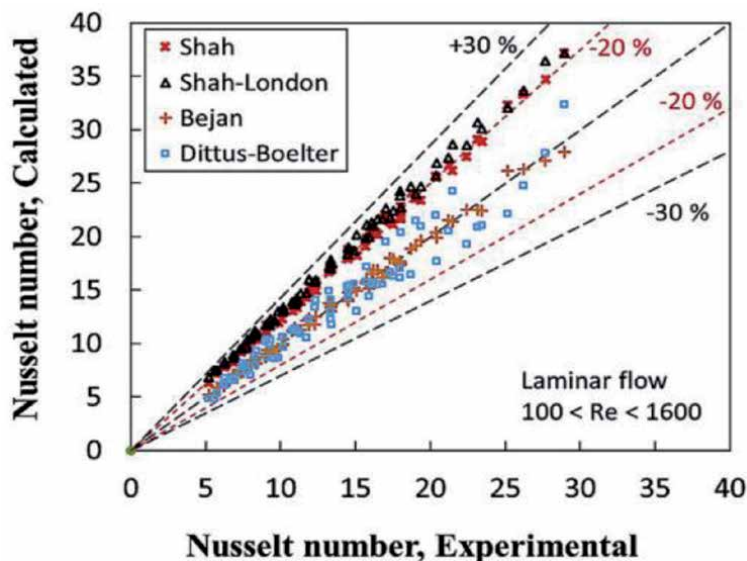
The numerical investigation on the Nanofluid-based triangular and trapezoidal grooved MCHS revealed that the water-based  $Al_2O_3$  Nanofluid was the best coolant for the trapezoidal grooved MCHS [73, 74]. In a numerical study conducted on  $Al_2O_3$ -water Nanofluid-based MCHS, the rise of Nanoparticles' concentration at the walls and non-uniform distribution of thermal conductivity was observed with increasing Discharge [75]. **Figure 20** shows the distribution of the Nanofluid thermal conductivity at the outlet.

Few studies used the advantages of both the geometries and the Nanofluids in the MCHS. Water-based Diamond Nanofluid has the best performance among the various Nanofluids used in the analysis of the wavy channeled MCHS [76]. M.M. Sarafraz et al. [77] witnessed a 76% improvement in the heat transfer performance of MCHS with a 20% increase in the pumping power at the  $Re$  higher than 1376. The variation of the Nu obtained from the experiments and existing correlations is shown in **Figure 21**.

The efficiency of an energy system can understand by finding its entropy generation. Some studies investigated the entropy generation of the MCHS to analyze its performance using various working fluids. In the first and second law thermodynamic analysis of offset strip-fin MCHS with CuO Nanofluid as coolant, it was found that the thermal characteristics of the MCHS improved with  $Re$  but the frictional entropy generation was also increased [78]. The rate of entropy generation of MCHS in the flow direction concerning the number of fins is presented in **Figure 22**.

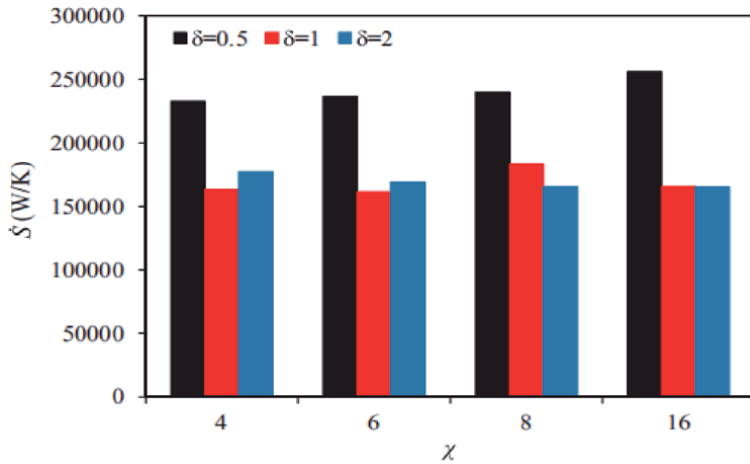
### 3.4 Magneto-hydrodynamics (MHD) influence

MHD is an interdisciplinary subject that has been used in various engineering problems like the design of MHD pumps and flows meters and cooling of nuclear reactors etc. In the field of microfluidics, MHD pipping is very favorable because of its uncomplicated design and less power consumption [79–82]. In the starting, conventional heat



**Figure 21.**

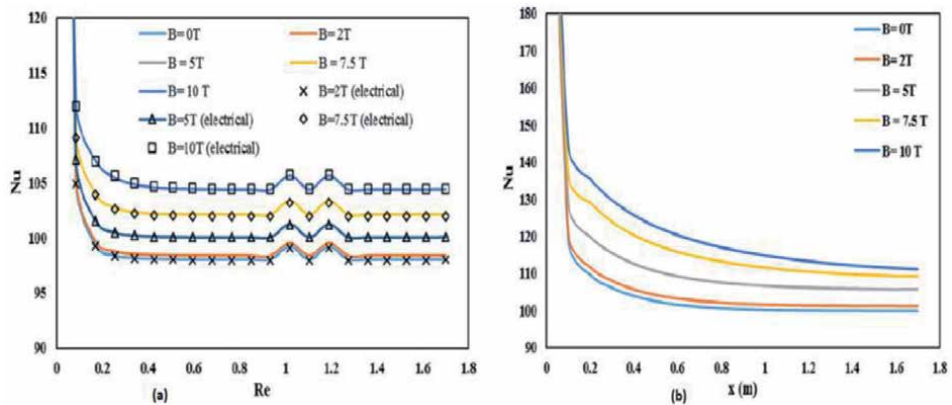
The variation of the nu obtained from the experiments and existing correlations [77].



**Figure 22.**  
 The entropy generation of MCHS in the flow direction with the number of fins [78].

exchangers with magnetic fluid are investigated to know its performance by applying it. The proportionality of friction factor and Nusselts number with the applied magnetic field was noticed in the study of the MHD effect on circular tube flow of  $Fe_3O_4$ -Water Nanofluid [83]. Variation of Nusselt number with Magnetic field effects is presented in **Figure 23**. The working fluid velocity was observed to be reduced with Lorentz force generated because of magnetic flux applied. The increase of the local heat transfer coefficient was witnessed experimentally when an external magnetic field was applied to the W-40 (magnetic Nanofluid) flow in a rectangular duct [84].

Few research studies about the MHD effect on micro-channels noticed the improvement of their hydraulic and thermal behavior. The decrease of the gradient of velocity at the wall with a rise in the index of Power-law flow was observed in the flow of non-Newtonian fluid flow in a microchannel under a transfer magnetic field [85]. The increment of the gradient of velocity near the wall and reduction of maximum velocity was found with the rising Hartmann number. The increase in the Joule heating and the viscous dissipation was observed to decrease the Nusselt number. Chunhong Yang et al. [86] studied the thermal behavior of an incompressible MHD flow in a rectangular microchannel by taking the combined influence of the viscous dissipation



**Figure 23.**  
 The nu variation with the magnetic field (a) in the range Re, (b) along the channel [83].

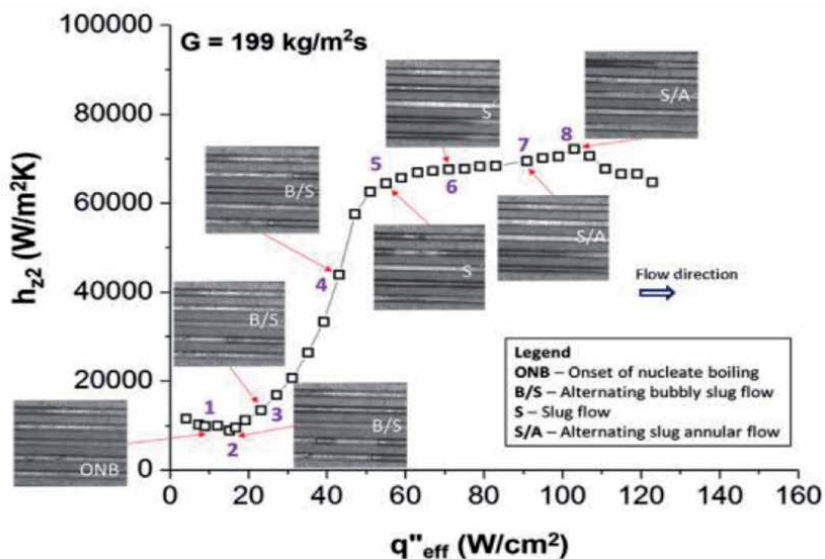


and the Joule heating. This analysis shows the decrease of normal velocity with increment in the Hartmann number ( $Ha$ ) without any applied lateral electric field. The increasing-decreasing trend of Velocity and temperature profiles was noticed with the rising the Hartmann number under the applied lateral electric field. The generation of entropy in the MCHS was diminished as the influence of the Lorentz force generated by the injected electric current and magnetic field applied transversely [87].

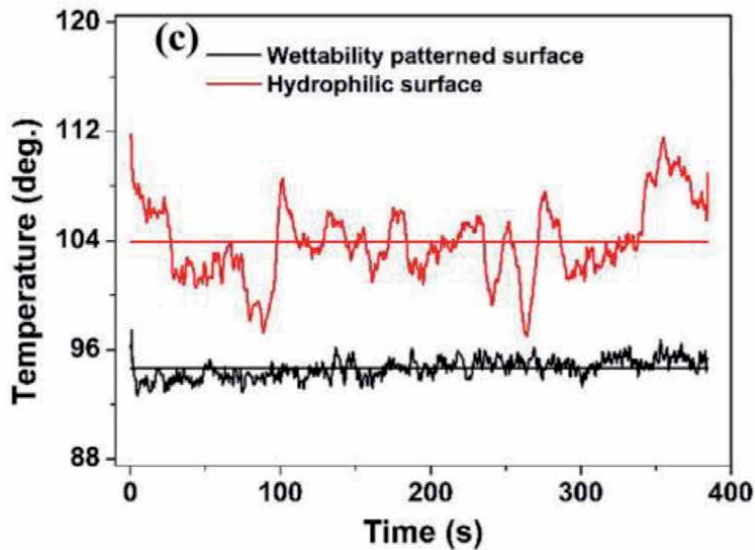
### 3.5 Flow boiling in MCHS

Flow boiling in the MCHS can vanish the heat fluxes in the range of 30 to 100  $W/cm^2$  with the acceptable channel surface temperatures [88]. The flow boiling implemented MCHSs were used for a variety of applications, like cooling of PEM fuel cells, thermal management of the IGBTs (insulated gate bipolar transistors), refrigeration systems, etc. [89]. Most of the researchers' attention is on estimating the impact of the mass flow rate, heat flux, vapor quality, and surface characteristics on the boiling heat transfer [90, 91]. Stable flow boiling is also one of the best way to enhance the heat transfer in the MCHS. The experimental analysis done by John Mathew et al. [92] on the copper hybrid MCHS with flow boiling revealed that the local heat transfer coefficient is consistent increases with the heat flux and becomes sensitive to the heat flux. The pressure loss was also found to increase in the 2-phase flow with heat flux under all mass flow rate conditions. **Figure 24** shows the variation of upstream heat transfer coefficient in the microchannel concerning the effective heat flux. A numerical study of Yang Luo et al. [93] on manifold MCHS with subcooled two-phase flow boiling proved that heat flux and the manifold ratio significantly influence the pressure drop and thermal resistance ( $R_{th}$ ) of the micro-channel. The authors suggested that the manifold ratios should be between 1 and 2 for low-pressure drop and the better thermal performance of the manifold heatsink.

The impact of the surface characteristics on the flow boiling of regasified and deionized water micro-channel was experimentally studied and found that the characteristics of the Cu microchannel surface are transient [88]. The heat transfer coefficients of the aged Cu microchannel surface were unchanged and even enhanced



**Figure 24.** Variation of upstream HT coefficient in the microchannel with respect to the heat flux with the images of flow visualization [92].



**Figure 25.**  
*Transient variation of heaters' temperature (lines represents the average temperature) [94].*

after proper cleaning. Hongzhao Wang et al. [94] examined the wettability patterned microchannel and homogeneous hydrophilic microchannel and found a 22% higher heat transfer coefficient for wettability patterned microchannel. The heat transfer coefficient was noticed to be improved for the wettability patterned channel with the mass flux. The transient variation of Heaters' temperature variation is shown in **Figure 25**.

The experimental and simulation analysis on microchannel with 2-phase continuous boiling revealed that heat transfer was improved at the fixed heat flux with increment in mass flux but it may tend to unstable boiling [95]. For the unstable boiling in a microchannel, the oscillation amplitude was observed to be influenced by the structural parameters of the microchannel and the thermal conductivity. In the experimental investigation on 2-phase flow regimes in a microchannel, the formation of the wave on the liquid film was observed in film flow regimes [96] and the wavelength of the waves on the liquid film is depending on flow rate of the gas and liquid.

Along with the MCHS performance improvement methods discussed above, a few other inventive methods were noticed in the literature. C.J. Ho et al. [97] examined the microencapsulated PCM (MEPCM) based MCHS under the sudden pulsed heat flux and disclosed that the layer of MEPCM layer not effective in controlling the temperature rise in the MCHS. At the high amplitude of heat flux pulse, the MEPCM layer has the improved cooling performance. Soumya Bandyopadhyay, Suman Chakraborty [98] investigated the thermophoretic force effect and the interfacial tension by studying Newtonian fluid dynamics in a microchannel with the consideration of temperature dependency of viscosity. Linda Arsenjuk et al. [99] investigated the slug flow in parallelized microchannel and obtained static fluid distribution with high-pressure loss. Zan Wu et al. [100] analyzed the slug flow in a square microchannel and correlated the velocity of the slug in terms of the Capillary number using bulk velocity and continuous phase viscosity.

#### 4. Conclusions

The advancements in the thermal performance enhancement methods for microchannel heat sinks are discussed so far. Each method is selected based on

heatsink application, the heat flux needs to be dissipated, space availability, etc. The primary conclusions drawn from this chapter are,

- The accuracy of the solution depends on the numerical method implemented to solve the fluid flow problem. The lattice Boltzmann method was considered an efficient numerical method to solve the fluid flow problems coupled with heat transfer in complex geometry.
- The geometry modification of the heat sink by adding the fins, changing the channel shape, flow pattern, etc., is the basic heat transfer enhancing technique but with increasing the complexity of the geometry the fabrication becomes difficult and expensive.
- The large pressure drop is also one of the disadvantages with the complex geometry of the heat sink.
- The microchannel heat sink developed with the phase changing process is well suited for the heat dissipation application where large fluctuations in the heat flux are involved.
- The flow boiling and jet impingement in the microchannel heat sink is considered the best methods to dissipate the large heat fluxes generated in the electronic components with the penalty of a large pressure drop.

## **5. Existing lacuna and future scope**

The major observations from the present chapter are

- Efficient Phase changing materials (PCM) based MCHS has to be developed and its influence on the heat transfer has to be analyzed thoroughly.
- High-pressure loss is the main limitation for the microfluidic systems, heat sinks with the low-pressure drop has to be developed
- There is more scope for electro-hydrodynamic and magneto-hydrodynamic studies in the field of microfluidics.
- The research on the influence of surface effects on the behavior fluid flow must be extended to analyze the thermal performance.
- Low-cost manufacturing methods for microfluidic devices are required as the existing fabrication is very expensive.



## Author details

Naga Ramesh Korasikha<sup>1</sup>, Thopudurthi Karthikeya Sharma<sup>1\*</sup>,  
Gadale Amba Prasad Rao<sup>2</sup> and Kotha Madhu Murthy<sup>2</sup>

1 NIT Andhra Pradesh, India

2 NIT Warangal, India

\*Address all correspondence to: [tk@nitandhra.ac.in](mailto:tk@nitandhra.ac.in)

## IntechOpen

---

© 2021 The Author(s). Licensee IntechOpen. This chapter is distributed under the terms of the Creative Commons Attribution License (<http://creativecommons.org/licenses/by/3.0>), which permits unrestricted use, distribution, and reproduction in any medium, provided the original work is properly cited. 

## References

- [1] Karoly R, Dumitru CD. Management of a Power System based on Renewable Energy. *Procedia Technol* 2014;12:693-697. <https://doi.org/10.1016/j.protcy.2013.12.551>.
- [2] Kohsri S, Planklang B. Energy management and control system for smart renewable energy remote power generation. *Energy Procedia*, 2011. <https://doi.org/10.1016/j.egypro.2011.09.021>.
- [3] Javied T, Rackow T, Franke J. Implementing energy management system to increase energy efficiency in manufacturing companies. *Procedia CIRP*, 2015. <https://doi.org/10.1016/j.procir.2014.07.057>.
- [4] Song H, Liu J, Liu B, Wu J, Cheng HM, Kang F. Two-Dimensional Materials for Thermal Management Applications. *Joule* 2018;2:442-463. <https://doi.org/10.1016/j.joule.2018.01.006>.
- [5] Habibi Khalaj A, Halgamuge SK. A Review on efficient thermal management of air- and liquid-cooled data centers: From chip to the cooling system. *Appl Energy* 2017;205:1165-1188. <https://doi.org/10.1016/j.apenergy.2017.08.037>.
- [6] Lakshminarayanan V, Sriraam N. The effect of temperature on the reliability of electronic components. *IEEE CONECCT 2014 - 2014 IEEE Int Conf Electron Comput Commun Technol* 2014;1-6. <https://doi.org/10.1109/CONECCT.2014.6740182>.
- [7] Kandlikar SG, Grande WJ. Evolution of microchannel flow passages-thermohydraulic performance and fabrication technology. *ASME Int Mech Eng Congr Expo Proc* 2002;59-72. <https://doi.org/10.1115/IMECE2002-32043>.
- [8] Mehendale SS, Jacobi AM, Shah RK. Fluid flow and heat transfer at micro- and meso-scales with application to heat exchanger design. *Appl Mech Rev* 2000;53:175-193. <https://doi.org/10.1115/1.3097347>.
- [9] Tuckerman DB, Pease RFW. High-Performance Heat Sinking for VLSI. *IEEE Electron Device Lett* 1981;EDL-2:126-129. <https://doi.org/10.1109/EDL.1981.25367>.
- [10] Missaggia LJ, Walpole JN, Liao ZL, Phillips RJ. Microchannel Heat Sinks For Two-Dimensional High-Power-Density Diode Laser Arrays. *IEEE J Quantum Electron* 1989;25:1988-1992. <https://doi.org/10.1109/3.35223>.
- [11] Peng XF, Peterson GP. Forced convection heat transfer of single-phase binary mixtures through microchannels. *Exp Therm Fluid Sci* 1996;12:98-104. [https://doi.org/10.1016/0894-1777\(95\)00079-8](https://doi.org/10.1016/0894-1777(95)00079-8).
- [12] Judy J, Maynes D, Webb BW. Characterization of frictional pressure drop for liquid flows through microchannels. *Int J Heat Mass Transf* 2002;45:3477-3489. [https://doi.org/10.1016/S0017-9310\(02\)00076-5](https://doi.org/10.1016/S0017-9310(02)00076-5).
- [13] Agostini B, Watel B, Bontemps A, Thonon B. Liquid flow friction factor and heat transfer coefficient in small channels: An experimental investigation. *Exp Therm Fluid Sci* 2004. [https://doi.org/10.1016/S0894-1777\(03\)00027-X](https://doi.org/10.1016/S0894-1777(03)00027-X).
- [14] Takács G, Szabó PG, Bognár G. Enhanced thermal characterization method of microscale heatsink structures. *Microelectron Reliab* 2016;67:21-28. <https://doi.org/10.1016/j.microrel.2016.09.019>.
- [15] Ramesh KN, Sharma TK, Rao GAP. Latest Advancements in Heat Transfer Enhancement in the Micro-channel Heat Sinks: A Review. *Arch Comput Methods Eng* 2020. <https://doi.org/10.1007/s11831-020-09495-1>.

- [16] Serafy C, Srivastava A, Yeung D. Unlocking the true potential of 3D CPUs with micro-fluidic cooling. *Proc Int Symp Low Power Electron Des* 2015;2015-October:323-6. <https://doi.org/10.1145/2627369.2627666>.
- [17] Zając P, Napieralski A. Novel thermal model of microchannel cooling system designed for fast simulation of liquid-cooled ICs. *Microelectron Reliab* 2018;87:245-258. <https://doi.org/10.1016/j.microrel.2018.06.020>.
- [18] Garrity PT, Klausner JF, Mei R. A flow boiling microchannel evaporator plate for fuel cell thermal management. *Heat Transf Eng* 2007;28:877-884. <https://doi.org/10.1080/01457630701378333>.
- [19] Datta M, Choi HW. Microheat exchanger for cooling high power laser diodes. *Appl Therm Eng* 2015;90:266-273. <https://doi.org/10.1016/j.applthermaleng.2015.07.012>.
- [20] Deng D, Xie Y, Chen L, Pi G, Huang Y. Experimental investigation on thermal and combustion performance of a combustor with microchannel cooling. *Energy* 2019;181:954-963. <https://doi.org/10.1016/j.energy.2019.06.034>.
- [21] Erp R Van, Kampitsis G, Matioli E. A manifold microchannel heat sink for ultra-high power density liquid-cooled converters. *Conf Proc - IEEE Appl Power Electron Conf Expo - APEC* 2019;2019-March:1383-9. <https://doi.org/10.1109/APEC.2019.8722308>.
- [22] Zhou W, Deng W, Lu L, Zhang J, Qin L, Ma S, et al. Laser micro-milling of microchannel on copper sheet as catalyst support used in microreactor for hydrogen production. *Int J Hydrogen Energy* 2014;39:4884-4894. <https://doi.org/10.1016/j.ijhydene.2014.01.041>.
- [23] Yuan D, Ci P, Tian F, Shi J, Xu S, Xin P, et al. The improvement of electrochemical etching process for silicon microchannel plates. *4th IEEE Int Conf Nano/Micro Eng Mol Syst NEMS* 2009;964-9. <https://doi.org/10.1109/NEMS.2009.5068734>.
- [24] Kikuchi T, Wachi Y, Sakairi M, Suzuki RO. Aluminum bulk micro-machining through an anodic oxide mask by electrochemical etching in an acetic acid/perchloric acid solution. *Microelectron Eng* 2013;111:14-20. <https://doi.org/10.1016/j.mee.2013.05.007>.
- [25] Jung PG, Jung ID, Lee SM, Ko JS. Fabrication of self-encapsulated nickel microchannels and nickel nanowells by reactive ion etching. *J Mater Process Technol* 2008;208:111-116. <https://doi.org/10.1016/j.jmatprotec.2007.12.132>.
- [26] Pan M, Zeng D, Tang Y. Feasibility investigations on multi-cutter milling process: A novel fabrication method for microreactors with multiple microchannels. *J Power Sources* 2009;192:562-572. <https://doi.org/10.1016/j.jpowsour.2009.03.024>.
- [27] Cheema MS, Dvivedi A, Sharma AK. Tool wear studies in fabrication of microchannels in ultrasonic micromachining. *Ultrasonics* 2015;57:57-64. <https://doi.org/10.1016/j.ultras.2014.10.018>.
- [28] Diao K, Zhao Y. Heat transfer performance of sintered Cu microchannels produced by a novel method. *Int J Heat Mass Transf* 2019;139:537-547. <https://doi.org/10.1016/j.ijheatmasstransfer.2019.05.020>.
- [29] Collins IL, Weibel JA, Pan L, Garimella S V. A permeable-membrane microchannel heat sink made by additive manufacturing. *Int J Heat Mass Transf* 2019;131:1174-1183. <https://doi.org/10.1016/j.ijheatmasstransfer.2018.11.126>.
- [30] haghhighinia A, Movahedirad S. Fluid micro-mixing in a passive microchannel: Comparison of 2D and

- 3D numerical simulations. *Int J Heat Mass Transf* 2019;139:907-916. <https://doi.org/10.1016/j.ijheatmasstransfer.2019.05.084>.
- [31] Salah SAS, Filali EG, Djellouli S. Numerical investigation of Reynolds number and scaling effects in micro-channels flows. *J Hydrodyn* 2017;29:647-658. [https://doi.org/10.1016/S1001-6058\(16\)60777-1](https://doi.org/10.1016/S1001-6058(16)60777-1).
- [32] Zhou YL, Chang H. Numerical simulation of hydrodynamic and heat transfer characteristics of slug flow in serpentine microchannel with various curvature ratio. *Heat Mass Transf Und Stoffuebertragung* 2019. <https://doi.org/10.1007/s00231-019-02664-4>.
- [33] Rostami J, Abbassi A. Conjugate heat transfer in a wavy microchannel using nanofluid by two-phase Eulerian-Lagrangian method. *Adv Powder Technol* 2016. <https://doi.org/10.1016/j.appt.2015.10.003>.
- [34] Li S, Chen R, Wang H, Liao Q, Zhu X, Wang Z, et al. Numerical investigation of the moving liquid column coalescing with a droplet in triangular micro-channels using CLSVOF method. *Sci Bull* 2015;60:1911-1926. <https://doi.org/10.1007/s11434-015-0924-7>.
- [35] Wang Z, Li S, Chen R, Zhu X, Liao Q, Ye D, et al. Numerical study on dynamic behaviors of the coalescence between the advancing liquid meniscus and multi-droplets in a microchannel using CLSVOF method. *Comput Fluids* 2018;170:341-348. <https://doi.org/10.1016/j.compfluid.2018.05.014>.
- [36] Ferrari A, Magnini M, Thome JR. A Flexible Coupled Level Set and Volume of Fluid (flexCLV) method to simulate microscale two-phase flow in non-uniform and unstructured meshes. *Int J Multiph Flow* 2017;91:276-295. <https://doi.org/10.1016/j.ijmultiphaseflow.2017.01.017>.
- [37] So RMC, Leung RCK, Kam EWS, Fu SC. Progress in the development of a new lattice Boltzmann method. *Comput Fluids* 2019;190:440-469. <https://doi.org/10.1016/j.compfluid.2019.04.009>.
- [38] Che Sidik NA, Aisyah Razali S. Lattice Boltzmann method for convective heat transfer of nanofluids - A review. *Renew Sustain Energy Rev* 2014;38:864-875. <https://doi.org/10.1016/j.rser.2014.07.001>.
- [39] Kamali R, Soloklou MN, Hadidi H. Numerical simulation of electroosmotic flow in rough microchannels using the lattice Poisson-Nernst-Planck methods. *Chem Phys* 2018;507:1-9. <https://doi.org/10.1016/j.chemphys.2018.04.008>.
- [40] Qasem NAA, Zubair SM. Compact and microchannel heat exchangers: A comprehensive review of air-side friction factor and heat transfer correlations. *Energy Convers Manag* 2018;173:555-601. <https://doi.org/10.1016/j.enconman.2018.06.104>.
- [41] Kumar P. Numerical investigation of fluid flow and heat transfer in trapezoidal microchannel with groove structure. *Int J Therm Sci* 2019;136:33-43. <https://doi.org/10.1016/j.ijthermalsci.2018.10.006>.
- [42] Sahar AM, Wissink J, Mahmoud MM, Karayiannis TG, Ashrul Ishak MS. Effect of hydraulic diameter and aspect ratio on single phase flow and heat transfer in a rectangular microchannel. *Appl Therm Eng* 2017;115:793-814. <https://doi.org/10.1016/j.applthermaleng.2017.01.018>.
- [43] Kim B. An experimental study on fully developed laminar flow and heat transfer in rectangular microchannels. *Int J Heat Fluid Flow* 2016;62:224-232. <https://doi.org/10.1016/j.ijheatfluidflow.2016.10.007>.
- [44] Soleimanikutanaei S, Ghasemisahebi E, Lin CX. Numerical study of heat transfer enhancement using

- transverse microchannels in a heat sink. *Int J Therm Sci* 2018;125:89-100. <https://doi.org/10.1016/j.ijthermalsci.2017.11.009>.
- [45] Kewalramani G V, Hedau G, Saha SK, Agrawal A. Empirical correlation of laminar forced convective flow in trapezoidal microchannel based on experimental and 3D numerical study. *Int J Therm Sci* 2019;142:422-433. <https://doi.org/10.1016/j.ijthermalsci.2019.05.001>.
- [46] Ghani IA, Kamaruzaman N, Sidik NAC. Heat transfer augmentation in a microchannel heat sink with sinusoidal cavities and rectangular ribs. *Int J Heat Mass Transf* 2017;108:1969-1981. <https://doi.org/10.1016/j.ijheatmasstransfer.2017.01.046>.
- [47] Chai L, Xia GD, Wang HS. Numerical study of laminar flow and heat transfer in microchannel heat sink with offset ribs on sidewalls. *Appl Therm Eng* 2016;92:32-41. <https://doi.org/10.1016/j.applthermaleng.2015.09.071>.
- [48] Xie J, Yan H, Sundén B, Xie G. The influences of sidewall proximity on flow and thermal performance of a microchannel with large-row pin-fins. *Int J Therm Sci* 2019;140:8-19. <https://doi.org/10.1016/j.ijthermalsci.2019.02.031>.
- [49] Chandra AK, Kishor K, Mishra PK, Siraj Alam M. Numerical Simulation of Heat Transfer Enhancement in Periodic Converging-diverging Microchannel. *Procedia Eng* 2015;127:95-101. <https://doi.org/10.1016/j.proeng.2015.11.431>.
- [50] Deng D, Chen L, Chen X, Pi G. Heat transfer and pressure drop of a periodic expanded-constrained microchannels heat sink. *Int J Heat Mass Transf* 2019;140:678-690. <https://doi.org/10.1016/j.ijheatmasstransfer.2019.06.006>.
- [51] Xia GD, Wang W, Jia YT, Yang YC, Xia GD, Wang W, et al. Accepted Manuscript 2019.
- [52] Liu H ling, Qi D hao, Shao X dong, Wang W dong. An experimental and numerical investigation of heat transfer enhancement in annular microchannel heat sinks. *Int J Therm Sci* 2019;142:106-120. <https://doi.org/10.1016/j.ijthermalsci.2019.04.006>.
- [53] Liu Y, Xu G, Sun J, Li H. Investigation of the roughness effect on flow behavior and heat transfer characteristics in microchannels. *Int J Heat Mass Transf* 2015;83:11-20. <https://doi.org/10.1016/j.ijheatmasstransfer.2014.11.060>.
- [54] Guo L, Xu H, Gong L. Influence of wall roughness models on fluid flow and heat transfer in microchannels. *Appl Therm Eng* 2015;84:399-408. <https://doi.org/10.1016/j.applthermaleng.2015.04.001>.
- [55] Yuan X, Tao Z, Li H, Tian Y. Experimental investigation of surface roughness effects on flow behavior and heat transfer characteristics for circular microchannels. *Chinese J Aeronaut* 2016;29:1575-1581. <https://doi.org/10.1016/j.cja.2016.10.006>.
- [56] Ji Y, Yuan K, Chung JN. Numerical simulation of wall roughness on gaseous flow and heat transfer in a microchannel. *Int J Heat Mass Transf* 2006;49:1329-1339. <https://doi.org/10.1016/j.ijheatmasstransfer.2005.10.011>.
- [57] Shi X, Li S, Mu Y, Yin B. Geometry parameters optimization for a microchannel heat sink with secondary flow channel. *Int Commun Heat Mass Transf* 2019;104:89-100. <https://doi.org/10.1016/j.icheatmasstransfer.2019.03.009>.
- [58] Michna GJ, Browne EA, Peles Y, Jensen MK. Single-phase microscale jet stagnation point heat transfer. *J Heat Transfer* 2009;131:1-8. <https://doi.org/10.1115/1.3154750>.

- [59] Elison B, Webb BW. Local heat transfer to impinging liquid jets in the initially laminar, transitional, and turbulent regimes. *Int J Heat Mass Transf* 1994;37:1207-1216. [https://doi.org/10.1016/0017-9310\(94\)90206-2](https://doi.org/10.1016/0017-9310(94)90206-2).
- [60] Lytle D, Webb BW. Air jet impingement heat transfer at low nozzle-plate spacings. *Int J Heat Mass Transf* 1994;37:1687-1697. [https://doi.org/10.1016/0017-9310\(94\)90059-0](https://doi.org/10.1016/0017-9310(94)90059-0).
- [61] Sabato M, Fregni A, Stalio E, Brusiani F, Tranchero M, Baritaud T. Numerical study of submerged impinging jets for power electronics cooling. *Int J Heat Mass Transf* 2019;141:707-718. <https://doi.org/10.1016/j.ijheatmasstransfer.2019.06.081>.
- [62] Abo-Zahhad EM, Ookawara S, Radwan A, El-Shazly AH, Elkady MF. Numerical analyses of hybrid jet impingement/microchannel cooling device for thermal management of high concentrator triple-junction solar cell. *Appl Energy* 2019;253:113538. <https://doi.org/10.1016/j.apenergy.2019.113538>.
- [63] Zhang Y, Wang S, Ding P. Effects of channel shape on the cooling performance of hybrid micro-channel and slot-jet module. *Int J Heat Mass Transf* 2017;113:295-309. <https://doi.org/10.1016/j.ijheatmasstransfer.2017.05.092>.
- [64] Husain A, Ariz M, Al-Rawahi NZH, Ansari MZ. Thermal performance analysis of a hybrid micro-channel, -pillar and -jet impingement heat sink. *Appl Therm Eng* 2016;102:989-1000. <https://doi.org/10.1016/j.applthermaleng.2016.03.048>.
- [65] Naphon P, Wiriyasart S, Arisariyawong T, Nakharintr L. ANN, numerical and experimental analysis on the jet impingement nanofluids flow and heat transfer characteristics in the micro-channel heat sink. *Int J Heat Mass Transf* 2019;131:329-340. <https://doi.org/10.1016/j.ijheatmasstransfer.2018.11.073>.
- [66] Robinson AJ, Schnitzler E. An experimental investigation of free and submerged miniature liquid jet array impingement heat transfer. *Exp Therm Fluid Sci* 2007;32:1-13. <https://doi.org/10.1016/j.expthermflusci.2006.12.006>.
- [67] Huang X, Yang W, Ming T, Shen W, Yu X. Heat transfer enhancement on a microchannel heat sink with impinging jets and dimples. *Int J Heat Mass Transf* 2017;112:113-124. <https://doi.org/10.1016/j.ijheatmasstransfer.2017.04.078>.
- [68] Yang YT, Tsai KT, Wang YH, Lin SH. Numerical study of microchannel heat sink performance using nanofluids. *Int Commun Heat Mass Transf* 2014;57:27-35. <https://doi.org/10.1016/j.icheatmasstransfer.2014.07.006>.
- [69] Ghale ZY, Haghshenasfard M, Esfahany MN. Investigation of nanofluids heat transfer in a ribbed microchannel heat sink using single-phase and multiphase CFD models. *Int Commun Heat Mass Transf* 2015;68:122-129. <https://doi.org/10.1016/j.icheatmasstransfer.2015.08.012>.
- [70] Abdollahi A, Mohammed HA, Vanaki SM, Sharma RN. Numerical investigation of fluid flow and heat transfer of nanofluids in microchannel with longitudinal fins. *Ain Shams Eng J* 2018;9:3411-3418. <https://doi.org/10.1016/j.asej.2017.05.011>.
- [71] Alfaryjat AA, Mohammed HA, Adam NM, Stanciu D, Dobrovicescu A. Numerical investigation of heat transfer enhancement using various nanofluids in hexagonal microchannel heat sink. *Therm Sci Eng Prog* 2018;5:252-262. <https://doi.org/10.1016/j.tsep.2017.12.003>.

- [72] Li J, Kleinstreuer C. Thermal performance of nanofluid flow in microchannels. *Int J Heat Fluid Flow* 2008;29:1221-1232. <https://doi.org/10.1016/j.ijheatfluidflow.2008.01.005>.
- [73] Kuppusamy NR, Mohammed HA, Lim CW. Numerical investigation of trapezoidal grooved microchannel heat sink using nanofluids. *Thermochim Acta* 2013;573:39-56. <https://doi.org/10.1016/j.tca.2013.09.011>.
- [74] Kuppusamy NR, Mohammed HA, Lim CW. Thermal and hydraulic characteristics of nanofluid in a triangular grooved microchannel heat sink (TGMCHS). *Appl Math Comput* 2014;246:168-183. <https://doi.org/10.1016/j.amc.2014.07.087>.
- [75] Shi X, Li S, Wei Y, Gao J. Numerical investigation of laminar convective heat transfer and pressure drop of water-based Al<sub>2</sub>O<sub>3</sub> nanofluids in a microchannel. *Int Commun Heat Mass Transf* 2018;90:111-120. <https://doi.org/10.1016/j.icheatmasstransfer.2017.11.007>.
- [76] Sakanova A, Keian CC, Zhao J. Performance improvements of microchannel heat sink using wavy channel and nanofluids. *Int J Heat Mass Transf* 2015;89:59-74. <https://doi.org/10.1016/j.ijheatmasstransfer.2015.05.033>.
- [77] Sarafraz MM, Yang B, Pourmehran O, Arjomandi M, Ghomashchi R. Fluid and heat transfer characteristics of aqueous graphene nanoplatelet (GNP) nanofluid in a microchannel. *Int Commun Heat Mass Transf* 2019;107:24-33. <https://doi.org/10.1016/j.icheatmasstransfer.2019.05.004>.
- [78] Al-Rashed AAAA, Shahsavar A, Entezari S, Moghimi MA, Adio SA, Nguyen TK. Numerical investigation of non-Newtonian water-CMC/CuO nanofluid flow in an offset strip-fin microchannel heat sink: Thermal performance and thermodynamic considerations. *Appl Therm Eng* 2019;155:247-258. <https://doi.org/10.1016/j.applthermaleng.2019.04.009>.
- [79] Kang HJ, Choi B. Development of the MHD micropump with mixing function. *Sensors Actuators, A Phys* 2011;165:439-445. <https://doi.org/10.1016/j.sna.2010.11.011>.
- [80] Das C, Wang G, Payne F. Some practical applications of magnetohydrodynamic pumping. *Sensors Actuators, A Phys* 2013;201:43-48. <https://doi.org/10.1016/j.sna.2013.06.023>.
- [81] Al-Hababbeh OM, Al-Saqqa M, Safi M, Abo Khater T. Review of magnetohydrodynamic pump applications. *Alexandria Eng J* 2016;55:1347-1358. <https://doi.org/10.1016/j.aej.2016.03.001>.
- [82] Xiao X, Kim CN. Magnetohydrodynamic flows in a hairpin duct under a magnetic field applied perpendicular to the plane of flow. *Appl Math Comput* 2014;240:1-15. <https://doi.org/10.1016/j.amc.2014.04.049>.
- [83] Bennia A, Bouaziz MN. CFD modeling of turbulent forced convective heat transfer and friction factor in a tube for Fe<sub>3</sub>O<sub>4</sub> magnetic nanofluid in the presence of a magnetic field. *J Taiwan Inst Chem Eng* 2017;78:127-136. <https://doi.org/10.1016/j.jtice.2017.04.035>.
- [84] Motozawa M, Chang J, Sawada T, Kawaguchi Y. Effect of magnetic field on heat transfer in rectangular duct flow of a magnetic fluid. *Phys Procedia* 2010;9:190-193. <https://doi.org/10.1016/j.phpro.2010.11.043>.
- [85] Kiyasatfar M, Pourmahmoud N. Laminar MHD flow and heat transfer of power-law fluids in square microchannels. *Int J Therm Sci* 2016;99:26-35.

<https://doi.org/10.1016/j.ijthermalsci.2015.07.031>.

[86] Yang C, Jian Y, Xie Z, Li F. Heat transfer characteristics of magneto-hydrodynamic electroosmotic flow in a rectangular microchannel. *Eur J Mech B/Fluids* 2019;74:180-190. <https://doi.org/10.1016/j.euromechflu.2018.11.015>.

[87] Ibáñez G, Cuevas S. Entropy generation minimization of a MHD (magnetohydrodynamic) flow in a microchannel. *Energy* 2010;35:4149-4155. <https://doi.org/10.1016/j.energy.2010.06.035>.

[88] Jayaramu P, Gedupudi S, Das SK. Influence of heating surface characteristics on flow boiling in a copper microchannel: Experimental investigation and assessment of correlations. *Int J Heat Mass Transf* 2019;128:290-318. <https://doi.org/10.1016/j.ijheatmasstransfer.2018.08.075>.

[89] Karayiannis TG, Mahmoud MM. Flow boiling in microchannels: Fundamentals and applications. *Appl Therm Eng* 2017;115:1372-1397. <https://doi.org/10.1016/j.applthermaleng.2016.08.063>.

[90] Thome JR. State-of-the-art overview of boiling and two-phase flows in microchannels. *Heat Transf Eng* 2006;27:4-19. <https://doi.org/10.1080/01457630600845481>.

[91] Bertsch SS, Groll EA, Garimella S V. Effects of heat flux, mass flux, vapor quality, and saturation temperature on flow boiling heat transfer in microchannels. *Int J Multiph Flow* 2009; 35:142-154. <https://doi.org/10.1016/j.ijmultiphaseflow.2008.10.004>.

[92] Mathew J, Lee PS, Wu T, Yap CR. Experimental study of flow boiling in a hybrid microchannel-microgap heat sink. *Int J Heat Mass Transf* 2019;135:1167-1191. <https://doi.org/10.1016/j.ijheatmasstransfer.2019.02.033>.

<https://doi.org/10.1016/j.ijheatmasstransfer.2019.02.033>.

[93] Luo Y, Li J, Zhou K, Zhang J, Li W. A numerical study of subcooled flow boiling in a manifold microchannel heat sink with varying inlet-to-outlet width ratio. *Int J Heat Mass Transf* 2019;139: 554-563. <https://doi.org/10.1016/j.ijheatmasstransfer.2019.05.030>.

[94] Wang H, Yang Y, He M, Qiu H. Subcooled flow boiling heat transfer in a microchannel with chemically patterned surfaces. *Int J Heat Mass Transf* 2019;140:587-597. <https://doi.org/10.1016/j.ijheatmasstransfer.2019.06.027>.

[95] Xia G, Lv Y, Cheng L, Ma D, Jia Y. Experimental study and dynamic simulation of the continuous two-phase instable boiling in multiple parallel microchannels. *Int J Heat Mass Transf* 2019;138:961-984. <https://doi.org/10.1016/j.ijheatmasstransfer.2019.04.124>.

[96] Vozhakov IS, Ronshin F V. Experimental and theoretical study of two-phase flow in wide microchannels. *Int J Heat Mass Transf* 2019;136:312-323. <https://doi.org/10.1016/j.ijheatmasstransfer.2019.02.099>.

[97] Ho CJ, Chiou YH, Yan WM, Ghalambaz M. Transient cooling characteristics of Al<sub>2</sub>O<sub>3</sub>-water nanofluid flow in a microchannel subject to a sudden-pulsed heat flux. *Int J Mech Sci* 2019;151:95-105. <https://doi.org/10.1016/j.ijmecsci.2018.11.017>.

[98] Bandyopadhyay S, Chakraborty S. Thermophoretically driven capillary transport of nanofluid in a microchannel. *Adv Powder Technol* 2018;29:964-971. <https://doi.org/10.1016/j.apt.2018.01.014>.

[99] Arsenjuk L, von Vietinghoff N, Gladius AW, Agar DW. Actively homogenizing fluid distribution and slug length of liquid-liquid segmented



flow in parallelized microchannels.  
Chem Eng Process - Process Intensif  
2020. <https://doi.org/10.1016/j.cep.2020.108061>.

[100] Wu Z, Cao Z, Sunden B. Flow patterns and slug scaling of liquid-liquid flow in square microchannels. Int J Multiph Flow 2019. <https://doi.org/10.1016/j.ijmultiphaseflow.2018.12.009>.



# Heat Pipes Heat Exchanger for HVAC Applications

*Anwar Barrak*

## Abstract

With increasing global demands for energy (especially in developing countries), energy production will increase, the wasted energy will increase, and the emission and pollution will increase also. That makes the researchers focus on recovering the wasted heat and enhancing the recovery devices to improve the energy-saving amount. Heat pipe technology is one of the promising methods of transfer heat efficiently between two species. There are three common types of heat pipe; conventional heat pipe, thermosyphon, and oscillating heat pipe. Each type contains three sections: evaporator, adiabatic, and condenser section. The heat pipe as a heat exchanger was investigated and experimentally used by many authors to recover the wasted energy in many engineering applications.

**Keywords:** heat transfer, heat exchanger, heat recovery, heat pipe, pulsating heat pipe

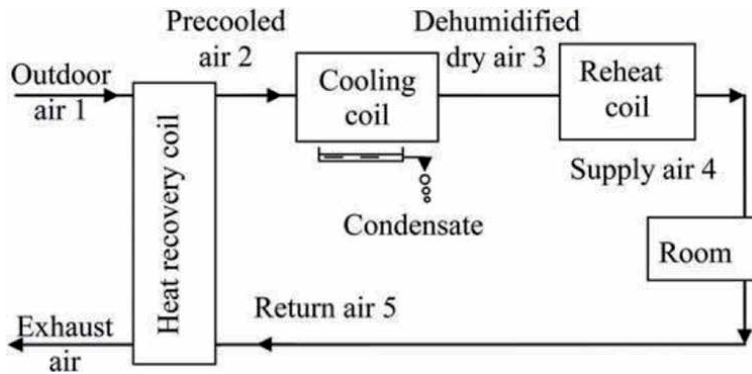
## 1. Introduction

The energy consumption of many countries has been increased mostly in growing countries. A rise in energy-consuming has been recognized because of the main developments in different sectors [1]. It is expected that energy-consuming even has a quicker increase in equatorial (hot) countries in comparison with the other countries. The energy side and global warming are the principal matters now and one of the main challenges for scientists and policymakers. One of the main processes that participate in the emissions lowering is an application of a heat recovery system to improve the thermal performance in the expression of energy-consuming. Air conditioning units are one of the important energy consumers, and commonly the running electrical cost of air conditioning systems accounts for about 50% of whole energy bills [2]. The heat will recover if the energy recovery applications are combined with air conditioning units to decrease the energy required of air conditioning units [3].

**Figure 1** shows the use of a heat recovery device in the HVAC system, a high temperature (hot) and humid inlet air is required in an occupied building. The return air (cold) can be used to precool the incoming outdoor (hot) air by employing a heat recovery coil. Conventional heat recovery coils include stationary finned or plate-type air-to-air heat exchangers or rotary heat wheels [4]. Heat pipe heat exchanger (HPHX) suggested as an efficient heat exchanger is for this purpose [3].

The advantages of using the heat recovery device in HVAC systems are:

1. Energy reduction and, thus, primary energy consumption, which led to reduce emission production.



**Figure 1.** Air conditioning system with precool and reheat coils [4].

2. Reduction in energy requirements and amounts of coolants used for the air conditioning system.
3. The operating costs are reduced [5].

The purpose of a heat pipe heat exchanger for heat recovery in hot and cold climates is widely known. The heat pipe exchanger offers a low air pressure drop, related to possible by loop configurations, and heat recovery applications can be extended to milder climates and still pay for themselves. A new possibility is ‘cooling’ recovery in the summertime, which is now economical enough to be considered. The application of heat pipe as a heat exchanger to recover wasted heat is participated to enhance the dehumidification capacity of a conventional cooling coil is one of the most attractive applications. The used heat pipe heat exchanger in HVAC systems as a dehumidifier device can decrease 10% the air relative humidity that leads to resulting in a remarkable enhancement of the quality of fresh air and a decrease in power demand. The heat pipe is a promising technology to enhance the quality of fresh air, and at the same time help save energy.

The objectives of this chapter are to view heat pipe technology, the mechanism of heat and mass transfer, and assess the performance of heat-pipe heat recovery units for the HVAC system. This chapter presents the updated development status of the heat pipe used as a heat exchanger used in the HVAC system to recover the wasted heat. In this chapter, the experimental and theoretical investigations of the heat pipe, Thermosyphon, and OHP are systematically summarized.

## 2. Heat pipe (HP)

The heat pipe is a very efficient passive device used to transfer heat. Heat pipes let height transfer rates over large space, with minimum temperature differences, simple structure, and easy control, and no required to pump [6]. Heat pipes consist of locked channels that are partially filled by a suitable working fluid. Heat pipes classify as a traditional heat pipe (HP), Thermosyphon heat pipe, and a pulsating/oscillating heat pipe (OHP) [7].

### 2.1 Conventional heat pipe (HP)

A heat pipe is a tube containing a wick structure filled partially with fluid at the saturated state is lined on the inner surface. It is divided into three sections,

as shown in **Figure 2**. An evaporator portion, where the heat is added and the liquid phase changes to vapor phase, a condenser region at the other end, where the heat is dissipated, and the condensation process occurs, and an adiabatic (insulated) zone in between, where no heat in or out in this section of the heat pipe and the two phases of working fluid (liquid and vapor) flow in contrary directions through the core and the wick [8].

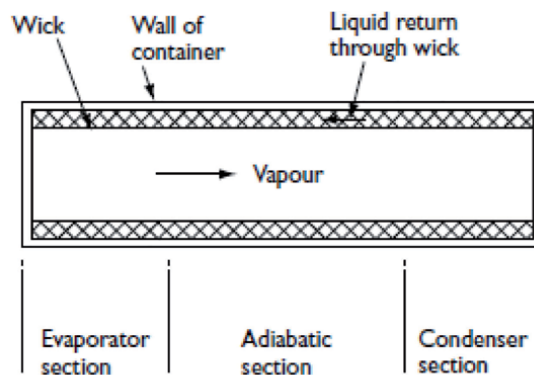
In the conventional heat pipe (HP), the condensed (liquid phase) goes back to the evaporator region by the capillary effect of the wick in the HP [7]. **Figure 3** shows the operation of a conventional heat pipe (HP).

1. Heat pipes have some advantages features compared to other conventional approaches to transfer heat like a finned heat sink.
2. In steady-state operation, a heat pipe can have an extremely high thermal conductance.
3. A heat pipe can transfer a high amount of heat over a relatively long distance with a comparatively small temperature differential.
4. Heat pipe with liquid metalworking fluids can have a higher thermal conductance in comparison to the best solid metallic conductors, silver or copper.

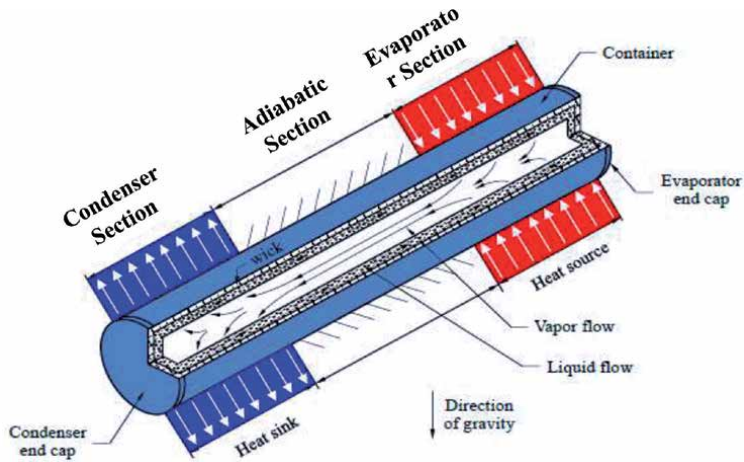
## 2.2 Thermosyphon heat pipe

Thermosyphon is a simple two-phase closed heat pipe but an effective heat transfer device. It is a wickless heat pipe with a small amount of liquid reservoir at the bottom. The best description of Thermosyphon is by dividing it into three sections, as shown in **Figure 4**. Heat input through the evaporator section will convert the liquid into vapor. The vapor rises and moves across the adiabatic region to the condenser section. The vapor condenses and gives up its latent heat in the condenser section. The liquid was then forced to back to the evaporator section as a liquid film by gravity force [10].

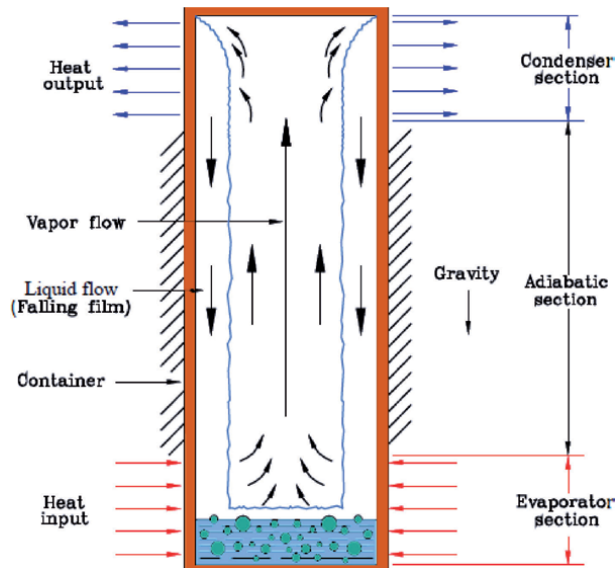
Thermosyphon is a wickless heat pipe, therefore gravity is the major driving force for condensate to return to the evaporator section, so the capillary limit is generally of no concern in the operation of the Thermosyphon. **Figure 4** shows the closed two-phase heat pipe (thermosyphon) [9].



**Figure 2.**  
*Conventional heat pipe [7].*



**Figure 3.**  
Schematic operation of a conventional heat pipe [9].



**Figure 4.**  
Schematic operation of a thermosyphon heat pipe [9].

### 3. Oscillating heat pipe (OHP)

Oscillating heat pipe (OHP) or pulsating heat pipe (PHP) is a relatively new development that was proposed by Akachi in the field of the heat pipe in cooling technology [11].

OHP is characterized by the following basic features (see **Figure 5**):

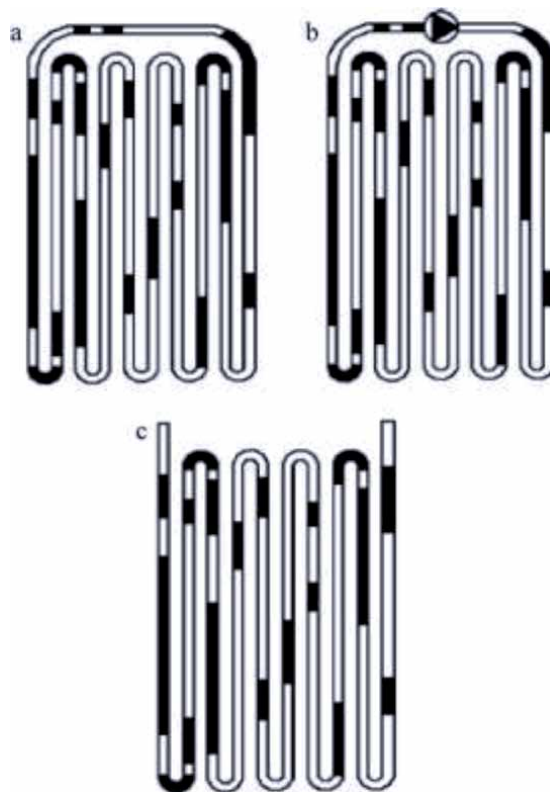
1. The structure of OHP is manufactured from a bending tube comprised of serpentine channel capillary dimensions with many turns, filled partially by a working fluid [13].
2. The OHPs are classified into three main types. **Figure 5a** illustrates the first type of OHP, which is a closed-loop oscillating heat pipe (CLOHP). The name

became from its long capillary tube forming a closed loop. While **Figure 5b** depicts the second type, which is a CLOHP with check valves; it is manufactured from a long capillary pipe with the joining ends to configure a closed loop. The closed-loop heat pipe/check valves contain one or more direction-control one-way check valves in the loop to make the working fluid circulate in one direction only. A closed-end oscillating heat pipe is a third type of heat pipe, which is manufactured from a long capillary tube with closed at both ends, as shown in **Figure 5c** [12].

3. No internal wick structure (simple manufacturing).
4. At least one heat-receiving section (evaporator), heat-dissipating section (condenser), and an optional in-between adiabatic section are present [13].

### 3.1 Operation of oscillating heat pipe (OHP)

When the evaporator section receives heat, the temperature in the evaporator region increases, which will lead to a rise in the vapor pressure in the channel, and causes the growth of bubbles size in the evaporator section, then bubbles move to the condenser zone by the difference between the pressure of the evaporator and condenser. During the movement of the vapor plug to the condenser section, which is under low temperature, so the condensation process occurs, and the vapor plug collapses. Then, the slug-train in the condenser section is pushed to the adjoining vapor plug, and the liquid slug moves to the evaporator section for nucleation.



**Figure 5.**  
*Types of oscillating heat pipes [12].*

At nucleation locations, dispersed bubbles generate and coalesce to grow in size as bubbles are continuously heated. The formation and growth of dispersed bubbles happen continuously when supplying the heat at the evaporator zone because the temperature of the inner wall of the tube was higher than the saturated temperature of the working fluid [11].

As the condenser cools, the pressure reduces, and a condensation process of bubbles accrues. This process pumps the working fluid again to the evaporator region and continuous between both sections and resulting in oscillating motion. The cycle gets completed in this way, and the same cycle is repeated again and again for heat transportation from the evaporator region to the condenser region.

### **3.2 Advantages of oscillating heat pipe (OHP)**

OHP is a highly effective thermal conductivity, thus resulting in a high level of temperature uniformity from the evaporator to the condenser. The operation of OHP can start at a low temperature to a high temperature, where the liquid and vapor phases can coexist. The manufacturing of OHP is almost by any shape. The OHP has some advantages and unique operating characteristics in comparison to a traditional heat pipe:

1. Part of the heat input at the evaporator zone of OHP will convert to the kinetic energy of the working fluid to maintain the oscillating/pulsating motion.
2. The liquid and vapor phases move in the same direction, and both phases do not interfere inside the OHP.
3. The evaporating and condensing heat transfer is significantly enhanced because liquid plugs that thermally driven in capillary tubes or channels that effectively produce thin films.
4. Oscillating/pulsating flows of working fluid inside capillary tubes/channels significantly improve the heat transfer by forced convection and the phase change (mass transfer).
5. The heat transferability of the OHP dramatically grows as the input power increases.
6. Wickless formations and low manufacturing expense.
7. The design of OHP can be independent of gravity [14].

### **4. Heat pipe heat exchanger (HPHX)**

A wide range of research investigations had been done to explain and understand the thermal performance and operational behavior of heat pipes technology when it is used as a heat exchanger for recovering the heat that is wasted in HVAC and other engineering applications. The literature studied many factors that affected the operating behavior and thermal performance of heat pipe heat exchanger (HPHX) like working fluid, heat input, inlet air temperature, and velocity, pipes geometry, and arrangement style.



#### 4.1 Review of heat pipe heat exchanger (HPHX)

This part will review the literature that investigated the recovering heat by using HPHX.

The heat pipe heat exchanger with staggered and inline arrays arrangement was investigated [15]. The heat pipe included sections with a height of 150 mm for the evaporator and condenser and 50 mm for the adiabatic zone. The heat pipe was fabricated from steel with a 20 mm inner diameter. They used 48 heat pipes put in an arrangement of eight rows. The results showed the effect of tube configuration, and the rate of heat transfer will increase by using a staggered configuration.

Noie [16] study experimentally and theoretically the influence of heat input, air temperature, and velocity on the performance of thermosyphon HPHX under steady-state operating conditions. The heat exchanger is comprised of six rows of 90 finned thermosyphon. The heat pipe had a length of 600 mm for the evaporator and condenser section and 100 mm for the adiabatic section and filled partially with water by 60% (from evaporator volume) filling ratio. The evaporator section was heated by air with temperature (100–250) °C & velocity (0.5–5.5) m/s, and the air was used to cool the condenser section at 25°C. The effectiveness-NTU method was used in the simulation program was developed to predict the outlet temperature. The results showed that the experimental and theoretical results were close. The results suggested avoiding the equal air velocity at the evaporator and condenser zones duo to the minimum effectiveness of heat pipe [16].

By using a heat exchanger with eight rows of thermosyphon in an HVAC system, Yau (2007) investigated experimentally the effect of the inlet air conditions on the sensible heat ratio (SHR). The results concluded that the SHR decreased by using HPHX with the HVAC system. These meant that the cooling coil capability for removing moisture with HPHX was enhancing, and it strongly recommended to install heat pipe heat exchangers with an HVAC system for moisture removal enhancement [17].

El-Baky and Mohamed [18] examined a heat pipe heat exchanger to recover heat by connecting it with ducts of inlet and return air streams. They investigated the influence of flow rate ratio, and inlet air temperature (32–40) °C. To help the liquid back from the condenser to the evaporator section, the heat pipes have 4 layers of the brass screen with a 0.125 mm wire diameter. The findings manifest that the effectiveness will be high as the inlet air temperature was near to the operating temperature of working fluid inside the heat pipe. The results revealed that increasing the inlet air temperature led to enhance the heat transfer rate and effectiveness for the evaporator and condenser section.

A loop type of heat pipe (LHP) was integrated into the window type air-conditioning system [19] to introduce and perform a possible reheat process in the system. This configuration presented an enhancement in the COP of the system with a reduction in energy consumption. The author concluded that the loop heat pipe could de enhance the thermal performance for the large capacity units due to the double effect LHP in the system.

Yau and Ahmadzadehtalatapeh [20] carry out an experimental investigation to study the thermal performance of a horizontal heat pipe heat exchanger. They used two rows of copper heat pipe filled partially with R134a as working fluid. They examined the influence of the inlet air velocity and variation of inlet air temperature (27–35°C). The mathematical simulation was used to predict the thermal resistance for one heat pipe and then compared with experimental findings that gave a good agreement between the experimental and theoretical results with increasing air velocity. The findings deduced that the sensible effectiveness for heat pipe decreased with increasing air velocity.

Jouhara and Merchant [21] preferred an experimental and theoretical study of the performance and saving energy of a tilted heat pipe heat exchanger (thermosyphons) in the HVAC system. The heat exchanger consisted of nine thermosyphons in arrangement inline configuration with fins at evaporator and condenser sections and filled partially with water. The investigation showed the impact of the heat input and inclination angles on the thermal performance of the system. They developed a simulation model to predict the thermal performance of the heat pipe. At 90 tilt angle, the results depicted that the HPHX had high performance and optimum effectiveness.

An experimental and theoretical analysis of heat pipe heat exchanger is presented [22]. The horizontal heat exchanger consisted from 6-row of finned heat pipe aimed to heat recovery in HAVAC system. The experimental test examined friendly substitutes as working fluid, and the results presented the alternative working fluid HFC152a had interesting heat transfer capabilities.

A study was conducted to investigate the effect of heat pipes rows on the thermal performance of heat exchanger experimentally and theoretically [23]. The heat exchanger was with three, six, and nine rows of the heat pipe, with four heat pipes in each row. The authors arranged heat pipes as a staggered configuration, and they investigated the effect of variation of inlet air temperature and velocity. In the theoretical part, the  $\epsilon$ -NTU method applied to estimate the temperature of air exiting the evaporator and the effectiveness and heat recovery. The results showed that the maximum effectiveness was 62.6% and achieved at the maximum number of rows 9 with inlet air conditions 45°C and 2 m/s.

## **4.2 Review of oscillating heat pipe heat exchanger (OHPHX)**

An oscillating heat pipe (OHP) is one of the promising heat pipe technologies. Compared with a traditional heat pipe, no wick structure inside the heat pipe, low cost, sensitive to low-temperature difference, and fast thermal response.

The operation of OHP does not need any power and there is no pump, so OHP considers as a passive device. The capillary effect plays an important role in the circulation fluid inside OHP between the evaporator and condenser section of OHP.

The principle of heat transporting by oscillating heat pipe depends on the pulsation phenomenon and the oscillation movement of working fluid in OHP. This phenomenon occurred because of the evaporation and condensation process (phase change) in the heat source (evaporator) and heat sink (condenser).

An OHP is a vacuum closed and a serpentine capillary tube (turns) and divided into the evaporator section (where the heat is added), condenser (where heat is rejected) section, and in-between adiabatic section. The OHP must have enough small inner diameter to let the liquid columns and vapor bubbles to coexist. The operation of an OHP begins when the evaporator section of OHP is subjected to heat, therefore, the evaporation process of working fluid starts, and the pressure of the vapor phase increases. So, the vapor bubble grew and pushed liquid plugs toward the condenser section (low-temperature region).

The condensation process at the condenser section induced a rise in the pressure variation between the evaporator section and the condenser section of OHP. Thus, the working fluid motion increased between hot and cold ends that lead to the heat transfer increased [24].

S. Rittidech et al. [25] used a prototype closed-end OHP made from copper with an inner diameter of 2 mm and 6 m total length of the tube. The eight turns OHP comprised only evaporator and condenser sections with a height of 190 mm for each one. They used 32 rows of OHP and used water and R123 as working fluid. The hot gas produced by a burner at a controlled velocity of 3.3 m/s with temperature

60, 70, 80°C. They noticed that the heat transfer rate and the thermal effectiveness increased by using R123 as a working fluid.

Oscillating heat pipe with check valve (OHP/CV) used in drier system [26]. CLOHP/CV with 20 turns made from copper filled partially by R134a with inner diameter 2 mm, evaporator, adiabatic, and condenser are 0.19 m, 0.08 m, and 0.19 m, respectively. The results showed that air humidity could be reduced from range (89–100) % to range (54–72) %.

An OHP was used to extend the tube surface of the heat exchanger instead of wire metal to overcome this limitation problem [27]. The copper OHP with 17 turns and 2.5 mm inner diameter is attached to both sides of the tubes. The working fluids were Acetone, R123, and Methanol by a 30% filling ratio. Furthermore, OHP with no working fluid was investigated to be a reference case that gives the same effect of wire metal features. The wind tunnel used to supply air at 25°C & rang (0.2–1.5) kg/s and the inlet temperature of water range (45 to 85) °C. The results revealed that the heat transfer and thermal performance of the OHPHX increased when the temperature of the inlet air increased. The using Methanol, R123, and acetone working fluids had higher thermal performance than the reference case by 10%.

Pracha et al. [28] used closed-loop OHP as the condenser for the vapor compression refrigeration system. The copper OHP was used with inner diameter 2.03 mm, the number of turn 250, and 80, 90, 100 mm as a length of the evaporator, condenser, and adiabatic sections respectively, and water as working fluid. The experimental work consists of two parts; the condenser unit and the OHP condenser part. For the same heat condition, the results showed that the OHP condenser system saved more electrical power, and the energy efficiency ratio (EER) increased by 18.9, 6.1, 13.4%, respectively. While for all cases, the coefficient of performance (COP) of the conventional condenser system is higher than the OHP condenser.

An OHP/CV is used as a heat recovery device in the drying chamber [29]. The cooper OHP/CV with inner diameter 2 mm, the length of the evaporator, adiabatic, and condenser section are 180, 200, and 180 mm, respectively. The working fluid was water by a 50% filling ratio. The result observed that the ratios of energy-saving were 56.66% and 28.13% for thermal and electrical energy, respectively.

Supirattanakul et al. [30] tested the different inlet air temperature at 50% relative humidity for the system with and without OHP/CV. The OHP/CV is made from copper with 56 turns, 2.03 mm inner diameter, and 220, 190, and 220 mm as a length of the evaporator, adiabatic, and condenser section, respectively, and the working fluid was R134a. The results revealed that energy is saved by 3.6% when OHP/CV was used in the system.

Pramod R and Ashish M [31] developed a closed-loop oscillating heat pipe by using a copper tube with a 2 mm inner diameter and bent to 10 turns. The lengths of the evaporator section, adiabatic section, and condenser section were 50 mm. The evaporator zone is heated by the oil path, while the condenser zone is cold by the water tank. Water, Acetone, Methanol, and Ethanol used as pure working fluids, and binary mixtures of (water/Acetone, water/Methanol, and Water/Ethanol) working fluids used by a filling ratio of 50%. The results of the study indicated that the thermal resistances smoothly decreased with rising heat input for both pure and binary (1:1 by volume) working fluid. The study also revealed that the temperature of working fluid (water/Methanol) at the evaporator section is low in high input heat, which gives a better performance of OHP than other binary working fluids.

The effects of putting fins in OHP were investigated [32]. They tested the finned and unfinned structure of OHP. The copper OHP was manufactured from a meandering tube by eight turns with a 2.5 mm inner diameter, and the lengths of the evaporator, adiabatic, and condenser sections were 50, 120, and 80 mm, respectively. They used copper wires by a 1 mm as fins, and the working fluids were

Methanol and Ethanol with a 50% filling ratio. The results revealed that Methanol had better thermal performance (lower thermal resistance) than Ethanol, and finned – inserted OHP presented lower thermal resistance than unfinned one.

The effect of using OHP/CV as a heat exchanger on energy-consuming in the split air unit was investigated [33]. They used HPHX to recover the wasted heat in an HVAC system. The authors made the ten turns OHP from copper tube with 1.65 mm inner diameter, and tested the OHP dry and with n-pentane by 70% filling ratio. At the evaporator section, the heat input was at a constant temperature of 45°C, while at the condenser section, the dissipation at 6°C with a constant volumetric ratio of 0.19 m<sup>3</sup>/s. The finding concluded that the OHP was able to regain wasted heat up to 240 W.

A. S. Barrak et al. [34] examined experimentally and theoretically the thermal performance of the oscillating heat pipe (OHP). The copper OHP had seven turns with 3.5 mm inner diameter, and 300 mm as the lengths of the condenser and evaporator, and 210 mm for adiabatic section. The water was working fluid of the OHP a filling ratio of 50%. The evaporator region is heated by hot air (35, 40, 45, and 50) °C with various face velocity (0.5, 1, and 1.5) m/s. The condenser section is cold by air at a temperature of 15°C. They developed a turbulent approach based on the k- $\epsilon$  model by using the volume of fluid (VOF) method to simulate heat and mass transfer inside OHP. The results revealed that the minimum thermal resistance was 0.2312°C/W at maximum heat input 107.75 W and maximum thermal resistance was 1.036°C/W at lower heat input 13.75 W. The simulation model showed a good agreement with experimental results with a maximum deviation of 15%.

Three working fluids (water, methanol, and binary solution) were used in OHPHX to improve the humidity removal of the cooling coil [35, 36]. They mixed water with methanol (binary fluid) by a ratio of 50:50 by volume and used it as working fluid in the OHP. The findings revealed that the dehumidification process was enhanced by 17% for water, 25% for methanol, and 21% for binary fluid. Authors notice 16% an enhancement in energy-saving ratio and an improvement in the thermal effectiveness of the OHPHX about 14% by using the binary fluid as a working fluid instead of water.

OHP was proposed as fins on the heat exchanger to enhance the heat transfer rate by increasing the surface area [37]. OHP was manufactured from copper with 3 mm inner diameter and R 134 s as a working fluid. The results showed 310 and 263% the enhancement by using OHP in the overall heat transfer coefficient for natural and forced convections.

The thermal effectiveness and thermal resistance of OHPHX were investigated [38]. The inner diameter of OHP was 5 mm and filled by HFE-7000 with a 35% and 50% filling ratio. The results presented that the behavior of OHP as a thermosiphon due to the inner diameter was not small enough to form the oscillating phenomena by vapor plugs and liquid slugs.

## **5. Conclusions**

Heat pipe heat exchanger is a new member of the heat recovery device in the HVAC system. The heat pipe has many advantages make it one of the promising device to enhance the value of energy saving in many engineering system and important research topics in the heat transfer area like simple structure, low cost, high heat transferability. The heat transfer performance of heat pipe is greatly influenced by many parameters, such as inner diameter, tilt angle, working fluids and filling ratio, and a turn's number for OHP, and many kinds of research have been done by investigating the heat transfer characteristics of the heat pipe.

Many experimental and theoretical investigations were conducted to study the heat and mass transfer in the heat pipe, and the thermal performance for the heat pipe and the system. The experimental part focused on the effect of certain parameters on the thermal performance and operation of the heat pipe heat exchanger, while the theoretical part focused on simulation and modeling the mechanism of mass and heat transfer operations.

From all those studies, the following conclusions are obtained:


1. The heat pipe heat exchanger as a heat recovery device has been successfully applied in conjunction with the HVAC system to enhance the energy-saving, cooling coil capacity, and dehumidification capability.
2. Despite the achievements gained from the theoretical studies, the mechanism of mass and heat transfer in the operation of OHP still has not been fully understood.
3. There are some questions and subjects that still need more investigations like; the chaotic behaviors in the OHP, the hydrodynamic and thermodynamic effects on the thermal performance, and the formation mechanism and transfer of heat and mass between the liquid plugs and vapor slugs. Finally, the Design techniques for the OHP heat exchange at present there is no reliable method.

## Author details

Anwar Barrak  
University of Technology, Baghdad, Iraq

\*Address all correspondence to: [anwar.barrak@yahoo.com](mailto:anwar.barrak@yahoo.com)

## IntechOpen

© 2021 The Author(s). Licensee IntechOpen. This chapter is distributed under the terms of the Creative Commons Attribution License (<http://creativecommons.org/licenses/by/3.0>), which permits unrestricted use, distribution, and reproduction in any medium, provided the original work is properly cited. 

## References

- [1] Hunt, V. D., 'Handbook of conservation and solar energy, trends and perspectives', Van Nostrand Reinhold Company, 1982.
- [2] Yau, Y. H., 'The use of a double heat pipe heat exchanger system for reducing energy consumption of treating ventilation air in an operating theatre – A full year energy consumption model simulation', *Energy and Buildings*, Vol. 40, pp. 917-925, 2008.
- [3] M. Ahmadzadehtalatapeh, and Y. H. Yau, 'Energy Conservation Potential of the Heat Pipe Heat Exchangers: Experimental Study and Predictions', *IJE TRANSACTIONS B: Applications* Vol. 25, No. 3, pp. 193-199, 2012.
- [4] K. S. Ong, 'Review of Heat Pipe Heat Exchangers for Enhanced Dehumidification and Cooling in Air Conditioning Systems', *International Journal of Low-Carbon Technologies*, 11, pp. 416-423, 2016.
- [5] ASHRAE Handbook HVAC Applications, SI Edition, 2011.
- [6] Amir Faghri, 'Review and Advances in Heat Pipe Science and Technology', *Journal of Heat Transfer*, Vol. 134, 2012.
- [7] Reay D, and Kew P. 'Heat pipes: theory, design and applications', fifth ed. Butterworth-Heinenmann, 2006.
- [8] Hassam Nasarullah Chaudhrya, Ben Richard Hughesa, and Saud Abdul Ghanib, 'A review of heat pipe systems for heat recovery and renewable energy applications', *Renewable and Sustainable Energy Reviews*, 16, pp.2249-2259, 2012.
- [9] Amir Faghri, 'Heat Pipes: Review, Opportunities and Challenges', *Frontiers in Heat Pipes (FHP)*, 5, 1, 2014.
- [10] A. Faghri, M.-M. Chen, and M. Morgan, 'Heat Transfer Characteristics in Two-Phase Closed Conventional and Concentric Annular Thermosyphons', *Journal of Heat Transfer*, Vol. 111/6, 11, 1989.
- [11] S. Thongdaeng, S. Rittidech and B. Bubphachot 'Internal flow patterns behavior of a top heat mode closed-loop oscillating heat pipe with check valves (THMCLOHP/CV)', *International Journal of the Physical Sciences* Vol. 7(29), pp. 5097-5105, 26 August, 2012.
- [12] W. Srimuang, and P. Amatachaya, 'A review of the applications of heat pipe heat exchangers for heat recovery', *Renewable and Sustainable Energy Reviews* 16, pp.4303-4315, 2012.
- [13] Khandekar S., Schneider M. and Groll M., 'Mathematical Modeling of Pulsating Heat Pipes: State of the Art and Future Challenges', *Heat and Mass Transfer Conf.*, pp. 856-862, Kolkata, India, 2002.
- [14] Hongbin Ma 'Oscillating Heat Pipes', Springer New York, Media New York 2015.
- [15] Yodrak L, Rittidech S, Poomsaad N. and Meena P., 2010, "Waste Heat Recovery by Heat Pipe Air-Preheater to Energy Thrift from the Furnace in a Hot Forging Process", *American Journal of Applied Sciences*, Vol.7, pp.675-681
- [16] Noie S. H., 2006, "Investigation of Thermal Performance of an Air-to-Air Thermosyphon Heat Exchanger Using e-NTU method, *Applied Thermal Engineering*, Vol.26, pp.559-567
- [17] Yau Y. H., 2007, "Application of a heat pipe heat exchanger to dehumidification enhancement in a HVAC system for tropical climates a baseline performance characteristics study", *International Journal of Thermal Sciences*, Vol.46 (2007), pp.164-1714.

- [18] El-Baky M. A. and Mohamed M. M., 2007, "Heat pipe heat exchanger for heat recovery in air conditioning", *Applied Thermal Engineering* Vol.27, pp.795-801
- [19] Alklaibi A. M., 2008, "Evaluating the possible configurations of incorporating the loop heat pipe into the air-conditioning systems" *international Journal of Refrigeration*, Vol. 31, pp.807-815.
- [20] Yau Y. H. and M. Ahmadzadehtalatapeh, 2010, *Experimental Investigation of the Thermal Performance of an Air-To-Air Horizontal Heat Pipe Heat Exchanger*, *International Journal of Mechanical and Materials Engineering (IJMME)*, Vol. 5 (2010), No. 1, pp.29-35.
- [21] Jouhara H. and Merchant H., 2012, "Experimental investigation of a thermosyphon based heat exchanger used in energy efficient air handling units", *Energy* Vol.39, pp. 82-89.
- [22] G. Righetti, C. Zilio, S. Mancin & G. A. Longo (2018) *Heat Pipe Finned Heat Exchanger for Heat Recovery: Experimental Results and Modeling*, *Heat Transfer Engineering*, 39:12, 1011-1023, DOI: 10.1080/01457632.2017.1358483
- [23] Ragil Sukarno, Nandy Putra, Imansyah Ibnu Hakim, Fadhil Fuad Rachman, Teuku Meurah Indra Mahlia, 'Multi-stage heat-pipe heat exchanger for improving energy efficiency of the HVAC system in a hospital operating room', *International Journal of Low-Carbon Technologies*, ctaa048, <https://doi.org/10.1093/ijlct/ctaa048>
- [24] Reay D, and Kew P. 'Heat pipes: theory, design and applications', fifth ed. Butterworth-Heinenmann, 2006
- [25] S. Rittidech, W. Dangeton, S. Soponronnarit, "Closed-ended oscillating heat-pipe (CEOHP) air-preheater for energy thrift in a dryer", *Applied Energy*, 81, 198-208, 2005.
- [26] P. Meena, S. Rittiched, N. Poomsaad, "Application of Closed Loop Oscillating Heat Pipe with Check Valve (CLOHP/CV) Air Preheater for Reduced Relative Humidity in Drying Systems), *Applied Energy*, vol. 84, issue 5, pages 553-564, 2007.
- [27] A Nuntaphan, S. Vithayasai, N. Vorayos, N. Vorayos, T. Kiatsiriroat, 'Use of oscillating heat pipe technique as extended surface in wire-on-tube heat exchanger for heat transfer enhancement', *International Communications in Heat and Mass Transfer* (37), 287-292, 2010.
- [28] Pracha Yeunyongkul, P. Sakulchangsattajai, and Afshin J. Ghajar "Experimental Investigation of Closed Loop Oscillating Heat Pipe as the Condenser for Vapor Compression Refrigeration", *International Refrigeration and Air Conditioning Conference at Purdue*, 2010.
- [29] S. Wannapakhe, T. Chaiwong, M. Dandee, S. Prompakdee " Hot Air Dryer with Closed – Loop Oscillating Heat Pipe with Check Valves for Reducing Energy in Drying Process" *Procedia Engineering* 32 (2012) 77-82, 2011.
- [30] P. Supirattanakul, S.Rittidech, B.Bubphachot, "Application of a closed-loop oscillating heat pipe with check valves (CLOHP/CV) on performance enhancement in air conditioning system." *Energy and Buildings journal*, G Model ENB-3133; No. of Pages5, 2011.
- [31] Pramod R. Pachgharea, Ashish M. Mahalle, "Thermal Performance of Closed Loop of Pulsating Heat Pipe Using Pure and Binary Working Fluids", *Frontiers in Heat Pipes (FHP)*, 3, 033002, 2012.

[32] M Lutfor Rahman, Sumaiya Nawrin, and Rasel A Sultan, Fariha Mir, and Mohammed Ali, 'Effect of fin and insert on the performance characteristics of close loop pulsating heat pipe CLPHP', *Procedia Engineering* 105, 129-136, 2015

[33] Govinda Mahajan, Heejin Cho, Scott M. Thompson, Harrison Rupp, Kevin Muse, "Oscillating heat pipes for waste heat recovery in HVAC systems", *Proceedings of the ASME*, 13-19, 2015.

[34] A. S. Barrak, A. A.M. Saleh and Z. H. Naji, "Experimental and Numerical Simulation for Thermal Investigation of Oscillating Heat Pipe Using VOF Model" *Engineering and Technology Journal*, Vol. 38, Part A, No. 1, pp. 88-104, 2020, <https://doi.org/10.30684/etj.v38i1A.286>

[35] A. S. Barrak, Ahmed. A. M. Saleh and Zainab. H. Naji, An experimental study of using water, methanol, and binary fluids in oscillating heat pipe heat exchanger, *Engineering Science and Technology, an International Journal*, <https://doi.org/10.1016/j.jestch.2019.05.010>

[36] A. S. Barrak, A. A. M. Saleh and Z. H. Naji, "Energy Saving of Air Conditioning System by Oscillating Heat Pipe Heat Recovery Using Binary Fluid," *2019 4th Scientific International Conference Najaf (SICN)*, Al-Najef, Iraq, (2020), pp. 178-183

[37] H. J. Mosleh, M. A. Bijarchi, M. B. Shafii, 'Experimental and numerical investigation of using pulsating heat pipes instead of fins in air-cooled heat exchangers', *Energy Conversion and Management* 181 (2019) 653-662.

[38] K. Yang, M. Jiang, C. Tseng, S. Wu, and J. Shyu, 'Experimental Investigation on the Thermal Performance of Pulsating Heat Pipe Heat Exchangers', *Energies*, 13, 269, 2020; doi:10.3390/en13010269



# EMbaffle® Heat Transfer Technology Step-Up in CO<sub>2</sub> Reduction

*Marco Rottoli, Daniele Agazzi, Marcello Garavaglia and Fabio Grisoni*

## Abstract

EMbaffle® is a proprietary shell and tube heat exchanger technology, designed to improve performance by pressure drops control, with suppressed tube vibrations. Developed to minimize fouling accumulation in crude oil units, the technology has proved to be effective in Gas treatment and Petrochemical, supporting the increase in gas-gas and cooling water flow rate per-unit demand, and in Renewable CSP, where Molten Salt units get a primary role in thermal storage and power efficiency. Diamond shape and baffle-grids number are the instruments for the design engineer to exploit exchanger efficiency against pressure drops, aimed to the desired performance with the optimized power consumption. Further to introduce the base of the technology, this work will also address the design of higher compact units by combining the grids performance with the improved exchanger tube surface. Experimental data to support the grid life under critical working conditions and actual performances with fluids density and viscosity are reported.

**Keywords:** shell&tube heat exchanger, increased thermo-hydraulic performance, reduced maintenance costs, improved plant reliability, energy efficiency & CO<sub>2</sub> reduction

## 1. Introduction

Shell & tube (S&T) heat exchangers are among the main process equipment involved in oil refineries, power industry and chemical plants. They are made of a pressure vessel in which is inserted a bundle of tubes. One fluid pass inside the tubes, while the other passes outside them. Tubes are generally supported by segmental baffles.

Although conventional segmental-baffles units prove well in the wide majority of the services, in several cases performances are not outstanding with negative impacts on maintenance costs and exchanger life, especially in case where large flow rates have to be processed, which can induce tube vibration issues.

If a dirty fluid is processed, fouling can be accumulated in the stagnation zones that are inherently created by segmental baffle geometry.

A possible remedy is the application of a longitudinal flow at the shell side. EMbaffle® technology promotes longitudinal flow at shell side, supporting the tubes with expanded metal grids.

The following paragraphs describes this technology, from general features to its inherent advantages, pressure drop and heat transfer characteristics.

Finally some technical advancements are reported, together with some design cases related to services where EMBaffle® technology proves its advantages over conventional segmental exchangers.

## **2. Longitudinal type heat exchanger technology**

Conventional S&T heat exchangers, widely used in Oil&Gas, Petrochemical, Chemical and Power Plants, are of the “segmental baffle” type, where the baffles support the tubes and govern the cross/longitudinal ratio of the shell flow direction through the bundle. The turbulent motion originated by the cross direction, normal to the exchanger tubes, determines the shell side heat transfer coefficients (HTC), that in many configurations controls the global value, and the consumed pressure drops. Decades of operational experience led to a widespread know-how in design and manufacture of safe, high performing and long-life segmental baffles heat exchangers, driving, at the same time, to claim for alternate design concepts in order to overcome the few critical limits of the technology.

Two matters in particular have been deeply addressed, depending on process flow rates and fluid nature (clean or dirty) [1, 2]:

- potential vibrations, induced by the cross component of high flow rates, may affect the exchanger tubes reliability;
- the flow recirculation, at the dead areas formed by the baffle outer diameter with the shell inner diameter, may induce, with dirty fluids, to progressive fouling accumulation, thus reducing the heat transfer surface and leading to potential tube local overheating and corrosion issues.

Further, the lowest design temperature approach, (typical for example of the very few degrees in Power generation pre-heaters), is limited because of the cross-flow component.

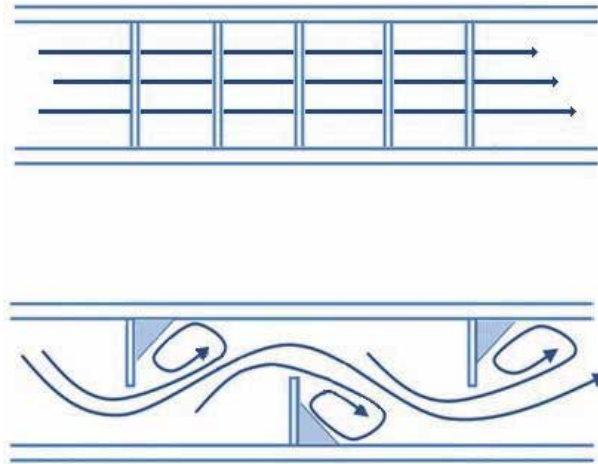
Helical and pure longitudinal flow design concepts have been exploited and exchangers have been developed to overcome some of the above criticalities.

In longitudinal flow solutions, design aims to reduced, up to the total suppression, the dead areas and the cross-flow component of a non-cross type Shell&Tube exchanger (**Figure 1**). The associated reduced drift and hydraulic resistance lead to significantly reduced pressure drops and the reduced span of tubes support elements grants a bundle compact assembly preventing potential vibration phenomena.

Among the longitudinal flow type heat exchangers, the Rod-Baffle is the pioneer. Conceived to suppress vibration issues by reducing the baffles span in shell side high flow rate and pure cross flow applications, in this technology, the tubes are supported by a repeated series of four regularly spaced-apart rod lines welded to a peripheral ring. The rod lines are disposed in alternate horizontal and vertical directions (one set of parallel rod lines at any single baffle), to form a square support, so that four baffles are required to fully confine the tube. The large free flow area left by the baffle determines a pure-like longitudinal flow in non-cross flow type HE.

It is the intent of this technology to govern a low value of pressure drops to suppress vibrations, accepting the resulting total Heat Transfer Coefficient as a consequent outcome.

Rod baffle basic concept was initially replicated by making use of strips in place of rods; only more recently solutions aimed to further reinforce the tubes



**Figure 1.**  
*Longitudinal vs. conventional S&T heat exchanger.*

confinement but taking care at the same time of the heat transfer performance have been developed.

### 3. EMbaffle® development

Aiming to grant all tubes confinement at any individual baffle, the EMbaffle® longitudinal flow type heat exchanger was then conceived and developed. Rods and strips are replaced by a patented Expanded Metal grid, (that's where EMbaffle name comes from). By making best use of the available shell side pressure drops, the unsupported tubes span can be easily managed to design the most stiff cage solution today available in the S&T heat exchangers market (**Figure 2**).

Initially thought to eliminate the dead areas in fouling applications, the grid geometries and baffles span impacts on fluid flow paths have been progressively explored, by both CFD analysis and experimental measurements, to establish design criteria aimed to maximize the shell side HTC making best use of the available pressure drops.

Two significant improvements in the longitudinal baffle technology are so achieved:

- Tubes full support at any baffle makes the technology ready to replace the Rod Baffle and “No Tube in the window” TEMA designs in most applications where



**Figure 2.**  
*EMbaffle® design – One baffle fully supporting each individual tube.*

vibration issues govern, with performance increasing under increased process flow rates within the same shell diameter constraints.

- Further, by making use of the reduced fouling accumulation and so the better use of the available pressure drops to improve global Heat Transfer Coefficient, the technology can replace in several processes different standard TEMA segmental baffle exchangers granting same/improved performances with reduced capex/opex costs.

Plant data and case studies will be proposed to offer a general view of EMbaffle design performance advantages when replacing traditional TEMA solutions.

#### 4. Principles of EMbaffle® technology

To overcome the lower performance in heat transfer, intrinsic of the longitudinal flow design when compared to cross flow, EMbaffle® technology makes use of the rhombus-like shape of the expanded metal baffle mesh to promote turbulence. The two tube pitches defined by the layout are named “long way of the diamond” (LWD) and “short way of the diamond” (SWD) (Figures 3 and 4).

Essentially, the baffle grids generate a local turbulence whose longitudinal extension and amplitude, other than by the fluid properties, are determined by the peculiar geometry of the grid mesh (Figure 5).

In Figures 6 and 7, the turbulence kinetic energy, as a measurement of the turbulence grade, is shown for different type of grid mesh shape with a specified grid span. The turbulence amplitude and extension are quite different for the different grids type.

Imposing a higher order of magnitude to the tube side heat transfer coefficient, the effect of the grids on the global heat transferred is studied by CFD analysis. As reported in Figure 8 the heat transfer coefficient development substantially replicates the local turbulence peak at the grid, but the decay slope is significantly lower granting the maintenance of a quite homogeneous value from grid to grid.

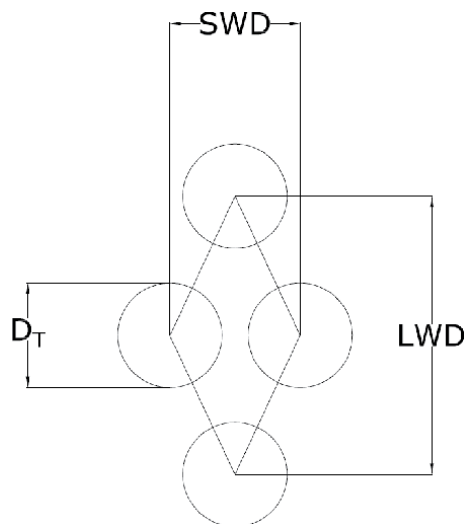
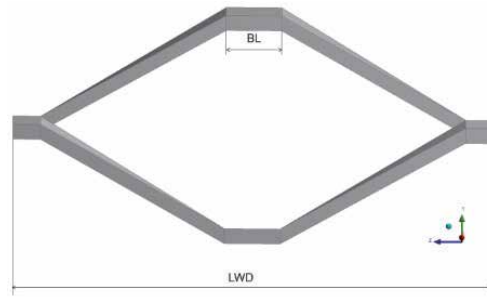
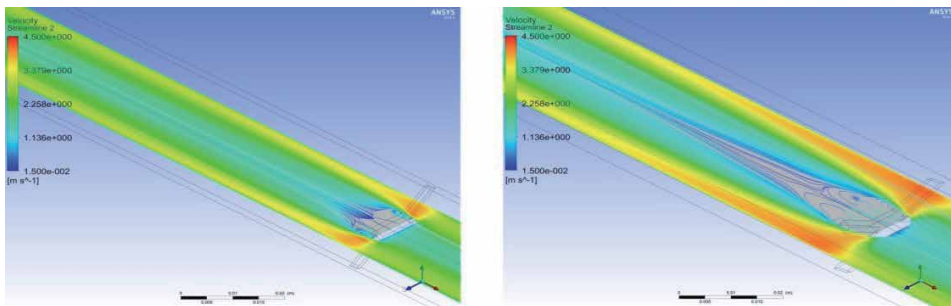


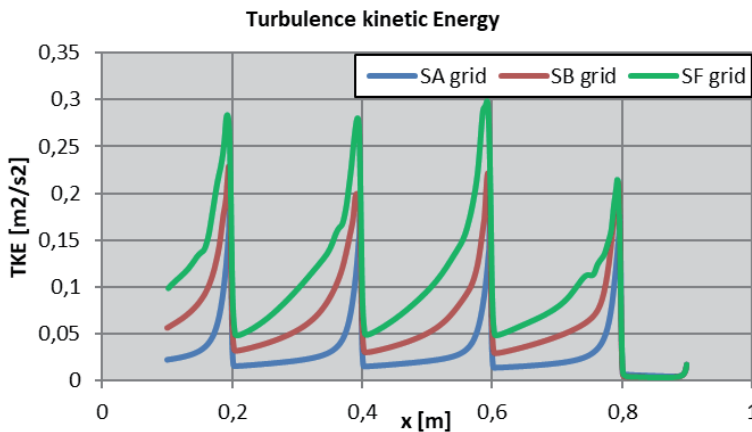
Figure 3.  
EMbaffle® –typical tube layout.



**Figure 4.**  
 EMbaffle® – Typical rhombus-like shape of grid mesh [3].



**Figure 5.**  
 EMbaffle® – Local flow velocity profile governed by the grid mesh shape induced turbulence.

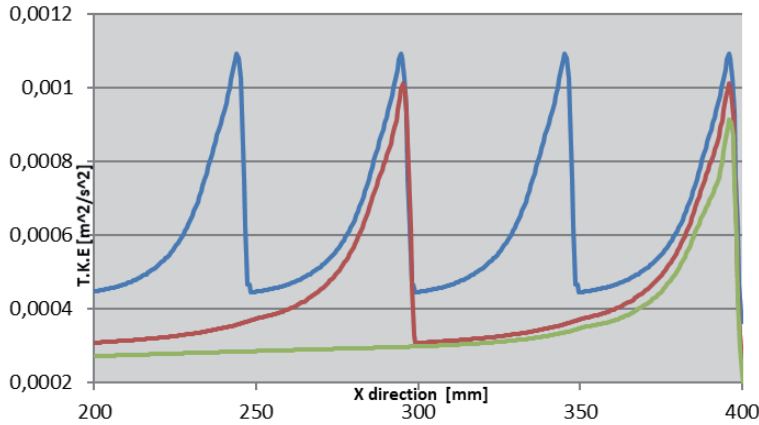


**Figure 6.**  
 CFD analysis of turbulent kinetic energy generated by different grid types, gas case [3].

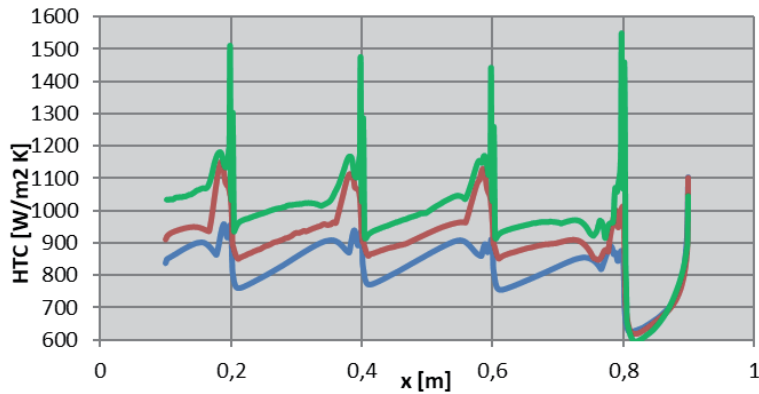
Grid mesh shape also allows for different tube count to be allocated within the same shell diameter, determining the total available heat exchange surface and the mean average flow velocity that governs the longitudinal contribution to the HTC.

Finally, increase or reduction in baffles span contributes, further to stronger or lighter tubes confinement, to the overall shell side HTC, with reversed impact on pressure drops.

The selection of grid type and grids span shall therefore be guided by the relevant boundary conditions as higher turbulence means higher pressure drops and overall HTC, while lower turbulence means lower pressure drops and lower total heat transferred.



**Figure 7.** CFD analysis of turbulent kinetic energy generated by different grid spans, liquid case [3].



**Figure 8.** From turbulence to heat transfer – Plot of HTC generated by different grid types [3].

## 5. Heat transfer in EMbaffle® technology

An important feature to design a S&T heat exchanger is the average temperature driving force  $\Delta T_m$  that can be calculated from the general global heat transfer equation:

$$Q = UA\Delta T_m \quad (1)$$

Where  $Q$  is the duty or heat transferred per unit time,  $U$  the overall heat transfer coefficient and  $A$  the heat transfer surface.

In general,  $\Delta T_m$  is determined by the approach temperatures, fluid properties and fluid arrangement. It can be calculated from the logarithmic mean temperature difference applying a correction factor:

$$\Delta T_m = \Delta T_{lm} F_t \quad (2)$$

$F_t$  is the correction factor and it depends on the S&T exchanger geometry (number of shell/tube passes and flow orientation), and distortion of the shell and tube fluid temperatures profile (thermal leakage through the longitudinal baffle, close approaches, temperature cross, bypass streams).

The correction factor  $F_t$  ranges from 0 to 1. Typically, values smaller than 0.8 indicate close temperature approaches and therefore an inadequate design for the given process conditions; the design may be easily improved by increasing the correction factor  $F_t$  switching to a counter-current type exchanger.

EMBaffle® allows to achieve a 100% counter-current configuration thanks to its pure longitudinal flow, maximizing the correction factor  $F_t$  to 1 and making the exchanger extremely performing where very tight temperature approaches are specified.

### 5.1 Heat transfer correlations

In EMBaffle® technology, the shell-side HTC is calculated using the following correlations for the Nusselt number in case of laminar and turbulent flow respectively:

$$Nu = C_L Re_h^{0.6} Pr^{0.4} \left( \frac{\mu_b}{\mu_w} \right)^{0.14} \quad (3)$$

$$Nu = C_T Re_h^{0.8} Pr^{0.4} \left( \frac{\mu_b}{\mu_w} \right)^{0.14} \quad (4)$$

The geometry coefficient functions,  $C_L$  and  $C_T$ , account for the enhancement due to the cross flow at the shell entrance and exit conditions. The Reynolds number is calculated as follows:

$$Re_h = \frac{\rho V_S D_h}{\mu_b} \quad (5)$$

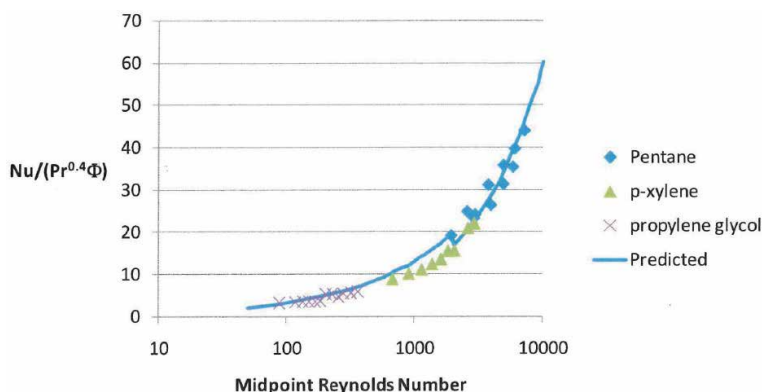
where  $V_S$  is the shell-side velocity and  $D_h$  is the characteristic diameter.

The shell-side velocity is calculated with the continuity equation, using the following expression for the shell-side flow area:

$$A_s = \frac{\pi}{4} (D_s^2 - N_T D_o^2) \quad (6)$$

The characteristic diameter is four times the nominal flow area divided by the wetted perimeter:

$$D_h = \frac{4 \left( \frac{1}{2} (LWD \times SWD) - \frac{\pi}{4} D_o^2 \right)}{\pi D_o} \quad (7)$$



**Figure 9.** Measured Nusselt number as a function of Reynolds number.

The above factors offer a large range of parameter options to provide the best solution in the light of the design constraints requested by the specific application.

Experimental tests had been conducted by different Institutions in order to validate the general heat transfer correlations and the coefficient  $C_L$  and  $C_T$  for different grid types. In **Figure 9** the measured Nusselt number  $A$  as a function of Reynolds Number is represented. The shift in prediction curve follows the change of Reynolds exponential dependence.

## 6. Pressure drops in EMbaffle® technology

Given the peculiar shape of the grids and the longitudinal flow patterns, EMbaffle® is characterized by reduced hydraulic resistance compared to conventional technologies. Due to this feature, in all cases where limited pressure drops are available EMbaffle® can still achieve low pressure drops for widely used TEMA types like E and F, while conventional segmental designs are forced to switch to “Low pressure drop” TEMA-types (G-, H-, J- or X). This results in a definitely more compact and thermo-hydraulically optimized design.

In EMbaffle® technology, shell-side pressure drop is the sum of the longitudinal flow component and the baffle flow component:

$$\Delta P = \Delta P_L + \Delta P_B \quad (8)$$

The expression for the longitudinal component is:

$$\Delta P_L = \frac{2\rho f_F L_T V_S^2}{D_p} \quad (9)$$

where  $D_p$  is the characteristic diameter,  $f_F$  the Fanning friction factor and  $L_T$  the length of the tubes. The characteristic diameter is calculated as follows:

$$D_p = \frac{4 \left[ \frac{\pi}{4} (D_s^2 - N_T D_o^2) \right]}{\pi D_o} \quad (10)$$

The friction factor is calculated with the following expression:

$$f_F = \begin{cases} \frac{16}{Re_p}, Re_p < 1189 \\ \frac{0.079}{Re_p^{0.25}}, Re_p \geq 1189 \end{cases} \quad (11)$$

The baffle pressure drop is calculated using the baffle velocity  $V_B$  and a baffle loss coefficient  $K_B$ :

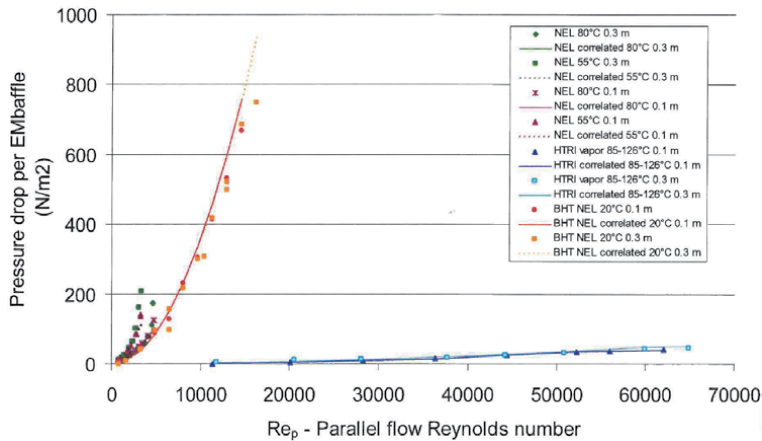
$$\Delta P_B = K_B N_B \frac{\rho V_B^2}{2} \quad (12)$$

$N_B$  is the number of the baffles. The baffle velocity is determined using the continuity equation with the following definition of the baffle flow area:

$$A_B = A_S - A_R - A_{EM} \quad (13)$$

$A_R$  is the ring area, while  $A_{EM}$  is the projected area of the EMbaffle grid.





**Figure 10.**  
 Measured pressure drops as a function of Reynolds number.

$K_B$  is the correlation factor accounting for the effect of entrance and exit cross flow, depending on the ratio  $A_B/A_S$  and the shell length and diameter ratio.

Experimental measurements have been conducted by different Institutions and heat exchangers Manufacturers to validate the above correlations.

The global measured pressure drops are strongly influenced by the entrance and exit cross flow, especially with short experimental heat exchangers, requiring the cross check of different experimental data.

In general, the correlations do not fit properly for very high viscous fluids and for extremely high Reynolds number, while fits with proper margin for low viscosity liquid and gases in Reynolds ordinary range of design (**Figure 10**).

In a straight comparison between a conventional S&T heat exchanger and the equivalent EMbaffle® heat exchanger under the same duty, EMbaffle® design often results in significant shell-side lower pressure drops, allowing in several experienced cases to sensibly increase the flow rate without asking for increased pump or compressor consumption.

## 7. Vibrations in EMbaffle® technology

Flow-induced vibrations are determined by the interaction of a cross flow with a physical body; this produces the shedding of alternating vortices, that transfers mechanical energy to the body. If one of the natural frequencies of the body is matched, such a configuration starts to vibrate. Vibration can be mechanical vibration of the tubes or acoustic resonance of the exchanger shell.

In all gas services and high flow-rate cooling services, prevent vibration is a relevant issue for equipment design. While demand of higher and higher flow-rates to be processed is growing, No-Tubes-In-Window (NTIW) design (i.e. the cut portion of the baffles do not accommodate exchanger tubes) with intermediate supports is often the conventional design solution adopted. The same solution approach can also be adopted when low pressure drops are available at the shell side.

However, removing tubes from the windows ends up in a larger shell diameter with impact on the capital cost; furthermore, NTIW heat exchangers are usually prone to acoustic vibrations, frequently imposing the adoption of a not desired

detuning longitudinal plate to suppress the phenomenon (this is typical for shell side Gas service heat exchangers).

Thanks to the strong bundle consistency and the full confinement of all tubes at any grid, EMbaffle® makes use of the full tube layout ensuring the filling of the complete shell section with consequent reduction of the equipment diameter and/or improved heat exchanger performance, while suppressing the risk of acoustic vibrations due to his longitudinal flow design (**Figure 11**).

The unsupported tubes span of the conventional TEMA heat exchanger is governed by the balance between longitudinal and cross flows, limiting the minimum value that can be reached.

The natural frequency of the tubes depends on the tube diameter and thickness, tube material and unsupported tube span, according to the following formula [4]:

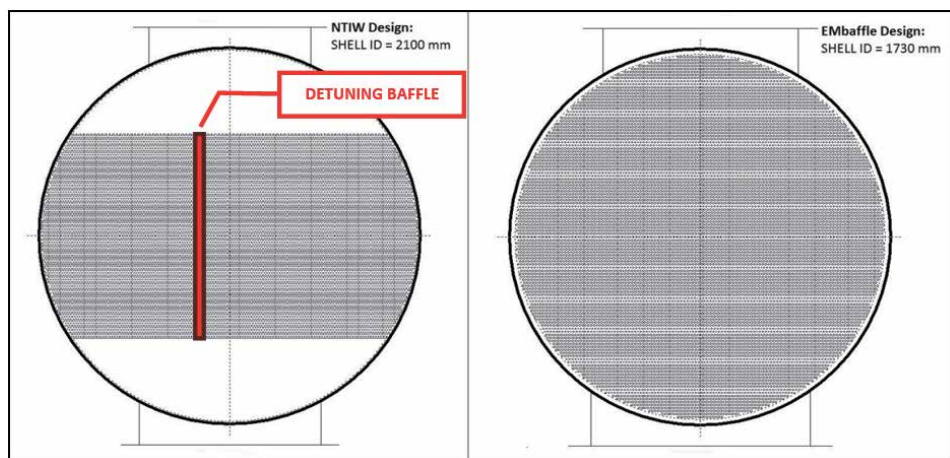
$$f_N = 0.04944C \left[ \frac{EIg_c}{W_e L^4} \right]^{0.5} \quad (14)$$

In an EMbaffle® exchanger, each tube is fully supported at every grid with a typical span ranging between 200 and 300 mm. This very close tube span significantly increases the natural frequency of the tubes, suppressing the risk of a frequency match and consequent vibration.

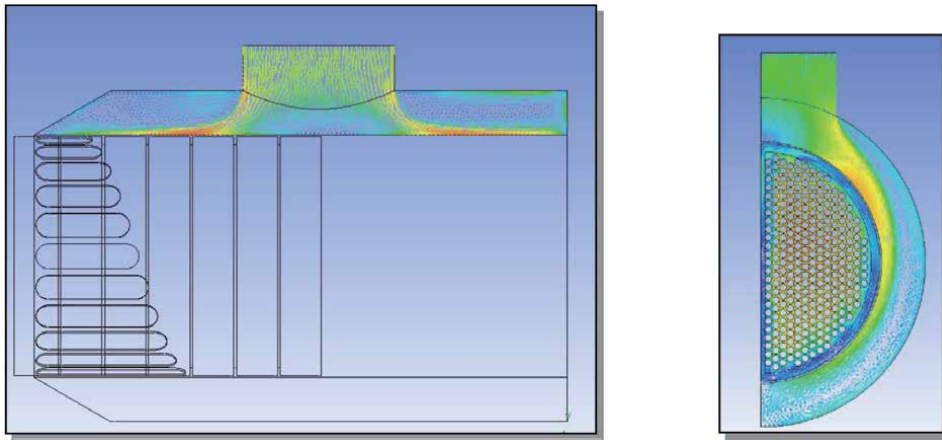
EMbaffle® is prone to good performances in condensing and boiling services too, e.g. cross-flow condensers, kettle-type reboilers, etc. where heat transfer coefficient is not substantially depending by the flow rate. Allowing the unrestricted shell-side flow thanks to the open structure, potential vibrations phenomena induced by phase transition are prevented, again allowing for a possible increase of shell side flow rate within the same exchanger constrains.

Concerns may apply to the shell-side fluid entrance region: here the flow suddenly changes from radial to longitudinal direction (vice versa at fluid exit), potentially stressing the tubes, specifically at bundle periphery as no annular space is left. Reducing the grids span in correspondence of the inlet/outlet nozzles, stronger tubes confinement can be configured as required to guarantee no vibrations.

The use of an annular chamber to distribute the flow entrance in homogeneous way through the full bundle circumference, further to provide an impingement protection to the directly exposed tubes, ensures at the same time the development of the longitudinal flow through the complete shell section since the first baffle pass.



**Figure 11.** EMbaffle® exploiting of the full shell area in comparison to NTIW in gas applications.



**Figure 12.**  
*Flow velocity distribution at EMbaffle® annular distributor – Top to bottom increased slot size case [5].*

Dedicated CFD analysis has been performed to study different annular distributor configurations aimed to optimize the fluid-dynamics through the distributor and reduce the relevant correlated pressure drops (**Figure 12**).

Several geometries were modeled in order to analyze the flow distribution and the performances of each case. The flow velocity distribution at the inlet nozzle is showing a large area of the annular distributor to be interested by flow recirculation, addressing the flow to concentrate on lateral and bottom sides, trend accentuated by clearance reduction.

Decreased Top to Bottom exchanger slots size, contrary to what it could be expected, seems to address to a better uniform flow speed trend, but the dispersion of the flow rates at the entrance cannot be avoided. The average pressure drops are not significantly impacted by the shape of the cut and this supports the simplest and cheapest construction solution of the annular inner shell.

Thanks to all above provisions, no relative motion between tube and grid is permitted and, therefore, no wearing nor fretting is observed and reported after years of continuous operations in potential vibration services.

## 8. Fouling in EMbaffle®

EMbaffle technology was originally conceived to enhance the shell side heat transfer by reducing fouling in heat exchange specific applications in refineries and petrochemical plants. By creating a uniform flow in the bundle, dead zones are omitted. By supporting the tubes using expanded metal grid the boundary layer is continuously interrupted thanks to the local increased velocity. By this approach the balance between fouling disposition and removal results at a lower fouling layer than in conventional heat exchangers.

EMbaffle® technology has then been applied to a variety of processes, where complexity of fouling mechanisms does not allow a predictable behavior. Further to the preliminary experimental results coming from authoritative Bodies, the actual performances in fouling reduction are finding systematic confirmation by the outcomes from a number of units installed and operating for several years.

Detailed monitoring of fouling development and study of growing rate had been originally concentrated on crude oil application, where fouling is strongly impacting the thermal and hydraulic performances of the exchangers. The overall heat transfer coefficient over time of a segmental baffle type heat exchanger and the same

exchanger with EMbaffle replacement bundle, have been monitored, adjusting shell side velocity and pressure drops in order to reproduce close process parameters for the two measurement campaigns.

Figures 13 and 14 report the plotted measurements and the related fitted distributions showing, over the constantly higher value, the quicker decay of the OHTC as a clear indication of the higher fouling grow rate of the segmental baffle exchanger.

From the measurements, the overall fouling factors can be extrapolated by using the following model:

$$U(t) = U_{\infty} + (U_0 - U_{\infty})e^{-\left[\frac{t-t_0}{t_f}\right]} \quad (15)$$

The fouling rate is derived from:

$$R(t) = \frac{1}{U(t)} - \frac{1}{h_i} \frac{D_o}{D_i} - \frac{D_o}{2\lambda} \ln\left(\frac{D_o}{D_i}\right) - \frac{1}{h_o} \quad (16)$$

The large variation in the early phase of both the segmental as of the EMbaffle run is reflected in the first part of the fouling plot. On the longer run the fouling of the EMbaffle is increasing relatively slow (Figure 15).

In order to assign the right value to exchanger performances, the method of optimum clean out time is used, where the optimum run time of the heat exchanger is based on cost evaluation, i.e. cost of decreased performance versus the cost of a clean-out (Figure 16).

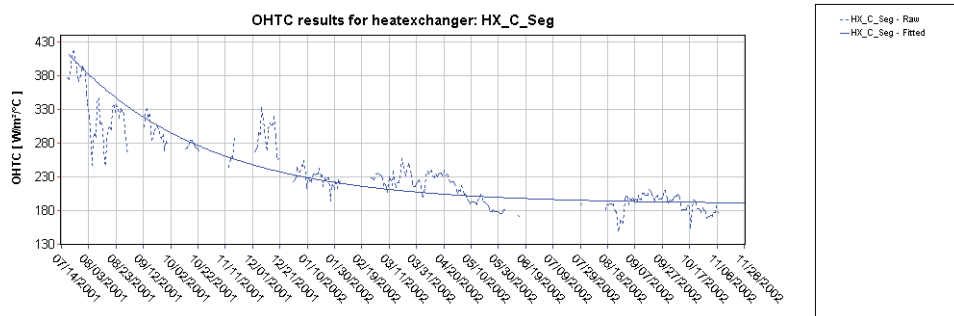


Figure 13. OHTC plot for the segmental baffle heat exchanger bundle [6].

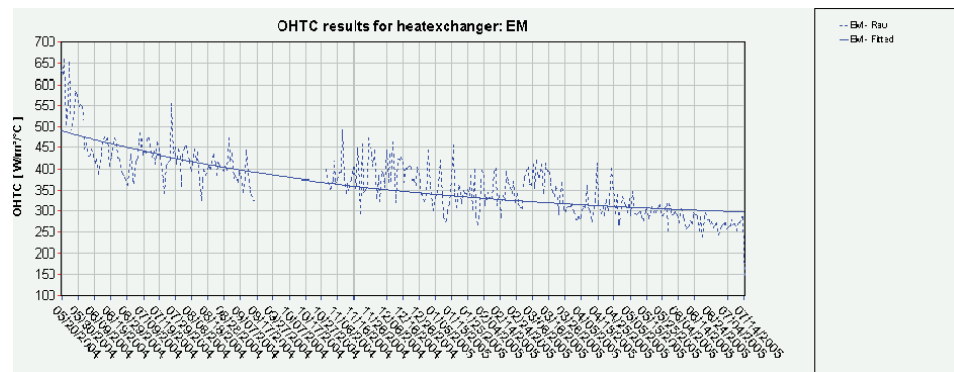
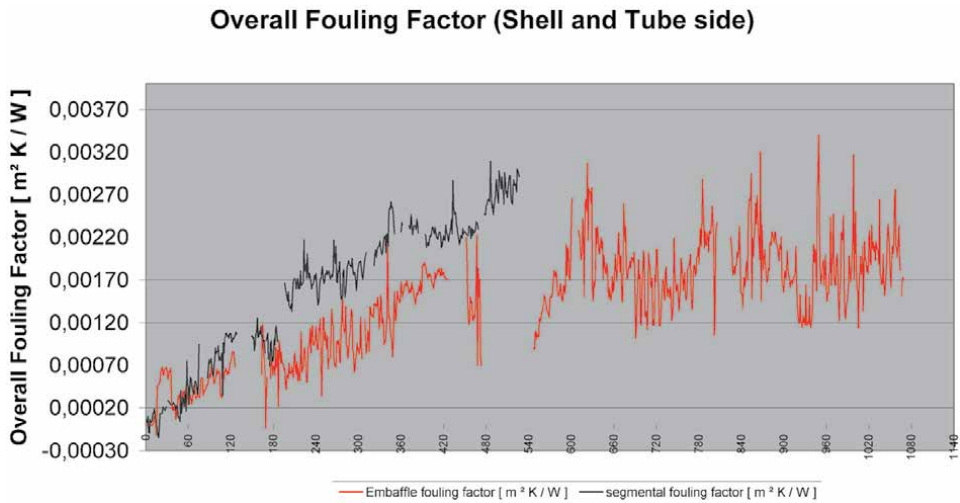


Figure 14. OHTC plot for the EMbaffle® heat exchanger bundle [6].



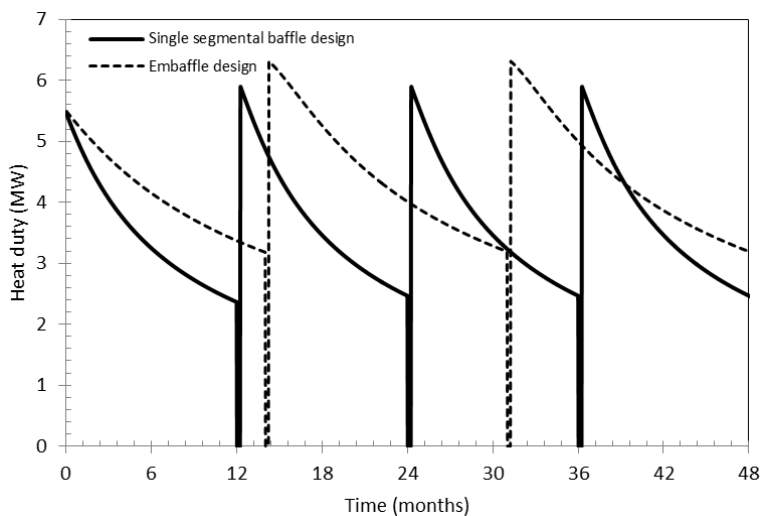
**Figure 15.**  
 Overall fouling factors plot for the EMbaffle® and segmental baffle heat exchanger bundles [6].

The following equation is used to calculate the maximum economic benefit connected with the ratio between the run time and number of cleaning steps

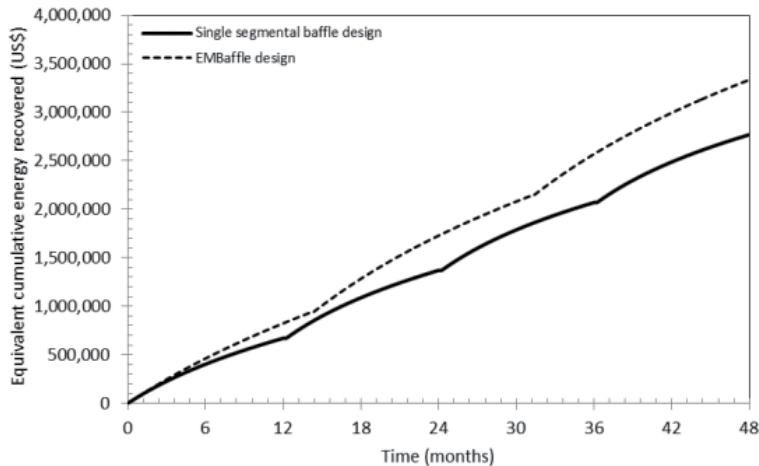
$$obj = C_E \int_0^{t_F} Q_E dt - N_c C_{cl} \quad (17)$$

Integral is calculated for the selected operating time.

In **Figure 17**, the economic benefit for a real case evaluated by comparing EMbaffle® performance with a parallel conventional unit on a base of 48 months operation is represented. Similar figures are of help in developing the best shut-down time at the light of the global plant configuration and performance.



**Figure 16.**  
 Comparison of overall heat duty performance of the EMbaffle® (dashed line) and the segmental baffle (solid line) heat exchanger bundles [7].



**Figure 17.** Comparison of energy recovered (US\$) using EMbaffle® vs. segmental S&T in a crude preheating unit [7].

## 9. Advancement in EMbaffle® design

Finned tubes are widely used when equipment size and weight reduction play an important role. EMbaffle® developed a dedicated low fin “enhanced tube” helical profile (profile and finning process under patenting), conceived to fit longitudinal flow design aimed to increase the heat transfer based on two mechanisms: increase of active external tube surface and promotion of turbulence.

Two interesting cases of fin application have been addressed and will be presented in following paragraphs: gas cooling and oil to molten salts heat transfer in CSP applications.

### 9.1 Gas cooling

Several experimental measurements have been taken to check the EMbaffle® correlations precision in predicting the global heat transfer coefficient for gas cooling with plain tubes.

Water flow rate at the tube side has been sized to grant a ten times higher tube side coefficient with respect to the predictable shell side coefficient, so that changes in exchanger performance can be attributed to shell side heat transfer only.

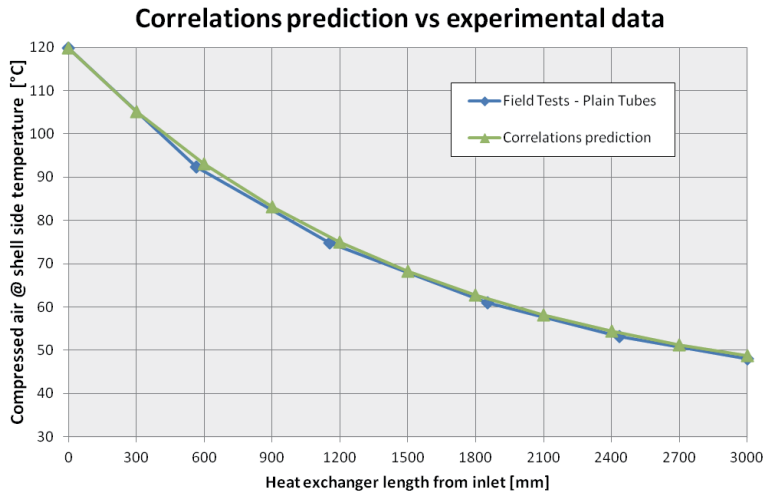
In **Figure 18**, the correspondence between the correlations predictions and the experimental measures is reported: the theoretical curve fits perfectly with the measured temperature values, with predicted outlet temperatures differing less than 1%.

In **Figure 19**, experimental data to compare finned against plain tubes heat transfer performances are reported. In test case, the outlet air temperature reduces from 51 °C of the plain tubes case to 43 °C for the finned case, showing a significant improvement in heat transfer and global duty.

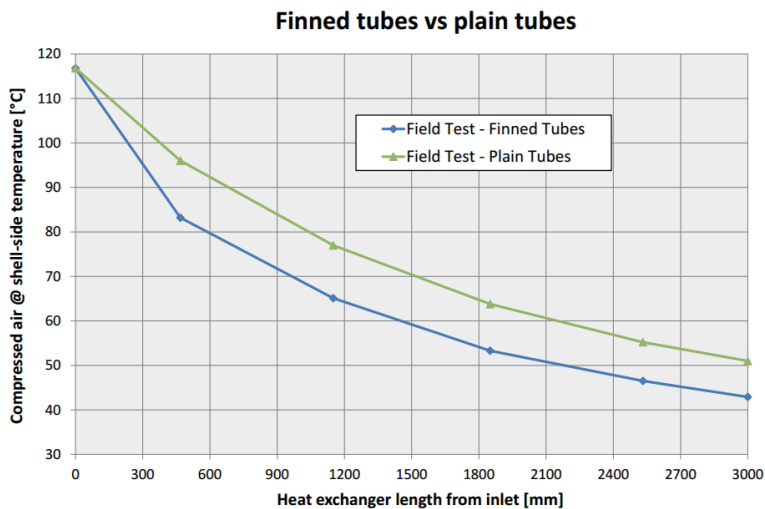
In the finned tubes test case, the air outlet temperature recorded for the plain tubes case has been reached at approx. 70% of the total tube length, showing a potential 30% tube length reduction.

These data allow to perform a design of the exchanger making use of the finned tube standard correlations to predict the temperature distribution profile and validate the global heat transferred.





**Figure 18.** Experimental data for gas cooling application: Comparison between experimental data versus correlations prediction for plain tubes.



**Figure 19.** Experimental data for gas cooling application: Comparison between EMbaffle® proprietary low fin tubes design vs. plain tubes.

Achieving a further significant reduction in the overall required tubes number and therefore of the equipment dimensions, the EMbaffle® finned tubes exchanger design is expected to prove successfully especially in offshore applications where compactness and lightness are of the essence.

More in general, the technology has a relevant impact on equipment costs containment for almost gas-gas and gas cooling processes and further tests shall be conducted to grant the continuous improvement of the performances in all gas applications.

Where tube-side can be the limiting factor, the use of enhanced features (inserts, inner surface micro-fins, etc.), to be applied in combination with shell side EMbaffle® grids, further to enhance the heat transfer, may also contribute to mitigate the fouling deposition on tubes side. The benefit of this combined

approach is therefore not only the increased heat recovery but also prolonged exchanger operating time through the reduction of fouling progress on both shell and tube sides.

For applications such as LNG vaporization, the combination between EMbaffle® and tube inserts is expected to be quite effective. On shell side, the EMbaffle® open structure will prevent the formation of dead zones guaranteeing, with the selection of proper grids span, the required tubes support, while inserts can mitigate the vaporizing issues at tubes inner surface by increasing the radial mixing.

## **9.2 Oil to molten salts in CSP**

A test campaign was carried out on the molten salt/thermal oil case to compare the performance between the use of bare tubes with finned tubes.

A heat exchanger based on EMbaffle technology with finned tubes was installed at the Concentrating Solar Platform centre in Almeria (Spain), the largest development and test center in Europe for molten salt application in CSP.

A test campaign was carried out using molten salt and thermal oil as media. A comparison has been made between the field test and an equivalent plain tube case calculated with the correlations.

Results shows an average 8% reduction in the overall heat transfer resistance. The consequent increase in performances is significant, even if not so high in absolute value: application of low fin tubes for this process shall be carefully evaluated.

## **9.3 Mechanical performance test**

The use of baffles made with “metal grid” instead of the more common “metal plate” suggests the need to verify their mechanical strength characteristics, especially in cases finned tubes are used and in the presence of processes with repeated thermal transients.

The different temperature distribution between the bundle support cage and the tubes during thermal transient brings to sliding of the tube inside the grid mesh, which could result mechanically harmful especially in the case of finned tubes.

In addition to the FEA for checking the static and dynamic stresses due to the accelerations induced on the tubes and on the grid, an experimental test was carried out to verify the consequences onto the grid subjected to the periodic longitudinal displacement of finned tubes in the most stringent conditions.

Two vertical baffles were positioned inside a horizontal cylindrical chamber and a finned tube was passed through them; weight and dimensions of tube were representative of the real exchanger conditions. A servomotor and a screw-nut type transmission were used to move the tube by operating a mechanical arm designed to transfer only a horizontal movement, minimizing any vertical thrust. The cylindrical chamber was filled with molten salts kept liquid with a system of heating resistances to maintain a temperature constantly above 380 °C.

Horizontal oscillatory movements (5 mm) equivalent to a 10-years working period of a exchanger with two daily transients were simulated to evaluate the effects of the relative wearing between the exchanger tube fin diameter and contact support points of the baffle grid diamond.

At the end of the test period the measurements of the outer diameter of the finned surface did show variation in height of the fins within 5% while no evidence of surface defect was registered on the contact profile of the grid mesh. Such a result is of extreme importance.



Other than confirming the good corrosion resistance of grid material in critical ambient conditions registered with standard corrosion tests formerly performed, it gives solid confirmation to the mechanical strength of the grid excluding at the same time any potential erosion defect on exchanger tubes surface in all EMbaffle technology application. This is of course further supported by the several years of service of the EMbaffle exchangers in different process services without reporting grids and/or tubes defect.

## 10. EMbaffle® design cases

Few design cases are presented in this paragraph as examples of how the application of EMbaffle® technology brings evident benefits.

### 10.1 DesignCase-1: overhead gas cooler

Two identical units (each one with two exchangers in parallel) have been installed in a platform. Using Sea water, the Overhead Gas Coolers were designed to cool high pressure acid natural gas from 110 °C down to 33 °C.

For this process the temperature approach between the fluids dictated a pure countercurrent arrangement, and the high water flow rate on the shell side did not allow the use of an F-shell TEMA type. Consequently a conventional segmental design in this case would have resulted in a much bigger and not-optimized geometry. A single pass for both tube and shell side exchanger would have been applied, with straight tubes and two tube sheets per exchanger.

The very limited shell-side available pressure drop in combination with the ability to accommodate large flow rates made this application very suitable for EMbaffle®, making possible the use of a F-shell TEMA type (**Figure 20**). The result was an optimized design, able to achieve a pure counter current arrangement with the application of U-tubes, which granted a single tube sheet per exchanger, reducing the weight. During the design stage a higher OHTC has been also exploited, with a consequent reduction in required heat transfer surface. Given the off-shore application, the reduction in size and weight obtained for the exchangers was particularly beneficial.



**Figure 20.**  
*EMbaffle® overhead gas cooler.*

Overhead Gas Cooler	Conventional design	EMbaffle® design	Units
<i>TEMA type</i>	BEM [8]	BFU [8]	—
<i>Number of equipments</i>	2 in parallel	2 in parallel	—
<i>Shell ID</i>	1780	1610	mm
<i>Tube length</i>	10000	7315	mm
<i>Baffle arrangement</i>	NTIW	EMbaffle	—
<i>Installed area</i>	3530	2609	m <sup>2</sup>
<i>SS pressure drop</i>	0.3	0.3	bar
<i>Duty</i>	50800	50800	kW
<i>Duty / Installed area</i>	14.4	19.5	kW/m <sup>2</sup>
<i>Weight</i>	118.2	73.3	tons

**Table 1.**

*Design comparison between EMbaffle® and conventional S&T for an overhead gas cooler.*

**Table 1** reports a comparison between a conventional S&T exchanger and the EMbaffle® type exchanger for this case.

The improvement described above are clearly depicted: EMbaffle® design is able to exploit the same duty of the conventional case with a 25% reduction of the installed surface area, providing the same shell-side pressure drop.

## 10.2 DesignCase-2: cycle gas cooler

**Figure 21** depicts a Cycle Gas Cooler, installed in a large chemical plant in North America. The function of the exchanger is to use Cycle water to cool the hot gas (placed at the tube side) from 100 °C to 40 °C.

Water flow rate was huge (more than 4000 tons per hour) and simply could not be accommodated in a single conventional baffle equipped heat exchanger. Two conventional units operating in parallel would have been necessary in order to guarantee a vibration-free design.

From the pressure drops point of view also, the single conventional unit would not have been an option resulting in pressure drops far above the allowable ones. In **Table 2** the straight comparison between the two designs is reported.



**Figure 21.**

*EMbaffle® cycle gas cooler.*

Cycle Gas Cooler	Conventional design	EMbaffle® design	Units
TEMA type	BEM [8]	BEM [8]	—
Number of equipments	2 in parallel	1	—
Shell ID	1740	1800	mm
Tube length	9760	11200	mm
Baffle arrangement	NTIW	EMbaffle	—
Installed area	3173	2335	m <sup>2</sup>
SS pressure drop	0.7	0.7	bar
Duty	69400	69400	kW
Duty / Installed area	21.9	29.7	kW/m <sup>2</sup>
Weight	126.6	79.2	tons

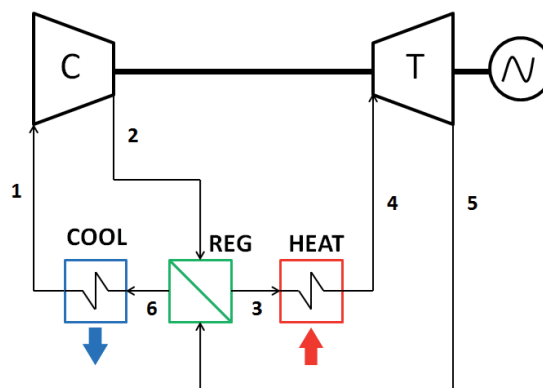
**Table 2.**  
 Design comparison between EMbaffle® and a conventional S&T for a cycle gas cooler.

### 10.3 CO<sub>2</sub>-based power generation plants

Challenge to avoid/reduce emission of carbon dioxide in power generation industry has been addressed in many ways, being its use as working fluid in power production plants one of the most promising.

**Figure 22** illustrates the supercritical Brayton-cycle and the relevant heat transfer units. High pressures involved and typically large gas flow rates may suggest adoption of S&T heat exchanger, being EMbaffle® one of the promising layout in consideration of the benefits envisaged in Gas Treatment and Purification chapter. Technology usually proves either as Gas Regenerator (path 2–3, 5–6), even in consideration of typical low temperature approach and pure countercurrent layout, and Gas Cooler (path 6–1); whereas large compression factors have to be achieved multistage Gas Intercoolers (not represented in the figure, along the path 1–2) are adopted. Depending on the application, Gas Heater design may rely on S&T layout or onto other piece of equipment (WHRU as example) depending onto the heat source medium.

**Table 3** reports a comparison between technologies for Gas Regenerator.



**Figure 22.**  
 Basic regenerative Brayton cycle for CO<sub>2</sub>-based power production plant.

CO <sub>2</sub> Regenerator	Conventional design	EMbaffle® design	Units
TEMA type	BEM [8]	BEM [8]	—
Number of equipments	1	1	—
Shell ID	2040	1600	mm
Tube length	23500	23500	mm
Baffle arrangement	NTIW	EMbaffle®	—
Installed area	5279	4324	m <sup>2</sup>
SS pressure drop	1.5	1.5	bar
Duty	48190	48190	kW
Duty / Installed area	9,1	11,1	kW/m <sup>2</sup>
Weight	207,1	124,4	tons

**Table 3.**

Design comparison between EMbaffle® and a conventional S&T for a CO<sub>2</sub> regenerator.

## Nomenclature

Symbol	Description	Units
$A$	Heat transfer area	[m <sup>2</sup> ]
$A_B$	Baffle flow area	[m <sup>2</sup> ]
$A_{EM}$	EMbaffle grid projected area	[m <sup>2</sup> ]
$A_R$	Ring area	[m <sup>2</sup> ]
$A_s$	Shell flow area	[m <sup>2</sup> ]
$C$	Tube span constant	[-]
$C_{cl}$	Cost of cleaning	[US\$/unit]
$C_E$	Cost of energy	[US\$/J]
$C_L$	Laminar heat transfer geometry function	[-]
$C_T$	Turbulent heat transfer geometry function	[-]
$D_h$	Characteristic diameter for Nu and Re <sub>h</sub>	[m]
$D_i$	Tube internal diameter	[m]
$D_P$	Characteristic diameter for Re <sub>P</sub>	[m]
$D_S$	Shell inner diameter	[m]
$D_o$	Tube outer diameter	[m]
$E$	Modulus of elasticity of tube material	[Pa]
$f_F$	Fanning friction factor	[-]
$F_t$	Correction factor depending on exchanger arrangement and approaches temperatures	[-]
$f_N$	Natural frequency	[Hz]
$g_c$	Conversion constant	[-]
$h$	Film transfer coefficient	[W/m <sup>2</sup> K]
$h_i$	Inner heat transfer coefficient	[W/m <sup>2</sup> K]
$h_o$	Outer heat transfer coefficient	[W/m <sup>2</sup> K]
$I$	Moment of inertia of tube	[m <sup>4</sup> ]
$K_b$	Hydraulic loss coefficient of baffle	[-]
$L$	Unsupported tube span	[m]
$LWD$	Long way of diamond	[m]
$N_B$	Number of baffles	[-]
$N_C$	Number of cleaning events	[-]
$N_T$	Number of tubes	[-]

$Nu$	Nusselt number	[-]
$obj$	Objective function value	[US\$]
$Pr$	Prandtl number	[-]
$Q$	Heat transferred	[W]
$Q_E$	Total accumulate heat exchanged	[MW]
$R(t)$	Actual fouling resistance at a specified time	[m <sup>2</sup> K/W]
$Re_h$	Heat transfer Reynolds number	[-]
$Re_p$	Longitudinal flow Reynolds number	[-]
$SWD$	Short way of diamond	[m]
$t$	Time	[s]
$t_0$	Time the heat exchanger has just been cleaned out or installed	[s]
$t_f$	Operating campaign time	[s]
$V_B$	Baffle velocity calculated from $A_b$	[m/s]
$V_s$	Shell-side velocity calculated from $A_s$	[m/s]
$U$	Overall heat transfer coefficient	[W/m <sup>2</sup> K]
$U_\infty$	Overall heat transfer coefficient at equilibrium	[W/m <sup>2</sup> K]
$U_0$	Overall heat transfer coefficient, initial	[W/m <sup>2</sup> K]
$W_e$	Effective mass per unit length	[kg/m]
$\Delta T_{lm}$	Logarithmic mean temperature difference	[K]
$\Delta T_m$	Average temperature driving force	[K]
$\Delta P$	Pressure Drop	[Pa]
$\Delta P_B$	Baffle flow pressure drop	[Pa]
$\Delta P_L$	Longitudinal flow pressure drop	[Pa]
$\lambda$	Wall thermal conductivity	[W/m K]
$\mu_b$	Bulk viscosity	[Pas]
$\mu_w$	Wall viscosity	[Pas]
$\rho$	Mass density	[kg/m <sup>3</sup> ]

## Author details

Marco Rottoli\*, Daniele Agazzi, Marcello Garavaglia and Fabio Grisoni  
 EMbaffle® Technology @ Brembana&Rolle SpA, Valbrembo, Italy

\*Address all correspondence to: [mrottoli@brembanarolle.com](mailto:mrottoli@brembanarolle.com)

## IntechOpen

© 2021 The Author(s). Licensee IntechOpen. This chapter is distributed under the terms of the Creative Commons Attribution License (<http://creativecommons.org/licenses/by/3.0>), which permits unrestricted use, distribution, and reproduction in any medium, provided the original work is properly cited. 

## **References**

- [1] K. Thulukkanam (2013) Heat Exchanger Design Handbook, sec. ed., CRC Press, Boca Raton, 312–314.
- [2] M. Stewart, O. T. Lewis (2013) Heat Exchanger Equipment Field Manual. Gulf Professional Publishing, Oxford.
- [3] F. Perrone, M. Brignone, G. Micali, M. Rottoli (2014). Grid geometry effects on pressure drops and heat transfer in an EMbaffle heat exchanger. International CAE Conference 2014, 27/28.10. 2014 Verona, Italy.
- [4] J. M. Chenoweth, FIVER – A new design concept to prevent tube damage from flow-induced vibration in shell-and-tube heat exchangers, Research Brief 1–10, Heat Transfer Research, Inc., College Station, TX (1983).
- [5] D. Agazzi, T. Odry, M. Rottoli (2016). CFD analysis of annular distributors for shell & tube heat exchangers. International CAE Conference 2016, 17/18.10. 2016 Parma, Italy.
- [6] E.J.J. van der Zijden, M. Brignone, M. Rottoli, C.F.J.M. van Lint (2013). EMbaffle® Heat Exchanger in fouling operation. Proceed. Int. Conf. Heat Exchangers Fouling and Cleaning, 324–328, 9/14.6.2013, Budapest, Hungary.
- [7] M. Brignone, F. Perrone, M. Rottoli, S.J. Pugh, E.M. Ishiyama (2015). EMbaffle® in refinery service. On-field study and data validation through SMARTPM®. Proceed. Int. Conf. Heat Exchangers Fouling and Cleaning, 7/12.6.2015, Enfield (Dublin), Ireland.
- [8] Tubular Exchanger Manufacturers Association, Inc. – Standards of the Tubular Exchanger Manufacturers Association – 9th Edition, 2007.

---

Section 5

# Thermal Management

---





# Managing Heat Transfer Issues in Thermoelectric Microgenerators

*Marc Salleras, Inci Donmez-Noyan, Marc Dolcet, Joaquin Santander, Denise Estrada-Wiese, Jose-Manuel Sojo, Gerard Gadea, Alex Morata, Albert Tarancon and Luis Fonseca*

## Abstract

This chapter deals with heat transfer challenges in the microdomain. It focuses on practical issues regarding this matter when attempting the fabrication of small footprint thermoelectric generators ( $\mu$ TEGs). Thermoelectric devices are designed to bridge a heat source (e.g. hot surface) and a heat sink (e.g. ambient) assuring that a significant fraction of the available temperature difference is captured across the active thermoelectric materials. Coexistence of those contrasted temperatures in small devices is challenging. It requires careful decisions about the geometry and the intrinsic thermal properties of the materials involved. The geometrical challenges lead to micromachined architectures, which silicon technologies provide in a controlled way, but leading to fragile structures, too. In addition, extracting heat from small systems is problematic because of the high thermal resistance associated to heat exchanged by natural convection between the surrounding air and small bare surfaces. Forced convection or the application of a cold finger clearly shows the usefulness of assembling a heat exchanger in a way that is effective and compliant with the mechanical constraints of micromachined devices. Simulations and characterization of fabricated structures illustrate the effectiveness of this element integration and its impact on the trade-off between electrical and thermal behavior of the active materials in device performance.

**Keywords:** thermoelectricity, silicon technology, micromachining, silicon nanowires, heat exchangers

## 1. Introduction

It is quite evident that extending or improving human senses has enabled human societies to prosper by acquiring information from their surroundings and gaining knowledge from it. Internet of Things (IoT) embody this trend today combining distributed sensing with high connectivity so that wise decisions and actions follow information gathering and analysis [1, 2]. Trillion Sensors is another paradigm onto which IoT is further exploited on the basis that the more extensive or intensive the deployment of sensor networks is, the more fruitful the knowledge that can be derived from them would be [3, 4].

Small dimensions (nanometers to micrometers) are appropriate in the sensitive part of sensors when they need to interact with phenomena or entities equally characterized by such small dimensions (light, molecules, living cells ...). An overall small size for the sensors themselves is not devoid of interest either. The smaller they are, the more sustainable their fabrication is in terms of materials and energy, and the more cost-effective they become. Small size is also enabling in itself, e.g. medical implants, as well as convenient, e.g. payloads.

Sensing requires energy. A certain provision of energy autonomy is needed for sensors to be deployed in remote locations, harsh environments, or where they need to remain temporary unattended. Batteries is a common way to provide such autonomy, but their charge is finite impeding long-term autonomy scenarios. Moreover, their recharge, replacement and disposal imply a logistic and environmental burden that will not be affordable when IoT gets to its full extent mobilizing tens of billions of devices and an even larger number of sensors.

Secondary batteries can be kept recharged by coupling them with energy harvesters able to draw energy present in the environment [5]. Heat is abundant in natural scenarios, and waste heat is also abundant in human-made scenarios due to laws of thermodynamics and our profuse use of thermal machines. When such heat gives rise to temperature gradients (a situation as simple as a hot surface exposed to air), thermoelectricity is a convenient way to extract electric energy from them [6, 7].

For that extraction to be optimum, the external thermal gradient needs to be fully transposed into the thermoelectric generator itself. Physical interaction of small devices with their environment may exploit profitably some scale factors when going down in dimensions, but, sometimes, small sizes pose a handicap or challenge for such interaction, too. This is the case when trying to cool down locally a part of a small device by exchanging heat with the surrounding air. This chapter tries to illustrate this point by sharing the issues and strategies the authors have dealt, and are dealing with, in their quest for silicon-based miniaturized thermoelectric generators.

## 2. Silicon-based thermoelectric generators

Silicon technology has been developed around an enabling and highly abundant semiconductor material. It is a mature technology apt to mass-production of devices with economy of scale and it is the champion technology of miniaturization. Not surprisingly, it boosted microelectronics in the XX century and nanoelectronics in the XXI century. In addition to the set of techniques that allow the fabrication of integrated circuits by depositing and patterning thin films on a silicon wafer, silicon technologies also developed micromachining techniques that allow carving and shaping the silicon wafers into structures that are able to interact with the environment. Sensors and actuators belong to the latter category. Since energy harvesters are environmental interacting devices and, application-wise, they should not be much larger than the sensors they will feed, it is only logical that their fabrication will similarly benefit from the silicon technologies toolbox. These technologies do not only excel in miniaturization but also in *integration* capabilities. This is an important aspect as well. Traditional thermoelectric generators are *assembled* from couples of semiconductor pellets, various millimeters in side, that are arranged electrically in series and thermally in parallel together with additional connecting strips and appropriate thermal elements. When going down in dimensions, assembly becomes harder and offers much less latitude for process automation. In this way, resourcing to technologies that inherently offer integration capabilities is convenient, if not a must.

## 2.1 Micro thermal device architecture

The traditional thermoelectric generators mentioned above feature a  $\pi$ -architecture, where the  $\pi$  symbol gives a visual clue about how each thermocouple is built assembling vertically two semiconductor pellets (*aka* legs) of different polarity (to add-up the contribution of both electrons and holes) and connecting them electrically with a horizontal conductive strip. Several of those thermocouples are then connected in 1D or 2D arrangements [8]. Such disposition is well adapted to exploit vertically occurring gradients: the bottom part is placed in contact with the heat source while the top part contacts the heat sink and the thermoelectric material in between translates the heat flowing through it (or the temperature difference spanning across it) into magnitudes of electrical relevance,  $V$  and  $I$ , and therefore power ( $V \cdot I$ ).

Silicon technologies are of planar nature. They enable massive parallelism at  $x$  and  $y$  directions for shaping *laterally* devices made from the superposition of several active thin films. Such shaping also involves patterning in the  $z$  direction, but the accumulated depth of the films is much lower than the lateral dimensions at play, leading to aspect ratios that are opposite to those that characterize  $\pi$ -shape thermocouples.

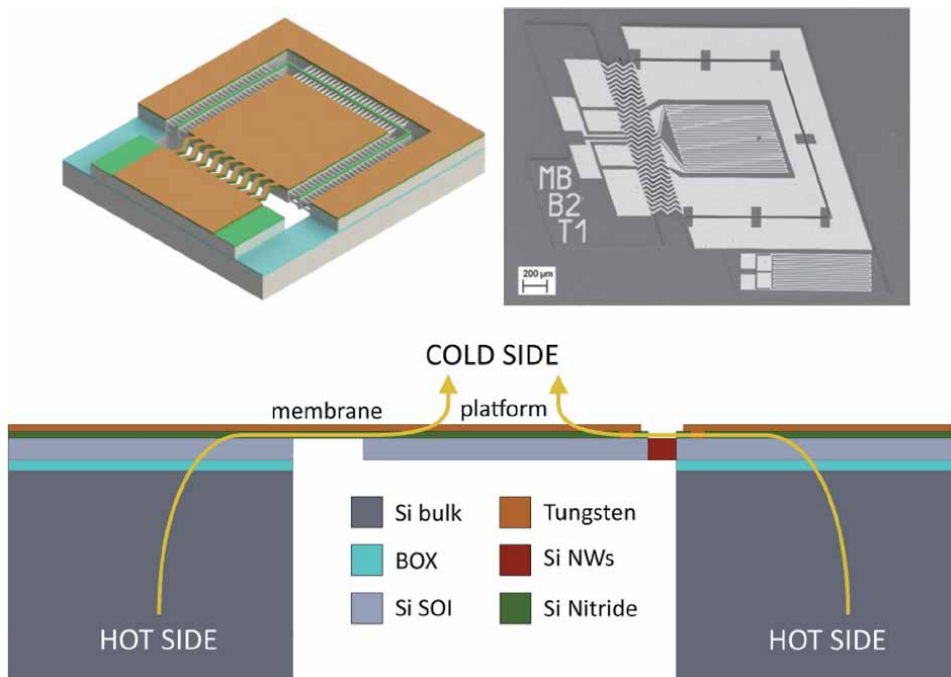
The main objective when defining the architecture and the technological route for a *micro* thermoelectric device is to obtain two areas of contrasted temperature in the *surface* of the chip since the thermoelectric materials will be arranged *laterally*. An architecture that translates an external vertical gradient into an internal lateral one is called *transversal*, and to make it possible a *thermal isolated platform* is defined.

The platform consists of a thin silicon area fabricated by eliminating the silicon beneath it. In order to preserve its thermal isolation from the surrounding bulk silicon, the physical connections between them should be minimized. Such connections are the mechanical supports that keep the platform in place (e.g. ancillary silicon bridges) and the thermoelectric materials themselves (and whatever supports they may need). In order to minimize the thermal conduction of these elements, they must be produced with *low thermal conductance* either by resorting to low thermal *conductivity* materials, when available and technologically feasible, or by acting on their *geometrical dimensions* making them long and thin.

**Figure 1** shows the schematics for such a device. Any hot surface in which this device is placed will act as a heat source. The top surface will be exposed to air acting as heat sink and will exchange heat with it. Due to their different thermal mass, the bulk rim area will hardly cool down, thus being the hot part of the device, while the platform will experience a larger decrease of temperature becoming the cold(er) part of it.

With respect to the thermoelectric material, the depicted device follows a uni-leg approach. Two thermoelectric materials are still at play, but a metal one replaces one of the semiconductor legs in order to close the circuit. Some thermoelectric performance is sacrificed because metals behave poorly thermoelectrically (they have higher thermal conductivities and close to zero Seebeck coefficients), but for the architecture presented and to keep processing simple, the use of a metal leg is technologically convenient.

Regarding the semiconductor thermoelectric material, one distinct feature of our approach is resorting to silicon materials, namely arrays of silicon nanowires (Si NWs). The rationale behind this option is to attempt the fabrication of *all-silicon* microgenerators, thus leveraging the full potential of silicon technologies. Thermoelectric performance of bulk silicon at ambient or moderate temperatures is bad because of its high thermal conductivity. Incidentally, this is the reason why it is



**Figure 1.**

From left to right and top to bottom: 3D sketch of an integrated planar micro-thermocouple; SEM image of a fabricated device; schematic cross-section of the device identifying the thermally isolated platform and other relevant elements, and the expected heat flow from hot to cold areas in a transversal architecture. The typical area for the platform of the devices discussed is  $1 \text{ mm}^2$ .

removed under the platform in the first place. However, nanostructuring of silicon in at least one dimension was shown to significantly lower its thermal conductivity when such spatial constraint is in the order or lower than the mean free paths of heat carriers (phonons) [9, 10].

Moreover, arrays of Si NWs can be conveniently grown as a post-process using a *bottom-up* method, known as CVD-VLS, which is mediated by previously deposited catalytic gold nanoparticles [11]. Following this procedure, this material can spontaneously fill the lateral void between the platform and the surrounding bulk silicon rim. Moreover, the NWs are attached quasi-epitaxially to the giving and receiving silicon walls minimizing any thermal and electrical contact resistance that could appear at those connection points [12]. Such minimization of parasitic resistances is an advantage of *micro-integration* when compared to *macro-assembly*. Further details on how Si NWs are grown and integrated in the proposed architecture can be found in our earlier published work [13–16].

The metal leg cannot be integrated in the same self-standing way. It is deposited as a thin film, so it needs a physical support. These ancillary supports need to be thermally optimized since they bridge the hot and cold areas. The nature of these supports has evolved across the different generations of our devices: from long and thin silicon bridges ( $400 \text{ μm} \times 100 \text{ μm} \times 15 \text{ μm}$ ) to wide and very thin  $\text{Si}_3\text{N}_4$  membranes ( $100 \text{ μm} \times 1000 \text{ μm} \times 0.3 \text{ μm}$ ). Since thermal conductivity of  $\text{Si}_3\text{N}_4$  is two orders of magnitude lower than the one of silicon, there is a net gain in thermal conductance, while enabling a shorter and wider (and less electrically resistive) metal leg.

The thermal impact on platform isolation of the *active* thermoelectric material, Si NWs, can be modulated by the nanowire length. The longer the nanowires are, the

higher their thermal resistance is. This leads to a platform better isolated from the bulk silicon rim and a larger resulting temperature difference ( $\Delta T$ ). Growing longer nanowires requires longer processing times, so a clever way of obtaining arbitrarily long nanowires in a reasonable time is to divide the span to be bridged by them into a number of consecutive trenches (see **Figure 1**). We usually cover lateral voids of several tens of microns by dividing them into 10 or 15  $\mu\text{m}$  wide trenches (as shown in the sketch of **Figure 1**). It must be noted that increasing the length of the NWs has a linear impact on their thermal conduction, but a sublinear impact on the overall thermal conductance of the device. NWs are just one of the several concurring heat leak paths across the platform and rim (metal legs, metal leg supports, platform mechanical supports, air itself), so increasing their length beyond the point where their thermal conductance starts competing with those of others makes no sense. Of course, another way to affect the thermal conduction of the thermoelectric material is choosing materials with lower thermal conductivity. In our case, and without moving beyond silicon compatible materials, SiGe NWs, which can be grown in a similar way, but exhibit better thermal properties, have been successfully integrated producing  $\Delta T$ s significantly larger than Si NWs, specially under natural convection and the absence of heat exchangers [17].

As said, longer NWs generally imply larger  $\Delta T$  and, thus, a larger thermovoltage. However, a resulting larger voltage is not necessarily associated to a larger power. Power ( $P$ ) goes as  $V^2/R$ , and since increasing the length of the NWs will also increase the electrical resistance of the device, a trade-off is established. Beyond certain NW length,  $V$  may still increase but  $P$  will decrease. The value at which this happens will not only depend on the balance of the thermal and electrical properties of the thermoelectric material, but also on the thermal relevance of the thermoelectric material in the thermal design of the overall device. This is of particular significance for this chapter as the way the platform exchanges heat with the ambient is an important element of the thermal resistance of the whole device and determines the corresponding internal  $\Delta T$  distribution. As commented, the goal of the thermal design of the device is to transpose most of the *external* gradient available to the active *internal* hot and cold areas. For that, the thermal resistance across platform and bulk silicon rim should be larger than the other two thermal resistances in series: the one of the hot part with the heat sink and the one of the cold part with the surrounding air. Being a solid–solid interface in usual application scenarios, keeping the former small poses no great problem; however, reducing the latter is much more challenging. As will be shown, the degree to which that reduction can be achieved would affect the tipping point of the thermal and electrical trade-off and impact also on materials and dimensional choices.

It must be noted that the heat transfer issues discussed in this chapter revolve about the challenge of exchanging heat in planar micromachined structures exhibiting very small exchange surfaces [18–22], while the particular nature of the thermoelectric material employed (e.g. NWs) is of no significance: the same conclusions will apply if silicon membranes, silicon-based thin films, or any other thermoelectric films of interest were considered instead.

## 2.2 Optimization considerations (load matching)

When considering the optimum design for a thermoelectric microgenerator ( $\mu\text{TEG}$ ) the generated power is the parameter which needs to be maximized. It is well known that for a given  $\mu\text{TEG}$  with its own internal resistance, the power that is transferred to the load is maximized when the internal resistance and the load resistance are equal. This case is usually known as load matching condition [23].

Considering the electrical circuit diagram shown in **Figure 2**, which represents a  $\mu$ TEG, formed by a voltage source ( $V_{OC}$ ) and its internal electrical resistance ( $R_{TEG}$ ), connected to a load resistance ( $R_L$ ), it is straightforward to evaluate the total dissipated power at the load as:

$$P_L = V_L \cdot I_L = I_L^2 \cdot R_L = \left( \frac{V_{oc}}{R_{TEG} + R_L} \right)^2 \cdot R_L \quad (1)$$

Finding the value of  $R_L$  which maximizes  $P_L$  implies after a few calculations the load matching condition,  $R_{TEG} = R_L$ . It is important to notice that the only parameter allowed to change in this optimization is the load resistance. Therefore, one can write the maximum power as:

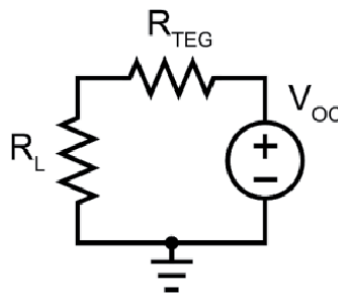
$$P_{L,max} = \frac{V_{oc}^2}{4R_L} = \frac{V_{oc}^2}{4R_{TEG}} \quad (2)$$

As can be seen in **Figure 3**, where the output power of a  $\mu$ TEG is plotted versus load resistance for three different internal resistances, each curve has a maximum for the load matching condition. But now the influence of the internal resistance is highlighted, where the lower its value, the greater the power output. In **Figure 3**, for example, halving the internal resistance can double the power output at the load matching condition. This highlights the importance of reducing the internal resistance when designing a  $\mu$ TEG.

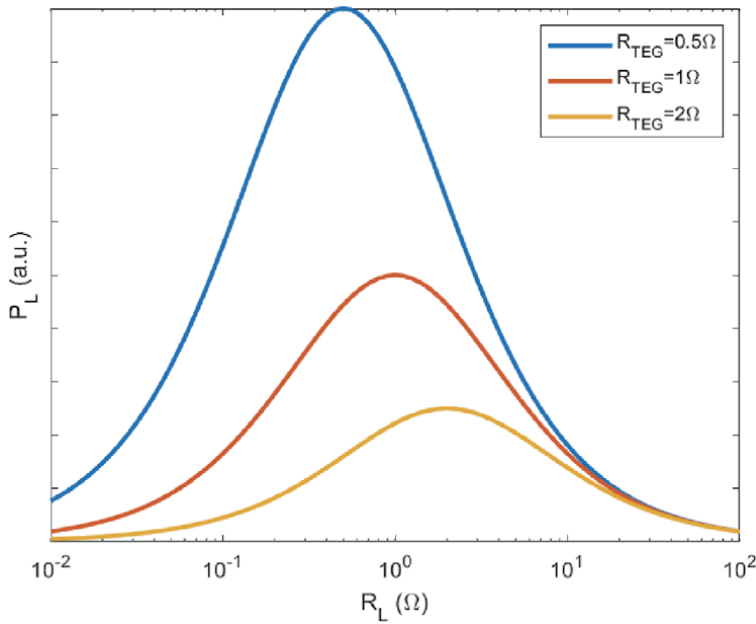
Some publications discussing load matching focus on the need to modify the internal resistance, increasing it, in order to match the load resistance [22]. According to **Figure 3**, this is in fact an error. It is always a better approach to minimize the internal resistance in order to increase the power output even further. Once the internal resistance is the minimum possible, then the load matching condition can be applied to maximize the power output. Actually, many integrated circuits exist which efficiently implement maximum power point tracking (MPPT) algorithms to extract the maximum power from a power source by modifying its load resistance.

This load matching approach can be analogously applied to the temperatures involved in the  $\mu$ TEG and is known as thermal matching. A simplified conductance network describing the  $\mu$ TEG ( $K_{TEG}$ ) in parallel with  $K_{LK}$  accounting for parasitic thermal leakages and in series with  $K_S$  representing the conductance to ambient (to both heat source and heat sink) is shown in **Figure 4**.

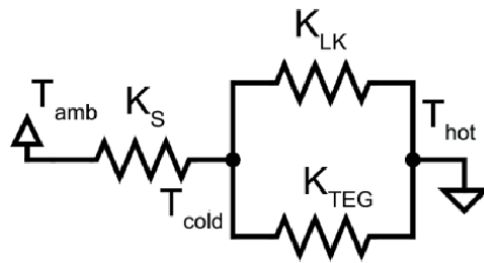
To explore which is the  $K_{TEG}$  value that maximizes  $P_{max}$ , as was done in the electrical case, Eq. (2) can be rewritten as:



**Figure 2.** Equivalent circuit of a  $\mu$ TEG, formed by a voltage source ( $V_{OC}$ ) and its internal resistance ( $R_{TEG}$ ), connected in series with a load resistance ( $R_L$ ).



**Figure 3.**  
 Power output of a  $\mu$ TEG versus load resistance for different  $R_{TEG}$  values.



**Figure 4.**  
 Simplified thermal conductance network describing the  $\mu$ TEG with parallel and series thermal conductances.

$$P_{L,max} = \frac{V_{oc}^2}{4R_{TEG}} = \frac{(S \cdot \Delta T)^2}{4R_{TEG}} \quad (3)$$

Where  $S$  is the Seebeck coefficient and  $\Delta T$  is the temperature difference across the  $\mu$ TEG, or  $T_{hot} - T_{cold}$  from **Figure 4**. Therefore:

$$\Delta T = \Delta T_A \frac{K_S}{(K_{TEG} + K_{LK} + K_S)} \quad (4)$$

Where  $\Delta T_A$  is the total available temperature difference,  $T_{amb} - T_{hot}$ .  $K_{TEG}$  is the internal thermal conductance of the  $\mu$ TEG and  $K_S$  represents the thermal conductance to the ambient.

When decreasing  $R_{TEG}$ , as deemed appropriated in the previous paragraphs, it is important to keep in mind that  $K_{TEG}$  is bound to increase, as they are inversely proportional. This is because of the implicit assumption that changing  $K_{TEG}$  implies a geometry modification, not a material property change and the geometry change affects both electrical resistance and thermal conductance of the  $\mu$ TEG. Ignoring any leakage contribution ( $K_{LK} = 0$  W/K) in Eq. (4), the power output (solid) and  $\Delta T$

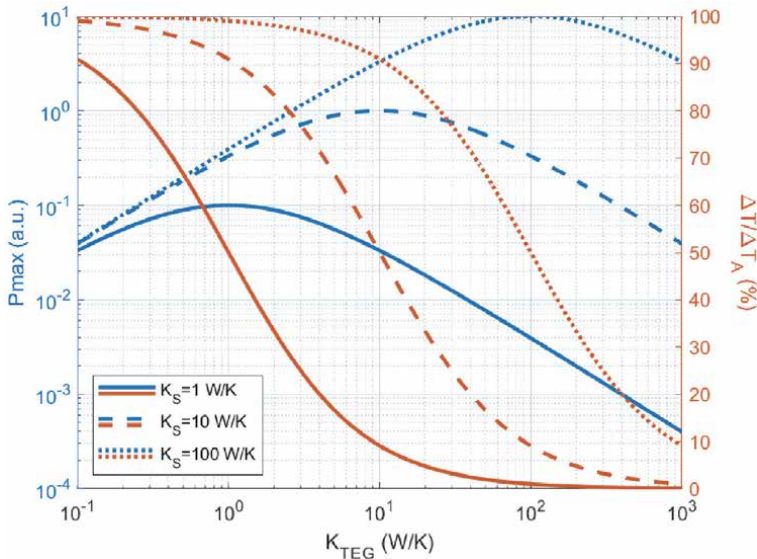
(dotted) versus  $K_{TEG}$  can be seen in **Figure 5**. Three different  $K_S$  cases have been considered to highlight the fact that, the larger  $K_S$ , the larger the power output, even for a constant  $K_{TEG}$ . It can be seen that when  $K_{TEG} = K_S$ , the maximum power condition when  $K_{LK} = 0$ , then the temperature drop across the  $\mu$ TEG is 50% of the available temperature difference.

Similar to the electrical case, many papers discussing thermal matching focus on reaching a temperature drop in the  $\mu$ TEG equal to the temperature drop across  $K_S$  [5, 24, 25]. When this  $K_S$  represents a heat exchanger, some authors suggest a low  $K_S$  heat exchanger to match  $K_{TEG}$  and therefore maximize the power output according. While this approach assures operation at the mathematical local maximum for a given  $K_S$ , it is a bad practice because it ignores the absolute maximum, which takes place at larger  $K_S$  values for a given  $K_{TEG}$ .

Looking at **Figure 5**, if  $K_{TEG} = 1$  W/K, this reasoning would imply that  $K_S = 1$  W/K would be necessary, and 50% of the total available temperature difference would drop across the  $\mu$ TEG. However, with a better heat exchanger,  $K_S = 10$  W/K or even  $K_S = 100$  W/K, then  $\Delta T$  will asymptotically approach  $\Delta T_A$ , and the power output will asymptotically reach:

$$P_{L,max} = \frac{(S \cdot \Delta T_A)^2}{4R_{TEG}} \quad (5)$$

In conclusion, both load matching and thermal matching are conditions that are mathematically true, but from a practical point of view, care must be taken when designing a  $\mu$ TEG to maximize its power output. First of all, its electrical internal resistance ( $R_{TEG}$ ) must be minimized, and after that, power output can be maximized by connecting a load which matches that of the  $\mu$ TEG, or simply an IC implementing an MPPT algorithm. On the thermal side, as  $R_{TEG}$  is minimized, the thermal conductance ( $K_{TEG}$ ) is consequently maximized. Then, as the  $\mu$ TEG is already optimized, and it is not possible to further increase  $K_{TEG}$ , the only option is to act on the external components, which in this case is the heat exchanger, and to choose one with an as large as possible  $K_S$ , so that almost all of the available  $\Delta T$  will be internally transferred to the  $\mu$ TEG.



**Figure 5.**  $P_{max}$  (left, blue curves) and  $\Delta T/\Delta T_A$  (right, red curves) versus  $K_{TEG}$  for different  $K_S$  values. For  $K_{TEG} = 1$ , thermal matching conditions would call for  $K_S = 1$ , but larger  $P_{max}$  values are possible for larger values of  $K_S$ .



### 3. Decreasing the platform thermal resistance

As mentioned before, the performance of  $\mu$ TEG devices depends on the temperature difference ‘seen’ by the thermocouples. Therefore, minimizing thermal resistances in series with those elements would improve the performance of the device. In this section, such improvement is demonstrated by decreasing the thermal resistance between the suspended platform and the ambient, usually the cold part, by favoring the heat flow locally. Two methods have been used to increase such heat exchange: (i) by forcing heat convection onto the platform and (ii) by contacting it with a cold mass. The promising results obtained from the experiments described in the next two subsections call for optimizing this effect through the development of a procedure to integrate a heat exchanging structure, which will be shown in section 4.

#### 3.1 Forced convection experiments

As the working scenario for the  $\mu$ TEG devices is dominated by a temperature difference between the hot and the cold parts, heat convection could play also an important role on how these temperatures are established. Convection is a mechanism of heat flux originated from the movement of the surrounding fluid, which will be typically air for the usual applications of the presented devices. Depending on how this movement is induced, convection can be classified as natural or forced.

Natural convection is based on the warming up of the air that is close to a heat source that, due to the lowering of its density, tends to move upwards, giving its place to colder air and so promoting the heat exchange. In forced convection, air is forced to move and then renew by an external force.

In order to demonstrate the improvement in the performance of the device, three different sets of experimental measurements have been performed on a device at three different convection conditions. The first one corresponds to natural convection, which occurs when the device is operated by letting it rest on top of a hot surface exposed to ambient at room conditions. The second and third sets of measurements correspond to forced convection regimes. In the second case, this is accomplished by the use of a standard CPU fan (see **Figure 6**) placed over the device, while in the third, an air jet, obtained through a syringe connected to the compressed air line in the laboratory, is directed towards the device. More details are available at [26].

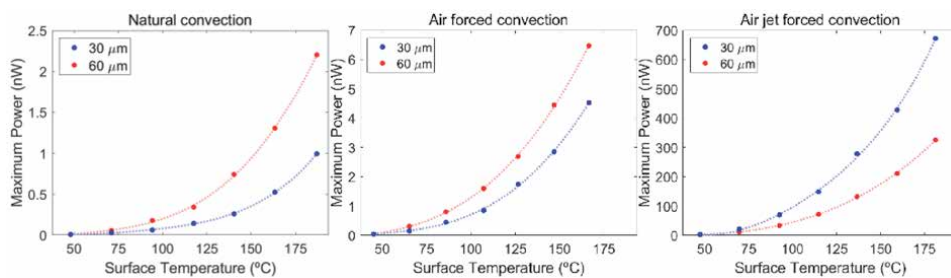
Such experimental measurements have been performed on two different devices, featuring 30 and 60  $\mu\text{m}$  long silicon NWs (by filling 3 and 6 trenches as described in section 2.1). Consequently, each one of the devices has different electrical and thermal resistances.

The obtained experimental results are shown in **Figure 7**. The devices have been measured at different temperatures of the hot plate (from 50 to 200  $^{\circ}\text{C}$  in 25  $^{\circ}\text{C}$  steps).

The measurement results show a very clear improvement in the performance as a result of forced convection. The maximum output power obtained when the device is mounted under the fan is multiplied by 3 when compared with the natural convection regime, while when under the more directed and higher flow air jet, the performance increases nearly three orders of magnitude: from a few nW to almost 0.7  $\mu\text{W}$ . Moreover, the more performant air convection is, the less relevant become the thermal properties of the thermoelectric material. In natural and air forced convection cases, the larger output power corresponds to the longest nanowires, whereas in the air jet forced convection the opposite is true. This happens because the longer nanowires also have a larger electrical resistance, and its larger thermal



**Figure 6.** Experimental setup used for the thermoelectrical characterization of  $\mu$ TEG devices under a forced convection regime induced by a CPU fan located on the top. The device is mounted on the thermal chuck of a Linkam station.



**Figure 7.** Maximum power versus chip surface temperature for three different heat convection regimes and on two different devices (adapted from [26]).

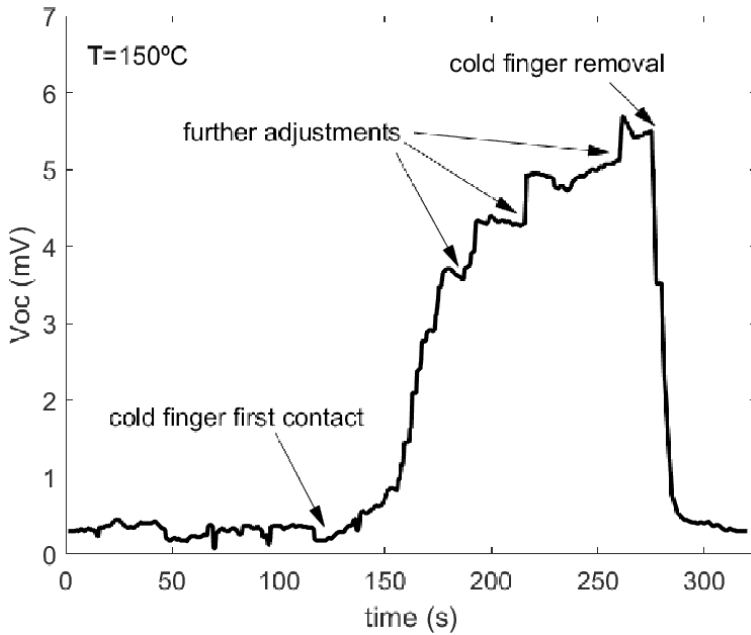
resistance is not significant in this case where the platform to ambient thermal resistance is enough to assure a large  $\Delta T$ .

### 3.2 Cold finger approach

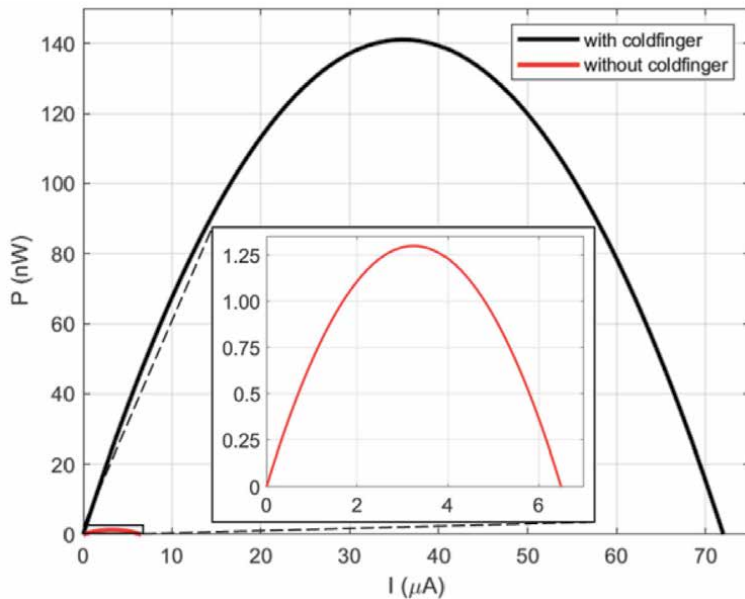
In the previous subsection, it has been experimentally demonstrated how important a good thermal connection with the surrounding ambient is in order to improve the overall performance of  $\mu$ TEG devices. Nevertheless, forced convection scenarios are not always available and artificially forcing them needs additional energy consuming devices. Therefore, in order to explore a passive strategy to diminish the thermal resistance to the surrounding ambient, the effect of contacting the microplatform with a metallic probe has been assessed. With this experiment, the feasibility of the addition of a heat exchanging structure as a general strategy for the reduction of the thermal resistance to the ambient will be demonstrated.

The experimental setup consists of a metallic probe dipped in thermally conducting paste, which is carefully positioned on the micro-platform by the use of a micro-manipulator.

The performance improvement obtained by means of this approach can be observed in **Figure 8**, which shows a plot of the Seebeck voltage output of the device placed on a hot plate at 150 °C when the cold finger is being attached. It can be observed that the voltage increases rapidly after contact, and it rises even more when the applied force to the cold finger is increased slightly, so demonstrating the reduction of the thermal resistance when the physical contact is improved.



**Figure 8.**  
*Voltage evolution while the cold finger is being attached and detached.*



**Figure 9.**  
*Power curves for a device, with and without the cold finger, on a hot plate at 250 °C.*

In **Figure 9** the power curves obtained from the same device at a hot plate temperature of 250 °C with and without the cold finger are shown. It can be seen an important improvement in the performance of two orders of magnitude, from 1.3 to 142 nW, so proving the effectiveness of the cold finger approach as a proof of concept validating the further development of more effective heat exchanging structures.

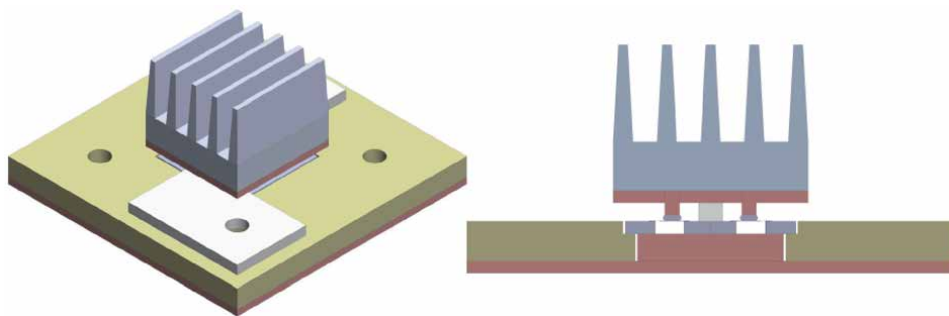
#### 4. Heat exchanger

The previous section highlights the importance of physically contacting the platform in order to improve heat extraction, and thus cooling it more efficiently. According to section 2.2 and the results shown in section 3.2, the need for a heat exchanger has been proven. In this section, we study the implementation of such component on the  $\mu$ TEG. This poses several problems from the technological point of view, especially considering the starting device architecture used to expose the thermoelectric material to a thermal gradient. The thermally isolated platform is a fragile structure and physically contacting it without caution might break it. A proper methodology with auxiliary components needs to be developed components to provide such contact safely.

The approach implies to have a thermally conductive piece contacting the platform and interfacing this part of the device with a heat exchanger of appropriate size. For this reason, such piece will be dubbed as ‘adapter’. The contact needs to be compliant to absorb any excess vertical displacement with deformation. The compliant part of this contact will be a certain amount of silver paste. A rigid spacer (PMMA), sitting both on the silicon bulk rim and the platform, will also be necessary to limit the maximum excursion of the adapter over the platform so that pressure between the heat exchanger on top and the platform below can be applied in a safe way. Finally, the heat exchanger itself, a commercial one of similar footprint is assembled onto our chip. In this case, our chip is 7x7 mm<sup>2</sup> and the smallest commercial heat exchanger found is 8x8 mm<sup>2</sup>. A PCB with a through-hole, to insert a copper plate improving the thermal conductance from the hot surface to the bulk silicon rim, and a slightly larger partial etch to fit the chip and facilitate the wire bonding to auxiliary copper traces, are included in the assembly as shown in **Figure 10**.

##### 4.1 Modeling results

The feasibility of the approach has been first tested building a physical model and solving finite element simulations (COMSOL) to evaluate the expected



**Figure 10.** Isometric, cross section and detailed view of the proposed approach to safely contact the thin silicon platforms.

improvement on performance. The thermal and electrical properties of the materials used in the model are listed in **Table 1**.

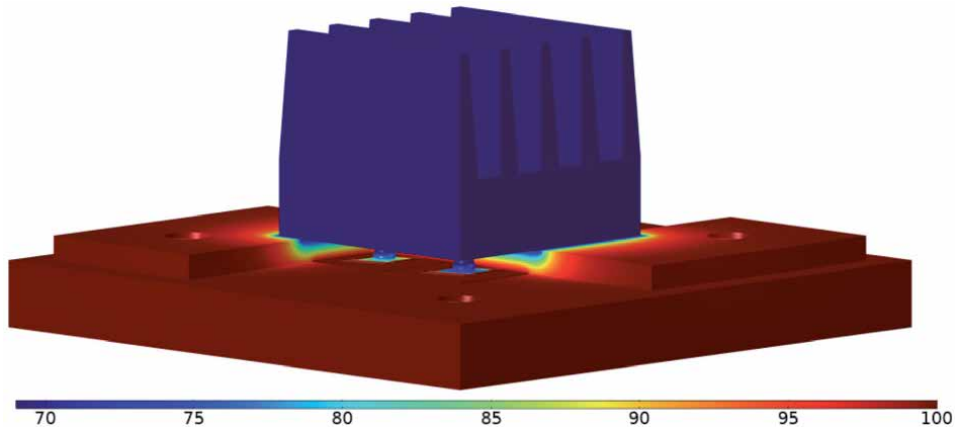
The model boundary conditions include a constant hot temperature at the bottom ( $T_{\text{hot}} = 100\text{ °C}$ ) and natural convection on the vertical and horizontal walls of the heat exchanger through a heat exchange coefficient directly calculated in COMSOL for an air ambient temperature of  $27\text{ °C}$ . When such element is not present, the heat exchange coefficient is applied directly on the platforms surface. **Figure 11** shows the temperature distribution for the whole model under such conditions. As it can be seen, even with a heat exchanger, the lowest temperature reached in the cold part is slightly below  $70\text{ °C}$  although the ambient temperature is  $27\text{ °C}$ . This is because the thermal resistance from the heat exchanger to the ambient is approximately one third of the total thermal resistance while the thermal resistance from the bottom of the PCB (actually most of this is from the silicon chip) to the heat exchanger is approximately two thirds of it.

	$\kappa\text{ (W}\cdot\text{m}^{-1}\cdot\text{K}^{-1}\text{)}$	$\sigma\text{ (S}\cdot\text{m}^{-1}\text{)}$	$S\text{ (V}\cdot\text{K}^{-1}\text{)}$
Silicon	150	$12\cdot 10^3$	
Silicon oxide	1.4	—	
Silicon nitride	30	—	
Silicon NWs	$25^{(1)}$	$12\cdot 10^3^{(1)}$	$250\cdot 10^{-6}$
Tungsten	174	$7.76\cdot 10^6^{(2)}$	
Thermal paste	5	—	
Copper	401	—	
FR4 (PCB)	0.3	—	
Spacer (PMMA)	0.2	—	

<sup>(1)</sup>Silicon NWs are modeled as a block, not individual nanowires, and the block material properties assume an occupation of only 5% of the total area with nanowires, while the remaining 95% has air material properties.

<sup>(2)</sup>Tungsten electrical conductivity is different from the bulk literature values. The sheet resistance on a real device has been measured to obtain this value.

**Table 1.**  
 Thermal and electrical properties of the materials used in the model.



**Figure 11.**  
 Temperature distribution for the whole model with  $T_{\text{hot}} = 100\text{ °C}$ .

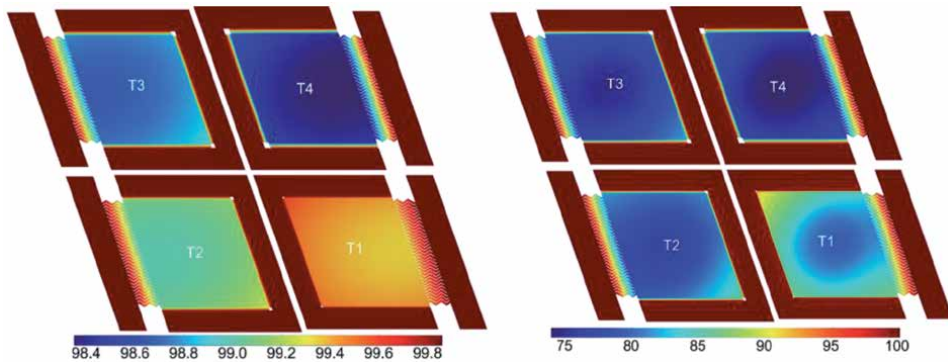
The internal temperature distribution for chips with four platforms with NW lengths of 10, 20, 30 and 40  $\mu\text{m}$  (T1 to T4) has been analyzed for the cases with or without heat exchanger. The difference is significant as shown in **Figure 12**. The temperature difference across the NWs in the best case reaches about 25  $^{\circ}\text{C}$  of the total 73  $^{\circ}\text{C}$  externally available, when the heat exchanger is in place (right). This means the thermal resistance of the nanowires is approximately twice the thermal resistance from the platform to the ambient through the heat exchanger.

On the other hand, for the case without heat exchanger (left), the temperature differences across the nanowires do not reach beyond 2  $^{\circ}\text{C}$ . In this case, the thermal resistance to the ambient is much larger than the nanowires thermal resistance, and a very small temperature drop develops across the active thermoelectric material.

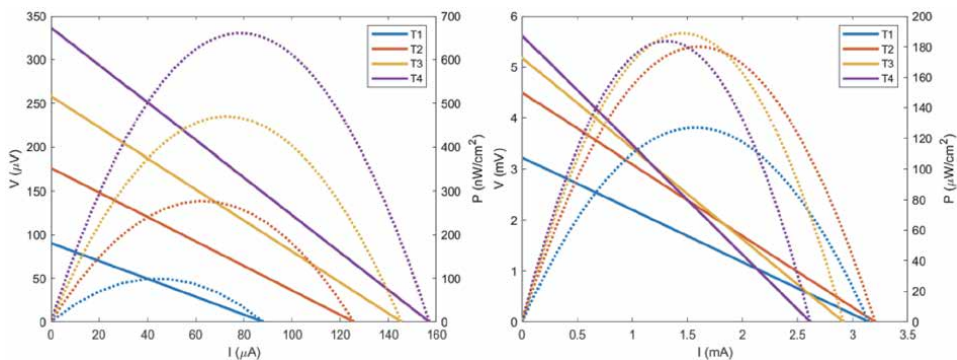
If the temperature solution from the finite element model is coupled to an electrical model through the Seebeck coefficient of the nanowires, the I-V curves and power output for each platform considering both scenarios can be obtained.

These results are shown in **Figure 13**, where the power output has been plotted as power density considering a device area of 2  $\text{mm}^2$ , large enough to contain the whole platform (approximately 1  $\text{mm}^2$ ) and space for additional contacts.

Clearly, a much larger power is obtained when the heat exchanger is in place due to the much higher  $\Delta T$  perceived by the NWs. In addition, the behavior of the four platforms evolve differently. Without the heat exchanger, voltage and power scale with the length of nanowires since their thermal resistance is the dominant part of the total device thermal resistance and such length is directly determining the



**Figure 12.** Temperature distribution for each platform (from T1 to T4) without heat exchanger (left) and with heat exchanger (right).



**Figure 13.** I-V curves (solid lines), and power output (dotted lines), versus current for T1-T4 devices, without (left) and with heat exchanger (right).

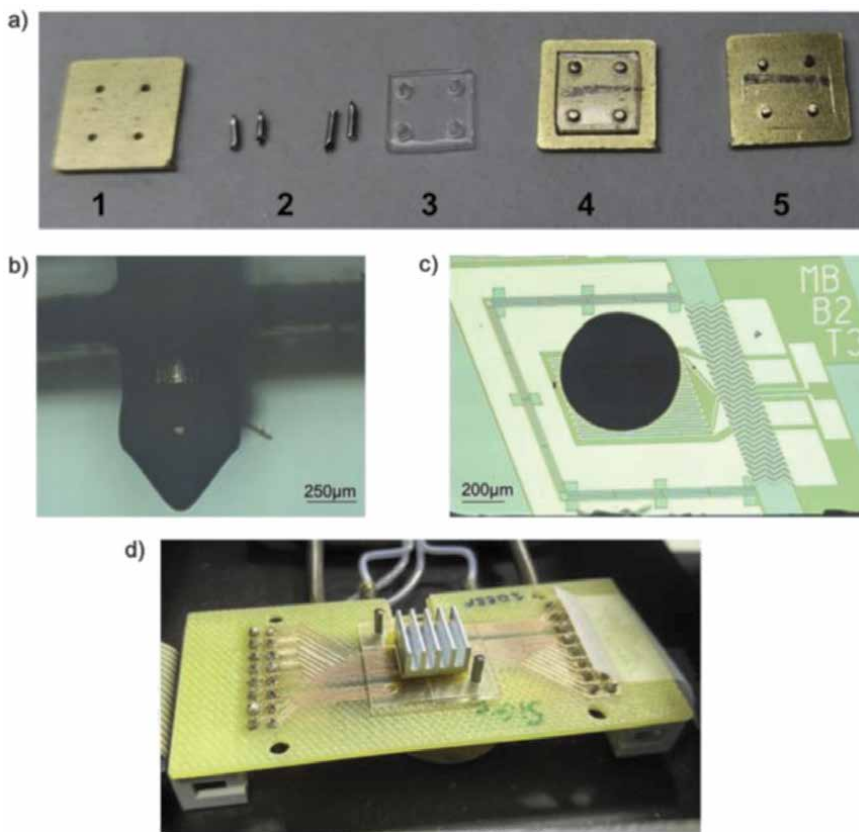


attained  $\Delta T$ . However, when the presence of the heat exchanger secures most of  $\Delta T$ , the positive effect of the lower thermal conductance of longer nanowires, which is still there, rapidly saturates and even reverse (see T4 vs. T3) because the detrimental impact of the increasing electrical resistance becomes dominant.

#### 4.2 Manual assembly and impact on measurements

The significant increase in the generated power when applying a forced convection or a cold finger and the results from the simulations including a heat exchanger directed our efforts to the construction of the previously described heat exchanger assembly on our  $\mu$ TEGs (see **Figure 10**).

The preparation sequence of the required components is given in **Figure 14a**. A heat exchanger adapter is made from four Cu wires (one per on-chip a device), with diameter similar to the size of the suspended platform (which they will contact after the assembly) inserted in a square brass piece and machined to the appropriate length. The tips of the wires are dipped with thermal paste (**Figure 14b**) to fill the gap between the Cu wires and the suspended platforms to guarantee good thermal contact (**Figure 14c**). A PMMA spacer with a thickness appropriately matching the length of the protruding Cu wires is then assembled between the heat exchanger adapter and the  $\mu$ TEG, and finally, the aluminum heat exchanger is placed on top of adapter using a thermal paste (**Figure 14d**). Further details can be found in [27] from which **Figures 14–17** have been adapted.



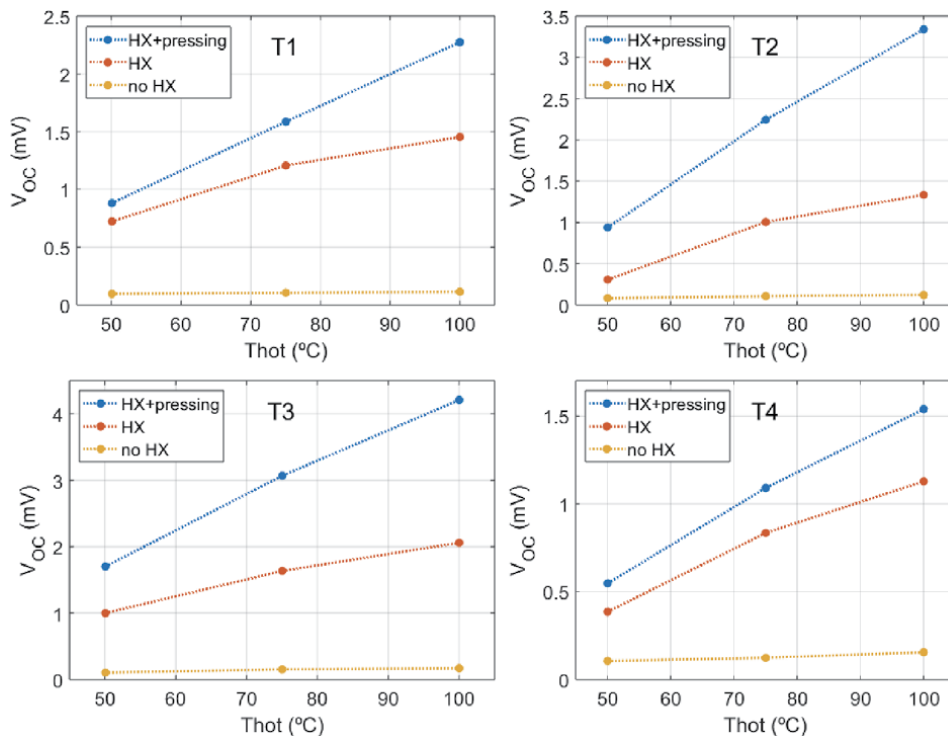
**Figure 14.** (a) Steps of the construction of the heat sink adapter. Optical microscope images of (b) the Cu wire dipped in thermal paste and (c) the footprint left on the platform of the test device. (d) An image of the final assembly.

Through the described integration scheme, a first evaluation of the performance improvement brought by a heat exchanger to the  $\mu$ TEG is enabled. In this study harvesting measurements with and without heat exchanger were performed by placing the assembled devices on a Linkam THMS 350 V heating stage at various temperatures in a natural convection environment. Three different cases were measured: without heat sink, with heat sink and with heat sink + pressing, where for the latter a force is applied on top of the assembly to reduce the thermal resistance of the thermal paste. Chips with different thermoelectric materials were measured: Si NWs, Si-Ge NWs and Si microbeams. At the current stage of technology maturity, a rather low number of devices has been measured, but the results shown in the next subsections correspond to significant devices of each category. In terms of measurement uncertainties, the most important source are thermal fluctuations that due to the thermoelectric nature of the device introduce variations in the measured V and I, which have been estimated to be below  $10 \mu\text{V}$  and  $1 \mu\text{A}$ , respectively.

#### 4.2.1 Measurements with Si NWs

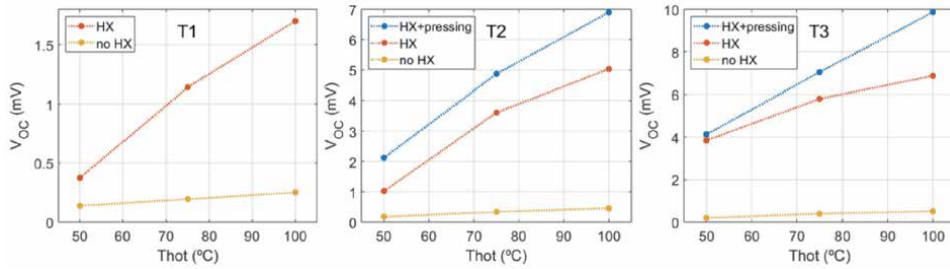
The Seebeck voltage vs. hotplate temperature curves for the Si NWs-based  $\mu$ TEGs with different number of trenches are shown in **Figure 15**. As anticipated, all the devices presented output voltages that scaled with the number of trenches (i.e. length of NWs). However, the reduction of the thermal resistance between the cold side (suspended platform) and the ambient when a heat exchanger is integrated resulted in a large increase of  $\Delta T$  across the NWs and hence higher overall voltages.

In terms of power, the maximum power densities obtained at hot plate temperatures of  $100 \text{ }^\circ\text{C}$  without the heat exchanger were in the range of  $0.05\text{--}0.1 \mu\text{Wcm}^{-2}$ .



**Figure 15.** Seebeck voltage vs. hot plate temperature for Si NWs-based  $\mu$ TEGs with different number of trenches (T1–T4) with and without heat exchanger.





**Figure 16.** Seebeck voltage vs. hot plate temperature for SiGe NWs-based  $\mu$ TEGs with different number of trenches (T1–T3) with and without heat exchanger.

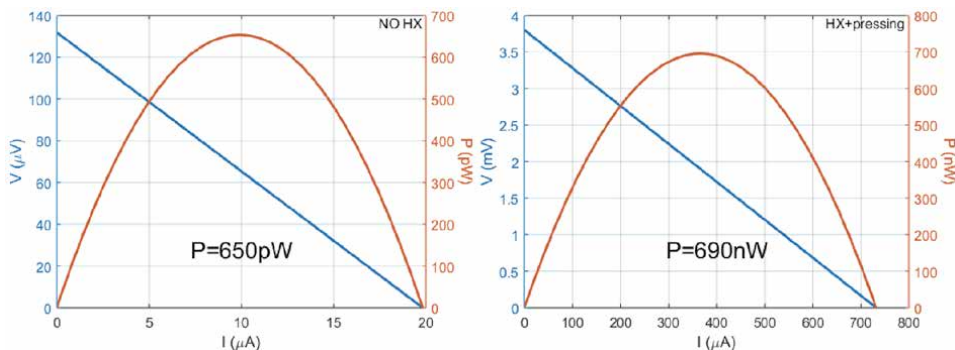
As expected, a tremendous increase in power density was observed after the integration of the heat exchanger + pressing, and values in the range 7–42  $\mu\text{Wcm}^{-2}$  were observed. No clear trends were observed with the number of trenches.

#### 4.2.2 Measurements with SiGe NWs

For devices with SiGe NWs, considerable higher Seebeck voltages were observed when compared to Si NWs (**Figure 16**), due to the higher thermal resistance resulting from the lower intrinsic thermal conductivity of the former. With and without heat exchanger, the devices performed better with increasing number of trenches. Also, power densities rose considerably with the integration of the heat exchanger. As already observed for the Si NWs, the voltage and generated power improved further when a slight pressure was applied to the heat exchanger. It is worth noticing that the maximum power thus obtained does not differ much for Si and SiGe NWs: 41.6  $\mu\text{Wcm}^{-2}$  vs. 45.2  $\mu\text{Wcm}^{-2}$ , respectively, considering a T3 device on a hotplate at 100 °C. This points to the dilution of the effect of better starting thermal properties when the heat exchanger is present.

#### 4.2.3 Measurements with Si microbeams

Si microbeams devices were fabricated to compare the performance of bulk Si with Si NWs. After the integration of the heat exchanger + pressing, the results presented in **Figure 17** show a remarkable three orders of magnitude increase in the generated power from  $\sim 650$  pW to  $\sim 690$  nW for a T1 device, i.e. from 32.5  $\text{nWcm}^{-2}$  to 34.5  $\mu\text{Wcm}^{-2}$ . This result evidences again that once the heat exchanger



**Figure 17.** I–V and power curves for the Si microbeams based  $\mu$ TEGs without heat exchanger (left) and with heat exchanger and pressing (right) for a hot plate temperature of 100 °C.

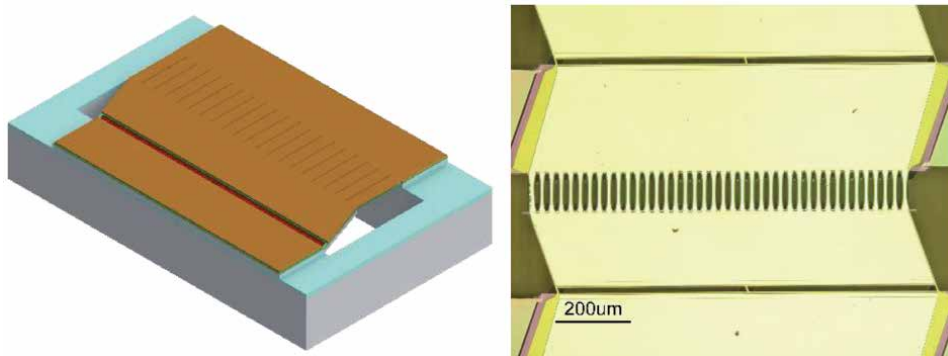
is in place, the thermal properties of the thermoelectric material become second order. Hence, by optimizing their electrical properties and ensuring a good  $\Delta T$  with the aid of a heat exchanger, it is possible to obtain high power densities even with high thermal conductivity thermoelectric materials such as Si microbeams.

### 4.3 Semiautomatic assembly with integration density

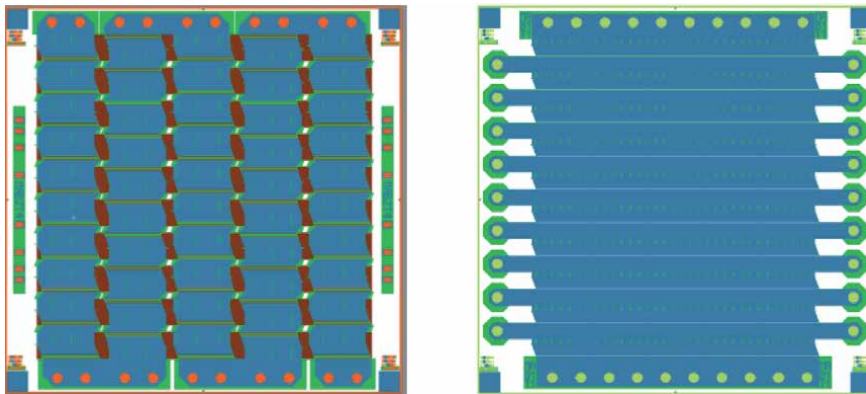
In order to translate the promising power densities of a single structure into useful absolute power levels, a certain number of thermocouples needs to be integrated and connected. The  $\mu$ TEGs design was modified to attain a higher integration density by reducing the number of active sides. The new thermocouple has a rectangular shape with one side featuring the membrane providing mechanical support and metallic connection, and the opposite side composed of the trenches to be filled with NWs. In **Figure 18**, a 3D schematic of the new unitary thermocouple is shown. The same cross-section profile of **Figure 1** still applies. With this new design, many elements can be integrated in the same chip: up to fifty thermocouples (each with an approximate size of  $5 \times 0.6 \text{ mm}^2$ ) fit in series or series-parallel configuration in a  $49 \text{ mm}^2$  chip, as shown in **Figure 19**. Both configurations would lead to the same harvested power, but the series one will scale up voltage while the parallel one will scale up current.

This compact design requires new components and a novel and more efficient approach for the integration of the heat exchanger in order to boost their thermal performance. A micromachined Si adapter (substituting the Cu wires, brass plate and PMMA spacer of the previous section) is necessary for the distribution of the force exerted on the platform by the heat exchanger, and different designs featuring the corresponding serial or parallel arrangements were fabricated. **Figure 20** (left) depicts the Si adapter designs where the central columns contact the platform of each thermocouple in the chip and the ones at the corners act as force distributors. Similar to the previous section, a commercial Al mini heat exchanger will be placed on top of the Si adapter to help the circulation of heat from the Si rim of the  $\mu$ TEG (warm side) through the thermoelectric material to the platform (cold side) to achieve the desired larger  $\Delta T$ . The heat flux representation through the assembly is shown in **Figure 20** (right).

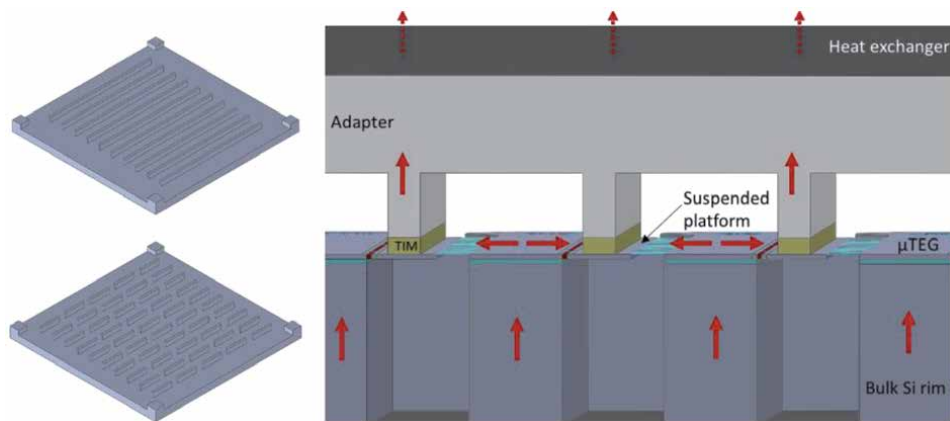
To achieve a good thermal contact, which is key for a maximum generated power, a thermal interface material (TIM) needs to be placed between the thermocouple and the adapter. To this aim, an inkjet printer (Dimatix) was chosen to deposit a controlled amount of TIM only on the columns of the adapter.



**Figure 18.** 3D schematic of the new thermocouple design (left) and an optical microscope image of the fabricated micromachined platform.



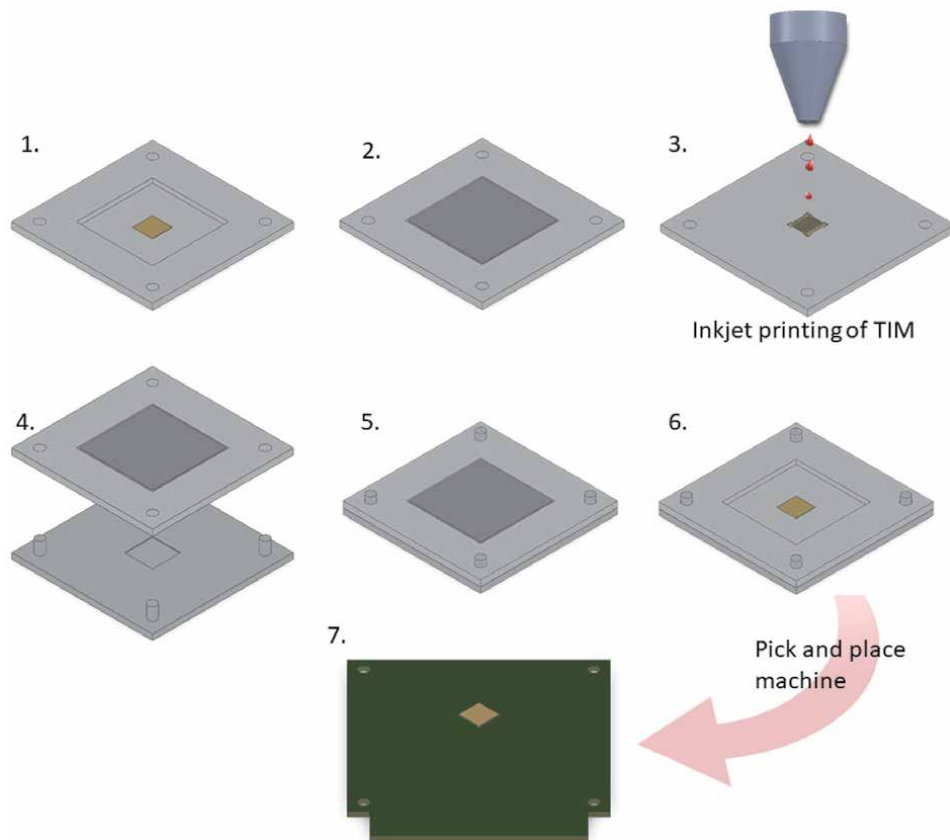
**Figure 19.** Layout of the new compact design featuring 50 thermocouples in serial connection (left) and serial connection of 10 arrangements of 5 thermocouples in parallel configuration (right).



**Figure 20.** Schematic of the different designs of the micromachined Si adapter (left). Heat flux through a parallel type  $\mu$ TEG, the adapter and the heat exchanger (right).

After dispensing the TIM, the adapter is placed face-down onto the thermocouple chip already wirebonded on a PCB. This is done with the help of a pick & place machine (Finetech) that enables proper chip alignment and attachment with a controlled gentle force (0.1 N). A holder with a removable lid for the adequate handling of the Si adapter during the process has been designed and 3D-printed. It allows accessing the corresponding side of the adapter, first to the inkjet printer, and then to the pick & place machine. The whole assembly process is depicted in **Figure 21**.

This is a still ongoing process. Two different inks are being tested to act as TIM between the adapter and the suspended platforms: a conductive silver nanoparticle ink (Agfa Orgacon SI-J20X) and a SU8 based polymeric ink (Micro Chem Prielex). The tests involve the assessment of the adequacy of the viscosity and adhesion of the TIM and the evaluation of the endurance of the  $\mu$ TEGs platforms during the assembly. Other TIM materials already used for the mainstream attachment of heat exchangers onto microprocessors can be also evaluated, as well as other ways of locally dispensing them, such as stamping. In any case, the goal is to obtain an integration route for the heat exchanger, without which no workable  $\Delta T$  would be possible in such miniaturized devices, that is prone to the automatic handling of the



**Figure 21.** New assembly route of the heat exchanger Si adapter onto the encapsulated  $\mu$ TEGs chip.

involved chips and it is compatible with their dimensional and mechanical endurance constraints.

## 5. Conclusions

With this chapter, the authors have tried to show the challenges to sort out when fabricating microgenerators ( $\mu$ TEGs) with planar silicon technologies. Such technologies offer a cost effective way of mass-production of miniaturized devices. However, the very nature of such technologies, the high thermal conductivity of bulk silicon and the typical thickness of the layers involved advises using silicon micromachining to enable areas of lateral thermal contrast. Such transversal architectures helps to translate naturally occurring vertical thermal gradients into internal lateral ones. In this way, a temperature difference will develop across a horizontally and self-standing laid thermoelectric material whose length is a design parameter. A material properties trade-off ensues: the longer the material, the higher its thermal resistance, increasing the attainable  $\Delta T$  and the obtained Seebeck voltage, but the larger will be its electrical resistance, reducing the power obtainable from that voltage. In addition, it has been shown that the overall attainable  $\Delta T$  is heavily influenced by the very poor heat exchange capabilities with the environment of small bare surfaces. Simulations and experiments show that the presence of a heat exchanger largely increase the effective  $\Delta T$ , but brings into play interesting heterogeneous integration challenges still to be fully solved in terms of an effective

but gentle attachment of an intermediate adapter that needs to be designed ad hoc for proper heat flow handling. The presence of the heat exchanger also affects the tilting point of the previously mentioned thermal/electrical trade-off, and thus on the final choice of materials. In the examples given, silicon-based materials have been used (silicon microbeams, silicon and silicon germanium nanowires), but similar structures could be devised for instance for any thermoelectric material in thin film form.

## Acknowledgements

This manuscript contains work supported by projects FP7-NMP-2013-SMALL-7 (Contract n. 604169) SiNERGY, TEC2016-78284-C3-1-R (AEI/FEDER, EU) MINAUTO and TEC2016-78284-C3-2-R (AEI/FEDER, EU) SIGGNAL. This research has made use of the infrastructure of the Spanish ICTS Network MICRONANOFABS (CNM site) partially supported by MINECO. I. Donmez-Noyan thanks the 'Programa de Doctorat en Ciència de Materials de la UAB' for the support in her formative activities.

## Author details

Marc Salleras<sup>1</sup>, Inci Donmez-Noyan<sup>1</sup>, Marc Dolcet<sup>1</sup>, Joaquin Santander<sup>1</sup>, Denise Estrada-Wiese<sup>1</sup>, Jose-Manuel Sojo<sup>2</sup>, Gerard Gadea<sup>2</sup>, Alex Morata<sup>2</sup>, Albert Tarancon<sup>2,3</sup> and Luis Fonseca<sup>1\*</sup>

1 Instituto de Microelectrónica de Barcelona, IMB-CNM (CSIC), Bellaterra, Spain

2 Institut de Recerca de l'Energia de Catalunya, IREC, Barcelona, Spain

3 Institució Catalana de Recerca i Estudis Avançats, ICREA, Barcelona, Spain

\*Address all correspondence to: [luis.fonseca@imb-cnm.csic.es](mailto:luis.fonseca@imb-cnm.csic.es)

## IntechOpen

© 2021 The Author(s). Licensee IntechOpen. This chapter is distributed under the terms of the Creative Commons Attribution License (<http://creativecommons.org/licenses/by/3.0>), which permits unrestricted use, distribution, and reproduction in any medium, provided the original work is properly cited. 

## References

- [1] Ashton A, That 'internet of things' thing, *RFID Journal* 2009. Available from: <https://www.rfidjournal.com/that-internet-of-things-thing> [Accessed: 2020-12-05]
- [2] Newman P, The Internet of Things 2020 Report, BI Intelligence. Preview available from <https://www.businessinsider.com/internet-of-things-report?IR=T> [Accessed: 2020-12-05]
- [3] Whalley S, TSensors and Exponential Abundance. 2017. Available from <https://www.aps.org/units/fiap/meetings/conference/upload/2-1-Whalley-Trillion-sensors.pdf> [Accessed: 2020-12-05]
- [4] Bryzek J, The Trillion Sensors (TSensors) Foundation for the IoT. 2015. Available from <http://www.iot-inc.com/wp-content/uploads/2015/11/2-Janusz.pdf> [Accessed: 2020-12-05]
- [5] Vullers RJM, van Schaijk R, Doms I, Van Hoof C, Mertens R: Micropower energy harvesting. *Solid-State Electronics*. 2009;53:684–693. DOI: 10.1016/j.sse.2008.12.011
- [6] Rowe DM, *CRC Handbook of Thermoelectrics*, CRC Press, 1995
- [7] Champier D: Thermoelectric generators: a review of applications. *Energy Conversion and Management*. 2017;140:167–18., DOI: 10.1016/j.enconman.2017.02.070
- [8] Snyder GJ, *Small Thermoelectric Generators*. 2008. Available from: [https://www.electrochem.org/dl/interface/fal/fal08/fal08\\_p54-56.pdf](https://www.electrochem.org/dl/interface/fal/fal08/fal08_p54-56.pdf) [Accessed: 2020-12-05]
- [9] Hochbaum AI, Chen R, Diaz Delgado R, Liang W, Garnett EC, Najarian M, Majumdar A, Yang P: Enhanced thermoelectric performance of rough silicon nanowires. *Nature*. 2008;451:163–167. DOI: 10.1038/nature06381
- [10] Boukai AI, Bunimovich Y, Tahir-Kheli J, Yu JK, Goddard III WA, Heath JR: Silicon nanowires as efficient thermoelectric materials. *Nature*. 2008; 451:168–171. DOI: 10.1038/nature06458
- [11] Gadea G, Morata A, Santos JD, Davila D, Calaza C, Salleras M, Fonseca L, Tarancon A: Towards a full integration of vertically aligned silicon nanowires in MEMS using silane as a precursor. *Nanotechnology*. 2015; 26:195302. DOI: 10.1088/0957-4484/26/19/195302
- [12] Gadea G, Sojo JM, Pacios M, Salleras M, Fonseca L, Morata A, Tarancon A: Enhanced thermoelectric figure of merit of individual Si nanowires with ultralow contact resistances. *Nano Energy*. 2020;57: 104191. DOI: 10.1016/j.nanoen.2019.104191
- [13] Dávila D, Tarancón A, Kendig D, Fernández-Regúlez M, Sabaté N, Salleras M, Calaza C, Cané C, Gràcia I, Figueras E, Santander J, San Paulo A, Shakouri A, Fonseca L: Planar thermoelectric microgenerators based on silicon nanowires. *Journal of Electronic Materials*. 2011;40(5): 851–855. DOI: 10.1007/s11664-011-1591-3
- [14] Davila D, Tarancon A, Fernandez-Regulez M, Calaza C, Salleras M, San Paulo A, Fonseca L: Silicon nanowire arrays as thermoelectric material for a power microgenerator. *Journal of Micromechanics and Microengineering*. 2011;21:104007. DOI: 10.1088/0960-1317/21/10/104007
- [15] Davila D, Tarancon A, Calaza C, Salleras M, Fernandez-Regulez M, San Paulo A, Fonseca L: Monolithically integrated thermoelectric energy harvester based on silicon nanowire arrays for powering micro/nanodevices.

Nano Energy. 2012;1:812–819. DOI: 10.1016/j.nanoen.2012.06.006

[16] Fonseca L, Santos JD, Roncaglia A, Narducci D, Calaza C, Salleras M, Donmez I, Tarancon A, Morata A, Gadea G, Belsito L, Zulian L: Smart integration of silicon nanowire arrays in all-silicon thermoelectric micro-generators. *Semiconductor Science and Technology*. 2016;31(8):084001. DOI: 10.1088/0268-1242/31/8/084001

[17] Donmez-Noyan I, Gadea G, Salleras M, Pacios M, Calaza C, Stranz A, Dolcet M, Morata A, Tarancon A, Fonseca L: SiGe nanowire arrays based thermoelectric microgenerator. *Nano Energy*. 2019;57:492–499. DOI: 10.1016/j.nanoen.2018.12.050

[18] Ziouche K, Yuan Z, Lejeune P, Lasri T, Leclercq D, Bougrioua Z: Silicon-based monolithic planar micro thermoelectric generator using bonding technology: *Journal of Microelectromechanical Systems*. 2017;26(1):45–47. DOI: 10.1109/JMEMS.2016.2633442

[19] Totaro T, Bruschi P, Pennelli G: Top down fabricated silicon nanowire networks for thermoelectric applications. *Microelectronic Engineering*. 2012;97:157–161. DOI: 10.1016/j.mee.2012.04.007

[20] Li Y, Buddharaju K, Singh N, Lee SJ: Top-Down Silicon Nanowire-Based Thermoelectric Generator: Design and Characterization. *Journal of Electronic Materials*. 2012;41(6):989–992. DOI: 10.1007/s11664-012-1901-4

[21] Tomita M, Oba S, Himeda Y, Yamato R, Shima K, Kumada T, Xu M, Takezawa H, Mesaki K, Tsuda K, Hashimoto S, Zhan T, Zhang H, Kamakura Y, Suzuki Y, Inokawa H, Ikeda H, Matsukawa T, Matsuki T, Watanabe T: Modeling, Simulation, Fabrication, and Characterization of a 10- $\mu\text{W}/\text{cm}^2$  Class Si-Nanowire Thermoelectric Generator for IoT

Applications. *IEEE Transactions on Electron Devices*. 2018;65(11):5180–5188. DOI: 10.1109/TED.2018.2867845

[22] Hu G, Edwards H, Lee M: Silicon integrated circuit thermoelectric generators with a high specific power generation capacity. *Nature Electronics*. 2019;2:300–306. DOI: 10.1038/s41928-019-0271-9

[23] Edwards H, Debord J, Tran T, Freeman D, Maggio, K. A Theory of Thermoelectric Energy Harvesting Systems. In Mescia, L., Losito, O., & Prudenzeno, F. (Ed.), *Innovative Materials and Systems for Energy Harvesting Applications*. IGI Global; 2015. P. 254–270. DOI: 10.4018/978-1-4666-8254-2.ch009

[24] Leonov V, Fiorini P, Vullers RJM: Theory and simulation of a thermally matched micromachined thermopile in a wearable energy harvester. *Microelectronics Journal*. 2011;42(4):579–584. DOI: 10.1016/j.mejo.2010.08.002

[25] Yuan Z, Ziouche K, Bougrioua Z, Lejeune P, Lasri T, Leclercq D: A planar micro thermoelectric generator with high thermal resistance. *Sensors and Actuators A: Physical*. 2015;221:67–76. DOI: 10.1016/j.sna.2014.10.026

[26] Santos JD, Salleras M, Donmez I, Gadea G, Calaza C, Morata A, Tarancon A, Fonseca L: Power Response of a Planar Thermoelectric Microgenerator Based on Silicon Nanowires at Different Convection Regimes. *Energy Harvesting and Systems*. 2016;3(4):335–342. DOI: [doi.org/10.1515/ehs-2016-0019](http://dx.doi.org/10.1515/ehs-2016-0019)

[27] Donmez-Noyan I, Dolcet M, Salleras M, Stranz A, Calaza C, Gadea G, Pacios M, Morata A, Tarancon A, Fonseca L: All-silicon thermoelectric micro/nanogenerator including a heat exchanger for harvesting applications. *Journal of Power Sources*. 2019;413:125–133. DOI: 10.1016/j.jpowsour.2018.12.029





# Transient Thermal Analysis of a Magnetorheological Knee for Prostheses and Exoskeletons during Over-Ground Walking

*Rafhael Milanezi de Andrade, André Palmiro Storch,  
Lucas de Amorim Paulo, Antônio Bento Filho,  
Claysson Bruno Santos Vimieiro and Marcos Pinotti*

## Abstract

Proper knee movement is essential for accomplishing the mobility daily tasks such as walking, get up from a chair and going up and down stairs. Although the technological advances in active knee actuators for prostheses and exoskeletons to help impaired people in the last decade, they still present several usage limitations such as overweight or limited mechanical power and torque. To address such limitations, we developed the Active Magnetorheological Knee (AMRK) that comprises a Motor Unit (MU), which is a motor-reducer (EC motor and Harmonic Drive) and a MR clutch, that works in parallel to a magnetorheological (MR) brake. Magnetorheological fluids, employed in the MR clutch and brake, are smart materials that have their rheological properties controlled by an induced magnetic field and have been used for different purposes. With this configuration the actuator can work as a motor, clutch or brake and can perform similar movements than a healthy knee. However, the stability, control, and life of magnetorheological fluids critically depend on the working temperature. By reaching a certain temperature limit, the fluid additives quickly deteriorate, leading to irreversible changes of the MR fluid. In this study, we perform a transient thermal analysis of the AMRK, when it is used for walking over-ground, to access possible fluid degradation and user's discomfort due overheating. The resulting shear stress in the MR clutch and brake generates heat, increasing the fluid temperature during the operation. However, to avoid overheating, we proposed a mode of operation for over-ground walking aiming to minimize the heat generation on the MR clutch and brake. Other heat sources inside the actuator are the coils, which generate the magnetic fields for the MR fluid, bearings, EC motor and harmonic drive. Results show that the MR fluid of the brake can reach up to 31°C after a 6.0 km walk, so the AMRK can be used for the proposed function without risks of fluid degradation or discomfort for the user.

**Keywords:** magnetorheological fluid, magnetorheological actuator, thermal analysis, prosthesis, exoskeleton

## **1. Introduction**

The gait is severely affected by lower-limb amputation and neuromotor diseases and to compensate the lost limb or impaired legs additional movements are required [1]. Walking and other daily activities, such as going up and down stairs, getting up and sitting down, can be severely impaired, reducing the mobility of the patient [2]. Over the years, researchers seek to develop suitable actuators for assistive lower-limb devices such as prosthesis and exoskeletons [3, 4]. In general, this kind of actuators can be divided into three major groups: passive, semi-active, and active [5, 6]. Passive devices do not require a power source for operation, they are designed for each type of application and do not allow performance adjustments [6]. Semi-active devices only dissipate energy through controllable dampers [7]. Active-type devices, on the other hand, are capable of supplying and dissipating energy in a controlled way [6, 8, 9]. Despite the disadvantages of semi-active and passive prostheses, the number of active prostheses is still small and only the Power Knee™ (PK, Ossur, Iceland) is available on the market. In addition, exoskeleton knee actuators still need to be improved to properly reproduce the knee gait kinematics for low energy consumption. Filho et al. [10], Garcia et al. [11], and Martinez-Villalpando and Herr [6] propose the use of linear actuators with a serial elastic element (SEA) between the femur and the tibia. This configuration has characteristics such as impact tolerance, low mechanical output impedance and passive storage of mechanical energy [12, 13]. However, they are heavy devices with high energy consumption, making it difficult to be used in prostheses or exoskeletons [9, 14].

On the other hand, magneto-rheological fluids (MR) are colloidal solutions composed by up to 50% of their volume of magnetically polarized micro particles mixed with an inert oil, usually mineral-based or silicone-based [15]. When the fluid is subjected to an external magnetic field, its particles begin to form columnar structures parallel to the magnetic flux lines; this behavior changes the rheological properties of the fluid, such as yield stress and others, in a reversible and proportional way to the induced magnetic field [16]; the response time is in order of milliseconds [17]. Due to these characteristics, MR fluids are used to develop devices for many applications in engineering and industry: vehicle suspensions [18], clutches [19], brakes [20], structural vibration damping [21], intelligent prosthesis [5, 22–24] and others. MR devices usually present low energy consumption and high torque-to-weight ratio [25, 26], which is important to increase the energy efficiency and reduce the weight of prostheses and exoskeletons' actuators [27].

Although the advances in actuators technology, the active actuators used in robotic devices are still heavy and bulky [28], and the passive and semi-active ones cannot properly reproduce the movement of a healthy knee. To address the shortcomings of the knee actuators, we developed the Active Magneto-Rheological Knee (AMRK) [29, 30]. The actuator employs a motor-unit (MU), composed by an EC 60 flat motor (Maxon Motors, Switzerland), harmonic drive CSG-14-100-2a (Harmonic Drive AG, Germany) and MR clutch, that works in parallel to a MR Brake. With this configuration the actuator has multifunctional working conditions and can reproduce movements similar to a healthy knee with low energy consumption [25, 26]. The system is assembled in a lightweight and compact structure and can be used as a prosthetic knee, a knee actuator for exoskeletons and in robotic functions [30].

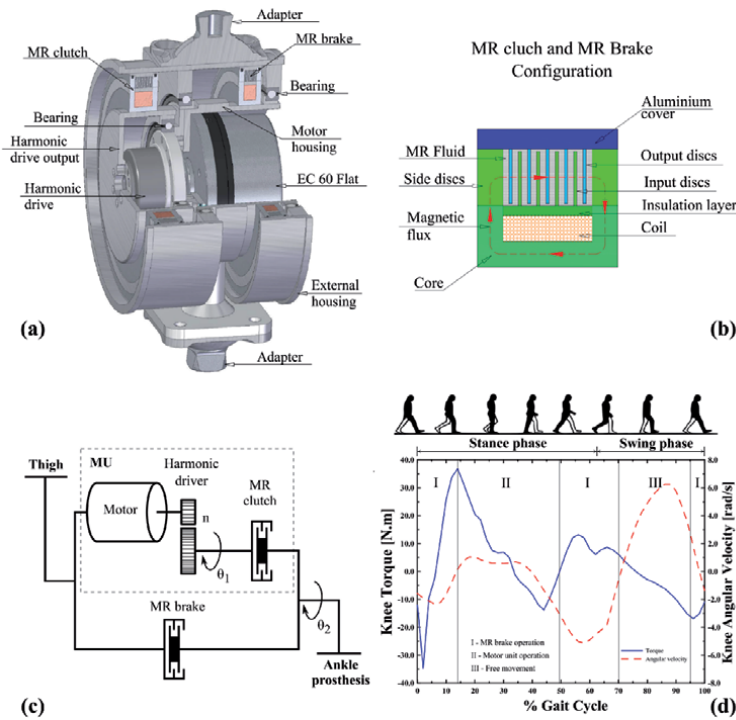
The MR Clutch and MR Brake of the AMRK present multi-disc configuration to improve the torque-to-mass ratio and compactness. With this configuration, the systems can work in full-slip and non-slip conditions. In the full-slip regime, there is a relative movement between the input and output and the torque is transmitted by the shear stress of the MR fluid [31], which is responsible for high heat generation. When in non-slip condition, there is no relative movement between the input

and output and the system works as a solid unit [32]. In this case, the heat generation is due just by Joule effect on the coil. The properties of the MR fluid strongly depend on the temperature, for this reason, the fluid shows different performances with the temperature variation [33]. The viscosity of the fluid changes with temperature variation, which results in a change in its shear stress. Moreover, MR fluids use additives to decrease sedimentation and increase the dispersion of particles, and such additives are also sensitive to temperature variation, some of it decompose when reaching about 100°C [34]. Moreover, cyclic operation under high and low temperatures can lead to irreversible changes in the MR fluid. It can run-out its rheological properties, leading to uncontrolled shear stress due to the influence of material agglomeration under magnetic field conditions [33]. Since high temperature deteriorates the MR fluid, the full-slip operation is the most critical working condition for the MR clutch and MR brake [35]. Some works in the literature present methodologies to evaluate how these properties change with temperature [36]. Chen et al. [33] proposed an experimental setup to evaluate an MR transmission under different temperatures, obtaining a set of torque and temperature curves with different current inputs. Zipster et al. [37] proposed an experimental setup that analyzes the MR fluid in flow mode, under different temperatures. Wang et al. [34] made a complete characterization of the MR fluid under different temperatures. Here we present a transient thermal analysis of the AMRK under over-ground working conditions to evaluate if the heat generation can deteriorate the MR fluid or be dangerous for the user. Since the full-slip operation increases heat production, we proposed an operating mode for the AMRK that minimizes the heat dissipation on the MR clutch and brake to avoid high working temperatures.

## 2. The active MR knee

The AMRK configuration is presented in **Figure 1**. The system consists of a motor unit (MU) (EC 60 flat motor, harmonic reducer CSG-14-100-2a and MR clutch) mounted in parallel to an MR brake, and can work as a motor, clutch and brake. This configuration allows the actuator to be controlled independently by the MU or by the brake MR, exploring thereby the advantages of each subsystem. The device is supported by two main structures: The external structure connects to the upper part of the prosthesis/exoskeleton, the internal one connects to the lower part of the prosthesis/exoskeleton through adapters. A pair of thin section bearings allows relative movement between the external and internal structures. The structures are made of 7075 aluminum alloy [5], as shown in **Figure 1(a)**. **Figure 1(b)** displays the configuration of the MR clutch and MR brake. The dynamic model of the AMRK is presented in **Figure 1(c)**, and the proposed actuator operating modes for over-ground walking are shown in **Figure 1(d)**.

The MR brake is housed between the external and internal structures and dissipates energy just when the knee joint should exert negative work during over-ground walking, operating mode I in **Figure 1(d)**. The MR brake is designed with a multi-disc configuration and hollow iron core to reduce mass and increase torque capacity [38], as displayed in **Figure 1(b)**. The output disks are connected to the aluminum cover, which is attached to the external structure of the actuator. The output disks are assembled interlayered with the input disks, which are attached to the iron core that is coupled to the internal structure. The MR fluid fills the space between disks. The magnetic field induced by the coil controls the yield stress of the MR fluid; in this way, the MR fluid can behave as a semi-solid or a Newtonian fluid depending on the action of the magnetic field. Consequently, the resistive torque of the brake is controlled by the input current on the brake coil [39].



**Figure 1.** The AMRK configuration and operation modes. (a) Cutaway view of the actuator. (b) configuration of the MR clutch and MR brake. (c) Dynamic model of the system. (d) Operating mode for over-ground walking used in the transient thermal analysis.

Active torque of the AMRK is required just when the knee exerts positive work, operating mode II in **Figure 1(d)**, and it is produced by the MU that comprises an EC motor, a harmonic drive (HD) and an MR clutch. The motor and HD stators are attached to the internal structure and the HD output is connected to the iron core of the MR clutch. The MR clutch has the same working principle as the MR brake, that is, when the magnetic field is activated, the MR fluid yield stress increases and prevents the relative movement between input and output disks. Thus, the torque produced by the motor-reducer is transferred to the external structure of the actuator controlled by the input current on the clutch coil. During swing phase, the knee rotates freely achieving high angular velocity. It can be accomplished by the AMRK as long as the MU is deactivated and the MR brake exerts low resistive torque to stabilize the joint, operating mode III in **Figure 1(d)**.

The torque supported by the MR brake and clutch follows the shear equation of a fluid between disks with relative angular movement [40], as shown below:

$$T = \int_{r_i}^{r_o} \tau_{MR} r_D dA \quad (1)$$

where  $\tau_{MR}$  is the shear stress of the MR fluid,  $r_D$  is the radius of the disks, and  $A$  is the effective contact area between disks and MR fluid. The contact area can be described in terms of the number of gaps ( $N$ ) filled by the MR fluid, and the internal ( $r_i$ ) and external ( $r_o$ ) radii of the disks. In addition, MR fluids behave like an ideal plastic fluid or Bingham plastic when subjected to magnetic field. Then the previous equation can be rewritten as:

$$T = 2N\pi \left[ \frac{\tau_y}{3} (r_o^3 - r_i^3) + \frac{\omega\mu_{MR}}{4h} (r_o^4 - r_i^4) \right] \quad (2)$$

where  $\tau_y$  is the yield stress of the MR fluid, which is a function of the magnetic field strength and can be obtained from the manufacturer's catalog,  $\mu_{MR}$  is the MR fluid viscosity,  $h$  is the gap thicknesses and  $\omega$  is the angular velocity of the disks.

As the magnetic circuit is composed by a set of elements in series, the magnetic flux is uniform throughout the circuit [41]. As the desired value for the magnetic flux density in the MR fluid area ( $B_{MR}$ ) is a design parameter, the magnetic flux can be described as follows:

$$\varphi = \pi (r_o^2 - r_i^2) B_{MR} \quad (3)$$

Similarly, the magnetic flux of a given circuit can also be described as a function of the number of coil's turns ( $N_b$ ), the current ( $I$ ) and the equivalent reluctance of the circuit ( $R_{eq}$ ) [41]:

$$\varphi = \frac{N_b I}{R_{eq}} \quad (4)$$

It worth noting that Eqs. (3) and (4) are just valid as long as there is no magnetic saturation in any elements of the magnetic circuit.

Eqs. (1)–(4) are used to construct a parametrized model to optimize the design variables (see [5]) for more details). **Table 1** presents the optimized value of the design variables after optimization process.

Variable	Optimal Value	
	MR Brake	MR Clutch
$T$ [N m]	35.0	55.4
$r_o$ [mm]	54	
$r_i$ [mm]	48.5	
$N$ [gaps]	14	20
$B_{MR}$ [T]	0.45	0.50
$I$ [A]	2.1	1.8
$N_t$ [turns]	164	226
$\tau_y$ [kPa]	27.3	30.3
$R_c$ [ohm]	4.34	6.05
$P$ [W]	19.2	19.6
$M$ [kg]	0.37	0.46

**Table 1.**  
 MR brake and MR clutch variables.

### 3. Thermal model of the actuator

In this section we present the procedure adopted to build the thermal model for the AMRK to carry out a transient temperature simulation across a long walk over the ground. We set up a model for each element that comprises the actuator: EC motor, harmonic drive, MR clutch, MR brake, bearings and housing. The detailed method used is described in the following subsections.

#### 3.1 Motor-reducer model

According to Maxon's Key Information for DC and EC motors [42], the losses of efficiency in the motor are divided into losses due to friction,  $P_{mec}$ , and due to the Joule effect,  $P_J$ , of the winding, which has resistance  $R_a$ . The energetic balance can be treated as:

$$P_{el} = P_{mec} + P_J \quad (5)$$

where  $P_{el}$  is the electrical power of the motor. The dissipation of power due Joule effect is given by:

$$P_J = R_a \cdot I_a^2 \quad (6)$$

where  $I_a$  is the input current in the motor armature.

The thermal properties of the motor are given by the supplier catalog. We considered the EC 60 flat model 411,678 for the analysis. The temperature of the motor housing can be predicted when the free surfaces are submitted to air as in [43]:

$$P_J = \frac{T_s - T_\infty}{R_{th2}} \quad (7)$$

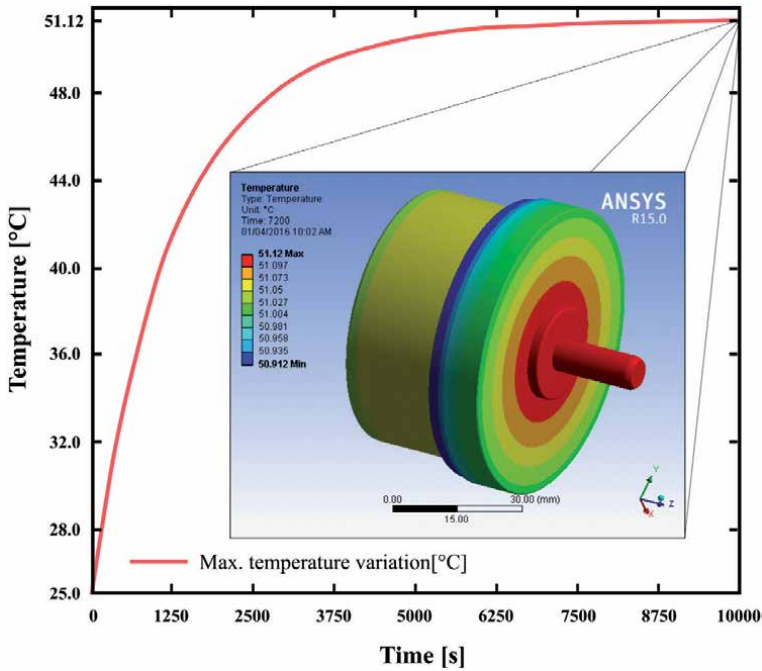
where  $T_s$  is the surface temperature,  $T_\infty$  is the environment temperature (25°C), and  $R_{th2}$  is the thermal resistance between the surface and the environment, which is given by the supplier catalog, and can also be described by the following equation [43]:

$$R_{th2} = \frac{1}{h_{comb} A_S} \quad (8)$$

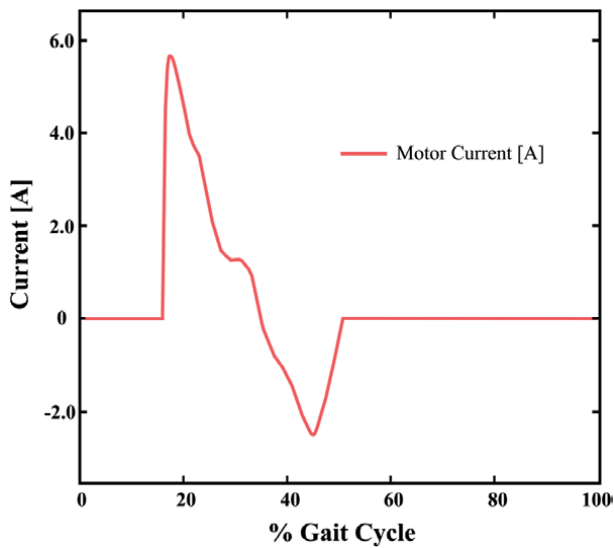
where  $h_{comb}$  is the combined heat transfer coefficient for convection and radiation and  $A_S$  is the heat transfer surface area. By rearranging Eq. (8), and considering the motor assembled in a plastic plate to reproduce the standard cooling conditions, as described in [44], the coefficient  $h_{comb} = 1.72 \times 10^{-5} \text{ W}/(\text{mm}^2 \text{ }^\circ\text{C})$  is obtained.

In order to validate the EC 60 motor thermal model to be used in the actuator, a transient simulation of the motor's temperature is shown in **Figure 2**. The external surface of the motor reaches a maximum temperature of 51.12°C in about 7200 s, which is very close to the temperature obtained by the Eq. (7) (51.15°C), thereby validating the used method.

As previously described, the motor is used just when positive work of the knee joint is required. For intermittent work, the supplier recommends using the average input current,  $I_{RMS}$ , in the motor armature during the cycle operation. The input current variation for the proposed working modes (**Figure 1(d)**) is presented in **Figure 3**.



**Figure 2.** Simulation of the motor's external temperature in nominal operating conditions. The highlighted color map represents the steady state temperature of the motor's surface.



**Figure 3.** Input current in the motor armature during the gait cycle.

We carried out a simulation considering the input current in the motor for the intermittent operating condition due to the gait cycle. A constant temperature of 28.86°C was obtained after 2 hours.

Regarding the harmonic drive, the heat generation ( $P_{HD}$ ) occurs basically due friction between its movable parts and it can be calculated as follows:

$$P_{HD} = \tau_f \omega N \tag{9}$$

where  $\tau_f$  is the friction torque that can be gathered from the supplier datasheet (Harmonic Drive AG, Germany), and  $\omega$  is the angular velocity of the knee joint, as shown in **Figure 1(d)**, and  $N$  is the HD reduction ratio ( $N = 100$ ). The presented intermittent working conditions for the CSG-14-100-2a, results in a RMS heat generation of 1.04 W.

### 3.2 MR clutch and MR brake

The proposed operating modes for the AMRK during over-ground walking consider that the MR clutch works in non-slip condition when the magnetic field is activated and in full-slip condition when no transmitting torque is required. Since the power is dissipated as heat in the MR fluid region and it is a function of the torque and the angular velocity between disks, the MR clutch does not present heat generation in the fluid area. On the other hand, the MR brake is always subjected to the full-slip operation and generates heat in the MR fluid region. However, the brake just works when braking torque or joint stabilization is required, thereby minimizing the heat generation.

The fluid used in the prototype is the MRF-140 CG, which has a recommended working temperature between  $-40^\circ\text{C}$  and  $130^\circ\text{C}$ , according to the manufacturer. However, Chen et al. [33] reported that there is a reduction in the yield stress of the MR fluid at temperatures around  $100^\circ\text{C}$ , due to the deterioration of some additives. For this reason, it is safe to limit the working temperature of the MR fluid to  $100^\circ\text{C}$ . Heat generation due to the sliding condition is given by [35]:

$$\dot{\Phi}_d = \frac{T\omega}{V_f} \quad (10)$$

where  $\dot{\Phi}_d$  is the volumetric generation of heat in the fluid,  $T$  and  $\omega$  are the torque and angular velocity of the knee, respectively, and  $V_f$  is the volume of the fluid.

The loss of electrical power due to the Joule effect on the coil can be written as [35].

$$\dot{\Phi}_c = \frac{I^2 R_C}{V_c} \quad (11)$$

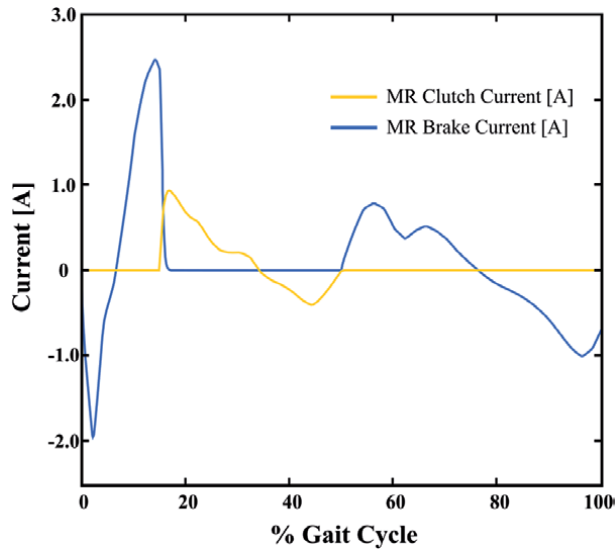
where  $\dot{\Phi}_c$  is the volumetric generation of heat in each coil,  $I$  is the electric current in the coil,  $R_C$  is the resistance of the coil, and  $V_c$  is the volume of the coil. The electrical current variation in the MR clutch/brake coils during the gait cycle for the proposed working modes is shown in **Figure 4**.

The other components to be modeled are the bearings and the convection coefficient on the free surfaces of the actuator. According to the NTN bearing catalog [45], bearing friction becomes a cause of heat generation that must be considered. Eq. (12) describes the heat generation applied to the bearings.

$$\dot{\Phi}_B = \frac{1.05 \times 10^{-4} \mu P d \Delta \omega}{2V_B} \quad (12)$$

where  $\dot{\Phi}_B$  is the volumetric heat generation in the bearing,  $\mu$  is the friction coefficient given by the manufacturer's datasheet,  $P$  is the load to which the bearing is subjected,  $\omega$  is the knee joint angular velocity,  $d$  is the inner diameter of the bearing, and  $V_B$  is the volume of the bearing.





**Figure 4.**  
*Input current on the MR Clutch and MR Brake coils during the gait cycle.*

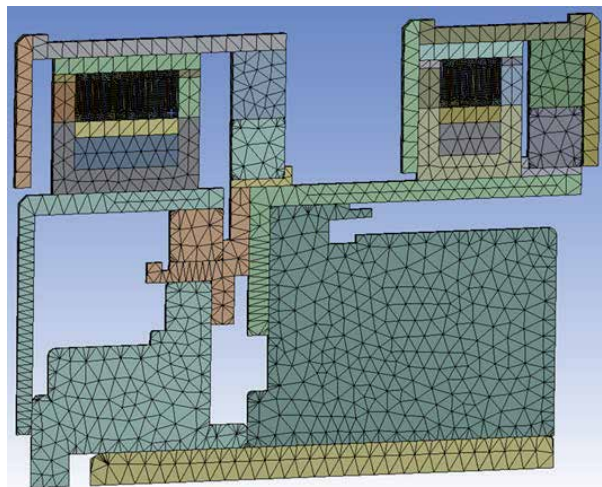
Natural convection and radiation are also considered for the components whose surfaces are exposed to the air. The heat transfer coefficient,  $h_T$ , composed by radiation and natural convection, is given by:

$$h_T = h_c + h_r \quad (13)$$

where  $h_c$  is the natural convection coefficient and  $h_r$  is the heat radiation coefficient. Here we considered  $h_T = 9.7 \times 10^{-6} \text{ W}/(\text{mm}^2 \text{ } ^\circ\text{C})$  [35].

### 3.3 FEM analysis

The 3D modeling of the AMRK is shown in **Figure 5**. Since the actuator presents an axisymmetric configuration, a part corresponding to 1/360 of the actuator was



**Figure 5.**  
*AMRK Discretized model reduced to 1/360 to improve time processing.*

Variable	Value
Motor heat generation	7.83E-6 W/mm <sup>3</sup>
Harmonic drive heat generation	3.83E-5 W/mm <sup>3</sup>
MR Brake coil heat generation	1.81E-4 W/mm <sup>3</sup>
MR Clutch coil heat generation	2.22E-5 W/mm <sup>3</sup>
Large bearings heat generation	3.98E-7 W/mm <sup>3</sup>
Small bearing heat generation	4.51E-7 W/mm <sup>3</sup>
MR fluid heat generation (MR brake)	1.03E-3 W/mm <sup>3</sup>
Motor heat transfer coefficient <sup>1</sup>	1.72E-5 W/mm <sup>2</sup> °C
Heat transfer coef. remaining components <sup>1</sup>	9.70E-6 W/mm <sup>2</sup> °C

<sup>1</sup>Room temperature = 25°C.

**Table 2.**  
Boundary conditions for the transient thermal analysis simulation.

simulated, to reduce the processing time. Unstructured tetrahedral elements were used for the model's mesh. Considering the dimensional differences of the actuator components, after a heuristic analysis of the actuator's mesh, different mesh sizes were adopted to obtain an acceptable precision of the results with reduced processing time. Mesh size for the MR fluid regions was 0.25 mm and for the other components we used mesh size of 2 mm.

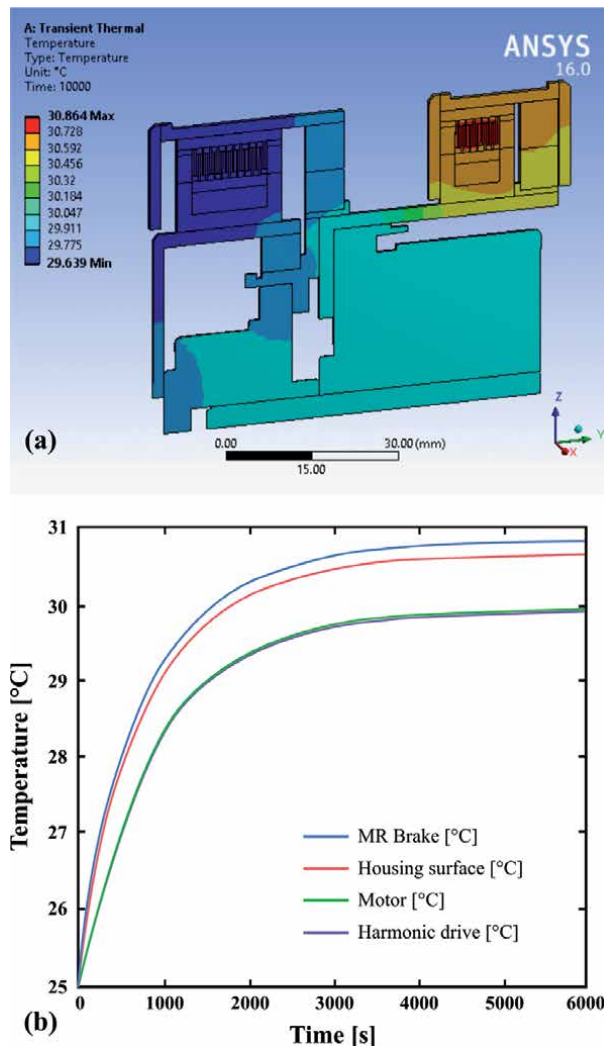
To perform the transient thermal analysis, the AMRK is subjected to the operating modes presented in **Figure 1(d)** for 10,000 seconds, which represents 10.0 km walk, to reach the steady state condition. In such a simulation when the MU is activated, operating mode II, the EC motor, HD, MR clutch coil and bearings are the heat sources. When the MR brake is activated, operating mode I and III, the MR fluid and the brake coil and the larger bearings are the heat sources. The values of the boundary conditions are given in **Table 2**.

## 4. Results and discussion

After build the thermal model of the AMRK, we carried out a transient thermal analysis considering the actuator is subjected to over-ground walking for a long period of time. The initial temperature of the actuator and environment was 25°C. **Figure 6(a)** presents the temperature color map for the steady state condition and **Figure 6(b)** shows the temperature variation across time in each component of the actuator.

After 6000 s of simulation, which represents a 6.0 km walk, the AMRK reached the steady state temperature distribution, **Figure 6(b)**. The simulation ran up to 10,000 s, but no change in the temperature distribution was observed, as presented in **Figure 6(a)**. The MR fluid is considered the most sensible element of the actuator to temperature rise and must be carefully evaluated. Moreover, for safe operation, it is important that the temperature of the copper wire does not exceed 150°C and the actuator's housing surface temperature does not exceed 43°C, so it does not cause injury to the user [46].

The maximum temperature observed after the simulation time was 30.86°C in the MR fluid region of the MR brake. As previously mentioned, the MR brake works in full-slip condition and dissipate energy as heat in the MR fluid region. The full-slip operation is the most critical condition for heat generation in MR fluid-based



**Figure 6.** Transient thermal analysis of the AMRK. (a) Temperature color map for steady state condition. (b) Temperature variation of actuator's components over time.

devices and can lead to critical temperatures [41]. However, unlike the common applications of shear transmissions, the proposed operating modes for the AMRK just activate the MR brake, which works in full-slip condition, when the knee is subjected to negative work, thereby reducing the heat generated. The MR clutch, as previously mentioned, works in non-slip condition and the heat is generated by Joule effect in the coil and not in the fluid area. Compared to previous applications of MR fluid-based transmissions, such as the shear transmission of Chen et al. [33] and the MR clutches proposed in Wang et al. [35, 41] and Leal-Junior et al. [36], where the temperature reached more than 120°C in full-slip condition, the temperature reached by the AMRK while working with the proposed operating modes, is not critical to the MR fluid integrity. On the other hand, from a braking torque control point of view, a more careful analysis should evaluate if this temperature increase can affect torque capacity of the MR brake. To improve the braking torque control in a rising temperature scenario a temperature-dependent shear stress, as proposed in [35], should be taken in to account.

The maximum temperature reached in the motor and harmonic drive was 29.94°C and 29.92°C, respectively, which are within the working limit temperature recommended by the supplier's catalog, up to 125°C and 120°C, respectively. The maximum temperature reached on the surface of the actuator was 30.68°C, which is not harmful to human skin [46]. These results validate the purpose usage of the AMRK as an actuator for knee replacement/assistance for over-ground walking.

## **5. Final remarks**

This work presented the thermal analysis of the Active Magneto-Rheological Knee actuator (AMRK) for lower-limb prostheses and exoskeletons. The AMRK is composed by a motor unit (EC motor, harmonic drive, and MR clutch), responsible for generating positive work, that works in parallel to a MR brake, used to dissipate energy when the knee is subjected to negative work conditions. The proposed configuration is designed to perform a proper walk with low energy consumption [25, 26]. The thermal model for the components of the MR actuator was presented. EC motor, harmonic drive, MR clutch, MR brake, and bearings were modeled to assess the thermal behavior of the knee when subjected to a long walk over the ground. The results indicate that the proposed operating modes are effective to avoid actuator overheating. The maximum temperatures reached in each component are within the tolerances established by the suppliers and no damage is caused to the system, as well as to the MR fluid. The external steady state temperature of the actuator is about 31°C, which does not represent risk for the user. Future work will consider evaluating the temperature of the system under more severe working conditions, such as going up and down stairs.

## **Acknowledgements**

This research was partially funded by grants from FAPES (Fundação de Amparo à Pesquisa e Inovação do Espírito Santo) TO 0480/2015 Project No. 67637574/15, TO 207/2018 Project No. 83276262, and TO 151/2021 Project No. 2021-8GJZ6. The authors honor Marcos Pinotti (in memoriam) for his important contribution to this work.

## **Conflict of interest**

The authors declare that there is no conflict of interest.

## Author details

Rafhael Milanezi de Andrade<sup>1,2\*</sup>, André Palmiro Storch<sup>1</sup>, Lucas de Amorim Paulo<sup>1</sup>, Antônio Bento Filho<sup>1</sup>, Claysson Bruno Santos Vimieiro<sup>2,3</sup> and Marcos Pinotti<sup>2</sup>

1 Laboratory of Robotics and Biomechanics, Department of Mechanical Engineering, Universidade Federal do Espírito Santo, Vitória, ES, Brazil

2 Bioengineering Laboratory, Department of Mechanical Engineering, Graduate Program in Mechanical Engineering, Universidade Federal de Minas Gerais, Belo Horizonte, MG, Brazil

3 Graduate Program in Mechanical Engineering, Pontifícia Universidade Católica de Minas Gerais, Belo Horizonte, MG, Brazil

\*Address all correspondence to: [rafhaelmilanezi@gmail.com](mailto:rafhaelmilanezi@gmail.com)

## IntechOpen

© 2020 The Author(s). Licensee IntechOpen. This chapter is distributed under the terms of the Creative Commons Attribution License (<http://creativecommons.org/licenses/by/3.0>), which permits unrestricted use, distribution, and reproduction in any medium, provided the original work is properly cited. 

## References

- [1] Cappozzo A, Figura F, Gazzani F, Leo T and Marchetti M, Angular displacements in the upper body of AK amputees during level walking *Prosthet. Orthot. Int.* 6 131-8, 1982.
- [2] Fatone S, Stine R, Gottipati P and Dillon M, Pelvic and spinal motion during walking in persons with transfemoral amputation with and without low back pain *Am. J. Phys. Med. Rehabil.* 95 438-47, 2016.
- [3] Bogue, R., *Robotic exoskeletons: a review of recent progress*, *Industrial Robot: An International Journal*, V. 42, n. 1, p. 5 – 10, 2015.
- [4] Pieringer, D. S., Grimmer, M., Russold, M. F. and Riener, R. “Review of the actuators of active knee prostheses and their target design outputs for activities of daily living,” Jul. 2017.
- [5] Andrade RM, Bento Filho A, Vimieiro CBS, and Pinotti M (2018) Optimal design and torque control of an active magnetorheological prosthetic knee. *Smart Materials and Structures* 27:105031.
- [6] Martinez-Villalpando. E. C., Her, H., 2009, Agonist-antagonist active knee prosthesis: A preliminary study in level-ground walking, *J.Rehabilitation Res. Development*, 46, 361-374;
- [7] Lauwerys, C., Swevers, J. and Sas, P., 2002, Linear control of car suspension using nonlinear actuator control, *Proceedings do ISMA2002*, Leuven-Bélgica;
- [8] Geng, Y., Yang, P., Xu, X., Chen, L., 2012 Design and simulation of Active Transfemoral Prosthesis. 24th Chinese Control and Decision Conference (CCDC). p. 3724-3728.
- [9] Andrade RM and Bonato P (2021) The Role Played by Mass, Friction, and Inertia on the Driving Torques of Lower-Limb Gait Training Exoskeletons. *IEEE Transactions on Medical Robotics and Bionics*, V. 3, n. 1, pp. 125-136, Feb. 2021. doi: 10.1109/TMRB.2021.3052014.
- [10] Filho, A. B., Andrade, R. M., Matos, M. C., 2014, Digital Prototyping of a Series Elastic Actuator for Exoskeletons, CONEM 2014;
- [11] Garcia, E., Arevalo, J. C., Munoz, G., 2011, On the biomimetic design of agile-robot legs. *Sensors*, Basel, Switzerland, 11, 11305;
- [12] Leal-Junior, A. G. ; Andrade, R. M. ; Bento Filho, A. *Series Elastic Actuator: Design, Analysis and Comparison. Recent Advances in Robotic Systems*. 1ed., InTech, p. 203-234, 2016a.
- [13] Fiorezi, GG.; Moraes, JS.; Ulhoa, PHF.; Andrade, RM *Biomimetic Design of a Planar Torsional Spring to an Active Knee Prosthesis Actuator Using FEM Analysis*, *Proceedings 2020*, V. 64, n. 1:30. Doi: 10.3390/IeCAT2020-08505.
- [14] Leal-Junior, A. G. ; Andrade, R. M. ; Bento Filho, A., *Linear Serial Elastic Hydraulic Actuator: Digital Prototyping and Force Control*, *IFAC-PapersOnLine*, 48 (6), 2015, 279-285.
- [15] Vicente, J. De, Klingenberg, DJ., Hidalgo-Alvarez, R. *Magnetorheological fluids: a review*. *Soft Matter*, v. 7, p. 3701-3710, 2011.
- [16] Leal-Junior, A. G., Campos, V., Díaz, C., Andrade, R. M., Frizera, A., Marques, C., A machine learning approach for simultaneous measurement of magnetic field position and intensity with fiber Bragg grating and magnetorheological fluid, *Optical Fiber Technology*, V. 56, 2020, 102184.
- [17] Yang, G., 2001, Large-scale magnetorheological fluid damper

for vibration mitigation: modeling, testing and control, PhD Dissertation University of Notre Dame, Indiana, USA.

[18] Sung, K. G., and Choi, S. B., 2008, Effect of an electromagnetically optimized magnetorheological damper on vehicle suspension control performance, *Proc. Inst. Mech. Eng.*, 222, 2307-19;

[19] Kavlicoglu, B. M., Gordaninejad, F., Evrensel, C., Fuchs, A. and Korol, G., 2006, A semi-active magnetorheological fluid limited slip differential clutch, *Trans. ASME, J. Vib. Acoust.*, 128, 604-10;

[20] Nguyen, Q. H. and Choi, S. B., 2010, Optimal design of an automotive magnetorheological brake considering geometric dimensions and zero-field friction heat, *Smart Mater. Struct.*, 19, 115024;

[21] Takashi, T., Sano, A., 2005, Fully Adaptive Vibration Control for Uncertain Structure Installed with MR Damper , American Control Conference, 2005. Proceedings of the 2005, 7, 4753 – 4759;

[22] Carlson, J. D., Matthis, W. and Toscano, J. R., 2001, Smart prosthetics based on magnetorheological fluids, *Proc. SPIE*, 4332, 308-16;

[23] Dong, S. F., Lu, K. Q., Sun, J. Q. and Rudolph, K., 2005, Rehabilitation device with variable resistance and intelligent control, *Med. Eng. Phys.*, 27, 249-55;

[24] Dong, S. F., Lu, K. Q., Sun, J. Q. and Rudolph, K., 2006, A prototype rehabilitation device with variable resistance and joint motion control, *Med. Eng. Phys.*, 28, 348-55;

[25] Andrade RM, Martins, JSR., Pinotti M, Bento Filho A and Vimieiro CBS (2021) Novel active magnetorheological knee prosthesis presents low energy

consumption during ground walking. *Journal of Intelligent Material Systems and Structures.* doi:10.1177/1045389X20983923

[26] M. Andrade, A. B. Filho, C. B. S. Vimieiro and M. Pinotti, “Evaluating Energy Consumption of an Active Magnetorheological Knee Prosthesis,” 2019 19th International Conference on Advanced Robotics (ICAR), Belo Horizonte, Brazil, 2019, pp. 75-80, doi: 10.1109/ICAR46387.2019.8981642

[27] Chen, J. Z.; Liao, W. H., 2006, A leg exoskeleton utilizing a magnetorheological actuator. Proceedings of IEEE International Conference on Robotics and Biomimetics. p. 824-829.

[28] Bento-Filho A, Tonetto CP, Andrade RM (2021) Four legged Guar robot: from inspiration to implementation, *Journal of Applied and Computational Mechanics.* doi:10.22055/JACM.2021.35212.2613.

[29] Andrade RM, (2018) Joelho magneto-reolgico para prteses transfemurais: prototipagem digital, fabricao e identificao experimental. Doctoral Thesis, Federal University of Minas Gerais, Belo Horizonte, May 2018. Available: <https://repositorio.ufmg.br/handle/1843/BUBD-AZ2MNM>.

[30] Andrade RM, Bento Filho A, Vimieiro CBS, and Pinotti M (2016) Atuador magneto- reolgico para prteses, exoesqueletos e outras aplicaoes robticas e uso. BR Patent Application BR102016024912A2.

[31] Kowol, P., Pilch, Z., 2015, Analysis of the magnetorheological clutch working at full slip state, *PRZEGLD ELEKTROTECHNICZNY*, 91, 108-111.

[32] Andrade, R. M., Paulo, L. A., Bento Filho, A., Vimieiro, C., 2017. Transient Thermal Analysis of a MR Clutch for Knee Prostheses and Exoskeletons,

- in: Proceedings of the 24th ABCM International Congress of Mechanical Engineering. <https://doi.org/10.26678/ABCM.COBEM2017.COB17-0311>
- [33] Chen, S., Huang, J., Jian, K., Ding, J., 2015, Analysis of Influence of Temperature on Magnetorheological Fluid and Transmission Performance, *Advances in Materials Science and Engineering*, 2015, 1-7.
- [34] Wang, D., Zi, B., Zeng, Y., Hou, Y., Meng, Q., 2014, Temperature-dependent material properties of the components of magnetorheological fluids, *J Mater Sci*, 49, 8459-8470.
- [35] Wang, D., Zi, B., Zeng, Y., Xie, F., Hou, Y., 2015, An investigation of thermal characteristics of a liquid-cooled magnetorheological fluid-based clutch, *Journal of Smart Materials and Structures*, 24, 1-13.
- [36] Leal-Junior, A. G. ; Andrade, R. M. ; Bento Filho, A. Transient Thermal Analysis Of A Magnetorheological Clutch. In: 16th Brazilian Congress of Thermal Sciences and Engineering - ENCIT 2016b.
- [37] Zipster, L., Richter, L., Lange, U., 2001, Magnetorheologic fluids for actuators, *Sensors and Actuators A*, 92, 318-325.
- [38] Rossa, C., Jaegy, A., Lozada, J., Micaelli, A. Design Considerations for Magnetorheological Brakes. *IEEE/ASME Transactions on Mechatronics*, v. 19, p. 1669-1680, 2014. DOI: 10.1109/TMECH.2013.2291966
- [39] Andrade RM, Sapienza S, and Bonato P (2019b) Development of a “transparent operation mode” for a lower-limb exoskeleton designed for children with cerebral palsy. *IEEE International Conference on Rehabilitation Robotics (ICORR)*. 512-517. doi:10.1109/ICORR.2019.8779432.
- [40] Guo, H. T., and Liao, W. H., 2012, A novel multifunctional rotary actuator with magnetorheological fluid, *Smart Mater. Struct.*, 21, 065012, (9pp);
- [41] Wang D and Hou Y 2013 Design and experimental evaluation of a multidisk magnetorheological fluid actuator *J. Intell. Mater. Syst. Struct.* 24 640-50.
- [42] Maxon DC motor and maxon EC motor Key information. Maxon Group. Available in: [https://www.maxongroup.com/medias/sys\\_master/8815460712478.pdf?attachment=true](https://www.maxongroup.com/medias/sys_master/8815460712478.pdf?attachment=true)
- [43] Cengel, Y. A., 2002, *Heat Transfer: A Practical Approach*, Second Edition. McGraw-Hill.
- [44] Craiu, O., Machedon, A., Tudorache, T., Morega, M., Modreanu, M., 2010, 3D Finite Element Analysis of a Small Power PM DC Motor, 12th International Conference on Optimization of Electrical and Electronic Equipment;
- [45] NTN Ball and Roller Bearings (Cat. No. 2203/E), NTN Corporation. Available in: <https://www.ntnglobal.com/en/products/catalog/en/2203/index.html>
- [46] Moritz, A. R., Henriques Jr., F. C., 1947, Studies of thermal injuries: II The relative importance of time and surface temperature in the causation of cutaneous burns. *AM J Pathol*; 23:695-720.



# Experimental Approaches to Measurement of Vapor Quality of Two-Phase Flow Boiling

*Mehdi Kabirnajafi and Jiajun Xu*

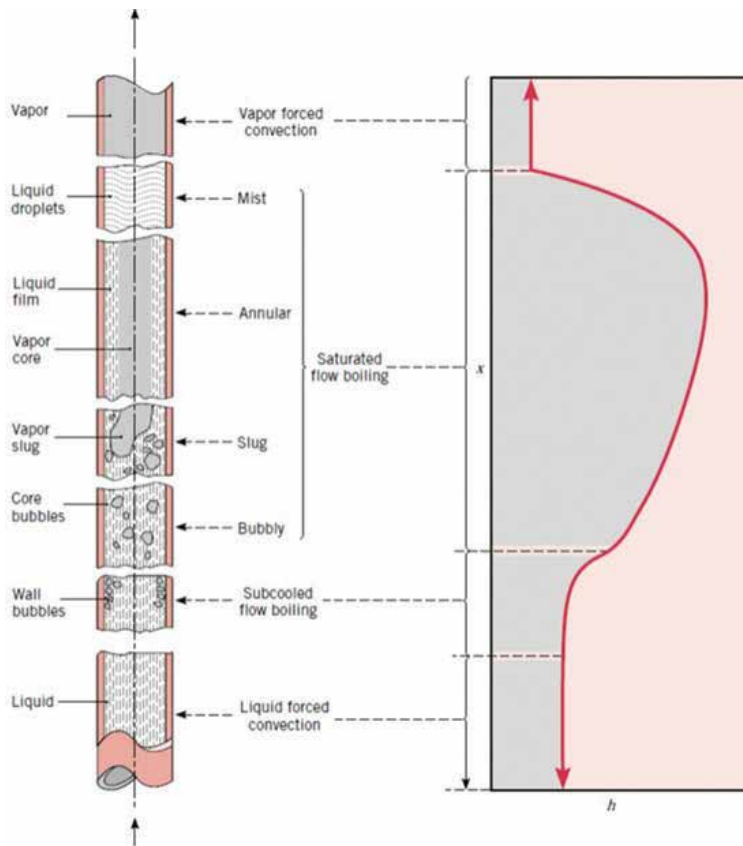
## Abstract

Vapor quality is one of the crucial parameters substantially affecting the flow boiling heat transfer coefficient. Hence, the reliability and accuracy of vapor quality measurements is of a great significance to accurately investigating the effect of vapor quality on the local flow boiling heat transfer coefficients. In the present study, various experimental approaches are represented to measure and control local vapor quality for flow boiling tests. Experimental approaches are classified based on the type of thermal boundary conditions imposed on the tube wall, that is, known constant wall heat flux and constant wall temperature (unknown variable wall heat flux). In addition, in-situ techniques are also investigated to measure local vapor quality regardless of the governing thermal boundary conditions within two-phase flow experiments. Finally, the experimental methodologies are compared based on their level of reliability and accuracy in measurement, costliness and affordability, and simplicity in execution to address their potential merits and demerits.

**Keywords:** vapor quality measurement, experimental methodologies, two-phase flow boiling, thermal boundary conditions

## 1. Introduction

Vapor quality is a crucial parameter which affects the flow boiling heat transfer behavior [1, 2]. **Figure 1** shows flow development inside a vertical tube under a constant wall heat flux, where the fluid moves in the upward direction. The figure also depicts various two-phase flow regimes in a vertical tube on the left and typical variations in local boiling heat transfer coefficient versus vapor quality on the right. From **Figure 1**, it can be inferred that flow boiling heat transfer coefficient is typically maximized in the range of vapor quality between 50% and 85%, while the smallest heat transfer coefficients tend to appear in the vapor forced convection region due to the low thermal conductivity of vapor as compared to that of the liquid. Accordingly, the accuracy of vapor quality measurements plays a significant role in properly investigating the impact of vapor quality on the local flow boiling heat transfer coefficient. On the other hand, in order to develop more efficient two-phase flow heat transfer systems, a specific range of vapor qualities should be targeted in design of thermal systems to achieve a higher range of boiling heat transfer coefficients. This also clearly highlights the significance of accurate vapor quality measurements at both the inlet and outlet of a test section.



**Figure 1.** Typical variations in heat transfer coefficient with vapor quality for forced-convection flow boiling in a tube [1].

Hardik and Prabhu [3] performed experiments to investigate the heat transfer and pressure drop of a diabatic two-phase water flow boiling in horizontal thin walled stainless steel tubes with different inner diameters under uniform wall heat flux conditions. To investigate the impact of vapor quality on the local boiling heat transfer coefficient, they measured vapor quality at the outlet of test section using a known range of uniform wall heat fluxes directly supplied by electrical heating tapes wrapped around the test sections. The effect of inlet vapor quality was not investigated in their study since a saturated liquid flow was provided at the inlet of test sections. In their study, the heat losses from the heating tapes were estimated using theoretical calculations of convective and radiative heat losses from the surface of test sections to the surroundings, and no single-phase experiments were conducted to empirically estimate heat losses at the same mass flux range of flow boiling tests.

A similar approach to measurement of outlet vapor quality was adopted by Yan *et al.* in two different studies [4, 5] to investigate the influence of crucial parameters, consisting of heat flux, mass flux, and vapor quality on the heat transfer performance of water flow boiling in a uniformly heated vertical nickel alloy tube as well as in a vertical 304 stainless steel (SS304) tube with twisted tape inserted under high heat flux conditions.

Although many experimental studies have been conducted to date to investigate the impact of local vapor quality on boiling heat transfer performance, majority of these studies have taken the similar approach to measure local vapor quality

only at the outlet of test section mainly under uniform wall heat flux boundary conditions using electrical heating [6–12]. There are limited studies investigating the effect of local vapor quality for other thermal boundary conditions [13, 14], while their techniques to measure local vapor quality are not reported clearly. Hence, there is a considerable gap in the literature concerning vapor quality measurement under other thermal boundary conditions (e.g. uniform wall temperature and unknown boundary conditions) than the uniform wall heat flux using electrical heating.

The measurement and control of local vapor quality for uniform wall heat flux conditions using heating tapes wrapped around the test section is simpler than that for uniform wall temperature or variable wall heat flux conditions where the latent heat for two-phase flow boiling is supplied by a hot-side fluid at test section. In the latter case, there is no opportunity for a direct control of vapor quality at test section unless using in-situ measurements of local density through the existing instruments with a currently low accuracy.

Concerning the existing gaps in the literature addressed above, the present study aims to investigate various experimental approaches to measure and control vapor qualities at both the inlet and outlet of a typical test section under different thermal boundary conditions imposed on a test section during two-phase flow boiling heat transfer process, including uniform wall temperature, uniform wall heat flux, and unknown boundary conditions. The experimental techniques are then compared based on their level of accuracy and overall uncertainty, costliness, as well as simplicity in implementation.

## 2. Heat loss considerations

Measurements of local vapor quality of a saturated boiling flow can strongly be affected by accuracy in estimating the heat losses and calibrating the latent heat supplies. This is due to the existence of latent heat during a boiling process with a constant saturation temperature of fluid while enthalpy increases with the increase of local vapor quality as a result of heat acquisition [1, 2]. This is therefore evident that inaccurate estimation of heat losses and imprecise calibration of latent heat supplies would pose unreliability in collected heat transfer data and large errors in results as well.

Although different theoretical and experimental approaches have been engaged to date to estimate heat loss during flow boiling, majority of these methods are based on the estimation of heat loss from single-phase flow [6, 9–15]. Indeed, single-phase experiments were conducted to estimate heat loss percentages for a range of mass fluxes and heat fluxes. Then, the same heat loss percentages derived from the single-phase flow were directly used for two-phase flow at the same mass fluxes [6, 9–11]. Alternatively, the heat losses extracted from single-phase flow for a range of mass and heat fluxes were developed for flow boiling over another range of mass and heat fluxes using either interpolation or extrapolation [12, 13, 15].

In this commonly applied methodology, the amounts of heat experimentally supplied for the test section ( $Q_{suppl}$ ) to increase the temperature of single-phase flow from a known value of  $T_{sp, in}$  at the inlet to another known value of  $T_{sp, out}$  at the outlet are monitored and recorded for a range of flow rates. On the other hand, the actual amounts of heat transferred to the fluid ( $Q_{transf}$ ) can be calculated by the following energy balance for a range of flow rates:

$$Q_{transf} = \dot{m} C_p (T_{sp, out} - T_{sp, in}) \quad (1)$$

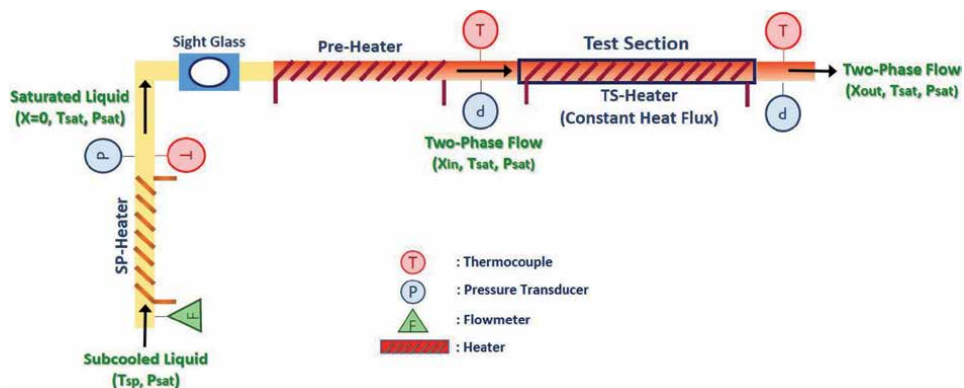
The difference between  $Q_{suppl}$  and  $Q_{transf}$  reveals the heat losses ( $Q_{loss} = Q_{suppl} - Q_{transf}$ ). A correlation is then developed by plotting the variations of heat transferred to the fluid ( $Q_{transf}$ ) versus heat supplied ( $Q_{suppl}$ ), which can be used for calibrating the heat supplies as an imperative step to further measure vapor qualities within the flow boiling tests.

### 3. Experimental approach for known uniform wall heat flux boundary conditions

After estimating heat losses and calibrating heat supplies for any of electrical heater units in a test setup, local vapor qualities at the inlet and outlet of a test section can be measured by energy balance on the enthalpy change of vaporization. **Figure 2** depicts the schematics of a typical setup to conduct measurements of vapor qualities under known constant wall heat flux boundary conditions using the electrical heating either through the direct resistance heating of the test tube or with the heating tapes wrapped around the tube.

As shown in **Figure 2**, while inlet vapor quality can be controlled using the heat-supplying unit located right before the test section (called Pre-Heater), local vapor quality at the outlet of test section may be controlled from the heat-supplying unit at the test section (called TS-Heater). The subcooled liquid at a certain pressure of  $P_{sat}$  with a bulk temperature of  $T_{sp}$  is warmed up by a heat-supplying unit (i.e. SP-Heater) in order to reach the state of saturated liquid ( $x = 0\%$ ) at the saturation temperature of  $T_{sat}$  corresponding to the system pressure of  $P_{sat}$ . Using the Pre-Heater located right before the test section, the saturated liquid therefore reaches a certain vapor quality at the inlet of the test section ( $x_{in}$ ) and is afterwards exposed to a known constant wall heat flux supplied by the TS-Heater at the test section to reach a two-phase flow of higher vapor quality at the outlet ( $x_{out}$ ), and then keeps recirculated.

To ensure the state of saturated liquid, the subcooled liquid is warmed up by the SP-Heater to reach a temperature infinitesimally lower than the saturation temperature of  $T_{sat}$  targeted for the flow boiling experiments. Using the sight glass shown in **Figure 2**, the state of saturated liquid is also directly observed in order to check whether or not there is any vapor bubble in the saturated liquid flow.



**Figure 2.** The experimental approach to measuring vapor qualities for uniform wall heat flux boundary conditions.

As represented in **Figure 2**, the inlet vapor quality is measured and controlled by adjusting the calibrated heat supplied by the Pre-Heater to take the saturated liquid ( $x = 0$ ) to the two-phase flow with a desired inlet quality of  $x_{in}$  as follows:

$$Q_{calib-pre} = (Q_{suppl-pre} - Q_{loss-pre}) = \dot{m} (h_{x[in]} - h_{f(x=0)}) \quad (2)$$

where  $h_x$  accounts for the enthalpy at vapor quality of  $x$ ,  $Q_{suppl-pre}$  is the heat experimentally supplied by the Pre-Heater,  $Q_{loss-pre}$  is the corresponding heat loss from this heat-supplying unit, and  $Q_{calib-pre}$  stands for the calibrated heat which is actually transferred to the boiling flow. Having the enthalpy of saturated liquid ( $h_{f(x=0)}$ ) known, the only unknown parameter in Eq. (2) is the enthalpy at the inlet of the test section from which the inlet vapor quality can simply be derived at the operating saturation temperature and pressure.

After having the inlet vapor quality known, the outlet vapor quality can be measured from the calibrated heat at the test section (TS-Heater) as follows:

$$Q_{calib-ts} = (Q_{suppl-ts} - Q_{loss-ts}) = \dot{m} (h_{x[out]} - h_{x[in]}) \quad (3)$$

where  $Q_{suppl-ts}$  is the heat experimentally supplied by the heating unit at the test section,  $Q_{loss-ts}$  is the corresponding heat loss from this heat-supplying unit, and  $Q_{calib-ts}$  stands for the calibrated heat which is actually transferred to the boiling flow. Having the inlet quality already measured, the only unknown parameter in Eq. (3) is the enthalpy at the outlet of the test section ( $h_{x[out]}$ ) from which the outlet vapor quality can be extracted at the operating saturation temperature and pressure.

This is important to point out that the outlet vapor quality derived from the test section contains an accumulated error arisen from earlier measurement of the inlet vapor quality. As clearly shown in Eq. (2), the inlet vapor quality can be measured and controlled by obtaining the enthalpy at the inlet of test section ( $h_{x[in]}$ ), which contains the uncertainties in measurement of mass flow rate ( $\dot{m}$ ), bulk fluid temperature ( $T_{sat}$ ), and calibrated heat supplies by the Pre-Heater ( $Q_{calib-pre}$ ). This measured value of inlet vapor quality ( $h_{x[in]}$ ) is used as a known parameter in Eq. (3) to obtain the vapor quality at the outlet of test section ( $h_{x[out]}$ ). The measured value of outlet vapor quality, in turn, contains uncertainties in measurement of bulk fluid temperature and calibrated heat supplies by the test section heater ( $Q_{suppl-ts}$ ) in addition to the earlier measurement error imposed by the value of inlet vapor quality, which eventually leads to the accumulation of more errors in measurement of outlet vapor quality through Eq. (3) as compared to that of inlet vapor quality.

#### 4. Experimental approaches for unknown variable heat flux or constant wall temperature boundary conditions

In the case of constant wall temperature boundary conditions for the test section, the wall heat flux is subject to change. The measurement and control of local vapor quality at the outlet of a test section under uniform wall temperature boundary conditions is more challenging than that of uniform wall heat flux boundary conditions. In a single loop of internal flow boiling, the outlet vapor quality is typically measured and controlled by directly monitoring the constant amounts

of surface heat flux provided by heating tapes wrapped around the test section. However, the use of hot fluid heating rather than electrical heating to generate constant wall temperature conditions does not allow the direct control of outlet vapor quality due to the unknown variable surface heat flux exchanged between the hot-side fluid (e.g. external condensation of steam or single-phase hot liquid) and the cold-side fluid (i.e. internal flow boiling).

#### 4.1 Approach I: auxiliary after-heater

**Figure 3** illustrates a typical case of constant temperature boundary conditions imposed by external condensation of steam on the test tube. The test section shown in this case is the place where external condensation and internal flow boiling occur simultaneously. The test section therefore functions as a cross flow heat exchanger whose both sides are manipulated with phase-change heat transfer processes. The test apparatus for this arrangement is to consist of two closed loops, including: external condensation loop (i.e. steam condensation over a horizontal tube) and internal boiling loop (i.e. two-phase flow boiling inside the tube).

Within the external condensation loop, saturated vapor of water at saturation temperature and pressure of  $T_{\text{sat,steam}}$  and  $P_{\text{sat,steam}}$  is provided by a steam generator and then enters the test chamber. After condensation of steam on the horizontal test tube due to the temperature difference between the saturated vapor and the tube surface (called subcooling), the condensate is driven by gravity and collected in a condensate reservoir to feed the steam generator and set a steady flow circulation in the external condensation loop. Regarding the internal boiling loop, the fluid is warmed up by the SP-Heater in order to reach the saturated liquid state ( $x = 0$ ) at the saturation temperature and pressure of  $T_{\text{sat}}$  and  $P_{\text{sat}}$ , respectively ( $T_{\text{sat}} < T_{\text{sat,steam}}$ ). Using the Pre-Heater located right before the test section, the saturated liquid therefore reaches a certain vapor quality at the inlet of the test section ( $x_{\text{in}}$ ) and is afterwards exposed to the latent heat released from the external condensation side to reach an unknown higher vapor quality at the outlet ( $x_{\text{out}}$ ).

The unknown outlet vapor quality can be measured by adding a calibrated heat-supplying unit (After-Heater) with power controller installed right after the test section in order to take the two-phase flow with unknown outlet quality to the known state of saturated vapor (i.e.  $x = 100\%$ ) at the same saturation temperature of  $T_{\text{sat}}$ . In this case, the energy balance is dictated as follows:

$$Q_{\text{calib-after}} = (Q_{\text{suppl-after}} - Q_{\text{loss-after}}) = \dot{m} (h_{g(x=1)} - h_{x[\text{out}]}) \quad (4)$$

where  $Q_{\text{suppl-after}}$  stands for the heat experimentally supplied by the After-Heater,  $Q_{\text{loss-after}}$  is the corresponding heat loss from this heat-supplying unit, and  $Q_{\text{calib-after}}$  accounts for the calibrated heat which is actually transferred to the boiling flow. Having the enthalpy of saturated vapor ( $h_{g(x=1)}$ ) known, the only unknown parameter in Eq. (4) is the enthalpy at the outlet of the test section ( $h_{x[\text{out}]}$ ) from which the outlet vapor quality can be extracted at the operating saturation temperature and pressure. Similar to the case of constant wall heat flux boundary conditions stated earlier, the inlet vapor quality can independently be measured and controlled by adjusting the calibrated heat supplied by the Pre-Heater using the Eq. (2).

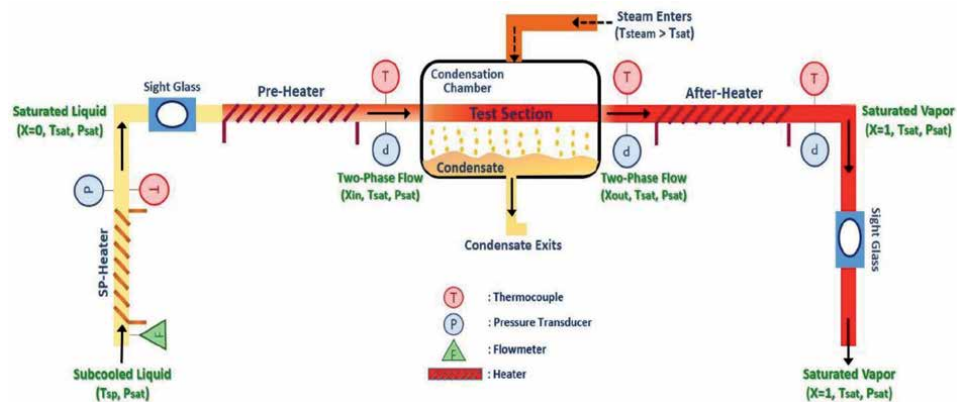
In this approach, to ensure the state of saturated vapor, the After-Heater located after the test section is adjusted to supply the required latent heat for the two-phase flow with a certain outlet quality to reach a temperature slightly higher than the constant saturation temperature, which would be the starting point of the superheated vapor state. As shown in **Figure 3**, using the sight glass installed after the

After-Heater, the state of saturated vapor is also directly observed in order to check whether or not there is any liquid droplet and/or humidity in the gas stream at the beginning of superheated state. Unlike the earlier approach to measuring local vapor quality at the outlet of test section under uniform wall heat flux conditions, this approach does not contain any accumulated errors arising from earlier measurements of inlet vapor qualities.

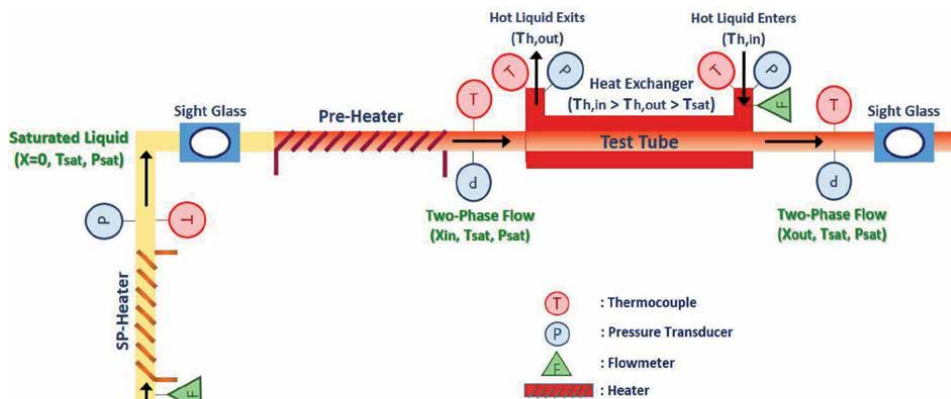
## 4.2 Approach II: auxiliary heat exchanger

In the second methodology for variable wall heat flux conditions, a tube-in-tube or shell-and-tube heat exchanger installed at the test section may be used for measuring and controlling local vapor quality at the outlet of test tube. Analogous to the earlier cases, the inlet vapor quality is measured and controlled by monitoring the calibrated heat supplied by the Pre-Heater using the Eq. (2).

As represented in **Figure 4**, a hot liquid single-phase flow with known mass flow rates and known temperatures and pressures at the inlet and outlet passes through



**Figure 3.**  
 The experimental approach to measuring vapor qualities for uniform wall temperature boundary conditions.



**Figure 4.**  
 The experimental approach to measuring vapor qualities for variable wall heat flux boundary conditions.

the outer tube (shell side), while the boiling flow of a known inlet vapor quality with a saturation temperature ( $T_{\text{sat}}$ ) lower than that of the heating liquid ( $T_h$ ) enters the inner tube of the counter-flow heat exchanger. After latent heat acquisition from the hot-side fluid, the internal boiling flow undergoes an unknown increase in vapor quality at the outlet of test tube whereas the heating liquid in the shell side experiences a temperature reduction as a result of sensible heat rejection yet its temperature at the outlet remains higher than the constant saturation temperature of internal boiling flow. The vapor quality at the outlet of the test tube can therefore be controlled by adjusting the mass flow rate of the hot liquid single-phase flow ( $\dot{m}_h$ ) at the shell side of the counter-flow heat exchanger.

The amounts of heat exchanged between the internal boiling flow and the heating liquid can be measured by writing down an energy balance as follows:

$$Q_{\text{rejected}} = \dot{m}_h C_p (T_{h,\text{in}} - T_{h,\text{out}}) = Q_{\text{gained}} = \dot{m} (h_{x[\text{out}]} - h_{x[\text{in}]}) \quad (5)$$

Aside from  $h_{x[\text{out}]}$ , all the other parameters in Eq. (5) are known. The enthalpy at the outlet of the test section ( $h_{x[\text{out}]}$ ) can thus be calculated and the vapor quality at the outlet of the test tube can be measured and controlled subsequently. Similar to the approach engaged to the uniform wall heat flux boundary conditions, the outlet vapor quality derived from this approach contains an accumulated error arisen from earlier measurement of the inlet vapor quality.

To keep the boiling fluid recirculated, this is evident that other components are required for the internal boiling loop, which are not shown in **Figures 2–4**. Subsequent to the test section or the After-Heater, the two-phase flow with a certain outlet quality or the saturated vapor is required to be condensed in a heat exchanger to reach the state of saturated liquid which is followed by a drop in temperature and pressure after passing through an expansion valve to reach the state of subcooled liquid prior to entering the pump in order to avoid the cavitation phenomenon. The liquid flow is then squeezed by a gear pump up to the desired saturation pressure to enter the SP-Heater.

## 5. In-situ measurement for any thermal boundary conditions

Regardless of the type of thermal boundary conditions governed on the test section, the local vapor quality of a two-phase flow boiling may be obtained through in-situ measurements.

Using the experimental approaches and/or instruments introduced here, first, the local density of two-phase flow at either of the inlet or outlet of a test section can be measured in-situ for any thermal boundary conditions that might be imposed on the test section. After obtaining the density, two independent thermodynamic properties of the flow at either inlet or outlet are known (*i.e.* density and either of saturation temperature or corresponding pressure) in order to look up the enthalpy of the two-phase flow at either inlet or outlet ( $h_{x[\text{in}]}$  or  $h_{x[\text{out}]}$ ). Having the local enthalpies known, the local vapor quality ( $x$ ) can be readily obtained via  $h_x = h_{f(x=0)} + x h_{fg}$  as the only unknown parameter left here. However, this is important to note that the accuracy of this approach is lower than those of the earlier approaches described so far in the present study due to the less accuracy of the limited experimental methodologies [16] and instruments [17–19] introduced to date to measure density of a two-phase flow.

Interest in the determination of two-phase flow density has brought about the design and development of various instruments to measure density in cryogenic flow



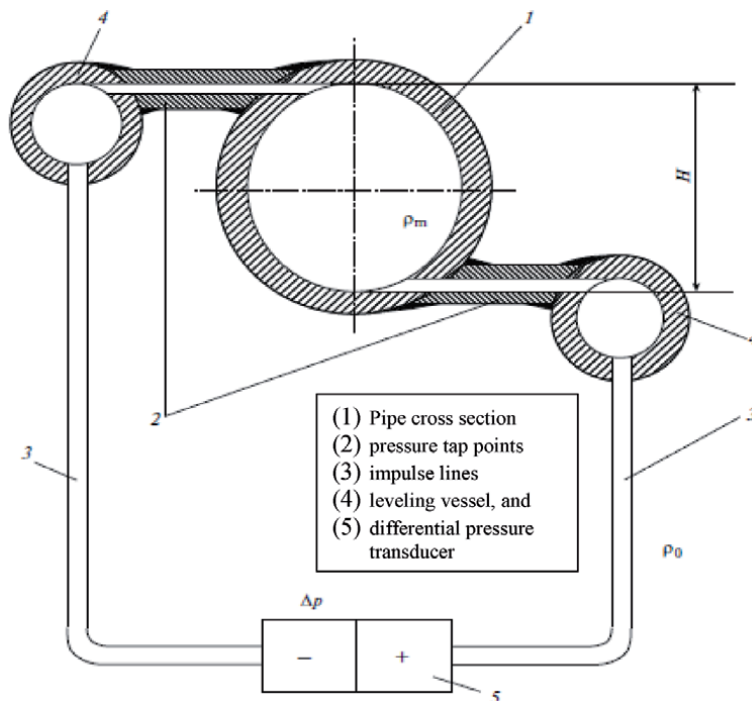
systems. The more promising of the methods suggested are based on either (i) measurements of the average dielectric constant or capacitance of the two-phase fluid or (ii) measurements of the nuclear radiation attenuation properties of the two-phase fluid. In principle, both of these measurable quantities are associated with the fluid density.

Turney and Snyder [17] used a capacitance density meter to measure the density of liquid and two-phase hydrogen flow. Most of their measured and calculated values of density exhibited a deviation up to  $\pm 15\%$  of the full-scale density. The advanced Coriolis meters have also been investigated for measurement of two-phase flow density [18, 19]. In this context, Reizner [18] has addressed the issues concerned to metering two-phase flow using the Coriolis meters. Technically, this is hard to retain flow-tube oscillations within two-phase flow due to the high and rapid damping of oscillations which is, by far, up to three orders of magnitude higher than that of the single-phase flow. Once the transmitter is not capable of maintaining the oscillations, the Coriolis meter is found to be “stalled”, and no measurements are provided. Even in the case of averting the stalling, large errors in measurements of mass flow and density are induced.

Although there is no specific instrument to accurately measure density of a two-phase flow, the technique(s) recently introduced by Boltenko [16] can measure the density with a reasonable accuracy. The range of uncertainty reported for his technique(s) is between 3% and 5%.

The following is a brief explanation of the proposed techniques to measure local density of a two-phase flow:

- i. *Gamma-raying Technique:* The method of Gamma-raying makes it possible to measure density of a two-phase flow both in steady and transient flow regimes as well as makes it possible to carry out ongoing record of  $\rho(t)$  with averaging over the time intervals which are remarkably shorter than the typical duration of an unsteady process ( $\tau > 0.1$  s) [20].



**Figure 5.** Schematic of the hydrostatic method to determine density of a two-phase flow [16].

- ii. *Hydrostatic Technique*: The hydrostatic method to determine the density of a two-phase flow is performed by the measurement of static pressures at two points of a channel. After measuring the static pressure difference between these two pressure tapping points, the average density of the two-phase flow can be obtained by the following correlation [21]:

$$\bar{\rho} = \frac{(\Delta P_{st} - \Delta P_{hyd})}{g H} \quad (6)$$

in which  $g$  is the gravitational acceleration,  $H$  is the pipe diameter,  $\Delta P_{hyd}$  accounts for the hydraulic resistance between the pressure tap points, and  $\Delta P_{st}$  stands for the hydrostatic pressure difference between the pressure tap points.

As can be seen from Eq. (6), it is possible to obtain  $\bar{\rho}$  only if  $\Delta P_{hyd}$  is known. Hence, the hydrostatic technique may be employed to measure  $\bar{\rho}$  for test sections with horizontal orientation. In the case of horizontal test tube  $\Delta P_{hyd} = 0$ , and then Eq. (6) reduces to:

$$\bar{\rho} = \frac{\Delta P_{st}}{g H} \quad (7)$$

**Figure 5** depicts schematics of the hydrostatic technique to measure the average density of a two-phase flow in a horizontal pipe.

## 6. Merits and demerits

In this section, the experimental approaches are sought to be compared based on their level of accuracy in measurement, affordability, and simplicity in implementation. Remarks, including merits and demerits, are expressed for each experimental technique described in the earlier sections in sequence.

### 6.1 Remarks on the approach for uniform wall heat flux conditions

The approach described in Section 3 is restricted to the investigation of the impact of local vapor quality on the heat transfer performance under known constant wall heat flux boundary conditions. Although the method is very affordable and simple to be implemented, accuracy of this methodology to measure local vapor quality is reliant heavily on the accuracy in estimating heat losses and calibrating heat supplies. Furthermore, it is important to note that the measurement of local vapor quality at the outlet of test section using this technique contains an accumulated error arisen from earlier measurement of local vapor quality at the inlet according to Eq. (3).

On the other hand, the measurement of flow boiling heat transfer data for horizontal test tubes using electrical heating has always been a subject of debate [22], where hot fluid heating is preferred to be used. In this regard, the following concerns are needed to be addressed: (i) for different types of stratified flow pattern, hot fluid heating induces practically uniform wall temperature boundary conditions for the tube perimeter, whereas electrical heating contributes to the circumferential heat conduction for the tube perimeter from the hot, dry-wall conditions at the top to the colder, wet-wall conditions at the bottom of the tube, leading to unknown thermal boundary conditions, (ii) for annular flow pattern with partial dryout at the top of the tube, electrical heating is not also advised due to the axial heat conduction along the tube.

## **6.2 Remarks on the approach I for constant wall temperature conditions**

Using the approach I described in Section 4.1, higher accuracy and lower uncertainty in vapor quality measurements can be achieved by conducting accurate estimation of heat losses as well as accurate calibration of heat supplies. Furthermore, measurement of local vapor quality at the outlet of test section using this technique does not contain any accumulated errors arising from earlier measurements of inlet vapor quality as represented in Eq. (4). This is while the approach is very affordable and simple in execution.

Taking advantage of the After-Heater located after the test section, this technique does not interfere with heat transfer data collected from the test section and does not pose the issues of circumferential and axial heat conduction caused by electrical heating for stratified and annular flow patterns within the test section.

## **6.3 Remarks on the approach II for variable wall heat flux conditions**

The approach II described in Section 4.2 is more expensive than the earlier techniques presented. The method is also not as simple as the earlier techniques in implementation. Using this approach, there is still accumulated error in measurement of outlet vapor quality arisen from the earlier measurement of inlet vapor quality, according to Eq. (5).

Moreover, the main drawback is that the methodology is likely to pose a higher overall uncertainty in measuring the local vapor qualities as compared to the earlier techniques described in Sections 3 and 4.1 since there will be higher number of points to be measured for temperature, pressure, and mass flow rate as indicated in Eq. (5). In this technique, five more precision instruments are required to be in service in order to measure flow rate of the hot-side fluid (one flow sensor), pressures (two pressure transducers), and temperatures (two thermocouple probes) at the inlet and outlet of the shell side of heat exchanger.

## **6.4 Remarks on the approaches for any thermal boundary conditions**

The major drawback of the in-situ measurements is that the techniques and/or instruments introduced to date pose a low accuracy to measure local density of a two-phase flow, which ultimately makes the overall uncertainty for vapor quality measurements undesirable. In addition, very accurate and expensive pressure transducers and/or expensive advanced Coriolis meters are required to be procured to implement this technique properly.

## **7. Conclusions**

Vapor quality plays a key role in flow boiling heat transfer behavior and can noticeably affect the local flow boiling heat transfer coefficient. To accurately investigate the effect of vapor quality on flow boiling behavior, accurate measurement of local vapor quality is critical.

In the present study, various experimental techniques were presented to measure and control vapor quality for flow boiling tests and were classified based on the type of thermal boundary conditions induced on the test tube wall. Moreover, in-situ measurements and techniques were also investigated to measure local density of two-phase flow and subsequently local vapor quality regardless of the governing thermal boundary conditions.

To provide a deeper insight to select an appropriate technique depending on researchers' choices, the experimental techniques were also compared based on their level of accuracy in measurement, affordability, and simplicity in implementation through addressing their potential weaknesses and strengths.

## **Acknowledgements**

We would like to acknowledge the financial support from NASA MUREP Institutional Research Opportunity Grant under Cooperative Agreement #80NSSC19M0196, National Science Foundation (NSF) for supporting this work via grant (HRD-1601156), and Department of Defense under contract: W911NF-20-1-0274.


## **Author details**

Mehdi Kabirnajafi and Jiajun Xu\*  
Center for Advanced Manufacturing in Space Technology and Applied Research (CAM-STAR), University of the District of Columbia, Washington, D.C., USA

\*Address all correspondence to: [jiajun.xu@udc.edu](mailto:jiajun.xu@udc.edu)

## **IntechOpen**

---

© 2020 The Author(s). Licensee IntechOpen. This chapter is distributed under the terms of the Creative Commons Attribution License (<http://creativecommons.org/licenses/by/3.0>), which permits unrestricted use, distribution, and reproduction in any medium, provided the original work is properly cited. 

## References

- [1] Bergman T.A., Levine A.S., Incropera F.P., Dewitt D.P., *Fundamentals of Heat and Mass Transfer*, John Wiley & Sons Inc., 7<sup>th</sup> Edition, 2011, ISBN 13 978-0470-50197-9.
- [2] Kabir M.M., Lee S., Investigation of the Effects of Simultaneous Internal Flow Boiling and External Condensation on the Heat Transfer Performance, Proceedings of ASME 2019 International Mechanical Engineering Congress and Exposition, IMECE2019-10697, V008T09A004, Nov. 2019, Salt Lake City, Utah.
- [3] Hardik BK, Prabhu SV. Boiling pressure drop and local heat transfer distribution of water in horizontal straight tubes at low pressure. *Int. J. Thermal Sciences*. 2016;**110**:65-82
- [4] Yan J, Bi Q, Liu Z, Zhu G, Cai L. Subcooled flow boiling heat transfer of water in a circular tube under high heat fluxes and high mass fluxes. *Fusion Engineering and Design*. 2015;**100**:406-418
- [5] Yan J, Bi Q, Cai L, Zhu G, Yuan Q. Subcooled flow boiling heat transfer of water in circular tubes with twisted-tape inserts under high heat fluxes. *Experimental Thermal and Fluid Science*. 2015;**68**:11-21
- [6] Lu Q, Chen D, Li C, He X. Experimental investigation on flow boiling heat transfer in conventional and mini vertical channels. *Int. J. Heat Mass Transf.* 2017;**107**:225-243
- [7] Trinh V, Xu J. An Experimental Study on Flow and Heat Transfer Characteristics of Ethanol/ Polyalphaolefin Nanoemulsion Flowing Through Circular Minichannels. *Nanoscale Research Letters*. 2017;**12**:216. DOI: 10.1186/s11671-017-1984-1
- [8] Poudel N., Acar M., Tran T., Xu J., An Experimental and Numerical Study of Convective Boiling of Nanoemulsion Inside Mini-Channels Heat Exchanger. Proceedings of ASME 2016 International Mechanical Engineering Congress and Exposition. Phoenix, Arizona. Nov. 11-17, 2016, V008T10A079.
- [9] Balasubramanian K, Jagirdar M, Lee PS, Teo CJ, Chou SK. Experimental investigation of flow boiling heat transfer and instabilities in straight microchannels. *Int. J. Heat Mass Transf.* 2013;**66**:655-671
- [10] Qu W, Siu-Ho A. Experimental study of saturated flow boiling heat transfer in an array of staggered micro-pin-fins. *Int. J. Heat Mass Transf.* 2009;**52**:1853-1863
- [11] Alam T, Lee PS, Yap CR, Jin L. Experimental investigation of local flow boiling heat transfer and pressure drop characteristics in microgap channel. *Int. J. Multiphase Flow*. 2012;**42**:164-174
- [12] Gedupudi S, Zu YQ, Karayiannis TG, Kenning DBR, Yan YY. Confined bubble growth during flow boiling in a mini/micro-channel of rectangular cross section Part I: Experiments and 1-D modelling. *Int. J. Therm. Sci.* 2011;**50**:250-266
- [13] Santini L, Cioncolini A, Butel MT, Ricotti ME. Flow boiling heat transfer in a helically coiled steam generator for nuclear power applications. *International Journal of Heat and Mass Transfer*. 2016;**92**:91-99
- [14] Sun ZC, Ma X, Ma LX, Li W, Kukulka DJ. Flow Boiling Heat Transfer Characteristics in Horizontal, Three-Dimensional Enhanced Tubes. *Energies*. 2019;**12**:927. DOI: 10.3390/en12050927

[15] Jagirdar M., Lee P.S., Methodology for More Accurate Assessment of Heat Loss in Microchannel Flow Boiling, IEEE 16th Electronics Packaging Technology Conference, 2014, Singapore, 630-634.

[16] Boltenko EA. Determination of the Density and Flow Rate of the Two-Phase Mixture under Steady and Emergency Conditions. Thermal Engineering. 2013;**60**(3):195-201

[17] Turney G.E., Snyder R.W., Measurement of Liquid and Two-Phase Hydrogen Densities with a Capacitance Density Meter. NASA Technical Notes, NASA TN D-5015, April 1969, Washington D.C.

[18] Reizner JR. Batch accuracy: the good, bad and ugly of Coriolis. March: InTech Magazine; 2005

[19] Hemp J., Yeung H., Coriolis Meter in Two Phase Conditions, IEE Seminar on Advanced Coriolis Mass Flow Metering, 2003, Ref No.03/10224, Oxford.

[20] Alkhutov NS et al. Measurements of the Density of the Two-Phase Mixture in Steady-State and Transient Regimes. Teploenerge\_tika. 2002;**9**:67-71

[21] Fedorov L.F., Rassokhin N.G., Processes of Steam Generation at Nuclear Power Plants, Ener\_goatomizdat, 1985, Moscow, in Russian.

[22] Thome J.R., The Heat Transfer Engineering Data Book III, PP PUBLICO Publications, 2016, ISBN-13: 9783934736375.





*Edited by Miguel Araiz Vega*

Thermal energy is present in all aspects of our lives, including when cooking, driving, or turning on the heat or air conditioning. Sometimes this thermal management is not evident, but it is essential for our comfort and lifestyle. In addition, heat transfer is vital in many industrial processes. Thermal energy analysis is a complex task that usually requires different approaches. With five sections, this book provides information on heat transfer problems and using experimental techniques and computational models to analyse them.

Published in London, UK

© 2021 IntechOpen

© Arina\_Bogachyova / iStock

**IntechOpen**

ISBN 978-1-83968-439-5



9 781839 684395